

Copyright
by
Aaron Chockla
2012

The Dissertation Committee for Aaron Michael Chockla Certifies that this is the approved version of the following dissertation:

**Solution Grown Silicon and Germanium Nanostructures:
Characterization and Application as Lithium Ion Battery Anode
Materials**

Committee:

Brian A. Korgel, Supervisor

C. Buddie Mullins

John G. Ekerdt

Emanuel Tutuc

James R. Chelikowsky

**Solution Grown Silicon and Germanium Nanostructures:
Characterization and Application as Lithium Ion Battery Anode
Materials**

by

Aaron Michael Chockla, B.Ch.E.; M.S.E.

Dissertation

Presented to the Faculty of the Graduate School of
The University of Texas at Austin
in Partial Fulfillment
of the Requirements
for the Degree of

Doctor of Philosophy

The University of Texas at Austin

May, 2012

Dedication

For my supportive parents, William and Sandra Chockla, and my loving fiancée, Melissa.

For all who have come before, making possible my success, and to those yet to come who may look on this work with greater vision than I.

Acknowledgements

We are—all of us—the sum product of our life experiences, encounters, and interactions. To acknowledge everyone who has impacted my life making it possible for me to be who I am and where I am today would require a manuscript longer than that which follows and a memory much better than mine. Nevertheless, I would like to thank those most responsible for my success at The University of Texas.

First and foremost, I would like to thank Dr. Brian Korgel who—during a one-on-one meeting in March, 2007—inspired me to pursue an advanced degree in the field of nanomaterials and who has provided me with endless insight, guidance, and support during the past five years. I would also like to thank Dr. C. Buddie Mullins for his support and advice and for inviting me to join his Li-ion battery sub-group meetings where I was free to share and discuss my thoughts and ideas. I further thank Dr. John Ekerdt, Dr. Emanuel Tutuc, and Dr. James Chelikowsky for their support and for agreeing to serve on my committee.

There are dozens of Korgel group members that deserve recognition for the contributions they have made to my success. I am indebted to Dayne Fanfare who taught me the fundamentals of semi-conductors and nanowire synthesis. Andrew Heitsch, Danielle Smith, and Reken Patel served as outstanding role models and sources of wisdom in my early years. Dr. Colin Hessel and Vincent Holmberg are two of the most influential and inspirational individuals I have had the pleasure of working. They have always made themselves available for advice and guidance and for that, I am grateful. Acknowledgment is well deserved for the people I have worked with on a daily basis: Timothy Bogart, Matthew Panthani, Chet Steinhagen, Vahid Akhavan, and Justin Harris, with whom I worked closely on most projects. Heartfelt thanks are in order for all

other Korgel group members, past and present, that I have been fortunate enough to work with, including Alex Knoop, Damon Smith, Mike Rasch, Brian Goodfellow, Jose Luis Hueso Martos, Kate Collier, Bonil Koo, Kate Shipman, and Hyun Park. I further value the numerous insightful and inspirational conversations had with the newest members of the Korgel group—Taylor Harvey, Jackson Stolle, Chris Bosoy, Xiaotang Lu, Julian Villarreal, and Yixuan Yu—and with all of the undergraduate researchers that I have had the pleasure of working with over the years, including Dariya Reed, Rebecca McKeever, Alejandro Maurer, and Danny Hellebusch. I would also like to thank members of Dr. Mullins' research group—Paul Abel, Yong-Mao Lin, Kyle Klavetter, and Nick Davy—for fruitful discussions pertaining to Li-ion batteries and electrochemistry. Finally, I would like to acknowledge my first year study group members, Dan Slanac, Costa Chrysostomou, and, in particular, Ross Gonzales Jr., for their support through first year classes and qualifying exams.

I also owe thanks to those who have helped me with characterization techniques along the way, including Dwight Romanovicz for help with SEM and TEM, Ji Ping Zhou for help with HRTEM, Haley Finley-Jones and Adam Rowland for ICPMS characterization, Hugo Celio for help with XPS, FTIR, and TGA, Karin Keller and Aaron Rogers for running countless mass spec samples, and last but not least, Vince Lynch for XRD training and data interpretation.

There are none more deserving of thanks than those who work behind the scenes to ensure that we graduate students are able to conduct our research without want or need. Thanks are due to Tijuana “T” Stockman for making sure my registration was complete every semester and for handling administrative details, Eddie Ibarra for expediently placing orders and keeping our labs stocked with chemicals and supplies, Kevin Haynes for assistance with shipping and receiving, the fine gentlemen in the cryo lab of the

physics department for keeping our supply of nitrogen tanks for the Schlenk line and glove boxes endless, and Jim Smitherman and Butch Cunningham for lab safety, various maintenance items, and for removing countless severed bolt fittings from our titanium reactor adaptors—I never seemed to learn the lesson. I would also like to express deep gratitude to Dr. Isaac Sanchez for taking a chance on a fellow Blue Hen and admitting me to the graduate Chemical Engineering program at The University of Texas.

I owe a great debt of gratitude to Dr. Abraham Lenhoff, my undergraduate research advisor at The University of Delaware for inspiring me to pursue advanced education, and to my graduate research mentors at the time, Andre Dumetz and Yu-Chia Cheng. Contributions are much appreciated from those whom I may have neglected to mention—not out of spite, but honest lack of memory—which have ensured my happiness in Austin and sanity in the lab. Finally, and most importantly, I would like to thank my family and friends for loving support and encouragement, helping me become who I am today.

**Solution Grown Silicon and Germanium Nanostructures:
Characterization and Application as Lithium Ion Battery Anode
Materials**

Aaron Michael Chockla, Ph.D.

The University of Texas at Austin, 2012

Supervisor: Brian A. Korgel

Solution-grown silicon and germanium nanowires were produced using various solvents and nanocrystalline seed materials. Silicon nanowires grown using monophenylsilane as the silicon source and gold catalyst seeds were made into a freestanding, lightweight, mechanically robust fabric and tested as a negative electrode material in lithium ion batteries. Annealing the fabric under reducing atmosphere converts the intrinsic poly(phenylsilane) shell into a highly conductive carbonaceous coating, improving Li storage behavior. Reduced graphite oxide (graphene) was studied as a freestanding support for gold-seeded germanium and silicon nanowires, the latter grown using trisilane. Graphene improves capacity retention for germanium nanowires but shows little improvement for silicon.

Slurry-cast films of nanowires were also tested as negative electrodes in lithium ion batteries using a variety of electrolyte solvent / binder combinations. Gold is detrimental to performance of silicon nanowires grown using trisilane. Removing gold through a simple wet etching procedure dramatically improves capacity retention. Silicon nanowires were also synthesized using in-situ formed tin seeds. Tin-seeded nanowires are easier to produce and outperform gold-seeded wires in lithium ion batteries. Germanium

nanowires perform exceptionally well under high current loads when cycled using electrolyte solutions that contain fluoroethylene carbonate and show promise for high-power applications.

Controlled synthesis of solution-grown germanium nanorods is demonstrated using nanocrystalline bismuth seeds. The addition of poly(vinylpyrrolidinone) / hexadecene copolymer leads to branched nanorods. Absorbance spectra were calculated using the discrete dipole approximation to compare against spectra obtained experimentally. The absorbance spectra and electric field internal to the nanorods depend highly on nanorod orientation. The presence of bismuth or gold at the tip of the nanorods also significantly alters the spectra and electric fields.

Ligand and surface chemistry of solution grown indium phosphide nanowires is also examined. Octylphosphonic acid and hexadecylamine are both essential for the growth of single crystalline indium phosphide nanowires. Potential solution synthesis routes to indium (III) oxide nanowires and indium phosphide nanowires with twinning superlattice structure are presented. Various phosphoric acid derivatives were tested in place of octylphosphonic acid and the efficacy of each is discussed.

Table of Contents

List of Tables	xviii
List of Figures	xix
Chapter 1: Introduction	1
1.1 Introduction to Lithium Ion Batteries	1
1.2 Introduction to Nanowire and Nanorod Synthesis	8
1.3 Growth Considerations and Germanium Nanorods	10
1.4 Surface Chemistry of Indium Phosphide Nanowires	12
1.5 Dissertation Outline	13
1.6 References	14
Chapter 2: Si Nanowire Fabric: an Electrode Material for Li-Ion Batteries [§]	22
2.1 Introduction	22
2.2 Experimental Section	24
2.2.1 Materials	24
2.2.2 Silicon Nanowire Synthesis	24
2.2.3 Material Characterization	25
2.2.4 LIB Anode Processing and Battery Testing	27
2.3 Results and Discussion	28
2.3.1 Si Nanowire Fabric	28
2.3.2 Electrochemical Performance of Si Nanowire Fabric Anodes	29
2.3.3 Composition of the Carbonaceous Shell on the Si Nanowires	34
2.3.4 Si Nanowire Structure after Electrochemical Cycling	39
2.4 Conclusion	42
2.5 Supporting Information	44
2.6 Acknowledgments	44
2.7 References	44

Chapter 3: Solvent Effects on Solution Phase Synthesis of Germanium Nanowires Seeded by Gold Nanocrystals [§]	48
3.1 Introduction.....	48
3.2 Experimental methods	49
3.2.1 Reagents.....	49
3.2.2 DPG decomposition and Ge nanowire growth reactions.....	50
3.2.3 Materials characterization.....	51
3.3 Results.....	52
3.3.1 SLS growth of Au-seeded Ge nanowires.....	52
3.3.2 The role of solvent impurities in Ge nanowire growth in.....	56
3.4 Discussion.....	60
3.4.1 DPG decomposition chemistry: the influence of Au	60
3.5 Conclusions.....	64
3.6 Acknowledgements.....	65
3.7 References.....	65
Chapter 4: Electrochemical Lithiation of Graphene-Supported Silicon and Germanium for Rechargeable Batteries [§]	68
4.1 Introduction.....	68
4.2 Experimental Details.....	69
4.2.1 Materials	69
4.2.2 Silicon nanowire synthesis.....	70
4.2.3 Germanium nanowire synthesis.....	71
4.2.4 Si nanocrystal synthesis	72
4.2.5 Reduced graphite oxide (RGO)	72
4.2.6 Anode preparation.....	73
4.2.7 Battery assembly and testing	74
4.2.8 Materials characterization.....	74
4.3 Results and Discussion	75
4.3.1 RGO supported nanowire and nanocrystal films.....	75
4.3.2 Electrochemical behavior of RGO.....	77
4.3.3 Electrochemical behavior of RGO supported Si nanowires	79

4.3.4	Electrochemical behavior of RGO supported Ge nanowires.....	81
4.3.5	Electrochemical behavior of RGO supported Si nanocrystals....	84
4.3.6	Extended behavior of RGO supported Si and Ge nanowires.....	86
4.4	Conclusions.....	88
4.5	Acknowledgements.....	89
4.6	References.....	90
Chapter 5:	Solution Grown Germanium Nanowires as a Negative Electrode Material in Lithium Ion Batteries.....	93
5.1	Introduction.....	93
5.2	Materials and Methods.....	94
5.2.1	Materials	94
5.2.2	Germanium nanowire synthesis.....	95
5.2.3	Anode preparation and battery assembly.....	96
5.2.4	Material characterization	96
5.3	Results and Discussion	97
5.3.1	Germanium nanowires thin films.....	97
5.3.2	Extended cycle life behavior.....	98
5.3.3	Rate test behavior.....	108
5.3.4	High-power testing.....	115
5.3.5	Electrical behavior	118
5.4	Conclusions.....	119
5.5	Acknowledgements.....	120
5.6	References.....	121
Chapter 6:	XPS Study of SEI Formation in Ge Nanowire Li-Ion Battery Negative Electrode Films	123
6.1	Introduction.....	123
6.2	Experimental Section.....	124
6.2.1	Materials	124
6.2.2	Germanium nanowire synthesis.....	125
6.2.3	Anode preparation and battery assembly.....	126

6.2.4	Battery disassembly and electrode cleaning	127
6.2.5	Material characterization	127
6.3	Results and Discussion	128
6.3.1	Cycling behavior	128
6.3.2	XPS of SEI formation using the EC:DEC electrolyte	130
6.3.3	XPS of SEI formation using the EC:DMC electrolyte	132
6.3.4	XPS of SEI formation using the FEC:DMC electrolyte	134
6.3.5	Germanium and germanium oxide signals	137
6.4	Conclusions	139
6.5	Acknowledgements	139
6.6	References	139
Chapter 7: Influence of Gold in Si Nanowire Lithium Ion Battery Anodes		143
7.1	Introduction	143
7.2	Experimental Section	144
7.2.1	Materials	144
7.2.2	Silicon nanowire synthesis	145
7.2.3	Removal of Au from Si nanowires	146
7.2.4	Anode preparation and battery assembly	147
7.2.5	Material characterization	148
7.3	Results and Discussion	149
7.3.1	Silicon nanowires and Au removal	149
7.3.2	Extended cycle life behavior	150
7.3.3	Rate test behavior	163
7.3.4	Electrical behavior	168
7.4	Conclusions	170
7.5	Acknowledgements	170
7.6	References	171
Chapter 8: In-situ Sn-seeded Si nanowires in Li Ion Batteries		174
8.1	Introduction	174
8.2	Experimental Section	175

8.2.1	Materials	175
8.2.2	Silicon nanowire synthesis.....	176
8.2.3	Anode preparation battery assembly.....	177
8.2.4	Material characterization	178
8.3	Results and Discussion	178
8.3.1	In-situ Sn-seeded Si nanowires.....	178
8.3.2	Extended cycle life behavior.....	181
8.3.3	Rate test behavior.....	190
8.3.4	Electrical behavior	196
8.4	Conclusions.....	198
8.5	Acknowledgements.....	198
8.6	References.....	198
Chapter 9:	Colloidal Synthesis of Germanium Nanorods ^s	201
9.1	Introduction.....	201
9.2	Experimental Section	202
9.2.1	Materials	202
9.2.2	Bi[N(SiMe ₃) ₂] ₃ preparation.....	202
9.2.3	Ge nanorod synthesis	203
9.2.4	Materials Characterization.....	205
9.3	Results and Discussion	205
9.3.1	Ge nanorods	205
9.3.2	Control of Ge nanorod dimensions	211
9.3.3	Branched nanorod growth.....	216
9.3.4	Reaction yield	219
9.4	Conclusions.....	219
9.5	Acknowledgements.....	220
9.6	References.....	220
Chapter 10:	Optical Properties of Colloidal Germanium Nanorods.....	224
10.1	Introduction.....	224
10.2	Experimental Details.....	224

10.2.1	Materials	224
10.2.2	Au-seeded Ge nanorod synthesis	225
10.2.3	Bi-seeded Ge nanorod synthesis	226
10.2.4	Materials characterization	227
10.3	Results and Discussion	227
10.3.1	Length Control of Bi-seeded Ge nanorods	227
10.3.2	Bi-seeded Ge nanorod optical properties	229
10.3.3	DDA calculations of Ge nanorod absorbance spectra.	230
10.3.3.1	The DDA Model	230
10.3.3.2	Calculated extinction cross-sections for Ge nanorods without metal tips.....	232
10.3.3.3	Calculated extinction cross-sections for Ge nanorods with Bi or Au tips.....	234
10.3.3.4	Electric field distribution within the Ge nanorods.....	236
10.3.3.5	DDA calculations: varying dipole geometry	239
10.4	Conclusions.....	245
10.5	Acknowledgements.....	246
10.6	References.....	246
Chapter 11: Role of Capping Ligands on Solution-Liquid-Solid (SLS) Growth of Indium Phosphide Nanowires		
11.1	Introduction.....	249
11.2	Experimental Section	250
11.2.1	Materials	250
11.2.2	Bi nanocrystal preparation	250
11.2.3	Indium (III) myristate preparation	252
11.2.4	Di-n-octylphosphonic acid preparation.....	252
11.2.5	InP nanowire Synthesis.....	253
11.2.6	Materials Characterization	254
11.3	Results and Discussion	257
11.3.1	Role of HDA and OPA on InP nanowire growth	257
11.3.2	Role of HDA and OPA on Bi nanocrystal seeds	264

11.3.3	Role of surfactants on InP nanowire growth.....	266
11.3.4	Effect phosphonic acids	267
11.4	Conclusions.....	271
11.5	Acknowledgements.....	272
11.6	References.....	272
Chapter 12:	Conclusions and Future Directions	275
12.1	Conclusions.....	275
12.1.1	Nanowire growth	275
12.1.2	Nanowires as negative electrodes in Li-ion batteries	275
12.1.3	Nanorods.....	277
12.1.4	Ligand chemistry	278
12.2	Future directions	278
12.3	References.....	281
Appendix A [§]	283
A.1	Solvents and reaction byproducts	283
A.2	Phenylgermane identification by mass spectrometry	285
Appendix B [§]	290
B.1	Cycle rates and additional characterization	290
B.2	Additional electrochemical characterization.....	291
B.3	References.....	296
Appendix C	297
C.1	Capacity retention using PC:DMC electrolyte	297
C.2	Rate test using PC:DMC electrolyte.....	299
Appendix D	302
D.1	XPS peak deconvolution of high resolution elemental scans ...	302
D.2	XPS characterization of uncycled Ge nanowire films	309
D.3	Ge composition: Ge ⁰ and GeO _x contributions	310

Appendix E	313
E.1 Electrochemistry of Si nanowires using PVdF binder	313
E.2 Electrochemistry of Au-removed Si nanowires	314
Appendix F	315
F.1 Sn-seeded Si nanowires with varying Si:Sn ratio	315
F.2 Electrochemistry Sn-seeded Si nanowires using PVdF	315
Appendix G ^s	317
G.1 Bi[N(Si(CH ₃) ₃) ₂] ₃ characterization	317
G.2 Control reactions without the addition of Bi nanocrystals	317
G.3 Optical properties of Ge nanorods	318
Appendix H	321
H.1 Bi and Au seeded Ge nanorod characterization	321
H.2 Supplemental discrete dipole approximation calculations	323
Appendix I	329
I.1 DOPA characterization	329
I.2 Bi nanocrystal and InP nanowire histogram data	329
I.3 Effect of <i>n</i> -octylphosphonic acid concentration	332
I.4 Effect of phosphoric acid derivatives	333
Bibliography	337
Vita	369

List of Tables

Table 2.1: Summary of the capacity retention Si nanowire fabric anodes annealed at the indicated temperatures.	32
Table 3.1: DPG conversion to Ge after 5 minutes at 380°C in various high boiling temperature solvents.	62
Table 5.1: Capacity retention of Ge nanowire films using various electrolyte solutions.	101
Table 7.1: Summary of first cycle capacity and retention in various battery formulations.	154
Table 7.2: Equivalent circuit parameters for electrochemical impedance spectra.	170
Table 8.1: Summary of first cycle capacity and retention in various battery formulations.	184
Table 9.1: Summary of nanorod reactions and dimensions.	219
Table 10.1: Ge nanorod dimensions determined from TEM.	229
Table 11.1: Reaction yield for reactions carried out in the presence of HDA and either H ₃ PO ₄ , OPA, DOPA or TOPO.	268
Table B1: C-rates determined from the theoretical charging capacities of Si, Ge and RGO. Cycling at a rate of 1C is equivalent to charging or discharging 1 g of battery material in 1 hour.	290

List of Figures

- Figure 1.1:** Comparison of the different battery technologies in terms of volumetric and gravimetric energy density. Reprinted from Ref 2.....1
- Figure 1.2:** Schematic (a) charge and (b) discharge cycles for a Li-ion battery with a LiCoO_2 cathode and graphite anode.3
- Figure 1.3:** Total cell capacity as a function of anode capacity using fixed cathode capacities of 137 mA h g^{-1} (LiCoO_2 , black) and 1637 mA h g^{-1} (sulfur, yellow).5
- Figure 1.4:** (a) Typical voltage profile and (b) corresponding differential capacity plot for a Si nanowire-based Li-ion battery negative electrode.6
- Figure 1.5:** Publications for Si and Ge Li ion battery negative electrode material by year. Search includes publications whose titles bear “lithium ion batteries” in conjunction with “Si / silicon” or “Ge / germanium”7
- Figure 1.6:** Nanowire growth mechanism. The arrow tracks the composition change as Si is added to Au. Schematics of the nanowires at various points during growth are shown (regions I, II, and III).10
- Figure 2.1:** (a) Photograph of mechanically flexible Si nanowire fabric. (b, c) SEM images of the fabric. (d) High-resolution TEM (HRTEM) image of a Si nanowire showing its crystallinity. (e) Fast Fourier transform (FFT) pattern from the HRTEM image in (d) showing a $\langle 110 \rangle$ growth direction. (f) Photographs of Si nanowire fabrics annealed at the indicated temperatures under a reducing atmosphere.28

Figure 2.2: (a) Galvanostatic cycling tests of Si nanowire fabric before and after annealing at 700, 800, 900, 1000, and 1100°C at a cycle rate of $C/20$ ($C = 3579 \text{ mA h g}^{-1}$).⁵⁻⁷ The inset shows discharge capacities after 20 cycles for batteries with nanowire fabric anodes annealed at various temperatures. (b) Galvanostatic cycling of a Si nanowire fabric anode annealed at 900°C.30

Figure 2.3: Current–potential measurements of Si nanowire fabric placed between two indium tin oxide (ITO) electrodes (inset). The nanowire fabric was annealed under a reducing atmosphere at the indicated temperatures. Measurements were made using $\sim 150 \mu\text{m}$ thick fabric samples with a contact area of 1 cm^231

Figure 2.4: Constant-current voltage profiles for Si nanowire fabric anodes annealed at (a) 800, (c) 900, (e) 1000, and (g) 1100°C with corresponding differential capacity curves (b, d, f, and h, respectively).34

Figure 2.5: Raman spectra of Si nanowire fabric before and after annealing under a reducing atmosphere at various temperatures. The Si (TO) peak at 521 cm^{-1} and carbon-related (D) and (G) bands at 1380 cm^{-1} and 1560 cm^{-1} are labeled.35

Figure 2.6: XPS data of O1s, C1s and Si2p states of Si nanowire fabric annealed at the temperature indicated. The intensities of all of the peaks are normalized, but the carbon signal decreased significantly relative to the Si signal as the annealing temperature was raised. Figure 2.7 plots the relative amounts of O, C and Si obtained from integration of the XPS peaks. The peak fitting procedures are described in the Experimental Section.37

Figure 2.7: Summary of compositional analysis extracted from the XPS data in Figure 2.6: (a) relative Si, C, and O content determined by integrating the O1s, C1s and Si2p peaks; (b) relative SiO, SiO _x , SiO ₂ content determined from the Si2p peak structure.....	38
Figure 2.8: XRD of Si nanowire fabric before and after annealing at the indicated temperatures under forming gas. The peak positions corresponding to diamond cubic Si (JCPDS: 00-027-1402) and silicon carbide (SiC, labeled ‘*’. JCPDS: 00-029-1131) are shown.	39
Figure 2.9: SEM images of Si nanowire fabric annealed at 900°C under forming gas: (a) prior to electrochemical cycling; (b) after 20 galvanostatic cycles without washing, and (c) after 20 galvanostatic cycles with washing with acetonitrile, H ₂ SO ₄ , and IPA.....	41
Figure 2.10: TEM and STEM images of Si nanowires annealed at 900°C under forming gas after 20 electrochemical cycles in a lithium cell. Two types of nanowires were observed in nearly equal proportions: (a) amorphous wires that appear to have a hollow core and (c) crystalline nanowires with a thick amorphous shell. (b, d) FFTs of the TEM images in (a) and (c). (e, f) STEM images and (g, h) corresponding EDS line scans at the positions indicated of (e, g) amorphous wires that appear to have a hollow core and (f, h) crystalline nanowires with a thick amorphous shell.....	42
Figure 3.1: SEM images of Ge nanowires formed by heating DPG in the presence of Au nanocrystals at 380°C for 10 minutes in (a) squalane, (b) squalene, (c) octacosane, (d) dotriacontane and (e) TOA. Ge nanowires could not be grown in TOP using Au seeds and DPG.....	53

Figure 3.2: XRD of the reaction products from the thermal decomposition of DPG at 380°C in (a) TOA without Au, and (b) TOA, (c) squalane, (d) octacosane, and (e) dotriacontane in the presence of Au nanocrystals, and (f) dotriacontane without Au nanocrystals. Diffraction patterns (b-f) index to diamond cubic Ge (JCPDS: 00-004-0545). Peaks labeled with “*” correspond to NaCl (JCPDS: 00-005-0628).....54

Figure 3.3: (a, b) TEM images of a Ge nanowire obtained by DPG decomposition in squalane in the presence of Au nanocrystals with (inset) corresponding FFT. (c, d) EDS acquired with the electron beam focused (c) on the wire and (d) at the nanowire tip. The Cu and C signals are from the TEM grid and support.55

Figure 3.4: (a) SEM and (b) TEM images of Ge nanowires obtained when DPG was heated in dotriacontane at 380°C without Au nanocrystals.56

Figure 3.5: (a, b) TEM images of a Ge nanowire obtained by DPG decomposition in dotriacontane at 380°C without adding gold nanocrystals. The inset in (b) is the FFT of the TEM image. (c, d) EDS data obtained from the core and the tip of the nanowire, respectively. The Cu peaks seen here are from the copper supported lacey carbon TEM grid.57

Figure 3.6: (a) EDS and (b) XRD of (inset) Ge nanowires grown in dotriacontane without Au. (b) XRD of (i) nanowires and (ii) solid byproduct isolated after heating dotriacontane. Ni and C signals are from the TEM grid. Diffraction peaks correspond to (i) diamond cubic Ge and (ii) NaCl (JCPDS: 00-005-0628).....59

Figure 3.7: Decomposition of diphenylgermane by phenyl redistribution. ($x=1, 2,$ or 3 ; $y=1, 2,$ or 3).....61

Figure 3.8: Illustration of two possible DPG decomposition routes leading to Au-seeded Ge nanowire growth: (a) homogeneous and (b) heterogeneous DPG decomposition. Pathway (b) as illustrated would not require phenyl redistribution and most likely does not occur.63

Figure 4.1: SEM images of LIB anodes of (a, b) Si nanowires, (c, d) Ge nanowires, (e, f) Si nanowire / RGO (75 % w/w Si), (g, h) Ge nanowire / RGO (75 % w/w Ge), and (i) RGO. The insets show photographs of the materials (13 mm in diameter). XRD (Figure B1 in Appendix B) confirmed that the nanowires were crystalline diamond cubic Si and Ge prior to electrochemical cycling.76

Figure 4.2: (a, b) TEM images of Si nanocrystals with accompanying FFT pattern (inset). (c) SEM of Si nanocrystals on graphene. The Si nanocrystal / graphene film in the inset is 13 mm in diameter.....77

Figure 4.3: (a) Charge (filled symbols) and discharge (open symbols) capacity of RGO cycled at various rates, along with corresponding (b) voltage profiles and (c, d) differential capacity curves.....78

Figure 4.4: (a) Charge (filled symbols) and discharge (open symbols) capacity of Si nanowire (squares) and Si nanowire / RGO (75% w/w Si, circles) anodes at various cycle rates. Discharge capacities of Si nanowire / RGO anodes with varying Si content are plotted in the inset with colors corresponding to the cycle rates in the capacity plot. The variation in discharge capacity is the result of capacity fade. (b) Voltage profiles of Si nanowire / RGO (75% w/w Si) anodes with (c, d) corresponding differential capacity curves.....80

Figure 4.5: Plots of (a, c, e, g) first cycle and (b, d, f, h) subsequent cycle differential capacity corresponding to the cycling data in Figure 4.4 for Si nanowire / RGO anodes with (a, b) 100%, (c, d) 75%, (e, f) 50%, and (g, h) 25% w/w Si.81

Figure 4.6: (a) Charge (filled symbols) and discharge (open symbols) capacity of Ge nanowire (squares) and Ge nanowire / RGO (75% w/w Ge) anodes (circles) cycled at different rates. Discharge capacities of Ge nanowire / RGO with varying Ge content are plotted in the inset with colors corresponding to the cycle rates in the capacity plot. The variation in discharge capacity is the result of capacity fade. (b) Voltage profiles and (c, d) corresponding differential capacity curves of the Ge nanowire / RGO (75% w/w Ge) anode.82

Figure 4.7: Plots of (a, c, e, g) first cycle and (b, d, f, h) subsequent cycle differential capacity corresponding to the cycling data in Figure 4.6 for Ge nanowire / RGO anodes with (a, b) 100%, (c, d) 75%, (e, f) 50%, and (g, h) 25% w/w Ge.84

Figure 4.8: (a) Charge (filled symbols) and discharge (open symbols) capacity with coulombic efficiencies of RGO with 70% w/w Si nanocrystals cycled at a rate of C/20. (b) The voltage profiles and (inset) differential capacity curves are shown for cycles 1 and 20.85

Figure 4.9: Lithium capacity of (a) Si nanowire / RGO (75% w/w Si) and (b) Ge nanowire / RGO (75% w/w Ge). The batteries were cycled at C/20 for 20 cycles followed by C/10 for the next 100 cycles.87

Figure 5.1: (a) SEM and (b) cross-sectional SEM of the Ge nanowire slurry cast on Cu foil, (c) TEM, (d) high resolution TEM with (inset) FFT down the [011] zone axis, and (e) XRD of as prepared Ge nanowires with the crystalline Ge reference pattern (JCPDS: 00-004-0545).98

Figure 5.2: (a) Comparison of charge capacity for various electrolytes with (b) charge capacity retention plotted relative to the 5th cycle charge capacity for each respective (c) electrolyte solvent system.100

Figure 5.3: (i) Charge and discharge capacities, coulombic efficiencies, (ii) voltage profiles and (iii) corresponding differential capacity curves for Ge nanowire batteries cycled galvanostatically using an electrolyte solution of 1.0M LiPF₆ dissolved in a 1:1 w/w mixture of (a) EC:DEC, (b) EC:DMC, EC:DMC + 3% w/w FEC, (d) FEC:DEC, or (e) FEC:DMC at cycles: 1, 2, 5, 10, 20, 50, and 100.....103

Figure 5.4: (a) Voltage profiles and (b) corresponding differential capacity plots comparing the first cycle charge and discharge characteristics for each electrolyte system.....105

Figure 5.5: Differential capacity color maps for (a.i-e.i) discharge (a.iii-e.iii) charge cycles with (a.ii-e.ii) waterfall plots for batteries cycled using electrolyte solvent mixtures of (a) EC:DEC, (b) EC:DMC, (c) EC:DMC with 3% FEC, (d) FEC:DEC, and (e) FEC:DMC.107

Figure 5.6: Comparison of charge capacity for various electrolytes at different charge rates.....109

Figure 5.7: (i) Rate cycle data, (ii) potential profiles and (iii) differential capacity plots for batteries cycled using electrolyte solvent mixtures of (a) EC:DEC, (b) EC:DMC, (c) EC:DMC with 3% FEC, (d) FEC:DEC, and (e) FEC:DMC at cycles: 10, 20, 25, 30, 35, 40, and 50..... 111

Figure 5.8: Differential capacity (a.i-e.i) discharge and (a.iii-e.iii) charge color maps and (a.ii-e.ii) waterfall plots for batteries cycled using electrolyte solvent mixtures of (a) EC:DEC, (b) EC:DMC, (c) EC:DMC with 3% FEC, (d) FEC:DEC, and (e) FEC:DMC at various rates for cycles 5 through 40. 114

Figure 5.9: Long term life cycling of batteries cycled using (a) FEC:DMC and (b) EC:DMC+FEC electrolyte solutions. The inset to (a) shows a cycles 1100 through 1200 with greater clarity, plotted with the temperature in Austin, Texas during a three day span. 116

Figure 5.10: Cycle data for Ge nanowire films cycled using EC:DMC+FEC (a) charged at 1C and discharged at various rates with or (b) charged at various rates and discharged at 1C with (c, d) voltage profiles and (e, f) differential capacity curves shown for cycles 2, 12, 22, 32, 42, 52, and 62..... 118

Figure 5.11: Impedance spectra of discharged batteries after 100 cycles using various electrolyte solutions at a rate of C/10. The data are offset by 200 units along the ordinate axis. 119

Figure 6.1: (a) SEM of Ge nanowires cycled with (b) EC:DEC, (c) EC:DMC, and (d) FEC:DMC electrolyte solutions. Capacity retention is relative to cycle 10..... 129

- Figure 6.2:** (a) High-resolution XPS elemental scans of F1s, O1s, C1s, P2p, Li1s, and Ge3d at various sputtering times and (b) corresponding elemental film compositions for batteries cycled with the EC:DEC electrolyte solution. The battery was disassembled in the lithiated state.132
- Figure 6.3:** (a) High-resolution XPS elemental scans of F1s, O1s, C1s, P2p, Li1s, and Ge3d at various sputtering times and (b) corresponding elemental film compositions for batteries cycled with the EC:DMC electrolyte solution. The battery was disassembled in the delithiated state.134
- Figure 6.4:** (a) High-resolution XPS elemental scans of F1s, O1s, C1s, P2p, Li1s, and Ge3d at various sputtering times and (b) corresponding elemental film compositions for batteries cycled with the FEC:DMC electrolyte solution. The battery was disassembled in the delithiated state.....137
- Figure 6.5:** Ratio of Ge⁰ to Ge suboxides as a function of sputtering time.138
- Figure 7.1:** (a) SEM of SFLS-grown Si nanowires. (b) Illustration of the Au etching procedure. (c) TEM images of nanowires prior to etching. Surface-bound Au nanocrystals are circled for reference. (d) TEM image of Si nanowires after etching—there are no longer Au nanocrystals present in the sample. (e) HRTEM image of a Si nanowire, shown growing in the <110> direction with (f) corresponding FFT pattern (imaged down the [011] zone axis). (g) SEM image of film of Au-removed Si nanowires in PVdF. (h) XRD of the Si nanowires (i) before and (ii) after Au removal (Si JCPDS: 00-027-1402, Au: 00-004-0784).....150

Figure 7.2: (a, c, e, g) Charge capacity cycle data for 100 cycles at C/10 and (b, d, f, h) capacity retention for Si nanowires in various electrolyte solutions: (a, b) as-prepared in PVdF; (c, d) Au-removed in PVdF; (e, f) as-prepared in NaAlg; (g, h) Au-removed in NaAlg. Capacity retention is relative to the 5th cycle for any given system. (i) Electrolyte solvent and (top) binder molecules are shown.....152

Figure 7.3: (i) Charge and discharge capacities with Coulombic efficiencies, (ii) voltage profiles and (iii) differential capacity plots for Si nanowires cycled using NaAlg binder and electrolyte solution of 1.0 M LiPF₆ in a 1:1 (w:w) solvent mixture of (a) EC:DEC, (b) EC:DMC, (c) EC:DMC + 3% (w/w) FEC, and (d) FEC:DMC at cycles 1, 2, 5, 10, 20, 50, and 100.156

Figure 7.4: (i) Charge and discharge capacities with Coulombic efficiencies, (ii) voltage profiles and (iii) differential capacity plots for Au-removed Si nanowires cycled using NaAlg binder and electrolyte solvent mixtures of (a) FEC:DEC or (b) FEC:DMC at cycles 1, 2, 5, 10, 20, 50 and 100.158

Figure 7.5: (a, c, e, g) Voltage profiles and (b, d, f, h) differential capacity plots for the first cycle of (a, c) as prepared Si nanowires and (b, d) Au-removed Si nanowires using (a-d) PVdF and (e-h) NaAlg as binders and the indicated electrolyte solvent combinations.....159

Figure 7.6: Color maps of differential capacity (i) discharge and (iii) charge profiles with (ii) corresponding waterfall plots for Si nanowires cycled using NaAlg binder with electrolyte solvent solutions of (a) EC:DEC, (b) EC:DMC, (c) EC:DMC+FEC, and (d) FEC:DMC.....161

Figure 7.7: Color maps of differential capacity (i) discharge and (iii) charge profiles with (ii) corresponding waterfall plots for Au-removed Si nanowires cycled using NaAlg binder and electrolyte solvent solutions of (a) FEC:DEC or (b) FEC:DMC.....163

Figure 7.8: Rate test data for batteries using NaAlg binder mixed with (a) as made Si nanowires and (b) Au-removed Si nanowires cycled at various rates with the indicated electrolyte solutions.....165

Figure 7.9: (i) Rate test data, (ii) voltage profiles and (iii) corresponding differential capacity plots for Au-removed Si nanowires mixed with NaAlg binder cycled using electrolyte solvent solutions of (a) FEC:DEC and (b) FEC:DMC at cycles 10, 20, 25, 30, 35, 40, and 50.166

Figure 7.10: Color maps of differential capacity (i) discharge and (iii) charge profiles and (ii) waterfall plots for Au-free nanowires cycled at various rates using NaAlg and electrolyte solvent solutions of (a) FEC:DEC or (b) FEC:DMC.....167

Figure 7.11: Impedance spectroscopy data after 100 cycles for samples of Si nanowires cycled (a, c) as prepared or (b, d) Au-removed mixed with (a, b) PVdF or (c, d) NaAlg as the binder and the electrolyte solvent solution mixtures shown. All spectra are taken in the delithiated state except for (c), which was lithiated. (a, b, d) curves are offset vertically by 350 ohms or (c) 75 ohms. (e) Equivalent circuit used to fit impedance data using resistance elements R_e (electrolyte), R_{sf} (surface), and R_{ct} (charge transfer), constant phase elements Q_{sf} and Q_{ct} and the Warburg diffusion element, Z_w169

Figure 8.1: Binary Si–Sn phase diagram and in-situ Sn-seeded Si nanowire growth mechanism.	179
Figure 8.2: (a) SEM and (b) TEM images of in-situ Sn-seeded Si nanowires. (c) Cross-sectional SEM image of a film of a Si nanowires mixed with PVdF. (d) HRTEM of a wire and seed (e) showing nanowire growth in the <211> direction from (f) a Sn seed with a d-spacing of 2.9Å corresponding to the (200) plane. (g) EDS spectra for the tip (i) and wire (ii) and (h) XRD (JCPDS: Si, 00-027-1402; β-Sn, 00-004-0673) confirm the material composition and SFLS growth mechanism...180	180
Figure 8.3: (a, c, e) Charge capacity and (b, d, f) capacity retention data for Sn-seeded Si nanowires (a, b) mixed with PVdF, (c, d) mixed with PVdF then annealed at 300°C under nitrogen for 12 hours, and (e, f) mixed with NaAlg. Capacity retention is relative to the 5 th cycle charge capacity. (g) Molecular representations of the electrolytes and binders used.	182
Figure 8.4: (a.i – e.i) Cycle data, (a.ii – e.ii) voltage profiles, (a.iii – e.iii), and corresponding differential capacity plots for Sn-seeded Si nanowires tested galvanostatically mixed with (a-c) PVdF and annealed or (d, e) NaAlg as the binder and an electrolyte solution solvent mixtures of (a) EC:DMC, (b, d) FEC:DEC or (c, e) FEC:DMC.	186
Figure 8.5: Comparison of 1 st cycle charge and discharge voltage profiles for films of Si nanowires mixed with (a) PVdF and annealed and (c) NaAlg using the indicated electrolyte solvent mixtures with (b, d) corresponding differential capacity plots.....	188

Figure 8.6: Differential (a.i-e.i) discharge and (a.iii-e.iii) charge capacity color maps with (a.ii-e.ii) corresponding waterfall plots for Sn-seeded Si nanowires with (a-c) PVdF and annealed or (d, e) NaAlg using electrolyte solvent mixtures of (a) EC:DMC, (b, d) FEC:DEC or (c, e) FEC:DMC. ...189

Figure 8.7: Cycle data for Sn-seeded Si nanowires mixed with (a) PVdF and annealed or (b) NaAlg using the electrolyte solutions shown and cycled at the rates indicated.....191

Figure 8.8: (a.i – e.i) Rate test data, (a.ii – e.ii) voltage profiles, and (a.iii – e.iii) differential capacity plots for nanowires mixed with (a-c) PVdF and annealed or (d, e) NaAlg and electrolyte solvents of (a) EC:DMC, (b, d) FEC:DEC or (c, e) FEC:DMC. * Cycles 20 and 25 in (d) and (e) are at C/20.....192

Figure 8.9: Differential (a.i-e.i) discharge and (a.iii-e.iii) charge capacity plots with (a.ii-e.ii) corresponding waterfall curves for Sn-seeded Si nanowires using either (a-c) PVdF and annealed or (d, e) NaAlg as binder and electrolyte solvent mixtures of (a) EC:DMC, (b, d) FEC:DEC or (c, e) FEC:DMC.....195

Figure 8.10: Impedance spectra of discharged batteries after (a, c, d) 100 cycles and (b) 1 cycle using film (2) with various electrolytes. The data are offset for clarity. (e) XRD data of film (2) (i) as prepared and (ii) after one full cycle.....197

Figure 9.1: TEM images of Ge nanorods grown with a Ge:Bi molar ratio of 20:1. The nanorods have Bi particles at the tips, as indicated in (b). XRD of these nanorods is shown in Figure 9.2.....206

Figure 9.2: XRD of the Ge nanorods with peaks indexed to diamond cubic Ge (JCPDS: 00-004-0545). The peaks labeled “*” correspond to orthorhombic Bi (JCPDS: 00-044-1246).....	207
Figure 9.3: High resolution TEM images of the Ge nanorods with (inset) corresponding FFT patterns. Indexing of the FFTs is consistent with diamond cubic Ge, with each nanorod being imaged down the [011] zone axis, as indicated. The growth direction of these nanorods is $\langle 111 \rangle$. A Bi particle is attached to the end of the nanorod in (a)..	208
Figure 9.4: (a) Illustration of the Ge nanorod growth process and (b) the Ge/Bi binary phase diagram. ²⁷ The polymer coating around that surrounds the Bi nanocrystals is not shown.....	210
Figure 9.5: (a) TEM image of Bi nanocrystals used to seed Ge nanorod growth; (b) histogram of Bi nanocrystal diameter determined by counting particles in a TEM image. The average diameter of these nanocrystals is 13.8 ± 1.5 nm. The average diameter of Bi nanocrystals observed at the Ge nanorod tips in Figure 9.1 is 15.9 ± 3.5 nm, which is close to this initial Bi seed diameter.....	211
Figure 9.6: (a-c) TEM images of Ge nanorods made with different Ge:Bi ratios. The accompanying histograms show the measured nanorod (d) length (L) and (e) diameter (d): (a,i) Ge:Bi = 20:1, $L = 170 \pm 20$ nm, $d = 11.4 \pm 1.9$ nm, (b,ii) Ge:Bi = 10:1, $L = 94 \pm 11$ nm, $d = 14.9 \pm 2.6$ nm, and (c,iii) Ge:Bi = 5:1, $L = 61 \pm 7$ nm, $d = 15.4 \pm 3.6$ nm.....	213

Figure 9.7: (a-c) TEM images of Ge nanorods made using Bi nanocrystals synthesized with different Na:Bi ratios. (d) and (e) show the corresponding histograms of length (L) and diameter (d): (a,i) Na:Bi = 1:1, $L = 110 \pm 18$ nm, $d = 10.6 \pm 1.7$ nm, (b,ii) Na:Bi = 4:1, $L = 170 \pm 20$ nm, $d = 11.4 \pm 1.9$ nm, and (c,iii) Na:Bi = 8:1, $L = 156 \pm 37$ nm, $d = 13.2 \pm 3.9$ nm.214

Figure 9.8: TEM images of Ge nanorods at different times after reactant injection at three different reaction temperatures: (a.i-a.v, ■) 300°C, (b.i-b.v, ●) 350°C, and (c.i-c.v, ▲) 400°C. Aliquots were taken from the nanorod reaction at 300°C after (a.i) 2 minutes, (a.ii) 4 minutes, (a.iii) 6 minutes, (a.iv) 10 minutes, and (a.v) 15 minutes. Aliquots were taken from the reaction at 350°C after (b.i) 1 minute, (b.ii) 2 minutes, (b.iii) 3 minutes, (b.iv) 4 minutes, and (b.v) 5 minutes. Aliquots were taken from the reaction at 400°C after (c.i) 30 seconds, (c.ii) 1 minute, (c.iii) 90 seconds, (c.iv) 2 minutes, and (c.v) 5 minutes. The average length, diameter, and Bi seed particle diameter are plotted in (d)-(f).215

Figure 9.9: TEM image of branched Ge nanorods grown at 350°C in the presence of (30% w/w) 1.5g PVP/HDE polymer. Typically the nanorods are made with 10 – 13.5% w/w polymer.216

Figure 9.10: TEM images and corresponding FFTs of branched Ge nanorods. 217

Figure 9.11: Summary of branching mechanisms. (a) Spontaneous branching resulting from starved growth and leading to twin, kink, and branch formation.^{40,48} (b) Catalyst fission into multiple seed particles that each nucleate a branch.⁵³ (c) Seed fusion,⁴⁰ (d) Geminate branching from multiple nuclei on a single seed particle that grow and then merge to create a branch point.⁴⁰ (e) Deposition of metal seed particles along the length of a nanorod that initiate the growth of a branch.^{44,52}218

Figure 10.1: TEM images of Ge nanorods isolated at different times during the reaction, (a) 30 sec, (b) 1 min, (c) 2 min, (d) 3 min, (e) 5 min, and (f) 10 min, along with their (g) absorbance spectra. The spectra in (g) are offset for clarity. The sharp peaks at 1400 nm are from chloroform. An absorbance spectrum for Bi nanocrystals in chloroform is provided in Supporting Information.....228

Figure 10.2: (a) Representation of a (i) dipole and interacting dipoles in a (ii) $2 \times 2 \times M$ arrangement (ii) without and (iii) with metal tips. M is the number of dipole layers needed to approximate the nanorod length. The real (n) and imaginary (k) components of the complex index of refraction for (b) Ge,³³ (c) Bi,^{34,35} and (d) Au³³ are shown.....230

Figure 10.3: Extinction spectra calculated using the DDA approximation for (a, b) 30 nm diameter Ge nanorods with varying aspect ratio (AR) or (c, d) nanorods with AR=20 and varying diameter D . (e, f) Relative contribution of absorption and scattering to the extinction cross-section of a 30 nm diameter nanorod with an aspect ratio of 20. Spectra were calculated with incident electric field polarized either (a, c, e) perpendicular or (b, d, f) parallel to the long axis of the nanorod. .233

Figure 10.4: Extinction spectra calculated using the DDA for Ge nanorods with (a, b) Bi and (c, d) Au tips. Simulations were performed with the incident electric field polarized either (a, c) perpendicular or (b, d) parallel to the length of the nanorods. (e, f, g, h) Relative contributions of scattering and absorption to the extinction cross-sections. The reported aspect ratios are determined by only considering the Ge portion of the nanorods and do not include the metal tip.....234

Figure 10.5: Scattering cross-sections (magnified by 10x compared to Figures 10.4e-h) calculated for 30 nm diameter Ge nanorods with (a, b) no metal tips, (c, d) Bi tips or (e, f) Au tips with the incident electric field polarized (a, c, e) perpendicular or (b, d, f) parallel to long axis of the nanorod.236

Figure 10.6: Internal electric field calculated using Equation (11) for a 30 nm diameter Ge nanorod with an aspect ratio of 20 with the polarization of the incident field oriented (a, b) perpendicular and (c, d) parallel to the nanorod length.238

Figure 10.7: Real (ϵ') and imaginary (ϵ'') parts of the complex dielectric function for (A) Ge, (b) Bi, and (c) Au.239

Figure 10.8: Internal electric fields calculated with the polarization of the incident electric field oriented parallel to the nanorod length for (a) corner dipoles (highlighted in blue) along the edges of the nanorod, (b) side dipoles along the faces of the nanorod and (c) central dipoles within the core of the nanorod. (d, e, f) Corresponding cross-sectional plots showing electric field contours for specific wavelengths.241

Figure 10.9: Intensity plots showing the local electric field near the tip of Ge nanorod (30 nm diameter; aspect ratio of 20) with Bi seeds for (a) perpendicular and (c) parallel incident electric fields with (b, d) corresponding cross-sectional plots showing constant wavelength contours.	242
Figure 10.10: (a) Critical angle for total internal reflection within a Ge nanorod suspended in chloroform. (b) Schematic for angle dependence of partial reflection / transmission versus total internal reflection of light impinging on an interface.....	244
Figure 10.11: Average internal electric field contour plots at 590 nm, calculated for a Ge nanorod 30 nm in diameter with an aspect ratio of 20) with incident electric fields at various angles (center plot) with corresponding surface plots for each angle (surrounding).	245
Figure 11.1: (a-d) SEM, (e-h) TEM, (i-l) HRTEM, and (m-p) corresponding FFT images of InP nanowires grown in the presence of (a, e, i, m) OPA and HDA, (b, f, j, n) OPA only, (c, g, k, o) HDA only, and (d, h, l, p) neither ligand.....	259
Figure 11.2: Diffraction patterns for InP nanowire reactions done in the presence of (i) HDA and OPA, (ii) OPA only, (iii) HDA only, and (iv) neither ligand. Reference patterns are included for InP (JCPDS: 00-032-0452), In ₂ O ₃ (JCPDS: 01-071-2194) and In (JCPDS: 00-005-0642).....	261
Figure 11.3: ATR-FTIR spectra collected for InP nanowires produced in the presence of (i) HDA and OPA, (ii) OPA only, (iii) HDA only or (iv) neither ligand. The signal between the 3750 cm ⁻¹ and 3000 cm ⁻¹ was magnified 10× to enhance features in this region.	262

Figure 11.4: XPS spectra of the In3d, P2p, and Bi4f regions for reactions done in the presence of (i) OPA and HDA, (ii) OPA only, (iii) HDA only and (iv) neither ligand.	264
Figure 11.5: TEM of Bi nanoparticles injected into hot solvent containing (a) HDA and OPA, (b) OPA only, (c) HDA only, and (d) neither ligand.	265
Figure 11.6: XPS spectrum of Bi seeds injected into reaction media containing (i) OPA and (ii) HDA and OPA.	266
Figure 11.7: Schematic diagram displaying the effect of (a) HDA and OPA on Bi nanocrystals and (b) the role of each in the reaction of InMyr ₃ with TMS ₃ P in the presence of Bi nanocrystals to form InP nanowires.	267
Figure 11.8: (a-d) SEM, (e-h) TEM, (i-l) HRTEM, and (m-p) corresponding FFT images of InP nanowires grown in the presence of HDA and (a, e, i, m) H ₃ PO ₄ , (b, f, j, n) OPA (c, g, k, o) DOPA, and (d, h, l, p) TOPO.	269
Figure 11.9: XRD InP nanowires grown in the presence of HDA and (i) H ₃ PO ₄ , (ii) OPA (iii) DOPA, and (iv) TOPO.....	270
Figure 11.10: XPS spectra of InP nanowires prepared in the presence of HDA and (i) H ₃ PO ₄ , (ii) OPA, (iii) DOPA or (iv) TOPO.....	271
Figure A1: Chemical structure, name, formula and molecular weight for (a) squalane, (b) squalene, (c) octacosane, (d) dotriacontane, (e) trioctylamine and (f) trioctylphosphine. Tri- <i>n</i> -octylamine and tri- <i>n</i> -phosphine both have coordinating groups, whereas the others are long chain hydrocarbons.	283
Figure A2: SEM images of reaction byproducts formed during SLS Ge nanowire growth: (a) kinked nanowires and (b) homogeneously nucleated amorphous Ge particles.....	284

Figure A3: TEM images of the solid reaction product obtained when DPG was heated in squalane at 400°C for 2 hrs in the absence of Au nanocrystals. The product is primarily necked amorphous Ge particles, but there are also a very small number of Ge nanowires that form, such as those in the TEM image in the inset.....285

Figure A4: Phenylgermanes observed by mass spectrometry: (a) monophenylgermane, (b) diphenylgermane, (c) monophenyldigermane, (d) triphenylgermane, (e) diphenyldigermane, (f) tetraphenylgermane, (g) triphenyldigermane, (h) tetraphenyldigermane and (g) pentaphenyldigermane. Molecules with similar molecular weights are displayed side-by-side for ease of comparison.287

Figure A5: (a) PCI-MS scans of (a) DPG as received from Gelest. (b) NCI-MS scans of aliquots taken from a DPG decomposition reaction in squalane at 380°C without Au nanocrystals. The reaction times are noted in minutes:seconds format next to each spectrum. Peaks are labeled that correspond to diphenylgermane (DPG), triphenylgermane (TPG) and tetraphenyldigermane (QPG₂).....289

Figure B1: XRD of (1) Ge nanowires and (2) Si nanowires. Data were acquired using a Rigaku R-Axis Spider Diffractometer with Image plate detector, Cu K_α radiation ($\lambda = 1.5418 \text{ \AA}$) at 40 kV and 40 mA, with samples on a 0.5 mm nylon loop, scanning for 10 min with sample rotation at 1° per second. Background scattering from the nylon loop has been subtracted. Reference patterns are provided for Ge (JCPDS: 00-004-0545), Au (JCPDS: 00-004-0784), and Si (JCPDS: 00-027-1402).291

Figure B2: (a) Voltage profiles and (b) differential capacity curves of Si nanowires (without RGO) corresponding to the capacity data in Figure 4.4a. 292

Figure B3: Expanded view of the differential capacity curves for Si nanowire/RGO (75% w/w Si) in the inset in Figure 4.4b. The curves are offset for clarity.293

Figure B4: (a) Voltage profiles and (b) differential capacity curves for Ge nanowires (without RGO) corresponding to the capacity data in Figure 4.6...294

Figure B5: Expanded view of the differential capacity curves in the inset of Figure 4.6b for Ge nanowire / RGO (75% w/w Ge). The curves are offset for clarity.295

Figure B6: Voltage profiles of (a) Si nanowire / RGO (75% w/w Si) and (b) Ge nanowire / RGO (75% w/w Ge) anodes corresponding to the capacity data plotted in Figure 9. The batteries were cycled at C/20 for 20 cycles and then C/10 for 100 cycles. The corresponding differential capacity curves are plotted in the insets.296

Figure C1: (a) Life cycle data, (b) voltage profiles, and (c) corresponding differential capacity plots for a battery cycled with PC:DMC.297

Figure C2: Differential capacity (a) discharge and (c) charge color maps with (b) waterfall plots for a battery cycled using an electrolyte solution of 1M LiPF₆ dissolved in a 1:1 w/w mixture of PC:DMC.298

Figure C3: (a) Capacities, (b) voltage profiles and (c) differential capacity plots for a battery cycled using a 1:1 w/w electrolyte solvent mixture of PC:DMC. The battery was cycled at the following rates (number of cycles): C/20 (10), C/10 (10), C/5 (5), C/2 (5), 1C (5), 2C (5), C/10 (10).300

Figure C4: Differential capacity (a) discharge and (c) charge color maps with (b) waterfall plots for a battery cycled at various rates using the PC:DMC electrolyte.....	301
Figure D1: Deconvoluted high-resolution XPS element scans of the Ge3d orbital at the indicated sputtering times for Ge nanowire films cycled using (a) EC:DEC, (b) EC:DMC, and (c) FEC:DMC.....	303
Figure D2: Deconvoluted high-resolution XPS element scans of the C1s orbital at the indicated sputtering times for Ge nanowire films cycled using (a) EC:DEC, (b) EC:DMC, and (c) FEC:DMC.....	304
Figure D3: Deconvoluted high-resolution XPS element scans of the O1s orbital at the indicated sputtering times for Ge nanowire films cycled using (a) EC:DEC, (b) EC:DMC, and (c) FEC:DMC.....	305
Figure D4: Deconvoluted high-resolution XPS element scans of the Li1s orbital at the indicated sputtering times for Ge nanowire films cycled using (a) EC:DEC, (b) EC:DMC, and (c) FEC:DMC.....	306
Figure D5: Deconvoluted high-resolution XPS element scans of the F1s orbital at the indicated sputtering times for Ge nanowire films cycled using (a) EC:DEC, (b) EC:DMC, and (c) FEC:DMC.....	307
Figure D6: Deconvoluted high-resolution XPS element scans of the P2p orbital at the indicated sputtering times for Ge nanowire films cycled using (a) EC:DEC, (b) EC:DMC, and (c) FEC:DMC.....	308
Figure D7: (a) High-resolution XPS elemental scans of F1s, O1s, C1s, P2p, Li1s, and Ge3d at various sputtering times and corresponding (b) atomic and (c) weight compositions of the Ge nanowire film prior to cycling.	310

Figure D8: Individual contributions from Ge 5/2, Ge 3/2, Ge ¹⁺ , Ge ²⁺ , Ge ³⁺ , and Ge ⁴⁺ for (a) uncycled and (b-d) cycled Ge nanowires using (b) EC:DEC, (c) EC:DMC, and (d) FEC:DMC.	311
Figure D9: Percent of Ge signal present as either Ge ⁰ or GeO _x for films cycled with various electrolytes.	312
Figure E1: (i) Charge / discharge capacities, coulombic efficiencies, (ii) voltage profiles and (iii) differential capacity for Si nanowires using PVdF and (a) EC:DEC, (b) EC:DMC, (c) EC:DMC+FEC, (d) FEC:DMC, and (e) PC:DMC.	313
Figure E2: (i) Charge / discharge capacities, coulombic efficiencies, (ii) voltage profiles and (iii) differential capacity for Au-removed Si nanowires using PVdF and (a) EC:DEC, (b) EC:DMC, or (c) FEC:DMC.....	314
Figure F1: TEM of in-situ Sn-seeded Si nanowires with a Si:Sn ratio of (a) 40:1 and (b) 400:1.....	315
Figure F2: Cycle data with coulombic efficiency for batteries assembled using Sn-seeded Si nanowires with PVdF binder and an electrolyte solvent solutions containing 1.0 M LiPF ₆ in a 1:1 w/w mixture of (a) EC:DEC, (b) EC:DMC, (c) EC:DMC + 3% w/w FEC, and (d) FEC:DMC...	316
Figure G1: Mass spectrometry of bismuth tris[bis(trimethylsilyl)]amide (Bi[N(Si(CH ₃) ₃) ₂] ₃) collected by positive ion chemical ionization.	317
Figure G2: Control reactions at (a) 350°C and (b) 400°C where the typical Ge nanorod procedure was followed except for the injection of Bi precursors. These results show that Ge nanorod growth requires the presence of Bi seeds to proceed through the SLS mechanism.....	318

Figure G3: TEM of Ge nanorods grown at 350°C after (a) 1 minute, (b) 2 minutes, (c) 3 minutes, (d) 4 minutes, and (e) 5 minutes with (f) absorbance spectra.	319
Figure G4: Absorbance spectra of branched and unbranched Ge nanorods and Bi nanocrystals.....	320
Figure H1: Ge nanorod sample at 30 seconds (or 1 minute) and 2 minutes showing the presence of Ge clusters in the reaction mixtures.....	321
Figure H2: Absorbance spectrum of Bi nanocrystals.....	322
Figure H3: TEM image of solution grown Au seeded Ge nanorods in squalane, TOPO and tri- <i>n</i> -dodecylamine.....	323
Figure H4: Extinction spectra of 200 nm long Ge nanorods with no metal tip with the incident electric field polarized (a) perpendicular and (b) parallel to the long axis of the nanorods.	324
Figure H5: Extinction cross-section calculations using the DDA with various dipole arrangements: (a) 2x2,(b) cross, (c) hexagon, and (d) 3x3, with the polarization of the incident electric field aligned (e) perpendicular and (f) parallel to the long axis of the nanorods.	325
Figure H6: Internal electric field using a parallel incident electric field for (a) edge and (b) central dipoles with (c, d) corresponding cross-sectional plots showing electric field contours for specific wavelengths for a dipole arrangement with a cross cross-section.....	326
Figure H7: Internal electric field using a parallel incident electric field for (a) face and (b) central dipoles with (c, d) corresponding cross-sectional plots showing electric field contours for specific wavelengths for a dipole arrangement with a hexagonal cross-section.	327

Figure H8: Intensity plots showing the local electric field near the tip of Ge nanorods with Au seeds for (a) perpendicular and (c) parallel incident electric fields with (b, d) corresponding cross-sectional plots showing constant wavelength contours.	328
Figure I1: Mass spectrometry of DOPA collected by positive ion chemical ionization.....	329
Figure I2: (a) TEM with (inset) diameter histogram of Bi nanocrystals ($d = 14.0 \pm 2.5$ nm) and (b) TGA analysis of the reaction product.	330
Figure I3: Nanowire histogram plots for InP nanowires grown in the presence of (a) HDA and OPA, (b) OPA only, (c) HDA only, or (d) no ligand. Nanowires were also grown in the presence of HDA and (e) H_3PO_4 , (f) OPA, (g) DOPA, or (h) TOPO.....	331
Figure I4: InP nanowires grown in the presence of HDA and (a) 10 mg, (b), 100 mg, and (c) 1000 mg OPA with (d) XRD spectra for each. Reference patterns are included for InP (JCPDS: 00-032-0452), In_2O_3 (JCPDS: 01-071-2194), and Bi (00-044-1246).	333
Figure I5: Phosphoric acid derivatives used in reactions included (1) phosphoric acid (H_3PO_4), (2) OPA, (3) DOPA, and (4) (TOPO).	334
Figure I6: TGA of InP nanowires grown in the presence of HDA and H_3PO_4 , OPA, DOPA, and TOPO.	335
Figure I7: TEM of InP nanowires grown in the presence of HDA and DOPA showing a high yield of nanocrystalline byproduct mixed in with the InP nanowires.	336

Chapter 1: Introduction

1.1 INTRODUCTION TO LITHIUM ION BATTERIES

The ubiquity of portable electronic devices—mp3 players, portable laptop computers, digital cameras, cell phones, and smart tablets—drives an increasing demand on power sources with high energy density. Lithium (Li) ion batteries are the power source of choice for mobile devices offering long life span through repeated rechargeability, flexible, lightweight design and high energy density as illustrated in Figure 1.1. Li-ion batteries boast energy densities among the highest current energy storage technologies¹ and show promise in satisfying the growing interest in battery powered electric cars.²

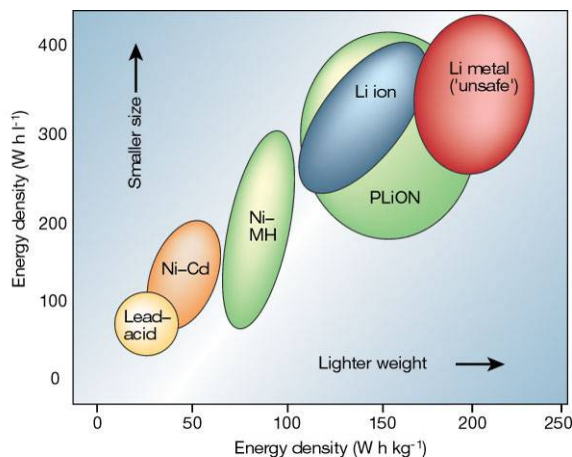
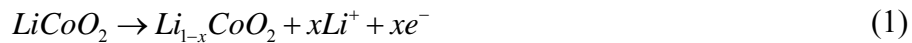


Figure 1.1: Comparison of the different battery technologies in terms of volumetric and gravimetric energy density. Reprinted from Ref 2.

Advance in energy storage technologies has been sluggish compared to solid-state memory capacity, which—according to Moore’s law—doubles every eighteen months. Li-ion battery technology has been particularly stagnant during the past several decades. A brief history of Li-ion battery development illustrates this point. Wittingham first

proposed lithium batteries in 1976, reporting titanium disulfide as a positive electrode material.³ Besenhard discovered reversible Li intercalation into graphite in the same year.^{4, 5} In 1979, Goodenough laid the foundation for modern Li-ion battery technology demonstrating a rechargeable Li-ion battery using lithium cobalt oxide (LiCoO₂) as the cathode. Since the mid 1980s, the cathode material has largely remained LiCoO₂ and the anode of choice has been graphite. The first commercial Li ion battery—made available by Sony in 1991—used these same materials. Li-ion battery technology has since seen little advance. Several challenges face progression of Li ion battery technology, including cost, safety, energy density, charge / discharge rate, and lifetime.⁶ These challenges manifest as material-related problems rooted in electrolyte stability and electrode storage capacity. A strong understanding of the inner workings of a Li-ion battery is necessary to overcome these challenges; a brief description follows.

Li-ion batteries operate by shuttling Li⁺ ions between the electrodes where they insert into the active material and form Li-containing compounds (e.g., LiCoO₂, LiC₆). Figure 1.2 shows a schematic charge / discharge cycle for a typical commercially available Li ion battery. In a brand new battery, Li is stored in the cathode as LiCoO₂. During the charge cycle, lithium oxidizes, dissociating from the metal oxide,



travels through an ion-permeable membrane, intercalates between individual graphite sheets in the anode, and is reduced:



Discharge traces the reverse process: Lithium de-intercalates from the graphite, diffuses into the cathode and reduces to reform LiCoO₂.

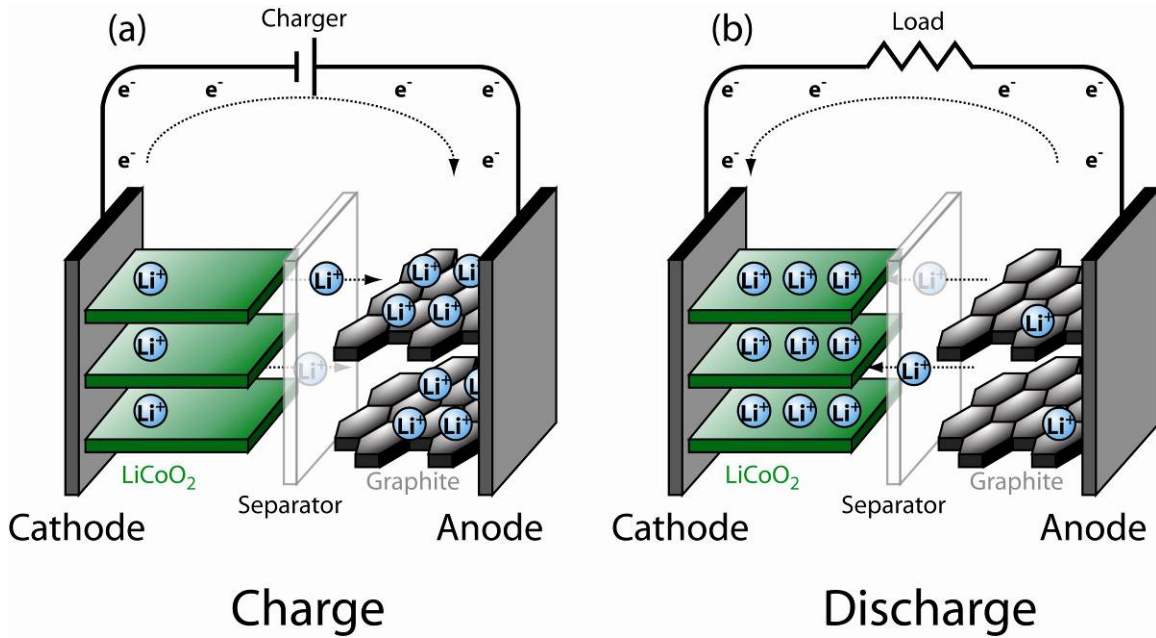


Figure 1.2: Schematic (a) charge and (b) discharge cycles for a Li-ion battery with a LiCoO_2 cathode and graphite anode.

The maximum capacity of an electrode is directly proportional to the amount of Li it can store. While volume occupied by the electrode material is important, capacities are typically reported on a per-mass basis. This speaks to a major deficiency of conventional Li ion batteries: low energy density, which is calculated as the product of capacity and discharge voltage. The maximum theoretical capacities of LiC_6 and LiCoO_2 are 372 mA h g^{-1} and 274 mA h g^{-1} , respectively. Due to large anisotropic structural changes that accompany delithiation of LiCoO_2 , the practical capacity of this material is only half of the theoretical maximum, or 137 mA h g^{-1} .⁷ The total capacity, Q_T , of the working cell can be calculated through:

$$Q_T = \frac{Q_A Q_C}{Q_A + Q_C} \quad (1)$$

where Q_A and Q_C are the capacities of the anode and cathode, respectively. From Equation (1), the maximum capacity for a LiCoO_2 / graphite battery is 100 mA h g^{-1} ,

assuming equal masses of each active material. This value serves as a benchmark for comparison and addressing this shortcoming is the main focus of this work.

Suitable electrode replacement materials are sought in an ongoing effort to realize Li-ion batteries with higher energy density and longer cycle life. There are several candidates on the cathode side, including lithium manganese oxide (LiMn_2O_4),^{8,9} lithium nickel oxide (LiNiO_2),¹⁰ lithium iron phosphate (LiFePO_4),¹¹ lithium vanadium oxide (LiV_2O_5),¹²⁻¹⁵ and their derivatives.^{10, 16-23} Sulfur (S) has a large Li storage capacity (1673 mA h g^{-1}) and moderate working voltage ($2.2 \text{ V vs. Li/Li}^+$) and is a good candidate for the positive electrode, though it lacks an intrinsic Li source.²⁴ Pre-lithiation of the electrode nullifies this point.²⁵ On the anode side, silicon (Si) is the leading candidate to replace graphite boasting a maximum theoretical capacity of 3579 mA h g^{-1} .²⁶⁻²⁸ Germanium (Ge) is also an attractive negative electrode material with a high theoretical capacity of 1624 mA h g^{-1} .²⁹ Figure 1.3 shows total battery capacity as a function of anode capacity illustrating the potential for improvements in Li-ion batteries by using the materials listed above. The black curve corresponds to a LiCoO_2 cathode and the yellow sulfur. The LiCoO_2 curve flattens out for anodes with a maximum theoretical capacity of around 1000 mA h g^{-1} , indicating a minimum capacity guideline for negative electrode materials. Not only do Si and Ge both surpass this threshold but, they also have low working potential relative to the standard Li reduction potential²⁶⁻²⁹ and are abundant earth metals, making them attractive negative electrode materials. Though Ge is expensive, it has a Li diffusion coefficient 400 times faster than Si³⁰ and performs better at high current densities, making it attractive in high power applications.^{31, 32} Ge also has a higher intrinsic conductivity than Si.

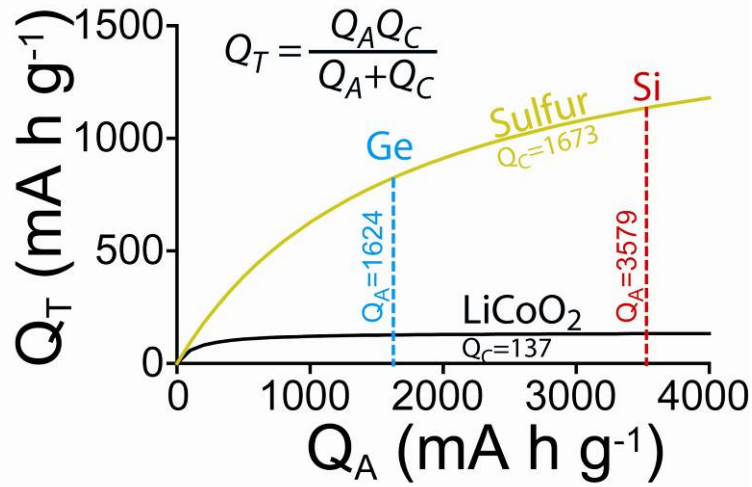


Figure 1.3: Total cell capacity as a function of anode capacity using fixed cathode capacities of 137 mA h g⁻¹ (LiCoO₂, black) and 1637 mA h g⁻¹ (sulfur, yellow).

Upon lithiation, Si forms an amorphous Li-Si compound (aLi_xSi). Further addition of Li causes formation of the Li₁₅Si₄ alloy.²⁶⁻²⁸



While other crystalline Li_xSi_{1-x} phases have been reported,³³ the reaction pathway shown above is the accepted mechanism for Si lithiation; Li₁₅Si₄ is the most lithiated phase that forms at room temperature. As lithium inserts into Si, the capacity increases and the potential difference between the anode and cathode drops. Figure 1.4a shows a typical voltage profile for a Si nanowire-based Li-ion battery negative electrode. The lithiation events described in Equation 3 occur at specific voltages and manifest as plateaus in the voltage profile due to phase-separation. For example, region I indicates a two-phase region consisting of Si and aLi_xSi, and region II indicates a two phase region consisting of aLi_xSi and Li₁₅Si₄. These equipotential lithiation sites are more easily seen using the differential capacity plot, shown in Figure 1.4b. Regions III and IV are identical to regions II and I, respectively, for the delithiation reaction.

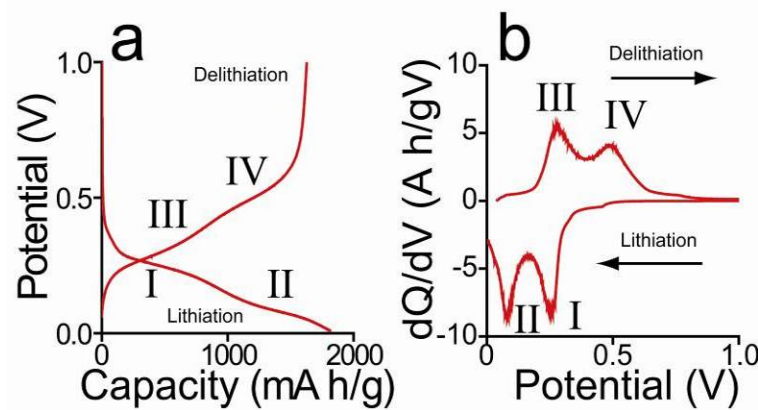
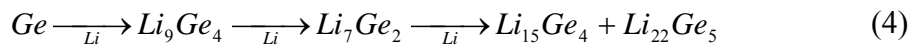


Figure 1.4: (a) Typical voltage profile and (b) corresponding differential capacity plot for a Si nanowire-based Li-ion battery negative electrode.

Ge undergoes a similar, though multi-stage, lithiation process:^{29, 34}



While Li-Si alloys were reported as early as 1976,³⁵ it took until the early 2000's for interest in Si as a negative electrode in Li-ion batteries to take off. Li-Ge alloys were explored in the 1960s,³⁶ though interest in Ge as a Li insertion material has piqued only recently as well (Figure 1.5). Early studies on Li-Si and Li-Ge alloys report formation of these compounds at temperatures greater than 400°C.³⁷ Reaction of bulk Si with Li suffers from poor reversibility, which prevented its use in Li-ion batteries. In 2001, Gao *et al.* overcame the challenges facing bulk Si cyclability and reported room temperature alloy formation in nanostructured Si and Ge, making these realistic negative electrode materials.³⁸

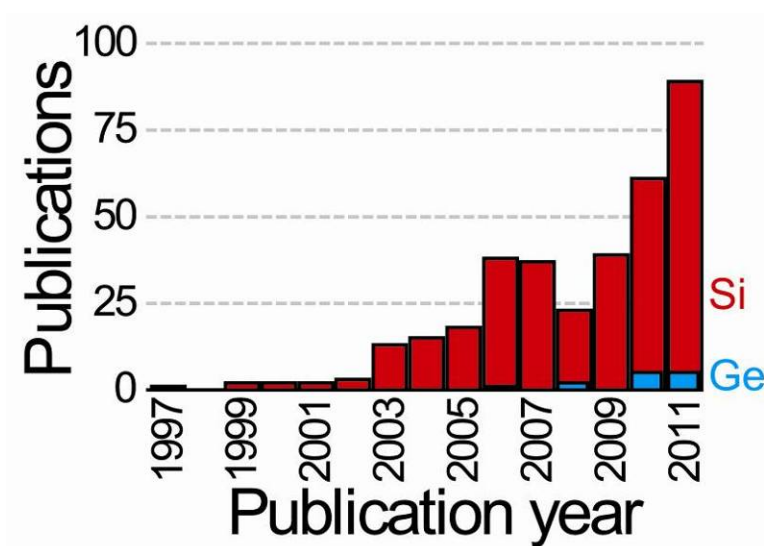


Figure 1.5: Publications for Si and Ge Li ion battery negative electrode material by year. Search includes publications whose titles bear “lithium ion batteries” in conjunction with “Si / silicon” or “Ge / germanium”.

In addition to enabling room temperature alloy formation, the use of nanostructured Si and Ge addressed another major drawback to using high-capacity Li insertion materials: volumetric expansion. During lithium insertion the Si and Ge lattices expand by up to 300% and repeated cycling pulverizes the electrode resulting in rapid capacity fade. Nanomaterials can accommodate strain better than their bulk counterparts and mitigate pulverization effects.³⁹⁻⁴¹

A wide variety of nanostructures have been explored as negative electrode materials in Li-ion batteries. Si and Ge thin films (i.e., grown using chemical vapor deposition–CVD–techniques) boast high capacities with minimal fade through hundreds of charge / discharge cycles.^{32-34, 41-64} Unfortunately, CVD processes are expensive and difficult to scale-up. A viable alternative to CVD techniques is the use of solution-grown nanowires. Nanowires are anisotropic single crystals hundreds of microns in length with narrow diameters (typically less than 50 nm), which can accommodate the stress that

accompanies volumetric expansion associated with Li insertion.³⁹⁻⁴¹ Furthermore, Si and Ge nanowires can be grown using high-throughput solution phase processes that are inexpensive compared to vapor phase approaches.⁶⁵⁻⁶⁹ Therefore, Si and Ge nanowires show great promise as Li ion battery negative electrodes.

The general approach to making nanomaterial-based Li-ion battery electrodes is to first prepare a slurry by mixing the active material (e.g., Si, Ge), conductive carbon, and a solvent-dispersed polymeric binder. This slurry is cast on a copper current collector, which serves to support the film and ensure efficient charge distribution throughout the electrode. Conductive carbon is necessary to increase film conductivity and is essential for most nanomaterial-based electrodes—especially semiconductors like Si and Ge. Binder chemistry is unique to the active material. The typical binder for Si and Ge nanomaterials is poly(vinylidene) fluoride (PVdF),⁷⁰ though green alternatives, such as carboxymethyl cellulose (CMC)^{71, 72} and alginate⁷³ have also been investigated. The search for stable electrolyte solutions is also an area of intense research.⁷⁴ For Si-based electrodes, fluoroethylene carbonate (FEC) appears to perform best.⁷⁵⁻⁷⁷ Research in these areas is ongoing. This work focuses on the use of Si and Ge nanowires as the active negative electrode material in Li-ion batteries. An introduction to nanowire synthesis follows.

1.2 INTRODUCTION TO NANOWIRE AND NANOROD SYNTHESIS

Nanowires are an interesting class of materials with a wide range of microelectronic applications in addition to high-performance Li-ion batteries.⁷⁸ They also function in logic gates,⁷⁹ memory devices,⁸⁰ light emitting devices,⁸¹ field effect transistors,⁸² chemical sensing,⁸³ and photovoltaics.⁸⁴ Since inception in 1959, photolithography has been the workhorse of the semiconductor industry⁸⁵ and has been

used as a top-down approach to fabricating nanowires with features as small as 40 nm.⁸⁶ Wagner *et al.* demonstrated a bottom-up approach to nanowire synthesis in a 1964 report showing growth of Si whiskers from gold (Au) droplets in a vapor phase process.⁸⁷ The growth mechanism was dubbed vapor-liquid-solid (VLS). Trentler *et al.* demonstrated a solution phase analog to VLS growth in 1995 reporting growth of InP, InAs, and GaAs nanowires in high boiling point solvents giving birth to solution-liquid-solid (SLS) growth mechanism.⁸⁸ Shortly thereafter, in 2002, Hanrath *et al.* developed the supercritical fluid-liquid-solid (SFLS) method, extending of SLS growth to Ge nanowires in supercritical solvents.⁸⁹ These three growth methods differ only in reaction media—the growth mechanism is otherwise identical. The naming convention for these techniques is born from the mechanism itself. The first phase in each title (e.g., vapor, solution, or supercritical fluid) refers to the reaction medium. The liquid-solid refers to the fact that the semiconductor forms a **liquid** alloy with the crystalline metal seed from which a **solid** single crystal nanowire extrudes. The growth mechanism is outlined below using Si nanowires seeded from Au nanocrystals as an example.

Figure 1.6 shows the binary phase diagram between Si and Au, which is used to rationalize the nanowire growth mechanism. The explanation that follows is unique to SLS and SFLS methods.⁹⁰ In a standard nanowire reaction, the Si precursor, typically an organometallic silane compound (i.e., monophenylsilane–MPS), is mixed with nanocrystalline Au seeds and introduced into the hot reaction solvent at a temperature above the Si-Au eutectic. The Si precursor rapidly thermally decomposes, liberating zero-valent Si atoms, which are free to alloy with the Au seeds (region I), eventually forming a Si-Au liquid droplet (region II). Further addition of Si atoms shifts the composition of the Si-Au beyond the liquidus line causing crystalline Si to precipitate and form the tip of the nanowire. A continued Si supply causes one-dimensional extrusion of the

semiconductor, forming the nanowire (region III). This process proceeds until the Si source is exhausted. Modifying the diameter of the seed metal catalyst controls the nanowire diameter.⁹¹ The semiconductor-metal atomic ratio controls the nanowire length.⁹²⁻⁹⁴

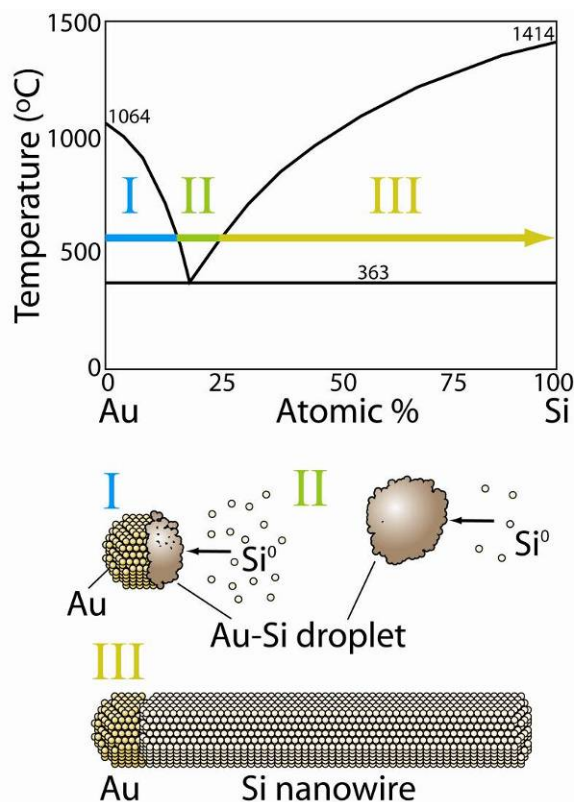


Figure 1.6: Nanowire growth mechanism. The arrow tracks the composition change as Si is added to Au. Schematics of the nanowires at various points during growth are shown (regions I, II, and III).

1.3 GROWTH CONSIDERATIONS AND GERMANIUM NANORODS

Nanorods are an interesting class of materials, as they can exhibit optical quantum confinement effects,^{95, 96} linear polarized photoluminescence,⁹⁷ and enhanced light absorption when the aspect ratio is sufficiently large.⁹⁸ Nanorod synthesis follows the same growth mechanism as nanowires, detailed above, though ligand chemistry and

atomic ratio between the semiconductor and metal seed are particularly important. Identifying an appropriate precursor is essential to the growth of high quality (i.e. straight, defect free, single crystalline) nanorods and nanowires alike. If a precursor decomposes too slowly, the catalyst seeds become starved resulting in growth defects that disrupt crystallinity (e.g., kinking and twinning). If decomposition occurs too rapidly, the system becomes flooded with excess semiconductor atoms that homogeneously nucleate forming undesired reaction byproducts (i.e., nanocrystals, amorphous particles, etc.). Seed catalyst selection is also critical; the metal seed must form a low eutectic with the semiconductor. Au and Bi are typical metals of choice.^{67, 69, 89, 91, 92, 96, 99-109} In the case of compound semiconductor nanowires (or nanorods of any material), solvent and ligand chemistry is also important.⁹²⁻⁹⁴ Coordinating solvents (e.g., tri-*n*-octylphosphine oxide, hexadecylamine, octylphosphonic acid, etc.) interact with nanostructures during growth and are used as capping ligands to control growth through arrested precipitation.

Germanium nanomaterials show interesting luminescent properties¹¹⁰ and can be used for biological imaging¹¹¹ and serve as the basis for new optical and electronic devices.¹¹²⁻¹¹⁴ Solvent dispersions of Ge nanocrystals have been utilized as inks to deposit thin films under relatively mild conditions showing potential for low-cost optical and electronic devices.¹¹⁴ Furthermore, Ge is an interesting optoelectronic material due to a high index of refraction, low optical dispersion, and infrared transparency.¹¹⁵ Ge nanowires exhibit interesting electronic,¹¹⁶ optical,⁹⁸ and mechanical properties.^{117, 118} Ge nanorods are particularly interesting as both length and diameter can be controlled, enabling finely tuned optical properties.⁹⁴ Synthesis and optical properties of Ge nanorods are explored in this work.

1.4 SURFACE CHEMISTRY OF INDIUM PHOSPHIDE NANOWIRES

Solution-processable nanowires can be grown under mild reaction conditions in scalable, low-cost, high-throughput processes using SLS techniques. By comparison, vapor phase processes require high temperature, high vacuum, are unscalable, and produce much less material. Nanowires of most semiconductor materials have been synthesized using solution methods, including group IV elements (e.g., Si^{65, 66, 69, 89, 92} and Ge^{65, 67, 68, 119}), III-V compound semiconductors such as gallium and indium pnictides (e.g., GaAs, InP, etc.),^{88, 91, 96, 101, 102, 120, 121} II-VI compound semiconductors like cadmium and zinc chalcogenides (e.g., CdSe, ZnS, etc.),^{99, 100, 103-105, 107-109, 122-124} and tetrael chalcogenides (IV-VI compound semiconductors–SnSe, PbS, etc.).¹²⁵⁻¹²⁸

Indium phosphide (InP) exhibits strong quantum confinement effects^{102, 106, 129, 130} and is an interesting material for optoelectronic applications.¹³¹ InP has a broader emission range and lower toxicity than CdSe, which has been studied in excruciating detail as an optoelectronic material.¹³² As such, there is great interest in developing and understanding the synthesis of InP nanomaterials. The surface chemistry of InP quantum dots has been an area of investigation of late and is relatively well understood.¹³²⁻¹³⁶ Surface chemistry of nanowires, grown via the solution-liquid-solid (SLS) growth mechanism, for example, remains ambiguous.^{91, 96, 101, 102, 106} There are also pronounced differences in the growth of SLS InP nanowires compared to vapor-liquid-solid (VLS) grown InP nanowires. For instance, SLS-grown InP nanowires exhibit zinc blende structure^{91, 96, 101, 102, 106} whereas VLS-grown nanowires show a mixture of the zinc blende and wurtzite phases, depending on the reaction conditions.¹³⁷⁻¹⁴² This point remains to be addressed directly, but as the phases differ in energy by only 6.8 meV per In-P atom pair,¹⁴³ the cause is likely due to the presence of the capping ligands in SLS syntheses

that form zinc blende structure preferentially. This work surveys the surface chemistry of InP nanowires, examining the efficacy of various ligands.

1.5 DISSERTATION OUTLINE

Growth of Si nanowires in supercritical fluids using MPS is well established and this material has previously been used as a negative electrode material in Li-ion batteries using the slurry method to prepare the electrode.¹⁴⁴ In this work, MPS-grown Si nanowires are again demonstrated as a negative electrode material, though as a freestanding fabric that does not require the addition of binder.¹⁴⁵ Through a simple anneal process the conductivity of the nanowire fabric is increased such that conductive carbon is also unnecessary. This work shows potential for fully flexible and mechanically robust batteries. Solution synthesis of Ge nanowires has also been previously reported, though using germanium (II) iodide (GeI_2) as the precursor and Bi as the seed catalyst.⁶⁸ Residual iodine can be corrosive, thus Au-seeded Ge nanowires were produced using diphenylgermane (DPG) as the Ge source in a variety of solvents; detailed synthesis of these nanowires is discussed.⁶⁷ The Ge nanowires were tested as negative electrodes in Li-ion batteries supported by reduced graphite oxide (RGO) in a flexible, mechanically robust, freestanding film. RGO-supported Si nanowires (grown using trisilane) were also tested. Graphene serves doubly as a binder and conductive agent. Results for RGO-supported negative electrode materials were lackluster and what follows is a detailed examination of electrochemical behavior of Si and Ge nanowires using the more conventional slurry methods. A variety of binders and electrolyte solutions were surveyed to optimize the performance of the nanowires. Ge has a Li diffusion coefficient 400 times that of Si and was tested under high current densities for potential high-power applications. The surface chemistry of these Ge nanowire films was also examined.

Trisilane grown Si nanowires contain Au in as high as 25% w/w and Au acts as an irreversible Li sink, which is detrimental to Si nanowire performance in Li-ion batteries.^{146, 147} As such, the effects of Au on the cycling behavior of Si nanowires were explored by removing Au through a wet etching process. Next, Au was eliminated from the reaction all together by using tin (Sn) as a seed material. Sn is an electrochemically active group IV element forming $\text{Li}_{22}\text{Sn}_5$ upon lithiation, which has a maximum theoretical capacity of 993 mA h g^{-1} . Diverging from work pertaining to Li-ion batteries, a detailed synthesis of Ge nanorods⁹⁴ follows with discussion of optical properties. Finally, ligand and surface chemistry is explored in solution-grown of InP nanowires.

1.6 REFERENCES

1. Tarascon, J. M.; Armand, M. *Nature* **2001**, *414*, 359-367.
2. Armand, M.; Tarascon, J. M. *Nature* **2008**, *451*, 652-657.
3. Whittingham, M. S. *Science* **1976**, *192*, 1126-1127.
4. Besenhard, J. O.; Eichinger, G. *J. Electroanal. Chem.* **1976**, *68*, 1-18.
5. Eichinger, G.; Besenhard, J. O. *J. Electroanal. Chem.* **1976**, *72*, 1-31.
6. Goodenough, J. B.; Kim, Y. *Chem. Mater.* **2009**, *22*, 587-603.
7. Alcantara, R.; Lavela, P.; Tirado, J. L.; Stoyanova, R.; Zhecheva, E. *J. Solid State Chem.* **1997**, *134*, 265-273.
8. Wakihara, M. *Mat. Sci. Eng. R* **2001**, *33*, 109-134.
9. Ohzuku, T.; Kitagawa, M.; Hirai, T. *J. Electrochem. Soc.* **1990**, *137*, 40-46.
10. Chang, C. C.; Scarr, N.; Kumta, P. N. *Solid State Ionics* **1998**, *112*, 329-344.
11. Padhi, A. K.; Nanjundaswamy, K. S.; Goodenough, J. B. *J. Electrochem. Soc.* **1997**, *144*, 1188-1194.
12. Bergstrom, O.; Gustafsson, T.; Thomas, J. O. *Acta Crystallogr. C* **1998**, *54*, 1204-1206.
13. Liu, G. Q.; Zeng, C. L.; Yang, K. *Electrochim. Acta* **2002**, *47*, 3239-3243.
14. Tsang, C.; Manthiram, A. *J. Electrochem. Soc.* **1997**, *144*, 520-524.
15. Murphy, D. W.; Christian, P. A.; Disalvo, F. J.; Carides, J. N. *J. Electrochem. Soc.* **1979**, *126*, 497-499.

16. Amarilla, J. M.; de Vidales, J. L. M.; Rojas, R. M. *Solid State Ionics* **2000**, *127*, 73-81.
17. Mohamedi, M.; Makino, A.; Dokko, K.; Itoh, T.; Uchida, I. *Electrochim. Acta* **2002**, *48*, 79-84.
18. Arora, P.; Popov, B. N.; White, R. E. *J. Electrochem. Soc.* **1998**, *145*, 807-815.
19. Sun, Y. K.; Hong, K. J.; Prakash, J.; Amine, K. *Electrochem. Commun.* **2002**, *4*, 344-348.
20. Alcantara, R.; Jaraba, M.; Lavela, P.; Tirado, J. L. *Electrochim. Acta* **2002**, *47*, 1829-1835.
21. Ramesh, T. N.; Lee, K. T.; Ellis, B. L.; Nazar, L. F. *Electrochem. Solid St.* **2010**, *13*, A43-A47.
22. Zhong, Q. M.; Bonakdarpour, A.; Zhang, M. J.; Gao, Y.; Dahn, J. R. *J. Electrochem. Soc.* **1997**, *144*, 205-213.
23. Chang, S. H.; Ryu, K. S.; Kim, K. M.; Kim, M. S.; Kim, I. K.; Kang, S. G. *J. Power Sources* **1999**, *84*, 134-137.
24. Zheng, G.; Yang, Y.; Cha, J. J.; Hong, S. S.; Cui, Y. *Nano Lett.* **2011**, *11*, 4462-4467.
25. Liu, N.; Hu, L.; McDowell, M. T.; Jackson, A.; Cui, Y. *ACS Nano* **2011**, *5*, 6487-6493.
26. Obrovac, M. N.; Christensen, L. *Electrochem. Solid St.* **2004**, *7*, A93-A96.
27. Li, J.; Dahn, J. R. *J. Electrochem. Soc.* **2007**, *154*, A156-A161.
28. Hatchard, T. D.; Dahn, J. R. *J. Electrochem. Soc.* **2004**, *151*, A838-A842.
29. Yoon, S.; Park, C.-M.; Sohn, H.-J. *Electrochem. Solid St.* **2008**, *11*, A42-A45.
30. Fuller, C. S.; Severiens, J. C. *Phys. Rev.* **1954**, *96*, 21-24.
31. Park, M.-H.; Cho, Y.; Kim, K.; Kim, J.; Liu, M.; Cho, J. *Angew. Chem. Int. Ed.* **2011**, *50*, 9647-9650.
32. Wang, J.; Du, N.; Zhang, H.; Yu, J.; Yang, D. *J. Mater. Chem.* **2011**, *22*, 1511-1515.
33. Kang, K.; Lee, H.-S.; Han, D.-W.; Kim, G.-S.; Lee, D.; Lee, G.; Kang, Y.-M.; Jo, M.-H. *App. Phys. Lett.* **2010**, *96*, 053110-3.
34. Graetz, J.; Ahn, C. C.; Yazami, R.; Fultz, B. *J. Electrochem. Soc.* **2004**, *151*, A698-A702.
35. Lai, S.-C. *J. Electrochem. Soc.* **1976**, *123*, 1196-1197.

36. Sangster, J.; Pelton, A. *J. Phase Equilib.* **1997**, *18*, 289-294.
37. Wen, C. J.; Huggins, R. A. *J. Solid State Chem.* **1981**, *37*, 271-278.
38. Gao, B.; Sinha, S.; Fleming, L.; Zhou, O. *Adv. Mater.* **2001**, *13*, 816-819.
39. Ryu, I.; Choi, J. W.; Cui, Y.; Nix, W. D. *J. Mech. Phys. Solids* **2011**, *59*, 1717-1730.
40. Zhang, X.; Shyy, W.; Sastry, A. M. *J. Electrochem. Soc.* **2007**, *154*, A910-A916.
41. Yao, Y.; McDowell, M. T.; Ryu, I.; Wu, H.; Liu, N.; Hu, L.; Nix, W. D.; Cui, Y. *Nano Lett.* **2011**, *11*, 2949-2954.
42. Baggetto, L.; Notten, P. H. L. *J. Electrochem. Soc.* **2009**, *156*, A169-A175.
43. Wang, D.; Yang, Z.; Li, F.; Liu, D.; Wang, X.; Yan, H.; He, D. *Mater. Lett.* **2011**, *65*, 1542-1544.
44. Rong, J. P.; Masarapu, C.; Ni, J.; Zhang, Z. J.; Wei, B. Q. *ACS Nano* **2010**, *4*, 4683-4690.
45. Fu, P. P.; Song, Y. J.; Zhang, H. F.; Yang, H. B.; Zhou, Z. X.; Wu, M. T.; Huang, L. H.; Xu, G. *Chinese J. Inorg. Chem.* **2006**, *22*, 1823-1827.
46. Maranchi, J. P.; Kumta, P. N.; Hepp, A. F. *Ceram. Trans.* **2005**, *161*, 121-129.
47. Jung, H. J.; Park, M.; Han, S. H.; Lim, H.; Joo, S. K. *Solid State Commun.* **2003**, *125*, 387-390.
48. Datta, M. K.; Maranchi, J.; Chung, S. J.; Epur, R.; Kadakia, K.; Jampani, P.; Kumta, P. N. *Electrochim. Acta* **2011**, *56*, 4717-4723.
49. Huang, R.; Fan, X.; Shen, W. C.; Zhu, J. *App. Phys. Lett.* **2009**, *95*, 133119-3.
50. Maranchi, J. P.; Hepp, A. F.; Kumta, P. N. *Electrochem. Solid St.* **2003**, *6*, A198-A201.
51. Kim, Y. J.; Kim, M. H.; Yang, J. H.; Park, J. W. *J. Korean Phys. Soc.* **2006**, *49*, 1196-1201.
52. Huang, R.; Zhu, J. *Mater. Chem. Phys.* **2010**, *121*, 519-522.
53. Munao, D.; Valvo, M.; van Erven, J.; Kelder, E. M.; Hassoun, J.; Panero, S. *J. Mater. Chem.* **2011**, *22*, 1556-1561.
54. Han, G. B.; Lee, J. N.; Choi, J. W.; Park, J. K. *Electrochim. Acta* **2011**, *56*, 8997-9003.
55. Li, H. X.; Cheng, F. Y.; Zhu, Z. Q.; Bai, H. M.; Tao, Z. L.; Chen, J. *J. Alloy. Compd* **2011**, *509*, 2919-2923.

56. Wen, Z. S.; Cheng, M. K.; Sun, J. C.; Wang, L. A. *Electrochim. Acta* **2010**, *56*, 372-375.
57. Hwang, C.-M.; Park, J.-W. *Thin Solid Films* **2010**, *518*, 6590-6597.
58. Laforge, B.; Levan-Jodin, L.; Salot, R.; Billard, A. *J. Electrochem. Soc.* **2008**, *155*, A181-A188.
59. Baggetto, L. C.; Hensen, E. J. M.; Notten, P. H. L. *Electrochim. Acta* **2010**, *55*, 7074-7079.
60. DiLeo, R. A.; Frisco, S.; Ganter, M. J.; Rogers, R. E.; Raffaelle, R. P.; Landi, B. J. *J. Phys. Chem. C* **2011**, *115*, 22609-22614.
61. Laïk, B.; Eude, L.; Pereira-Ramos, J.-P.; Cojocaru, C. S.; Pribat, D.; Rouvière, E. *Electrochim. Acta* **2008**, *53*, 5528-5532.
62. Ruffo, R.; Hong, S. S.; Chan, C. K.; Huggins, R. A.; Cui, Y. *J. Phys. Chem. C* **2009**, *113*, 11390-11398.
63. Chakrapani, V.; Rusli, F.; Filler, M. A.; Kohl, P. A. *J. Phys. Chem. C* **2011**, *115*, 22048-22053.
64. Yu, C. J.; Li, X.; Ma, T.; Rong, J. P.; Zhang, R. J.; Shaffer, J.; An, Y. H.; Liu, Q.; Wei, B. Q.; Jiang, H. Q. *Adv. Eng. Mater.* **2012**, *2*, 68-73.
65. Hanrath, T.; Korgel, B. A. *Adv. Mater.* **2003**, *15*, 437-440.
66. Heitsch, A. T.; Akhavan, V. A.; Korgel, B. A. *Chem. Mater.* **2011**, *23*, 2697-2699.
67. Chockla, A. M.; Korgel, B. A. *J. Mater. Chem.* **2009**, *19*, 996-1001.
68. Lu, X.; Fanfair, D. D.; Johnston, K. P.; Korgel, B. A. *J. Am. Chem. Soc.* **2005**, *127*, 15718-15719.
69. Heitsch, A. T.; Fanfair, D. D.; Tuan, H.-Y.; Korgel, B. A. *J. Am. Chem. Soc.* **2008**, *130*, 5436-5437.
70. Li, J.; Christensen, L.; Obrovac, M. N.; Hewitt, K. C.; Dahn, J. R. *J. Electrochem. Soc.* **2008**, *155*, A234-A238.
71. Ding, N.; Xu, J.; Yao, Y. X.; Wegner, G.; Lieberwirth, I.; Chen, C. H. *J. Power Sources* **2009**, *192*, 644-651.
72. Key, B.; Bhattacharyya, R.; Morcrette, M.; Seznec, V.; Tarascon, J. M.; Grey, C. P. *J. Am. Chem. Soc.* **2009**, *131*, 9239-9249.
73. Kovalenko, I.; Zdyrko, B.; Magasinski, A.; Hertzberg, B.; Milicev, Z.; Burtovyy, R.; Luzinov, I.; Yushin, G. *Science* **2011**, *334*, 75-79.
74. Zhang, S. S. *J. Power Sources* **2006**, *162*, 1379-1394.

75. Etacheri, V.; Haik, O.; Goffer, Y.; Roberts, G. A.; Stefan, I. C.; Fasching, R.; Aurbach, D. *Langmuir* **2012**, *28*, 965-976.
76. Choi, N.-S.; Yew, K. H.; Lee, K. Y.; Sung, M.; Kim, H.; Kim, S.-S. *J. Power Sources* **2006**, *161*, 1254-1259.
77. Nakai, H.; Kubota, T.; Kita, A.; Kawashima, A. *J. Electrochem. Soc.* **2011**, *158*, A798-A801.
78. Chan, C. K.; Peng, H.; Liu, G.; McIlwrath, K.; Zhang, X. F.; Huggins, R. A.; Cui, Y. *Nat. Nano.* **2008**, *3*, 31-35.
79. Huang, M. H.; Mao, S.; Feick, H.; Yan, H.; Wu, Y.; Kind, H.; Weber, E.; Russo, R.; Yang, P. *Science* **2001**, *292*, 1897-1899.
80. Duan, X.; Huang, Y.; Lieber, C. M. *Nano Lett.* **2002**, *2*, 487-490.
81. Gudiksen, M. S.; Lauhon, L. J.; Wang, J.; Smith, D. C.; Lieber, C. M. *Nature* **2002**, *415*, 617-620.
82. Cui, Y.; Lieber, C. M. *Science* **2001**, *291*, 851-853.
83. Cui, Y.; Wei, Q.; Park, H.; Lieber, C. M. *Science* **2001**, *293*, 1289-1292.
84. Kayes, B. M.; Atwater, H. A.; Lewis, N. S. *J. App. Phys.* **2005**, *97*, 114302-11.
85. Xia, Y.; Whitesides, G. M. *Angew. Chem. Int. Ed.* **1998**, *37*, 550-575.
86. Totzeck, M.; Ulrich, W.; Gohnermeier, A.; Kaiser, W. *Nat. Photon.* **2007**, *1*, 629-631.
87. Wagner, R. S.; Ellis, W. C. *App. Phys. Lett.* **1964**, *4*, 89-90.
88. Trentler, T. J.; Hickman, K. M.; Goel, S. C.; Viano, A. M.; Gibbons, P. C.; Buhro, W. E. *Science* **1995**, *270*, 1791-1794.
89. Hanrath, T.; Korgel, B. A. *J. Am. Chem. Soc.* **2002**, *124*, 1424-1429.
90. VLS nanowires are typically grown in a chemical vapor deposition method wherein a substrate is coated with a thin layer of the seed metal and placed in a high temperature reature under high vacuum. The organometalic precursor is then introduced, and the reaction mechanism follows the description in the main text.
91. Wang, F.; Yu, H.; Li, J.; Hang, Q.; Zemlyanov, D.; Gibbons, P. C.; Wang; Janes, D. B.; Buhro, W. E. *J. Am. Chem. Soc.* **2007**, *129*, 14327-14335.
92. Heitsch, A. T.; Hessel, C. M.; Akhavan, V. A.; Korgel, B. A. *Nano Lett.* **2009**, *9*, 3042-3047.
93. Hessel, C. M.; Heitsch, A. T.; Korgel, B. A. *Nano Lett.* **2009**, *10*, 176-180.

94. Chockla, A. M.; Harris, J. T.; Korgel, B. A. *Chem. Mater.* **2011**, *23*, 1964-1970.
95. Kan, S.; Mokari, T.; Rothenberg, E.; Banin, U. *Nat. Mater.* **2003**, *2*, 155-158.
96. Wang, F.; Buhro, W. E. *J. Am. Chem. Soc.* **2007**, *129*, 14381-14387.
97. Alivisatos, A. P. *Science* **1996**, *271*, 933-937.
98. Smith, D. A.; Holmberg, V. C.; Rasch, M. R.; Korgel, B. A. *J. Phys. Chem. C* **2010**, *114*, 20983-20989.
99. Grebinski, J. W.; Hull, K. L.; Zhang, J.; Kosel, T. H.; Kuno, M. *Chem. Mater.* **2004**, *16*, 5260-5272.
100. Puthussery, J.; Lan, A.; Kosel, T. H.; Kuno, M. *ACS Nano* **2008**, *2*, 357-367.
101. Fanfair, D. D.; Korgel, B. A. *Cryst. Growth Des.* **2005**, *5*, 1971-1976.
102. Shweky, I.; Aharoni, A.; Mokari, T.; Rothenberg, E.; Nadler, M.; Popov, I.; Banin, U. *Mater. Sci. Eng. C* **2006**, *26*, 788-794.
103. Goebel, J. A.; Black, R. W.; Puthussery, J.; Giblin, J.; Kosel, T. H.; Kuno, M. *J. Am. Chem. Soc.* **2008**, *130*, 14822-14833.
104. Wang, F.; Buhro, W. E. *Small* **2010**, *6*, 573-581.
105. Ouyang, L.; Maher, K. N.; Yu, C. L.; McCarty, J.; Park, H. *J. Am. Chem. Soc.* **2006**, *129*, 133-138.
106. Yu, H.; Li, J. B.; Loomis, R. A.; Wang, L. W.; Buhro, W. E. *Nat. Mater.* **2003**, *2*, 517-520.
107. Zhen, L.; Andreas, K.; Anton, M.; Alf, M. *Small* **2008**, *4*, 1698-1702.
108. Fanfair, D. D.; Korgel, B. A. *Cryst. Growth. Des.* **2008**, *8*, 3246-3252.
109. Dong, A.; Wang, F.; Daulton, T. L.; Buhro, W. E. *Nano Lett.* **2007**, *7*, 1308-1313.
110. Chou, N. H.; Oyler, K. D.; Motl, N. E.; Schaak, R. E. *Chem. Mater.* **2009**, *21*, 4105-4107.
111. Lambert, T. N.; Andrews, N. L.; Gerung, H.; Boyle, T. J.; Oliver, J. M.; Wilson, B. S.; Han, S. M. *Small* **2007**, *3*, 691-699.
112. Heath, J. R.; Shiang, J. J.; Alivisatos, A. P. *J. Chem. Phys.* **1994**, *101*, 1607-1615.
113. She, M.; King, T.-J. *IEEE Tran. Electron Dev.* **2003**, *50*, 1934-1940.
114. Holman, Z. C.; Kortshagen, U. R. *Langmuir* **2009**, *25*, 11883-11889.
115. Claey, C. *Germanium-Based Technologies: From Materials to Devices* **2007**.
116. Hanrath, T.; Korgel, B. A. *J. Phys. Chem. B* **2005**, *109*, 5518-5524.

117. Smith, D. A.; Holmberg, V. C.; Korgel, B. A. *ACS Nano* **2010**, *4*, 2356-2362.
118. Smith, D. A.; Holmberg, V. C.; Lee, D. C.; Korgel, B. A. *J. Phys. Chem. C* **2008**, *112*, 10725-10729.
119. Gerung, H.; Boyle, T. J.; Tribby, L. J.; Bunge, S. D.; Brinker, C. J.; Han, S. M. *J. Am. Chem. Soc.* **2006**, *128*, 5244-5250.
120. Zhaoping, L.; Kai, S.; Wen-Bin, J.; Dan, X.; Yen-Fu, L.; Jiye, F. *Chemistry* **2009**, *15*, 4546-4552.
121. Yujie, X.; Yi, X.; Zhengquan, L.; Xiaoxu, L.; Shanmin, G. *Chemistry* **2004**, *10*, 654-660.
122. Xi, L.; Tan, W. X. W.; Boothroyd, C.; Lam, Y. M. *Chem. Mater.* **2008**, *20*, 5444-5452.
123. Yu, H.; Li, J.; Loomis, R. A.; Gibbons, P. C.; Wang, B.; Buhro, W. E. *J. Am. Chem. Soc.* **2003**, *125*, 16168-16169.
124. Kuno, M.; Ahmad, O.; Protasenko, V.; Bacinello, D.; Kosel, T. H. *Chem. Mater.* **2006**, *18*, 5722-5732.
125. Liu, S.; Guo, X.; Li, M.; Zhang, W.-H.; Liu, X.; Li, C. *Angew. Chem. Int. Ed.* **2011**, *50*, 12050-12053.
126. Cho, K.-S.; Talapin, D. V.; Gaschler, W.; Murray, C. B. *J. Am. Chem. Soc.* **2005**, *127*, 7140-7147.
127. Wang, Z.; Zhao, B.; Zhang, F.; Mao, W.; Qian, G.; Fan, X. *Mater. Lett.* **2007**, *61*, 3733-3735.
128. Zhang, L.; Yu, J. C.; Mo, M.; Wu, L.; Kwong, K. W.; Li, Q. *Small* **2005**, *1*, 349-354.
129. Mičić, O. I.; Sprague, J.; Lu, Z.; Nozik, A. J. *App. Phys. Lett.* **1996**, *68*, 3150-3152.
130. Mičić, O. I.; Jones, K. M.; Cahill, A.; Nozik, A. J. *J. Phys. Chem. B* **1998**, *102*, 9791-9796.
131. Duan, X.; Huang, Y.; Cui, Y.; Wang, J.; Lieber, C. M. *Nature* **2001**, *409*, 66-69.
132. Cros-Gagneux, A.; Delpech, F.; Nayral, C. I.; Cornejo, A.; Coppel, Y.; Chaudret, B. *J. Am. Chem. Soc.* **2010**, *132*, 18147-18157.
133. Moreels, I.; Martins, J. C.; Hens, Z. *Sensor. Actuat. B-Chem.* **2007**, *126*, 283-288.
134. Hens, Z.; Moreels, I.; Martins, J. C. *ChemPhysChem* **2005**, *6*, 2578-2584.

135. Guzelian, A. A.; Katari, J. E. B.; Kadavanich, A. V.; Banin, U.; Hamad, K.; Juban, E.; Alivisatos, A. P.; Wolters, R. H.; Arnold, C. C.; Heath, J. R. *J. Phys. Chem.* **1996**, *100*, 7212-7219.
136. Mičić, O. I.; Ahrenkiel, S. P.; Nozik, A. J. *App. Phys. Lett.* **2001**, *78*, 4022-4024.
137. Dick, K. A.; Caroff, P.; Bolinsson, J.; Messing, M. E.; Johansson, J.; Deppert, K.; Wallenberg, L. R.; Samuelson, L. *Semicond. Sci. Tech.* **2010**, *25*, 024009.
138. Caroff, P.; Dick, K. A.; Johansson, J.; Messing, M. E.; Deppert, K.; Samuelson, L. *Nat. Nanotechnol.* **2009**, *4*, 50-55.
139. Algra, R. E.; Verheijen, M. A.; Borgstrom, M. T.; Feiner, L. F.; Immink, G.; van Enkevort, W. J. P.; Vlieg, E.; Bakkers, E. *Nature* **2008**, *456*, 369-372.
140. Kriegner, D.; Wintersberger, E.; Kawaguchi, K.; Wallentin, J.; Borgstrom, M. T.; Stangl, J. *Nanotechnology* **2011**, *22*, 425704.
141. Algra, R. E.; Vonk, V.; Wermeille, D.; Szweryn, W. J.; Verheijen, M. A.; van Enkevort, W. J. P.; Bode, A. A. C.; Noorduyn, W. L.; Tancini, E.; de Jong, A. E. F.; Bakkers, E. P. A. M.; Vlieg, E. *Nano Lett.* **2011**, *11*, 44-48.
142. Xiong, Q.; Wang, J.; Eklund, P. C. *Nano Lett.* **2006**, *6*, 2736-2742.
143. Akiyama, T.; Sano, K.; Nakamura, K.; Ito, T. *Jpn. J. App. Phys.* **2006**, *45*, L275-L278.
144. Chan, C. K.; Patel, R. N.; O'Connell, M. J.; Korgel, B. A.; Cui, Y. *ACS Nano* **2010**, *4*, 1443-1450.
145. Chockla, A. M.; Harris, J. T.; Akhavan, V. A.; Bogart, T. D.; Holmberg, V. C.; Steinhagen, C.; Mullins, C. B.; Stevenson, K. J.; Korgel, B. A. *J. Am. Chem. Soc.* **2011**, *133*, 20914-20921.
146. Yuan, L.; Liu, H. K.; Maarroof, A.; Konstantinov, K.; Liu, J.; Cortie, M. J. *New Mater. Electr. Sys.* **2007**, *10*, 95-99.
147. Taillades, G.; Benjelloun, N.; Sarradin, J.; Ribes, M. *Solid State Ionics* **2002**, *152-153*, 119-124.

Chapter 2: Si Nanowire Fabric: an Electrode Material for Li-Ion Batteries[§]

2.1 INTRODUCTION

The demand for portable electronic devices has been steadily rising, in part because of the increasing global dependence on mobile information, entertainment, and communication. These devices require portable power sources. Lithium ion (Li^+) batteries (LIBs) have become widely used because of their high energy density, but there is a strong desire to improve many aspects of LIBs, including cost, safety, energy density, capacity, cycle life, and rate capability.¹ The recent interest in using LIBs in automobiles has heightened the search for new materials that can achieve higher energy density and prolonged cycle life.²

A LIB functions by shuttling Li^+ between the anode and cathode. The typical cathode in a commercially available LIB is composed of a lithium metal oxide (i.e., LiCoO_2) and the anode of graphite. The LIB capacity is limited in part by the intercalation of Li^+ by the graphitic anode material; thus, higher capacity batteries require anode materials that can accommodate more Li^+ . The theoretical capacity of the graphite anode is 372 mA h g^{-1} .^{3, 4} Lithium-alloying materials have the potential for significantly higher storage capacities. For instance, Si alloys with Li^+ at room temperature to form $\text{Li}_{15}\text{Si}_4$, which corresponds to a much higher theoretical capacity of 3579 mA h g^{-1} .⁵⁻⁷ However, Si undergoes an enormous volume expansion of nearly 300% when fully lithiated.⁸ Bulk crystalline Si cannot tolerate the stresses associated with these lithiation / delithiation cycles and crumbles, resulting in battery failure.⁹ On the other hand, Si nanostructures have been found to tolerate extreme volume changes with cycling.^{7, 10-21} Thin Si films have realized capacities above 2000 mA h g^{-1} .^{12, 13, 19} Si nanoparticles have

[§] This chapter appears in *Journal of the American Chemical Society* **2011**, *133*, 20914-20921.

also been explored, but with overall specific capacities that have been limited by the need for a conductive carbon matrix to ensure electrical contact with the electrode.^{11, 18} Si nanowires have been promising.^{7, 14-17, 20, 21} For example, Cui and co-workers achieved a capacity of 2725 mA h g⁻¹ with very good stability, retaining more than 1400 mA h g⁻¹ after 700 cycles using an interconnected amorphous Si hollow nanosphere thin-film electrode.²² Unfortunately, these electrode materials are very expensive at present and cannot be produced in the significant quantities needed for commercial LIB applications.^{12, 13, 19}

Solvent-based processes for nanowire synthesis, such as supercritical-fluid–liquid–solid (SFLS) and solution–liquid–solid (SLS) growth, can produce large amounts of Si nanowires at relatively low cost.²³⁻²⁸ In a 10 mL laboratory-scale reactor, hundreds of milligrams of nanowires with lengths of >100 μm can be produced in a few hours,^{23, 26} which is sufficient to create nanowire-based nonwoven fabrics several inches on a side.²⁷ These nanowires exhibit excellent mechanical properties, are highly flexible, and have strength-to-weight ratios greater than those of both carbon fiber and Kevlar.^{27, 29} This fabric material is thin (thickness of 50–150 μm) and has a paper like appearance and feel. The first fabrics consisting entirely of one-dimensional nanomaterials were made from carbon nanotubes (CNTs) because of their mechanical strength, flexibility, and large aspect ratio and the ability to produce the material in macroscopic quantities.^{30, 31} Metal oxide nanowires of cryptomelane-M ($K_{2-x}Mn_8O_{16}$) that could be synthesized in large quantities by hydrothermal methods have been used to form macroscopic freestanding membranes.³² Recently, SFLS synthesis has been used to produce Ge nanowire fabric.^{27, 33} Fabric-like materials consisting of CNTs and graphene sheets have recently been explored as electrodes for flexible LIB applications^{11, 21, 34-37} and as electrode supports for other materials, as in graphene–silicon,^{11, 37} CNT–Si nanowire,^{21, 34} and CNT–Li₄Ti₆O₁₂

electrodes.^{21, 35} Here we demonstrate the creation of a Si nanowire fabric and show that it can function as a standalone anode material without the need for additional conductive fillers (activated carbon) or polymeric binders. For good battery performance, it was necessary to convert a thin polyphenylsilane³⁸ coating on the Si nanowires to carbon by annealing under forming gas (7% H₂ in N₂) at 900°C. This thin layer provides the electrical conductivity needed for efficient Li⁺ charging and discharging of the layer. The LIB performance of the Si nanowire fabric and the role of the shell on the cycling behavior are reported.

2.2 EXPERIMENTAL SECTION

2.2.1 Materials

All chemicals were used as received without further purification. Dodecanethiol (DDT, ≥98%), hydrogen tetrachloroaurate trihydrate (≥99.9%), sodium borohydride (≥98%), toluene (anhydrous, ACS grade, 99.8%), ethanol (99.9%), tetraoctylammonium bromide (TOAB, 98%), and chloroform (99.8%) were purchased from Sigma-Aldrich. Monophenylsilane (MPS, >95%) was obtained from Gelest, and LiPF₆ [1.0 M in a 1:1 ethylcarbonate (EC, >99.95%)/ diethyl carbonate (DEC, >99.98%) mixture] was purchased from Novolyte. For battery assembly, Celgard 2400 membranes (25 μm, purchased from Celgard) were used as separators, and Li metal (99.9%) was obtained from Alfa Aesar.

2.2.2 Silicon Nanowire Synthesis

Si nanowires were synthesized by gold (Au) nanocrystal-seeded SFLS growth in toluene using the synthetic procedures detailed in previous reports.³⁸ Briefly, MPS and 2 nm Au nanoparticles³⁹ were mixed together in a 290:1 Si: Au mole ratio and diluted with anhydrous toluene to achieve an MPS concentration of 156 mM. Nanowires were then

grown in a flow-through sealed titanium reactor at 490°C and 10.3 MPa. After the reaction, the nanowires were collected from the reactor walls and washed with chloroform (10 mL) and ethanol (5 mL) several times via centrifugation at 8000 rpm. The nanowires were then dispersed in chloroform to a concentration of 5 mg mL⁻¹ and stored in a vial under ambient conditions prior to use.

2.2.3 Material Characterization

Scanning electron microscopy (SEM) images were acquired using a Zeiss Supra 40 scanning electron microscope with an in-lens arrangement, a working voltage of 5 keV, and a working distance of 5 mm. SEM samples were imaged on silicon wafers obtained from SEH. Transmission electron microscopy (TEM) images were digitally acquired using either a FEI Tecnai Spirit BioTwin transmission electron microscope operated at 80 kV or a JEOL 2010F field-emission microscope operated at 200 kV. TEM samples were prepared by drop-casting from chloroform dispersions onto 200 mesh lacey carbon copper TEM grids (Electron Microscopy Sciences).

X-ray diffraction (XRD) was carried out using a Rigaku R-Axis Spider diffractometer with an image-plate detector and Cu K_α radiation ($\lambda = 1.5418 \text{ \AA}$) operated at 40 kV and 40 mA. Measurements were taken on samples on a 0.5 mm nylon loop. Samples were scanned for 10 minutes while rotating at 1 deg/s under ambient conditions. The data were integrated from $2\theta = 20$ to 80° . Background scattering from the nylon loop was subtracted from the sample measurement.

X-ray photoelectron spectroscopy (XPS) was performed on a Kratos photoelectron spectrophotometer with monochromatic Al K_α radiation (1487 eV). The Si nanowire fabric was secured on the experimental tray using double-sided Cu tape. Spectra were collected at 0.1 eV intervals using an integration time of 800 ms through a

tungsten coil set at 4.8 V bias with respect to the sample. Data were collected continuously under high vacuum (10^{-9} Torr). The effect of sample charging on the XPS data was corrected by shifting the Si^0 $2p_{3/2}$ peak to a binding energy of 99.3 eV.

The XPS results were analyzed using CasaXPS software. Background subtraction was done using a Shirley background model. Peak areas were deconvoluted as Voigt functions (30% Gaussian character). The Si2p region was deconvoluted as Si^0 $2p_{3/2}$, Si^0 $2p_{1/2}$, Si^{1+} , Si^{2+} , Si^{3+} , and Si^{4+} peaks placed at 99.3, 99.9, 100.1, 101.1, 102.1, and 103.2 eV, respectively. The zero-valent Si spin splits were assumed to have the same full width at half-maximum (FWHM), and the area of the $2p_{1/2}$ peak was set as half the area of the $2p_{3/2}$ peak. Similarly, one FWHM value was used for all of the other oxide peaks; however, for simplicity, the other oxidative states were not divided into their respective spin splits. Values for the FWHM of the oxidized states were constrained by placing the FWHM between 1.8 and 2.2 times the zero-valent peaks.

The C1s region was deconvoluted into three peaks placed at 284, 284.7, and 285.5 eV. These binding energies correspond to Si–C, C–C, and C–O bonding, respectively. The O1s region was deconvoluted into two peaks. The first peak, placed at 532.5 eV, corresponds to SiO_2 and C–O bonding. The second peak, placed at 533.9 eV, relates to O_2 adsorbed on the surface of the wires. Only one FWHM was used to generate the peaks for each species of C and O.

Raman spectroscopy was performed using a Renishaw inVia microscope equipped with a 514.5 nm argon ion laser in backscattering configuration. The Stokes Raman signal at 521 cm^{-1} for single-crystalline bulk Si oriented with the [110] direction normal to the laser was used to calibrate the instrument. The beam was focused using an optical microscope with a 50 \times objective lens. Spectra were taken on freestanding sheets

of nanowire fabric lying on glass slides by single scans from 100 to 2000 cm^{-1} at 5% laser power (0.2 mW).

2.2.4 LIB Anode Processing and Battery Testing

Si nanowire fabric was prepared by sonicating nanowire dispersions (5–10 mg mL^{-1} Si nanowires in chloroform) for 1 hour. The dispersions were drop-cast into a Teflon trough and left overnight to dry. After drying, the fabric was peeled from the trough using tweezers (and a thin razor blade wedged between the fabric and trough bed when necessary) and cut into 1 cm \times 1 cm squares that were loaded into quartz boats and heated under a moderate flow of forming gas in a tube furnace.

Batteries were prepared within an argon-filled glovebox using a Cu foil current collector. The Si nanowire fabric was placed on the Cu current collector to serve as the anode material. The electrolyte was a 1.0 M solution of LiPF_6 in a 1:1 w/w EC : DEC mixture (Novolyte). A few drops of electrolyte were deposited over the nanowire fabric. A Celgard 2400 separator membrane (25 μm thick) was then added, followed by Li metal foil (99.9%, Alfa Aesar) as the counter electrode. Galvanostatic measurements were made using an Arbin BT-2143 test unit that was cycled between 3 V and 10 mV vs. Li/Li^+ at a rate of $C/20$ ($C = 3579 \text{ mA h g}^{-1}$)⁵⁻⁷.

After cycling, the batteries were disassembled, and the anode was cleaned by soaking the fabric in acetonitrile overnight and then rinsing with 0.5 M sulfuric acid for 1 minute, until bubbling subsided. The anode was then placed in a vial and soaked in isopropyl alcohol (IPA) for several minutes. The IPA was decanted, and the anode was soaked two more times in the same way and then dried in air before SEM and TEM imaging.

2.3 RESULTS AND DISCUSSION

2.3.1 Si Nanowire Fabric

Figure 2.1 shows a photograph and SEM images of Si nanowire fabric made by casting concentrated dispersions of SFLS-grown nanowires in toluene into a Teflon trough. The fabric is composed of highly entangled nanowires. It is $\sim 50\ \mu\text{m}$ thick and relatively porous, containing $\sim 90\%$ void volume. The Si nanowire fabric is pliable with good mechanical integrity. Even though the nanowires are single crystalline Si, a material that is brittle in bulk form, they are mechanically flexible and strong because of their narrow diameter.²⁷

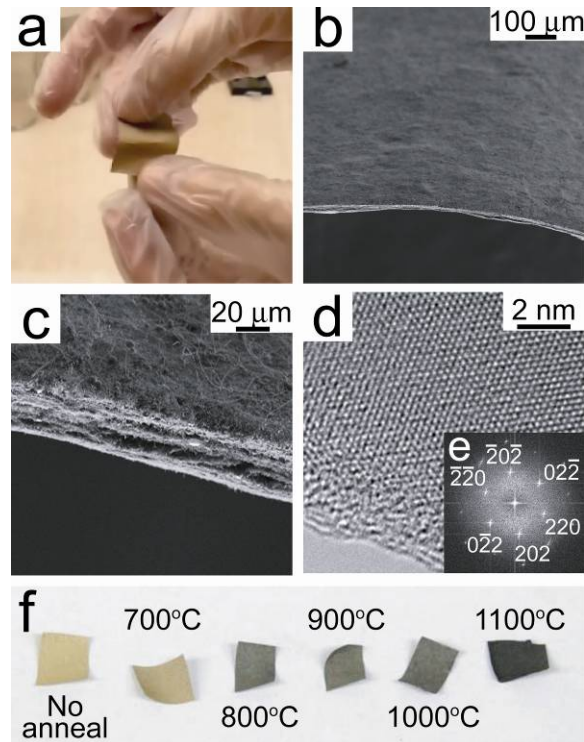


Figure 2.1: (a) Photograph of mechanically flexible Si nanowire fabric. (b, c) SEM images of the fabric. (d) High-resolution TEM (HRTEM) image of a Si nanowire showing its crystallinity. (e) Fast Fourier transform (FFT) pattern from the HRTEM image in (d) showing a $\langle 110 \rangle$ growth direction. (f) Photographs of Si nanowire fabrics annealed at the indicated temperatures under a reducing atmosphere.

2.3.2 Electrochemical Performance of Si Nanowire Fabric Anodes

1 cm × 1 cm squares of Si nanowire fabric were tested as standalone Si-based anode materials without added conductive carbon or binder for a LIB. The as-made Si nanowire fabric performed poorly. As shown in Figure 2.2a, the capacity in the first cycle was just under 600 mA h g⁻¹ but then dropped to nearly zero after only a couple of cycles. Tests of the electrical conductivity showed that the nanowire fabric is electrically insulating with a conductivity of ~0.2 nS m⁻¹. The nanowire fabric must be sufficiently conductive to facilitate efficient lithium alloying with Si.⁴⁰

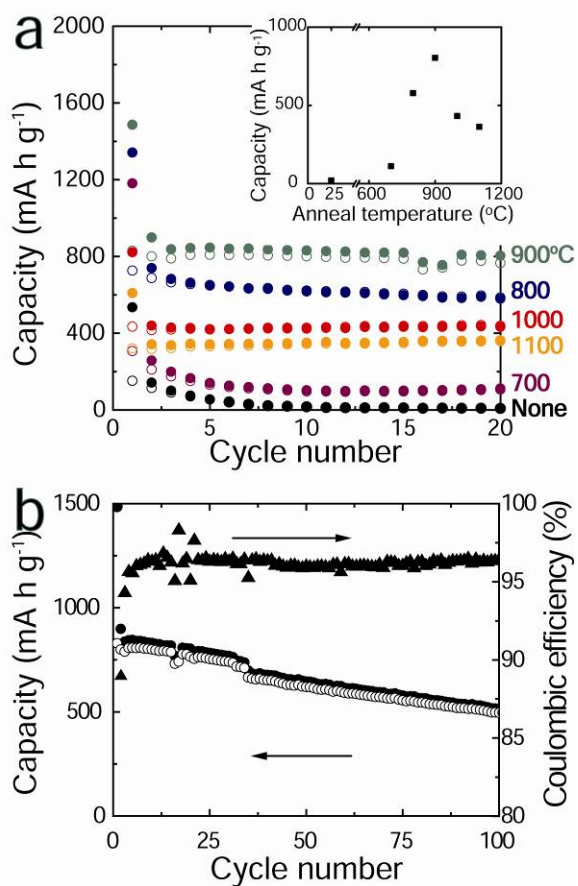


Figure 2.2: (a) Galvanostatic cycling tests of Si nanowire fabric before and after annealing at 700, 800, 900, 1000, and 1100°C at a cycle rate of $C/20$ ($C = 3579 \text{ mA h g}^{-1}$).⁵⁻⁷ The inset shows discharge capacities after 20 cycles for batteries with nanowire fabric anodes annealed at various temperatures. (b) Galvanostatic cycling of a Si nanowire fabric anode annealed at 900°C.

The electrical conductivity of the Si nanowire fabric was enhanced significantly by annealing under a reducing atmosphere at temperatures greater than 700°C. Figure 2.3 shows current–potential curves for nanowire fabric annealed at various temperatures. Annealing at temperatures between 700 and 1000°C led to conductivities ranging from 70 to 150 nS/m. Fabric annealed at 1100°C had a conductivity of 1400 nS m⁻¹.

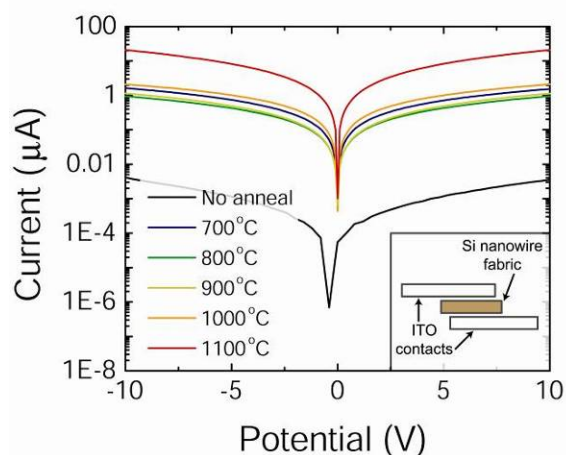


Figure 2.3: Current–potential measurements of Si nanowire fabric placed between two indium tin oxide (ITO) electrodes (inset). The nanowire fabric was annealed under a reducing atmosphere at the indicated temperatures. Measurements were made using $\sim 150\ \mu\text{m}$ thick fabric samples with a contact area of $1\ \text{cm}^2$.

Figure 2.1f shows photographs of Si nanowire fabric after annealing under forming gas at various temperatures. The fabric turns increasingly black with increasing annealing temperature. The Si nanowires produced by the SFLS process using monophenylsilane as a reactant have a thin polyphenylsilane shell on their surface.³⁸ Annealing under a reducing environment transforms this shell material to carbon, which provides the significantly enhanced electrical conductivity. When the nanowires are annealed in the presence of oxygen and water, the shell material oxidizes to a defective and insulating SiO_2 layer.

The annealed Si nanowire fabric performed well in galvanostatic cycling tests. Figure 2.2a shows the capacity (with cycling at a $C/20$ rate, where $C = 3579\ \text{mA h g}^{-1}$, corresponding to $\text{Li}_{15}\text{Si}_4$)⁵⁻⁷ for Si nanowire fabric annealed under a reducing atmosphere at various temperatures. All of the nanowire samples exhibited a large initial irreversible capacity loss during the first cycle, which is typical for Si anode materials and results from formation of solid–electrolyte interphase (SEI) layers upon cycling to low

potentials. The nanowire fabric annealed to 700°C performed better than the as-made nanowires, but the capacity was still very limited. On the other hand, nanowires annealed at 900°C performed quite well and retained a cycling capacity of 800 mA h g⁻¹ after 20 cycles. As shown in Figure 2.2b, the capacity was still higher than 500 mA h g⁻¹ after 100 cycles. When the nanowires were annealed at even higher temperature (>900°C), they did not perform as well. The Figure 2.2a inset shows a plot of the discharge capacity after 20 cycles for Si nanowire fabric electrodes annealed at various temperatures. The highest performance was achieved with nanowires annealed at 900°C. Table 2.1 summarizes the capacity retention data of the Si nanowire fabric annealed at various temperatures.

Table 2.1: Summary of the capacity retention Si nanowire fabric anodes annealed at the indicated temperatures.

Temperature (°C)	Capacity (m Ah g ⁻¹)			Retention (%)	
	1 st Cycle	2 nd Cycle	20 th Cycle	C _{ret1} [§]	C _{ret2} [†]
No anneal	534	142	8	2	6
700°C	1180	257	111	9	43
800°C	1341	738	579	43	78
900°C	1485	898	804	54	89
1000°C	821	439	433	57	99
1100°C	608	341	363	60	106

[§]Amount of charge capacity retained after 20 cycles compared to the first charging cycle.

[†]Amount of charge capacity retained after 20 cycles compared to the second charging cycle.

Figure 2.4 shows the constant-current voltage profiles and differential capacity (dQ/dV) curves for the first and 20th cycles of batteries with Si nanowires annealed at 800, 900, 1000, and 1100°C. Each constant-current voltage profile shows two plateaus during the charge cycle, corresponding to the lithiation of crystalline silicon and the formation of the Li₁₅Si₄ phase.⁶ The discharge cycles have a steeper slope than the charge cycles (corresponding to a broader peak in the dQ/dV curves), indicating that delithiation occurs over a relatively broad range of potentials, which is consistent with amorphous

silicon. The dQ/dV plots provide a better illustration of the potentials at which the lithiation and delithiation events occur. Each of the first-cycle charge curves in the dQ/dV plots shows a peak between 150 and 200 mV, corresponding to lithiation of crystalline Si. This peak is shifted slightly in the 900°C sample (Figure 2.4d) to ~250 mV. A peak near 50 mV is also observed for each sample and is attributed to the formation of $\text{Li}_{15}\text{Si}_4$.⁶ By the 20th cycle, the first lithiation event has shifted to ~300 mV, which falls in the range expected for lithiation of amorphous Si (a-Si).⁴¹ The second lithiation event has a significantly reduced intensity, indicating a marked consumption of crystalline silicon. The first discharge cycle shows a prominent peak at ~450 mV, which corresponds to the delithiation potentials of a-Si and $\text{Li}_{15}\text{Si}_4$.⁴¹ Lithium extraction during the 20th cycle occurs at the a-Si delithiation potential (300 mV).⁴¹

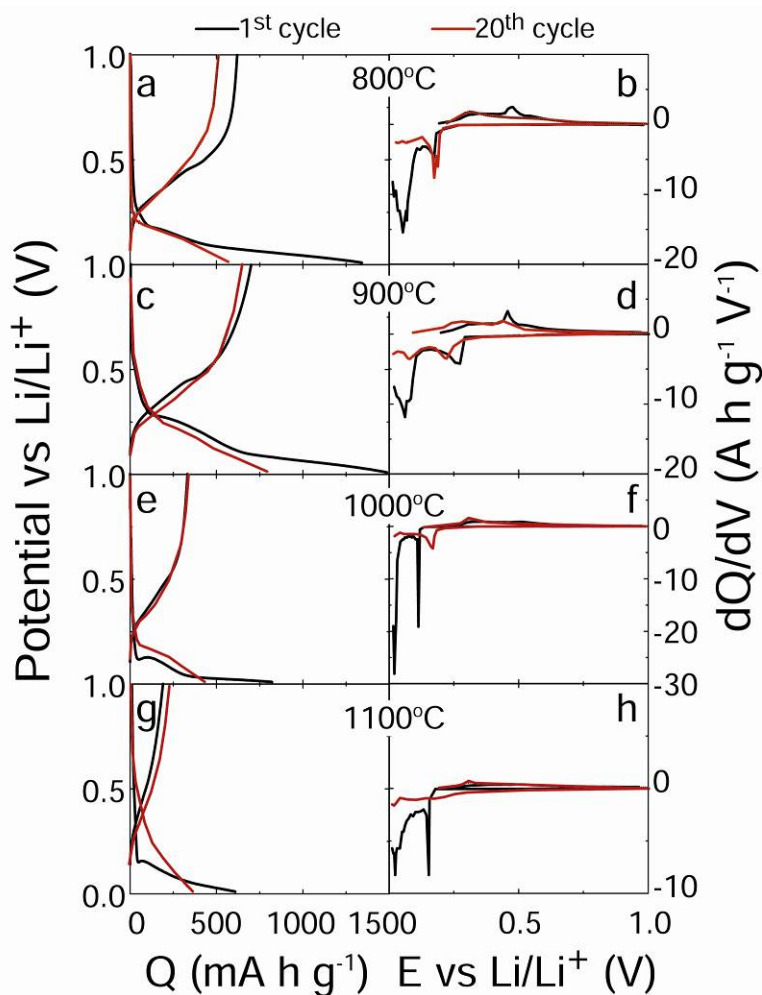


Figure 2.4: Constant-current voltage profiles for Si nanowire fabric anodes annealed at (a) 800, (c) 900, (e) 1000, and (g) 1100°C with corresponding differential capacity curves (b, d, f, and h, respectively).

2.3.3 Composition of the Carbonaceous Shell on the Si Nanowires

Raman spectroscopy, XPS, and XRD were used to determine the composition of the shell material formed after annealing the nanowires under forming gas. Figure 2.5 shows Raman spectra of nanowires as-made and after annealing at various temperatures. The as-made nanowires exhibit the characteristic Si transverse optical (TO) band at 521 cm^{-1} along with a smaller peak at 495 cm^{-1} that is most likely related to stacking faults.⁴²⁻

⁴⁵ After annealing of the nanowires at 700°C, the nanowire spectra still have the characteristic Si-related peaks, but there is a significant sloping baseline due to fluorescence from the sample. This fluorescence is due to a chemical change in the shell material that is probably related to the phenyl species. With increasing annealing temperature, the fluorescence signal diminishes in intensity. Nanowires annealed at 900°C and above have almost no fluorescent background. The nanowires annealed at 800°C and higher exhibit two prominent bands at ~ 1350 and ~ 1600 cm^{-1} , corresponding to disordered (D) and graphitic (G) carbon.⁴⁶⁻⁴⁹ These peaks are not present in the Raman spectra of the as-made nanowires nor in the spectra of the nanowires annealed at 700°C. It appears that the fluorescent species formed as a result of annealing at 700°C is converted to the carbon that forms at higher annealing temperatures.

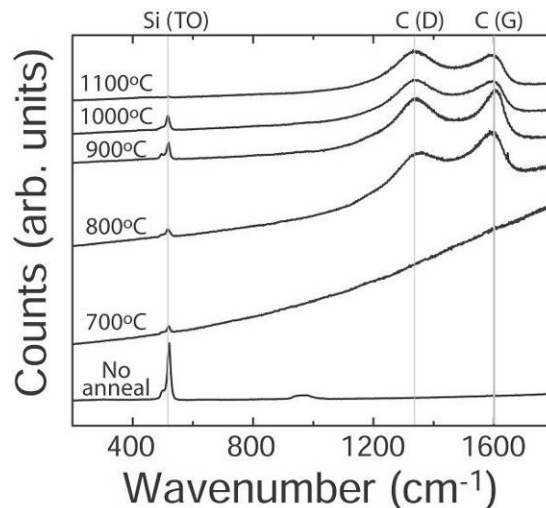


Figure 2.5: Raman spectra of Si nanowire fabric before and after annealing under a reducing atmosphere at various temperatures. The Si (TO) peak at 521 cm^{-1} and carbon-related (D) and (G) bands at 1380 cm^{-1} and 1560 cm^{-1} are labeled.

The much improved battery performance of the Si nanowire fabric after annealing results from the formation of the electrically conductive carbon layer on the nanowires. It is obvious from the change in color of the nanowire fabric from its typical pale-yellow to black that the shell material has been converted to carbon, as confirmed by the Raman spectra. But why does the battery performance diminish when the nanowires are heated above 900°C? The Raman spectra show that the same carbon species that helped to achieve good battery response are still present on the nanowires annealed at 1000 and 1100°C, and the electrical conductivity of the nanowires is also high (Figure 2.3). However, XPS (Figures 2.6 and 2.7) and XRD (Figure 2.8) reveal that a significant amount of Si oxidation and some SiC formation occur when the nanowires are annealed at these higher temperatures. The XRD patterns in Figure 2.8 show that the nanowires are still composed predominantly of crystalline Si after annealing, indicating that the oxidation and carbide formation occurs only on the nanowire surface. It appears that residual oxygen or water, most likely contained initially in the poly(phenylsilane) shell, oxidizes the surfaces of the nanowires. Nanowires annealed at 1100°C no longer have a measurable Si⁰ XPS peak, and the entire Si signal corresponds to either Si⁴⁺ or Si²⁺. XRD also indicates that some of the surface carbon reacts with the underlying Si to form SiC. The SiC diffraction peaks are very broad, indicating that the crystalline SiC domains are extremely small, which is consistent with the lack of a SiC-related Raman signal at 790 cm⁻¹.⁵⁰ The Si⁰ signal does not show up in the XPS or Raman spectra because the surface layer becomes too thick to penetrate. Additionally, there is a noticeable decrease in the relative carbon signal in the XPS spectra, along with the appearance of a relatively strong XPS signal at higher binding energy of 285.5 eV, indicating that the carbonaceous layer has also oxidized to some extent (Figures 2.6 and 2.7).

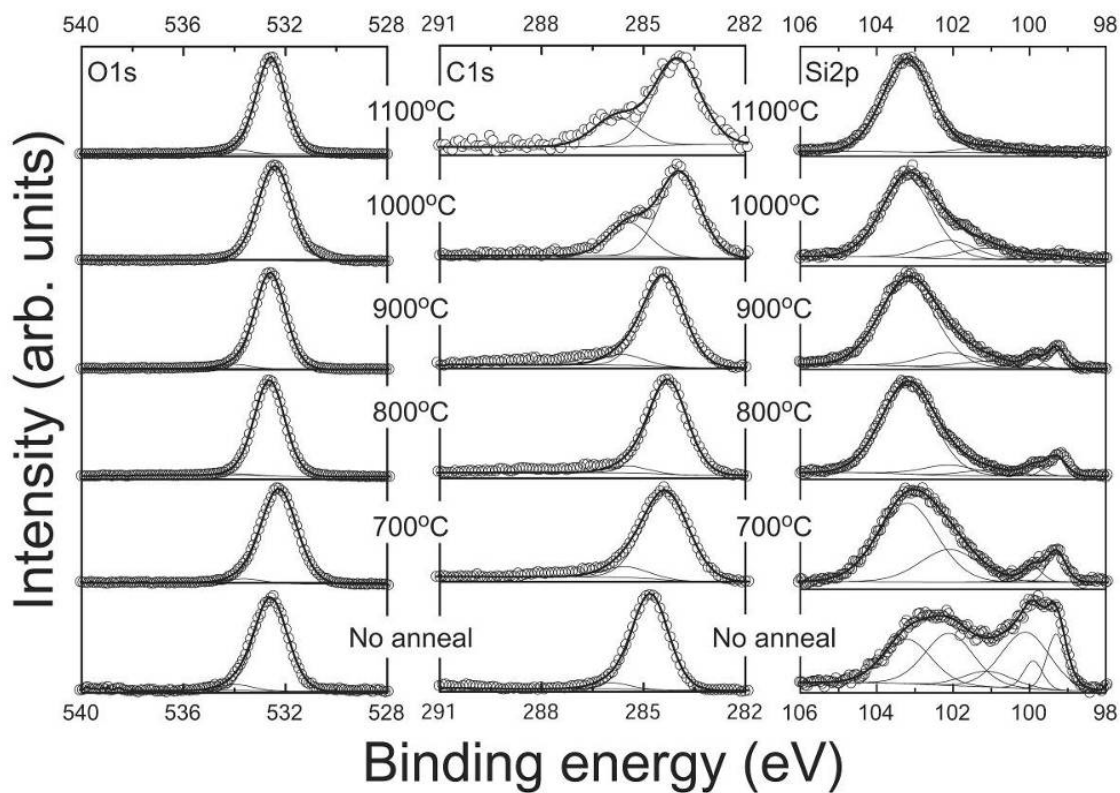


Figure 2.6: XPS data of O1s, C1s and Si2p states of Si nanowire fabric annealed at the temperature indicated. The intensities of all of the peaks are normalized, but the carbon signal decreased significantly relative to the Si signal as the annealing temperature was raised. Figure 2.7 plots the relative amounts of O, C and Si obtained from integration of the XPS peaks. The peak fitting procedures are described in the Experimental Section.

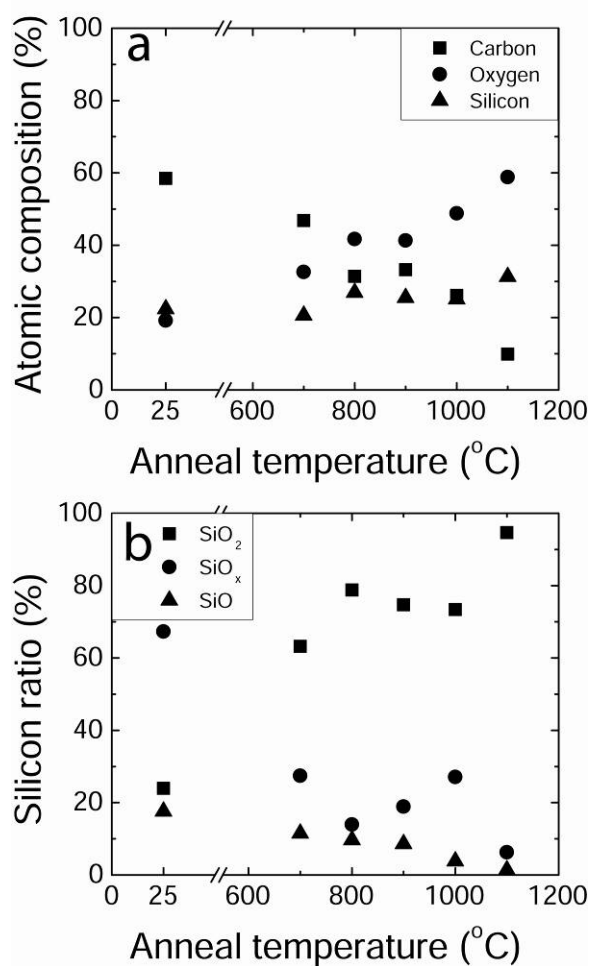


Figure 2.7: Summary of compositional analysis extracted from the XPS data in Figure 2.6: (a) relative Si, C, and O content determined by integrating the O1s, C1s and Si2p peaks; (b) relative SiO, SiO_x, SiO₂ content determined from the Si2p peak structure.

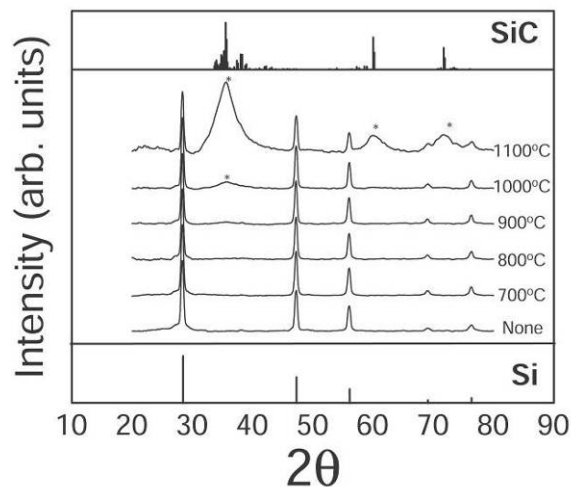


Figure 2.8: XRD of Si nanowire fabric before and after annealing at the indicated temperatures under forming gas. The peak positions corresponding to diamond cubic Si (JCPDS: 00-027-1402) and silicon carbide (SiC, labeled ‘*’. JCPDS: 00-029-1131) are shown.

The oxide and SiC that forms at the nanowire surface after annealing at 1000 and 1100°C is most likely responsible for the reduced lithiation/delithiation of the nanowire fabric. SiC is known to be electrochemically inactive for lithiation,⁵¹ and the oxide layer creates an electrically insulating barrier between the Si core and the electrolyte that is not conducive to battery performance.

2.3.4 Si Nanowire Structure after Electrochemical Cycling

The coin cell housing was disassembled after cycling to examine the structural integrity of the nanowires by SEM and TEM. Figure 2.9 shows SEM images of the Si nanowire fabric that had been annealed at 900°C under forming gas before and after 20 galvanostatic cycles. The nanowires removed from the coin cell housing were covered with an organic surface coating, presumably comprised of ROCO₂Li and ROLi species associated with reduction of the EC/DEC solvent.¹⁴ Rinsing the nanowires with acetonitrile, H₂SO₄, and IPA removed the organic coating (SEI layer). In comparison

with the nanowires prior to electrochemical cycling, the nanowires appear to be larger in diameter. TEM images of the nanowires after galvanostatic cycling showed two different populations of nanowires in nearly equal proportions. As shown in Figure 2.10, some nanowires were amorphous and appeared to have hollowed cores. Others had a crystalline core with a thick amorphous shell. Nanoprobe energy-dispersive spectroscopy (EDS) maps of Si, O, and C composition across the nanowire diameters showed that nanowires with crystalline cores had a higher concentration of Si in the center, with a measurable amount of carbon and oxygen mostly at the nanowire surface. The amorphous nanowires with the hollow cores had a high concentration of Si in the shell, along with C and O. It appears that the structural integrity of these Si nanowires was lost during lithium cycling, with a rupture of the shell. The presence of the nanowires with crystalline cores may indicate that these nanowires were not involved in the electrochemical cycling. These issues require further study.

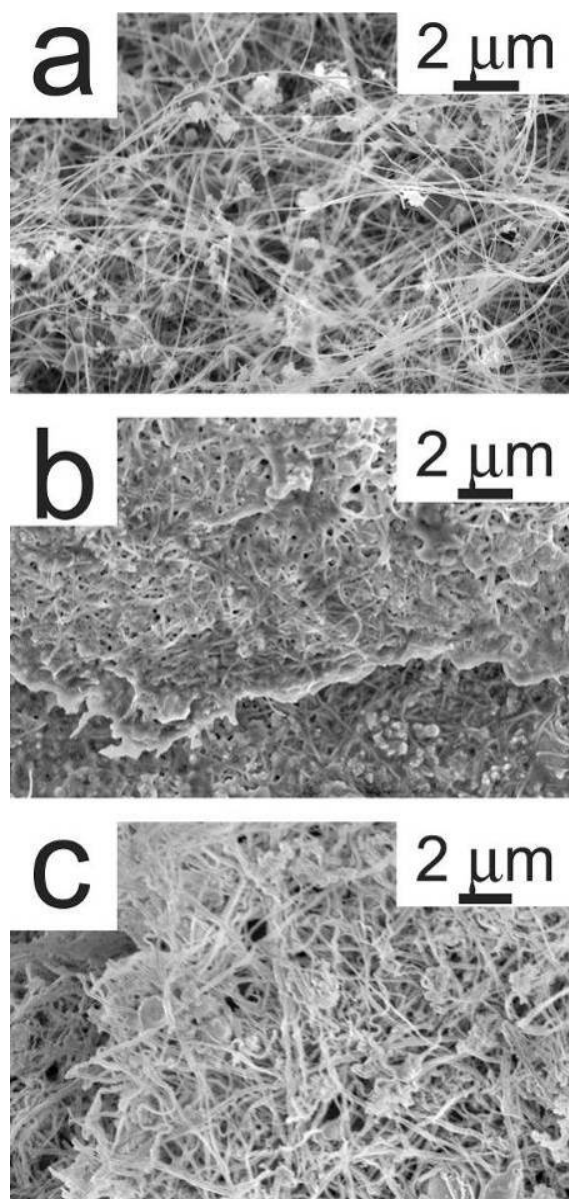


Figure 2.9: SEM images of Si nanowire fabric annealed at 900°C under forming gas: (a) prior to electrochemical cycling; (b) after 20 galvanostatic cycles without washing, and (c) after 20 galvanostatic cycles with washing with acetonitrile, H₂SO₄, and IPA.

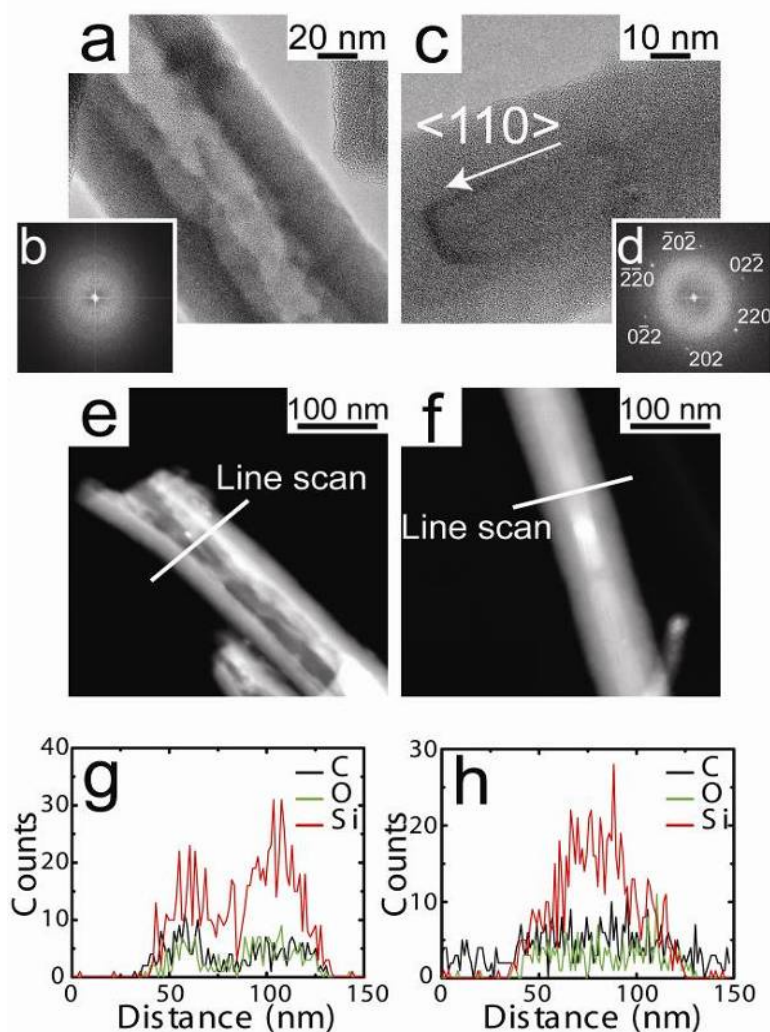


Figure 2.10: TEM and STEM images of Si nanowires annealed at 900°C under forming gas after 20 electrochemical cycles in a lithium cell. Two types of nanowires were observed in nearly equal proportions: (a) amorphous wires that appear to have a hollow core and (c) crystalline nanowires with a thick amorphous shell. (b, d) FFTs of the TEM images in (a) and (c). (e, f) STEM images and (g, h) corresponding EDS line scans at the positions indicated of (e, g) amorphous wires that appear to have a hollow core and (f, h) crystalline nanowires with a thick amorphous shell.

2.4 CONCLUSION

A nonwoven fabric of Si nanowires has been reported. The fabric has the look and feel of tissue paper yet is composed entirely of crystalline Si. Annealing the nanowire

fabric at 900°C under reducing atmosphere (forming gas) leads to good performance as an anode in a Li⁺ battery without addition of carbon binder. The key to their good performance is the presence of a thin electrically conductive carbon layer on the nanowires. When the nanowires were annealed above 900°C, the battery performance diminishes because of the formation of a surface barrier layer of SiO₂ and SiC under the conducting carbonaceous coating that prevents efficient lithiation and delithiation.

This study has shown that the surface composition of Si nanowires plays a critical role in their effectiveness as an anode material in an LIB. Si nanowires can alloy with lithium, but their capacity and cycling stability all rely on the quality of the surfaces. In the present case of Si nanowires grown by the SFLS process with monophenylsilane as a reactant, a residual poly(phenylsilane) shell can be converted from an inactive layer to a coating that enables Si nanowire lithiation/delithiation. The coating is conformal and uniform and does not require a separate materials deposition step. Carbon binder, which would lower the specific capacity of the material, need not be added. This Si nanowire fabric represents a mechanically flexible silicon anode material with the potential to be applied in lightweight paper-based or plastic LIBs. Future research needs to focus on understanding the cycling durability and the factors that limit performance, including the formation and stability of the solid–electrolyte interphase layer. Another issue that requires further consideration is the influence of the nanowire density on performance. Since the nanowire fabric has 90% void volume, the volumetric capacity of the nanowire fabric is relatively low. The specific capacity of 800 mA h g⁻¹ corresponds to a volumetric capacity of 186 mA h cm⁻³, which is significantly lower than the value for graphite (777–867 mA h cm⁻³). However, it should be possible to increase the volumetric capacities of the nanowire fabric by densifying the films with pressure. An estimation of the maximum volumetric capacity of a densified Si nanowire fabric looks compelling,

with a maximum of $1864 \text{ mA h cm}^{-3}$, which is more than a factor of 2 higher than that of graphite. The influence of volumetric expansion and contraction upon lithiation and delithiation on cycling stability, however, would still need to be understood.

2.5 SUPPORTING INFORMATION

Movies showing the fabrication and handling of Si nanowire fabric. This material is available free of charge via at <http://pubs.acs.org>.

2.6 ACKNOWLEDGMENTS

Authors that contributed to this work include: Justin T. Harris, Vahid A. Akhavan, Timothy D. Bogart, Vincent C. Holmberg, Chet Steinhagen, C. Buddie Mullins, Keith J. Stevenson, and Brian A. Korgel. We thank Kate Collier for HRTEM images of Si nanowires. Financial support of this research was provided in part by the Robert A. Welch Foundation (F-1464) and the Air Force Research Laboratory (FA-8650-07-2-5061). C.B.M. and K.J.S. acknowledge financial support from the Welch Foundation (F-1436 to C.B.M. and F-1529 to K.J.S.). V.C.H. acknowledges the Fannie and John Hertz Foundation and the National Science Foundation Graduate Research Fellowship Program for financial support. Raman spectroscopic characterization was supported as part of the program “Understanding Charge Separation and Transfer at Interfaces in Energy Materials (EFRC: CST)”, an Energy Frontier Research Center funded by the U.S. Department of Energy, Office of Science, Office of Basic Energy Sciences, under Award DE-SC0001091.

2.7 REFERENCES

1. Goodenough, J. B.; Kim, Y. *Chem. Mater.* **2010**, *22*, 587
2. Armand, M.; Tarascon, J. M. *Nature* **2008**, *451*, 652
3. Dahn, J. R.; Zheng, T.; Liu, Y.; Xue, J. S. *Science* **1995**, *270*, 90

4. Winter, M.; Besenhard, J. O.; Spahr, M. E.; Novák, P. *Adv. Mater.* **1998**, *10*, 725
5. Weydanz, W. J.; Wohlfahrt-Mehrens, M.; Huggins, R. A. *J. Power Sources* **1999**, *81*, 237
6. Obrovac, M. N.; Christensen, L. *Electrochem. Solid-State Lett.* **2004**, *7*, A93
7. Chan, C. K.; Peng, H.; Liu, G.; McIlwrath, K.; Zhang, X. F.; Huggins, R. A.; Cui, Y. *Nat. Nanotechnol.* **2008**, *3*, 31
8. Xu, Y. H.; Yin, G. P.; Zuo, P. J. *Electrochim. Acta* **2008**, *54*, 341
9. Boukamp, B. A.; Lesh, G. C.; Huggins, R. A. *J. Electrochem. Soc.* **1981**, *128*, 725
10. Chan, C. K.; Patel, R. N.; O'Connell, M. J.; Korgel, B. A.; Cui, Y. *ACS Nano* **2010**, *4*, 1443
11. Lee, J. K.; Smith, K. B.; Hayner, C. M.; Kung, H. H. *Chem. Commun.* **2010**, *46*, 2025
12. Graetz, J.; Ahn, C. C.; Yazami, R.; Fultz, B. *Electrochem. Solid-State Lett.* **2003**, *6*, A194
13. Kasavajjula, U.; Wang, C.; Appleby, A. J. *J. Power Sources* **2007**, *163*, 1003
14. Chan, C. K.; Ruffo, R.; Hong, S. S.; Huggins, R. A.; Cui, Y. *J. Power Sources* **2009**, *189*, 34
15. Hu, L.; Wu, H.; Hong, S. S.; Cui, L.; McDonough, J. R.; Bohy, S.; Cui, Y. *Chem. Commun.* **2010**, *47*, 367
16. Kang, K.; Lee, H.-S.; Han, D.-W.; Kim, G.-S.; Lee, D.; Lee, G.; Kang, Y.-M.; Jo, M.-H. *Appl. Phys. Lett.* **2010**, *96*, 053110-3
17. Laïk, B.; Eude, L.; Pereira-Ramos, J.-P.; Cojocaru, C. S.; Pribat, D.; Rouvière, E. *Electrochim. Acta* **2008**, *53*, 5528
18. Lee, J.-K.; Kung, M. C.; Trahey, L.; Missaghi, M. N.; Kung, H. H. *Chem. Mater.* **2009**, *21*, 6
19. Maranchi, J. P.; Hepp, A. F.; Kumta, P. N. *Electrochem. Solid-State Lett.* **2003**, *6*, A198
20. Peng, K.; Jie, J.; Zhang, W.; Lee, S.-T. *Appl. Phys. Lett.* **2008**, *93*, 033105-3
21. Huang, R.; Fan, X.; Shen, W.; Zhu, J. *Appl. Phys. Lett.* **2009**, *95*, 133119-3
22. Yao, Y.; McDowell, M. T.; Ryu, I.; Wu, H.; Liu, N.; Hu, L.; Nix, W. D.; Cui, Y. *Nano Lett.* **2011**, *11*, 2949
23. Heitsch, A. T.; Fanfair, D. D.; Tuan, H.-Y.; Korgel, B. A. *J. Am. Chem. Soc.* **2008**, *130*, 5436

24. Lee, D. C.; Hanrath, T.; Korgel, B. A. *Angew. Chem., Int. Ed.* **2005**, *44*, 3573
25. Holmes, J. D.; Johnston, K. P.; Doty, R. C.; Korgel, B. A. *Science* **2000**, *287*, 1471
26. Hanrath, T.; Korgel, B. A. *Adv. Mater.* **2003**, *15*, 437
27. Smith, D. A.; Holmberg, V. C.; Korgel, B. A. *ACS Nano* **2010**, *4*, 2356
28. Heitsch, A. T.; Akhavan, V. A.; Korgel, B. A. *Chem. Mater.* **2011**, *23*, 2697
29. Smith, D. A.; Holmberg, V. C.; Lee, D. C.; Korgel, B. A. *J. Phys. Chem. C* **2008**, *112*, 10725
30. de Heer, W. A.; Bacsá, W. S.; Châtelain, A.; Gerfin, T.; Humphrey-Baker, R.; Forro, L.; Ugarte, D. *Science* **1995**, *268*, 845
31. Endo, M.; Muramatsu, H.; Hayashi, T.; Kim, Y. A.; Terrones, M.; Dresselhaus, M. S. *Nature* **2005**, *433*, 476
32. Yuan, J.; Liu, X.; Akbulut, O.; Hu, J.; Suib, S. L.; Kong, J.; Stellacci, F. *Nat. Nanotechnol.* **2008**, *3*, 332
33. Holmberg, V. C.; Patel, R. N.; Korgel, B. A. *J. Mater. Res.* **2011**, *26*, 2305
34. Choi, J. W.; Hu, L.; Cui, L.; McDonough, J. R.; Cui, Y. *J. Power Sources* **2010**, *195*, 8311
35. Hu, L.; Wu, H.; La Mantia, F.; Yang, Y.; Cui, Y. *ACS Nano* **2010**, *4*, 5843
36. Ng, S. H.; Wang, J.; Guo, Z. P.; Chen, J.; Wang, G. X.; Liu, H. K. *Electrochim. Acta* **2005**, *51*, 23
37. Wang, J.-Z.; Zhong, C.; Chou, S.-L.; Liu, H.-K. *Electrochem. Commun.* **2010**, *12*, 1467
38. Tuan, H.-Y.; Korgel, B. A. *Chem. Mater.* **2008**, *20*, 1239
39. Saunders, A. E.; Sigman, M. B.; Korgel, B. A. *J. Phys. Chem. B* **2004**, *108*, 193
40. Choi, H. S.; Park, C. R. "Towards High Performance Anodes with Fast Charge/Discharge Rate for LIB Based Electrical Vehicles." <http://www.intechopen.com/articles/show/title/towards-high-performance-anodes-with-fast-charge-discharge-rate-for-lib-based-electrical-vehicles>
41. Obrovac, M. N.; Krause, L. J. *J. Electrochem. Soc.* **2007**, *154*, A103
42. Lopez, F. J.; Hemesath, E. R.; Lauhon, L. J. *Nano Lett.* **2009**, *9*, 2774
43. Davidson, F. M.; Lee, D. C.; Fanfair, D. D.; Korgel, B. A. *J. Phys. Chem. C* **2007**, *111*, 2929

44. Wang, R.-P.; Zhou, G.-W.; Liu, Y.-L.; Pan, S.-H.; Zhang, H.-Z.; Yu, D.-P.; Zhang, Z. *Phys. Rev. B* **2000**, *61*, 16827
45. Hessel, C. M.; Rasch, M. R.; Hueso, J. L.; Goodfellow, B. W.; Akhavan, V. A.; Puvanakrishnan, P.; Tunnel, J. W.; Korgel, B. A. *Small* **2010**, *6*, 2026
46. Tuinstra, F.; Koenig, J. L. *J. Chem. Phys.* **1970**, *53*, 1126
47. Lespade, P.; Al-Jishi, R.; Dresselhaus, M. S. *Carbon* **1982**, *20*, 427
48. Ferrari, A. C.; Robertson, J. *Phys. Rev. B* **2000**, *61*, 14095
49. Ferrari, A. C. *Solid State Commun.* **2007**, *143*, 47
50. Monika, W.; Wang, Y.; Zerda, T. W. *J. Phys. Condens. Matter* **2005**, *17*, 2387
51. Timmons, A.; Todd, A. D. W.; Mead, S. D.; Carey, G. H.; Sanderson, R. J.; Mar, R. E.; Dahn, J. R. *J. Electrochem. Soc.* **2007**, *154*, A865

Chapter 3: Solvent Effects on Solution Phase Synthesis of Germanium Nanowires Seeded by Gold Nanocrystals[§]

3.1 INTRODUCTION

Semiconductor nanowires have been proposed for use in a variety of different applications because of their unique physical properties,¹⁻⁹ their ability to be dispersed in solvents¹⁰ and combined with polymers and organic and biological molecules,^{1-3,11,12} and deposited under mild conditions on a variety of different kinds of substrates.¹³ To realize many envisioned nanowire applications—such as structural nanowire/polymer composites, low-cost functional coatings, batteries and printable electronics that require large quantities of nanowires—strategies are needed to generate large quantities of semiconductor nanowires.

Solution-based synthetic routes, including solution-liquid-solid (SLS)¹⁴ and supercritical fluid-liquid-solid (SFLS)^{15,16} growth, are capable of producing large amounts of crystalline nanowires with controlled diameter.¹⁷ Like vapor-liquid-solid (VLS) growth,¹⁸ SLS and SFLS methods use metal nanocrystals to seed and promote nanowire crystallization via the formation of a eutectic with the semiconductor.¹⁷ Thus far, the most successful solution method for Group IV semiconductor (i.e., Si and Ge) nanowires has been SFLS.^{19,20} SFLS growth utilizes solvents heated and pressurized above their critical point, which enables reaction temperatures as high as ~650°C to be reached.²¹ These high temperatures have enabled the use of a wide variety of different metal seeds and reactants for Si and Ge nanowire growth.^{22,23} However, the high pressures of SFLS are not ideal for large scale, commercial nanowire production. SLS reactions on the other hand are carried out under ambient pressure, but the reaction temperatures are limited by the boiling point of the solvent.¹⁷ Because of the relatively

[§] This chapter appears in *Journal of Materials Chemistry* **2009**, *19*, 996-1001.

limited temperature range of solvent boiling points, there have been very few reports of SLS-grown Si and Ge nanowires.^{24,25} In this contribution, we demonstrate the SLS growth of Ge nanowires using Au nanocrystals as seeds.

There are a number of solvents with boiling temperatures exceeding the Au:Ge eutectic, including squalane ($T_b \sim 420^\circ\text{C}$), squalene ($T_b > 380^\circ\text{C}$), octacosane ($T_b \sim 430^\circ\text{C}$), dotriacontane ($T_b \sim 460^\circ\text{C}$), tri-*n*-octylamine ($T_b \sim 380^\circ\text{C}$) and tri-*n*-octylphosphine ($T_b \sim 360^\circ\text{C}$); yet, Au-seeded SLS Ge nanowire growth has not been previously demonstrated. Both SFLS and VLS growth of Ge nanowires are well established,^{19,26} but the Ge reactant chemistries used in these methods do not necessarily apply to SLS growth. Gaseous germane for example, which is the common reactant for VLS growth, cannot be fed directly into a solvent for SLS growth and it was our previous belief that diphenylgermane ($\text{Ge}(\text{C}_6\text{H}_5)_2\text{H}_2$; DPG)—which works very well for SFLS Ge nanowire growth—would be too unreactive for SLS growth.²⁴ However, this has turned out not to be the case, and Au nanocrystals were found to significantly enhance the DPG decomposition in some high boiling solvents, (i.e., squalane and squalene) and have produced significant quantities of crystalline Ge nanowires.

3.2 EXPERIMENTAL METHODS

3.2.1 Reagents

All reactions were carried out using standard airless procedures using a nitrogen-filled glove box and a Schlenk line. Squalane (99%), squalene (>98%), octacosane (99%), dotriacontane (97%), tri-*n*-octylamine (TOA, 98%), tri-*n*-octylphosphine (TOP, >97%) and toluene (>99.5%) were purchased from Sigma-Aldrich. Diphenylgermane (DPG, >95%) was obtained from Gelest. Dodecanethiol-coated Au nanocrystals (2.6 ± 0.4 nm diameter) were synthesized following literature procedures.²⁷

Stock solutions of 300 mM DPG were prepared in a nitrogen-filled glove box by adding 75 μL of DPG to 1.33 mL of the solvent used for the reaction. For reactions in octacosane and dotriacontane, DPG stock solutions were prepared in toluene as octacosane and dotriacontane are solids at room temperature. For SLS nanowire growth, 3.3 μL of a dispersion of 35.6 mg mL^{-1} Au nanocrystals in toluene were added to the DPG stock solution before injection into the reaction flask, corresponding to a Ge:Au mole ratio of 1250:1 in the injection solution.

3.2.2 DPG decomposition and Ge nanowire growth reactions

The solvent—either 4 mL of squalane, squalene, TOA, or TOP, or 5g of octacosane or dotriacontane—was added to a 4-neck flask and attached to a Schlenk line, heated to 100°C under vacuum (<500 mTorr) for 30 minutes, and then blanketed with nitrogen. The solvent was then heated to 380°C. For DPG decomposition reactions, 1 mL of Au-free DPG reactant solution was removed from the glove box in a syringe and rapidly injected into the reaction flask. For SLS nanowire growth, a Au nanocrystal/DPG reactant solution was injected.

The reactions were carried out at 380°C for 5 minutes. The flask was removed from the heating mantle, and once the flask cooled to $\sim 100^\circ\text{C}$ 15 mL of toluene were added. The temperature was reduced further to $\sim 50^\circ\text{C}$ and the flask was sonicated for 5 to 10 seconds to redisperse the reaction product from the flask walls. The reaction solution was then transferred to a centrifuge tube and spun at 8000 rpm for 5 minutes. The supernatant was discarded. The precipitate was resuspended in 10 mL of chloroform and 2 mL of ethanol and centrifuged again at 8000 rpm for 5 minutes. The supernatant was again discarded and the precipitate saved for characterization.

3.2.3 Materials characterization

Ge nanowires and other reaction products were characterized using a variety of techniques, including scanning and transmission electron microscopy (SEM and TEM), energy dispersive X-ray spectroscopy (EDS), X-ray diffraction (XRD) and mass spectrometry.

SEM was performed using a Zeiss Supra 40 SEM with an in-lens arrangement, a working voltage of 5 keV and a working distance of 5 mm. SEM samples were imaged on 1cm × 1cm silicon wafers (from S.E.H.). TEM images were acquired digitally with either a Philips EM208 TEM (operated at 80 kV) or a field emission JEOL 2010F TEM (operated at 200 kV). EDS data were acquired on a JEOL 2010F TEM equipped with an Oxford Inca EDS detector. The TEM samples were prepared by drop-casting from chloroform onto 200 mesh copper lacey carbon TEM grids (Electron Microscopy Sciences).

XRD was performed using a Bunker-Nonius D8 Advance diffractometer with Cu K_{α} radiation ($\lambda = 1.54 \text{ \AA}$). Around 3–5 mg of sample was deposited onto quartz substrates and analyzed using a rotating sample holder and collecting data for 4 to 6 hours. The generator voltage and amperage were 40 mV and 40 mA, respectively, with a scan rate of 12 deg min^{-1} in 0.02 deg intervals.

Inductively coupled plasma mass spectrometry (ICPMS) was performed using a GBC Optimass 8000 ICPMS. For ICPMS, 1g of solvent (squalane, squalene, octacosane, dotriacontane, TOA or TOP) was combined with 5g of concentrated nitric acid (15.8 N) and stirred for 20 min at 70 °C to extract any trace metal ions into the aqueous phase. Squalene was stirred at room temperature due to side reactions observed when heated to 70 °C. The aqueous phase was then diluted by adding a 1 mL aliquot to 50 mL of a 1% (w/w) nitric acid solution and analyzed.

3.3 RESULTS

3.3.1 SLS growth of Au-seeded Ge nanowires

Ge nanowires could be produced by Au nanocrystal-seeded SLS growth in squalane, squalene, dotriacontane, octacosane and trioctylamine at 380°C by the thermal decomposition of DPG. Figure 3.1 shows SEM images of Ge nanowires obtained in these reactions. The nanowires are crystalline and composed of diamond cubic Ge as confirmed by XRD (Figure 3.2). The highest quality nanowires were obtained in squalane (Figure 3.1a). Figure 3.3 shows a TEM image of a 30 nm diameter Au-seeded Ge nanowire grown in squalane. The fast Fourier transform (FFT) of the TEM image matches crystalline Ge and indicates that the nanowire has a $\langle 110 \rangle$ growth direction. EDS collected with the electron beam focused on the nanowire and the tip showed the presence of Ge in the wire and Au at the tip, thus confirming that the nanowire grew by the SLS mechanism from the Au seed.

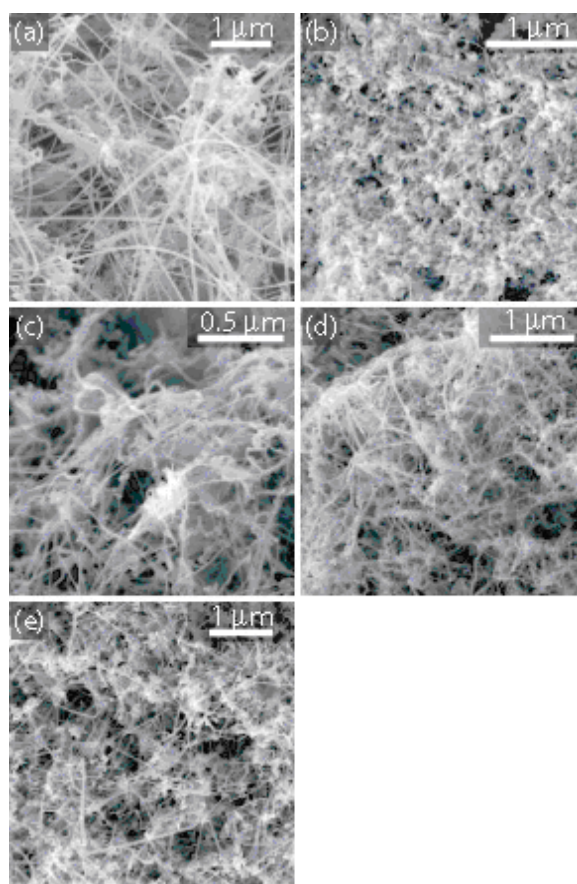


Figure 3.1: SEM images of Ge nanowires formed by heating DPG in the presence of Au nanocrystals at 380°C for 10 minutes in (a) squalane, (b) squalene, (c) octacosane, (d) dotriacontane and (e) TOA. Ge nanowires could not be grown in TOP using Au seeds and DPG.

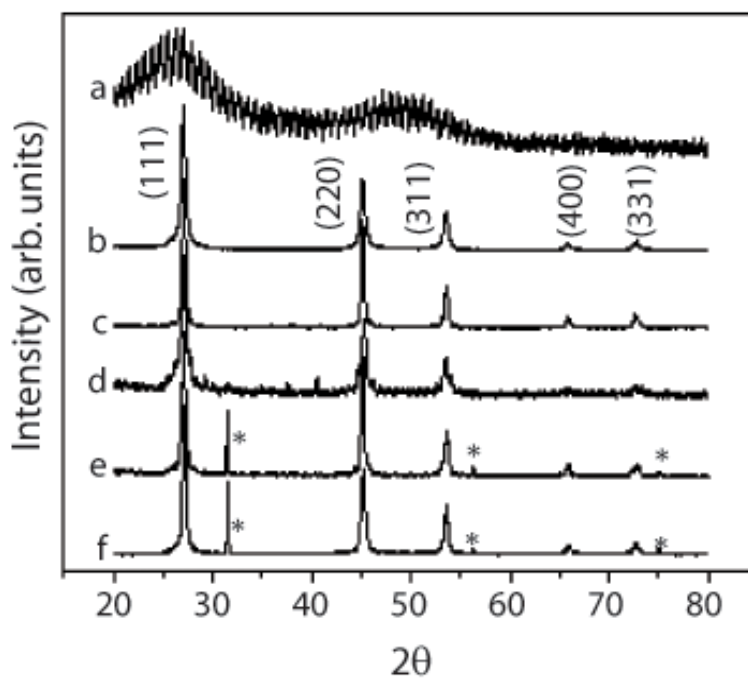


Figure 3.2: XRD of the reaction products from the thermal decomposition of DPG at 380°C in (a) TOA without Au, and (b) TOA, (c) squalane, (d) octacosane, and (e) dotriacontane in the presence of Au nanocrystals, and (f) dotriacontane without Au nanocrystals. Diffraction patterns (b-f) index to diamond cubic Ge (JCPDS: 00-004-0545). Peaks labeled with “*” correspond to NaCl (JCPDS: 00-005-0628).

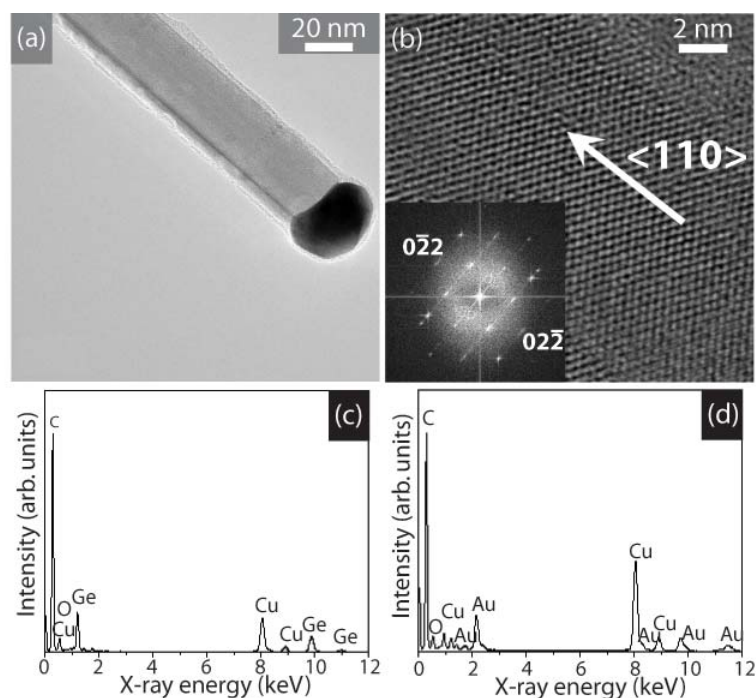


Figure 3.3: (a, b) TEM images of a Ge nanowire obtained by DPG decomposition in squalane in the presence of Au nanocrystals with (inset) corresponding FFT. (c, d) EDS acquired with the electron beam focused (c) on the wire and (d) at the nanowire tip. The Cu and C signals are from the TEM grid and support.

The nanowire yield and quality were quite good in all of the solvents except in TOP, in which Ge nanowires could not be produced. Nonetheless, some undesired reaction products were also observed in the reactions, including amorphous Ge particles, heavily kinked nanowires, and nanowires with significant surface deposition. Figure A2 in Appendix A shows SEM images of typical impurities. Amorphous Ge particles result from homogeneous Ge nucleation and growth that is unassociated with the Au seed particles; kinking results when the seed particle becomes starved for Ge; and sidewall deposition is a consequence of DPG decomposition that is too fast.^{28,29} It should be possible to eliminate most of these undesired byproducts by optimizing the reaction conditions.

3.3.2 The role of solvent impurities in Ge nanowire growth in

Crystalline Ge nanowires were also obtained in relatively high yield when DPG was heated at 380°C in dotriacontane without Au nanocrystals. In all of the other solvents, Au nanocrystals were needed to induce crystalline Ge nanowire growth. Figure 3.4 shows SEM and TEM images of the Ge nanowires obtained under these conditions; the nanowires are straight and appear to be of reasonable quality. EDS (Figure 3.5c) of the nanowires confirmed that they were composed of Ge and XRD (Figure 3.2f) confirmed that the nanowires were indeed crystalline, diamond cubic Ge. The addition of Au nanocrystals to the reactions in dotriacontane also led to crystalline Ge nanowires, but the product yields were similar to the reactions carried out in the absence of Au. The Ge nanowires formed without Au nanocrystals present were heavily twinned, like the nanowire in Figure 3.5.

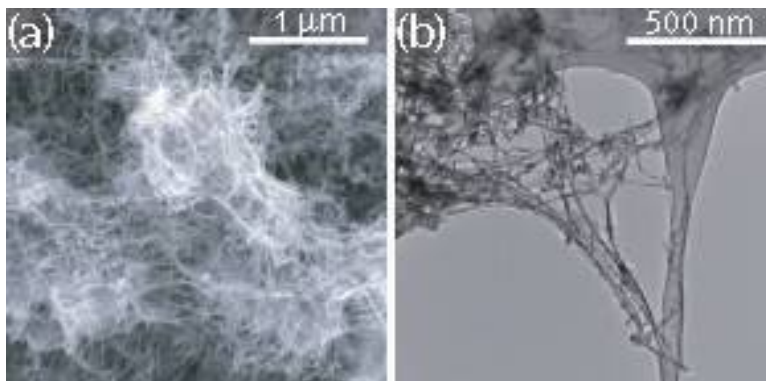


Figure 3.4: (a) SEM and (b) TEM images of Ge nanowires obtained when DPG was heated in dotriacontane at 380°C without Au nanocrystals.

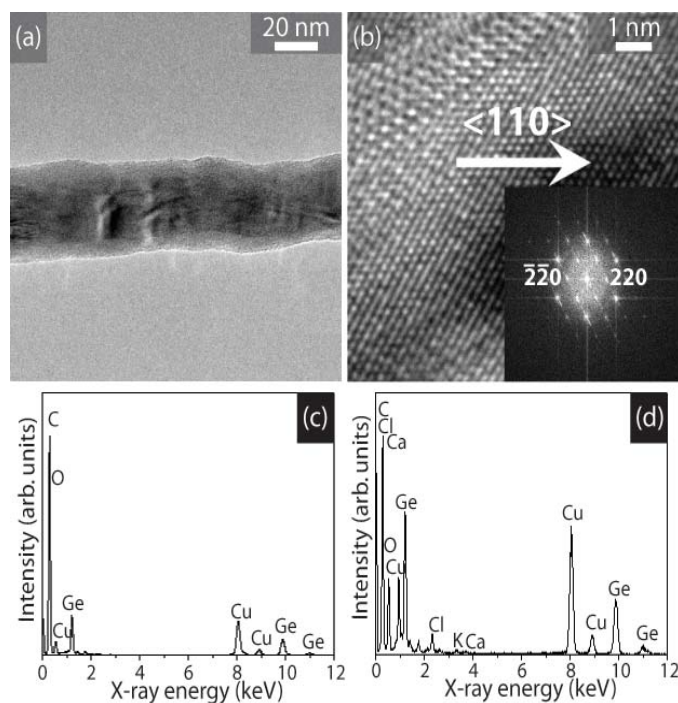


Figure 3.5: (a, b) TEM images of a Ge nanowire obtained by DPG decomposition in dotriacontane at 380°C without adding gold nanocrystals. The inset in (b) is the FFT of the TEM image. (c, d) EDS data obtained from the core and the tip of the nanowire, respectively. The Cu peaks seen here are from the copper supported lacey carbon TEM grid.

Although “unseeded” Ge nanowire growth was at first surprising to us, there are in fact several reports of Ge nanowires grown in solution without the intentional addition of seeds.^{30–34} In our case, however, EDS and XRD of the nanowires and ICPMS of the dotriacontane showed that impurities in the dotriacontane were actually responsible for the formation of the Ge nanowires in the absence of Au nanocrystals. Diffraction peaks for NaCl were observed (Figure 3.6) to be present in the sample by XRD of the nanowire product. Heating pure dotriacontane (without adding DPG) at 400°C for 2 hours was found to produce a solid byproduct that was found to be NaCl by XRD (Figure 3.6).³⁵ TEM showed an accumulation of material at the tips of the nanowires, which EDS showed to be composed of Cu and other impurities at the tip of the wire (Figure 3.6).

ICPMS of pure dotriacontane also showed that Cu was present in the solvent. In fact, pure dotriacontane took on a slight red hue when heated at 400°C for 2 hours, most likely from this Cu impurity. ICPMS of the other solvents did not show the presence of contaminants and crystalline Ge nanowires did not form in these solvents unless Au nanocrystals were added to the reactions. In the absence of Au nanocrystals, only amorphous Ge particles were formed (Appendix A, Figure A3).

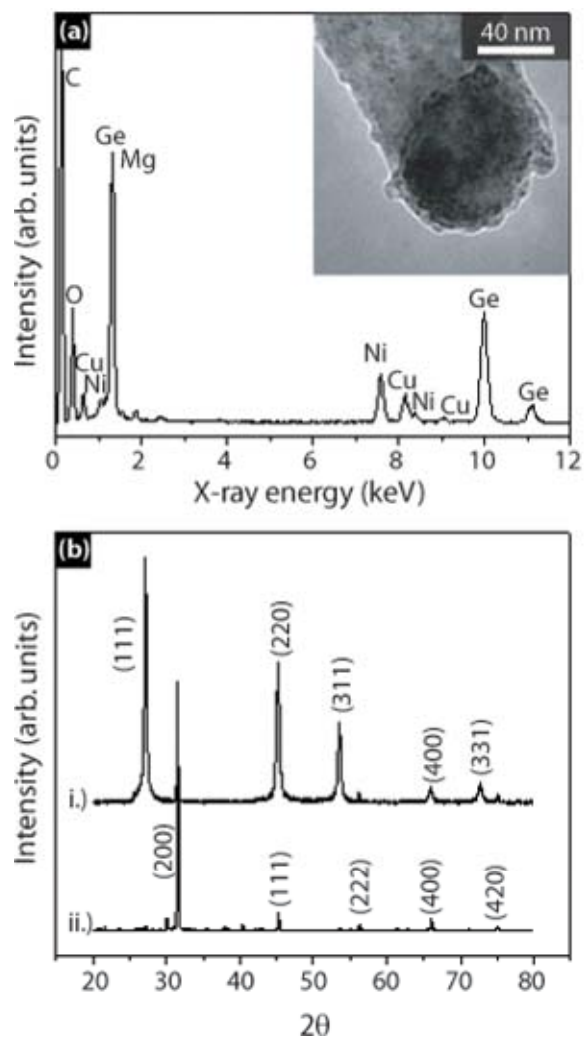


Figure 3.6: (a) EDS and (b) XRD of (inset) Ge nanowires grown in dotriacontane without Au. (b) XRD of (i) nanowires and (ii) solid byproduct isolated after heating dotriacontane. Ni and C signals are from the TEM grid. Diffraction peaks correspond to (i) diamond cubic Ge and (ii) NaCl (JCPDS: 00-005-0628).

3.4 DISCUSSION

3.4.1 DPG decomposition chemistry: the influence of Au

Au promotes nanowire growth by the SLS mechanism because the reaction temperature of 380°C is higher than the Au:Ge eutectic (360°C). Ge forms a liquid solution with the Au nanocrystals as DPG decomposes, eventually saturating the seed particle and then crystallizing from it in the form of a nanowire.¹⁸ There are no reported studies of DPG decomposition at 380 °C in solution at ambient pressure.³⁶ In squalane in the absence of Au nanocrystals, DPG decomposition is in fact very slow and one would not expect DPG to be a suitable reactant for SLS nanowire growth. However, when Au nanocrystals are added to the reaction, the solution turns instantaneously black due to the formation of Ge from DPG. Au plays a significant role in the rate of DPG conversion to Ge in squalane (and squalene) at 380°C, in addition to promoting crystallization of the nanowires.

Mass spectrometry of the reaction byproducts from a DPG decomposition reaction in squalane at 380°C (see Figures A4 and A5 in Appendix A) revealed that DPG decomposes by phenyl redistribution, leading to tetraphenylgermane (QPG) and germane as reaction end products as described in Figure 3.7. Phenylsilanes also decompose by a similar redistribution pathway in organic solvents at elevated temperature.^{22,37}

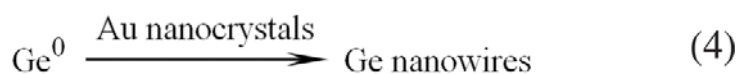
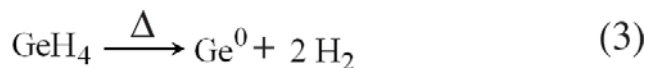
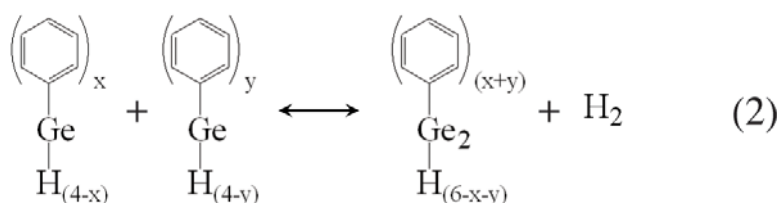
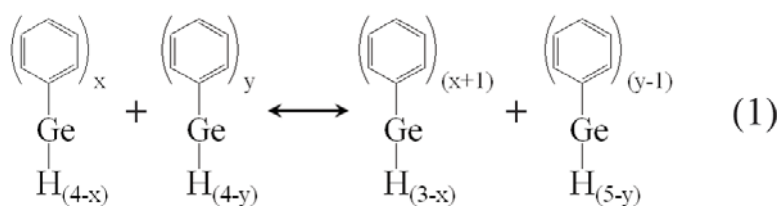


Figure 3.7: Decomposition of diphenylgermane by phenyl redistribution. ($x=1, 2, \text{ or } 3$; $y=1, 2, \text{ or } 3$).

Table 3.1 lists the measured DPG conversion to Ge nanowires after 5 minutes for reactions carried out in various solvents. In all of the solvents except TOP, the addition of Au nanocrystals led to the theoretical yield of Ge from DPG. In some of the solvents under some conditions, the measured DPG conversion was slightly higher than 50%, which could be due to the presence of QPG in the weighed product, as it is insoluble and not easily separated from nanowires, which in turn are not reasonably dispersible in solvents. In the absence of Au, there was almost no observable DPG decomposition to Ge in squalane and squalene at 380°C after 5 minutes. In octacosane, TOA and dotriacontane, however, there was significant conversion of DPG to Ge when Au was not present in the reaction. The Ge product obtained from octacosane and TOA was composed of amorphous Ge particles and the Ge product from dotriacontane was

crystalline nanowires. As established above, there is an impurity in dotriacontane that promotes crystalline nanowire growth, which also appears to catalyze DPG decomposition. In octacosane and TOA, no such impurity was identified.

Table 3.1: DPG conversion to Ge after 5 minutes at 380°C in various high boiling temperature solvents.

	Boiling point (°C)	Conversion [†] with Au (%)	Conversion [†] without Au (%)
Squalane	420	52.8	0
Squalene	420	25.0	0
Octacosane	430	30.0	43.6**
Dotriacontane	460	42.7	65.2*
Trioctylamine	360	77.0	66.0**
Trioctylphosphine [§]	360	0	0

* Crystalline Ge

** Amorphous Ge

[§] By applying a slight back pressure, TOP could be refluxed at 380°C

[†] The theoretical maximum conversion of DPG to Ge by phenyl redistribution is 50%, since tetraphenylgermane is thermally stable at 380°C

DPG decomposes to Ge by phenyl redistribution, and in squalane and squalene the Au nanocrystals greatly enhance the decomposition rate. Figure 3.8 provides two possible reaction pathways involving DPG and Au nanocrystals. In a homogeneous DPG decomposition pathway, DPG would first undergo redistribution to germane (GeH₄) in solution, and then decompose to Ge which is free to diffuse into the Au nanocrystal. In a heterogeneous decomposition pathway, DPG (or another phenylgermane species) adsorbs to the Au nanocrystal surface and then decomposes to Ge by disproportionation. This second heterogeneous decomposition pathway for phenylgermanes seems unlikely, as it requires (1) the adsorption of at least two phenylgermane reactant species and (2) the final desorption of QPG as a reaction byproduct; however, metals (although not Au) are well-known catalysts for phenyl redistribution reactions of phenylsilanes,^{23,37} and perhaps Au is catalyzing phenylgermane disproportionation. Another heterogeneous reaction

pathway might involve the adsorption of GeH_4 from solution, followed by hydrogen desorption and then Ge incorporation into the seed. Au is in fact known to catalyze silane (SiH_4) decomposition by such a heterogeneous pathway, in which the Au surface enhances the rate of hydrogen desorption.^{38,39} The problem with this reaction pathway is that in squalane and squalene in the absence of Au there is almost no Ge formed, and there is no observed bubbling of GeH_4 gas out of the reaction flask. One other variation might be that DPG (or other phenylgermanes) adsorbs to the Au nanocrystal surface, rearranges to GeH_4 and then the Au surface enhances the decomposition of GeH_4 . Again, this reaction pathway requires the adsorption of multiple phenylgermanes on the nanocrystal surface (unless direct Ge–C thermolysis were possible, which is unlikely) and eventually QPG desorption.

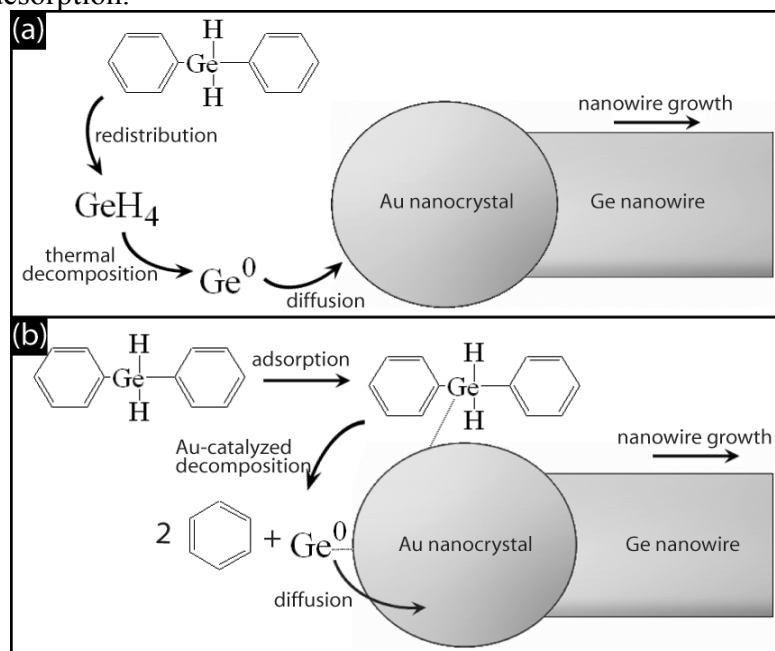


Figure 3.8: Illustration of two possible DPG decomposition routes leading to Au-seeded Ge nanowire growth: (a) homogeneous and (b) heterogeneous DPG decomposition. Pathway (b) as illustrated would not require phenyl redistribution and most likely does not occur.

3.5 CONCLUSIONS

Significant quantities of Ge nanowires could be produced in solution at 380°C using DPG as a reactant and Au nanocrystals to promote SLS nanowire growth. The Au nanocrystals were also found to greatly increase the rate of DPG decomposition to Ge in squalane and squalene. DPG decomposes to Ge by phenyl redistribution to GeH₄ and GePh₄. A few plausible reaction pathways involving the Au nanocrystals were proposed.

Au had less influence on DPG decomposition rates in dotriacontane, TOA and octacosane, but was needed to crystallize Ge nanowires, except in dotriacontane; crystalline Ge nanowires formed in dotriacontane without adding Au nanocrystals, but it was found that impurities in the solvent (e.g., Cu and NaCl) seeded nanowire growth. No such impurities were found by ICPMS in TOA and octacosane. Therefore, it is possible that squalane and squalene actually retard DPG decomposition (in the absence of Au); however, it is not clear why this would be the case since there is no obvious functional group common to these molecules expected to interact with Ge (see Appendix A for a summary of the solvent chemical structures). At any rate, Au may be serving as a catalyst for DPG decomposition in squalane and squalene, or may simply serve as a Ge sink and shift the equilibrium toward Ge formation. Further mechanistic studies are needed to clarify the details of this relatively complicated reaction chemistry.

In summary, SLS growth can be used to produce high aspect ratio crystalline nanowires. In contrast to gas-phase VLS methods, which are limited to batch reactions on substrate surfaces, SLS nanowire growth can be used to produce large quantities of nanowires, as needed for applications like printed electronics and nanowire /polymer composites. The purity of the solution reaction environment, however, is more difficult to maintain than in high vacuum gas-phase conditions and it remains to be seen how significantly impurities affect the physical properties of nanowires grown in solution.

There may be a tradeoff in purity and yield of nanowires, and perhaps this will be one of the deciding factors about which nanowire growth method—either gas phase or solution phase—is used. More research is needed, testing and comparing the physical properties of nanowires made both in solution and in the gas phase in order to answer this question. At any rate, the solution chemical synthesis of semiconductor nanowires provides a general high-yield strategy to produce crystalline semiconductor nanowires that opens the door for many possible technological applications like polymer /nanowire composites that are simply impossible using VLS-CVD growth methods.

3.6 ACKNOWLEDGEMENTS

Brian A. Korgel made significant contributions to this work. We acknowledge the Robert A. Welch Foundation, the Office of Naval Research, and the Air Force Research Laboratory for financial support of this work. We also thank Dayne Fanfair and Andrew Heitsch for helpful discussions, Aaron Rogers for assistance with the PCI/NCI-MS measurements, and Adam Rowland for assistance with the ICPMS measurements.

3.7 REFERENCES

1. Law, M.; Goldberger, J.; Yang, P. *Annu. Rev. Mater. Res.* **2004**, *34*, 83
2. Lu, W.; Lieber, C. M. *J. Phys. D: Appl. Phys.* **2006**, *39*, R387
3. Yogeswaran U.; Chen, S.-M. *Chem. Sensors* **2008**, *8*, 290
4. Hu, J.; Odom, T. W.; Lieber, C. M. *Acc. Chem. Res.* **1999**, *32*, 435
5. Duan, X.; Huang, Y.; Cui, Y.; Wang J.; Lieber, C. M. *Nature* **2001**, *409*, 66
6. Y. Cui and C. M. Lieber, *Science* **2001**, *409*, 66
7. Smith, D. A.; Holmberg, V.; Lee, D. C.; Korgel, B. A. *J. Phys. Chem. C* **2008**, *112*, 10725
8. Lozano, K.; Hernandez, C.; Petty, T.; Sigman, M. B.; Korgel, B. A. *J. Coll. Int. Sci.* **2006**, *297*, 618
9. Sigman, M. B.; B. A. Korgel, B. A. *J. Am. Chem. Soc.* **2005**, *127*, 10089

10. Colli, A.; Fasoli, A.; Beecher, P.; Servati, P.; Pisana, S.; Fu, Y.; Flewitt, A. J.; Milne, W. I.; Robertson, J.; Ducati, C.; De Franceschi, S.; Hofmann, S.; Ferarri, A. C. *J. Appl. Phys.* **2007**, *102*, 034302
11. Hsieh, G. W.; Beecher, P.; Li, F. M.; Servati, P.; Colli, A.; Fasoli, A.; Chu, D.; Nathan, A.; Ong, B.; Robertson, J.; Ferrari, A. C.; Milne, W. I. *Physica E* **2008**, *40*, 2406
12. Vivekchanc, S. R. C.; Kam, K. C.; Gundiah, G.; Govindaraj, A.; Cheetham A. K.; Rao C. N. R. *J. Mater. Chem.* **2005**, *15*, 4922
13. McAlpine, M. C.; Friedman, R. S.; Jin, S.; Lin, K.; Wang, W. U.; Lieber, C. M. *Nano Lett.* **2003**, *3*, 1531
14. Trentler, T. J.; Hickman, K. M.; Goel, S. C.; Viano, A. M.; Gibbons P. C.; Buhro, W. E. *Science* **1995**, *270*, 1791–1796
15. Holmes, J. D.; Johnston, K. P.; Doty R. C.; Korgel, B. A. *Science* **2000**, *287*, 1471–1473
16. Hanrath T.; Korgel, B. A. *Adv. Mater.* **2003**, *15*, 437
17. Wang, F.; Dong, A.; Sun, J.; Yu H.; Buhro, W. E. *In org. Chem.* **2006**, *45*, 7511
18. Wagner R. S.; Ellis, W. C. *Appl. Phys. Lett.* **1964**, *4*, 89
19. Hanrath, T.; Korgel, B. A. *J. Am. Chem. Soc.* **2002**, *124*, 1424
20. Tuan, H.-Y.; Korgel, B. A. *Chem. Mater.* **2008**, *20*, 1239
21. Smith, D. K.; Lee, D. C.; Korgel, B. A. *Chem. Mater.* **2006**, *18*, 3356
22. Lee, D. C.; Hanrath, T.; Korgel, B. A. *Angew. Chem. Intl. Ed.* **2005**, *44*, 3573–3577
23. Tuan, H.-Y.; Lee, D. C.; Korgel, B. A. *Angew. Chem. Intl. Ed.* **2006**, *31*, 5184–5187
24. Lu, X.; Fanfair, D. D.; Johnston, K. P.; Korgel, B. A. *J. Am. Chem. Soc.* **2005**, *127*, 15718
25. Heitsch, A. T.; Fanfair, D. D.; Tuan, H.-Y.; Korgel, B. A. *J. Am. Chem. Soc.* **2008**, *130*, 5436
26. Wu, Y. Y.; Yang, P. D. *J. Am. Chem. Soc.*, **2001**, *123*, 3165
27. Saunders, A. E.; Sigman Jr., M. B.; Korgel, B. A. *J. Phys. Chem. B* **2004**, *108*, 193
28. Fanfair, D. D.; Korgel, B. A. *Crystal Growth Des.* **2008**, *8*, 3246
29. Lu, X.; Hanrath, T.; Johnston K. P.; Korgel, B. A. *Nano Lett.* **2003**, *3*, 93

30. Heath J. R.; LeGoues, F. K. *Chem. Phys. Lett.* **1993**, 208, 263
31. Zaitseva, N.; Dai, Z. R.; Grant, C. D.; Harper J.; Saw, C. *Chem. Mater.* **2007**, 19, 5174
32. Ge, M.; Liu, J. F.; Wu, H.; Yao, C.; Zeng, Y.; Fu, Z. D.; Zhang S. L.; Jiang, J. *Z. J. Phys. Chem. C* **2007**, 111, 11157
33. Zaitseva, N.; Harper, J.; Gerion D.; Saw, C. *Appl. Phys. Lett.* **2005**, 86, 053105.
34. Gerung, H.; Boyle, T. J.; Tribby, L. J.; Bunge, S. D.; Brinker C. J.; Han, S. M. *J. Am. Chem. Soc.* **2006**, 128, 5244
35. From correspondence with Sigma: one purification step for dotriacontane is a brine wash that may leave residual alkali and alkaline species.
36. DPG is typically used as the reactant for SFLS growth of Ge nanowires, which is often carried out at 380 °C, but under very high pressures, greater than at least 50 bar (Ref. 19).
37. Gilman H.; Miles, D. H. *J. Org. Chem.* **1958**, 23, 326
38. Speier Jr., J. L.; Zimmerman, R. E. *J. Am. Chem. Soc.* **1955**, 77, 6395
39. Russell, G. A. *J. Am. Chem. Soc.* **1959**, 81, 4815

Chapter 4: Electrochemical Lithiation of Graphene-Supported Silicon and Germanium for Rechargeable Batteries[§]

4.1 INTRODUCTION

Rechargeable lithium ion batteries (LIBs) are used widely to power portable electronic devices. They have high energy density, high operating voltage, low self-discharge and require little maintenance. However, more advanced applications are demanding batteries with increased capacity, faster charging and discharging and longer cycle life.^{1,2} The most demanding applications like battery-powered automobiles and utility-scale power storage for intermittent renewable energy sources like solar cells and wind need unprecedented power density.³

Improved LIBs require advances in electrode materials. The battery capacity is limited by the amount of lithium that can be incorporated into the negative (anode) and positive (cathode) electrodes, which have theoretical lithium storage capacities of 372 mA h g⁻¹ (graphite) and 135 mA h g⁻¹ (LiCoO₂).^{2,4} Graphite has good lithium storage capacity and chemical stability, low irreversible capacity loss and low cost,^{5,6} but there are materials with much higher theoretical capacities. Si and Ge for example have theoretical capacities of 3579 mA h g⁻¹ and 1600 mA h g⁻¹, respectively.⁷⁻¹⁰ Increasing the anode capacity to about 1000 mA h g⁻¹ without any change in the cathode material would significantly improve the total battery capacity compared to what is possible using graphite.⁴

Lithiation of Si and Ge causes a large volume expansion (300% v/v) that leads to pulverization of bulk crystals and battery failure.¹¹ Nanoparticles, nanowires and nanotubes can withstand these changes without cracking and have been widely studied for high capacity anodes in LIBs.^{2, 12-19} However, the long-term cycling stability of Si

[§] This chapter was accepted for publication in *The Journal of Physical Chemistry C* **April, 2012**

and Ge anodes is sensitive to the additional components in the battery, including electrically conductive additives (Si and Ge are poor conductors), polymeric binder and electrolyte.^{2, 10,15-27} There has been significant recent interest in using graphene as a battery additive because it has a high electrical conductivity, mechanical durability, and chemical stability.^{28, 29} As a stand-alone electrode material, graphene can store more Li than graphite because Li can adsorb to both sides of a single graphene sheet.³⁰⁻³⁶ Furthermore, graphene can be produced in significant quantities by reducing exfoliated graphene oxide.^{37, 38} Reduced graphite oxide (RGO) has been studied as a LIB host for a variety of nanocrystals, including Mn_3O_4 ,³⁹ Co_3O_4 ,^{40, 41} SnO_2 ,⁴² Fe_3O_4 ,⁴³ and Si,⁴⁴ and it has been shown to provide increased capacity in most of these instances. Here, we study the LIB performance of RGO-supported Si and Ge nanowires, as well as Si nanocrystals, focusing on the role of the RGO in the electrochemical lithiation reaction. In all cases, RGO improved the LIB performance of these nanomaterials. However, the lithiation reactions were dominated by RGO unless the Si and Ge loading was relatively high (50 % w/w) and the cycling rate was slow ($< C/10$). Only in the case of the Ge nanowires was lithiation competitive with RGO at faster cycling rates.

4.2 EXPERIMENTAL DETAILS

4.2.1 Materials

All reagents were used as received without further purification. Dodecanethiol (DDT, $\geq 98\%$), tetrachloroaurate trihydrate ($\geq 99.9\%$), sodium borohydride ($\geq 98\%$), toluene (ACS grade and anhydrous, 99.8%), ethanol (99.9%), potassium permanganate ($\geq 99\%$), sulfuric acid (95.0-98.0%), hydrogen peroxide ($>30\%$ solution in water), hydrazine monohydrate (98%), tetraoctylammonium bromide (TOAB, 98%), and chloroform (99.8%) were purchased from Sigma Aldrich. LiPF_6 (1.0M in a 1:1 mixture

of ethylcarbonate [EC, >99.95%] : diethyl carbonate [DEC, >99.98%]) was purchased from Novolyte. Batteries were assembled using Celgard 2400 membranes (Celgard, 25 μ m) as separators and Li metal (Alfa Aesar, 99.9%) as the counter electrode. Diphenylgermane (DPG, >95%) was purchased from Gelest. Graphite (sp-1) powder was purchased from Bay Carbon. Methanol (99.98%), hydrochloric acid (25% v/v) and alumina filters (13mm diameter, Whatman brand) were purchased from Fisher and hydrofluoric acid (48–51% v/v) from EMD Chemical. Trisilane (99.99%) was purchased from Voltaix.

4.2.2 Silicon nanowire synthesis

Si nanowires were synthesized by gold nanocrystal-seeded supercritical fluid-liquid-solid (SFLS) growth using trisilane as the Si reactant in toluene.⁴⁵ All procedures were performed within a nitrogen-filled glove box. A reactant solution of trisilane and Au nanocrystals in toluene is made first. Trisilane is added (0.25 mL) to 0.85 mL of toluene-dispersed 2 nm diameter dodecanethiol-capped Au nanocrystals⁴⁶ at a concentration of 32.4 mg mL⁻¹ to give a 40:1 Si:Au mole ratio. Nanowire growth is carried out in a flow-through high pressure sealed titanium reactor at 450°C. Before injecting the reactant solution, the reactor is heated to 450°C then pressurized with toluene to 6.9 MPa with a closed effluent line. The reactant solution is injected over the course of 1 minute with the reactor effluent remaining closed and the reactor pressure increases to 15.2 MPa. Immediately after injecting the reactant solution, the inlet line is closed and the reactor is removed from the heating block and allowed to cool to room temperature. After the reactor has cooled, it is removed from the glovebox and opened. The nanowires are extracted from the reactor with additional toluene. The crude reaction product, typically dispersed in about 20 mL of toluene, is centrifuged at 8000 rpm for 5

minutes and the supernatant is discarded. The nanowires are then washed two more times by redispersion in 20 mL of toluene followed by centrifugation. The nanowires are redispersed in toluene at a concentration of 1 mg mL^{-1} and stored as a stock solution in a vial under ambient conditions prior to use.

4.2.3 Germanium nanowire synthesis

Ge nanowires were synthesized by Au nanocrystal-seeded solution-liquid-solid (SLS) growth.⁴⁷ 10 mL of squalane was added to a 4-neck flask attached to an air-free Schlenk line heated to 100°C under vacuum ($<500 \text{ mTorr}$) for 30 minutes, and then blanketed with nitrogen. The solvent was then heated to 380°C while, in a nitrogen-filled glove box, an injection solution containing 0.375 mL of DPG and 0.55 mL of a Au nanoparticle dispersion (1 mg mL^{-1} in toluene) diluted with 1 mL squalane was plunged into a syringe. The syringe containing the reactant solution was removed from the glove box and rapidly injected into the reaction flask and stirred vigorously for 5 minutes. At the end of the 5 minute reaction, the flask was removed from the heating mantle and cooled to $\sim 100^\circ\text{C}$, at which point 10 mL of toluene was added. The temperature was reduced further to $\sim 50^\circ\text{C}$ and the flask was sonicated for 5 to 10 seconds to redisperse the reaction product from the flask walls. The reaction solution was then transferred to a centrifuge tube, additional toluene ($\sim 10 \text{ mL}$) was added, and the mixture was centrifuged. After centrifugation, the supernatant was discarded, toluene ($\sim 10 \text{ mL}$) was added, and the mixture was centrifuged once more. The supernatant was again discarded. Nanowires were dispersed in toluene at a concentration of 1 mg mL^{-1} and stored under ambient conditions prior to use. These stock solutions were used directly to fabricate the LIB anodes as described below.

4.2.4 Si nanocrystal synthesis

Si nanocrystals were synthesized by the thermal decomposition of HSQ.^{48, 49} HSQ was heated under inert atmosphere to 1300°C where it was annealed for 1h under forming gas (7%H₂, 93% N₂) to yield a dark glassy material composed of Si nanocrystals in SiO₂. This material was mechanically ground to a powder and added to an aqueous solution of hydrofluoric (10 mL HF, 48% v/v) and hydrochloric (1 mL HCl, 25% v/v) acids. After 6 hours in the dark, the SiO₂ has etched away to yield a dispersion of hydrogen-terminated Si nanocrystals, which was then transferred to a plastic centrifuge tube. 3 mL of ethanol are added to the beaker which is then sonicated for 3 mins to collect nanocrystals that aggregated on the walls of the beaker. This residue was added to the centrifuge tube with the previously collected nanocrystals and the tube was centrifuged at 8000 rpm for 3 minutes. The supernatant was discarded, 5 mL of ethanol was added to the centrifuge tube, and the tube was placed in the bath sonicator for 5 mins to redisperse the Si nanocrystals. The solution was centrifuged at 8000 rpm for 3 minutes. This was repeated twice with ethanol and once with chloroform. After the final wash cycle, the Si nanocrystals were dispersed into chloroform and stored in a vial under ambient conditions for later use.

4.2.5 Reduced graphite oxide (RGO)

RGO was made from graphite oxide (GO) prepared by a modified Hummers method.³⁷ Graphite powder (3 g) was dispersed in a 250 mL round bottom flask with 50 mL concentrated sulfuric acid stirring at 600 rpm. 7 g KMnO₄ is added slowly, making sure that the temperature does not exceed 35°C. The temperature is maintained at 35°C for 2 hr. H₂O₂ is added until the solution ceases to bubble (about 20 mL). Then, 50 mL of DI water is added and the flask is heated to 95°C for 4 hr. The solution becomes brown and viscous indicating the formation of GO. After cooling to room temperature, the

resulting mixture is stirred overnight. The viscous, brown dispersion of GO is filtered through a Buchner funnel and resuspended in water (repeated twice). After a third filtration, the GO is suspended in a 0.1% solution of hydrochloric acid by sonication for 3 hr. The dispersion is then centrifuged for 10 min at 8000 rpm. The final brown paste is placed on a piece of Fisherbrand filter paper (Qualitative P5, medium porosity, slow flow rate) and dried under vacuum overnight at room temperature. About 5.5 g of GO is obtained from 3 g of graphite powder.

GO is reduced to RGO using procedures similar to Park and coworkers.³⁸ A stock solution of RGO was prepared by adding GO to water at a concentration of 3 mg mL⁻¹ and exfoliating via sonication for one hour. An additional 9 volumes of dimethylformamide (DMF) were added to the suspension and sonicated again for an hour. A stable suspension of graphene oxide is formed at a final concentration of 0.3 mg mL⁻¹ GO in a 9:1 ratio of dimethylformamide and water. GO is then chemically reduced to RGO by adding 1 μ L hydrazine monohydrate per mL of solution and stirred with heating for 12 hr at 80°C.

4.2.6 Anode preparation

LIB anodes were prepared by combining the 1 mg mL⁻¹ stock solutions of Si or Ge nanowires in toluene with the prepared RGO dispersions in the appropriate amounts to yield mixtures of RGO with Si or Ge nanowires at wt% of 0 (i.e. RGO only), 25, 50, 75, 100 (i.e. nanowires only). The nanowire/RGO dispersions were vacuum filtered through a 13 mm diameter Whatman filter (FisherSci) with 0.02 μ m pores.⁴⁴ About 3-5 mg of material was needed to uniformly cover the filter. The retentate film was then rinsed with isopropanol. The alumina filter and retentate film were placed in a vacuum chamber attached to an air-free Schlenk line for overnight drying. After drying, the

anodes were carefully lifted off the filter with the help of a razor blade and tweezers and assembled into a coin cell using Li foil as the counter electrode.

Silicon nanocrystals were combined with RGO by mixing Si nanocrystals (1.4 mg dispersed in ethanol) with RGO (0.6 mg dispersed in 2 mL water / DMF) giving a Si nanocrystal composition of 70% w/w). The mixture was sonicated for 30 minutes and vacuum filtered (13 mm Whatman filter with 0.02 μm pore size). The retentate films were rinsed with ethanol. The filter was removed from the flask and dried under vacuum overnight before lifting the nanocrystal / RGO film off the filter.

4.2.7 Battery assembly and testing

Batteries were prepared in an argon-filled glovebox using a Cu foil current collector. RGO-supported anode materials were placed on the Cu current collector. A few drops of electrolyte solution (1.0M solution of LiPF_6 in a 1:1 (w/w) mixture of EC:DEC) were deposited on the anode material. A Celgard 2400 separator membrane (25 μm thick) was added followed by a few additional drops of electrolyte and Li metal foil as the counter electrode. A top casing was added to complete the battery before crimping.

Galvanostatic measurements were made with an Arbin BT-2143 test unit with cycling between 3 V and 10 mV vs Li/Li^+ using the following cycling schedule unless otherwise noted: 20 cycles at $C/20$, 20 cycles at $C/10$, 20 cycles at $C/5$, 10 cycles at $C/2$, 10 cycles at C , 20 cycles at $C/20$. Table B1 in Appendix B provides the theoretical capacities used to determine the cycle rate, C , for all of the materials studied.

4.2.8 Materials characterization

Scanning electron microscopy (SEM) images were acquired using a Zeiss Supra 40 SEM with an in-lens arrangement, a working voltage of 5 keV and a working distance

of 5 mm. SEM samples were imaged on silicon wafers (S.E.H). Transmission electron microscopy (TEM) images were digitally acquired using a JEOL 2010F TEM operated at 200 kV. TEM samples of Si nanocrystals were prepared on 200 mesh lacey-carbon copper TEM grids (Electron Microscopy Sciences) with a layer of drop-cast graphene. The Si nanocrystals were drop-cast from chloroform dispersions onto the grids.

4.3 RESULTS AND DISCUSSION

4.3.1 RGO supported nanowire and nanocrystal films

Si nanowires were grown by the supercritical fluid-liquid-solid (SFLS) method,⁴⁵ Ge nanowires were grown by the solution-liquid-solid (SLS) method,⁴⁷ and Si nanocrystals were produced by a thermal decomposition of hydrogen silsesquioxane (HSQ).^{48, 49} These nanomaterials were mixed well with RGO. Figures 4.1 and 4.2 show images of the materials used in the lithiation studies. The anode layers were 100–200 μm thick with relatively uniform thickness and composition.

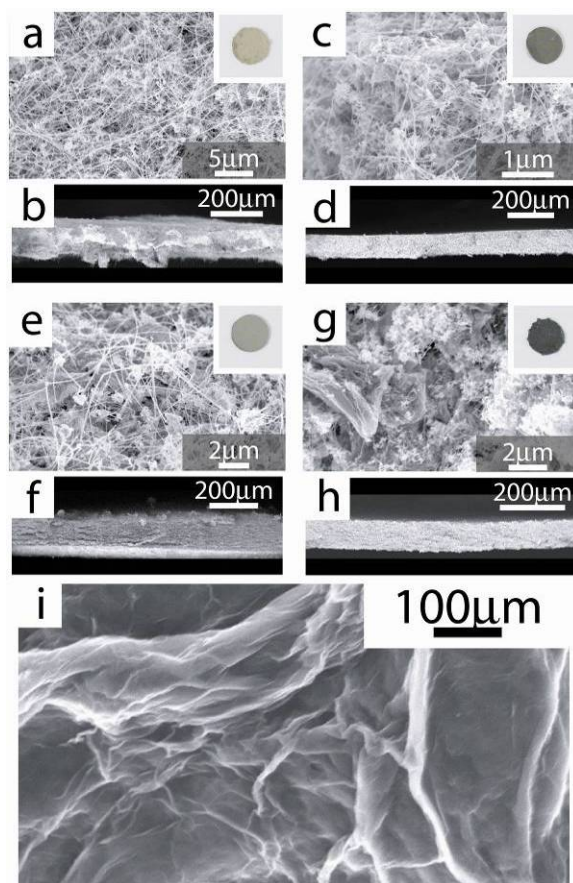


Figure 4.1: SEM images of LIB anodes of (a, b) Si nanowires, (c, d) Ge nanowires, (e, f) Si nanowire / RGO (75 % w/w Si), (g, h) Ge nanowire / RGO (75 % w/w Ge), and (i) RGO. The insets show photographs of the materials (13 mm in diameter). XRD (Figure B1 in Appendix B) confirmed that the nanowires were crystalline diamond cubic Si and Ge prior to electrochemical cycling.

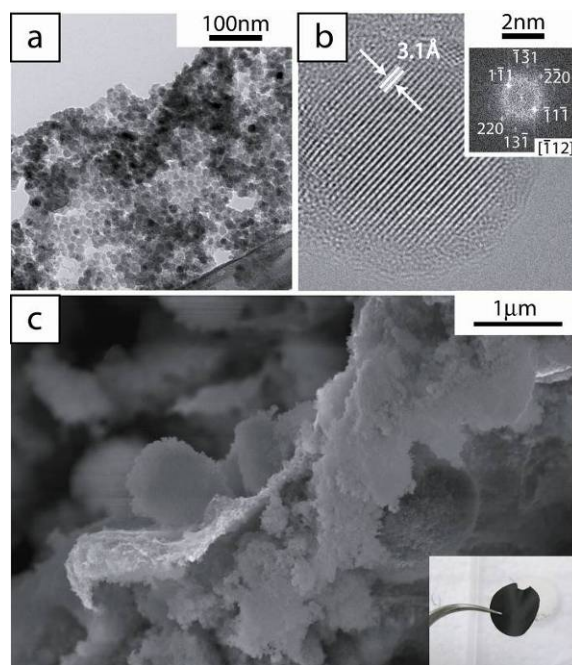


Figure 4.2: (a, b) TEM images of Si nanocrystals with accompanying FFT pattern (inset). (c) SEM of Si nanocrystals on graphene. The Si nanocrystal / graphene film in the inset is 13 mm in diameter.

4.3.2 Electrochemical behavior of RGO

Figure 4.3 shows the capacity and associated voltage and differential capacity curves for RGO anodes. The voltage profiles are consistent with reported RGO lithiation, with a first-cycle lithiation peak at 800 mV and a secondary lithiation event beginning around 250 mV and intensifying down to the cutoff voltage (10 mV).³⁶ The first cycle charge capacity at a rate of C/20 was nearly 1200 mA h g⁻¹ and then dropped steadily to 350 mA h g⁻¹, where it stabilized after 20 cycles. An increase in cycle rate led to decreased capacity. For instance, the capacity was about 200 mA h g⁻¹ at a rate of C/5 and near 100 mA h g⁻¹ at a rate of 1C. Reducing the cycle rate again to C/20 led to a return to higher capacity approaching 400 mA h g⁻¹. These capacities are slightly higher at faster cycling rates than previously reported for RGO. For example, Wang *et al.*³⁴ observed a first cycle capacity of 700 mA h g⁻¹ with an immediate decrease to 100 mA h

g^{-1} in the second cycle at a rate of $C/7.5$. The capacity of RGO anodes is known to be sensitive to the preparation method.³⁵ The high irreversible first cycle capacity is results from electrochemical reactions contributing to the solid-electrolyte interphase (SEI) layer formation. Reversible capacities slightly exceeding the theoretical maximum of graphite (372 mA h g^{-1}) at low cycle rate ($C/20$) indicate that Li^+ adsorption is occurring on both sides of individual graphene sheets.^{30,32}

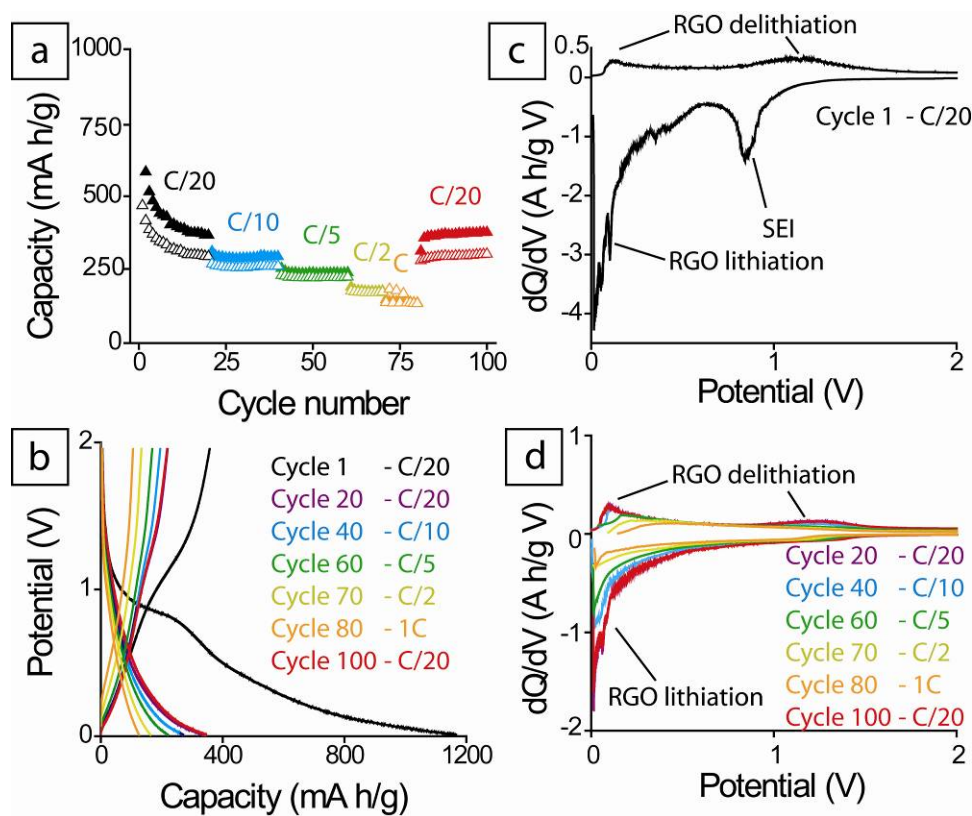


Figure 4.3: (a) Charge (filled symbols) and discharge (open symbols) capacity of RGO cycled at various rates, along with corresponding (b) voltage profiles and (c, d) differential capacity curves.

4.3.3 Electrochemical behavior of RGO supported Si nanowires

Figure 4.4 shows the electrochemical performance of Si nanowires with and without RGO added. Both samples showed a high irreversible capacity. The Si nanowires had an initial capacity of 1100 mA h g^{-1} at a cycle rate of C/20 and after 20 cycles, the capacity was less than 500 mA h g^{-1} . An increase in rate to C/10 led to a loss of lithiation capacity, but a reduction in cycle rate back to C/20 restored the capacity of greater than 500 mA h g^{-1} . The capacity was not stable and continuously dropped with increased cycling. Figure B.2 in Appendix B provides the voltage and differential capacity data for the Si nanowires, which confirmed that lithiation of the Si nanowires was occurring in the early cycles, but decreased significantly with more cycling. Adding RGO to the Si nanowires stabilized the electrodes to a small extent; for example, there was still measurable capacity when the rate was increased from C/20 to C/10, but was low and dropped to less than 100 mA h g^{-1} . A return in capacity similar to the RGO-free nanowires was observed when the rate was decreased again to C/20, but the capacity was lower (about 300 mA h g^{-1}) and still declining steadily with each subsequent cycle. The voltage and differential capacity curves for the Si nanowire / RGO anode (75% w/w Si) are shown in Figure 4.4b and an expanded view of the differential capacity data is shown in Figure B3 in Appendix B. The signatures of Si lithiation and delithiation are again present,^{7,12} confirming that Si participates in the electrochemical reaction. Interestingly, when the cycle rate returned to C/20 after cycling at faster rates, the electrochemical features corresponding to Si lithiation and delithiation were quite weak (cycle 100) even though a higher capacity was restored, indicating that Si was not fully participating in the de/lithiation reactions. The reason for this requires further study, but the significant capacity fade indicates that there are competing irreversible electrochemical reactions.

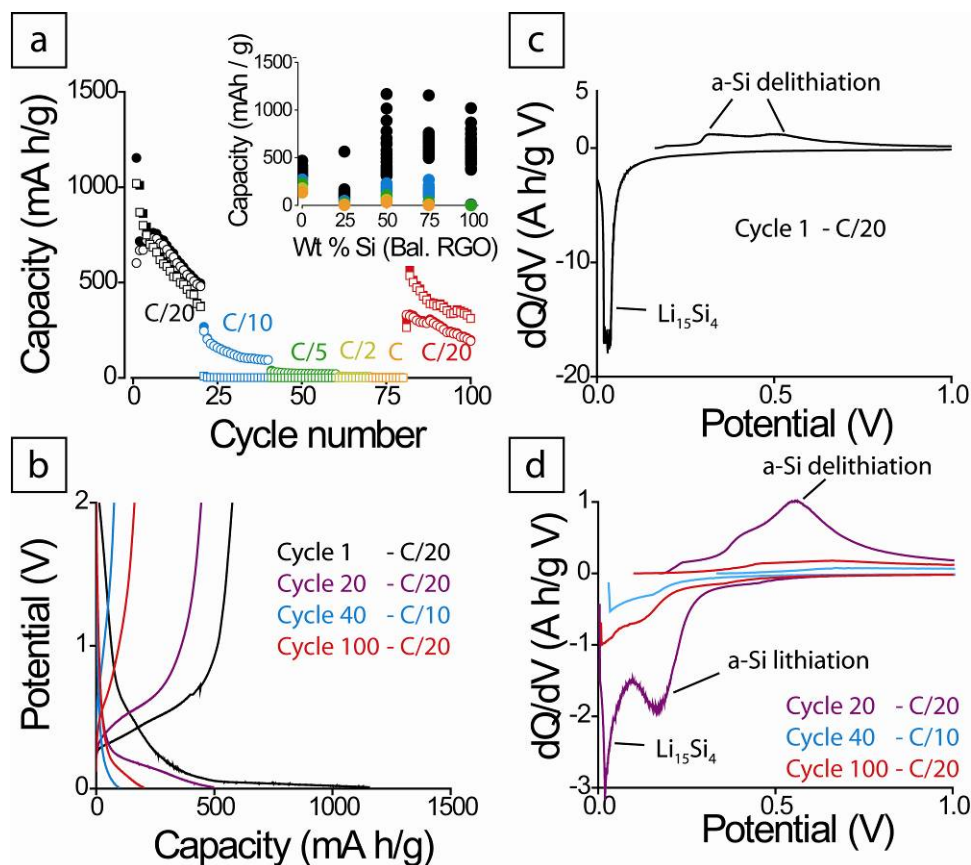


Figure 4.4: (a) Charge (filled symbols) and discharge (open symbols) capacity of Si nanowire (squares) and Si nanowire / RGO (75% w/w Si, circles) anodes at various cycle rates. Discharge capacities of Si nanowire / RGO anodes with varying Si content are plotted in the inset with colors corresponding to the cycle rates in the capacity plot. The variation in discharge capacity is the result of capacity fade. (b) Voltage profiles of Si nanowire / RGO (75% w/w Si) anodes with (c, d) corresponding differential capacity curves.

Figure 4.5 shows differential capacity curves for Si nanowire/RGO anodes with different Si content. With only 25% w/w Si, most of the lithiation and delithiation is related to RGO. The lithiation peak at 800 mV for example is characteristic of RGO and not Si. With 75% w/w Si, there is no evidence of RGO lithiation at a cycle rate of C/20 and the capacity is due solely to Si lithiation. At higher cycle rates, RGO may be participating in the lithiation reaction as the two distinctive Si peaks at 100 mV and 200

mV (most clearly observed in the cycle 20 in Figure 4.5b) are not clearly distinguishable and lithiation is occurring at a continuous range of potential below 250 mV down to the cutoff voltage (10 mV), which is characteristic of graphene.

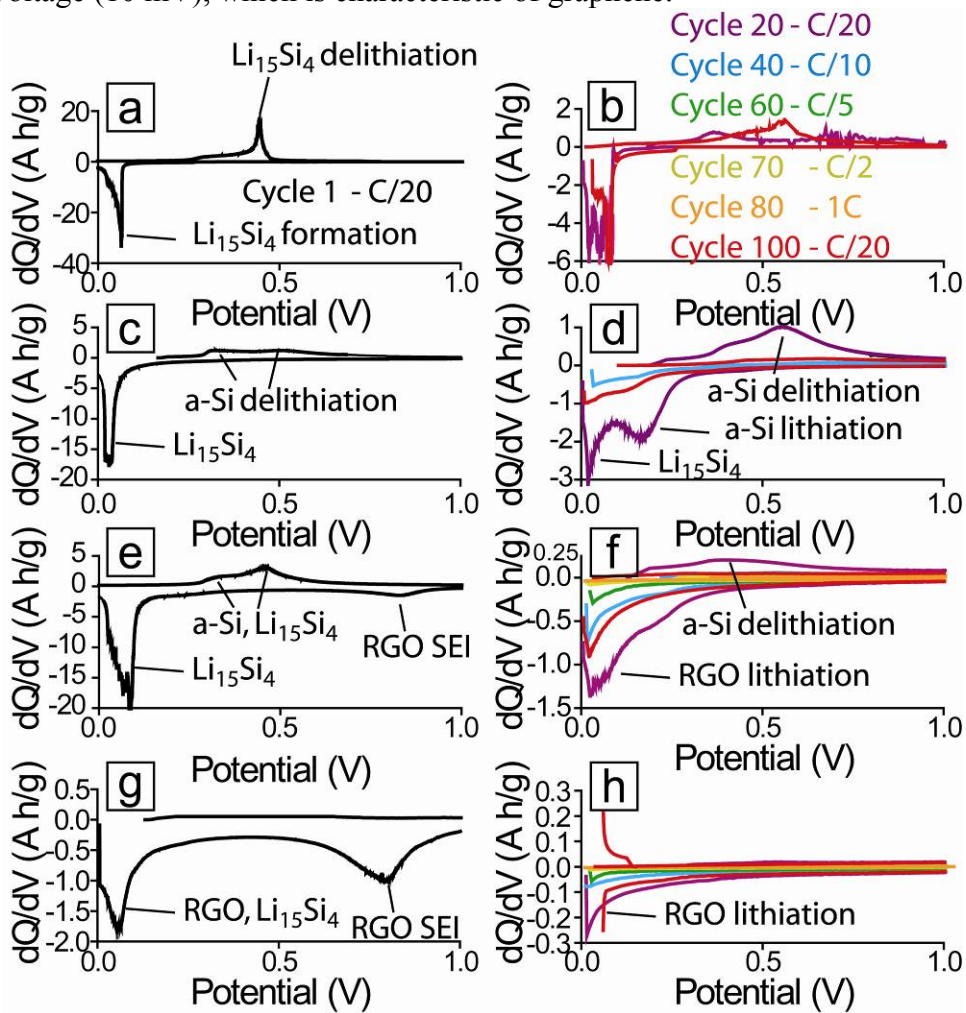


Figure 4.5: Plots of (a, c, e, g) first cycle and (b, d, f, h) subsequent cycle differential capacity corresponding to the cycling data in Figure 4.4 for Si nanowire / RGO anodes with (a, b) 100%, (c, d) 75%, (e, f) 50%, and (g, h) 25% w/w Si.

4.3.4 Electrochemical behavior of RGO supported Ge nanowires

Figure 4.6 shows capacity data for Ge nanowires with different amounts of RGO. The Ge nanowires performed significantly better than the Si nanowires, especially when

RGO was added. There was still significant irreversible capacity, but the capacity began to stabilize at about 600 mA h g^{-1} after 20 cycles at C/20. An increase in cycle rate led to a decrease in capacity, but RGO provided a significant stabilizing effect at higher cycling rates. At rates of C/2 and 1C, Ge nanowires without RGO exhibited zero capacity whereas Ge nanowires with RGO (75% w/w Ge) had capacities of 50 and 100 mA h g^{-1} . Again slowing the cycling rate to C/20 after 80 cycles led to an increase in capacity, to just above 500 mA h g^{-1} for the Ge nanowires with RGO (75% w/w Ge).

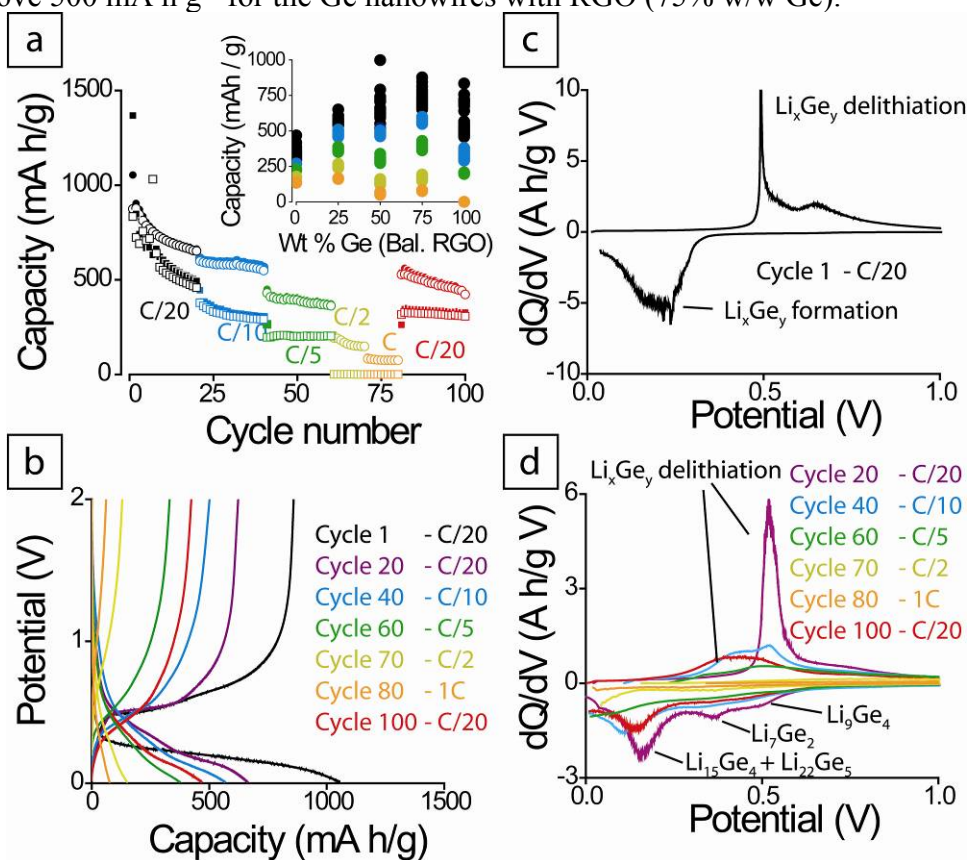


Figure 4.6: (a) Charge (filled symbols) and discharge (open symbols) capacity of Ge nanowire (squares) and Ge nanowire / RGO (75% w/w Ge) anodes (circles) cycled at different rates. Discharge capacities of Ge nanowire / RGO with varying Ge content are plotted in the inset with colors corresponding to the cycle rates in the capacity plot. The variation in discharge capacity is the result of capacity fade. (b) Voltage profiles and (c, d) corresponding differential capacity curves of the Ge nanowire / RGO (75% w/w Ge) anode.

The voltage profiles and differential capacity data of Ge nanowire/RGO anodes (Figures 4.6b and 4.7) confirm that the Ge is participating in the electrochemical reactions. Figures B.4 and B.5 in Appendix B provide voltage curves and differential capacity data for Ge nanowires corresponding to the capacity data in Figure 4.6 and an expanded view of the differential capacity curves for the Ge nanowire/RGO (75% w/w Ge) anode in the inset in Figure 4.6b. When there is less than 50% w/w Ge, there is significant lithiation of RGO (i.e., the pronounced lithiation peak at 800 mV), similar to the Si nanowire / RGO materials. But at 75% w/w Ge, lithiation appears to be exclusively occurring by insertion into Ge, except at faster cycling rates. The lithiation peaks observed at 0.1-0.3 V and 0.3-0.5 V in the differential capacity data are consistent with values reported for galvanostatic cycling of Ge.^{10,50, 51} When cycled at C/5, a broad peak at around 100 mV is present, which may still indicate the lithiation of Ge, but at faster rates, lithiation begins to occur at 250 mV and increases steadily down to the cutoff voltage (10 mV), which is characteristic of RGO lithiation. The 200 mV and 400 mV lithiation peaks reappear when the cycle rate is reduced to C/20, indicating that Ge is again being lithiated.

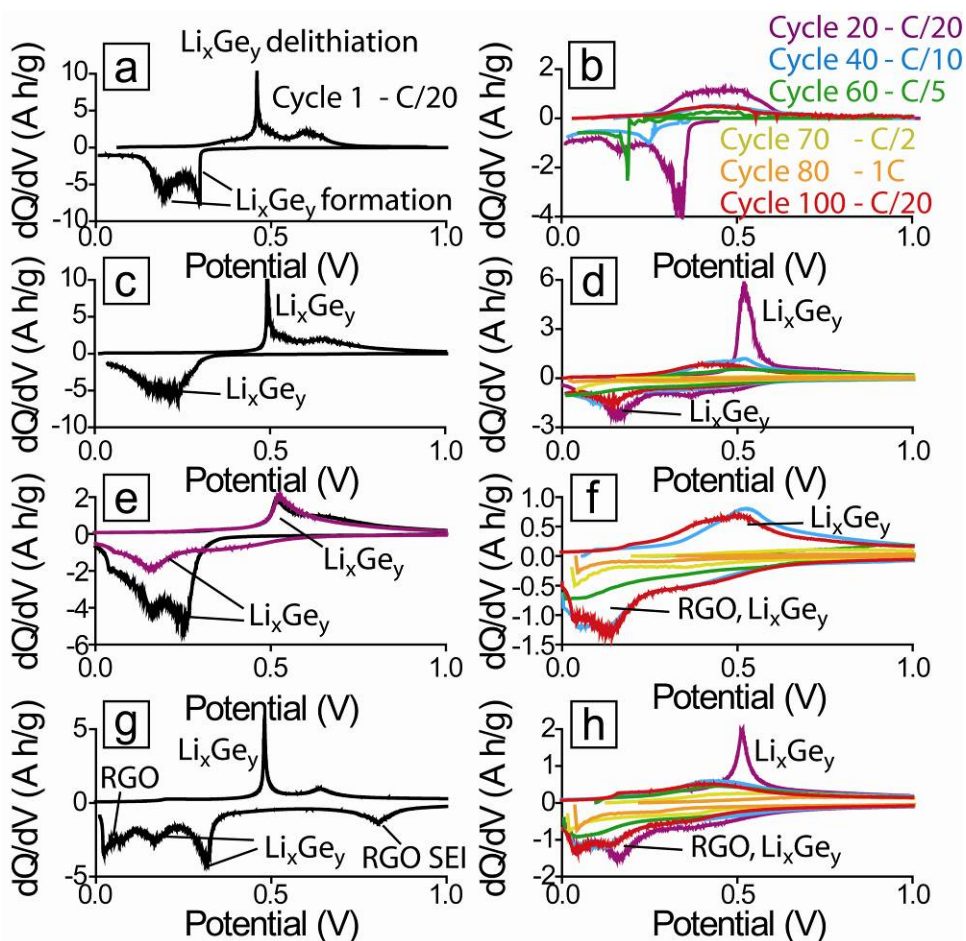


Figure 4.7: Plots of (a, c, e, g) first cycle and (b, d, f, h) subsequent cycle differential capacity corresponding to the cycling data in Figure 4.6 for Ge nanowire / RGO anodes with (a, b) 100%, (c, d) 75%, (e, f) 50%, and (g, h) 25% w/w Ge.

4.3.5 Electrochemical behavior of RGO supported Si nanocrystals

Figure 4.8 shows electrochemical data for RGO with 70% w/w Si nanocrystals. The material initially performs similar to those of Lee *et al.*⁴⁴ with initial charge capacity nearing 3000 mA h g^{-1} , but there is much more significant capacity fade. The differential capacity curves in the inset of Figure 4.8b confirm that Si is being lithiated, with no evidence of RGO lithiation (i.e., no peak at 800 mV). Lee *et al.*⁴⁴ observed capacities of greater than 2200 mA h g^{-1} after 50 cycles in their Si nanoparticle/graphene anodes.

Compared to Lee *et al.*,⁴⁴ the nanocrystals used here are smaller (5nm vs. 20-25 nm diameter), which may lead to a larger amount of surface oxide that could lower the capacity. The amount of Si used here was slightly higher (70% compared to 60% w/w), leaving less available volume for expansion upon lithiation. Finally, the cycling rate used here was faster (C/20 vs C/40). More stable cycling should be possible using a more appropriate binder, like polyvinylidene fluoride (PVdF).^{52,53}

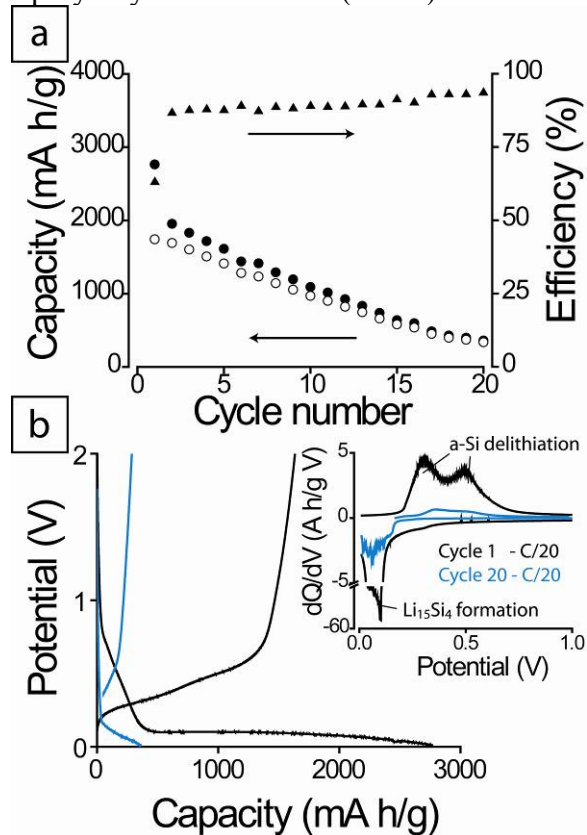


Figure 4.8: (a) Charge (filled symbols) and discharge (open symbols) capacity with coulombic efficiencies of RGO with 70% w/w Si nanocrystals cycled at a rate of C/20. (b) The voltage profiles and (inset) differential capacity curves are shown for cycles 1 and 20.

4.3.6 Extended behavior of RGO supported Si and Ge nanowires

The Ge nanowire / RGO (75% w/w Ge) gave the best cycling performance of the materials studied here. Figure 4.9 shows the cycling performance of the RGO-supported Ge and Si nanowires. There was significant capacity fade in both materials, but especially in the case of the Si nanowire/RGO anode at the faster cycling rate of C/10. The Ge nanowire / RGO anode exhibits an initially high capacity of 1050 mA h g^{-1} (the theoretical capacity for this composition is 1308 mA h g^{-1}) and retained much of this, decreasing only to 800 mA h g^{-1} after 20 cycles. At higher charging rate of C/10, the capacity of Ge nanowire / RGO was still around 500 mA h g^{-1} and gradually faded to 350 mA h g^{-1} after 100 cycles. Figure B6 in Appendix B provides the voltage profiles and differential capacity curves. In the Si nanowire / RGO anode, the differential capacity plots indicate that a significant amount of RGO lithiation is occurring after cycle 20 when the rate was increased to C/10. This is also the case for the Ge nanowire/RGO anode, but the characteristic lithiation and delithiation peaks of Ge are still present, indicating that Ge lithiation rates are faster than Si and still competitive with RGO at these faster cycling rates. This likely relates to the much higher solid state Li diffusion in Ge than Si.¹⁰

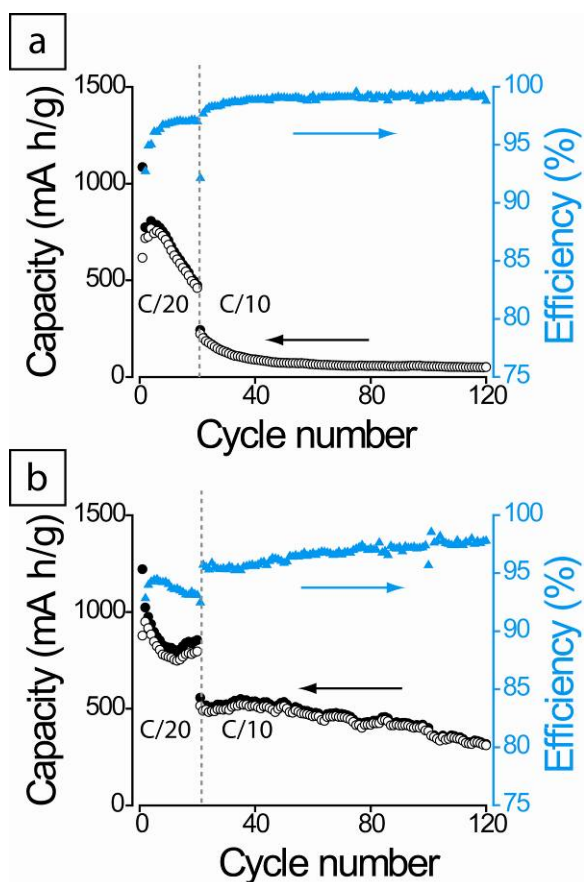


Figure 4.9: Lithium capacity of (a) Si nanowire / RGO (75% w/w Si) and (b) Ge nanowire / RGO (75% w/w Ge). The batteries were cycled at C/20 for 20 cycles followed by C/10 for the next 100 cycles.

The much better performance of the Ge/RGO anodes compared to Si also probably relates to the significant presence of Au in the Si nanowires used in this study (See XRD data in Figure B1 of Appendix B). The Si nanowires were grown by the SFLS process using trisilane as a reactant, which requires relatively large amounts of Au seeds.⁴⁵ Typical Si: Au molar ratios are 40:1, compared to about 600:1 for Si nanowires grown by SFLS using monophenylsilane (MPS). Trisilane is much more reactive than MPS, however, and yields a significantly higher Si nanowire production rate,⁴⁵ which is economically desirable. Nonetheless, Au accounts for nearly 25% by weight of the Si

nanowire anode, which is known to contribute significant irreversible capacity.^{54, 55} In previous studies, Si nanowires grown by SFLS using monophenylsilane with significantly less Au (<1% w/w) have exhibited much better cycling performance than the trisilane-grown Si nanowires.^{19, 20} The Au content in SLS-grown Ge nanowires is also relatively low—less than 1% w/w Au.⁴⁷

4.4 CONCLUSIONS

The capacities reported here are well below the theoretical capacities of Si and Ge, but these can be improved significantly by selecting more appropriate electrolyte,^{52, 53} binder²¹ and processing methods.²² A low capacity can also result from poor adhesion to the copper collector, which was not optimized. Previous reports of very high capacity near the theoretical limit³⁹⁻⁴⁴ have utilized materials anchored by covalent linkage or electrostatic interaction with RGO. Yang *et al.*⁴¹ observed reduced capacity retention in electrode materials made by mechanical mixing of Co₃O₄ nanoparticles with RGO compared to materials made with intentional chemisorption of the nanoparticles to the RGO. Additionally, slurries typically used in LIBs are formulated to evenly coat the current collector to ensure good electrical contact—the surfaces of the anodes studied here are relatively rough and were simply placed into physical contact with the current collector and may not provide the best electrical contact. Nonetheless, the data show that RGO can significantly help stabilize electrochemical lithiation of Si and Ge nanomaterials and improve cycle life and capacity retention.

RGO itself can serve as an LIB anode material, but when combined with Si or Ge nanowires, RGO does not participate in the electrochemical lithiation reaction when the Si/Ge loading is relatively high—greater than about 50% w/w—and when the charging rate is relatively slow—in this case, slower than C/10. At lower Si/Ge loading and faster

cycling rates, RGO lithiation does occur and under most of these conditions dominates the electrochemical behavior. The stabilizing effect of RGO was more pronounced for Ge than Si, most likely because of the lower concentration of Au in the Ge sample, but also because of the higher Li diffusion in Ge than Si. Ge has a lower theoretical capacity than Si, but Li diffusion is much faster in Ge, by a factor of 400,¹⁰ and has the potential for much faster charge/discharge rates than Si. Much higher capacities were observed in the Ge nanowire/RGO materials at faster cycling rates compared to the Si nanowire/RGO materials. Park *et al.*¹⁶ reported a capacity of 600 mA h g⁻¹ for Ge nanotubes at a current load of 20 A g⁻¹ corresponding to a cycle rate of 12.3C. A charge rate of C/3 is considered viable for commercial applications. High cycle rates of 10C have been observed for Si with capacities of up to 1250 mA h g⁻¹,¹⁷ but only in thin vapor-deposited films. For high rate applications, Ge appears to be more promising than Si, at least in the case of composite materials in which competitive electrochemical lithiation can occur.

4.5 ACKNOWLEDGEMENTS

Authors that contributed to this work include: Matthew G. Panthani, Vincent C. Holmberg, Colin M. Hessel, Dariya K. Reid, Timothy D. Bogart, Justin T. Harris, C. Buddie Mullins, and Brian A. Korgel. Financial support of this research was provided by the Robert A. Welch Foundation (F-1464) and the Air Force Research Laboratory (FA-8650-07-2-5061). JTH acknowledges financial support as part of the program “Understanding Charge Separation and Transfer at Interfaces in Energy Materials (EFRC: CST),” an Energy Frontier Research Center funded by the U.S. Department of Energy Office of Science, Office of Basic Energy Sciences, under Award No. DE-SC0001091.

4.6 REFERENCES

1. Tarascon, J.-M.; Armand, M. *Nature* **2001**, *414*, 359-367.
2. Kasavajjula, U.; Wang, C.; Appleby, A. J. *J. Power Sources* **2007**, *163*, 1003-1039.
3. Armand, M.; Tarascon, J.-M. *Nature* **2008**, *451*, 652-657.
4. Yoshio, M.; Tsumura, T.; Dimov, N. *J. Power Sources* **2005**, *146*, 10-14.
5. S. Basu, U.S. Patent No. 4,304,825, **Dec 8, 1981**.
6. S. Basu, U.S. Patent No. 4,423,125, **Dec 27, 1983**.
7. Obrovac, M. N.; Christensen, L. *Electrochem. Solid-State Lett.* **2004**, *7*, A93-A96.
8. Weydanz, W. J.; Wohlfahrt-Mehrens, M.; Huggins, R. A. *J. Power Sources* **1999**, *81-82*, 237-242.
9. Gao, B.; Sinha, S.; Fleming, L.; Zhou, O. *Adv. Mater.* **2001**, *13*, 816-819.
10. Graetz, J.; Ahn, C. C.; Yazami, R.; Fultz, B. *J. Electrochem. Soc.* **2004**, *151*, A698-A702.
11. Boukamp, B. A., Lesh, G. C., Huggins, R. A. *J. Electrochem. Soc.* **1981**, *128*, 725-729.
12. Obrovac, M. N.; Krause, L. J. *J. Electrochem. Soc.* **2007**, *154*, A103-A108.
13. Liu, C.; Li, F.; Ma, L.-P.; Cheng, H.-M. *Adv. Mater.* **2010**, *22*, E28-E62.
14. Chan, C. K.; Peng, H.; Liu, G.; McIlwrath, K.; Zhang, X. F.; Huggins, R. A.; Cui, Y. *Nature Nanotech.* **2008**, *3*, 31-35.
15. Chan, C. K.; Zhang, X. F.; Cui, Y. *Nano Lett.* **2007**, *8*, 307-309.
16. Park, M.-H.; Cho, Y.; Kim, K.; Kim, J.; Liu, M.; Cho, J. *Angew. Chem. Int. Ed.* **2011**, *50*, 9647-9650.
17. Yao, Y.; McDowell, M. T.; Ryu, I.; Wu, H.; Liu, N.; Hu, L.; Nix, W. D.; Cui, Y. *Nano Lett.* **2011**, *11*, 2949-2954.
18. Teki, R.; Datta, M. K.; Krishnan, R.; Parker, T. C.; Lu, T.-M.; Kumta, P. N.; Koratkar, N. *Small* **2009**, *5*, 2236-2242.
19. Chan, C. K.; Patel, R. N.; O'Connell, M. J., Korgel, B. A., Cui, Y. *ACS Nano* **2010**, *4*, 1443-1450.
20. Chockla, A. M.; Harris, J. T.; Akhavan, V. A.; Bogart, T. D.; Holmberg, V. C.; Steinhagen, C.; Mullins, C. B.; Stevenson, K. J.; Korgel, B. A. *J. Am. Chem. Soc.* **2011**, *133*, 20914-20921.

21. Kovalenko, I.; Zdyrko, B.; Magasinski, A.; Hertzberg, B.; Milicev, Z.; Burtovyy, R.; Luzinov, I.; Yushin, G. *Science* **2011**, *334*, 75-29.
22. Li, J.; Christensen, L.; Obrovac, M. N.; Hewitt, K. C.; Dahn, J. R. *J. Electrochem. Soc.* **2008**, *155*, A234-A238.
23. Cho, Y. J.; Kim, H. S.; Im, H.; Myung, Y.; Jung, G. B.; Lee, C. W.; Park, J.; Park, M.-H.; Cho, J.; Kang, H. S. *J. Phys. Chem. C* **2011**, *115*, 9451-9457.
24. Kim, H.; Cho, J. *Nano Lett.* **2008**, *8*, 3688-3691.
25. Choi, J. W.; Hu, L.; Cui, L.; McDonough, J. R.; Cui, Y. *J. Power Sources* **2010**, *195*, 8311-8316.
26. Wang, W.; Kumta, P. N. *ACS Nano* **2010**, *4*, 2233-2241.
27. Magasinski, A.; Dixon, P.; Hertzberg, B.; Kvit, A.; Ayala, J.; Yushin, G. *Nat. Mater.* **2010**, *9*, 353-358.
28. Singh, V.; Joung, D.; Zhai, L.; Das, S.; Khondaker, S. I.; Seal, S. *Prog. Mat. Sci.* **2011**, *56*, 1178-1271.
29. Dikin, D. A.; Stankovich, S.; Zimney, E. J.; Piner, R. D.; Dommett, G. H. B.; Evmenenko, G.; Nguyen, S. T.; Ruoff, R. S. *Nature* **2007**, *448*, 457-460.
30. Yoo, E.; Kim, J.; Hosono, E.; Zhou, H.; Kudo, T.; Honma, I. *Nano Lett.* **2008**, *8*, 2277-2282.
31. Liu, Y.; Xue, J. S.; Zheng, T.; Dahn, J. R. *Carbon* **1996**, *34*, 193-200.
32. Suzuki, T.; Hasegawa, T.; Mukai, S. R.; Tamon, H. *Carbon* **2003**, *41*, 1933-1939.
33. Liang, M.; Zhi, L. *J. Mater. Chem.* **2009**, *19*, 5871-5878.
34. Wang, C.; Li, D.; Too, C. O.; Wallace, G. G. *Chem. Mater.* **2009**, *21*, 2604-2606.
35. Pan, D.; Wang, S.; Zhao, B.; Wu, M.; Zhang, H.; Wang, Y.; Jiao, Z. *Chem. Mater.* **2009**, *21*, 3136-3142.
36. Matsuo, Y.; Sugie, Y. *Carbon* **1998**, *36*, 301-303.
37. Park, S.; An, J.; Piner, R. D.; Jung, I.; Yang, D.; Velamakanni, A.; Nguyen, S. T.; Ruoff, R. S. *Chem. Mater.* **2008**, *20*, 6592-6594.
38. Park, S.; An, J.; Jung, I.; Piner, R. D.; An, S. J.; Li, X.; Velamakanni, A.; Ruoff, R. S. *Nano Lett.* **2009**, *9*, 1593-1597.
39. Wang, H.; Cui, L.-F.; Yang, Y.; Sanchez Casalongue, H.; Robinson, J. T.; Liang, Y.; Cui, Y.; Dai, H. *J. Am. Chem. Soc.* **2010**, *132*, 13978-13980.
40. Wu, Z.-S.; Ren, W.; Wen, L.; Gao, L.; Zhao, J.; Chen, Z.; Zhou, G.; Li, F.; Cheng, H.-M. *ACS Nano* **2010**, *4*, 3187-3194.

41. Yang, S.; Feng, X.; Ivanovici, S.; Müllen, K. *Angew. Chem. Int. Ed.* **2010**, *49*, 8408-8411.
42. Wang, D.; Kou, R.; Choi, D.; Yang, Z.; Nie, Z.; Li, J.; Saraf, L. V.; Hu, D.; Zhang, J.; Graff, G. L.; Liu, J.; Pope, M. A.; Aksay, I. A. *ACS Nano* **2010**, *4*, 1587-1595.
43. Zhou, G.; Wang, D.-W.; Li, F.; Zhang, L.; Li, N.; Wu, Z.-S.; Wen, L.; Lu, G. Q.; Cheng, H.-M. *Chem. Mater.* **2010**, *22*, 5306-5313
44. Lee, J. K.; Smith, K. B.; Hayner, C. M.; Kung, H. H. *Chem. Comm.* **2010**, *46*, 2025-2027.
45. Heitsch, A. T.; Akhavan, V. A.; Korgel, B. A. *Chem. Mater.* **2011**, *23*, 2697-2699.
46. Saunders, A. E.; Sigman, M. B.; Korgel, B. A. *J. Phys. Chem. B* **2004**, *108*, 193-199.
47. Chockla, A. M.; Korgel, B. A. *J. Mater. Chem.* **2009**, *19*, 996-1001.
48. Hessel, C. M.; Henderson, E. J.; Veinot, J. G. C. *Chem. Mater.* **2006**, *18*, 6139-6146.
49. Hessel, C. M.; Reid, D.; Panthani, M. G.; Rasch, M. R.; Goodfellow, B. W.; Wei, J.; Fujii, H.; Akhavan, V.; Korgel, B. A. *Chem. Mater.* **2012**, *24*, 393-401.
50. Laforge, B.; Levan-Jodin, L.; Salot, R.; Billard, A. *J. Electrochem. Soc.* **2008**, *155*, A181-A188.
51. Yoon, S.; Park, C.-M.; Sohn, H.-J. *Electrochem. Solid-State Lett.* **2008**, *11*, A42-A45.
52. Choi, N.-S.; Yew, K. H.; Lee, K. Y.; Sung, M.; Kim, H.; Kim, S.-S. *J. Power Sources* **2006**, *161*, 1254-1259.
53. Nakai, H.; Kubota, T.; Kita, A.; Kawashima, A. *J. Electrochem. Soc.* **2011**, *158*, A798-A801.
54. Taillades, G.; Benjelloun, N.; Sarradin, J.; Ribes, M. *Solid State Ionics* **2002**, *152*, 119-124.
55. Yuan, L.; Liu, H. K.; Maarroof, A.; Konstantinov, K.; Liu, J.; Cortie, M. *J. New Mater. Electrochem. Syst.* **2007**, *10*, 95-99.

Chapter 5: Solution Grown Germanium Nanowires as a Negative Electrode Material in Lithium Ion Batteries

5.1 INTRODUCTION

The invention of the lithium ion battery ushered in an era of unparalleled personal electronic device portability, evident by the ubiquity of cellular phones, laptop computers, mp3 players and smart tablets. This change in lifestyle has fostered increased demand for longer lasting, higher capacity, cheap, sustainable power supplies.¹ The automotive industry is also moving toward using Li-ion batteries to power cars, but developmental hurdles remain.² Unfortunately, battery technology has been relatively stagnant during the past several decades; since the mid 1980s, the cathode material has been a Li metal oxide compound (largely LiCoO_2) with a graphite anode.³ Recently, much effort has been made to improve the capacity of Li ion batteries, particularly by replacing graphite with a material that can store more lithium.⁴ Germanium is one such candidate.

Graphite forms LiC_6 upon lithiation which has a maximum theoretical capacity of 372 mA h g^{-1} . Compare this to Ge, which forms $\text{Li}_{22}\text{Ge}_5$,^{5, 6} a compound with a maximum theoretical capacity of 1624 mA h g^{-1} . The main argument against Ge is the cost. In 2009, the price of Ge was $\$950 / \text{kg}$ and fluctuated between $\$380 / \text{kg}$ and $\$1490 / \text{kg}$ during the preceding decade.⁷ There is no shortage of supply, however; as Ge is abundant in the earth's crust.⁸ The natural abundance of Ge in the Earth's lithosphere, for instance, is about 1.6 ppm,⁹ which translates to about $2 \cdot 10^{18} \text{ kg}$ —an amount large enough to fill a 130-foot deep pool the size of the United States—yet the worldwide production of Ge in 2011 reached only 118 tonnes.¹⁰ The price of Ge is maintained by low demand.

A large volumetric expansion (300%) accompanies lithium insertion into the Ge lattice. Bulk Ge pulverizes within the first few charge / discharge cycles and becomes unusable as an electrode material. The primary method of mitigating pulverization has been to use nanomaterials, which are resilient to mechanical stresses associated with this expansion.¹¹⁻¹³ Studies have been conducted to explore the viability of Ge as an anode material in Li ion batteries but have focused on thin film germanium.^{6, 8, 14-19} Studies on solution-processable nanomaterials such as nanoparticles,¹⁹⁻²¹ nanowires²²⁻²⁵ and nanotubes²⁶ have been explored as well. In addition to increased Li storage, Ge has a large Li diffusion coefficient²⁷ making it attractive in high power applications.^{14, 26} We report a scalable method for high throughput synthesis of solution processable Ge nanowires using the SLS growth mechanism.²⁸ Various electrolyte solutions were tested, including the fluorethylene carbonate (FEC) additive.²⁹⁻³¹

5.2 MATERIALS AND METHODS

5.2.1 Materials

All reactions were carried out using standard airless procedures using a nitrogen-filled glove box and a Schlenk line. All reagents and solvents were used as received and without further purification. Dodecanethiol (DDT, $\geq 98\%$), tetrachloroaurate trihydrate ($\geq 99.9\%$), sodium borohydride ($\geq 98\%$), toluene (anhydrous, 99.8%), ethanol (99.9%), tetraoctylammonium bromide (TOAB, 98%), propylene carbonate (PC, anhydrous, 99.7%), lithium hexafluorophosphate (LiPF_6 , $\geq 99.99\%$), poly (vinylidene fluoride) (PVdF, average MW $\sim 534,000$ by GPC), 1-methyl 2-pyrrolidinone (NMP, 99.5%), chloroform (99.8%) and squalane (99%) were purchased from Sigma-Aldrich and diphenylgermane (DPG, $>95\%$) from Gelest. Conductive carbon super C65 was supplied by TIMCAL. Fluoroethylene carbonate (FEC, $>98\%$) was obtained from TCI America.

Electrolytes were either purchased—as 1.0M solutions of LiPF_6 in a 1:1 w/w mixture of ethylcarbonate (EC) : diethyl carbonate (DEC) (Novolyte) or 1.0M LiPF_6 in a 1:1 mixture of EC : dimethyl carbonate (DMC) (EMD chemicals)—or prepared in one of four ways: LiPF_6 was either dissolved at a concentration of 1.0M in 1:1 w/w mixture of (1) FEC:DEC, (2) FEC:DMC, (3) PC : DMC or (4) by adding 3% w/w FEC to the EC:DMC solution purchased from EMD chemicals. Celgard 2400 membranes (25 μm) were used as separators in battery assembly and were purchased from Celgard. Li metal foil (1.5 mm 99.9%) was purchased Alfa Aesar.

5.2.2 Germanium nanowire synthesis

Dodecanethiol-coated Au nanocrystals (2 nm diameter) were synthesized following literature procedures³² and were stored in a nitrogen-filled glove box dispersed in toluene at a concentration of 1 mg mL⁻¹. Ge nanowires were produced using a modified literature method.²⁸ In short, 10 mL squalane were added to a 4-neck flask and attached to a Schlenk line, heated to 100°C with vigorous stirring under vacuum (<500 mTorr) for 30 minutes, and then blanketed with nitrogen. The solvent was then heated to 380°C. An injection solution containing 0.27 5mL of the Au nanocrystal stock solution was combined with 0.375 mL DPG, diluted with 1 mL squalane and plunged into a syringe. The reaction solution-containing syringe was removed from the glove box and injected into the reaction flask containing squalane at 380°C. The reaction lasted 5 minutes, then the flask was removed from the heating mantle and allowed to cool to room temperature. Toluene (10 mL) was then added to the reaction mixture. The flask was removed from the Schlenk line and sonicated for a few seconds to remove product that had adhered to the flask walls. The reaction solution was then transferred to a centrifuge tube and spun at 8000 rpm for 5 minutes. The supernatant was discarded and the

precipitate was resuspended in 10 mL of chloroform and 2 mL of ethanol and centrifuged again at 8000 rpm for 5 minutes. This washing procedure was carried out a third time before the Ge nanowire product was dried down by rotovap to get an accurate weight. One reaction produces roughly 40 mg of Ge nanowires. Two such reactions were needed to generate enough material to make a slurry to be used in Li ion battery testing.

5.2.3 Anode preparation and battery assembly

The Ge nanowire slurry was prepared by dispersing Ge nanowires (81.1 mg) in 2 mL toluene and bath sonicating for 1 hour. Meanwhile, 23.2 mg PVdF and 11.6 mg conductive carbon were dissolved in 1 mL NMP and bath sonicated for 1 hour. The Ge nanowire and PVdF / carbon black suspensions were mixed (70:20:10 w/w solid content of Ge : PVdF : carbon black) and wand sonicated for an additional 30 minutes. The solution was then reduced by rotovap to yield a thick slurry. The slurry was cast onto Cu foil using a 200 μm film applicator and vacuum dried overnight at 100°C.

Batteries were assembled in an argon-filled glovebox. Ge nanowire anodes were hole-punched (1 cm diameter) from the Cu foil supported slurry film. The electrolyte was a 1.0 M solution of LiPF_6 in a 1:1 w/w mixture of either (1) EC:DEC, (2) EC:DMC, (3) EC:DMC + 3% w/w FEC, (4) FEC:DEC, (5) FEC:DMC, or (6) PC:DMC. A few drops of electrolyte were deposited over lithium foil counter electrode and again atop the separator membrane (25 μm thick, Celgard) before the adding the Ge anode.

5.2.4 Material characterization

Scanning electron microscopy (SEM) images were acquired using a Zeiss Supra 40 SEM with an in-lens arrangement, a working voltage of 5 keV and a working distance of 5 mm. SEM samples were imaged on silicon wafers (S.E.H). Transmission electron microscopy (TEM) images were digitally acquired using either a FEI Tecnai Spirit

BioTwin TEM operated at 80 kV or a field emission JEOL 2010F TEM operated at 200 kV. TEM samples were prepared by drop-casting from chloroform dispersions onto 200 mesh lacey-carbon copper TEM grids (Electron Microscopy Sciences).

X-ray diffraction (XRD) was carried out using a Rigaku R-Axis Spider Diffractometer with Image plate detector with Cu k_{α} ($\lambda = 1.5418 \text{ \AA}$) radiation operated at 40 kV and 40 mA. Measurements were taken on samples on a 0.5 mm nylon loop. Samples were scanned for 10 minutes while rotating at 1° per second under ambient conditions. The data were integrated from $2\theta = 20$ to 80 . Background scattering from the nylon loop was subtracted from the sample measurement.

AC electrochemical impedance spectroscopy (EIS) measurements were made using an Electrochemical Analyzer (CH Instruments, model CHI 604D) over a frequency range of 0.01 to 100,000 Hz. Galvanostatic measurements were made using an Arbin BT-2143 test unit that cycling between 2 V and 10 mV vs Li/Li⁺ at various rates. Capacities are reported based on the active material only.

5.3 RESULTS AND DISCUSSION

5.3.1 Germanium nanowires thin films

Figure 5.1 shows Ge nanowires grown using the SLS growth method used in this study. Ge nanowires were combined with PVdF and cycled at a rate of C/10 ($C = 1620 \text{ mA h g}^{-1}$) using electrolyte solutions consisting of 1.0 M LiPF₆ dissolved in a variety of 1:1 w/w solvent mixtures, including: **(1)** EC:DEC, **(2)** EC:DMC, **(3)** EC:DMC + 3% w/w FEC (hereafter referred to as EC:DMC+FEC), **(4)** FEC:DEC, **(5)** FEC:DMC, and **(6)** PC:DMC. In recent studies, the primary electrolyte solution has been some combination of EC, DEC, and DMC.^{8, 14, 16, 22, 25, 33} Several recent studies have shown that FEC stabilizes the cycle life behavior for Si nanostructures,²⁹⁻³¹ but has yet to be tested in Ge

systems. PC:DMC was also tested. PC is known to interact unfavorably toward the intercalation of Li in graphite,³⁴ but the effect on germanium is unknown.

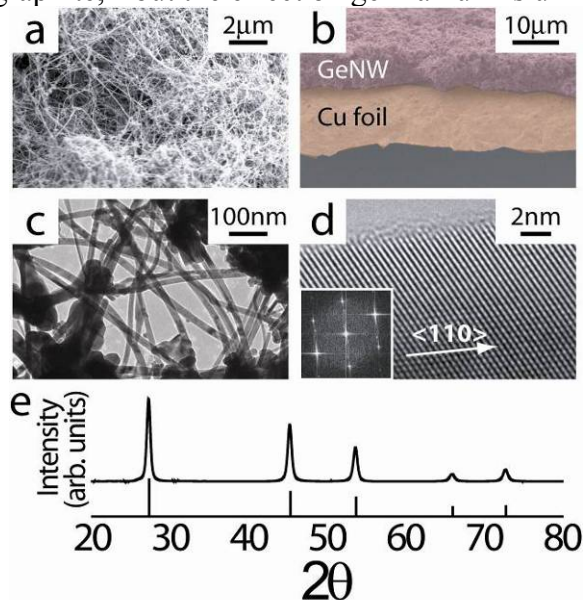


Figure 5.1: (a) SEM and (b) cross-sectional SEM of the Ge nanowire slurry cast on Cu foil, (c) TEM, (d) high resolution TEM with (inset) FFT down the [011] zone axis, and (e) XRD of as prepared Ge nanowires with the crystalline Ge reference pattern (JCPDS: 00-004-0545).

5.3.2 Extended cycle life behavior

Charge/discharge cycle results and capacity retention data are shown in Figure 5.2 and summarized in Table 5.1. First cycle capacities ranged between 1300 and 1900 mA h g⁻¹. Some capacities exceed the theoretical maximum of Ge due to Li consuming side reactions during the first cycle, attributed to solid-electrolyte-intefphase (SEI) layer formation. Irreversible capacity losses were below 25% for most electrolytes, though electrolyte (5) had an irreversible loss of 50%. While the addition of FEC to the electrolytes increased the irreversible losses (comparing electrolyte (4) to (1), or electrolyte (5) to (2), for example), the capacity retention for these electrolyte systems were the best. For example, electrolytes (3)–(5) (i.e., FEC-containing electrolytes)

exhibited capacity retention between 75% and 98%. In general, DEC-containing electrolytes, (1) and (4), out-performed the DMC analogues, (2) and (5). It appears that DEC is more stable in Ge nanowire films; further characterization is shown in Chapter 6 that substantiate this claim. Electrolyte (6) performed poorly; additional data pertaining to this system can be found in Appendix C. Of further interest here is that we achieve high capacities with good cyclability for Ge nanowires cycled with PVdF binder without a high temperature anneal. In contrast, Si requires heat treatment of up to 300°C under inert atmosphere to achieve reasonable cycle behavior.^{35, 36} As the purpose of the anneal is to distribute the binder / conductive carbon more uniformly over the active material,^{35, 36} it is likely that PVdF forms a better coating on Ge nanowires than it does Si during slurry casting. The Ge nanowires studied here require only a 100°C vacuum anneal to dry residual NMP and capacity retention is much better than reported in references 35 and 36.

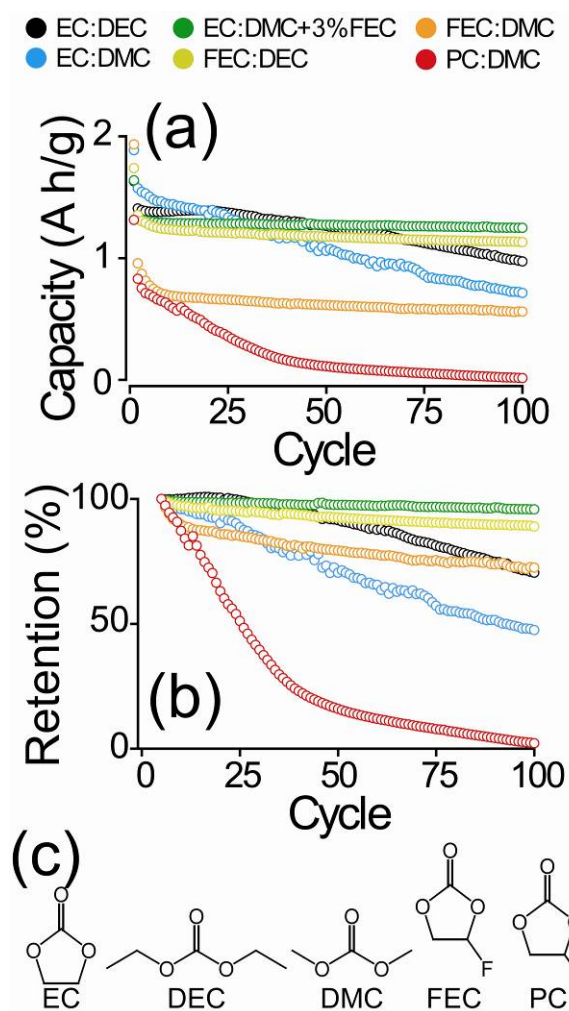


Figure 5.2: (a) Comparison of charge capacity for various electrolytes with (b) charge capacity retention plotted relative to the 5th cycle charge capacity for each respective (c) electrolyte solvent system.

Table 5.1: Capacity retention of Ge nanowire films using various electrolyte solutions.

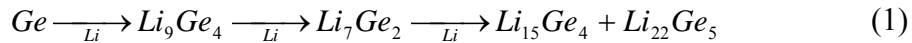
Electrolyte	Capacity (mA h g ⁻¹)				Retention (%)	
	Cycle 1	1 st cycle loss (%)	Cycle 5	Cycle 100	Q _{ret1} ^a	Q _{ret5} ^b
EC:DEC	1630	223 (13.7)	1382	973	59.7	70.4
EC:DMC	1885	311 (16.5)	1504	714	37.9	47.5
EC:DMC+FEC	1639	301 (18.4)	1303	1248	76.1	95.8
FEC:DEC	1738	385 (22.2)	1271	1131	65.0	89.0
FEC:DMC	1933	975 (50.5)	774	561	29.0	72.5
PC:DMC	1313	484 (36.8)	699	15	1.2	2.2

^a Charge capacity retention of the 100th cycle relative to the 1st cycle

^b Charge capacity retention of the 100th cycle relative to the 5th cycle

Figure 5.3 shows electrochemical data for electrolytes (1)–(5). Coulombic efficiencies ranged between 95 and 100%. The coulombic efficiencies for electrolytes (1), Figure 5.3a.i, and (2), Figure 5.3b.i, ranged between 95% and 98%. Coulombic efficiencies for electrolytes (3)–(5) approached 99% indicated better charge and Li⁺ transport through SEI layers formed from electrolyte solutions containing FEC. The voltage profiles show constant over-potential for these electrolytes as well, whereas electrolytes (1) and (2) show a gradual increase due to progressively increasing internal resistances within the battery due to continued SEI growth during cycling, for example. We present electrochemical impedance spectroscopy (EIS) data below to substantiate this claim.

All electrolytes show a first cycle plateau in the voltage profiles at 350–400mV and another at 150–200mV. These peaks correspond to lithiation of Ge and formation of Li_xGe_{1-x} compounds. Lithiation behavior beyond the first cycle depends on the electrolyte used. Batteries cycled using electrolytes (1)–(3), for example, show three distinct lithiation peaks—at 500 mV, 400 mV, and between 150 mV and 200 mV, respectively—which likely correspond to the multi-stage lithiation process reported by Yoon *et al.*⁵



In Ref. 5, the Li_9Ge_4 phase was observed for a cut-off potential of 220 mV. When the potential was lowered to 170 mV, the Li_7Ge_2 phase was reported. Cycling to 0V yields $Li_{15}Ge_4$.⁵ Only the first cycle differential plots were reported in Ref. 5, though, making further comparison to our results difficult. The peak situated between 350 mV and 400 mV in the first cycle corresponds to Li insertion into crystalline Ge⁸ and disappears in subsequent cycles where it is replaced by higher-potential broad peaks. This indicates Ge amorphization during the first cycle. This first cycle peak could also be due to SEI formation. For electrolytes (1)–(3), three distinct lithiation peaks are observed—at 400 mV, 500 mV, and between 150 mV and 200 mV—corresponding to the various stages of lithiation described by the reaction pathway above. FEC-containing electrolyte solutions show attenuation of the 500 mV peak with progressive cycling. The 400mV peak is more intense in these samples as well. This indicates that FEC causes a fundamental difference in the way Ge films are lithiated (i.e., instead of a three-stage process, only two lithiation events are observed). Further characterization is required to determine the nature of lithiation in the presence of FEC. The lithiation peak between 150 mV and 200m V persists during all cycles, indicating formation of $Li_{15}Ge_4$ and $Li_{22}Ge_5$. The delithiation peaks occur at the same potential (500 mV) for all electrolytes during each cycle. This potential is consistent with previous observations for Li removal from Ge.^{5, 8, 16, 19, 22, 25, 33} Subtle differences between the differential plots are presented more lucidly in Figures 5.4 and 5.5.

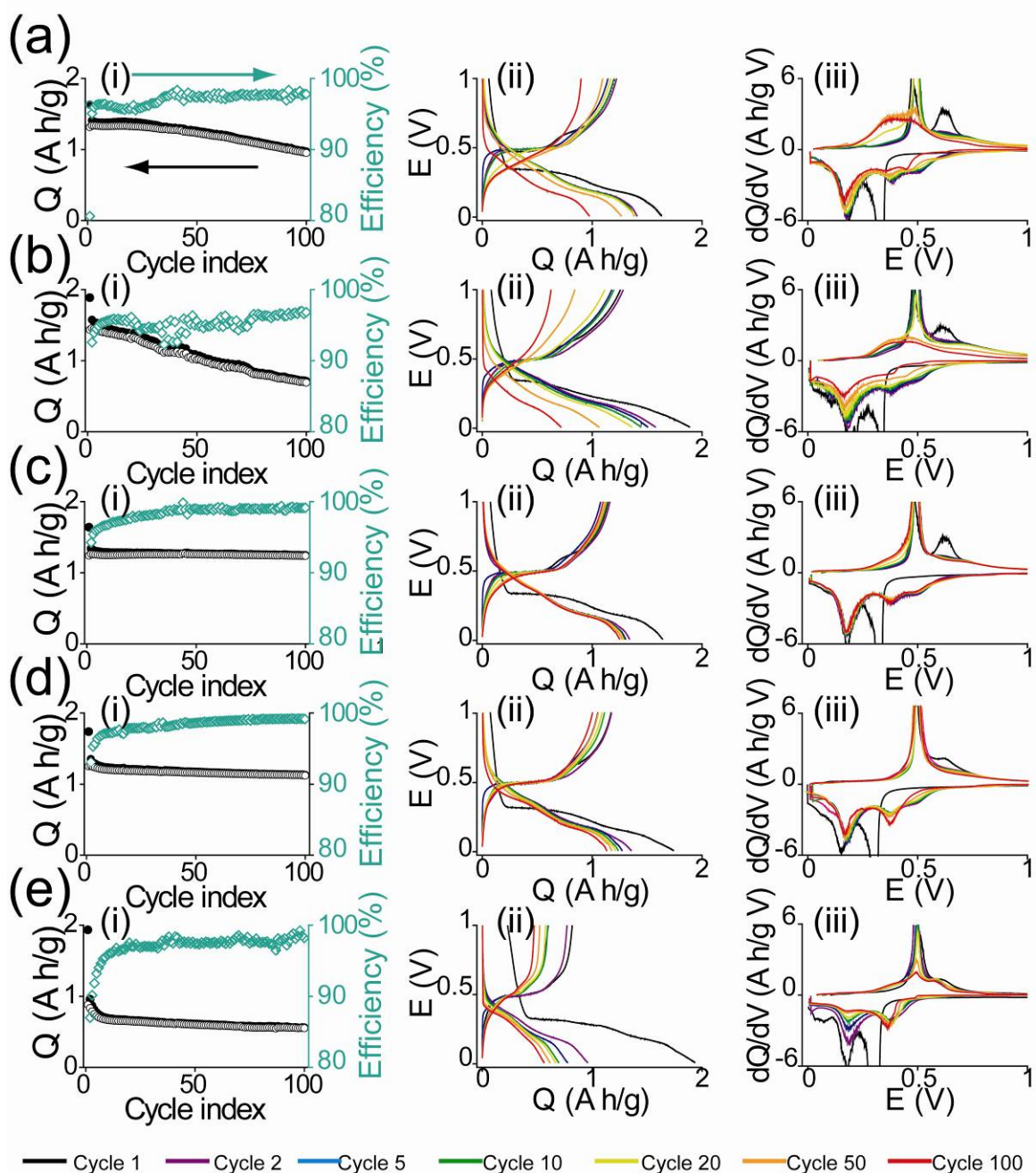


Figure 5.3: (i) Charge and discharge capacities, coulombic efficiencies, (ii) voltage profiles and (iii) corresponding differential capacity curves for Ge nanowire batteries cycled galvanostatically using an electrolyte solution of 1.0M LiPF₆ dissolved in a 1:1 w/w mixture of (a) EC:DEC, (b) EC:DMC, EC:DMC + 3% w/w FEC, (d) FEC:DEC, or (e) FEC:DMC at cycles: 1, 2, 5, 10, 20, 50, and 100.

Figure 5.4 compares the first cycle voltage profiles and differential capacity plots for all batteries tested. Over-potentials are independent of electrolyte. As previously mentioned, both charge and discharge plateaus occur in the same potential windows in the voltage profiles for all electrolytes tested (Figure 5.4a.). Equivalently, all charge and discharge peaks occur at the same potentials in the differential capacity plots (Figure 5.4b). For electrolyte systems where EC was used, a second delithiation peak is observed around 600 mV. This has been observed for other Ge systems using EC-containing electrolytes, though the cause remains to be understood.^{5, 16, 19, 22} This peak is observed only during the first cycle and is attributed to EC decomposition during SEI formation. Electrolyte (6) has a higher over-potential due to increased internal resistances within the battery (see impedance data below).

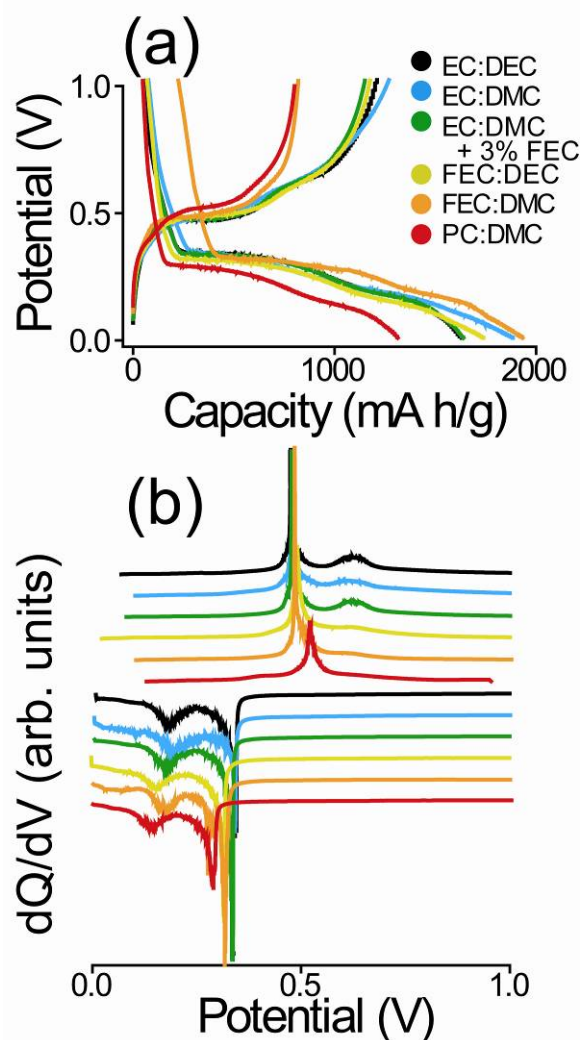


Figure 5.4: (a) Voltage profiles and (b) corresponding differential capacity plots comparing the first cycle charge and discharge characteristics for each electrolyte system.

Electrochemical data are shown in greater detail in Figure 5.5. A gradual decline in signal intensity with increasing cycle number is observed as a general trend for all batteries—an expected trend as the electrode degrades with aging. In the differential charge plots, electrolytes (3)–(5) retain intense lithiation signals at 350 mV. This feature manifests itself in the color map as the vertical green band centered at the same potential.

Batteries cycled with electrolytes (1) and (2) show the 350 mV peak for early cycles, but it fades rapidly. The lower potential lithiation peak also fades during cycling for electrolytes (1) and (2) while remaining constant for the electrolytes (3) and (4). Electrolyte (5) shows interesting behavior; the high-potential lithiation peak remains while the low-potential peak fades, indicating increased resistance to $\text{Li}_{15}\text{Ge}_4$ and Li_1Ge_5 formation with this electrolyte. The capacitive behavior is, instead, associated with lithiation of a-Ge or lower Li-content Li-Ge alloys with lithiation events around 350mV (e.g., Li_9Ge_4 , Li_7Ge_2).

Delithiation trends can be classified into FEC-containing (3-5) and FEC-free (1), (2) electrolyte solutions. Electrolytes (1) and (2) have a sharp delithiation peak centered at 500 mV that fades within 20-30 cycles and merges with a lower potential (400 mV) broad peak. Adding FEC—e.g., electrolytes (3), (4), and (5)—improves the cycling behavior which manifests as a strong delithiation peak that remains centered at 500 mV. Peak broadening is still observed for (3) and (5), although it takes more cycling to realize. Peak broadening is not observed for (4). The delithiation peak in electrolyte (5) fades gradually, but instead of forming a broad peak at lower potentials, the peak remains at 500 mV and forms a small shoulder at higher potentials (600 mV) which also fades by cycle 100. These data indicate a fundamental difference in interaction between EC with DMC than FEC with DMC in regards to SEI formation. FEC stabilizing effects in Ge nanowire films are examined in greater detail in Chapter 6.

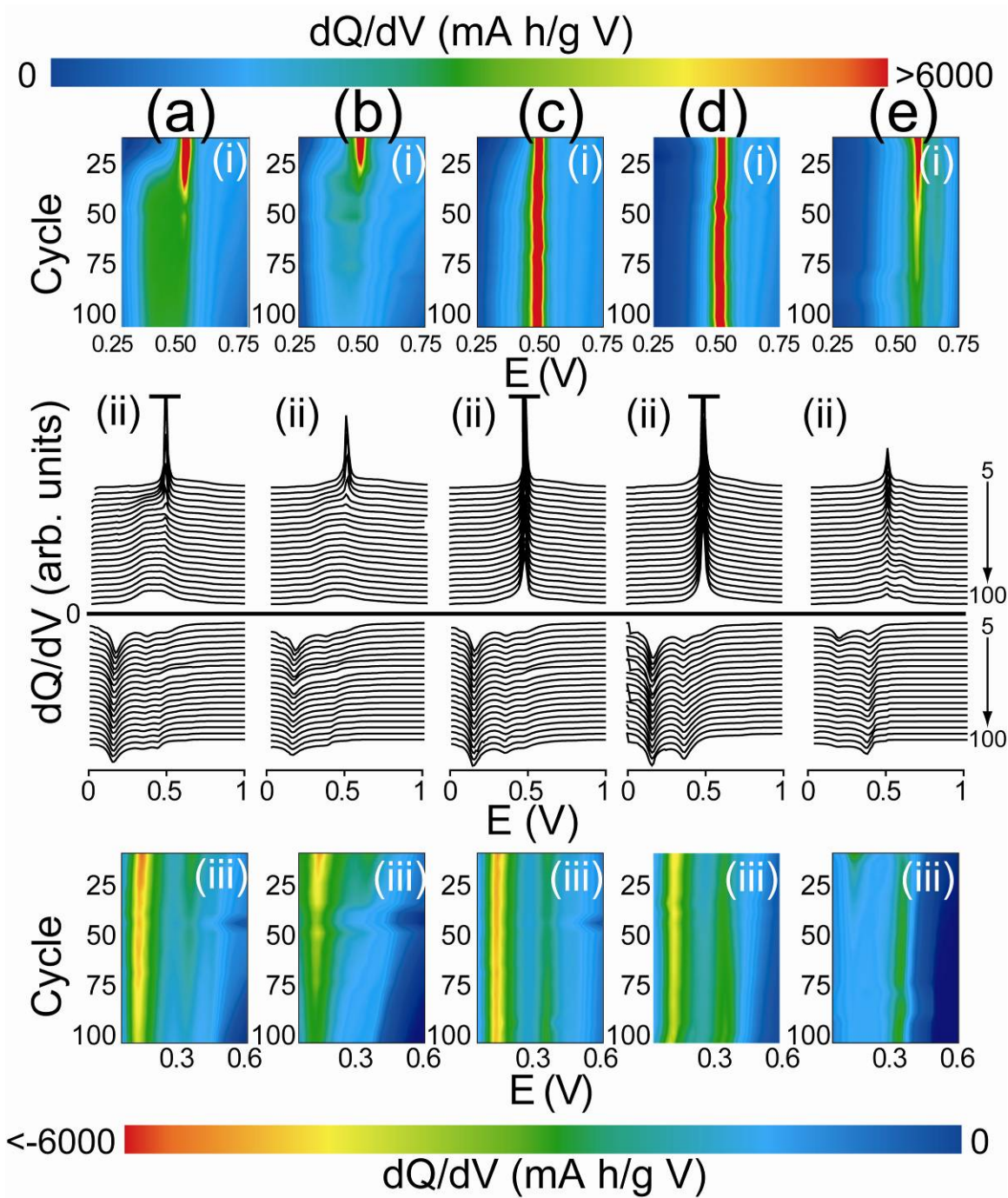


Figure 5.5: Differential capacity color maps for (a.i-e.i) discharge (a.iii-e.iii) charge cycles with (a.ii-e.ii) waterfall plots for batteries cycled using electrolyte solvent mixtures of (a) EC:DEC, (b) EC:DMC, (c) EC:DMC with 3% FEC, (d) FEC:DEC, and (e) FEC:DMC.

5.3.3 Rate test behavior

A battery should perform well (i.e. high capacity retention for thousands of cycles) at a rate no slower than $C/3$ to be considered commercially viable, where C corresponds to the current density required to fully charge or discharge the battery in 1 hour. A new set of batteries was fabricated and tested at various rates to evaluate the performance of SLS-grown Ge nanowires under operating conditions typical for the commercial end user. The same set of electrolytes used above was used here and results are shown in Figure 5.6. These data show similar performance trends to what we report above; electrolyte solutions containing FEC perform better than those without. Capacities above 1000 mA h g^{-1} were achieved for electrolytes (1), (3), and (4) up to a cycle rate of $C/2$ and only showed slight drop in capacity when the rate was increased to C and $2C$. Electrolyte (1) shows an unusual trend for rates between $C/2$ and $2C$ in that it settles in to the new rate by gradually increasing in capacity during each 5-cycle test. The other electrolyte solutions either hold steady at each rate, or decay slightly. This is a commonly observed trend that remains to be understood. One explanation is that volume change exposes previously inaccessible regions to electrolyte by new cracks that form in the SEI layer during expansion of the active material.^{16,37} The phenomenon is electrolyte-dependent and could also be due to re-dissolution of SEI with continuous cycling. When the rate is reduced to $C/10$ for the final 10 cycles (cycles 41–50), all batteries except PC:DMC return to the same capacities as the first $C/10$ test (cycles 11–20) indicating that the Ge nanowire material is not damaged at higher cycling rates.

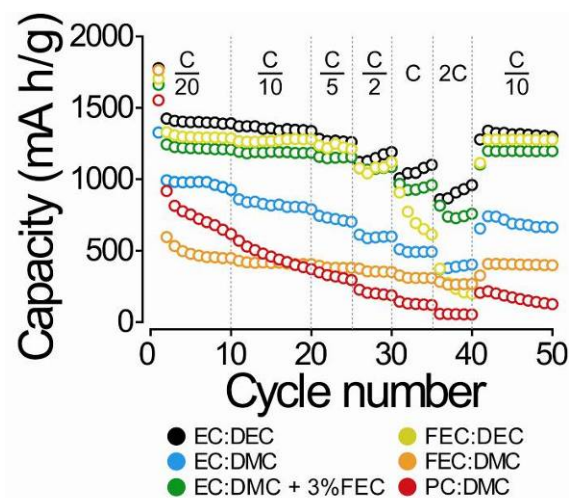


Figure 5.6: Comparison of charge capacity for various electrolytes at different charge rates.

Electrochemical data for the rate cycle tests are shown in Figure 5.7. Electrolytes (1) and (2) show gradual capacity fade during cycling with coulombic efficiencies between 90 and 100%. At the 11th and 21st cycles—where the rate changes from C/20 to C/10 and C/10 to C/5, respectively, the drop in capacity is very small. When the rate is increased to C/2 at the 26th cycle the capacity drops 100 to 200 mA h g⁻¹. The implications of this observation are two fold: (1) the Ge nanowire film has good electrical and ionic conductivity and (2) Li diffusion through the active Ge material is not a rate limiting step for rates of C/5 or slower. For these two electrolytes when the rate changes to C/2, C, or 2C, (cycles 25, 31, and 36, respectively), a larger capacity drop is observed, followed by a gradual increase in capacity as the battery relaxes into the new rate. This effect is especially pronounced for electrolyte (1). The voltage profiles and differential capacity plots for electrolytes (1) and (2) exhibit a shift in the lithiation and delithiation peaks to lower potentials for rates between C/2 and 2C. This effect is shown more clearly in Figure 5.10 below.

Batteries cycled using FEC-containing electrolytes exhibit better capacity retention and show smaller drops in capacity (less than 50 mA h g^{-1}) at rate change cycles. For instance, electrolytes **(3)** and **(4)** show charge and discharge capacity curves that are relatively continuous through 25 cycles—a span over which 2 rate changes occur—with efficiencies of 99% and higher. At faster cycle rates, these two electrolytes behave similar to **(1)** and **(2)** exhibiting $100\text{--}200 \text{ mA h g}^{-1}$ drops in capacity at rate change cycles. Electrolyte **(5)** has the largest first cycle capacity loss and records the lowest capacities aside from electrolyte **(6)**. Capacity retention for this system is the best, however. This system shows a difference in capacity of 150 mA h g^{-1} between cycles 10 (rate = $C/20$) and 40 (rate = $2C$). Contrast this point to electrolyte **(4)** which shows a capacity difference of 1100 mA h g^{-1} between the same cycles. If the first cycle irreversible capacity loss could be reduced, electrolyte **(5)** would be the best electrolyte systems for high power applications. Comparing **(5)** with **(3)** shows that, in order to do this, FEC should be used as an additive in small amounts only and not as a main component in the electrolyte solvent. The differential capacity plots show lithiation and delithiation events at the same potentials discussed above with a few nuances. The subtleties are discussed further in Figure 5.8.

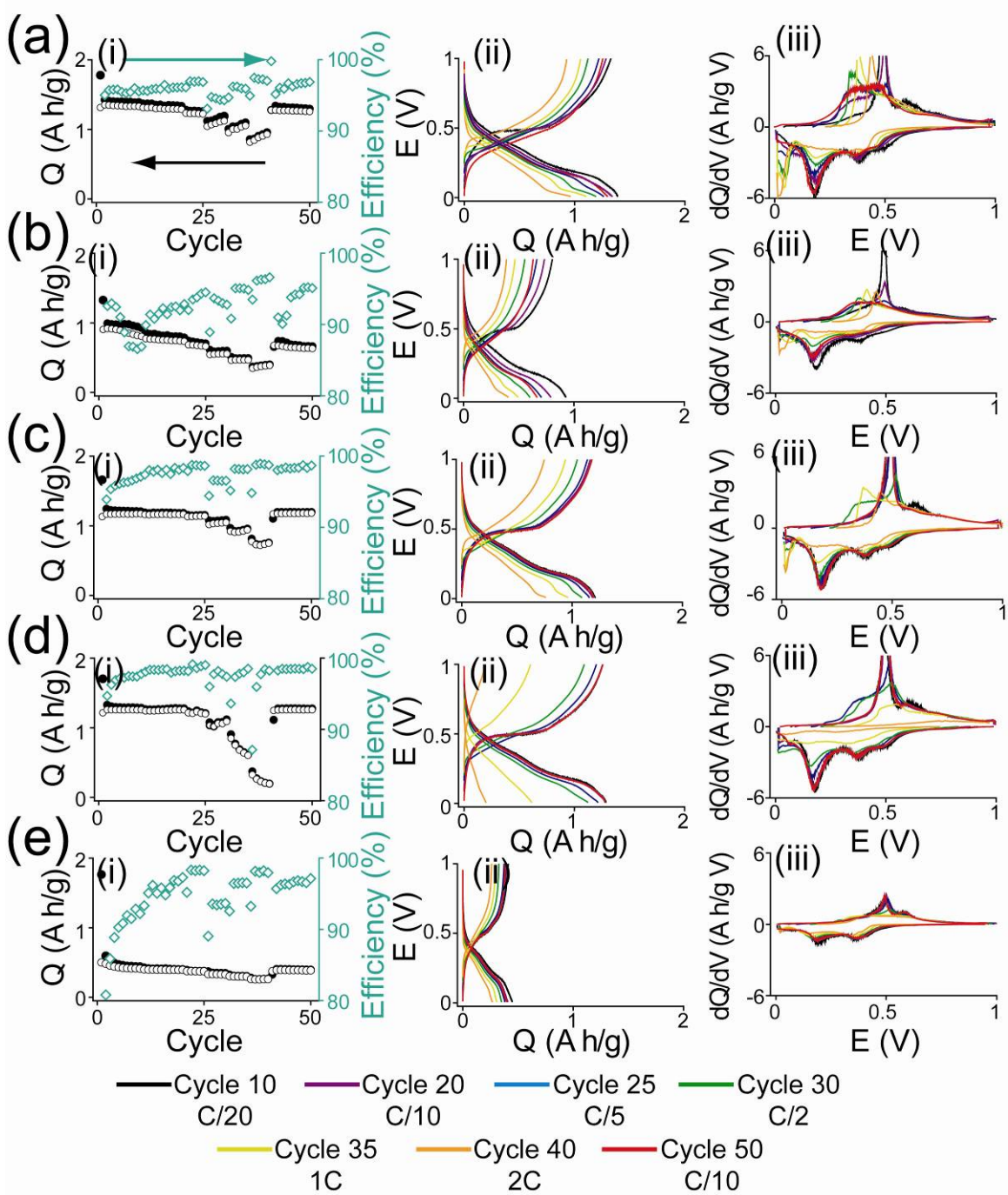


Figure 5.7: (i) Rate cycle data, (ii) potential profiles and (iii) differential capacity plots for batteries cycled using electrolyte solvent mixtures of (a) EC:DEC, (b) EC:DMC, (c) EC:DMC with 3% FEC, (d) FEC:DEC, and (e) FEC:DMC at cycles: 10, 20, 25, 30, 35, 40, and 50.

Detailed electrochemical data are shown in Figure 5.8 for batteries cycled at various rates using electrolytes (1)–(5). At cycle 21 electrolyte- and rate-dependent differences in delithiation behavior are observed. For rates between C/5 and 2C (between cycles 21 and 40 cycles) delithiation shifts first to 350 mV (cycles 21–25) then shifts to higher potentials in ~50 mV increments when the cycle rate is further increased. This effect is more pronounced for electrolyte (2) but also occurs for electrolyte (1). To illustrate, for electrolyte (1), between cycles 26 and 30 (cycle rate = C/2) delithiation occurs at 350 mV. At 1C (cycles 31–35), the peak moves to 400 mV, at 2C (cycles 36–40) the peak is centered at 450 mV. In contrast, FEC-containing electrolytes exhibit delithiation at 500 mV through 30 cycles (i.e., up to a cycle rate of C/2). A second peak was observed around 400 mV for these cycles as well. At rates of 1C and 2C, (between cycles 30 and 40), the delithiation peak reduces in intensity but remains at 500 mV for electrolytes (4) and (5). At cycle rates of 1C and 2C electrolytes (3) and (4) follow the same trend.

Delithiation occurs within previously observed ranges reported for Li removal from Ge (i.e., 300 mV–500 mV). Few studies comment on electrochemical behavior and, to the best of our knowledge at the time of writing this, no study exists that focuses on rate-dependent electrochemical behavior for Ge. While we suspect the anomalous trends in electrolytes (1) and (2) may be due to altered phase formations due to kinetic limitations within the films, further studies are necessary to explain the observed behavior in light of the nanowire microstructure and film composition.

Lithium insertion data are shown in Figures 5.8a.iii–5.8e.iii. Electrolytes (1) and (2) lithiate at ~250 mV through cycle 25 (up to a rate of C/5). Starting at cycle 26 and through cycle 40, the 250 mV peak is significantly reduced in intensity and a second peak appears at potentials lower than 50 mV. Electrolyte (3) shows the same behavior starting

at cycle 31 and extending through cycle 40. FEC-containing electrolyte solutions are resistant to shifts in lithiation potential, showing two prominent lithiation peaks centered around 350 mV and 250 mV. As observed in the delithiation data, when the cycle rate is relaxed back to C/10, the lithiation peaks resume at their initial potential values.

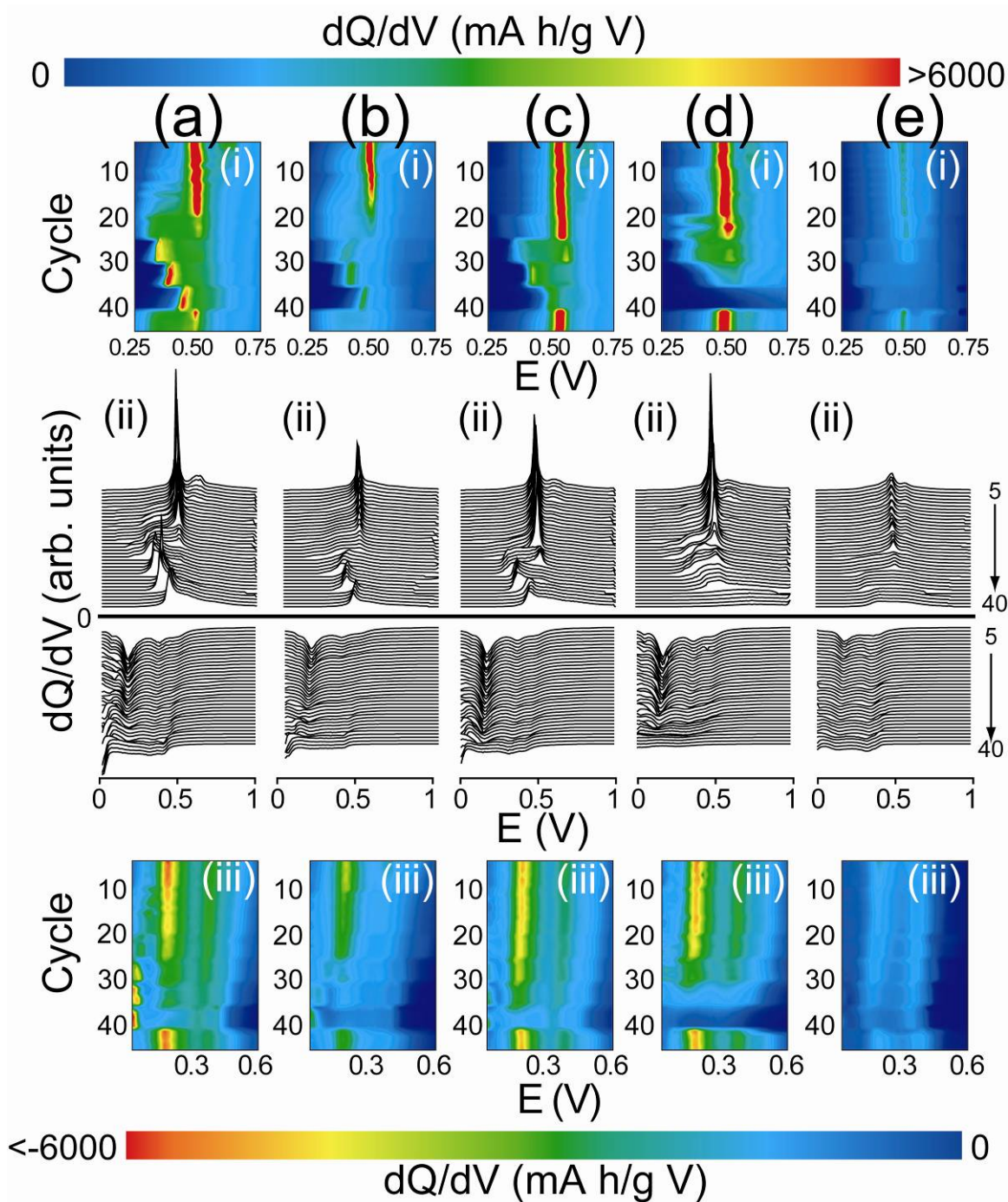


Figure 5.8: Differential capacity (a.i-e.i) discharge and (a.iii-e.iii) chargecolor maps and (a.ii-e.ii) waterfall plots for batteries cycled using electrolyte solvent mixtures of (a) EC:DEC, (b) EC:DMC, (c) EC:DMC with 3% FEC, (d) FEC:DEC, and (e) FEC:DMC at various rates for cycles 5 through 40.

5.3.4 High-power testing

Electrolyte (3) showed the best cycle performance in previous tests. Capacity retention was 95.8% after 100 cycles and the first cycle capacity loss was limited to 18.4%. Electrolyte (4) performed comparable with retention of 89% and first cycle loss of 22.2%. These batteries were cycled further at a rate of 1C to determine the long-term stability under conditions more typical of commercial use. The data for these additional cycles are shown in Figure 5.9. The first 100 cycles at a rate of C/10 are shown for reference. Electrolyte (3) showed good cycle behavior with capacities above 1000 mA h g⁻¹ through 300 cycles at 1C. During the final 200 cycles, the battery experienced rapid fade and the final capacity at cycle 600 was 200 mA h g⁻¹. Electrolyte (4) displays some fluctuation, but holds between 600 and 700 mA h g⁻¹ through 1200 cycles at 1C. While a more systematic study is needed to truly explain the data, we attribute the fluctuations to small temperature changes. To support this claim, the lab temperature where the batteries are tested is generally held around 75°F. Between cycles 750 and 1050, the room temperature dropped to ~60°F, indicated with by the ΔT span in Figure 5.9a, and capacities dropped to ~400mA h g⁻¹. The temperature was increased back to 75°F, and the capacity returned to 600–700mA h g⁻¹. The inset to Figure 5.9a shows cycles 1100–1200, which occurred over a three day span. Plotted with these data is the ambient temperature during a three day span in Austin, Texas. Small temperature differences inside the building come with temperature fluctuations outside. These data show a correlation between the capacity and the temperature. Whether the effect is due to the electrolyte or the Ge nanowires remains to be understood, but these results indicate Ge nanowires cycled with electrolyte (4) may be a good candidate for high-temperature lithium storage for high-power applications, such as powering automobiles.

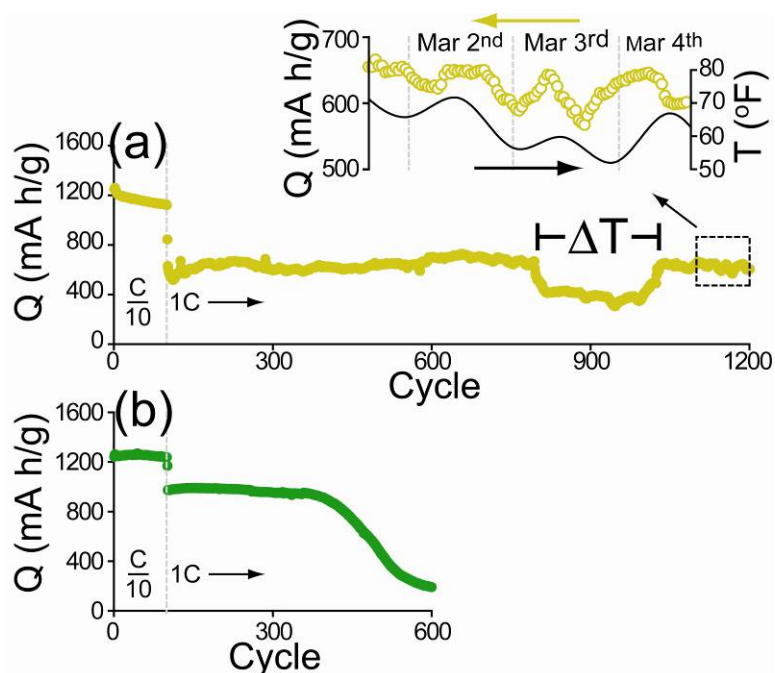


Figure 5.9: Long term life cycling of batteries cycled using (a) FEC:DMC and (b) EC:DMC+FEC electrolyte solutions. The inset to (a) shows a cycles 1100 through 1200 with greater clarity, plotted with the temperature in Austin, Texas during a three day span.

Germanium is known to perform very well at high charge rates.^{8, 14, 26} Above, we showed that at rates of 1C and 2C, the performance of the battery begins to suffer. Graetz *et al.* have reported capacities of 400 mA h g⁻¹ when a fast charge rate (1000C) is followed by a slow discharge (1C). In light of these results, Ge nanowire films were tested using different charge and discharge rates; for example, one battery was charged at 1C and discharged at various rates—up to 20C—and another was charged at various rates and discharged at 1C. Results are shown in Figure 5.10; electrolyte (3) was used for these batteries. The first two charge/discharge cycles were done at C/20 to condition the electrode. For the battery with a constant charge rate of 1C—battery (a)—the capacity was 1050 mA h g⁻¹ for discharge rate of 1C and only dropped to 900 when the rate was increased to 10C. A significant drop-off was observed at 20C where the discharge

capacity was 400 mA h g^{-1} . The battery fully recovered when the discharge rate was reduced to 1C. Similar capacities were achieved for the battery with a constant discharge rate—battery (b). Interesting to note that battery (b) shows gradual increases in capacity at each new charge rate, whereas battery (a) shows constant capacities. When the charge rate is 10C or 20C, though, the coulombic efficiency exceeds 100%. The reason behind this is unclear and requires further investigation. Voltage profiles and differential capacity curves show trends similar to those observed above. Battery (a) shows a strong lithiation peak at 200mV independent of discharge rate while the delithiation peak shifts to higher potentials. Similarly, battery (b) shows a shift in the 200mV lithiation peak to lower potentials while delithiation occurs at a constant potential independent of charge rate. Differences in these observed over-potentials are likely due to the non-equilibrium nature of the system. Alternatively, the lithiation pathways and intermediate Li-Ge alloy phases that form during lithiation could be altered by the higher current density. Fast cycling conditions such as these have been observed for Ge nanotubes produced via the Kirkendall effect with reported capacity of 650 mA h g^{-1} at 10C.²⁶ We show that slowly charging the battery before rapid discharge improves discharge behavior. These results point to Ge as a great candidate for high power devices requiring fast charge and discharge characteristics.

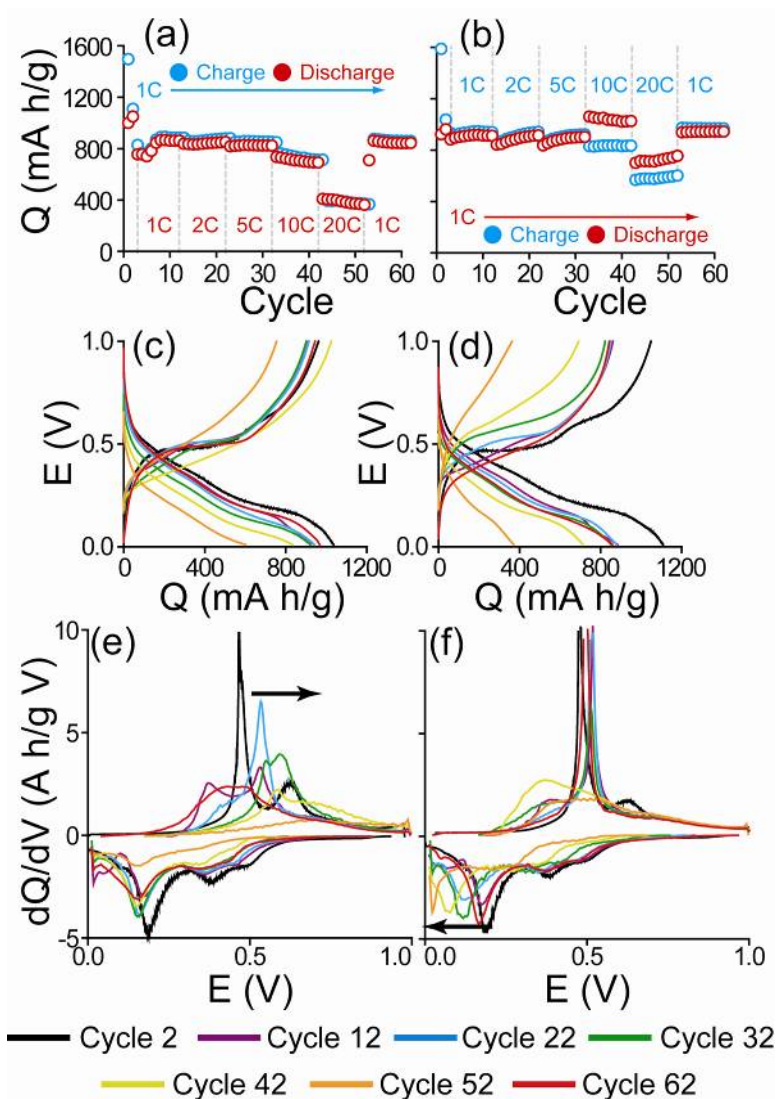


Figure 5.10: Cycle data for Ge nanowire films cycled using EC:DMC+FEC (a) charged at 1C and discharged at various rates with or (b) charged at various rates and discharged at 1C with (c, d) voltage profiles and (e, f) differential capacity curves shown for cycles 2, 12, 22, 32, 42, 52, and 62.

5.3.5 Electrical behavior

Electrochemical impedance spectroscopy (EIS) measurements were made after 100 charge/discharge cycles at C/10, shown in Figure 5.11. Each film shows characteristic impedance features, namely a high-frequency semi-circular resistive

element coupled with a high frequency diffusion element. The size of the semi-circle is indicative of the film resistance; the larger the semi-circle, the more resistive the film. The steepness of the low-frequency slope provides information about Li^+ diffusion within the film. A 45° slope is associated with semi-infinite diffusion in a planar electrode. Slopes steeper than 45° are characteristic of finite Li^+ diffusion typical of thin films.³⁸ FEC-containing electrolyte solutions have lower impedance than FEC-free electrolytes, evident by the quick transition from the high- to low-frequency regimes (e.g., FEC-based electrolytes do not form a full semi-circle), which accounts for the improved cycling behavior of FEC-containing electrolytes.

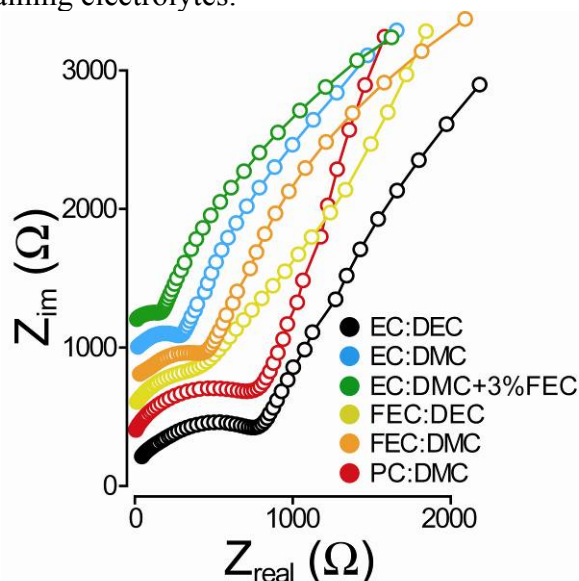


Figure 5.11: Impedance spectra of discharged batteries after 100 cycles using various electrolyte solutions at a rate of $C/10$. The data are offset by 200 units along the ordinate axis.

5.4 CONCLUSIONS

We report electrochemical behavior of Ge nanowire films cycled using a variety of electrolyte solvents and evaluate the efficacy of each. We found that the PVdF binder does not require a high temperature anneal to achieve high capacities when Ge is used as

the anode material. Fluoroethylene carbonate serves as an excellent additive to the EC:DMC electrolyte solution when used in small amounts (3% w/w). When used in greater amounts, (i.e., in a 1:1 w/w mixture with DEC), batteries perform exceptionally well. Ge nanowire films cycled with EC:DMC+FEC and FEC:DEC at 1C showed high capacities and great cycle retention through hundreds of cycles. Furthermore, EC:DMC+FEC showed high capacities for discharge rates up to 20C when a slow charge rate was used.

Electrochemical behavior was also examined in great detail. FEC was found to enhance coulombic efficiency for Ge nanowire batteries. Furthermore, batteries cycled with FEC-containing electrolytes had lower film resistances as measured by electrochemical impedance spectroscopy than FEC-free electrolytes. Different lithiation trends were observed and depended on the electrolyte and cycle rate. The ramifications of these data are discussed in light of the differential capacity peaks. These results show that Ge nanowires are a great candidate for high power commercial applications. High charge and discharge rate tests show that lithiation and delithiation behavior depends on the cycle rate. These tests also show that Ge nanowires cycled with electrolyte FEC:DEC may be a good candidate for high-temperature lithium storage for high-power applications, such as powering automobiles. Surface characterization studies are presented in Chapter 6 that explain electrolyte dependent differences in the SEI layers.

5.5 ACKNOWLEDGEMENTS

Authors contributing to this work include: Kyle Klavetter, Justin T. Harris, C. Buddie Mullins, and Brian A. Korgel. Paul Abel and Yong-Mao Lin were also very helpful with discussions pertaining to EIS and electrochemistry. We thank TIMCAL for supplying the conductive carbon used in slurry formation.

5.6 REFERENCES

1. Armand, M.; Tarascon, J. M. *Nature* **2008**, *451*, 652-657.
2. Goodenough, J. B.; Kim, Y. *Chem. Mater.* **2009**, *22*, 587-603.
3. Yoshino, A., Nakajima, T., Sanechika, K. U.S. Patent No. 4,668,595. **May 9, 1986.**
4. Winter, M.; Besenhard, J. O.; Spahr, M. E.; Novák, P. *Adv. Mater.* **1998**, *10*, 725-763.
5. Yoon, S.; Park, C.-M.; Sohn, H.-J. *Electrochem. Solid St.* **2008**, *11*, A42-A45.
6. Baggetto, L.; Notten, P. H. L. *J. Electrochem. Soc.* **2009**, *156*, A169-A175.
7. *U.S. Geological Survey, Mineral Commodity Summaries, January 2010.*
8. Graetz, J.; Ahn, C. C.; Yazami, R.; Fultz, B. *J. Electrochem. Soc.* **2004**, *151*, A698-A702.
9. Höll, R.; Kling, M.; Schroll, E. *Ore Geol. Rev.* **2007**, *30*, 145-180.
10. *U.S. Geological Survey, Mineral Commodity Summaries, 2011.*
11. Yao, Y.; McDowell, M. T.; Ryu, I.; Wu, H.; Liu, N.; Hu, L.; Nix, W. D.; Cui, Y. *Nano Lett.* **2011**, *11*, 2949-2954.
12. Zhang, X.; Shyy, W.; Sastry, A. M. *J. Electrochem. Soc.* **2007**, *154*, A910-A916.
13. Ryu, I.; Choi, J. W.; Cui, Y.; Nix, W. D. *J. Mech. Phys. Solids* **2011**, *59*, 1717-1730.
14. Wang, J.; Du, N.; Zhang, H.; Yu, J.; Yang, D. *J. Mater. Chem.* **2012**, *22*, 1511-1515.
15. Hwang, C.-M.; Park, J.-W. *Thin Solid Films* **2010**, *518*, 6590-6597.
16. Laforge, B.; Levan-Jodin, L.; Salot, R.; Billard, A. *J. Electrochem. Soc.* **2008**, *155*, A181-A188.
17. Wang, D.; Yang, Z.; Li, F.; Liu, D.; Wang, X.; Yan, H.; He, D. *Mater. Lett.* **2011**, *65*, 1542-1544.
18. Baggetto, L. C.; Hensen, E. J. M.; Notten, P. H. L. *Electrochim. Acta* **2010**, *55*, 7074-7079.
19. DiLeo, R. A.; Frisco, S.; Ganter, M. J.; Rogers, R. E.; Raffaele, R. P.; Landi, B. J. *J. Phys. Chem. C* **2011**, *115*, 22609-22614.
20. Cheng, J.; Du, J. *CrystEngComm* **2012**, *14*, 397-400.
21. Xue, D.-J.; Xin, S.; Yan, Y.; Jiang, K.-C.; Yin, Y.-X.; Guo, Y.-G.; Wan, L.-J. *J. Am. Chem. Soc.* **2012**, *134*, 2512-2515.

22. Seo, M.-H.; Park, M.; Lee, K. T.; Kim, K.; Kim, J.; Cho, J. *Energ. Environ. Sci.* **2011**, *4*, 425-428.
23. Liu, X. H.; Huang, S.; Picraux, S. T.; Li, J.; Zhu, T.; Huang, J. Y. *Nano Lett.* **2011**, *11*, 3991-3997.
24. Ko, Y. D.; Kang, J. G.; Lee, G. H.; Park, J. G.; Park, K. S.; Jin, Y. H.; Kim, D. W. *Nanoscale* **2011**, *3*, 3371-3375.
25. Chan, C. K.; Zhang, X. F.; Cui, Y. *Nano Lett.* **2007**, *8*, 307-309.
26. Park, M.-H.; Cho, Y.; Kim, K.; Kim, J.; Liu, M.; Cho, J. *Angew. Chem. Int. Ed.* **2011**, *50*, 9647-9650.
27. Fuller, C. S.; Severiens, J. C. *Phys. Rev.* **1954**, *96*, 21-24.
28. Chockla, A. M.; Korgel, B. A. *J. Mater. Chem.* **2009**, *19*, 996-1001.
29. Etacheri, V.; Haik, O.; Goffer, Y.; Roberts, G. A.; Stefan, I. C.; Fasching, R.; Aurbach, D. *Langmuir* **2012**, *28*, 965-976.
30. Choi, N.-S.; Yew, K. H.; Lee, K. Y.; Sung, M.; Kim, H.; Kim, S.-S. *J. Power Sources* **2006**, *161*, 1254-1259.
31. Nakai, H.; Kubota, T.; Kita, A.; Kawashima, A. *J. Electrochem. Soc.* **2011**, *158*, A798-A801.
32. Saunders, A. E.; Sigman, M. B.; Korgel, B. A. *J. Phys. Chem. B* **2003**, *108*, 193-199.
33. Lee, H.; Kim, H.; Doo, S.-G.; Cho, J. *J. Electrochem. Soc.* **2007**, *154*, A343-A346.
34. Aurbach, D.; Ein-Eli, Y. *J. Electrochem. Soc.* **1995**, *142*, 1746-1752.
35. Li, J.; Christensen, L.; Obrovac, M. N.; Hewitt, K. C.; Dahn, J. R. *J. Electrochem. Soc.* **2008**, *155*, A234-A238.
36. Chen, Z.; Christensen, L.; Dahn, J. R. *Electrochem. Commun.* **2003**, *5*, 919-923.
37. Magasinski, A.; Zdyrko, B.; Kovalenko, I.; Hertzberg, B.; Burtovyy, R.; Huebner, C. F.; Fuller, T. F.; Luzinov, I.; Yushin, G. *ACS App. Mater. Inf.* **2010**, *2*, 3004-3010.
38. Ruffo, R.; Hong, S. S.; Chan, C. K.; Huggins, R. A.; Cui, Y. *J. Phys. Chem. C* **2009**, *113*, 11390-11398.

Chapter 6: XPS Study of SEI Formation in Ge Nanowire Li-Ion Battery Negative Electrode Films

6.1 INTRODUCTION

Lithium (Li)-ion battery technology has witnessed sluggish advance since commercialization by Sony in 1991; the internal working materials used have remained largely unchanged. In an effort to improve the capacity and cycle life of Li-ion batteries, a myriad of new positive and negative electrode materials with high lithium storage capabilities have been explored. Graphite serves as the negative electrode material and forms LiC_6 upon lithiation, a compound with a maximum theoretical capacity of 372 mA h g^{-1} . There is much interest in replacing graphite with a material can store more lithium;¹ germanium (Ge) is one such candidate. Ge alloys with Li to form $\text{Li}_{22}\text{Ge}_5$ upon lithiation and boasts a maximum theoretical capacity of 1624 mA h g^{-1} .² Furthermore, Li diffuses very quickly into and out of Ge,³ making it particularly attractive for high power applications. For example, Ge thin films have been cycled as fast as 1000C , where C is the current density required to fully charge or discharge the battery in 1 hour.² However, thin film deposition methods are high-cost and low-throughput processes that are unattractive from a commercial stand-point. A recent report of Ge nanotubes produced via the Kirkendall effect shows high capacities and good retention cycle rates as high as 20C .⁴ Similar results are reported in Chapter 5 for solution grown Ge nanowires as well. Commercialization potential for these Ge nanowires was also shown with capacities between 600 and 700 mA h g^{-1} through 1000 cycles at a rate of 1C .

Electrolyte chemistry plays a critical role in battery efficacy.⁵ The anode operates at a low working potential relative to the standard reduction potential of lithium where the electrolyte solutions are unstable and reduce to form a solid electrolyte interphase

(SEI) layer on the electrode surface.^{6,7} The SEI forms during the first cycle and results in a large first cycle irreversible capacity loss. This passivating layer grows with continued cycling and affects the electronic and ionic transport through the film.⁸ Formation of the SEI layer is dependent on the stability of the electrolyte within the voltage range of the battery. Additives such as fluoroethylene carbonate (FEC) and vinylene carbonate (VC) can be introduced to reduce first cycle capacity losses and improve cyclability.^{5, 8-13} A good SEI layer is thin and completely passivates the surface of the electrode, preventing further electrolyte reduction.¹⁴ Several recent studies detail the surface behavior of cycled Si-based Li-ion battery negative electrodes,^{8, 11, 12} focusing on the effect of fluoroethylene carbonate (FEC), an additive known to drastically improve the cyclability of Si thin film^{8, 12} and nanowire¹¹ electrodes in small quantities. Fluorinated carbonates resist oxidation, have low melting points, and are less flammable than their non-fluorinated counterparts. Many such compounds have received much attention in general due to performance enhancement in various systems.^{5, 8, 11-13, 15, 16} To the best of our knowledge, no such studies have been done for Ge nanowire electrodes. In fact, until recently, FEC had not been used in conjunction with Ge-based electrodes (see Chapter 5). Here, we study SEI layers formed on films of solution-grown Ge nanowires cycled as the negative electrode material in Li-ion batteries using various FEC-containing and FEC-free electrolyte solutions.

6.2 EXPERIMENTAL SECTION

6.2.1 Materials

All reactions were carried out using standard airless procedures in a nitrogen-filled glove box and a Schlenk line. All reagents and solvents were used as received and without further purification. Dodecanethiol (DDT, $\geq 98\%$), tetrachloroaurate trihydrate

($\geq 99.9\%$), sodium borohydride ($\geq 98\%$), toluene (anhydrous, 99.8%), ethanol (99.9%), tetraoctylammonium bromide (TOAB, 98%), dimethyl carbonate (DMC, $\geq 99\%$), lithium hexafluorophosphate (LiPF_6 , $\geq 99.99\%$), poly-(vinylidene fluoride) (PVdF, average MW $\sim 534,000$ by GPC), 1-methyl 2-pyrrolidinone (NMP, 99.5%), chloroform (99.8%) and squalane (99%) were purchased from Sigma-Aldrich and diphenylgermane (DPG, $>95\%$) from Gelest. Conductive carbon super C65 was supplied by TIMCAL. Fluoroethylene carbonate ($>98\%$) was obtained from TCI America. Electrolytes were either purchased—as 1.0M solutions of LiPF_6 in a 1:1 w/w mixture of ethylcarbonate (EC) : diethyl carbonate (DEC) (Novolyte) or 1.0M LiPF_6 in a 1:1 mixture of EC : DMC (EMD chemicals)—or prepared by dissolving LiPF_6 at a concentration of 1.0M in a 1:1 w/w mixture of FEC:DMC. For battery assembly, Celgard 2400 membranes (25 μm) were used as separators, purchased from Celgard, and Li metal foil (1.5 mm 99.9%) as the counter electrode, purchased from Alfa Aesar.

6.2.2 Germanium nanowire synthesis

Dodecanethiol-coated Au nanocrystals (2 nm diameter) were synthesized following literature procedures¹⁷ and were stored in a nitrogen-filled gloved box, dispersed in at a concentration of 1 mg Au nanocrystals per mL toluene. Ge nanowires were produced using a modified literature method. In short, 10 mL squalane were added to a 4-neck flask and attached to a Schlenk line, heated to 100°C with vigorous stirring under vacuum (<500 mTorr) for 30 minutes, and then blanketed with nitrogen. The solvent was then heated to 380°C. An injection solution containing 0.275 mL of the Au nanocrystal stock solution was combined with 0.375 mL DPG, diluted with an additional 1 mL squalane and plunged into a syringe. The syringe containing the reactant solution was removed from the glove box and injected into the reaction flask with squalane heated

to 380°C. The reaction lasted 5 minutes, after which the flask was removed from the heating mantle to cool to room temperature. Toluene (10 mL) was added to the reaction mixture, and the flask was removed from the Schlenk line and sonicated for a few seconds to remove product that had adhered to the flask walls. The reaction solution was then transferred to a centrifuge tube and spun at 8000 rpm for 5 minutes. The supernatant was discarded and the precipitate was resuspended in 10 mL of chloroform and 2 mL of ethanol and centrifuged again at 8000 rpm for 5 minutes. This washing procedure was carried out a third time before the Ge nanowire product was dried down by rotovap to get an accurate weight. One reaction produces roughly 40 mg of Ge nanowires. Two such reactions were needed to generate enough material for electrochemical testing.

6.2.3 Anode preparation and battery assembly

The Ge nanowire slurry was prepared by dispersing the nanowires (81.1 mg) in 2 mL toluene and bath sonicating for 1 hour. Meanwhile, 23.2 mg PVdF and 11.6 mg carbon black were dissolved in 1 mL NMP and bath sonicating for 1 hour. The Ge nanowire and PVdF / carbon black suspensions (70:20:10 w/w solid content of Ge : PVdF : carbon black) were mixed and wand sonicating for an additional 30 minutes. The solution was then reduced by rotovap to yield a thick slurry. The slurry was cast onto Cu foil—which acts as the current collector for the battery—using a 200 μm film applicator and vacuum dried overnight at 100°C.

Batteries were assembled in an argon-filled glovebox. Ge nanowire anodes were punched from the Cu foil (1 cm diameter) supported slurry film. The electrolyte was a 1.0 M solution of LiPF_6 in a 1:1 w/w mixture of either (1) EC:DEC, (2) EC:DMC, or (3) FEC:DMC. A few drops of electrolyte were deposited over lithium foil and again atop a

Celgard 2400 separator membrane (25 μ m thick, Celgard) before the adding the Ge anode and crimping the completed battery.

6.2.4 Battery disassembly and electrode cleaning

Batteries were disassembled in an argon filled glovebox after cycling. EC:DEC and EC:DMC batteries were cycled through 100 galvanostatic charge/discharge cycles using an Arbin BT-2143 test unit sweeping between 2 V and 10 mV vs Li/Li⁺ at a rate of C/10 ($C = 1620 \cdot 70\%$ for Ge content + $370 \cdot 30\%$ for C content = 1326 mA h g⁻¹) and were brought into the glovebox in the delithiated state. The FEC:DMC battery was lithiated after 100 cycles before bringing it into the glovebox. Coin cells were opened inside the glovebox and placed in a vial to which 3 mL DMC was added to dilute any residual electrolyte salt on the surface of the film. The vial was shaken gently and allowed to sit for several hours. This cleaning procedure was done a total of 3 times, decanting the liquid from the vial and replacing with fresh DMC each time. The films were then transferred in an air-free chamber designed to transfer samples from the glovebox to the x-ray photoelectron spectroscopy (XPS) chamber without oxygen exposure.

6.2.5 Material characterization

Scanning electron microscopy (SEM) images were acquired using a Zeiss Supra 40 SEM with an in-lens arrangement, a working voltage of 5 keV and a working distance of 5 mm. SEM samples were imaged on silicon wafers (S.E.H). XPS spectra were recorded using a commercial X-ray photoelectron spectrometer (Kratos Axis Ultra), utilizing a monochromatic Al K $_{\alpha}$ X-ray source ($h\nu = 1486.5$ eV), hybrid optics (employing a magnetic and electrostatic lens simultaneously) and a multi-channel plate detector coupled to a hemispherical analyzer. The Ge nanowire films were secured on

the experimental tray using double-sided Cu tape. The photoelectron take-off angle was normal to the surface of the sample and 45° with respect to the X-ray beam. All spectra were recorded using a single sweep and an aperture slot of 300 μm by 700 μm. High-resolution spectra were collected with 20 eV pass energy. Spectra were collected at 0.1 eV intervals and 2000 ms integration time through a tungsten coil set at 4.8 V bias with respect to the sample. The pressure in the analysis chamber was typically 3·10⁻⁹ Torr during data acquisition. Sputtering was carried out using 4 keV Ar⁺ ions with a ~1.6 μA current measured at the sample.

Casa XPS analysis software was used to determine the stoichiometry of samples from corrected peak areas and employing Kratos sensitivity factors for each element of interest. The effect of sample charging on the XPS data was corrected by shifting the F1s, Li-F peak to a binding energy of 685.1 eV. Background subtraction was done using a Shirley background model. Peak areas were deconvoluted as Voigt functions (30% Gaussian character).

The chamber for transporting air sensitive samples from a glove box to an ultra-high vacuum chamber for X-ray photoelectron spectroscopy analysis was built at the Surface Analysis Laboratory of the Texas Materials Institute (TMI) at UT-Austin. The design of the interface contains a set of built-in figure of merits that were used to verify that samples were not exposed to traces of oxygen and water during transport.

6.3 RESULTS AND DISCUSSION

6.3.1 Cycling behavior

Figure 6.1 shows SEM and cycling behavior of Ge nanowires cycled using electrolyte solutions consisting of 1.0M LiPF₆ in a 1:1 w/w mixture of: (1) ethylene carbonate : diethyl carbonate (EC:DEC), (2) ethylene carbonate : dimethyl carbonate

(EC:DMC), and (3) fluoroethylene carbonate : dimethyl carbonate (FEC:DMC).¹⁸ EC:DEC (Figure 6.1b) and EC:DMC (Figure 6.1c) behave similarly, with first cycle irreversible capacity losses of 13.7% and 16.5%, respectively, and both show steady capacity fade. EC:DEC shows better retention after 100 cycles holding 70.5% capacity compared to 49.5% exhibited by EC:DMC. FEC:DMC has much greater first cycle loss (50.5%) but shows the best capacity retention at 80.8%. After cycling, batteries were brought into the glovebox and disassembled. To explain the differences in cycling behavior and explore the differences in SEI layers, Ge nanowire electrodes were sputtered with Ar⁺ ions and probed intermittently using X-ray photoelectron spectroscopy (XPS) creating elemental depth profiles, shown in Figures 6.2–6.4. The EC:DMC and FEC:DMC batteries were opened in the discharged state and the EC:DEC battery was disassembled in a lithiated state.

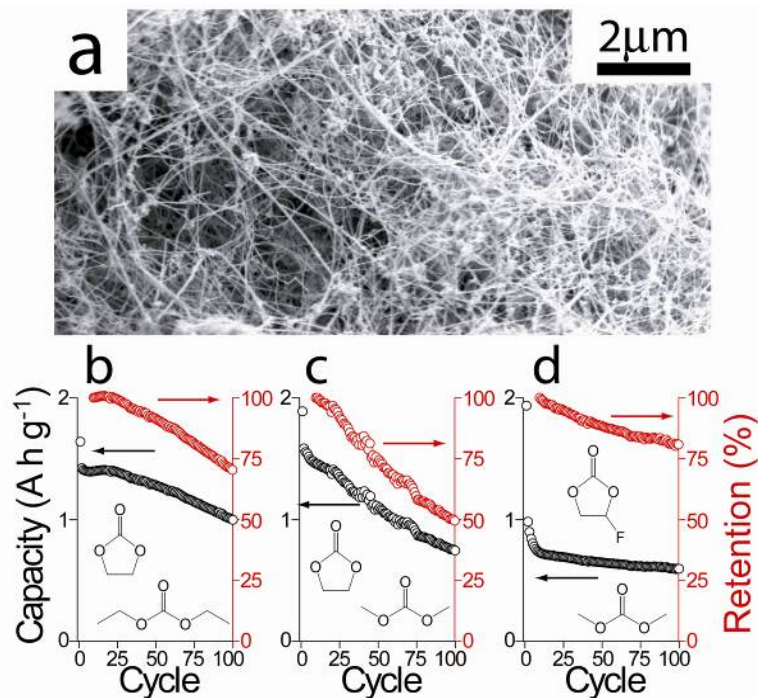


Figure 6.1: (a) SEM of Ge nanowires cycled with (b) EC:DEC, (c) EC:DMC, and (d) FEC:DMC electrolyte solutions. Capacity retention is relative to cycle 10.

6.3.2 XPS of SEI formation using the EC:DEC electrolyte

Ge nanowire films cycled with the EC:DEC electrolyte, presented in Figure 6.2, show little change in the F1s signal between scans. LiF is present throughout the film, evident by the strong signal in both the F1s (684.8 eV)¹⁹ and Li1s (55.5 eV).¹⁹ A small shoulder in the F1s signal present at higher energies corresponds to PVdF (687.5 eV).²⁰ No peak is observed for LiPF₆ (688.5 eV).²¹ The Li1s signal shifts slightly with sputtering time. LiF is present at the surface and as the signal shifts due to a combination of Li₂CO₃ (53.6 eV–54.6 eV), LiOR (53.6 eV), and Li₂O (53.3 eV) species in film.²² The 290.7 eV peak in the C1s signal indicates the presence of carbonates (e.g., O-C-O₂) in the un-sputtered scan.^{19, 23-27} The carbonate signal fades with increasing sputter time. The peak at 287 eV corresponds to (CH₂OCO₂Li)₂, the reduction product of EC.^{23, 28-30} DEC reduces to CH₃CH₂OLi, which manifests in a peak at 285 eV.^{14, 23, 30} Aliphatic carbon (e.g., conductive carbon and PVdF) also contributes to this signal (284.9 eV).³¹ Sputtering into the film results in a reduction in the carbonate signal along with the EC and DEC decomposition product signals. Etheral and alkoxy carbon (i.e., R-O-R') is present through the 2-minute scan (288 eV).²⁶ Furthermore, a small amount of oxylates may be present—due to the formation of CO₂,³² for example—evident by the small shoulder at 289 eV.²⁴ A peak centered at 282.5 eV corresponding to LiCH₂R³³ evolves during sputtering times of 5 minutes and longer. This shows that the decomposed carbonate species are concentrated near the surface of the SEI layer. The O1s signal corroborates information obtained from the Li1s and C1s spectra. The carbonate signal (i.e., Li₂CO₃, ROCO₂Li) dominates the un-sputtered O1s scan (532.4 eV).^{22, 24} This signal decreases in intensity through the 5-minute scan while LiOH, LiOR, (531.2 eV)^{22, 33} and Li₂O (528.3 eV)^{22, 33} peaks appear. The Ge3d signal shows Ge suboxides concentrated near the surface of the SEI—likely due to the high oxygen content in this region—with Ge⁰

appearing deeper into the film. The Ge^{3+} signal dominates the $\text{Ge}3d$ signal at the surface. As this battery was opened in the lithiated state, this indicates Li-induced reduction of Ge^{4+} near the surface. This becomes more evident when compared to the EC:DMC battery data, shown below, which exhibits a strong Ge^{4+} signal at the surface. This also implies lithiation of GeO_2 , analogous to LiMO_2 ($M = \text{Co}, \text{Mn}, \text{etc.}$) where M can switch between the M^{3+} and M^{4+} oxidation state during cycling. GeO_2 forms Li_2O upon lithiation and has poor reversibility.³⁴ Given the high GeO_x content at the surface, this is a likely cause for the gradual capacity fade for this battery. Sputtering into the film reveals a transition from Ge^{3+} to Ge^{4+} (32.5 eV),¹⁹ lower suboxides, and Ge^0 ; the $\text{Ge } 5/2$ (29.4 eV)¹⁹ and $\text{Ge } 3/2$ (30.0 eV)³⁵ are visible starting with the 5-minute scan, though shifted to lower binding energies. Differential charging is prevalent in surface-passivated films and is the likely cause for this and other similar drifting signals observed throughout the manuscript.^{36, 37} The shift in the Ge signal may also be due to formation of Li-Ge alloys would have the same effect.³⁸ The drop lines shown for the Ge spectra correspond to the values used to calculate the composition and not the literature values listed above. The P2p signal was not detected in any scan. Figures D1–D6 in Appendix D show peak deconvolutions for each element.

The SEI region is evident from the atomic elemental composition changes with sputtering time shown in Figure 6.2b. Carbon and oxygen drop 15% and 5%, respectively, within the first 5 minutes of sputtering and then level off for the final two scans. Lithium content increases by 20% and fluorine peaks at 12% in the 20-second scan, then levels off to 8% by 5 minutes. The germanium signal increases gradually from less than 1% to 5% after 30 minutes of sputtering. The SEI layer appears to be sputtered through within 5 minutes, given that the compositions vary only slightly in the last two scans for all elements.

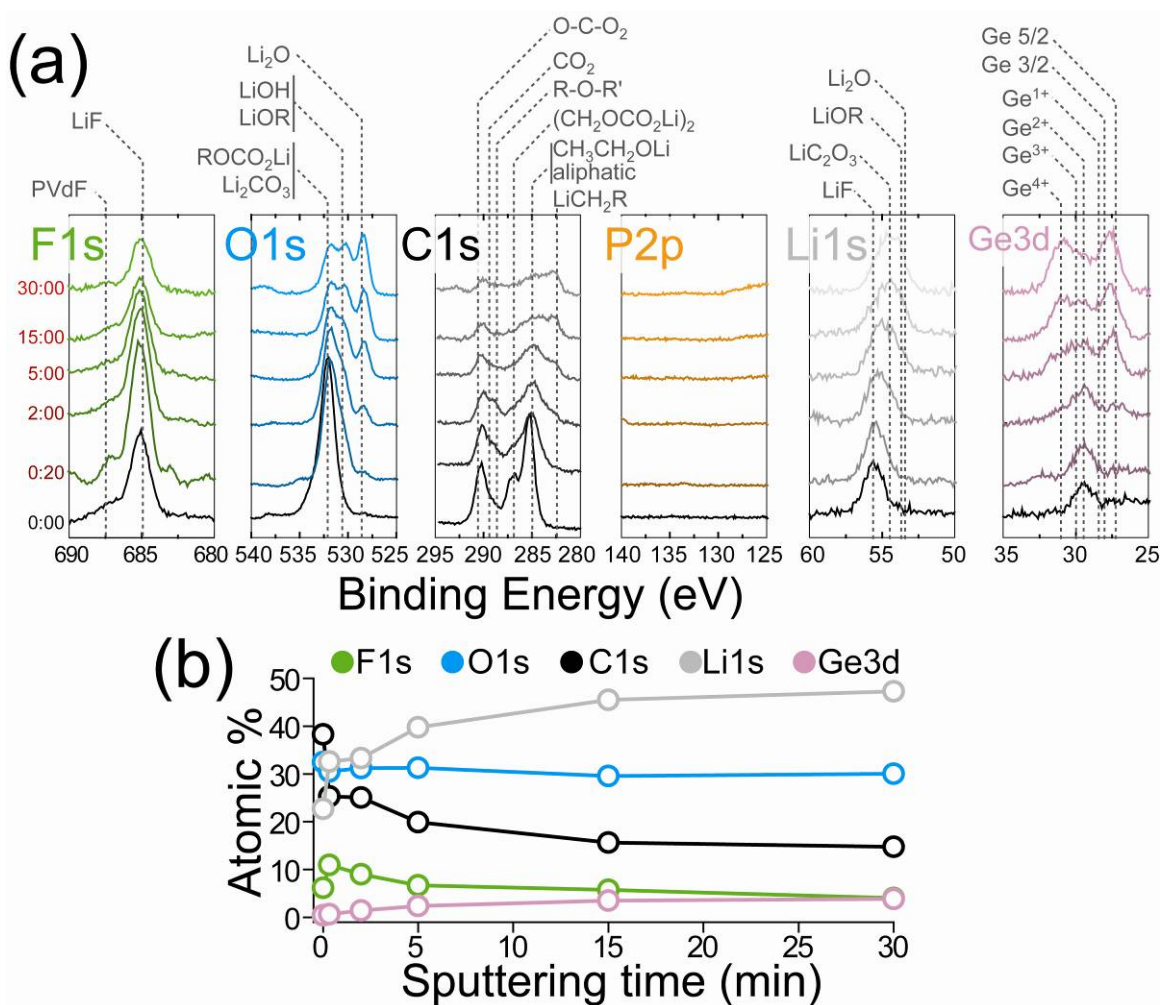


Figure 6.2: (a) High-resolution XPS elemental scans of F1s, O1s, C1s, P2p, Li1s, and Ge3d at various sputtering times and (b) corresponding elemental film compositions for batteries cycled with the EC:DEC electrolyte solution. The battery was disassembled in the lithiated state.

6.3.3 XPS of SEI formation using the EC:DMC electrolyte

Ge nanowire films cycled with EC:DMC, shown in Figure 6.3, exhibit similar behavior to films cycled with EC:DEC. The F1s signal shows a strong LiF peak with a small PVdF shoulder throughout the film. The Li1s signal contains various Li compounds (e.g., LiF, Li₂CO₃, LiOH, and LiOR). The O1s signal confirms the presence of these oxidized Li compounds. The relative intensities of the LiOH, LiOR, and Li₂O peaks to

the Li_2O_3 peak are lower for the EC:DMC electrolyte than for EC:DEC. The un-sputtered C1s signal shows a more intense carbonate peak than was exhibited for the EC:DEC electrolyte. Furthermore, the peak at 287 eV is more defined in this spectrum indicating a SEI layer rich in decomposed carbonates that is thicker for EC:DMC compared to EC:DEC. The carbonate peaks persist throughout the sputtered film while the electrolyte decomposition signals fade revealing aliphatic and LiCH_2R signals within the film. The thick SEI layer conceals the Ge3d for the first few scans. After 5 minutes of sputtering, a mixture of oxidation states, primarily Ge^{4+} and Ge^0 , emerges. The Ge^{3+} peak is not intense here as it was for the lithiated film using EC:DEC. This further indicates lithiation of GeO_2 and is the likely cause for the observed capacity fade for this battery as well. The P2p signal, again, was not detected in any scan.

The SEI region is evident from the atomic elemental composition changes with sputtering time shown in Figure 6.2b. Carbon and oxygen drop 15% and 5%, respectively, within the first 5 minutes of sputtering and then level off for the final two scans. Lithium and fluorine increase by 15% and 5%, respectively, within the first 5 minutes of sputtering and also level off. The germanium signal increases gradually from less than 1% to ~10% after 30 minutes of sputtering. The SEI layer is sputtered clean within 5 minutes. The individual element scans confirm this, as the 15- and 30-minute scans are nearly identical for all elements with compositions that differ only slightly from the 5-minute scan.

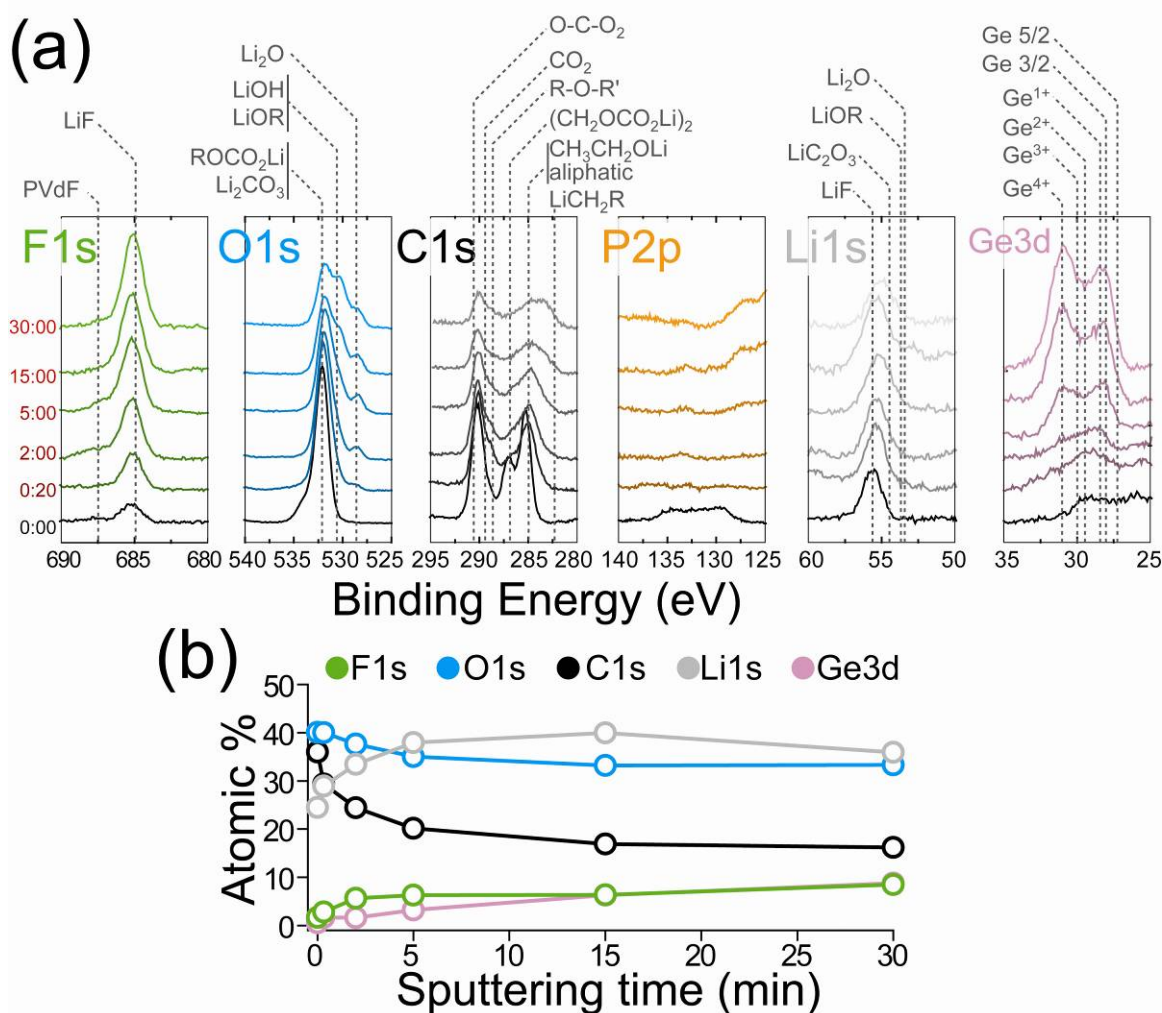


Figure 6.3: (a) High-resolution XPS elemental scans of F1s, O1s, C1s, P2p, Li1s, and Ge3d at various sputtering times and (b) corresponding elemental film compositions for batteries cycled with the EC:DMC electrolyte solution. The battery was disassembled in the delithiated state.

6.3.4 XPS of SEI formation using the FEC:DMC electrolyte

Surface chemistry for Ge nanowire films cycled with FEC:DMC, shown in Figure 6.4, differs significantly from films cycled with either EC:DEC or EC:DMC. The first notable difference is the presence of a P2p signal at 134.7 eV corresponding to LiPF₆ hydrolysis products of the form Li_xPF_yO_z (e.g., LiPOF₂, Li₂PFO₃).^{39, 40} This species is

also present in the F1s spectra at 688.5 eV⁴⁰ in the un-sputtered and 20-second scans and is concentrated at in the surface layer. Similar to EC:DEC and EC:DMC, LiF is present throughout the film, evident by the strong signal in both the F1s and Li1s spectra. The PVdF shoulder is also present throughout. Unlike the previous films, the Li1s signal does not change with sputtering time. Lithium is present as a mixture of LiF, Li₂CO₃, LiOH, and LiOR. The O1s region corroborates the Li1s signal, showing a mixture of Li₂CO₃, LiOH, and LiOR. Li₂O is not observed at all for the FEC:DMC electrolyte. These data, coupled with the C1s spectrum, indicates less electrolyte decomposition in comparison to the EC:DEC and EC:DMC electrolytes. The carbonate signal at 290 eV is present only as a small shoulder in the C1s signal, and only for the un-sputtered and 20-second scans. Furthermore, the EC decomposition peak at 287 eV is only a small shoulder on the large 285 eV peak and only for the unsputtered film. The Ge3d signal shows markedly different behavior than for the EC:DEC and EC:DMC electrolytes. Ge suboxides are present in much lower quantities. The majority of the signal is instead due to zero-valent Ge. The oxides that are present are predominantly Ge¹⁺ and Ge²⁺. This is in stark contrast to the EC:DEC and EC:DMC electrolytes wherein the suboxide signals were dominated by Ge³⁺ and Ge⁴⁺. The initial Ge nanowire film surface has roughly equal Ge⁴⁺ and Ge⁰ contributions (see Figure D7 in Appendix D). HF is present due to the FEC solvent and reacts with GeO₂ to form gaseous GeF₄. This explains why the Ge⁴⁺ signal is lower here in than for FEC-free electrolytes. Minimized electrolyte decomposition and preservation of zero-valent Ge allows for extended cyclability and good capacity retention because there is less Li₂O formation.

There is a noticeably higher concentration of lithium and fluorine in the surface layer of the SEI, further indicating enhanced Li consumption through reaction with HF and subsequent deposition of LiF on the surface of the film. HF also reacts with LiOH,

Li_2O , and Li_2O_3 to produce LiF which accounts for the high fluorine content.²⁶ The carbon and oxygen signals witness a sharp drop between the un-sputtered and 20-second scan and the phosphorous signal fades as well. After the 2-minute sputter, compositions change by less than a few percent for all elements indicating a thinner SEI layer for the FEC:DMC electrolyte than the previous two cases. This is consistent with reports of FEC-based electrolytes forming SEI layers on Si nanowires.¹¹ The fluorine signal is much stronger for FEC:DMC than it is for EC:DMC and EC:DEC. In addition to increased Li consumption, the $\text{Li}_x\text{PF}_y\text{O}_z$ salts are present, enhancing the fluorine signal. There is still a huge first cycle irreversible capacity loss to consider. Given that the carbonaceous electrolyte does not decompose very much, evolution of HF from the FEC electrolyte likely hinders first cycle capacity, creating more LiF , which precipitates out on the surface of the electrode. The thin SEI layer allows for good charge and ion transport, allowing for good capacity retention and extended cyclability.

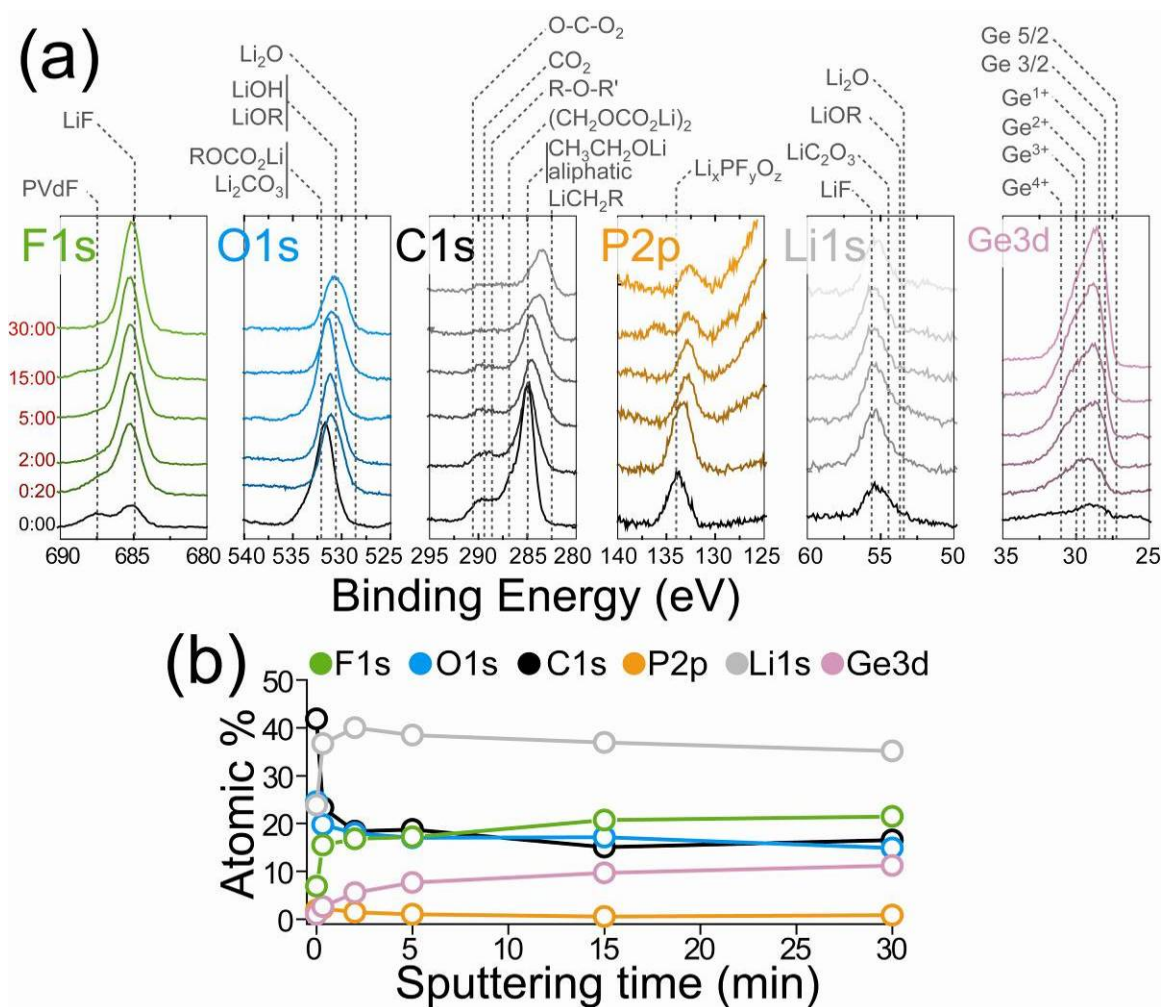


Figure 6.4: (a) High-resolution XPS elemental scans of F1s, O1s, C1s, P2p, Li1s, and Ge3d at various sputtering times and (b) corresponding elemental film compositions for batteries cycled with the FEC:DMC electrolyte solution. The battery was disassembled in the delithiated state.

6.3.5 Germanium and germanium oxide signals

Alkyl carbonate solvents (e.g., EC, DMC, DEC, and FEC) are reduced to Li-containing salts (Li₂CO₃, LiCH₂R, LiPOF₂, Li₂PFO₃, etc.), which passivate the electrode surface, forming the SEI layer.^{7, 11, 26, 39, 40} Introducing additives (e.g., FEC) into the electrolyte solution can modify the SEI layer.^{5, 8, 11, 12} LiF is present in every film and comes from the reaction of HF with these various Li salts. HF is produced through LiPF₆

hydrolysis¹¹ and—for the FEC electrolyte—from the dehydrofluorination of FEC yielding VC, another proved Li-ion battery performance enhancing electrolyte additive.^{41, 42} Furthermore, PVdF can dehydrofluorinate and generate additional HF.²⁰ The presence of HF and Li in the Ge nanowire films significantly alter the oxidation state of Ge.

The atomic ratio of zero-valent Ge to the sum total of Ge suboxide species was calculated for films cycled using each electrolyte solution and at each scan time, shown in Figure 6.5. The ratio of Ge⁰ to GeO_x is two to three times lower for EC:DMC than FEC:DMC. EC:DEC also has a higher Ge⁰ to GeO_x ratio by comparison. The oxide signal is mainly Ge³⁺ and Ge⁴⁺ for EC:DEC whereas the suboxides are predominantly in the Ge¹⁺ and Ge²⁺ state for FEC:DMC (see Figure D8). The similarities between the FEC:DMC and EC:DEC curves are due to the fact that the latter is lithiated, which results in reduction of the suboxide signals. For sake of comparison, the Ge⁰ to GeO_x ratio for an uncycled Ge nanowire film is 1.2 at the surface and 1.8 after sputtering for 20 seconds and 30 minutes.

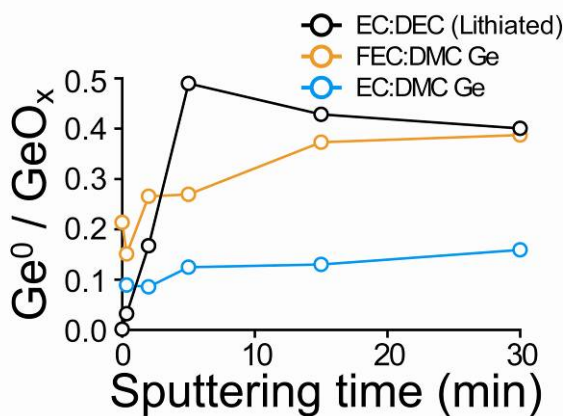


Figure 6.5: Ratio of Ge⁰ to Ge suboxides as a function of sputtering time.

6.4 CONCLUSIONS

Here, we examined SEI layers formed on Ge nanowire films cycled as negative electrodes in Li-ion batteries using mixtures (1:1 w/w) of EC:DEC, EC:DMC, and FEC:DMC as the electrolyte solvents. The EC:DMC solvent mixture produces the thickest SEI layer and performs poorly, exhibiting steady capacity fade with cycling. The EC:DEC electrolyte also forms a thick SEI layer, though XPS indicates that the layer is not as thick as that formed by EC:DMC. This is also evident by the improved capacity retention relative to EC:DMC. EC:DEC also exhibits steady capacity fade. Given the high content of oxides Ge in the film, this fade is attributed to partial irreversible GeO₂ lithiation. Furthermore, the SEI layers are rich in decomposed carbonate solvents. The oxygen rich environment acts as an additional sink to Li⁺ ions through irreversible formation of Li₂O and various organic Li salts. The FEC:DMC electrolyte forms a thin SEI layer compared to EC:DEC and EC:DMC. Though this film exhibits the largest first cycle irreversible capacity loss—attributed to a higher concentration of HF resulting in enhanced LiF formation—it also shows the best capacity retention, attributed to limited Ge oxidation, maintained by the increased presence of HF.

6.5 ACKNOWLEDGEMENTS

Authors contributing to this work include: Timothy D. Bogart, Hugo Celio, and Brian A. Korgel. Vincent C. Holmberg and Vahid A. Akhavan were extremely helpful with XPS analysis techniques. We thank TIMCAL for supplying the conductive carbon used in slurry formation.

6.6 REFERENCES

1. Winter, M.; Besenhard, J. O.; Spahr, M. E.; Novák, P. *Adv. Mater.* **1998**, *10*, 725-763.
2. Graetz, J.; Ahn, C. C.; Yazami, R.; Fultz, B. *J. Electrochem. Soc.* **2004**, *151*, A698-A702.

3. Fuller, C. S.; Severiens, J. C. *Phys. Rev.* **1954**, *96*, 21-24.
4. Park, M.-H.; Cho, Y.; Kim, K.; Kim, J.; Liu, M.; Cho, J. *Angew. Chem. Int. Ed.* **2011**, *50*, 9647-9650.
5. Zhang, S. S. *J. Power Sources* **2006**, *162*, 1379-1394.
6. Peled, E. *J. Electrochem. Soc.* **1979**, *126*, 2047-2051.
7. Chan, C. K.; Ruffo, R.; Hong, S. S.; Cui, Y. *J. Power Sources* **2009**, *189*, 1132-1140.
8. Nakai, H.; Kubota, T.; Kita, A.; Kawashima, A. *J. Electrochem. Soc.* **2011**, *158*, A798-A801.
9. Shiraishi, S.; Kanamura, K.; Takehara, Z.-I. *J. Electrochem. Soc.* **1999**, *146*, 1633-1639.
10. Aurbach, D.; Gamolsky, K.; Markovsky, B.; Gofer, Y.; Schmidt, M.; Heider, U. *Electrochim. Acta* **2002**, *47*, 1423-1439.
11. Etacheri, V.; Haik, O.; Goffer, Y.; Roberts, G. A.; Stefan, I. C.; Fasching, R.; Aurbach, D. *Langmuir* **2012**, *28*, 965-976.
12. Choi, N.-S.; Yew, K. H.; Lee, K. Y.; Sung, M.; Kim, H.; Kim, S.-S. *J. Power Sources* **2006**, *161*, 1254-1259.
13. Möller, K. C.; Hodal, T.; Appel, W. K.; Winter, M.; Besenhard, J. O. *J. Power Sources* **2001**, *97-98*, 595-597.
14. Aurbach, D.; Ein-Eli, Y.; Markovsky, B.; Zaban, A.; Luski, S.; Carmeli, Y.; Yamin, H. *J. Electrochem. Soc.* **1995**, *142*, 2882-2890.
15. Sato, K.; Zhao, L.; Okada, S.; Yamaki, J.-i. *J. Power Sources* **2011**, *196*, 5617-5622.
16. Smart, M. C.; Ratnakumar, B. V.; Ryan-Mowrey, V. S.; Surampudi, S.; Prakash, G. K. S.; Hu, J.; Cheung, I. *J. Power Sources* **2003**, *119-121*, 359-367.
17. Chockla, A. M.; Korgel, B. A. *J. Mater. Chem.* **2009**, *19*, 996-1001.
18. These data are reported in Chapter 5 and are shown again here for reference.
19. Briggs, D. S.; Seah, M.P. *Practical Surface Analysis, second edition* **1993**.
20. Andersson, A. M. *Surface phenomena in Li-ion batteries, Ph.D. thesis, Acta Universitatis Upsaliensis, Uppsala* **2001**.
21. Andersson, A. M.; Herstedt, M.; Bishop, A. G.; Edström, K. *Electrochim. Acta* **2002**, *47*, 1885-1898.
22. Kanamura, K.; Takezawa, H.; Shiraishi, S.; Takehara, Z. *J. Electrochem. Soc.* **1997**, *144*, 1900-1906.

23. Aurbach, D.; Weissman, I.; Schechter, A.; Cohen, H. *Langmuir* **1996**, *12*, 3991-4007.
24. Dedryvere, R.; Laruelle, S.; Grugeon, S.; Gireaud, L.; Tarascon, J. M.; Gonbeau, D. *J. Electrochem. Soc.* **2005**, *152*, A689-A696.
25. Kanamura, K.; Tamura, H.; Takehara, Z.-I. *J. Electroanal. Chem.* **1992**, *333*, 127-142.
26. Kanamura, K.; Tamura, H.; Shiraishi, S.; Takehara, Z.-I. *J. Electrochem. Soc.* **1995**, *142*, 340-347.
27. Kanamura, K.; Tamura, H.; Shiraishi, S.; Takehara, Z.-I. *Electrochim. Acta* **1995**, *40*, 913-921.
28. Aurbach, D.; Markovsky, B.; Shechter, A.; Ein-Eli, Y.; Cohen, H. *J. Electrochem. Soc.* **1996**, *143*, 3809-3820.
29. Aurbach, D.; Ein-Ely, Y.; Zaban, A. *J. Electrochem. Soc.* **1994**, *141*, L1-L3.
30. Aurbach, D.; Zaban, A.; Schechter, A.; Ein-Eli, Y.; Zinigrad, E.; Markovsky, B. *J. Electrochem. Soc.* **1995**, *142*, 2873-2882.
31. Charlier, J.; Detalle, V.; Valin, F.; Bureau, C.; Lecayon, G. *J. Vac. Sci. Technol. A* **1997**, *15*, 353-364.
32. Vogdanis, L.; Martens, B.; Uchtmann, H.; Hensel, F.; Heitz, W. *Makromol. Chem.* **1990**, *191*, 465-472.
33. Schechter, A.; Aurbach, D.; Cohen, H. *Langmuir* **1999**, *15*, 3334-3342.
34. Kim, Y.; Hwang, H.; Lawler, K.; Martin, S. W.; Cho, J. *Electrochim. Acta* **2008**, *53*, 5058-5064.
35. Moulder, J. F. S., W. F.; Sobol, P. E.; Bomben, K. D. *Handbook of X-Ray Photoelectron Spectroscopy* **1992**.
36. Dedryvère, R.; Foix, D.; Franger, S.; Patoux, S.; Daniel, L.; Gonbeau, D. *J. Phys. Chem. C* **2010**, *114*, 10999-11008.
37. Ehinon, K. K. D.; Naille, S.; Dedryvère, R.; Lippens, P. E.; Jumas, J. C.; Gonbeau, D. *Chem. Mater.* **2008**, *20*, 5388-5398.
38. Philippe, B.; Dedryvre, R. M.; Allouche, J.; Lindgren, F.; Gorgoi, M.; Rensmo, H. K.; Gonbeau, D.; Edström, K. *Chem. Mater.* **2012**, *24*, 107-1115.
39. Aurbach, D.; Zaban, A. *J. Electroanal. Chem.* **1995**, *393*, 43-53.
40. Andersson, A. M.; Abraham, D. P.; Haasch, R.; MacLaren, S.; Liu, J.; Amine, K. *J. Electrochem. Soc.* **2002**, *149*, A1358-A1369.
41. Mogi, R.; Inaba, M.; Jeong, S.-K.; Iriyama, Y.; Abe, T.; Ogumi, Z. *J. Electrochem. Soc.* **2002**, *149*, A1578-A1583.

42. McMillan, R.; Slegel, H.; Shu, Z. X.; Wang, W. J. *Power Sources* **1999**, 81-82, 20-26.

Chapter 7: Influence of Gold in Si Nanowire Lithium Ion Battery Anodes

7.1 INTRODUCTION

Lithium-silicon alloys have been extensively explored for use as high capacity negative electrode materials in lithium ion batteries (LIBs).¹ Silicon can store an enormous amount of lithium and boasts a maximum theoretical capacity (3579 mA h g⁻¹)²⁻⁴ ten times greater than graphite (370 mA h g⁻¹), the commercial standard in LIBs. Si offers the greatest power density of known Li insertion materials. Si is also inexpensive and abundant, with a low working potential relative to the reduction potential of Li/Li⁺. Si alloys with Li, by becoming amorphous (a-Si) and then forming Li₁₅Si₄.^{2, 3, 5}



Unfortunate for battery applications, lithiation leads to a massive volume expansion of up to 300%, which leads to electrode pulverization and battery failure. Nanostructured materials can tolerate these mechanical stresses and remain intact.⁶⁻⁸ Si nanowires (and other nanostructures) have received much attention for high capacity LIB anodes.⁹⁻²³

We have demonstrated that, through a simple annealing process, supercritical fluid-liquid-solid (SFLS) grown Si nanowires using monophenylsilane as the Si source show good cycle behavior and high capacities as Li insertion materials without the addition of conductive carbon or binder typically required for Si nanostructured electrodes (see Chapter 2). We have also reported graphene-supported SFLS Si nanowires synthesized using trisilane as a freestanding lithium insertion that exhibits poor cycle performance due to the presence of excess gold (see Chapter 4). Trisilane-

grown Si nanowires are attractive because the SFLS process can produce up to 100 mg of material in a single lab-scale reactor batch. Conventional CVD methods for Si nanowires yield only microgram quantities after reaction times of 4 to 20 minutes.^{12, 13, 16, 19} By comparison, SFLS reactions in our lab can produce Si nanowires at 6–8 g hr⁻¹. Au is present in significant amounts, at a concentration of about 25% w/w. Au is a poor Li insertion material and forms Li₁₅Au₄ irreversibly.^{24, 25} Given the high-throughput nature of SFLS methods,²⁶ it is of great interest to determine the cause of the poor performance and improve the cycle behavior. In this study, the influence of Au in the Li storage performance of Si nanowires was studied. Si nanowires were grown using trisilane as a reactant in the SFLS process and then tested in slurry-cast films. Polyvinylidene fluoride (PVdF) and sodium alginate (NaAlg) were tested as a binders and fluoroethylene carbonate (FEC) as an electrolyte additive in various standard electrolyte solutions.²⁷⁻³⁰ Batteries were tested using nanowires with and without Au removal.

7.2 EXPERIMENTAL SECTION

7.2.1 Materials

All reactions were carried out using standard airless procedures using a nitrogen-filled glove box. All reagents and solvents were used as received and without further purification. Dodecanethiol (DDT, ≥98%), tetrachloroaurate trihydrate (≥99.9%), sodium borohydride (≥98%), toluene (anhydrous, 99.8%), propylene carbonate (PC, anhydrous, 99.7%), ethanol (99.9%), tetraoctylammonium bromide (TOAB, 98%), lithium hexafluorophosphate (LiPF₆, ≥99.99%), poly (vinylidene fluoride) (PVdF, average MW ~534,000 by GPC), alginic acid sodium salt (NaAlg, Lot# MKBG5630V), 1-methyl 2-pyrrolidinone (NMP, 99.5%), chloroform (99.8%) and squalane (99%) were purchased from Sigma-Aldrich and trisilane (Si₃H₈, 100%) from Voltaix. Conductive

carbon super C65 was supplied by TIMCAL. Hydrofluoric acid (HF, 48%) was purchased from EMD Chemicals and hydrochloric acid (HCl, 12.1 N) and nitric acid (HNO₃, 15.8 N) were bought from Fisher. Fluoroethylene carbonate (>98%) was obtained from TCI America. Electrolyte solutions were either purchased—as 1.0 M solutions of LiPF₆ in a 1:1 w/w mixture of ethylcarbonate (EC) : diethyl carbonate (DEC) (Novolyte) EC : dimethyl carbonate (DMC, EMD chemicals)—or prepared in one of three ways: LiPF₆ was dissolved at a concentration of 1.0 M in 1:1 w/w mixture of either (1) FEC:DEC or (2) FEC:DMC, or (3) FEC was added at a concentration of 3% w/w to the 1.0 M LiPF₆ in EC:DMC solution purchased from EMD chemicals. Celgard 2400 membranes (25µm, Celgard) were used as separators, and Li metal foil (1.5 mm 99.9%) as the counter electrode, purchased from Alfa Aesar.

7.2.2 Silicon nanowire synthesis

Si nanowires were grown from using Au nanocrystal seeds using published SFLS methods..²⁶ Dodecanethiol-capped Au nanocrystals (2 nm diameter) were synthesized following established procedures³¹ and stored in a nitrogen-filled gloved box dispersed in toluene at a concentration of 50 mg mL⁻¹. Si nanowire synthesis was carried out in a nitrogen-filled glove box. A reactant solution is made by mixing 0.25 mL of trisilane with 0.55 mL of the Au nanocrystal dispersion in toluene and diluting with an additional 0.3 mL of toluene. Nanowire growth is carried out in a flow-through high pressure sealed titanium reactor at 450°C. Before injecting the reactant solution, the reactor is heated to 450°C then pressurized with toluene to 6.9 MPa with a closed effluent line. The reactant solution is injected over the course of 1 minute with the reactor effluent remaining closed. The reactor pressure increases to 15.2 MPa during the 1 minute reaction. Immediately after injecting the reactant solution, the inlet valve is closed and

the reactor is removed from the heating block and allowed to cool to room temperature. After the reactor has cooled, it is removed from the glovebox and opened. The nanowires are extracted from the reactor with additional toluene (~15mL). The crude reaction product is centrifuged (all centrifugations steps were done at 8000 rpm for 5 minutes) and the supernatant is discarded. The nanowires are then washed two more times by redispersion in 20 mL toluene followed by centrifugation. The nanowires are dried down using a rotovap to determine an accurate weight (typical product yield is ~100 mg) before being dispersed in chloroform and stored in a vial under ambient conditions prior to use.

7.2.3 Removal of Au from Si nanowires

Au was removed from the nanowires using a two-step etching process. For the first etch, approximately 100 mg of nanowires were dispersed in 80 mL of CHCl_3 and added to a plastic beaker containing a 40 mL HF etching solution composed of HF, deionized water (DI H_2O), and ethanol in a 1:1:1 (v/v) ratio. The mixture was emulsified with vigorous stirring for 30 minutes. After etching, the stirring was stopped to allow phase separation. The nanowires tend to stick to the liquid-liquid interface, so the top phase (*aq*) is extracted with a plastic pipette, being careful to not harvest the nanowires trapped at the interface. The organic phase containing the Si nanowires is added to a plastic centrifuge tube with 10 mL fresh DI H_2O . The centrifuge tube is then shaken vigorously, then let stand to allow phase separation. This process is repeated once more and EtOH (10 mL) is added to the remaining solution prior to centrifugation at 8000 rpm for 5 minutes. The solution is washed three additional times by centrifugation and redispersion in CHCl_3 , discarding the supernatant each time before finally dispersing the nanowires in 20 mL CHCl_3 .

For the second etch the Si nanowire suspension is added with an additional 60 mL CHCl_3 to a glass beaker containing a 50 mL *aqua regia* solution (1:3 HNO_3 : HCl v/v). The mixture was emulsified with vigorous stirring for 2 hours. After etching, the stirring is stopped allowing phase separation. The CHCl_3 phase is removed via pipette and the remaining Si nanowire suspension in *aqua regia* is centrifuged at 8000 rpm for 5 minutes. After centrifugation, the *aqua regia* is carefully removed with a pipette and the Si nanowires are redispersed in 10 mL DI H_2O . The wires are washed twice with DI H_2O (10 mL) and twice with EtOH. The wires are dried down via rotovap to get an accurate weight before making slurry solutions.

7.2.4 Anode preparation and battery assembly

Slurries were prepared by combining Si nanowires with either PVdF or NaAlg and conductive carbon and in a 70:20:10 (w/w) ratio. Four separate Si nanowire slurries were prepared by dispersing the nanowires (typically 80-100 mg) in 2 mL ethanol and bath sonication for 1 hour. Meanwhile, two conductive carbon / PVdF in 1 mL NMP and two conductive carbon / NaAlg in 1 mL DI H_2O suspensions were prepared and bath sonicated for 1 hour. Si nanowire and carbon / binder solutions were mixed in the following combinations: (1) as made Si nanowires with PVdF, (2) Au-removed Si nanowires with PVdF, (3) as made Si nanowires with NaAlg, and (4) Au-removed Si nanowires with NaAlg. Slurries generally required a few additional mL of EtOH or DI H_2O to form a uniform suspension. Slurries were wand sonicated for 30 minutes and reduced by rotovap yielding viscous dispersions, then cast onto Cu foil using a 200 μm film applicator and vacuum dried overnight at 100°C.

Batteries were assembled in an argon-filled glovebox. Si nanowire anodes were hole-punched (1 cm diameter) from the Cu foil supported slurry film. The electrolyte

was a 1.0 M solution of LiPF_6 in a 1:1 w/w mixture of either (1) EC:DEC, (2) EC:DMC, (3) EC:DMC + 3% w/w FEC, (4) FEC:DEC, (5) FEC:DMC, or (6) PC:DMC. A few drops of electrolyte were deposited over the Li foil counter electrode and on top of a Celgard 2400 separator membrane (25 μm thick, Celgard) before the adding the Si anode and crimping the completed battery.

AC electrochemical impedance spectroscopy (EIS) measurements were obtained using an Electrochemical Analyzer (CH Instruments, model CHI 604D) over a frequency range of 0.01 to 100,000 Hz. Galvanostatic measurements were made using an Arbin BT-2143 test unit sweeping between 2 V and 10 mV vs Li/Li^+ at various rates. Capacities are reported based on the active material only.

7.2.5 Material characterization

Scanning electron microscopy (SEM) images were acquired using a Zeiss Supra 40 SEM with an in-lens arrangement, a working voltage of 5 keV and a working distance of 5 mm. Transmission electron microscopy (TEM) images were digitally acquired using either a FEI Tecnai Spirit BioTwin TEM operated at 80 kV or a field emission JEOL 2010F TEM operated at 200 kV. TEM samples were prepared by drop-casting from chloroform dispersions onto 200 mesh lacey-carbon copper TEM grids (Electron Microscopy Sciences).

X-ray diffraction (XRD) was performed with a Rigaku R-Axis Spider Diffractometer with Image plate detector with $\text{Cu } k_\alpha$ ($\lambda = 1.5418 \text{ \AA}$) radiation operated at 40 kV and 40 mA. Samples were measured on a 0.5 mm nylon loop, scanning for 10 min with 1° per second sample rotation under ambient conditions. The diffraction data were integrated radially from $2\theta = 20$ to 80. Background scattering from the nylon loop was subtracted.

7.3 RESULTS AND DISCUSSION

7.3.1 Silicon nanowires and Au removal

The relatively high concentration of Au nanocrystals needed for the SFLS synthesis using trisilane leads to a significant amount of Au present in the sample.^{26, 32, 33} A two-step etching procedure illustrated in Figure 7.1b was used to remove Au from the nanowires. Au etching requires two steps because of a thin layer of Si coating the Au at the tips of the nanowires. The first step uses HF to remove the thin Si shell, exposing the Au tip; the second uses *aqua regia* to etch the seed particles.^{32, 33} TEM and XRD confirmed the efficacy of the etching procedure. For example, Figures 7.1c and 7.1d show TEM images of the Si nanowires before and after etching. Before etching, there are Au nanocrystals at the nanowire tips and associated with the nanowire surface. After etching, there are no longer any visible Au nanocrystals in the TEM images of the nanowires. XRD also shows that the Au initially present in the nanowire sample is removed (Figure 7.1h).

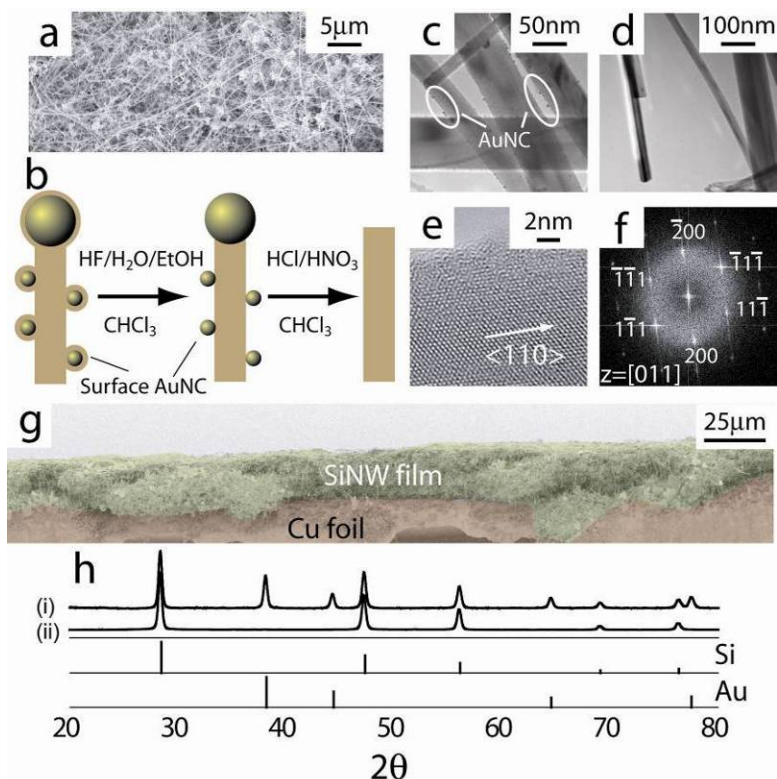


Figure 7.1: (a) SEM of SFLS-grown Si nanowires. (b) Illustration of the Au etching procedure. (c) TEM images of nanowires prior to etching. Surface-bound Au nanocrystals are circled for reference. (d) TEM image of Si nanowires after etching—there are no longer Au nanocrystals present in the sample. (e) HRTEM image of a Si nanowire, shown growing in the $\langle 110 \rangle$ direction with (f) corresponding FFT pattern (imaged down the $[011]$ zone axis). (g) SEM image of film of Au-removed Si nanowires in PVdF. (h) XRD of the Si nanowires (i) before and (ii) after Au removal (Si JCPDS: 00-027-1402, Au: 00-004-0784).

7.3.2 Extended cycle life behavior

Si nanowire films were prepared in one of four nanowire / binder combinations and cycled galvanostatically against Li foil. Combinations included: **(1)** as-made nanowires mixed with PVdF, **(2)** Au-removed nanowires mixed with PVdF, **(3)** as-made nanowires mixed with NaAlg, and **(4)** Au-removed nanowires mixed with NaAlg. Six electrolyte solutions of 1.0 M LiPF_6 in a variety of solvents were also tested, including:

(A) EC:DEC, (B) EC:DMC, (C) EC:DMC + 3% w/w FEC, (D) FEC:DEC, (E) FEC:DMC, and (F) PC:DMC. Standard electrolytes contain a combination of EC, DEC, and DMC and are used commonly in both research and commercially. Several recent studies have shown FEC to stabilize cycle life in batteries with Si powders,²⁷⁻²⁹ but has yet to be tested for Si nanowires. Figure 7.2 shows galvanostatic cycling data for Si nanowire/binder combinations (1)–(4) cycled at a rate of C/10 for 100 charge/discharge cycles. C is the current density required to fully lithate or delithiate the electrode in 1 hour. The different colored curves correspond to the electrolyte system shown at the top of the figure next to the dot of the same color. Table 7.1 summarizes the battery data: first cycle charge capacity, irreversible first cycle capacity loss, and percent capacity retention of cycle 100 relative to cycles 1 and 5.

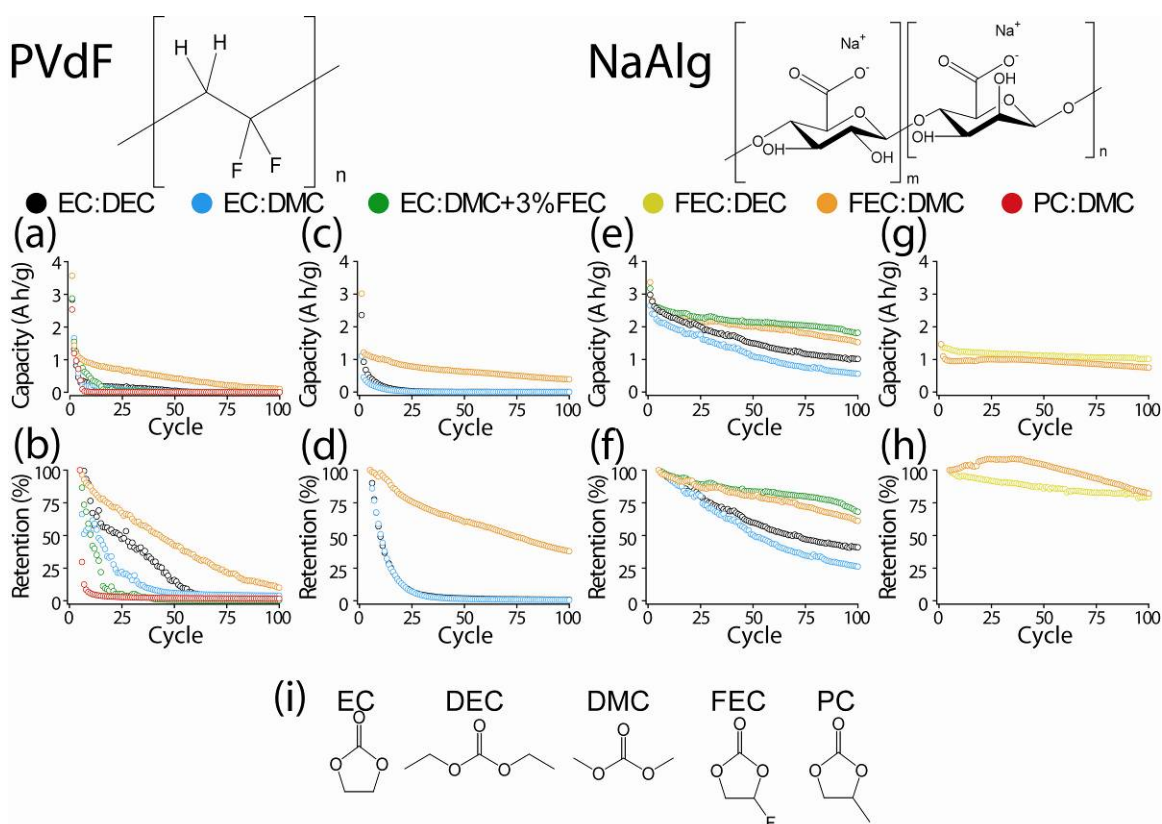


Figure 7.2: (a, c, e, g) Charge capacity cycle data for 100 cycles at $C/10$ and (b, d, f, h) capacity retention for Si nanowires in various electrolyte solutions: (a, b) as-prepared in PVdF; (c, d) Au-removed in PVdF; (e, f) as-prepared in NaAlg; (g, h) Au-removed in NaAlg. Capacity retention is relative to the 5th cycle for any given system. (i) Electrolyte solvent and (top) binder molecules are shown.

First cycle charge capacities were between 1100 and 3600 mA h g^{-1} . Only three of the fourteen systems tested had first cycle charge capacities below 2300 mA h g^{-1} while five had capacities above 3000 mA h g^{-1} . PVdF based systems performed poorly beyond the first cycle with irreversible capacity losses of 39% to 68%. The Si nanowires with Au removed performed particularly poorly when mixed with PVdF; first cycle irreversible capacity losses were greater than 50%. With PVdF binder and Au removed Si nanowires, electrolyte (E) performed the best with 35.4% charge capacity retention of

cycle 100 relative to cycle 5. All other systems show capacity retention below 4%. According to previous reports, Si / PVdF films must be annealed above 250°C to realize high capacities with good retention.³⁴ After annealing films (1) and (2) for 12 hours under N₂ flow at 300°C, they still performed poorly and were not tested further.

Films (3) and (4) contain NaAlg and greatly outperformed the PVdF-containing films (1) and (2). Film (4) was cycled with FEC-containing (i.e., **D** and **E**) electrolytes only. These had the lowest first cycle capacity (1455 mA h g⁻¹ for electrolyte (**D**) and 1466 mA h g⁻¹ for **E**) but had the best capacity retention after 100 cycles (77.3% and 78.6%, respectively) relative to the 5th cycle charge capacity. Electrolyte (**E**) had the highest first cycle irreversible capacity loss for all four films, ranging between 21.3% for film (3) and 68% for film (2).

Interactions between the binder and active Si material are critical to electrode longevity. The porous texture of the Si–C–binder film is important for the stable reaction between Si and Li. Furthermore, binders that undergo a self-healing process during lithium insertion and removal maintain the integrity of the electrode and improve cycle life.^{35, 36} This is true for binders that exhibit hydrogen bonding, which break and reform as the electrode material expands and contracts (e.g., carboxymethylcellulose–CMC, NaAlg, etc.). Carboxylic acid groups in NaAlg interact with the surface of conductive carbon and Si in this way to provide efficient electronic and Li⁺ ion transport. The use of NaAlg shows improved cycle life for the Si nanowire anode performance compared to PVdF.³⁰ Heat treatment of PVdF forms an even distribution on Si powder electrodes and is responsible for the improved performance over un-annealed PVdF films.³⁴ Our results indicate that the binder does not interact as strongly with the Si nanowire surface and as such, performance suffers; we do not observe improved cycling after PVdF heat-treatment with Si nanowires as was previously observed for Si particles.^{30, 34} We focus

on NaAlg films (**3** and **4**) in the electrochemical analysis below. Data for the Si nanowire/PVdF combination are provided as supporting information in Appendix E.

Table 7.1: Summary of first cycle capacity and retention in various battery formulations.

Film	Electrolyte [‡]	Capacity (mA h g ⁻¹)				Retention (%)	
		Cycle 1	1 st cycle loss (%)	Cycle 5	Cycle 100	Q _{ret1} ^a	Q _{ret5} ^b
PVdF	EC:DEC	2838	1151 (40.6)	310	3	0.1	1.0
PVdF	EC:DMC	3564	1391 (39.0)	337	13	0.4	3.8
PVdF	EC:DMC+FEC	2873	1143 (39.8)	858	3	0.1	0.3
PVdF	FEC:DMC	3572	1557 (43.6)	1038	100	2.8	9.6
PVdF	PC:DMC	2534	1260 (49.7)	366	5	0.2	1.3
PVdF [†]	EC:DEC	2358	1240 (52.6)	438	3	0.1	0.8
PVdF [†]	EC:DMC	1109	656 (59.2)	247	1	0.1	0.6
PVdF [†]	FEC:DMC	3013	2048 (68)	1103	390	12.9	35.4
NaAlg	ED:DEC	2978	443 (15.9)	2503	1012	34.0	40.4
NaAlg	EC:DMC	2650	446 (16.8)	2171	560	21.1	25.8
NaAlg	EC:DMC+FEC	3172	512 (16.1)	2589	1815	57.2	70.1
NaAlg	FEC:DMC	3362	718 (21.3)	2528	1526	45.4	60.3
NaAlg [†]	FEC:DEC	1455	372 (25.6)	1317	1017	69.9	77.3
NaAlg [†]	FEC;DMC	1466	695 (47.4)	955	751	51.2	78.6

[†] Au-removed Si nanowires

^a Charge capacity retention of the 100th cycle relative to the 1st cycle

^b Charge capacity retention of the 100th cycle relative to the 5th cycle

Figure 7.3 shows electrochemical data for film (**3**) with electrolytes (**A**), (**B**), (**C**), and (**E**). Coulombic efficiencies ranged between 95 and 100%. The coulombic efficiencies for electrolytes (**A**), Figure 7.3a.i, and (**B**), Figure 7.3b.i, settled between 95% and 98% after the 10th cycle. Electrolyte (**C**), Figure 7.3c.i, settled around 99% through about 90 cycles at which point the battery performance began to degrade; this battery had the best capacity retention for this series (70.1%) and low first cycle irreversible loss (16.1%). Electrolyte (**E**), Figure 7.3d.i, held steady at 99% though 100 cycles and also had good capacity retention relative to the 5th cycle (60.3%). The voltage profiles show increased over-potential as cycling progresses due primarily to a shift in lithiation to lower potentials. This effect is more pronounced for electrolytes (**A**) and (**B**) in Figures 7.3a.ii and 7.3b.ii, respectively, where the initial lithiation event occurs at

lower and lower potentials as the cycling progresses. The reason behind this is unclear, but since the shift is more pronounced in batteries that show worse retention behavior, it is likely due to kinetic and transport limitations that evolve as the battery cycles longer and increased internal resistances due to SEI growth with continued cycling. The differential capacity plots share similar characteristics, with lithiation peaks between 50 mV and 100 mV and between 200 mV and 250 mV. These potentials correspond to $\text{Li}_{15}\text{Si}_4$ crystallization and a-Si lithiation, respectively.^{3, 5} Delithiation profiles show a plateau (or differential peak) near 500 mV for early cycles and 250 mV for later cycles corresponding to the delithiation potentials of $\text{Li}_{15}\text{Si}_4$ and a-Si, respectively.^{3, 5}

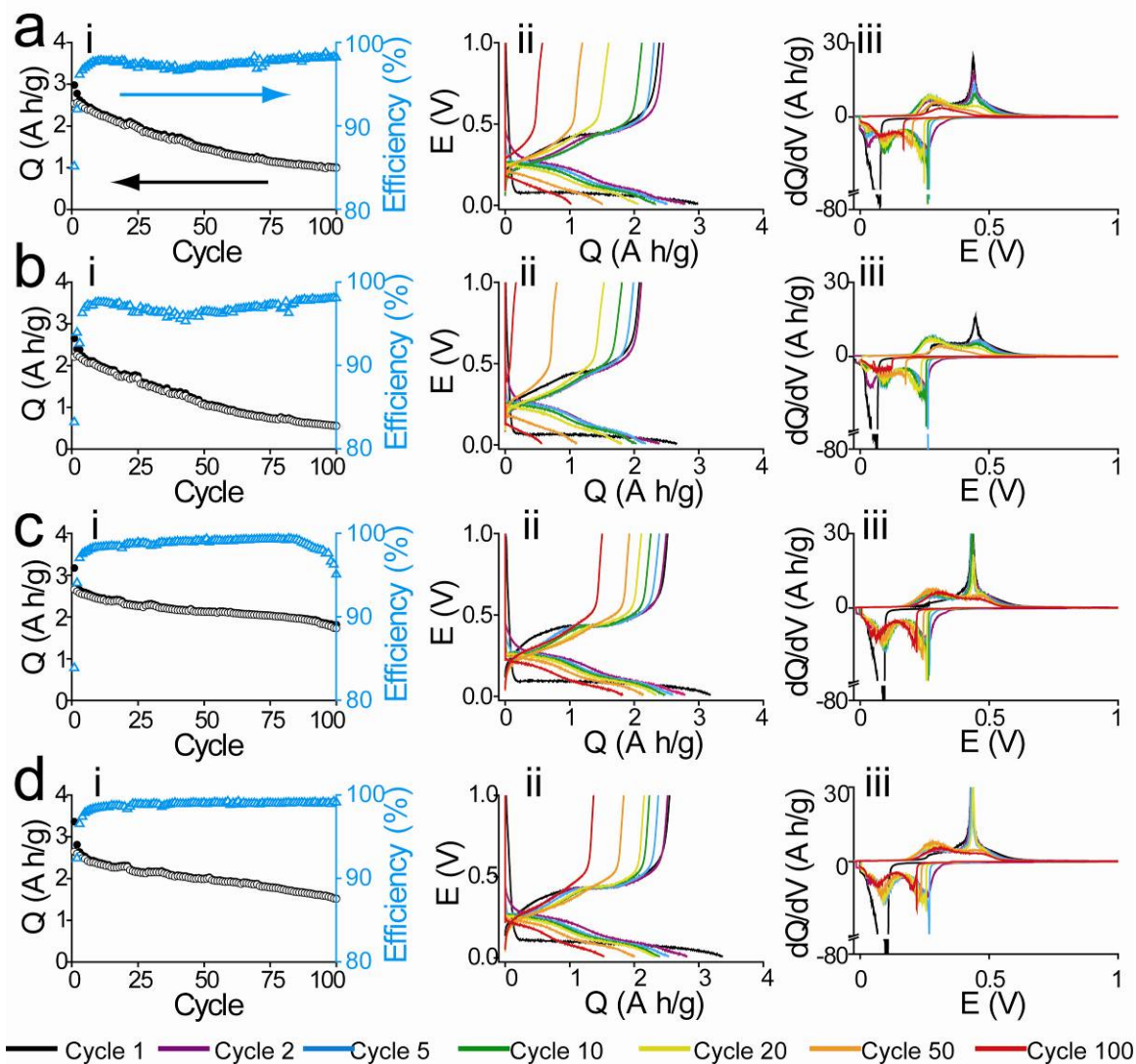


Figure 7.3: (i) Charge and discharge capacities with Coulombic efficiencies, (ii) voltage profiles and (iii) differential capacity plots for Si nanowires cycled using NaAlg binder and electrolyte solution of 1.0 M LiPF₆ in a 1:1 (w:w) solvent mixture of (a) EC:DEC, (b) EC:DMC, (c) EC:DMC + 3% (w/w) FEC, and (d) FEC:DMC at cycles 1, 2, 5, 10, 20, 50, and 100.

Electrochemical data for film (4) with electrolytes (D) and (E) are shown in Figure 7.4. Coulombic efficiencies for these systems were at least 98%, similar to film (3). The voltage profiles show stable over-potentials for electrolyte (D) and a slight

increase for (E). Differential capacity plots show (de)lithiation at similar potentials observed for film (3), (i.e. charge peaks around 100 mV and 250 mV and discharge peaks at 250 mV and 500 mV). While these batteries had much lower first cycle capacities than the rest of the batteries tested—1455 mA h g⁻¹ for electrolyte (D) and 1466 mA h g⁻¹ for (E)—they also exhibited the highest capacity retention after 100 cycles (77.3 and 78.6%, respectively). The reduction in first cycle capacity of film (4) is likely due to SiO₂ on the surface of the nanowires. SiO_x electrodes have been studied³⁷⁻⁴¹ and have capacities of at most 1600 mA h g⁻¹.⁴¹ Furthermore, SiO₂ is electrochemically inactive⁴² with respect to lithium insertion in the potential ranges studied here. The presence of these two species would lower the measured specific capacity of our Si nanowires films. The source of SiO_x is likely from *aqua regia*, the strong oxidizing agent used to remove Au from the tips and surface of the nanowires. A second HF etch after Au-removal step would remove the SiO₂ coating and improve the capacity of these films, but doing so would likely be detrimental to capacity retention. The oxidized nanowire surface plays a key role in realizing improved capacity retention. Li reacts with the oxidized surface of the Si nanowire to form silicates and Li₂O.^{37, 38, 40, 43, 44} This layer is also transparent to Li⁺ transport allowing lithiation of the nanowire core. The Li_ySiO_x is stronger than Si and limits expansion of the Si nanowire core.⁴⁴ Furthermore, SiO_x lithiates to a lesser degree than Si and undergoes more mild expansion by comparison.³⁹ While this limits the extent of lithiation, it in turn improves the cycle life of the battery. This effect is dependent on the oxide thickness⁴⁴ and can be engineered. Furthermore, NaAlg interacts strongly with the polar oxidized Si nanowire surface, and stabilizes cycling behavior. A systematic study varying the oxide thickness of the wires is required to truly optimize the system. Differential capacity data are discussed in greater detail below.

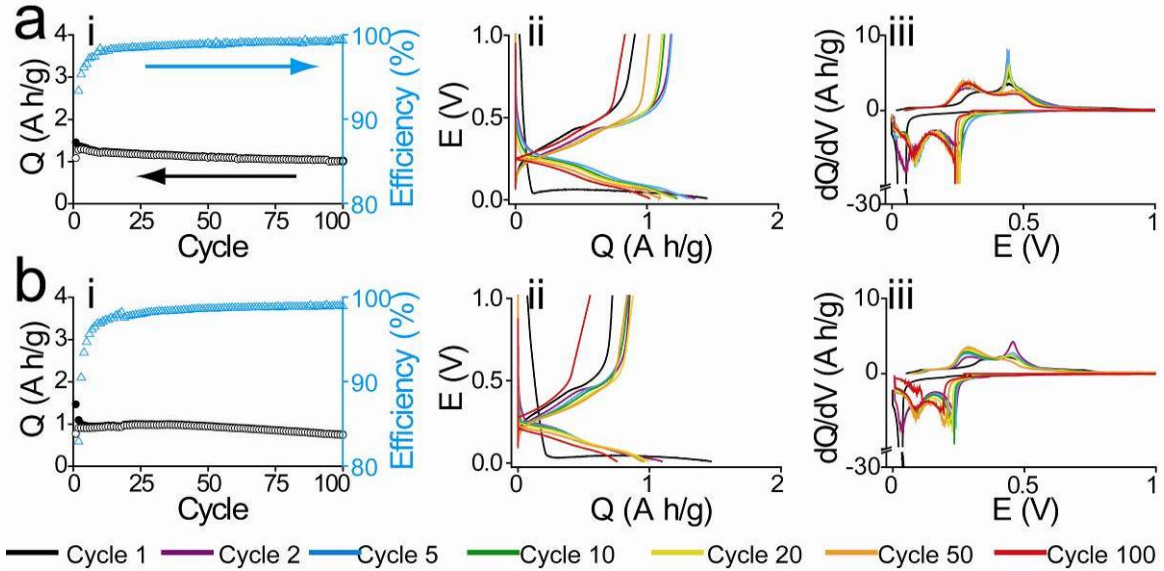


Figure 7.4: (i) Charge and discharge capacities with Coulombic efficiencies, (ii) voltage profiles and (iii) differential capacity plots for Au-removed Si nanowires cycled using NaAlg binder and electrolyte solvent mixtures of (a) FEC:DEC or (b) FEC:DMC at cycles 1, 2, 5, 10, 20, 50 and 100.

Figure 7.5 compares the first cycle voltage profiles and differential capacity plots for all Si nanowire film / electrolyte combinations tested. Over-potentials are independent of electrolyte for any given film and vary slightly depending on whether the wires are as made (average over potential ~ 350 mV) or Au-removed (average over-potential ~ 400 mV). The difference in over-potential is due to the presence of Au, which is present in the Si nanowire films at a weight percent of roughly 19%. Au-removed nanowires have a larger over-potential because crystalline Si lithiates below potentials of 50 mV whereas Au lithiates at a slightly higher potential of 100 mV,^{24, 25} All systems have near identical first cycle lithiation behavior, with a sharp peak appearing at potentials at or below 100 mV when Au is present, corresponding to lithiation of crystalline Si and Au, and below 50 mV when Au is removed, corresponding to lithiation of crystalline Si.^{2, 3, 5} Discharge behavior can be generalized as well based on whether or

not Au is present. Films (1) and (3) show sharp delithiation peaks at 500 mV for all but electrolyte (F). Propylene carbonate is known to damage graphite due to poor SEI formation^{45, 46} and is likely responsible for absence of the sharp delithiation peak. Instead, a broad hump is observed at 300 mV, which is the potential for a-Si delithiation. In contrast, films (2) and (4) show broad peaks that span the potential range from 300 mV to 500 mV when Au is removed. The sharp 500 mV peak is not observed, presumably due to the presence of a SiO_x coating on the nanowires.³⁷⁻⁴⁰

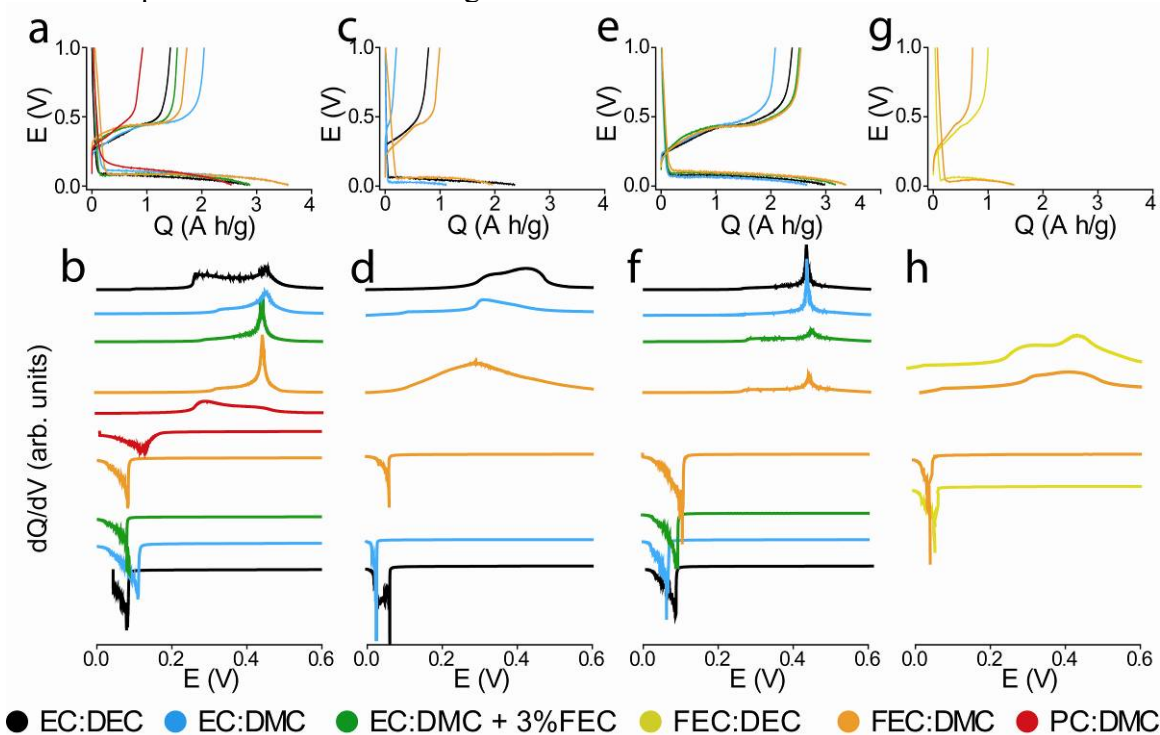
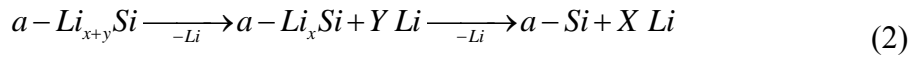


Figure 7.5: (a, c, e, g) Voltage profiles and (b, d, f, h) differential capacity plots for the first cycle of (a, c) as prepared Si nanowires and (b, d) Au-removed Si nanowires using (a-d) PVdF and (e-h) NaAlg as binders and the indicated electrolyte solvent combinations.

Electrochemical data for films (3) and (4) are shown in greater detail in Figures 7.6 and 7.7. Trends in lithiation and delithiation potentials are similar for the two films and independent of electrolyte solvent. Two prominent lithiation peaks are observed at

250 mV (a-Si lithiation) and 100 mV (Li₁₅Si₄ formation). For electrolytes **(A)** and **(B)**, as cycling progresses, these two peaks drift to lower potentials and fade in intensity, merging eventually into a single broad peak at around 150 mV to 200 mV. Electrolytes **(C)** and **(E)** retain strong lithiation peaks throughout the entire cycle test that show only slight drift to lower potentials. FEC is stable in Si systems for up to several hundred cycles⁴⁷ before a drastic decline in performance is observed. The scope of these experiments is not long enough to probe the failure modes of the FEC electrolytes.

Electrolytes **(A)** and **(B)** exhibit similar delithiation trends, shown in Figure 7.6a.i and 7.6b.i, respectively. Early discharge cycles exhibit a sharp peak at 500 mV attributed to delithiation of Li₁₅Si₄.⁴⁸ This peak disappears by cycle 20 as it forms a shoulder on the lower potential peak centered at 300 mV, attributed to delithiation of a-Si.^{22, 48} Electrolytes **(C)** and **(E)** show somewhat contrasting behavior. The sharp Li₁₅Si₄ peak is present at 500 mV, but the a-Si delithiation peak at 300 mV peak is initially absent. As cycling progresses, two broad lithiation peaks are observed, consistent with previous reports of the Si delithiation. These peaks are rationalized as low- and high-potential delithiation of a-Si in two separate single phase regions:



The fade of the sharp peak at 500 mV indicates that the Li₁₅Si₄ phase forms less as cycling progresses. For electrolytes **(A)** and **(B)** This is also seen by the reduction in the Li₁₅Si₄ formation peak at potentials below 100 mV. Electrolytes **(C)** and **(E)** retain sharp Li₁₅Si₄ lithiation peak through 100 cycles and a strong Li₁₅Si₄ delithiation peak through at least 30 cycles. A stable SEI layer is formed that is more transparent to electron and Li⁺ ion flow for FEC-containing versus FEC-free electrolytes and is responsible for the differences in electrochemical behavior.

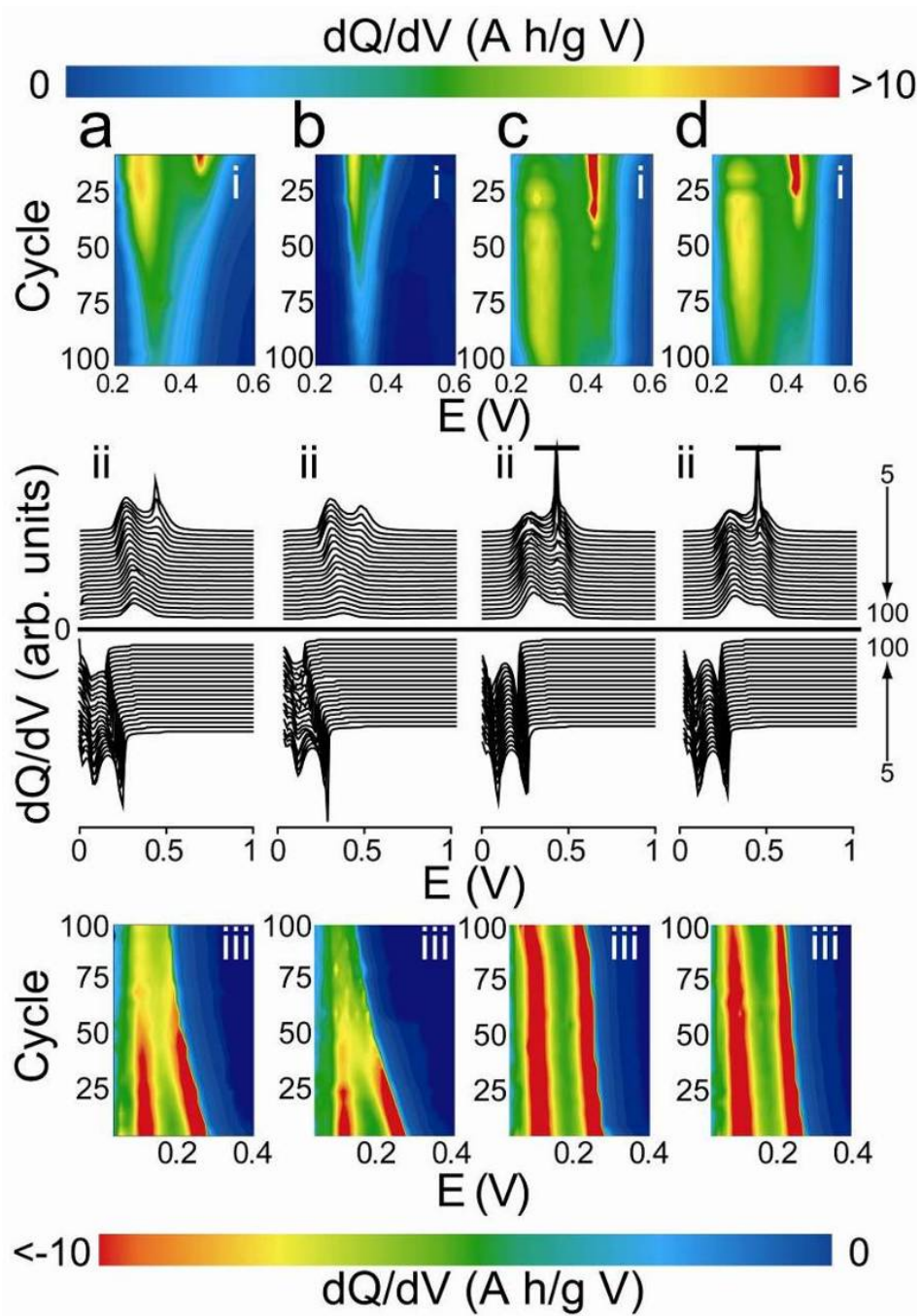


Figure 7.6: Color maps of differential capacity (i) discharge and (iii) charge profiles with (ii) corresponding waterfall plots for Si nanowires cycled using NaAlg binder with electrolyte solvent solutions of (a) EC:DEC, (b) EC:DMC, (c) EC:DMC+FEC, and (d) FEC:DMC.

Figure 7.7 shows a similar set of data for film **(4)** using electrolytes **(D)** and **(E)**. As discussed above, these films show lower initial capacities, but the highest capacity retention out of all batteries tested. The same general lithiation and delithiation trends are observed as for film **(3)** with electrolytes **(D)** and **(E)**; namely, the presence of two lithiation peaks—at 250 mV and 100 mV—that gradually fade with increased cycling, and two delithiation peaks—at 500 mV and 300 mV—that undergo a shift in intensity from the 500 mV peak, which is more intense initially, then fades as the 300 mV peak grows. The obvious difference between these nanowires and those reported above is the absence of Au. Au is known to lithiate to form $\text{Li}_{15}\text{Au}_4$, but with very low ($\sim 100 \text{ mA h g}^{-1}$) reversible capacity.^{24, 25} Au, present in films **(1)** and **(3)** at a mass content of nearly 20%, acts as a significant sink of both electrons and Li^+ ions. As such, these films exhibited poor capacity retention. Au-removal mitigates this irreversible effect, shown here.

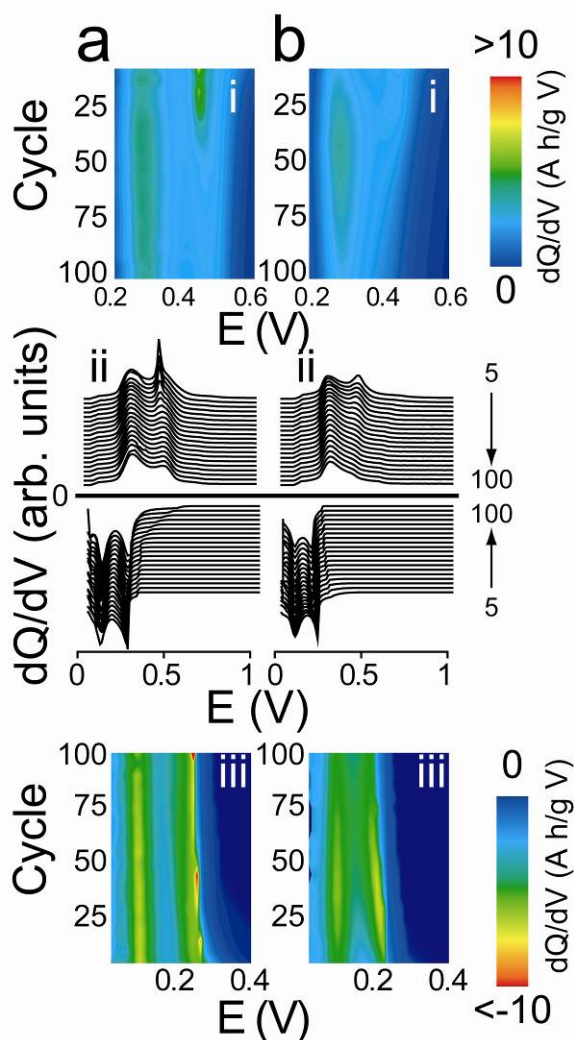


Figure 7.7: Color maps of differential capacity (i) discharge and (iii) charge profiles with (ii) corresponding waterfall plots for Au-removed Si nanowires cycled using NaAlg binder and electrolyte solvent solutions of (a) FEC:DEC or (b) FEC:DMC.

7.3.3 Rate test behavior

Due to superior performance in the tests above, films (3) and (4) were tested at faster rates using electrolytes (A), (B), and (E); results are shown in Figure 7.8. At rates faster than C/20, the batteries registered zero capacity. A similar observation was made for SFLS Si nanowires grown using the trisilane precursor and supported with a free-

standing film of graphene. The poor performance was attributed to the presence of gold (see Chapter 4). Data shown in Figure 7.8b corroborate this claim. Figure 7.8b shows rate test data for batteries cycled using film (4) and electrolytes (D) and (E) at various rates. These two electrolyte systems performed well with capacities of $\sim 1500 \text{ mA h g}^{-1}$ sustained through rates up to C/5 (i.e., through 25 cycles) with electrolyte (E) boasting slightly higher capacities. Further increasing the rate to C/2, C, and 2C resulted in capacitive drop-off of $400\text{--}500 \text{ mA h g}^{-1}$ at each rate change cycle (cycles 26, 31, 36). Electrolyte (E) stored no lithium at a rate of 2C while electrolyte (D) registered capacities of $\sim 400 \text{ mA h g}^{-1}$. These data indicate that the SEI formed using DEC is slightly more stable and has better charge and ion transfer properties than that formed by DMC. When the rate was reduced to C/10 for the final 10 cycles, the capacity returned to the same level as cycles 10-20 (i.e., the first set of cycles at C/10), showing that the film was not damaged by the harsher cycling conditions and the capacity drop at faster cycling rates are due to kinetic limitations rather than film degradation effects. A further point of interest is that cycling at C/20 for the first few cycles yields capacities nearly twice the values reported above (e.g., $\sim 2000 \text{ mA h g}^{-1}$ vs $\sim 1000 \text{ mA h g}^{-1}$) observed above where cycling began at C/10.

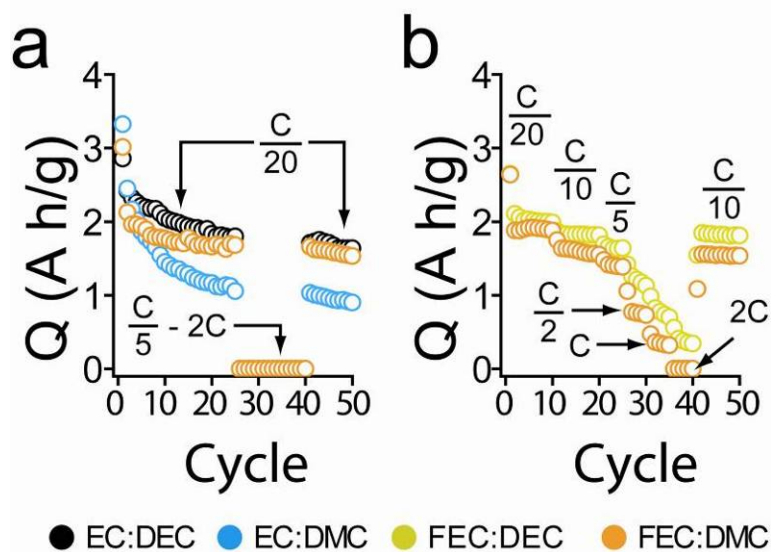


Figure 7.8: Rate test data for batteries using NaAlg binder mixed with (a) as made Si nanowires and (b) Au-removed Si nanowires cycled at various rates with the indicated electrolyte solutions.

Electrochemical data for film (4) with electrolytes (D) and (E) are shown in Figure 7.9. The coulombic efficiencies for these samples were typically between 98% and 100% after the first 10 cycles. For cycles where the rate was changed, the efficiency often dropped to as low as 90% for one cycle, then returned to between 98% and 100%. The over-potentials are consistent for all cycles and both electrolytes, but increase as the cycle rate increases, likely due to kinetic or transport limitations within the film. These limitations arise from poor lithium diffusion in Si and poor electron conductivity of Si. The differential capacity plots show peaks at the expected potentials, following the same general trends observed above.

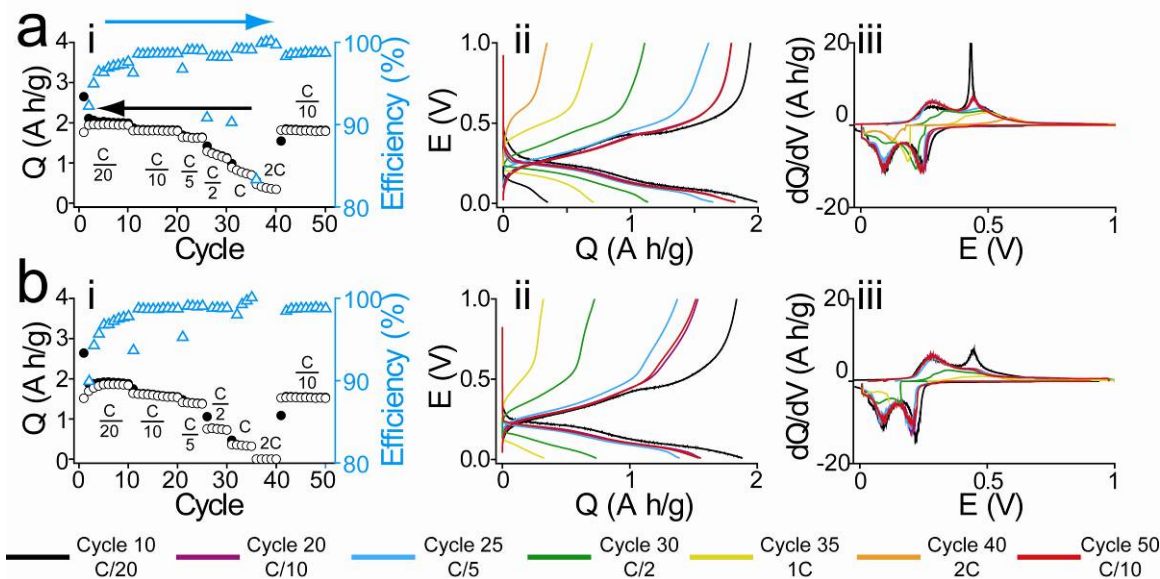


Figure 7.9: (i) Rate test data, (ii) voltage profiles and (iii) corresponding differential capacity plots for Au-removed Si nanowires mixed with NaAlg binder cycled using electrolyte solvent solutions of (a) FEC:DEC and (b) FEC:DMC at cycles 10, 20, 25, 30, 35, 40, and 50.

Detailed electrochemical data are shown in Figure 7.10 for batteries cycled using film (4) and electrolytes (D) and (E). The lithiation and delithiation peaks are characteristic of lithiation of α -Si (250 mV) and formation of $\text{Li}_{15}\text{Si}_4$ (<100 mV) and α -Si delithiation (300 mV and 500 mV). A few slight differences are observed for increased rates for both electrolytes. First, the 250 mV lithiation peak drifts to lower potentials with increased cycle rate. This shift is most pronounced in Figure 7.10a.iii. The peaks shift back to their initial potentials at cycle 41 where the rate is reduced to C/10. Between cycles 25 and 41, however, the 100 mV peak no longer appears, indicating that $\text{Li}_{15}\text{Si}_4$ does not form at the faster cycling rates of C/2, C, and 2C.

Delithiation trends differ from observations made around Figure 7.7. At cycle 21 (rate = C/5) the 300 mV peak begins to shift to higher potentials. This is in contrast to observations presented above where the 500 mV peak decreased in intensity and merged

into the 300 mV peak. This trend is observed for both electrolytes and becomes more pronounced with increasing cycle rate. At cycle 41, when the rate is relaxed to C/10, the peaks resume the positions and intensities as during cycles 11-20 (i.e. the first set of cycles at C/10). While the observed trends point to kinetic limitations in the Si nanowire film, a more detailed study is necessary to determine the true nature of the peak shifts.

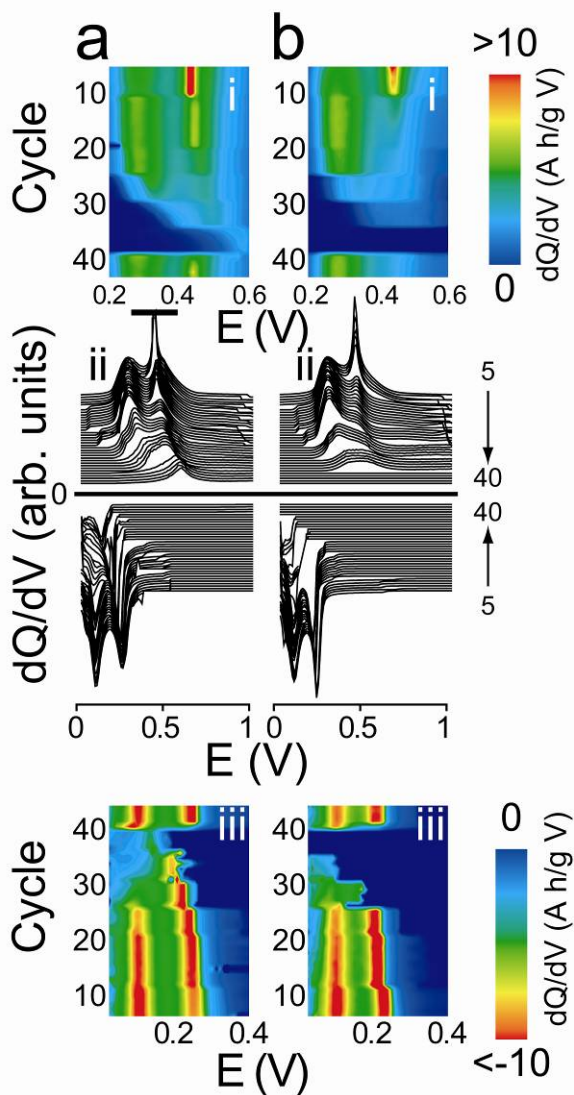


Figure 7.10: Color maps of differential capacity (i) discharge and (iii) charge profiles and (ii) waterfall plots for Au-free nanowires cycled at various rates using NaAlg and electrolyte solvent solutions of (a) FEC:DEC or (b) FEC:DMC.

7.3.4 Electrical behavior

Electrochemical impedance spectroscopy (EIS) measurements were made after 100 galvanostatic charge / discharge cycles at C/10 and are shown in Figure 7.11. Interpretation and translation of the equivalent circuit^{12, 49} shown in Figure 7.11e to the actual battery remains unclear. Nevertheless, each film shows characteristic impedance features (i.e. high-frequency semi-circular resistive component coupled to a low-frequency linear diffusion region). The size of the semi-circle is indicative of the film resistance. The larger the circle, the more resistive the film, and the steepness of the low-frequency region provides information about Li^+ diffusion within the film. Slopes of 45° are associated with semi-infinite diffusion whereas slopes steeper than 45° are characteristic of finite Li^+ diffusion in thin film electrodes. Electrolyte solutions with FEC have lower impedance than electrolytes without FEC, evident by the smaller semi-circle region. The film resistance estimated based on the equivalent shown in Figure 7.11e is tabulated in Table 7.2. The R_{ct} element is typically associated with resistance to charge transfer, which we calculate to be an order of magnitude lower for FEC:DMC compared to EC:DMC; FEC-containing electrolytes form less resistive films.

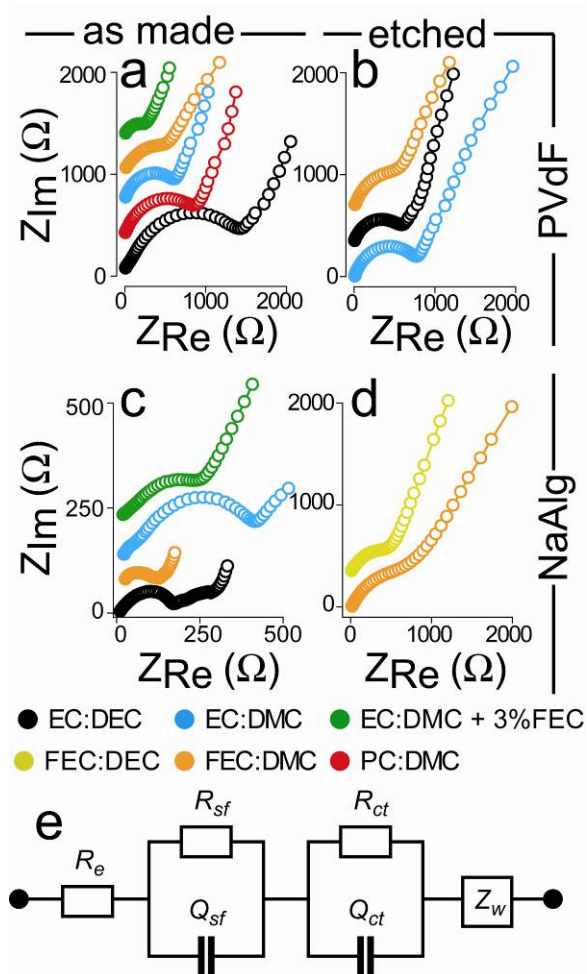


Figure 7.11: Impedance spectroscopy data after 100 cycles for samples of Si nanowires cycled (a, c) as prepared or (b, d) Au-removed mixed with (a, b) PVdF or (c, d) NaAlg as the binder and the electrolyte solvent solution mixtures shown. All spectra are taken in the delithiated state except for (c), which was lithiated. (a, b, d) curves are offset vertically by 350 ohms or (c) 75 ohms. (e) Equivalent circuit used to fit impedance data using resistance elements R_e (electrolyte), R_{sf} (surface), and R_{ct} (charge transfer), constant phase elements Q_{sf} and Q_{ct} and the Warburg diffusion element, Z_w .

Table 7.2: Equivalent circuit parameters for electrochemical impedance spectra.

Film	Electrolyte [‡]	R_{np} (Ω)	Y_o ($\Omega^{-1}s^n$) ^a ·10 ⁶	n^a
NaAlg	EC:DMC	453.0	25.0	0.63
NaAlg	FEC:DMC	46.5	6.4	0.76
NaAlg [†]	FEC:DMC	65.0	2.1	0.95

[†] Au-removed Si nanowires

^a Y_o and n are the two elements used to fit the constant phase element $Q_{dl,2}$

7.4 CONCLUSIONS

We set out to explain why SFLS Si nanowires grown using trisilane performed poorly in an earlier report. Here, we show that Au is responsible for the poor cycling behavior and that capacity retention can be improved through a simple etching process. Silicon nanowires grown by Au seeded SFLS growth were tested as a Li ion battery electrode material using a variety of binder and electrolyte combinations with and without removing Au from the nanowires. PVdF films showed poor cycle behavior, even when annealed according to previous reports. NaAlg films, however, interact with Si surfaces and were found to show marked improvement on the cycle behavior, but capacity retention still suffered. By removing the Au tips, the initial capacity was reduced, but the capacity retention was significantly improved. FEC-based electrolyte systems showed the best cycle behavior. Further investigations are underway to explore the surface chemistry of the Au-removed Si nanowires similar to data shown in Chapter 6. Better understanding of the surface chemistry will provide the means to optimize the engineering of Si nanowires that have high capacity and good cycle retention.

7.5 ACKNOWLEDGEMENTS

Authors contributing to this work include: Timothy D. Bogart, Colin M. Hessel, Kyle Klavetter, C. Buddie Mullins, and Brian A. Korgel. Paul Abel and Yong-Mao Lin

were also very helpful with discussions pertaining to EIS and electrochemistry. We thank TIMCAL for supplying the conductive carbon used in slurry formation.

7.6 REFERENCES

1. Szczech, J. R.; Jin, S. *Energ. Environ. Sci.* **2011**, *4*, 56-72.
2. Li, J.; Dahn, J. R. *J. Electrochem. Soc.* **2007**, *154*, A156-A161.
3. Obrovac, M. N.; Christensen, L. *Electrochem. Solid St.* **2004**, *7*, A93-A96.
4. Reports have shown the existence of the $\text{Li}_{22}\text{Si}_5$ phase which has a maximum theoretical capacity of 4200, but most studies indicate $\text{Li}_{15}\text{Si}_4$ is the high Li content Li-Si alloy that forms at room temperatures.
5. Hatchard, T. D.; Dahn, J. R. *J. Electrochem. Soc.* **2004**, *151*, A838-A842.
6. Yao, Y.; McDowell, M. T.; Ryu, I.; Wu, H.; Liu, N.; Hu, L.; Nix, W. D.; Cui, Y. *Nano Lett.* **2011**, *11*, 2949-2954.
7. Zhang, X.; Shyy, W.; Sastry, A. M. *J. Electrochem. Soc.* **2007**, *154*, A910-A916.
8. Ryu, I.; Choi, J. W.; Cui, Y.; Nix, W. D. *J. Mech. Phys. Solids* **2011**, *59*, 1717-1730.
9. Gao, B.; Sinha, S.; Fleming, L.; Zhou, O. *Adv. Mater.* **2001**, *13*, 816-819.
10. Huang, R.; Fan, X.; Shen, W.; Zhu, J. *App. Phys. Lett.* **2009**, *95*, 133119-3.
11. Cui, L.-F.; Ruffo, R.; Chan, C. K.; Peng, H.; Cui, Y. *Nano Lett.* **2008**, *9*, 491-495.
12. Ruffo, R.; Hong, S. S.; Chan, C. K.; Huggins, R. A.; Cui, Y. *J. Phys. Chem. C* **2009**, *113*, 11390-11398.
13. Kang, K.; Lee, H.-S.; Han, D.-W.; Kim, G.-S.; Lee, D.; Lee, G.; Kang, Y.-M.; Jo, M.-H. *App. Phys. Lett.* **2010**, *96*, 053110-3.
14. Cho, Y. J.; Kim, H. S.; Im, H.; Myung, Y.; Jung, G. B.; Lee, C. W.; Park, J.; Park, M.-H.; Cho, J.; Kang, H. S. *J. Phys. Chem. C* **2011**, *115*, 9451-9457.
15. Foll, H.; Carstensen, J.; Ossei-Wusu, E.; Cojocar, A.; Quiroga-Gonzalez, E.; Neumann, G. *ECS Transactions* **2010**, *33*, 131-141.
16. Chakrapani, V.; Rusli, F.; Filler, M. A.; Kohl, P. A. *J. Phys. Chem. C* **2011**, *115*, 22048-22053.
17. Hu, L.; Wu, H.; Hong, S. S.; Cui, L.; McDonough, J. R.; Bohy, S.; Cui, Y. *Chem. Commun.* **2011**, *47*, 367-369.

18. Chockla, A. M.; Harris, J. T.; Akhavan, V. A.; Bogart, T. D.; Holmberg, V. C.; Steinhagen, C.; Mullins, C. B.; Stevenson, K. J.; Korgel, B. A. *J. Am. Chem. Soc.* **2011**, *133*, 20914-20921.
19. Laïk, B.; Eude, L.; Pereira-Ramos, J.-P.; Cojocaru, C. S.; Pribat, D.; Rouvière, E. *Electrochim. Acta* **2008**, *53*, 5528-5532.
20. Peng, K.; Jie, J.; Zhang, W.; Lee, S.-T. *App. Phys. Lett.* **2008**, *93*, 033105-3.
21. Chan, C. K.; Patel, R. N.; O'Connell, M. J.; Korgel, B. A.; Cui, Y. *ACS Nano* **2010**, *4*, 1443-1450.
22. Chan, C. K.; Ruffo, R.; Hong, S. S.; Huggins, R. A.; Cui, Y. *J. Power Sources* **2009**, *189*, 34-39.
23. Liu, X. H.; Zhang, L. Q.; Zhong, L.; Liu, Y.; Zheng, H.; Wang, J. W.; Cho, J.-H.; Dayeh, S. A.; Picraux, S. T.; Sullivan, J. P.; Mao, S. X.; Ye, Z. Z.; Huang, J. Y. *Nano Lett.* **2011**, *11*, 2251-2258.
24. Yuan, L.; Liu, H. K.; Maarroof, A.; Konstantinov, K.; Liu, J.; Cortie, M. *J. New Mater. Electr. Sys.* **2007**, *10*, 95-99.
25. Taillades, G.; Benjelloun, N.; Sarradin, J.; Ribes, M. *Solid State Ionics* **2002**, *152-153*, 119-124.
26. Heitsch, A. T.; Akhavan, V. A.; Korgel, B. A. *Chem. Mater.* **2011**, *23*, 2697-2699.
27. Etacheri, V.; Haik, O.; Goffer, Y.; Roberts, G. A.; Stefan, I. C.; Fasching, R.; Aurbach, D. *Langmuir* **2012**, *28*, 965-976.
28. Choi, N.-S.; Yew, K. H.; Lee, K. Y.; Sung, M.; Kim, H.; Kim, S.-S. *J. Power Sources* **2006**, *161*, 1254-1259.
29. Nakai, H.; Kubota, T.; Kita, A.; Kawashima, A. *J. Electrochem. Soc.* **2011**, *158*, A798-A801.
30. Kovalenko, I.; Zdyrko, B.; Magasinski, A.; Hertzberg, B.; Milicev, Z.; Burtovyy, R.; Luzinov, I.; Yushin, G. *Science* **2011**, *334*, 75-79.
31. Saunders, A. E.; Sigman, M. B.; Korgel, B. A. *J. Phys. Chem. B* **2003**, *108*, 193-199.
32. Heitsch, A. T.; Hessel, C. M.; Akhavan, V. A.; Korgel, B. A. *Nano Lett.* **2009**, *9*, 3042-3047.
33. Hessel, C. M.; Heitsch, A. T.; Korgel, B. A. *Nano Lett.* **2009**, *10*, 176-180.
34. Li, J.; Christensen, L.; Obrovac, M. N.; Hewitt, K. C.; Dahn, J. R. *J. Electrochem. Soc.* **2008**, *155*, A234-A238.
35. Bridel, J. S.; Azaïs, T.; Morcrette, M.; Tarascon, J. M.; Larcher, D. *Chem. Mater.* **2009**, *22*, 1229-1241.

36. Mazouzi, D.; Lestriez, B.; Roue, L.; Guyomard, D. *Electrochem. Solid St.* **2009**, *12*, A215-A218.
37. Miyachi, M.; Yamamoto, H.; Kawai, H.; Ohta, T.; Shirakata, M. *J. Electrochem. Soc.* **2005**, *152*, A2089-A2091.
38. Sun, Q.; Zhang, B.; Fu, Z.-W. *Appl. Surf. Sci.* **2008**, *254*, 3774-3779.
39. Yang, J.; Takeda, Y.; Imanishi, N.; Capiglia, C.; Xie, J. Y.; Yamamoto, O. *Solid State Ionics* **2002**, *152*, 125-129.
40. Nagao, Y.; Sakaguchi, H.; Honda, H.; Fukunaga, T.; Esaka, T.. *Electrochem. Soc.* **2004**, *151*, A1572-A1575.
41. Hu, Y.-S.; Demir-Cakan, R.; Titirici, M.-M.; Müller, J.-O.; Schlögl, R.; Antonietti, M.; Maier, J. *Angew. Chem. Int. Ed.* **2008**, *47*, 1645-1649.
42. Saint, J.; Morcrette, M.; Larcher, D.; Laffont, L.; Beattie, S.; Pérès, J. P.; Talaga, D.; Couzi, M.; Tarascon, J. M. *Adv. Funct. Mater.* **2007**, *17*, 1765-1774.
43. Netz, A.; Huggins, R. A.; Weppner, W. *J. Power Sources* **2003**, *119-121*, 95-100.
44. McDowell, M. T.; Lee, S. W.; Ryu, I.; Wu, H.; Nix, W. D.; Choi, J. W.; Cui, Y. *Nano Lett.* **2011**, *11*, 4018-4025.
45. Aurbach, D.; Ein-Eli, Y. *J. Electrochem. Soc.* **1995**, *142*, 1746-1752.
46. Aurbach, D.; Gofer, Y.; Langzam, J. *J. Electrochem. Soc.* **1989**, *136*, 3198-3205.
47. Coowar, F.; Abdelsalam, M. E.; Lain, M. *U.K. Patent No. 2481124*, **Dec 14, 2011**.
48. Obrovac, M. N.; Krause, L. *J. Electrochem. Soc.* **2007**, *154*, A103-A108.
49. Zhao, J.; Wang, L.; He, X.; Wan, C.; Jiang, C. *Int. J. Electrochem. Sci.* **2010**, *5*, 478-488.

Chapter 8: In-situ Sn-seeded Si nanowires in Li Ion Batteries

8.1 INTRODUCTION

Silicon (Si) nanostructures have received great attention since the turn of the century as a potential replacement for graphite as the working anode material in Li ion batteries,¹ primarily due to the fact that Si (3579 mA h g^{-1})²⁻⁴ exhibits a ten-fold improvement on the maximum theoretical capacity of graphite (372 mA h g^{-1}). Accompanying this enormous Li storage capacity comes a great penalty; the Si lattice expands by up to 300% in order to form the $\text{Li}_{15}\text{Si}_4$ phase, which results in electrode pulverization leading to battery failure. Silicon nanostructures mitigate pulverization effects associated with Li cycling⁵⁻⁷ and are a particularly attractive class of materials. Furthermore, Si offers the greatest power density of known Li insertion materials, is an inexpensive and abundant element, and has a low working potential relative to the Li/Li^+ reduction potential.

Chapter 2 showed good cycle behavior and high capacities by annealing a free-standing nanowire fabric composed of Si nanowires grown using the supercritical fluid-liquid-solid (SFLS) method with monophenylsilane as the Si source and gold (Au) catalyst seeds without conventional addition of conductive carbon or binder.⁸ In Chapter 4 we also reported graphene-supported SFLS Si nanowires synthesized using trisilane as a freestanding lithium insertion. These membranes exhibit poor cycle performance, which we later showed (in Chapter 7) could be improved by etching Au from the nanowire product. Trisilane-grown SFLS wires can be produced at an astounding rate of 6 to 8 g hr^{-1} using lab scale equipment⁹ compared to conventional CVD processes, which produce aerial mass loadings on the order of $\mu\text{g cm}^{-1}$.¹⁰⁻¹³ In an effort to avoid the use of Au altogether yet exploit the high throughput SFLS process, we turn to tin (Sn) as a seed

material. We simplify the SFLS process by simultaneous injection of trisilane with a molecular Sn precursor–bis[bis(trimethylsilyl)amino] tin (II), or SnHMDS₂–instead of Sn nanocrystals, which are difficult to synthesize and oxidize easily.¹⁴⁻¹⁶ This injection mixture forms Sn nanocrystals in-situ which seeds the growth of Si nanowires.

Sn has been used recently in the CVD growth of Si nanowires¹⁷ and is an attractive seed material due to its electrochemical behavior; Sn forms an alloy with Li (Li₂₂Sn₅) with a capacity (993 mA h g⁻¹),¹⁸⁻²² nearly three times that of graphite, and has been independently explored as a graphite replacement,²² though Sn also exhibits massive volumetric expansion upon lithiation of ~260%.²³ In this study, we evaluate Li storage performance of in-situ Sn seeded Si nanowires grown using trisilane and SnHMDS as the Si and Sn sources, respectively. In accordance with previous results, we test heat-treated polyvinylidene fluoride (PVdF) and sodium alginate (NaAlg) as binders and fluoroethylene carbonate (FEC) as an electrolyte additive in various standard electrolyte solutions.²⁴⁻²⁸

8.2 EXPERIMENTAL SECTION

8.2.1 Materials

All reagents and solvents were used as received and without further purification. Toluene (anhydrous, 99.8%), ethanol (99.9%), lithium hexafluorophosphate (LiPF₆, ≥99.99%), poly (vinylidene fluoride) (PVdF, average MW ~534,000 by GPC), alginic acid sodium salt (NaAlg, Lot# MKBG5630V), 1-methyl 2-pyrrolidinone (NMP, 99.5%), chloroform (99.8%) and bis[bis(trimethylsilyl)amino] tin(II) (SnHMDS₂, Lot# 10396PKV) were purchased from Sigma-Aldrich and trisilane (Si₃H₈, 100%) was obtained from Voltaix. Conductive carbon super C65 was supplied by TIMCAL. Fluoroethylene carbonate (>98%) was obtained from TCI America. Electrolytes were

either purchased—as 1.0 M solutions of LiPF_6 in a 1:1 w/w mixture of ethylcarbonate (EC) : diethyl carbonate (DEC) (Novolyte) or 1.0M LiPF_6 in a 1:1 mixture of EC : dimethyl carbonate (DMC) (EMD chemicals)—or prepared in one of three ways: LiPF_6 was either dissolved at a concentration of 1.0 M in 1:1 w/w mixture of (1) FEC:DEC or (2) FEC:DMC or (3) FEC was added at a 3% w/w to the EC:DMC solution purchased from EMD chemicals. For battery assembly, Celgard 2400 membranes (25 μm) were used as separators, purchased from Celgard, and Li metal foil (1.5 mm 99.9%), used as the counter electrode, from Alfa Aesar.

8.2.2 Silicon nanowire synthesis

Si nanowires were synthesized in a nitrogen filled glovebox using standard air-free procedures. A modified supercritical fluid-liquid-solid (SFLS) method⁹ was developed into a new in-situ tin-seeded growth process using trisilane and bis[bis(trimethylsilyl)amino] tin (II) $[(\text{TMS}_2\text{N})_2\text{Sn}]$ as the Si and Sn sources, respectively, in supercritical toluene. A reactant solution of trisilane and SnHMDS in toluene is first made. Trisilane is added (0.25 mL) to a mixture of 116 μL SnHMDS dispersed in 0.7 mL toluene to give a 20:1 Si:Sn mole ratio. Nanowire growth is carried out in a flow-through high pressure sealed titanium reactor at 450°C. Before injecting the reactant solution, the reactor is heated to 450°C then pressurized with toluene to 6.9 MPa with a closed effluent line. The reactant solution is injected over the course of 1 min with the reactor effluent remaining closed. The reactor pressure increases to 13.1 MPa during the course of the reaction. Immediately after the 1 minute injection the reactant solution, the reactor inlet is closed and the sealed reactor is removed from the heating block and allowed to cool to room temperature. After the reactor has cooled, it is removed from the glovebox and opened. The nanowires are extracted from the reactor with ~20 mL

additional toluene. The crude reaction product is centrifuged at 8000 rpm for 5 minutes and the supernatant is discarded. The nanowires are then washed two more times by redispersion in 20 mL of toluene followed by centrifugation. The nanowires were dried down via rotovap to determine an accurate weight and stored in a vial under ambient conditions prior to use. A typical reaction yields approximately 100 mg of product.

8.2.3 Anode preparation battery assembly

Slurries were prepared by combining Si nanowires with either PVdF or NaAlg and conductive carbon and in a 70:20:10 w/w ratio. Two separate slurries were prepared by dispersing the nanowires (typically 80-100 mg) in 2 mL ethanol and bath sonication for 1 hour. Meanwhile, PVdF and conductive carbon were suspended in 1 mL NMP or NaAlg and conductive carbon in 1 mL DI H₂O and bath sonicated for 1 hour. The Si nanowires were mixed with the appropriate binder solutions. Slurries generally required a few additional mL of EtOH or DI H₂O to form a uniform suspension. Slurries were wand sonicated for 30 minutes and reduced by rotovap yielding viscous dispersions, then cast onto Cu foil using a 200 μ m film applicator and vacuum dried overnight at 100°C.

Batteries were assembled in an argon-filled glovebox. Si nanowire anodes were hole-punched from the Cu foil supported slurry film. The electrolyte was a 1.0 M solution of LiPF₆ in a 1:1 w/w mixture of either **(A)** EC:DEC, **(B)** EC:DMC, **(C)** EC:DMC + 3% w/w FEC, **(D)** FEC:DEC, or **(E)** FEC:DMC. A few drops of electrolyte were deposited over the Li foil counter electrode and on top of a Celgard 2400 separator membrane (25 μ m thick, Celgard) before the adding the Si anode and crimping the completed battery.

AC electrochemical impedance spectroscopy (EIS) measurements were obtained using an Electrochemical Analyzer (CH Instruments, model CHI 604D) over a frequency

range of 0.01 to 100,000 Hz. Galvanostatic measurements were made using an Arbin BT-2143 test unit sweeping between 2 V and 10 mV vs Li/Li⁺ at various rates. Capacities are reported based on the active material only.

8.2.4 Material characterization

Scanning electron microscopy (SEM) images were acquired using a Zeiss Supra 40 SEM with an in-lens arrangement, a working voltage of 5 keV and a working distance of 5 mm. Transmission electron microscopy (TEM) samples were prepared by drop-casting from chloroform dispersions onto 200 mesh lacey-carbon copper TEM grids (Electron Microscopy Sciences). Images were digitally acquired using either a FEI Tecnai Spirit BioTwin TEM operated at 80 kV or a field emission JEOL 2010F TEM operated at 200 kV. Energy-dispersive X-ray spectroscopy (EDS) data were acquired on the JEOL 2010F TEM with its Oxford Inca EDS detector.

X-ray diffraction (XRD) was performed with a Rigaku R-Axis Spider Diffractometer with Image plate detector with Cu k_α ($\lambda = 1.5418 \text{ \AA}$) radiation operated at 40 kV and 40 mA. Samples were measured on a 0.5 mm nylon loop, scanning for 10 min with 1° per second sample rotation under ambient conditions. The diffraction data were integrated from $2\theta = 20$ to 80. Background scattering from the nylon loop was subtracted.

8.3 RESULTS AND DISCUSSION

8.3.1 In-situ Sn-seeded Si nanowires

In-situ Sn-seeded Silicon nanowires are grown via the SFLS growth mechanism,²⁹ shown in Figure 8.1. Sn is a low melting point metal that forms a eutectic with Si at 232°C making it a good seed candidate for SFLS Si nanowire synthesis. Unlike conventional SFLS syntheses,^{9, 29, 30} however, Sn nanocrystals are not injected into the reactor pre-synthesized. Instead, a molecular Sn source–bis[bis(trimethylsilyl)amino] tin

(II), or $(\text{TMS}_2\text{N})_2\text{Sn}$ —is injected simultaneously with trisilane to form Sn nanocrystals in-situ just prior to Si nanowire formation.

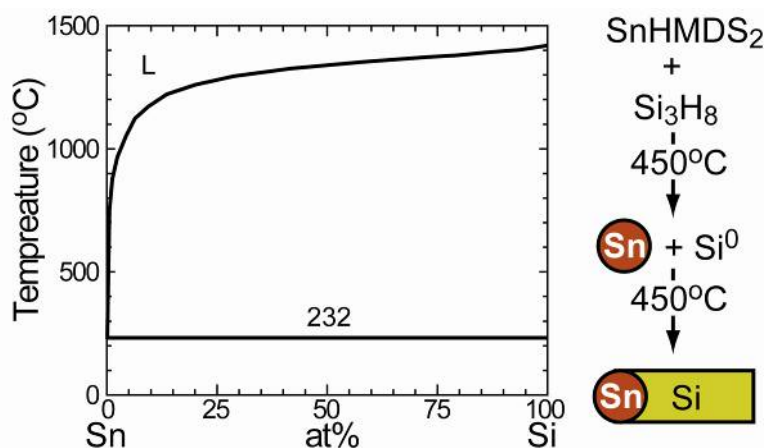


Figure 8.1: Binary Si–Sn phase diagram and in-situ Sn-seeded Si nanowire growth mechanism.

In-situ Sn-seeded Silicon nanowires grown via the SFLS growth mechanism are shown in Figure 8.2. Due to the extreme reactivity of trisilane, a low Si:Sn mole ratio is required to realize the growth of nanowires.^{9, 31, 32} For wires tested in batteries, a Si:Sn ratio of 20:1 was used, though wires were successfully synthesized at a ratio of 40:1 as well (see Figure F1 in Appendix F). HRTEM images are shown for a Si nanowire with the Sn tip in Figure 8.2d with magnified images of the highlighted regions shown in Figure 8.2e—showing the Sn tip—and Figure 8.2f—showing the wire with accompanying FFT pattern. Wires were found to grow in the [211] direction. The most common growth directions for SFLS grown Si nanostructures are [110], and [111] directions.^{9, 30, 31, 33, 34} EDS spectra were taken of the Sn tip (Figure 8.2g.i) and the Si wire (Figure 8.2g.ii) confirming composition and the SFLS growth mechanism. XRD was also done to confirm crystallinity (Figure 8.2h). The diffraction pattern shows single crystal cubic Si

nanowires mixed with tetragonal β -Sn. These results illustrate the successfully in-situ seeding of Si nanowires with Sn nanocrystals via the SFLS mechanism; Sn nanocrystals form in solution prior to super-saturation with Si and subsequent nanowire growth.

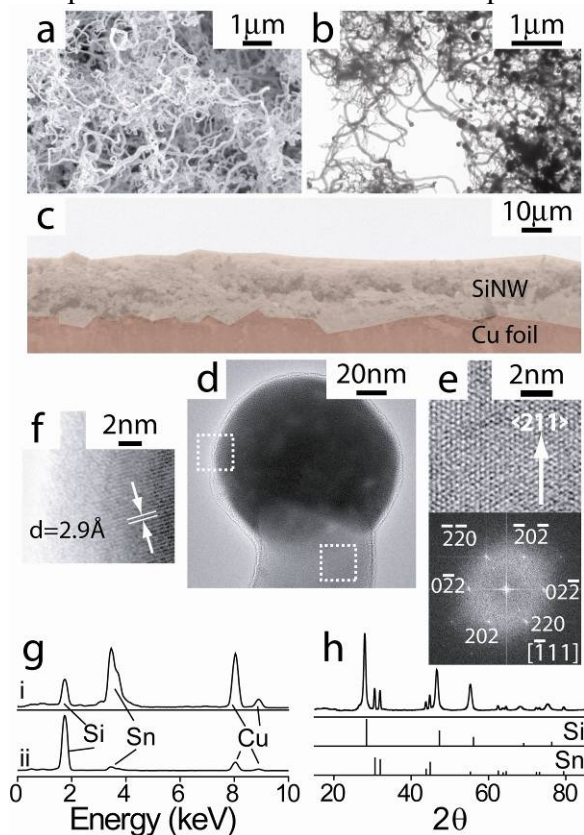


Figure 8.2: (a) SEM and (b) TEM images of in-situ Sn-seeded Si nanowires. (c) Cross-sectional SEM image of a film of a Si nanowires mixed with PVdF. (d) HRTEM of a wire and seed (e) showing nanowire growth in the $\langle 211 \rangle$ direction from (f) a Sn seed with a d-spacing of 2.9 \AA corresponding to the (200) plane. (g) EDS spectra for the tip (i) and wire (ii) and (h) XRD (JCPDS: Si, 00-027-1402; β -Sn, 00-004-0673) confirm the material composition and SFLS growth mechanism.

The synthesis parameter space is currently being explored to improve the nanowire morphology. In contrast to pre-synthesized metal seed materials—Au for example, which produces high quality, single crystal, defect free Si nanowires⁹—using the

molecular $(\text{TMS}_2\text{N})_2\text{Sn}$ source produces kinked and tortuous wires. In this synthesis method, there are no ligands in the reaction mixture that would serve to cap the nanocrystals and control size as Sn nucleates to form the tip. Without capping agents on the surfaces of the wires, they are free to aggregate and form large particles, as shown in Figure 8.2c. Adding capping agents such as poly-(vinyl pyrrolidone), or poly(2-ethyl-2-oxazoline), which have been shown to stabilize colloiddally grown Sn nanocrystals,^{14, 16} could help stabilize the particles as they form in-situ which would produce longer, thinner Si nanowires. The Si:Sn ratio was increased to 400:1 to try to grow longer Si nanowires, but Si_3H_8 decomposes too rapidly and homogeneously nucleates to form a-Si particles (Figure F1).

8.3.2 Extended cycle life behavior

Sn-seeded Si nanowires were tested galvanostatically using one of three binder systems and one of five electrolyte systems to determine the optimal set of materials. The binder systems were either **(1)** polyvinylidene fluoride (PVdF), **(2)** PVdF with a subsequent 12 hour anneal at 300°C under an inert nitrogen stream, or **(3)** sodium alginate (NaAlg). Electrolyte solutions consisted of 1.0M LiPF_6 dissolved in a 1:1 w/w mixture of **(A)** EC:DEC, **(B)** EC:DMC, **(C)** EC:DMC + 3% w/w FEC (hereafter referred to as EC:DMC+FEC), **(D)** FEC:DEC, and **(E)** FEC:DMC. Batteries were cycled galvanostatically for 100 cycles at a rate of $C/10$, where C is the current density required to fully lithiate or delithiated the electrode in 1 hour ($C = 3579 \text{ mA h g}^{-1}$ for Si).²⁻⁴ Capacity and retention data for films **(1)**–**(3)** are shown in Figure 8.3. Capacity retention data were calculated relative to the 5th cycle charge capacity. Table 8.1 summarizes the cycle data: first cycle charge capacity, irreversible first cycle capacity loss, and percent capacity retention of cycle 100 relative to cycles 1 and 5.

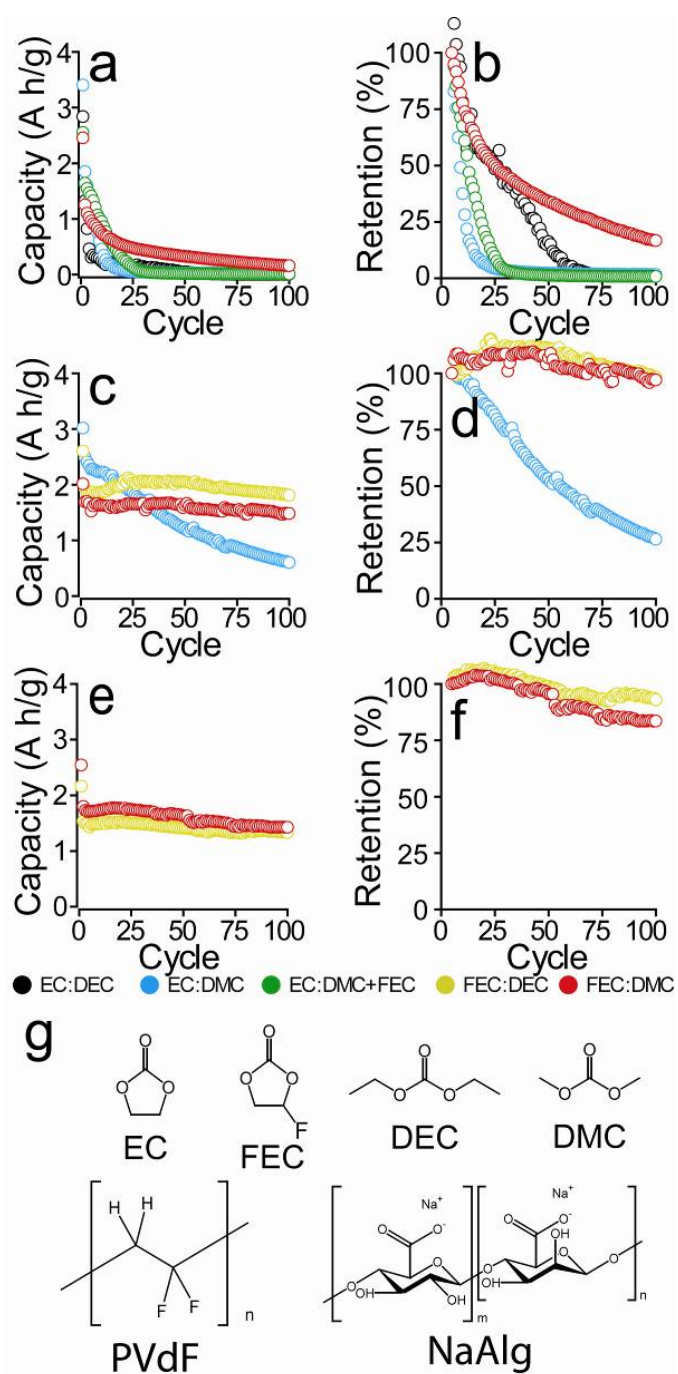


Figure 8.3: (a, c, e) Charge capacity and (b, d, f) capacity retention data for Sn-seeded Si nanowires (a, b) mixed with PVdF, (c, d) mixed with PVdF then annealed at 300°C under nitrogen for 12 hours, and (e, f) mixed with NaAlg. Capacity retention is relative to the 5th cycle charge capacity. (g) Molecular representations of the electrolytes and binders used.

PVdF films performed poorly with capacity of less than 2% after 100 cycles for electrolytes **(A)**, **(B)**, and **(C)**, and 16.7% for **(E)**. These data clearly indicate two points: (1) PVdF is not a good binder system without processing (heat treatment, for example);²⁶ (2) FEC-containing electrolytes outperform FEC-free electrolytes. This latter point has been reported for Si particles^{24, 25, 27} and we recently observed this for Au seeded and Au removed Si nanowires as well (see Chapter 7). Film **(2)** was made by annealing film **(1)** at 300°C for 12 hours under nitrogen flow—in accordance with previous reports²⁶—and provides an enormous increase in battery performance. This is in contrast to observations made using the same Au seeded Si nanowires mentioned above where we did not see improvement in cycle behavior for an annealed film (Chapter 7). By annealing the PVdF film and focusing on FEC containing electrolytes, we were able to improve capacity retention drastically. Electrolyte **(B)** was tested for this film to compare against the unannealed film. Film **(2)** batteries cycled with electrolyte **(B)** showed capacity retention of 26.3%, a 10% increase over the best performing battery from film **(1)**. Electrolytes **(D)** and **(E)** perform the best with capacity retention values of 98.3% and 97.1%, respectively. First cycle capacities for the annealed films were in the same range (i.e. 2000–3000 mA h g⁻¹) as the unannealed film. There was, however, a marked reduction in the first cycle irreversible capacity loss. Whereas unannealed films had first cycle losses between 35.7% and 53.3%, the losses for annealed PVdF films were much lower, ranging between 16.0% and 25.7%. Heat treatment of PVdF improves the cycle behavior as it generates an even polymer / conductive carbon distribution around the active Si matrix.²⁶ While this has been reported for Si particles, we did not observe this behavior for Au seeded Si nanowires. The wires produced here are shorter and are therefore capable of packing more densely, facilitating PVdF / conductive carbon redistribution process during the anneal.

NaAlg—recently shown to improve cyclability of Si particles²⁸—was tested with in-situ seeded Si nanowires in parallel with annealed PVdF films. NaAlg is ecologically friendly (produced by brown algae) and does not require a lengthy high-temperature anneal to produce good results. Film (3) was tested using electrolytes (D) and (E) exhibiting first cycle capacities of 2161 mA h g⁻¹ and 2542 mA h g⁻¹, respectively with first cycle losses around 29% for both electrolytes. Capacity retention of these films was also high, with values of 93% and 83.5%, respectively. Our previous report of Au removed Si nanowires cycled with the NaAlg binder had the highest capacity retentions in that study and is attributed to the self-healing process that takes place from hydrogen bonds between sugar-like moieties in the binder (e.g., carboxymethylcellulose–CMC, NaAlg, etc.)^{28, 35, 36} and the partially oxidized Si surface that break and reform as the electrode material expands and contracts during lithium insertion and removal (Chapter 7).

Table 8.1: Summary of first cycle capacity and retention in various battery formulations.

Binder	Electrolyte	Capacity (mA h g ⁻¹)				Retention (%)	
		Cycle 1	1 st cycle loss (%)	Cycle 5	Cycle 100	Q _{ret1} ^a	Q _{ret5} ^b
PVdF	EC:DEC	2838	1514 (53.3)	310	3	0.1	1.0
PVdF	EC:DMC	3406	1558 (45.7)	1222	20	0.6	1.6
PVdF	EC:DMC+FEC	2552	910 (35.7)	1410	11	0.4	0.8
PVdF	FEC:DMC	2457	1205 (49.0)	961	161	6.5	16.7
PVdF [†]	EC:DMC	3016	524 (17.4)	2278	600	19.9	26.3
PVdF [†]	FEC:DEC	2604	669 (25.7)	1843	1811	69.5	98.3
PVdF [†]	FEC:DMC	2014	322 (16.0)	1527	1483	73.6	97.1
NaAlg	FEC:DEC	2161	624 (28.9)	1427	1327	61.4	93.0
NaAlg	FEC:DMC	2542	745 (29.3)	1707	1426	56.1	83.5

[†] PVdF film annealed for 12 hours at 300°C under a nitrogen atmosphere

^a Charge capacity retention of the 100th cycle relative to the 1st cycle

^b Charge capacity retention of the 100th cycle relative to the 5th cycle

Analysis beyond this point focuses on films (2) and (3) with film (1) data relegated to Appendix F in Figure F2. Charge and discharge capacities and corresponding

coulombic efficiency curves are shown in Figure 8.4 for films (2) and (3) cycled with various electrolytes. All electrolyte / binder combinations had coulombic efficiencies of at least 98%—except for film (2) cycled with electrolyte (B), which had a coulombic efficiency of at least 95%. Voltage profiles and differential capacity curves are also shown with similar lithiation and delithiation features for all binder / electrolyte combinations. Namely, two plateaus (or peaks in the differential curves) are observed around 250 mV and below 100 mV during charge cycles and at 300 mV and 500 mV during discharge cycles. These values correspond to the lithiation of a-Si (250 mV) and formation of $\text{Li}_{15}\text{Si}_4$ (below 100 mV).^{3, 37} As cycling progresses, these peaks drift to slightly lower potentials, due to increased internal resistance within the battery (we show impedance measurements below to substantiate this statement) that may be due SEI growth over time, or gradual pulverization of the active material. Delithiation profiles show plateaus (or differential peaks) centered around 500 mV and 250 mV corresponding to the delithiation potentials of $\text{Li}_{15}\text{Si}_4$ and a-Si, respectively.^{3, 37} From these data, it is difficult to discern directly whether or not Sn is storing lithium and contributing to capacitive behavior of the battery. Sn has a theoretical capacity of 992 mA h g^{-1} (corresponding to the $\text{Li}_{22}\text{Sn}_5$ alloy),¹⁸⁻²⁰ and Li insertion into and removal from Sn occurs at 400 mV and 500 mV, respectively.^{19, 20} The Sn signal would not be as strong as Si as Sn is less present in the film and Si has higher Li storage capacity, thus peaks associated with Si are more intense. As such, Sn lithiation and delithiation peaks in the differential capacity plots are convoluted in with the Si peaks. However, we present ex-situ XRD evidence below that suggests lithiation of Sn. Surface characterization experiments of cycled films study the films in greater depth are ongoing (similar to Chapter 6).

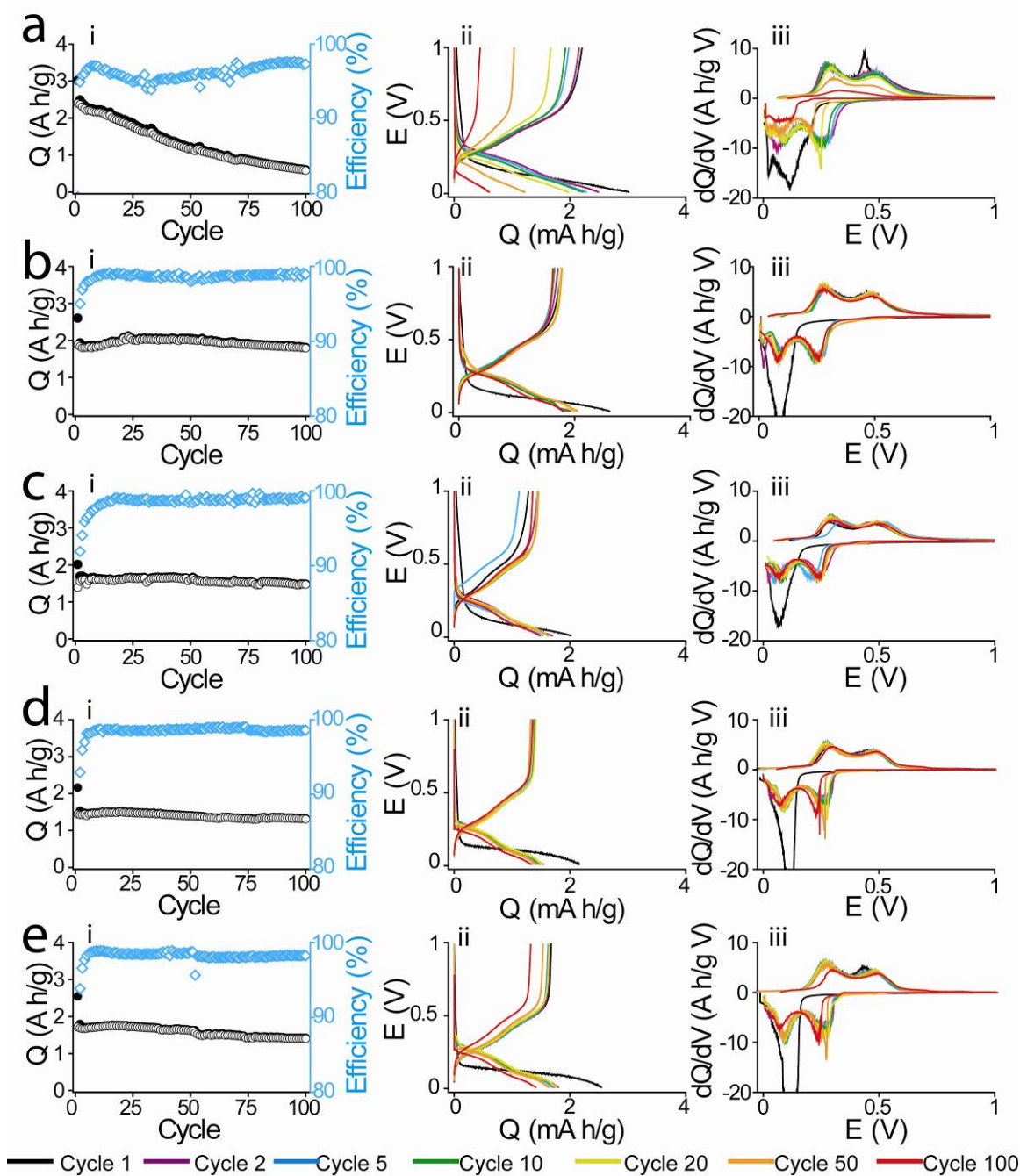


Figure 8.4: (a.i – e.i) Cycle data, (a.ii – e.ii) voltage profiles, (a.iii – e.iii), and corresponding differential capacity plots for Sn-seeded Si nanowires tested galvanostatically mixed with (a-c) PVdF and annealed or (d, e) NaAlg as the binder and an electrolyte solution solvent mixtures of (a) EC:DMC, (b, d) FEC:DEC or (c, e) FEC:DMC.

First cycle charge and discharge voltage profiles and corresponding differential capacity curves are shown in Figure 8.5 for films **(2)** and **(3)**. The over-potentials are nearly the same for both electrolytes. Comparison with previous results for Au seeded Si nanowires (Chapter 7) shows small differences in the voltage profiles and differential peaks. Au seeded and Au removed Si nanowires exhibit strong lithiation peaks at 100 mV and 50 mV, respectively. Lithiation of Au occurs at near identical potentials to Si and the contributions of each are difficult to deconvolute. Here, we observe more broad lithiation peaks centered between 100 mV and 150 mV. While discrete peaks are not observed at higher potentials, as observed for the lithiation of Sn powder, Sn coated carbonaceous anodes show gradual sloping lithiation curve over a range of potentials below 500 mV,^{20, 38, 39} consistent with the observations made here. Electrolytes **(D)** and **(E)** behave the same in both binder systems. There is a strong lithiation peak at 100 mV and two broad delithiation humps at 300 mV and 500 mV. Annealed PVdF films using electrolyte **(B)** have a stronger delithiation peak at 500 mV. This peak is stronger for this battery because more Li was able to be removed—specifically from $\text{Li}_{15}\text{Si}_4$ —during discharge. This also manifests itself in the low irreversible loss (17.4%) shown in Table 8.1 (second lowest of all batteries tested). FEC-containing electrolytes outperform this battery over the course of the 100-cycle test because the SEI layer is more stable.

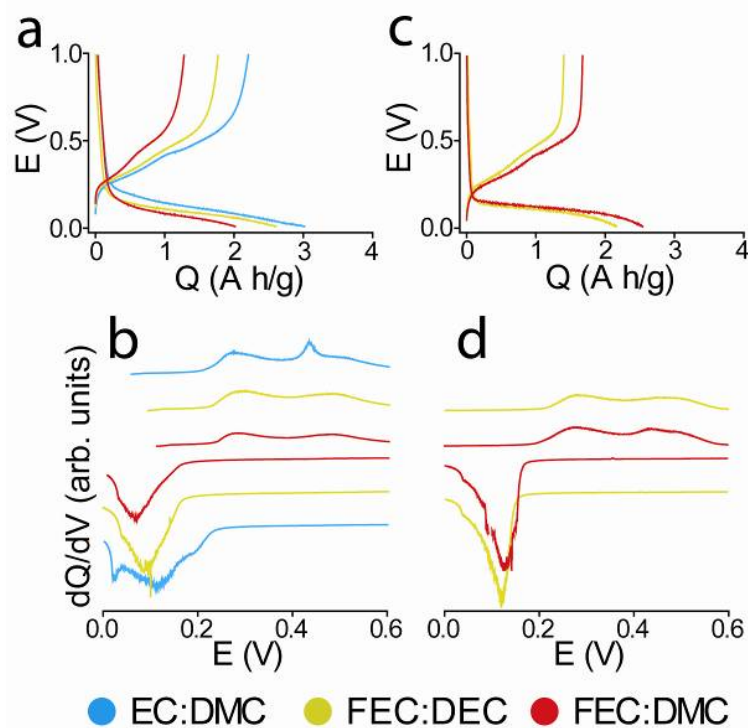


Figure 8.5: Comparison of 1st cycle charge and discharge voltage profiles for films of Si nanowires mixed with (a) PVdF and annealed and (c) NaAlg using the indicated electrolyte solvent mixtures with (b, d) corresponding differential capacity plots.

Electrochemical data for films (2) and (3) are shown in greater detail in Figure 8.6. Lithiation and delithiation behavior for electrolytes (D) and (E) are very similar to one another, but differ slightly from (B). The differences lie primarily in the long-term cyclability behavior where the differential peaks fade and shift to lower potentials for electrolyte (B) whereas two prominent peaks centered at 250 mV and 100 mV persist through the entire test for electrolytes with FEC. There is a slight difference in peak intensities between films (2) and (3). Film (2) peaks are roughly equal in intensity whereas film (3) shows a 300 mV peak slightly more intense than the 100 mV peak.

Delithiation behavior is similar independent of electrolyte and / or binder. All systems show two peaks—at 300 mV and 500 mV—with the 300 mV peak being slightly

more intense. The EC:DMC battery (Figure 8.6a.i) fades faster and the peaks can be seen merging into a single broad delithiation peak around 300 mV. All FEC-containing electrolytes (Figure 8.6b.i–8.6e.i) show both peaks persist through 100 cycles, but show signs of fading toward the later cycles.

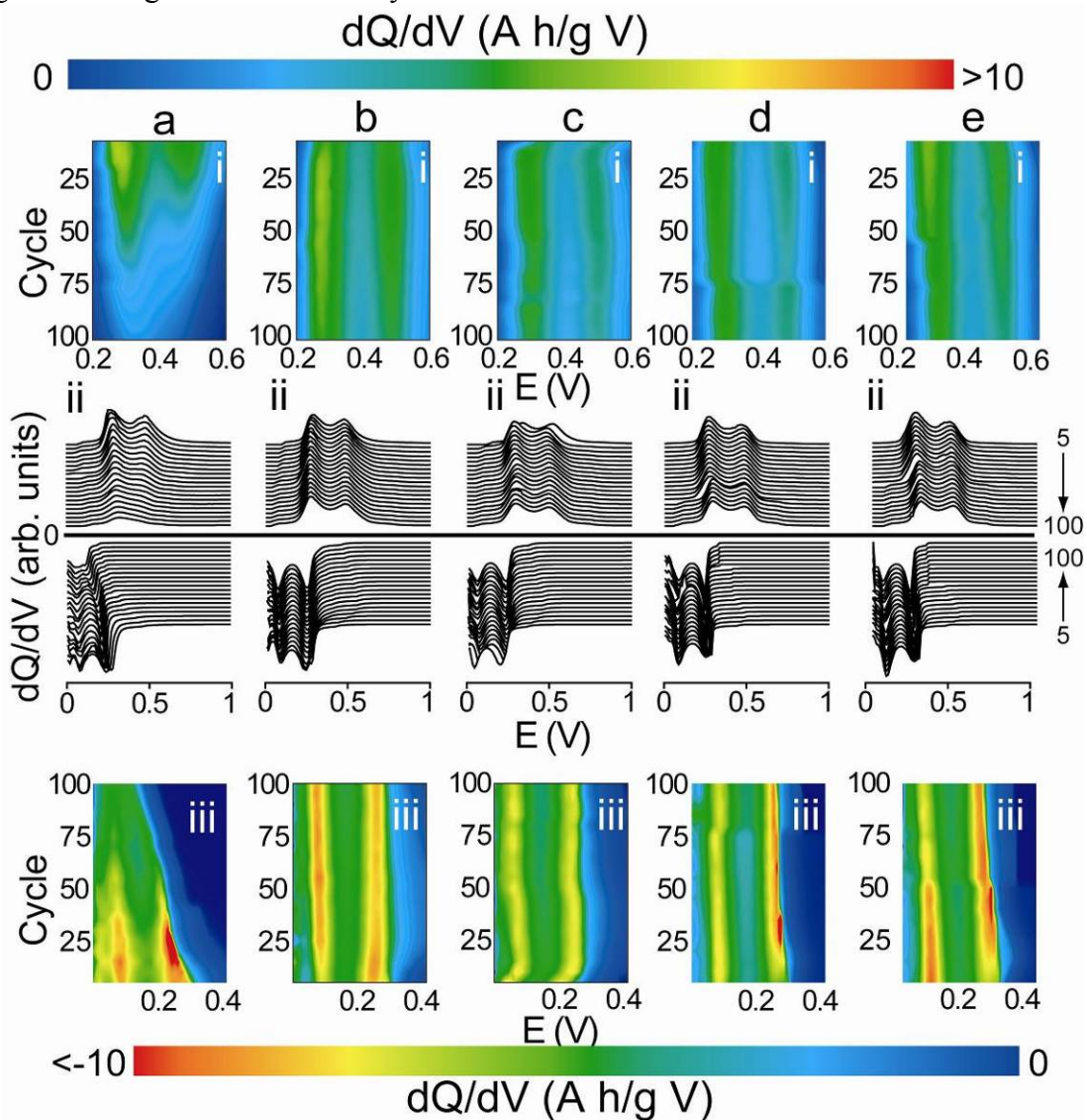


Figure 8.6: Differential (a.i-e.i) discharge and (a.iii-e.iii) charge capacity color maps with (a.ii-e.ii) corresponding waterfall plots for Sn-seeded Si nanowires with (a-c) PVdF and annealed or (d, e) NaAlg using electrolyte solvent mixtures of (a) EC:DMC, (b, d) FEC:DEC or (c, e) FEC:DMC.

8.3.3 Rate test behavior

Silicon nanowires were cycled at faster rates to determine their potential for high-power applications potential of the batteries. Film (2) was cycled at various rates using electrolytes (B), (D), and (E), and film (3) was cycled using (D) and (E) only. Both sets of data, shown in Figure 8.7, show similar trends; at rates faster than $C/10$ (2) or $C/20$ (3), the capacity fades rapidly. Electrolyte (B) performed as well as FEC-containing electrolytes in this study until the final 10 cycles when the cycle rate was returned to $C/10$ where electrolytes (D) and (E) rebounded to the same capacities ($\sim 2000 \text{ mA h g}^{-1}$) as the first set of $C/10$ cycles (cycles 11-20) and held steady while (B) returned to a value slightly lower ($\sim 1700 \text{ mA h g}^{-1}$) and continued to fade to 1500 mA h g^{-1} . Non-FEC containing electrolytes typically show good results through 30-50 cycles before starting to degrade.^{24, 25, 27} Film (3) capacities also rebounded to high values (1600 mA h g^{-1}) for both electrolytes at cycle 40 when the rate was reduced to $C/10$ after cycling at rates of $C/2$, C , and $2C$. These data are shown in greater detail below. To be considered commercially viable, batteries should show good capacity retention through thousands of cycles at a rate of $C/3$ or faster. Here, at a rate of $C/2$, the capacities were above 1000 mA h g^{-1} for all binder / electrolyte combinations showing promise for potential commercialization of these materials. Further work is required to stabilize capacity retention at these faster rates.

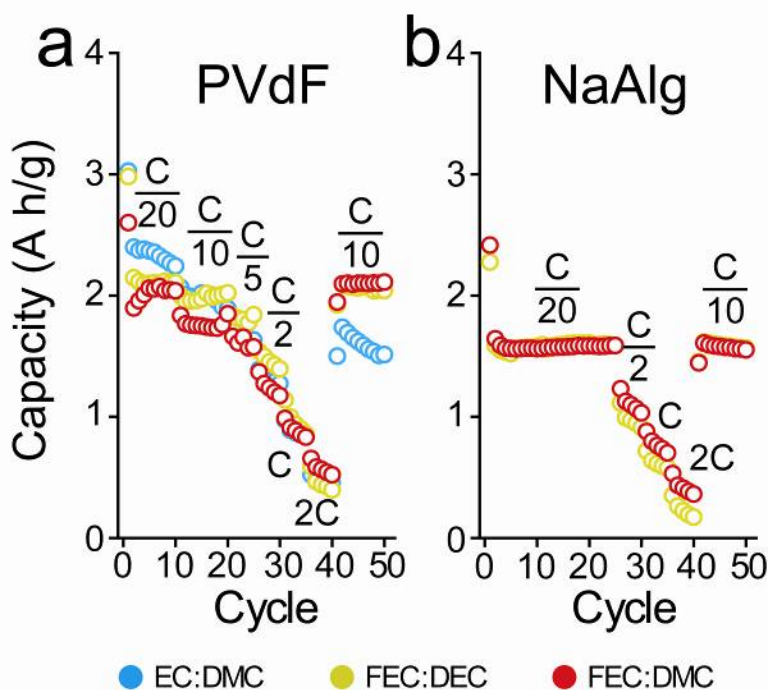


Figure 8.7: Cycle data for Sn-seeded Si nanowires mixed with (a) PVdF and annealed or (b) NaAlg using the electrolyte solutions shown and cycled at the rates indicated.

Electrochemical data for films (2) and (3) cycled at various rates are shown in Figure 8.8. The coulombic efficiencies for electrolyte (B) was between 90% and 100% and between 98% and 100% for FEC-containing electrolytes (except where the efficiency dropped around 95% for cycles where the rate was changed) for both PVdF and NaAlg films. The voltage profiles and differential capacity plots show plateaus and peaks at expected potentials and follow the same general trends observed previously for all binder / electrolyte combinations. These data are presented in greater detail using Figure 8.9.

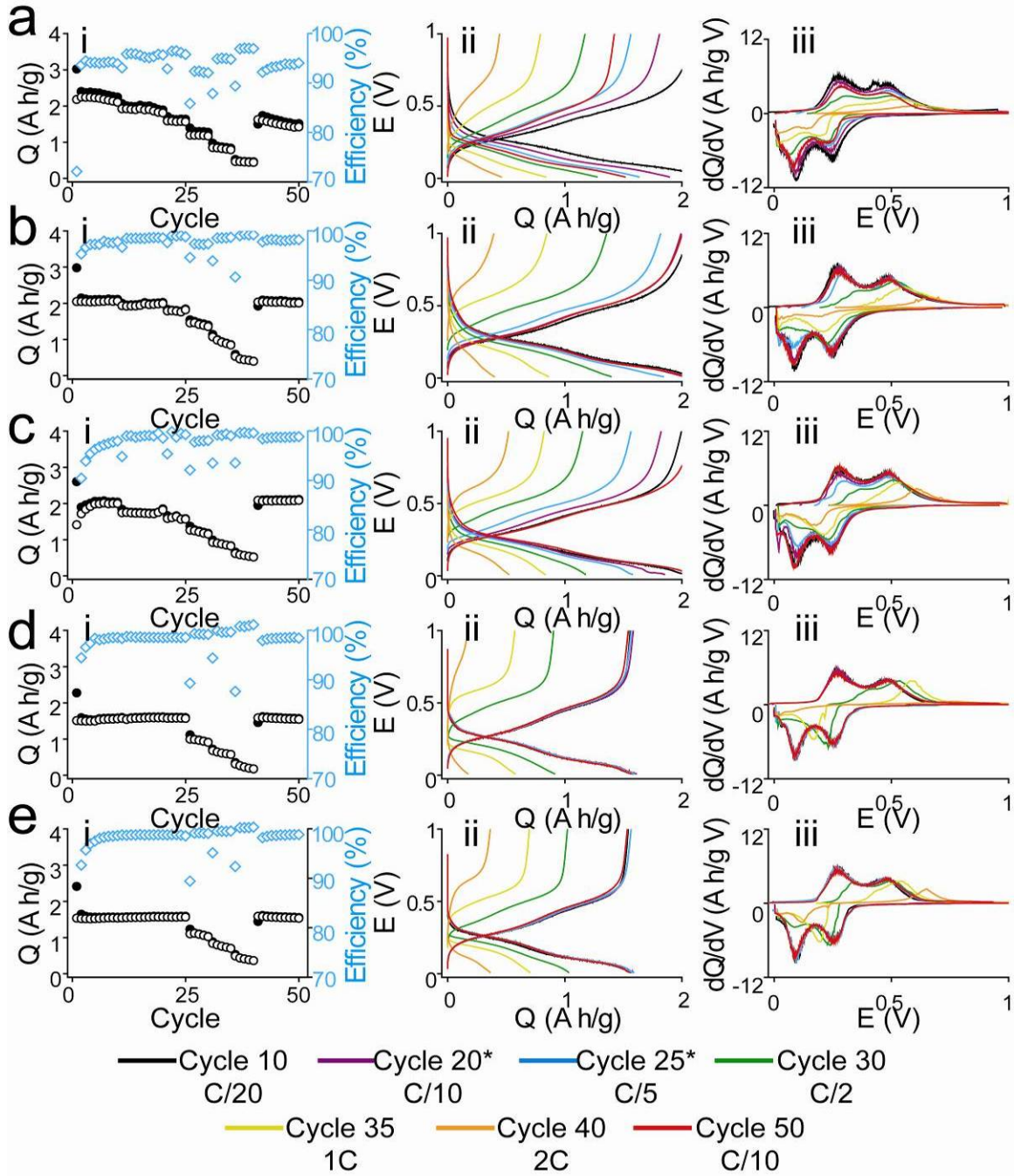


Figure 8.8: (a.i – e.i) Rate test data, (a.ii – e.ii) voltage profiles, and (a.iii – e.iii) differential capacity plots for nanowires mixed with (a-c) PVdF and annealed or (d, e) NaAlG and electrolyte solvents of (a) EC:DMC, (b, d) FEC:DEC or (c, e) FEC:DMC. * Cycles 20 and 25 in (d) and (e) are at C/20.

Figure 8.9 shows data analogous to Figure 8.6 for the rate test data shown in Figures 8.8. Discharge (Figures 8.9a.i–8.9e.i) and charge (Figures 8.9a.iii–8.9e.iii) color maps are shown with the same data illustrated as waterfall plots in Figures 8.9a.ii–8e.ii for Si nanowires mixed with PVdF and annealed (Figures 8.9a–8.9c) and NaAlg (Figures 8.9d and 8.9e) using various electrolyte solutions. The lithiation (100 mV and 250 mV) and delithiation peak (300 mV and 500 mV) locations are at the same potentials as discussed earlier. A few slight differences occur when the rate is increased, however. The lithiation potential for all batteries is between 200 mV and 250 mV with a second lithiation event occurring at potentials at or slightly below 100 mV. These peaks persist through the 25th cycle (i.e. through rates of C/20, C/10, and C/5), at which point there is a noticeable shift to lower potentials. This shift is more pronounced and easier to see for FEC-containing batteries where the 200 mV peak is more intense and undergoes shifts as large as 100 mV to lower potentials between cycles 25 and 40 (Figure 8.9b.iii–8.9e.iii). Between cycles 30 and 40 (i.e., at cycle rates of 1C and 2C) the two peaks are merged in a single broad hump. The broad peak is situated between the 100 mV and 250 mV. The lower potential peak is generally attributed to the formation of $\text{Li}_x\text{Si}_{1-x}$ phases, thus the merging of the two lithiation peaks at an intermittent potential implies that the rate is too fast to form this phase and that the film is limited kinetically. This explains why the capacity is reduced at higher rates and also why the capacity is able to return to the same values as prior to vigorous cycling when the rate is relaxed to C/10. At cycle 41, the peaks resume the positions and intensities as during cycles 11-20 (i.e. the first set of cycles at C/10). The delithiation behavior at faster rates is also slightly different than what we observed at C/10. Earlier, we noted a marked difference in the peak appearance and evolution between PVdF and NaAlg binders. Namely, the 250 mV peak grows in intensity for NaAlg films whereas it is present from the start in PVdF films. This

observation is made again here (Figures 8.9d.iii, 8.9e.iii). For PVdF films (Figures 8.9a.iii–8.9c.iii), the 100 mV peak—which was initially weaker and grew in intensity—was present and very intense from the onset of cycling. This could be due to the fact that the first 10 cycles were at C/20 here whereas previously, the early cycles were done at C/10. As mentioned above, it is difficult to tell from the electrochemical data whether or not Sn is lithiating and contributing to the capacitive behavior of the battery.

Delithiation follows similar behavior as lithiation. All batteries tested show delithiation peaks at 300 mV and 500 mV. Starting with the 21st cycle both peaks begin to reduce in intensity and the 300 mV peak begins to shift to higher potentials and merge with the 500 mV peak. Between cycles 30 and 40, there is a single broad peak, similar to lithiation behavior. This, again, has kinetic implications. At cycle 41, when the rate is relaxed to C/10, the peaks resume the positions and intensities as during cycles 11-20 (i.e. the first set of cycles at C/10). A more rigorous detailed in-situ study is necessary to determine exactly what phases are being produced at higher rates, which would explain the shifts in peak intensities and locations. To the best of our knowledge at the time of writing this manuscript, no such study has been performed.

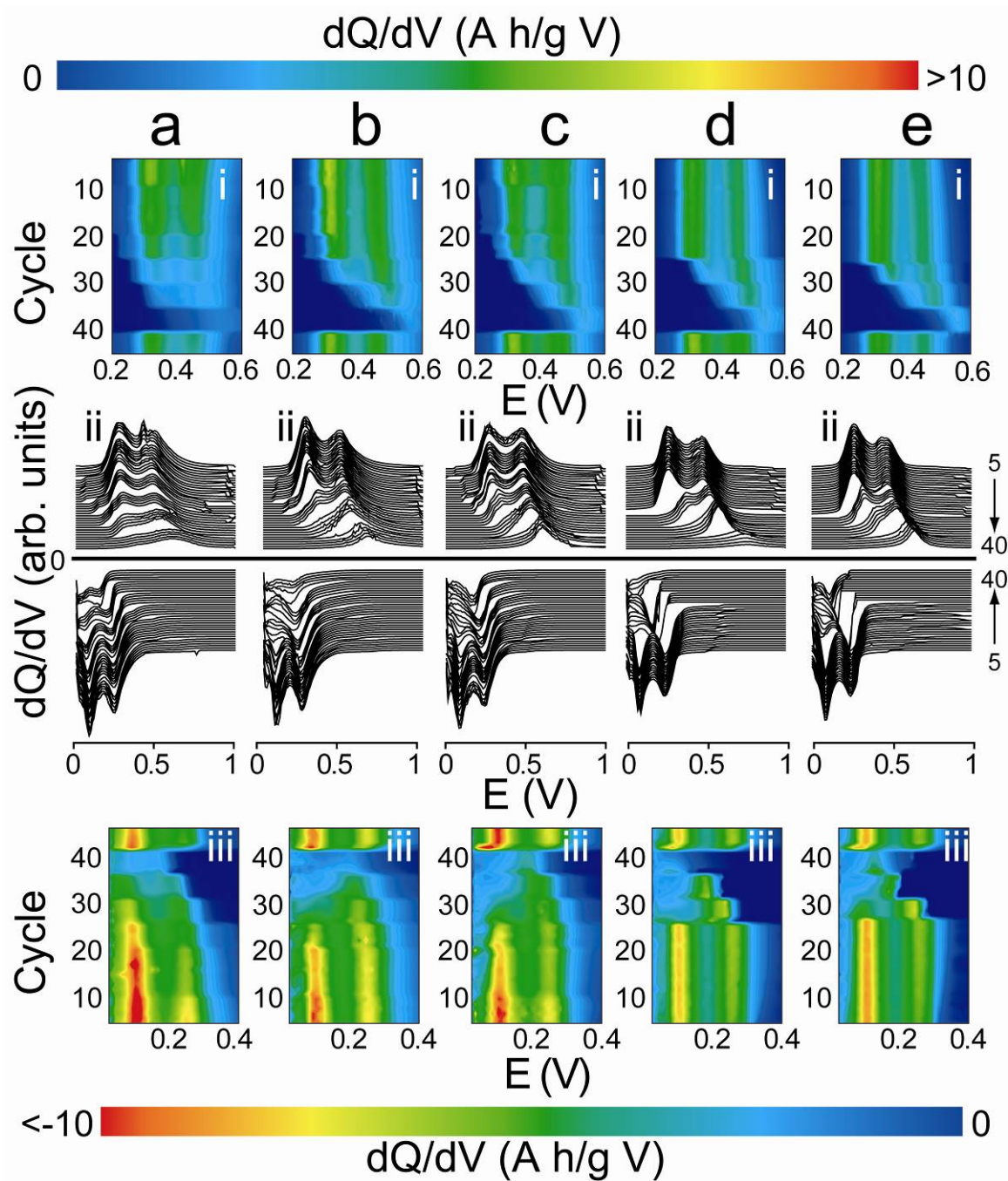


Figure 8.9: Differential (a.i-e.i) discharge and (a.iii-e.iii) charge capacity plots with (a.ii-e.ii) corresponding waterfall curves for Sn-seeded Si nanowires using either (a-c) PVdF and annealed or (d, e) NaAlg as binder and electrolyte solvent mixtures of (a) EC:DMC, (b, d) FEC:DEC or (c, e) FEC:DMC.

8.3.4 Electrical behavior

Electrochemical impedance spectroscopy (EIS) measurements were made after 100 galvanostatic cycles at $C/10$, shown in Figure 8.10. Each film shows characteristic impedance features, namely a high-frequency semi-circular resistive element coupled with a high frequency diffusion element. The size of the semi-circle is indicative of the film resistance; the larger the semi-circle, the more resistive the film. The steepness of the low-frequency slope provides information about Li^+ diffusion within the film. A 45° slope is associated with semi-infinite diffusion in a planar electrode. Slopes steeper than 45° are characteristic of finite Li^+ diffusion that occurs in a thin film.¹¹ FEC-containing electrolyte solutions have higher impedance than those without FEC, evident by the quick transition from the high- to low-frequency regimes (e.g., FEC-based electrolytes do not form a full semi-circle). Measurements were also made after the first cycle using film **(1)** and electrolytes **(B)** and **(E)** and are plotted in Figure 8.10b together with measurements taken after 100 cycles. These data show progressive impedance as the batteries cycle and is the cause of the differential peak shifts reported in Figure 8.4. Finally, XRD measurements were taken on film **(1)** as prepared and after one full charge-discharge cycle using electrolyte **(E)** the highlighted areas show regions where Si and Sn peaks are present in (i) and absent in (ii) indicating consumption of those crystalline materials. The Sn seeds participate in Li storage.

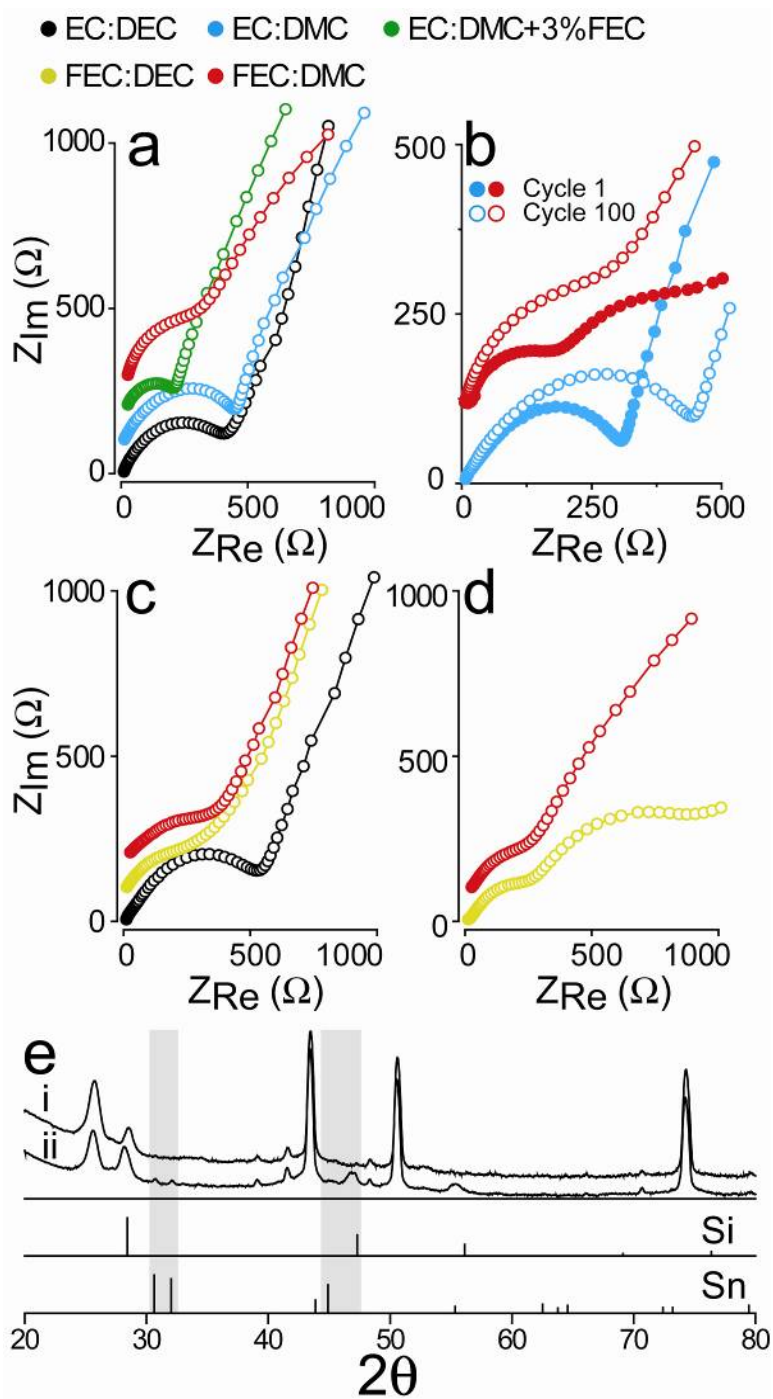


Figure 8.10: Impedance spectra of discharged batteries after (a, c, d) 100 cycles and (b) 1 cycle using film (2) with various electrolytes. The data are offset for clarity. (e) XRD data of film (2) (i) as prepared and (ii) after one full cycle.

8.4 CONCLUSIONS

We report simplified single-step solution phase synthesis of Si nanowires using a new in-situ seeding process from Sn nanocrystals. An organometallic Sn source is injected into the reactor with trisilane. Sn nanocrystals form before the growth of Si nanowires via the SFLS growth mechanism. This process does not require pre-fabrication of nanocrystal seeds as is the general convention and offers a reduced cost-method for producing nanowires. The wires are tested as a Li ion battery negative electrode material using a variety of binders and electrolytes. For binders, as prepared PVdF films perform poorly but show drastic improvement upon heat treatment. The NaAlg binder also shows good cycle behavior. For electrolytes, FEC-based systems showed the best capacity retention. We further show that Sn is active in Li storage. Additional investigations to explore the surface chemistry of cycled films are ongoing. Better understanding of chemistry internal to the battery will provide the means for optimizing the system.

8.5 ACKNOWLEDGEMENTS

Authors contributing to this work include: Kyle Klavetter, C. Buddie Mullins, and Brian A. Korgel. Paul Abel and Yong-Mao Lin were also very helpful with discussions pertaining to EIS and electrochemistry. Reken N. Patel was helping in develop in-situ seeded synthesis. We thank TIMCAL for supplying the conductive carbon used in slurry formation.

8.6 REFERENCES

1. Szczech, J. R.; Jin, S. *Energ. Environ. Sci.* **2011**, *4*, 56-72.
2. Li, J.; Dahn, J. R. *J. Electrochem. Soc.* **2007**, *154*, A156-A161.
3. Obrovac, M. N.; Christensen, L. *Electrochem. Solid St* **2004**, *7*, A93-A96.
4. Reports have shown the existance of the $\text{Li}_{22}\text{Si}_5$ phase, which has a maximum theoretical capacity of 4200, but most studies indicate $\text{Li}_{15}\text{Si}_4$ is the hight Li content Li-Si alloy that forms at room temperatures

5. Zhang, X.; Shyy, W.; Sastry, A. M. *J. Electrochem. Soc.* **2007**, *154*, A910-A916.
6. Yao, Y.; McDowell, M. T.; Ryu, I.; Wu, H.; Liu, N.; Hu, L.; Nix, W. D.; Cui, Y. *Nano Lett.* **2011**, *11*, 2949-2954.
7. Ryu, I.; Choi, J. W.; Cui, Y.; Nix, W. D. *J. Mech. Phys. Solids* **2011**, *59*, 1717-1730.
8. Chockla, A. M.; Harris, J. T.; Akhavan, V. A.; Bogart, T. D.; Holmberg, V. C.; Steinhagen, C.; Mullins, C. B.; Stevenson, K. J.; Korgel, B. A. *J. Am. Chem. Soc.* **2011** *133*, 20914-20921.
9. Heitsch, A. T.; Akhavan, V. A.; Korgel, B. A. *Chem. Mater.* **2011**, *23*, 2697-2699.
10. Laïk, B.; Eude, L.; Pereira-Ramos, J.-P.; Cojocaru, C. S.; Pribat, D.; Rouvière, E. *Electrochim. Acta* **2008**, *53*, 5528-5532.
11. Ruffo, R.; Hong, S. S.; Chan, C. K.; Huggins, R. A.; Cui, Y. *J. Phys. Chem. C* **2009**, *113*, 11390-11398.
12. Kang, K.; Lee, H.-S.; Han, D.-W.; Kim, G.-S.; Lee, D.; Lee, G.; Kang, Y.-M.; Jo, M.-H. *App. Phys. Lett.* **2010**, *96*, 053110-3.
13. Chakrapani, V.; Rusli, F.; Filler, M. A.; Kohl, P. A. *J. Phys. Chem. C* **2011**, *115*, 22048-22053.
14. Jo, Y. H.; Jung, I.; Choi, C. S.; Kim, I.; Lee, H. M. *Nanotechnology* **2011**, *22*, 8.
15. Zou, C.-D.; Gao, Y.-L.; Yang, B.; Zhai, Q.-J. *T. Nonferr. Metal. Soc.* **2010**, *20*, 248-253.
16. Chou, N. H.; Schaak, R. E. *J. Am. Chem. Soc.* **2007**, *129*, 7339-7345.
17. Rathi, S. J.; Jariwala, B. N.; Beach, J. D.; Stradins, P.; Taylor, P. C.; Weng, X.; Ke, Y.; Redwing, J. M.; Agarwal, S.; Collins, R. T. *J. Phys. Chem. C* **2011**, *115*, 3833-3839.
18. Winter, M.; Besenhard, J. R. O. *Electrochim. Acta* **1999**, *45*, 31-50.
19. Courtney, I. A.; Tse, J. S.; Mao, O.; Hafner, J.; Dahn, J. R. *Phys. Rev. B* **1998**, *58*, 15583-15588.
20. Todd, A. D. W.; Ferguson, P. P.; Fleischauer, M. D.; Dahn, J. R. *Int. J. Energ. Res.* **2010**, *34*, 535-555.
21. *ASM International's Binary Alloy Phase Diagrams 2nd ed.* **1990**.
22. Robert A, H. *J. Power Sources* **1999**, *81-82*, 13-19.

23. Beaulieu, L. Y.; Eberman, K. W.; Turner, R. L.; Krause, L. J.; Dahn, J. R. *Electrochem. Solid St.* **2001**, *4*, A137-A140.
24. Etacheri, V.; Haik, O.; Goffer, Y.; Roberts, G. A.; Stefan, I. C.; Fasching, R.; Aurbach, D. *Langmuir* **2012**, *28*, 965-976.
25. Choi, N.-S.; Yew, K. H.; Lee, K. Y.; Sung, M.; Kim, H.; Kim, S.-S. *J. Power Sources* **2006**, *161*, 1254-1259.
26. Li, J.; Christensen, L.; Obrovac, M. N.; Hewitt, K. C.; Dahn, J. R. *J. Electrochem. Soc.* **2008**, *155*, A234-A238.
27. Nakai, H.; Kubota, T.; Kita, A.; Kawashima, A. *J. Electrochem. Soc.* **2011**, *158*, A798-A801.
28. Kovalenko, I.; Zdyrko, B.; Magasinski, A.; Hertzberg, B.; Milicev, Z.; Burtovyy, R.; Luzinov, I.; Yushin, G. *Science* **2011**, *334*, 75-79.
29. Hanrath, T.; Korgel, B. A. *J. Am. Chem. Soc.* **2002**, *124*, 1424-1429.
30. Hanrath, T.; Korgel, B. A. *Adv. Mater.* **2003**, *15*, 437-440.
31. Heitsch, A. T.; Hessel, C. M.; Akhavan, V. A.; Korgel, B. A. *Nano Lett.* **2009**, *9*, 3042-3047.
32. Hessel, C. M.; Heitsch, A. T.; Korgel, B. A. *Nano Lett.* **2009**, *10*, 176-180.
33. Cui, Y.; Lauhon, L. J.; Gudixsen, M. S.; Wang, J.; Lieber, C. M. *App. Phys. Lett.* **2001**, *78*, 2214-2216.
34. Lu, X.; Hanrath, T.; Johnston, K. P.; Korgel, B. A. *Nano Lett.* **2002**, *3*, 93-99.
35. Bridel, J. S.; Azaïs, T.; Morcrette, M.; Tarascon, J. M.; Larcher, D. *Chem. Mater.* **2009**, *22*, 1229-1241.
36. Mazouzi, D.; Lestriez, B.; Roue, L.; Guyomard, D. *Electrochem. Solid St.* **2009**, *12*, A215-A218.
37. Hatchard, T. D.; Dahn, J. R. *J. Electrochem. Soc.* **2004**, *151*, A838-A842.
38. Zheng, Y. X.; Xie, J.; Song, W. T.; Liu, S. Y.; Cao, G. S.; Zhao, X. B. *J. Mater. Res.* **2011**, *26*, 2719-2724.
39. Wu, P.; Du, N.; Liu, J.; Zhang, H.; Yu, J.; Yang, D. *Mater. Res. Bull.* **2011**, *46*, 2278-2282.

Chapter 9: Colloidal Synthesis of Germanium Nanorods[§]

9.1 INTRODUCTION

Colloidal synthetic methods have been developed for germanium (Ge) nanocrystals,¹⁻⁸ which have enabled studies of how quantum confinement affects the optical and electronic properties of Ge.¹⁻⁷ These nanocrystals have been explored as luminescent materials⁴ for biological imaging² and as the basis of new optical and electronic devices.^{1,7,8} Solvent dispersions of Ge nanocrystals have also been utilized as inks to deposit thin films under relatively mild conditions showing potential for low-cost optical and electronic devices.⁸ To date, however, Ge nanorods with controlled length and thickness have not been made.

Nanorods are particularly interesting nanostructures, as they can exhibit size-dependent shifts in their optical properties due to quantum confinement in both axial and radial dimensions.^{9,10} Their anisotropic shape can also lead to other unique effects, such as linear polarized photoluminescence¹¹ and enhanced light absorption when the aspect ratio is sufficiently large.¹² Nanorods of many other semiconductors, including CdE (E = S^{13, 14}, Se^{14, 15}, Te¹⁵), ZnE (E = O¹⁶, S¹⁷, Se¹⁸), InP^{10, 19}, InAs,¹⁹ and Si²⁰ have been made using colloidal routes, such as oriented attachment,²¹⁻²⁴ ligand-assisted growth²⁵⁻³⁰, and metal nanocrystal-assisted solution-liquid-solid (SLS) growth.^{10,19,20} The SLS approach has proven particularly successful for generating nanorods from materials that do not exhibit a strongly preferred crystallographic growth direction, like those with cubic crystal structure such as Si²⁰, InP¹⁰ and InAs.⁹

Here, we demonstrate SLS growth of Ge nanorods in a high boiling solvent. An appropriate combination of reaction solvent and precursor, seed metal and capping

[§] This chapter appears in *Chemistry of Materials* **2011**, 23, 1964-1970.

ligands was identified. Bismuth (Bi) nanocrystals were used as seeds, similar to recent studies using Bi to seed SLS growth of Ge nanowires.³¹⁻³³ Diphenylgermane (DPG) was used as the Ge reactant, with relatively low Ge:Bi ratios. Capping ligands were found to be necessary to prevent aggregation and stabilize the nanorods. Trioctylphosphine oxide (TOPO) was found to be a successful capping ligand.

9.2 EXPERIMENTAL SECTION

9.2.1 Materials

Anhydrous tetrahydrofuran (THF, Sigma Aldrich, $\geq 99.9\%$), sodium bis(trimethylsilyl)amide ($\text{NaN}[\text{SiMe}_3]_2$, Sigma Aldrich, 1.0 M in THF), bismuth (III) chloride (BiCl_3 , Sigma Aldrich, $\geq 98\%$), diphenyl ether (DPE, Sigma Aldrich, $\geq 99\%$), tri-*n*-octylphosphine oxide (TOPO, Sigma Aldrich, 99%), squalane (Sigma Aldrich, 99%), anhydrous toluene (Sigma Aldrich, 99.8%), anhydrous hexane (Sigma Aldrich, 95%), and diphenylgermane (DPG, Gelest, $>95\%$) were purchased and used without further purification. Polyvinylpyrrolidone-hexadecane (PVP-HDE) copolymer (Ganex V-216, MW = 7300 g mol⁻¹, product ID 72289D) was obtained from ISP Technologies, Inc.

9.2.2 $\text{Bi}[\text{N}(\text{SiMe}_3)_2]_3$ preparation

$\text{Bi}[\text{N}(\text{SiMe}_3)_2]_3$ was prepared according to literature methods.³⁴ In a typical procedure, 10 mL of 1.0 M $\text{NaN}(\text{SiMe}_3)_2$ (10 mmol of Na) in THF is added to a three-neck round bottom flask in a nitrogen-filled glove box. The flask is sealed, removed from the glove box and connected to a Schlenk line. THF is evaporated under vacuum to leave a yellow powder. The flask is blanketed with nitrogen and 20 mL anhydrous toluene is added. The solution is chilled to 0°C using an ice bath. Separately, in a glove box, 1.06 g BiCl_3 (3.35 mmol of Bi) is dissolved in 3 mL THF. 15 mL of toluene is then added to this solution and the entire mixture is transferred by syringe to the Schlenk flask

containing the $\text{NaN}(\text{SiMe}_3)_2$ / toluene mixture. The ice bath is removed and the reaction mixture is stirred for 1 hour at room temperature. The solvent is then evaporated under vacuum and blanketed with nitrogen. 10 mL anhydrous hexane is added to dissolve the product. The flask is sealed and brought into a nitrogen-filled glove box. The solution is transferred to a vial that is wrapped with paraffin film and electrical tape to avoid oxygen exposure. The vial is placed in a centrifuge tube, removed from the glove box and centrifuged. After centrifugation, the tube is returned to the glove box and the vial is removed. The supernatant is collected and filtered using a Millipore 0.22 μm hydrophobic Durapore membrane syringe filter (Fisher Scientific). The filtrate is an optically clear, yellow solution, which is transferred to a three-neck flask, removed from the glove box, and attached to a Schlenk line. The solvent is evaporated under vacuum leaving the $\text{Bi}[\text{N}(\text{SiMe}_3)_2]_3$ product, which is dissolved in anhydrous THF to a concentration of 0.25 M. The product is used without further purification and is stored in a glove box. Figure G1 in Appendix G shows that exclusive synthesis of $\text{Bi}[\text{N}(\text{SiMe}_3)_2]_3$ was successful via mass spec. A typical preparation yields 1.0–1.25 g of $\text{Bi}[\text{N}(\text{SiMe}_3)_2]_3$.

9.2.3 Ge nanorod synthesis

Ge nanorods were synthesized by first generating a reagent solution of Bi nanocrystals, followed by the addition of the Ge reactant solution. This process of using a crude reaction mixture of Bi nanocrystals as opposed to purified Bi nanocrystals as a reagent was found to provide the most reliable and reproducible results. The reagent solution of Bi nanocrystals was first prepared using a modification of established methods.³⁵ A polymer solution with either 0.5 g or 0.68 g PVP/HDE copolymer in 4.5 or 4.32g of DPE, respectively (i.e. solutions of 10 or 13.5 wt% copolymer), was degassed on a Schlenk line under vacuum with vigorous stirring for 1 hour at 70°C.³⁶ In some

reactions, more PVP-HDE copolymer was added to the reactions and found to induce branched growth. The polymer solution was then blanketed with nitrogen and heated to 180°C. While degassing the polymer solution, a reactant solution for the Bi nanocrystals of Na[N(SiMe₃)₂] and Bi[N(SiMe₃)₂]₃ was prepared in a glove box. 19 μL of 1.0 M Na[N(SiMe₃)₂] in THF (19 μmol Na) and 19 μL of 0.25 M Bi[N(SiMe₃)₂]₃ in THF (4.75 μmol Bi) were combined in 500 μL of THF to obtain a 4:1 mixture of Na to Bi. Once the polymer / THF solution had finished degassing, it was heated to 180°C and then the Na/Bi reactant solution was rapidly injected. The solution turns black immediately upon injection, indicating the formation of Bi nanocrystals.

After stirring the Bi nanocrystal reactant mixture for 30 min at 180°C, 2 g of TOPO dissolved in 5 mL of toluene and 4 mL of squalane were added by syringe. The temperature was lowered to 150°C, and placed under vacuum for 60 minutes to evaporate DPE. The flask was then blanketed in nitrogen and heated to 350°C.

Under vigorous stirring, a Ge reactant solution of 18 μL of DPG (95 μmol, which corresponds to a Ge:Bi molar ratio of 20:1 in the reaction mixture) dissolved in 500 μL squalane was rapidly injected into the hot Bi nanocrystal mixture. The heating mantle was removed five minutes later to allow the reaction mixture to cool to room temperature.

Once the temperature fell to 100°C, 10 mL of toluene was injected to prevent the solidification of TOPO. After cooling to room temperature, 10 mL of ethanol was added and the mixture was centrifuged at 10000 rpm for 5 min to precipitate the nanorods. The supernatant was discarded. The precipitate was resuspended in 5 mL of chloroform and 5 mL of ethanol, followed by another centrifugation. The supernatant was again discarded. The precipitate was redispersed in chloroform and stored in air. A typical reaction produces 10 to 15 mg of Ge nanorods.

9.2.4 Materials Characterization

The Ge nanorods were characterized by transmission electron microscopy (TEM), energy dispersive X-ray spectroscopy (EDS) and X-ray diffraction (XRD). The TEM images were acquired digitally on either a FEI Tecnai Spirit BioTwin TEM operated at 80 kV or a field emission JEOL 2010F TEM operated at 200 kV. For TEM, nanorods were drop-cast from chloroform dispersions onto carbon-coated 200 mesh copper TEM grids (Electron Microscopy Sciences). Energy-dispersive X-ray spectroscopy (EDS) data were acquired on the JEOL 2010F TEM with its Oxford Inca EDS detector.

X-ray diffraction (XRD) was performed using a Bunker-Nonius D8 Advance diffractometer with Cu K α radiation ($\lambda=1.54$ Å). Data were acquired from purified nanorods (1~3 mg) dropcast on a quartz substrate using a rotating sample holder with generator voltage and amperage of 40 mV and 40 mA, respectively, at a scan rate of 12 deg min $^{-1}$ in 0.02 deg intervals, with typical collection times of 4 to 6 hours.

9.3 RESULTS AND DISCUSSION

9.3.1 Ge nanorods

Figure 9.1 shows TEM images of Ge nanorods synthesized by decomposing DPG at 350°C in squalane in the presence of TOPO and Bi nanocrystals at a Ge:Bi molar ratio of 20:1. These nanorods had an average length of 170 ± 20 nm and diameter of 11.4 ± 1.9 nm. XRD (Figure 9.2) and high-resolution TEM images (Figure 9.3) confirmed that the nanorods are crystalline and composed of diamond cubic Ge. TEM also shows that the nanorods had Bi nanocrystals at their tips, confirming the SLS mechanism for nanorod growth. Control reactions were done at 350°C and 400°C where Bi nanocrystals were not formed in order to ensure that unseeded growth of Ge nanorods does not occur. The results to these control reactions are shown in Figure G2 in Appendix G. In a survey

of 20 nanorods, the $\langle 111 \rangle$ direction was the only growth direction observed for germanium nanorods,³⁷ as shown in Figure 9.3, which may be the cause for the high relative intensity of the $\langle 111 \rangle$ peak in the XRD spectrum. The XRD diffraction patterns also show peaks that correspond to orthorhombic Bi due to the Bi seeds.

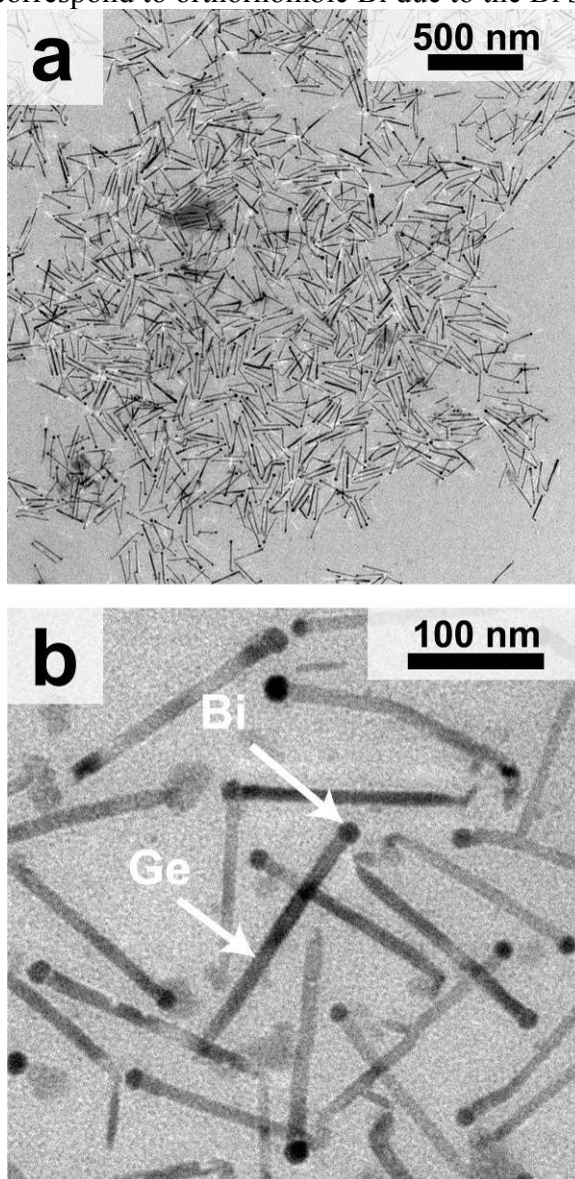


Figure 9.1: TEM images of Ge nanorods grown with a Ge:Bi molar ratio of 20:1. The nanorods have Bi particles at the tips, as indicated in (b). XRD of these nanorods is shown in Figure 9.2.

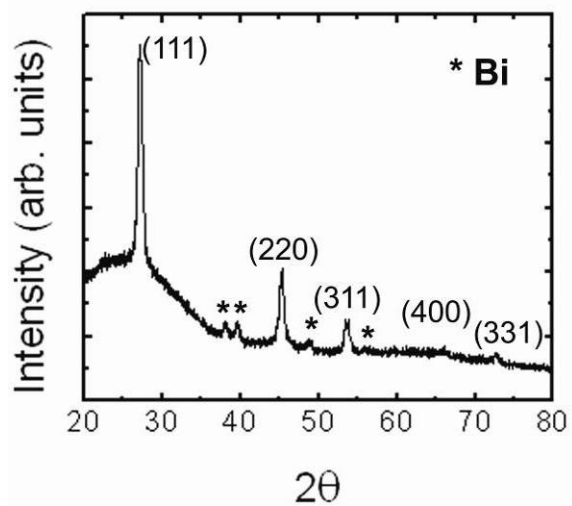


Figure 9.2: XRD of the Ge nanorods with peaks indexed to diamond cubic Ge (JCPDS: 00-004-0545). The peaks labeled “*” correspond to orthorhombic Bi (JCPDS: 00-044-1246).

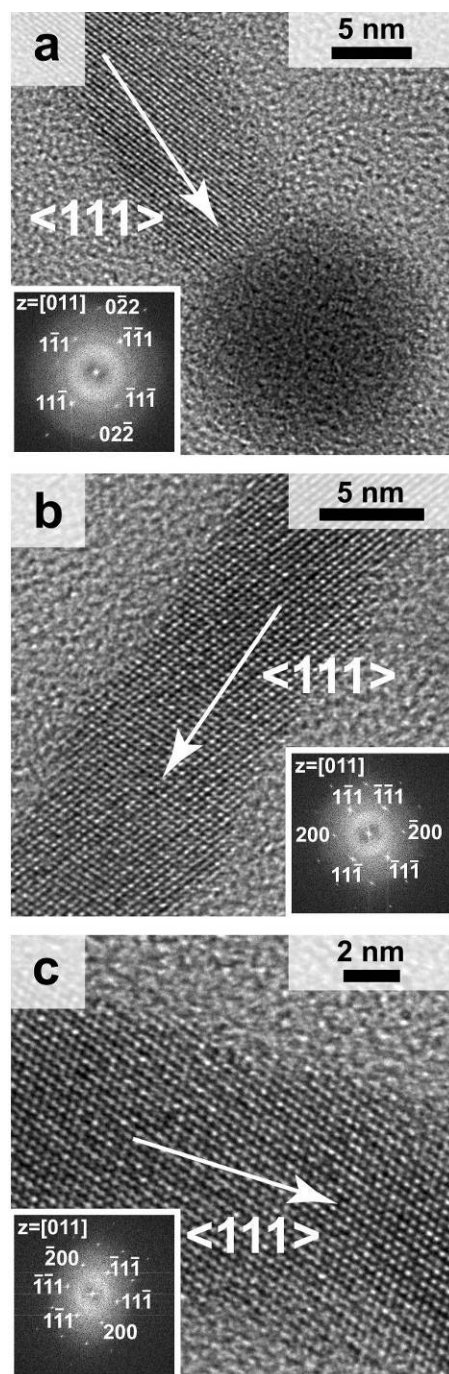


Figure 9.3: High resolution TEM images of the Ge nanorods with (inset) corresponding FFT patterns. Indexing of the FFTs is consistent with diamond cubic Ge, with each nanorod being imaged down the [011] zone axis, as indicated. The growth direction of these nanorods is $\langle 111 \rangle$. A Bi particle is attached to the end of the nanorod in (a).

The SLS mechanism for Ge nanorod growth, as illustrated in Figure 9.4, proceeds because Bi forms a eutectic with Ge at relatively low temperature, below the boiling point of the solvent. The reaction temperature is also high enough to thermally decompose DPG.³² TOPO serves as a capping ligand that prevents aggregation and helps control nanorod growth. Reactions carried out without TOPO led to reaction product that was heavily aggregated and very polydisperse. The PVP/HDE polymer stabilizes the Bi nanocrystals during nanorod growth and helps prevent aggregation of the seeds during growth. When Bi nanocrystals were first synthesized and purified prior to nanorod growth, very inconsistent results were obtained. The dispersion stability of the Bi nanocrystals is apparently very sensitive to the amount of polymer present in the reaction mixture and the most reliable method to produce Ge nanorods utilized the crude Bi nanocrystal reaction media to carry out the nanorod synthesis. The remaining byproducts from the Bi nanocrystal reaction did not appear to interfere with Ge nanorod growth. The Bi nanocrystals observed at the tips of the Ge nanorods were found to have similar diameter as the nanocrystals prior to nanorod growth, indicating that there is little agglomeration of the seed particles during the reaction. To characterize the Bi seeds, a reaction was done and stopped prior to DPG injection. The product was isolated and TEM of the resulting Bi nanocrystals is shown in Figure 9.5.

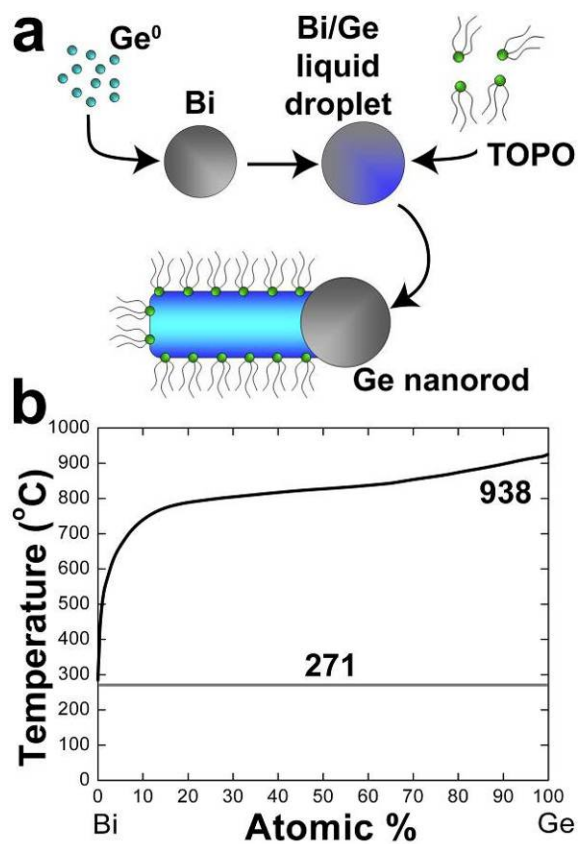


Figure 9.4: (a) Illustration of the Ge nanorod growth process and (b) the Ge/Bi binary phase diagram.²⁷ The polymer coating around that surrounds the Bi nanocrystals is not shown.

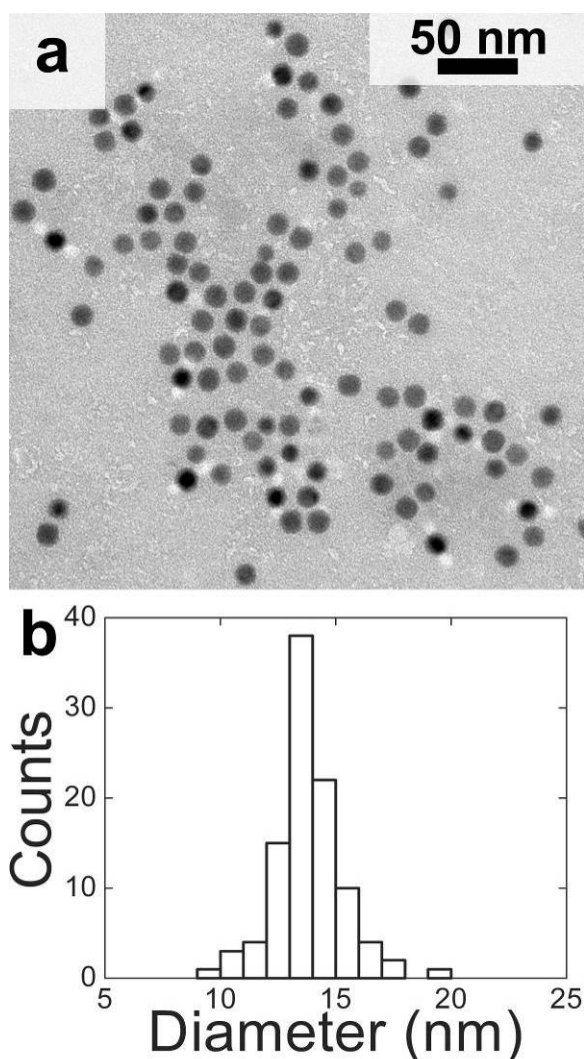


Figure 9.5: (a) TEM image of Bi nanocrystals used to seed Ge nanorod growth; (b) histogram of Bi nanocrystal diameter determined by counting particles in a TEM image. The average diameter of these nanocrystals is 13.8 ± 1.5 nm. The average diameter of Bi nanocrystals observed at the Ge nanorod tips in Figure 9.1 is 15.9 ± 3.5 nm, which is close to this initial Bi seed diameter.

9.3.2 Control of Ge nanorod dimensions

The average length of the nanorods could be varied from 60 nm up to 170 nm by raising the amount of Ge relative to the amount of Bi in the reaction. Figure 9.6 shows TEM images and corresponding length and diameter distributions of the Ge nanorods

made with varying Ge:Bi ratio. Unlike the nanorod length, the nanorod diameter could not be systematically varied. This was primarily because the Bi seed diameter could not be easily manipulated. For example, higher ratios of Na[N(SiMe₃)₂] to Bi[N(SiMe₃)₂]₃ in the Bi nanocrystal synthesis were explored for making smaller diameter Bi nanocrystals, as described in Ref 35, but we found that this did not lead to smaller diameter nanorods. In fact, as shown in Figure 9.7, higher initial Na:Bi ratios only led to more polydisperse samples.

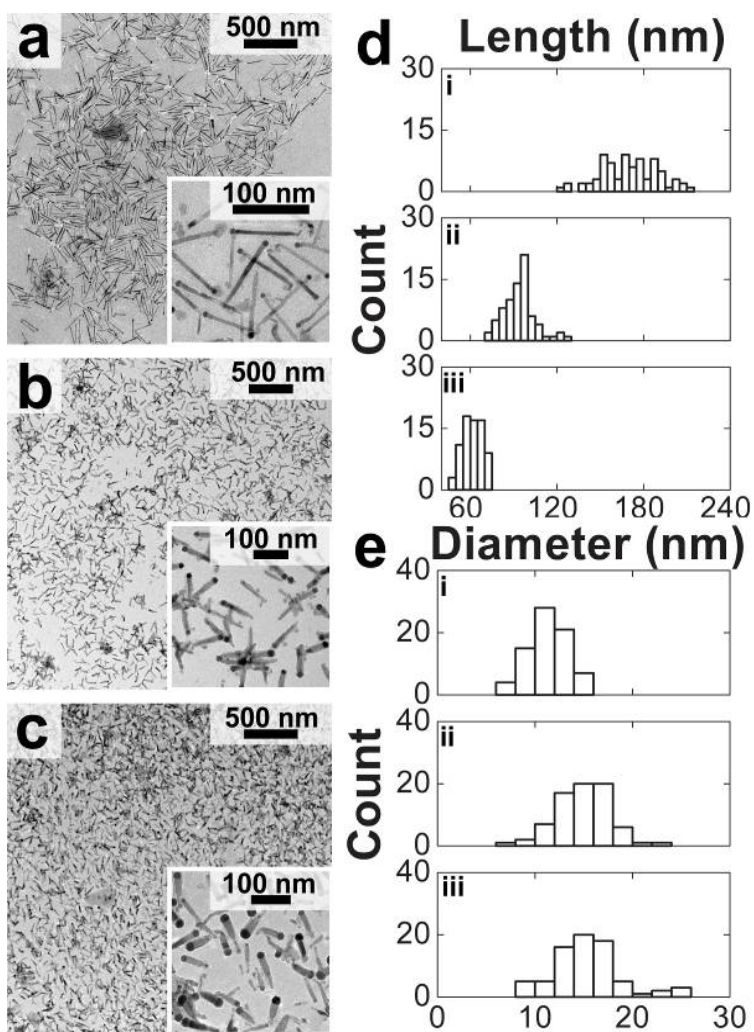


Figure 9.6: (a-c) TEM images of Ge nanorods made with different Ge:Bi ratios. The accompanying histograms show the measured nanorod (d) length (L) and (e) diameter (d): (a,i) Ge:Bi = 20:1, $L = 170 \pm 20$ nm, $d = 11.4 \pm 1.9$ nm, (b,ii) Ge:Bi = 10:1, $L = 94 \pm 11$ nm, $d = 14.9 \pm 2.6$ nm, and (c,iii) Ge:Bi = 5:1, $L = 61 \pm 7$ nm, $d = 15.4 \pm 3.6$ nm.

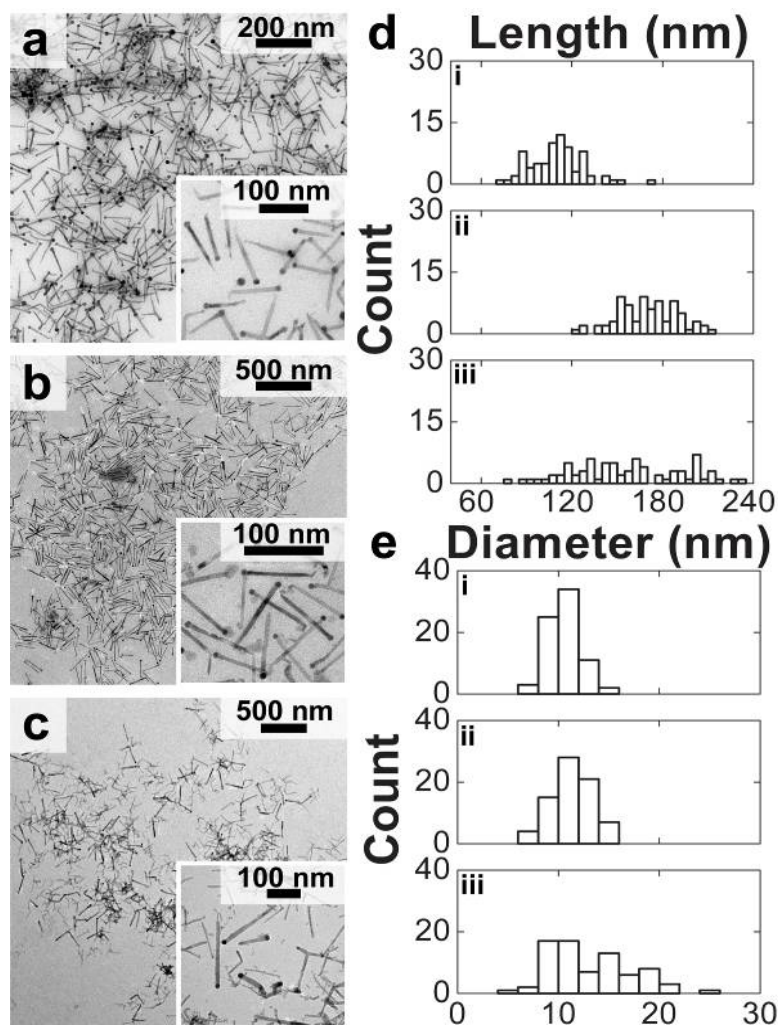


Figure 9.7: (a-c) TEM images of Ge nanorods made using Bi nanocrystals synthesized with different Na:Bi ratios. (d) and (e) show the corresponding histograms of length (L) and diameter (d): (a,i) Na:Bi = 1:1, $L = 110 \pm 18$ nm, $d = 10.6 \pm 1.7$ nm, (b,ii) Na:Bi = 4:1, $L = 170 \pm 20$ nm, $d = 11.4 \pm 1.9$ nm, and (c,iii) Na:Bi = 8:1, $L = 156 \pm 37$ nm, $d = 13.2 \pm 3.9$ nm.

The nanorod dimensions were also sensitive to the reaction temperature. Figure 9.8 shows TEM images of Ge nanorods obtained at different times after injecting reactants at three different growth temperatures: 300°C, 350°C and 400°C. The nanorod growth rate was significantly higher at higher temperature. Increased reaction

temperature also led to slight increases in nanorod diameter, as nanorods grown at 400°C had a measurable increase in average nanorod diameter from 10 nm to 20 nm.

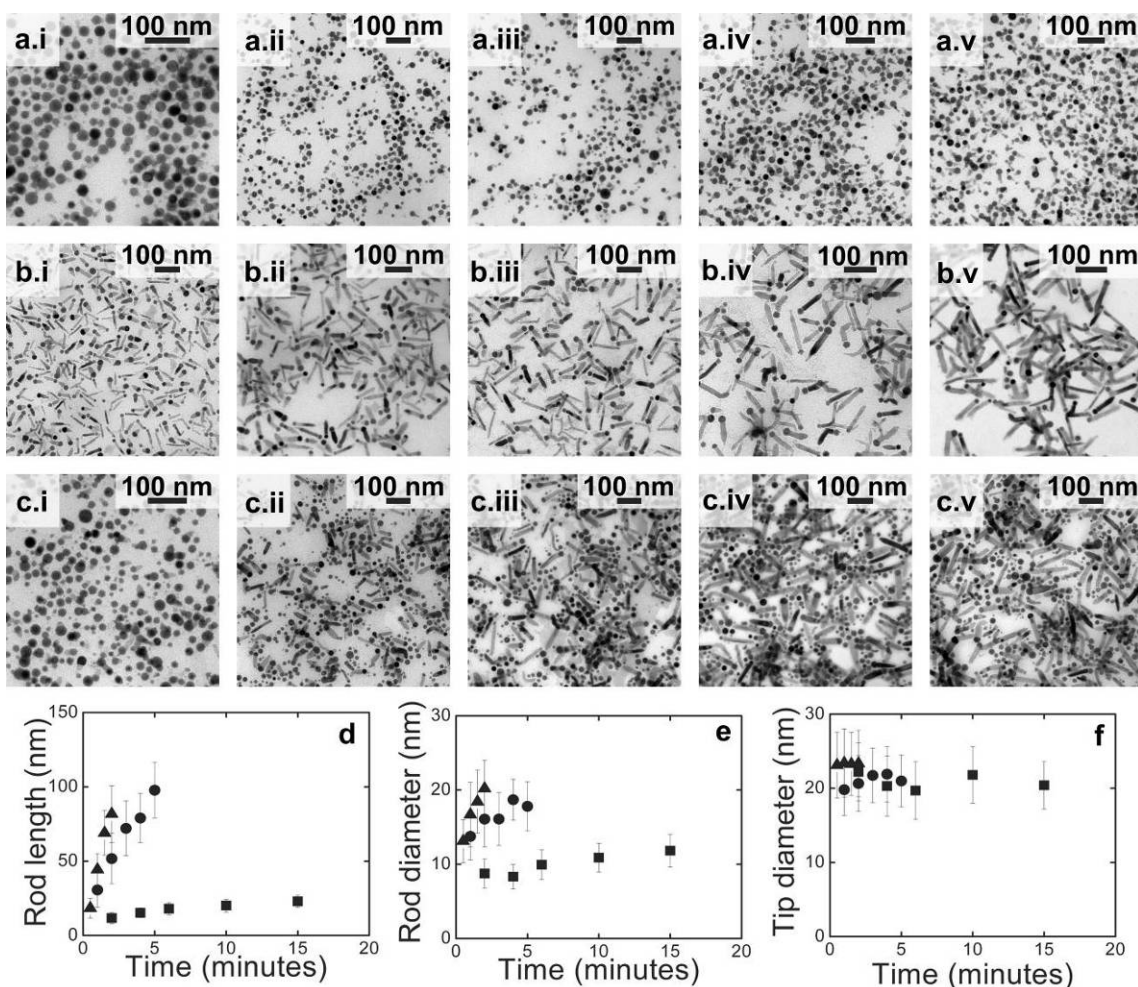


Figure 9.8: TEM images of Ge nanorods at different times after reactant injection at three different reaction temperatures: (a.i-a.v, ■) 300°C, (b.i-b.v, ●) 350°C, and (c.i-c.v, ▲) 400°C. Aliquots were taken from the nanorod reaction at 300°C after (a.i) 2 minutes, (a.ii) 4 minutes, (a.iii) 6 minutes, (a.iv) 10 minutes, and (a.v) 15 minutes. Aliquots were taken from the reaction at 350°C after (b.i) 1 minute, (b.ii) 2 minutes, (b.iii) 3 minutes, (b.iv) 4 minutes, and (b.v) 5 minutes. Aliquots were taken from the reaction at 400°C after (c.i) 30 seconds, (c.ii) 1 minute, (c.iii) 90 seconds, (c.iv) 2 minutes, and (c.v) 5 minutes. The average length, diameter, and Bi seed particle diameter are plotted in (d)-(f).

9.3.3 Branched nanorod growth

In the process of studying the Ge nanorod growth reactions, a new batch of PVP/HDE was needed at one point.³⁶ The new batch of polymer gave branched Ge nanorods. The branching could be eliminated by further decreasing the polymer concentration in the reaction. An excess of PVP/HDE polymer led to branching of the Ge nanorods.

Figure 9.9 shows a TEM image of a typical sample of branched Ge nanorods and Figure 9.10 shows high resolution TEM images of several branch points in the nanorods. Most of the branched nanorods exhibited grain boundaries near the branch points, with some of the arms extending in the $\langle 111 \rangle$ direction.³⁷ There was no noticeable relationship between the relative orientations of the nanorod arms. Furthermore, the grain boundaries do not appear to be twin defects.

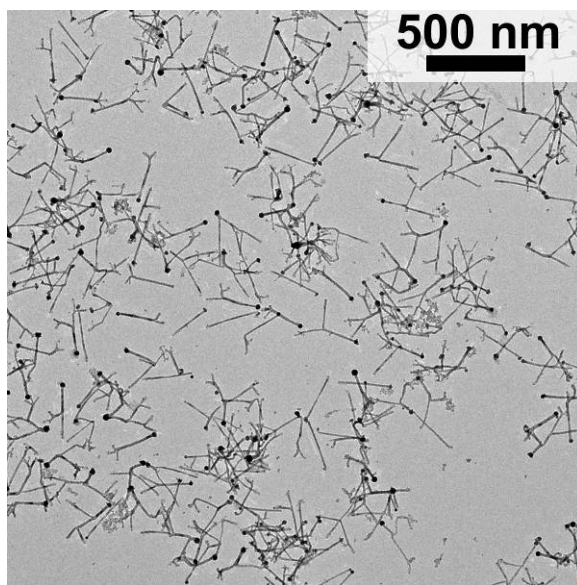


Figure 9.9: TEM image of branched Ge nanorods grown at 350°C in the presence of (30% w/w) 1.5g PVP/HDE polymer. Typically the nanorods are made with 10 – 13.5% w/w polymer.

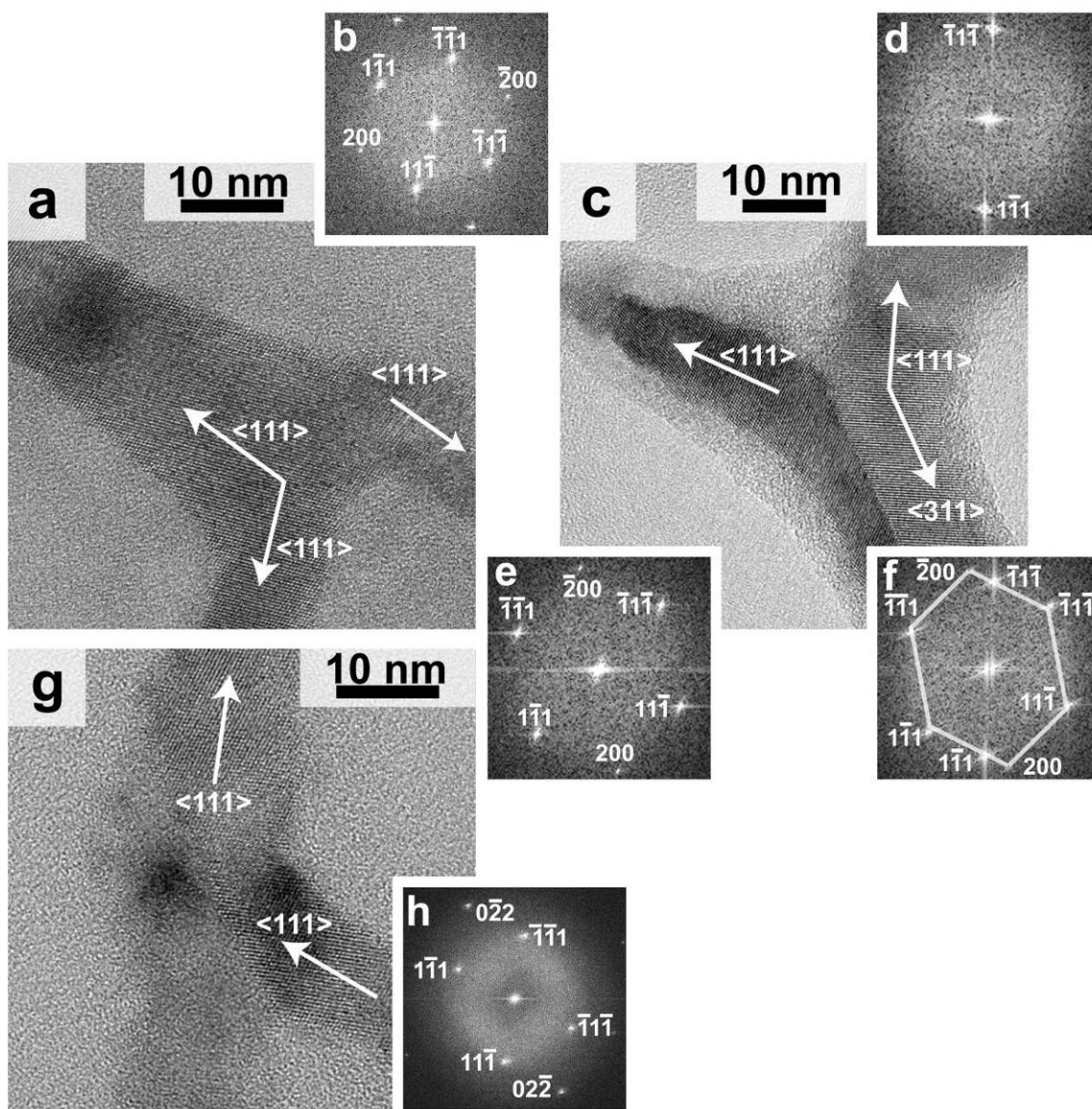


Figure 9.10: TEM images and corresponding FFTs of branched Ge nanorods.

Branched growth has been observed in many other nanorods and nanowires, including CdSe,³⁸⁻⁴⁰ CdS,⁴¹ CdTe,^{39, 42} InAs,⁴³ GaP,⁴⁴ ZnO,^{45, 46} MgO,⁴⁷ ZnSe,⁴⁸⁻⁵⁰ PbSe,⁵¹ ZnS,³⁸ GaN⁵² and Si.⁵² Figure 9.11 summarizes a variety of branching mechanisms that have been observed. Based on the analysis of many TEM images and the fact that there was no obvious relationship between the crystallographic growth directions of the arms,

it appears that the Ge nanorod branching results from the fusion of seed particles from two initially distinct nanorods—the mechanism illustrated in Figure 9.11c. Furthermore, the Bi seeds at the tips of the branched nanorods are correspondingly larger than those observed at the tips of nanorods that are not branched. Initially separate nanorods collide and merge and then continue to grow a unified arm from the branch point. At the branch points, the rod diameters increase, as does the average tip diameter (30.2 ± 4.5 nm).

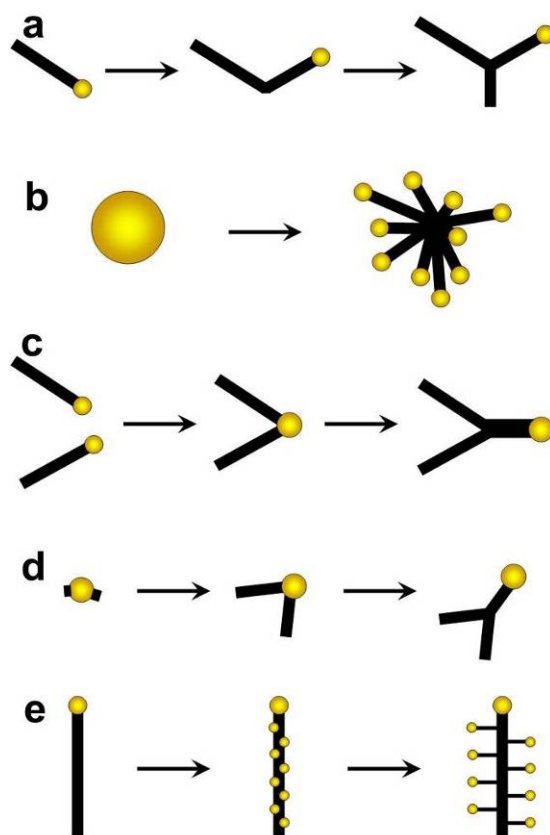
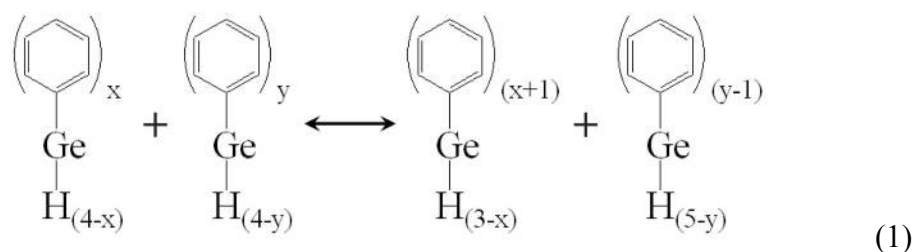


Figure 9.11: Summary of branching mechanisms. (a) Spontaneous branching resulting from starved growth and leading to twin, kink, and branch formation.^{40,48} (b) Catalyst fission into multiple seed particles that each nucleate a branch.⁵³ (c) Seed fusion,⁴⁰ (d) Geminant branching from multiple nuclei on a single seed particle that grow and then merge to create a branch point.⁴⁰ (e) Deposition of metal seed particles along the length of a nanorod that initiate the growth of a branch.^{44,52}

9.3.4 Reaction yield

Table 9.1 summarizes the dimensions of the nanorods, along with the yields, of various Ge nanorod reactions. The Ge:Bi and Na:Bi ratios, as well as reaction temperature, influenced the nanorod dimensions and the reaction yield. In all cases, the reaction yields are less than 50%. This is due to the decomposition pathway of DPG to Ge. In this temperature range in solution, DPG decomposes to GeH₄ and tetraphenylgermane (QPG) by phenyl redistribution:⁵



QPG ends up as a reaction byproduct as it does not decompose, making the theoretical maximum conversion of DPG to Ge 50%.⁵⁴ Reactions carried out at 350°C had conversions of Ge from DPG ranging from 18 to 35%.

Table 9.1: Summary of nanorod reactions and dimensions.

Na:Bi	Ge:Bi	Temp (°C)	Rod <i>L</i> (nm)	Rod <i>D</i> (nm)	Tip <i>D</i> (nm)	Conversion (%)
4:1	5:1	350	61 ± 7	15.4 ± 3.6	19.5 ± 3.5	27 ± 13
4:1	10:1	350	94 ± 11	14.9 ± 2.6	16.7 ± 2.7	34 ± 12
8:1	20:1	350	156 ± 37	13.2 ± 3.9	15.2 ± 4.0	27 ± 17
4:1	20:1	350	170 ± 20	11.4 ± 1.9	13.1 ± 2.2	35 ± 13
1:1	20:1	350	110 ± 18	10.6 ± 1.7	13.4 ± 3.2	18 ± 9
4:1	20:1	300	21 ± 4	11.8 ± 2.2	20.4 ± 3.2	1.2 ± 0.5
4:1	20:1	400	82 ± 19	20.2 ± 3.8	23.3 ± 3.5	28 ± 12

9.4 CONCLUSIONS

A colloidal synthetic method has been developed to produce Ge nanorods. It relies on Bi nanocrystals to seed SLS growth using diphenylgermane as a reactant that is decomposed in a high temperature boiling solvent. TOPO was also essential as a capping

ligand for obtaining redispersible, crystalline nanorods with relatively narrow size distributions. Increased amounts of PVP-HDE copolymer led to significant branching of the nanorods.

This method yields Ge nanorods with diameters of 10-15 nm and systematically tunable length. Thus, there is the potential for studying the influence of quantum confinement on optical properties of Ge. The nanorod diameter, however, needs to be slightly smaller, in the sub-10 nm diameter range for this. The ability to synthesize much smaller diameter Bi nanocrystals would be able to yield this material. Studies are underway to develop a method to produce nanorods of much narrower diameter.

9.5 ACKNOWLEDGEMENTS

Authors that contributed to this work include: Justin T. Harris and Brian A. Korgel. We thank ISP Technologies, Inc. for providing samples of PVP / HDE copolymer and J. P. Zhou for assistance in acquiring TEM images. Funding was provided by the Robert A. Welch Foundation (Grant no. F-1464).

9.6 REFERENCES

1. Heath, J. R.; Shiang, J. J.; Alivisatos, A. P. *J. Chem. Phys.* **1994**, *101*, 1607.
2. Lambert, T. N.; Andrews, N. L.; Gerung, H.; Boyle, T. J.; Oliver, J. M.; Wilson, B. S.; Han, S. M. *Small* **2007**, *3*, 691.
3. Wilcoxon, J. P.; Provencio, P. P.; Samara, G. A. *Phys. Rev. B* **2001**, *64*, 035417.
4. Chou, N. H.; Oyler, K. D.; Motl, N. E.; Schaak, R. E. *Chem. Mater.* **2009**, *21*, 4105.
5. Codoluto, S. C.; Baumgardner, W. J.; Hanrath, T. *Cryst. Eng. Comm.* **2010** *12*, 2903.
6. Lee, D. C.; Pietryga, J. M.; Robel, I.; Werder, D. J.; Schaller, R. D.; Klimov, V. I. *J. Am. Chem. Soc.* **2009**, *131*, 3436.
7. Min, S.; Tsu-Jae, K. *IEEE Electron Device* **2003**, *50*, 1934.
8. Holman, Z. C.; Kortshagen, U. R. *Langmuir* **2009**, *25*, 11883

9. Kan, S.; Mokari, T.; Rothenberg, E.; Banin, U. *Nat. Mater.* **2003**, *2*, 155
10. Wang, F. D.; Buhro, W. E. *J. Am. Chem. Soc.* **2007**, *129*, 14381.
11. Alivisatos, A. P. *Science* **1996**, *271*, 933.
12. Smith, D. A.; Holmberg, V. C.; Rasch, M. R.; Korgel, B. A. *J. Phys. Chem. C* **2010**, *114*, 20983.
13. Li, Y.; Li, X.; Yang, C.; Li, Y. *J. Mater. Chem.* **2003**, *13*, 2641.
14. Chen, C.-C.; Chao, C.-Y.; Lang, Z.-H. *Chem. Mater.* **2000**, *12*, 1516.
15. Bunge, S. D.; Krueger, K. M.; Boyle, T. J.; Rodriguez, M. A.; Headley, T. J.; Colvin, V. L. *J. Mater. Chem.* **2003**, *13*, 1705.
16. Le, H. Q.; Chua, S. J.; Koh, Y. W.; Loh, K. P.; Chen, Z.; Thompson, C. V.; Fitzgerald, E. A. *Appl. Phys. Lett.* **2005**, *87*, 101908.
17. Zhang, D.; Qi, L.; Cheng, H.; Ma, J. *J. Colloid Interface Sci.* **2002**, *246*, 413.
18. Lv, R.; Cao, C.; Zhai, H.; Wang, D.; Liu, S.; Zhu, H. *Solid State Commun.* **2004**, *130*, 241.
19. Shweky, I.; Aharoni, A.; Mokari, T.; Rothenberg, E.; Nadler, M.; Popov, I.; Banin, U. *Mater. Sci. Eng. C* **2006**, *26*, 788.
20. Heitsch, A. T.; Hessel, C. M.; Akhavan, V. A.; Korgel, B. A. *Nano Lett.* **2009**, *9*, 3042.
21. Barnard, A. S.; Xu, H.; Li, H.; Pradhan, N.; Peng, X. *Nanotechnology* **2006**, *17*, 5707.
22. Cho, K.-S.; Talapin, D. V.; Gaschler, W.; Murray, C. B. *J. Am. Chem. Soc.* **2005**, *127*, 7140.
23. Barnard, A. S.; Xu, H. *J. Phys. Chem. C* **2007**, *111*, 18112.
24. Tang, Z.; Kotov, N. A.; Giersig, M. *Science* **2002**, *297*, 237.
25. Joo, J.; Son, J. S.; Kwon, S. G.; Yu, J. H.; Hyeon, T. *J. Am. Chem. Soc.* **2006**, *128*, 5632.
26. Manna, L.; Scher, E. C.; Alivisatos, A. P. *J. Am. Chem. Soc.* **2000**, *122*, 12700.
27. Peng, X.; Manna, L.; Yang, W.; Wickham, J.; Scher, E.; Kadavanich, A.; Alivisatos, A. P. *Nature* **2000**, *404*, 59.
28. Peng, Z. A.; Peng, X. *J. Am. Chem. Soc.* **2000**, *123*, 183.
29. Saunders, A. E.; Ghezelbash, A.; Sood, P.; Korgel, B. A. *Langmuir* **2008**, *24*, 9043.
30. Shieh, F.; Saunders, A. E.; Korgel, B. A. *J. Phys. Chem. B* **2005**, *109*, 8538.

31. Lu, X.; Fanfair, D. D.; Johnston, K. P.; Korgel, B. A. *J. Am. Chem. Soc.* **2005**, *127*, 15718.
32. Chockla, A. M.; Korgel, B. A. *J. Mater. Chem.* **2009**, *19*, 996.
33. Zaitseva, N.; Dai, Z. R.; Grant, C. D.; Harper, J.; Saw, C. *Chem. Mater.* **2007**, *19*, 5174.
34. Carmalt, C. J.; Comptom, N. A.; Errington, N. J.; Fisher, G. A.; Moenandar, I.; Norman, N. C. *Inorg. Synth.* **1996**, *31*, 98.
35. Wang, F. D.; Tang, R.; Yu, H.; Gibbons, P. C.; Buhro, W. E. *Chem. Mater.* **2008**, *20*, 3656.
36. During the course of the experiments, we ran out of PVP/HDE copolymer and ordered more. The second batch of polymer led to branching of the nanorods. Therefore, the amount of polymer used was reduced (and optimized) from 0.5 g to 0.67 g in order to obtain the highest quality nanorods without branching.
37. The growth direction was determined by imaging by high resolution TEM of 20 nanorods. All of the nanorods that were imaged exhibited <111> growth direction.
38. Moore, D.; Ding, Y.; Wang, Z. L. *Angew. Chem. Int. Ed.* **2006**, *45*, 5150.
39. Kanaras, A. G.; Sonnichsen, C.; Liu, H. T.; Alivisatos, A. P. *Nano Lett.* **2005**, *5*, 2164.
40. Grebinski, J. W.; Hull, K. L.; Zhang, J.; Kosel, T. H.; Kuno, M. *Chem. Mater.* **2004**, *16*, 5260.
41. Zhang, J.; Yang, Y.; Jiang, F.; Li, J.; Xu, B.; Wang, S.; Wang, X. *J. Cryst. Growth* **2006**, *293*, 236.
42. Kuno, M.; Ahmad, O.; Protasenko, V.; Bacinello, D.; Kosel, T. H. *Chem. Mater.* **2006**, *18*, 5722.
43. May, S. J.; Zheng, J. G.; Wessels, B. W.; Lauhon, L. J. *Adv. Mater.* **2005**, *17*, 598.
44. Dick, K. A.; Deppert, K.; Larsson, M. W.; Martensson, T.; Seifert, W.; Wallenberg, L. R.; Samuelson, L. *Nat. Mater.* **2004**, *3*, 380.
45. Lao, J. Y.; Huang, J. Y.; Wang, D. Z.; Ren, Z. F. *J. Mater. Chem.* **2004**, *14*, 770.
46. Wei, Q.; Meng, G. W.; An, X. H.; Hao, Y. F.; Zhang, L. D. *Nanotechnology* **2005**, *16*, 2561.
47. Hao, Y. F.; Meng, G. W.; Ye, C. H.; Zhang, X. R.; Zhang, L. D. *J. Phys. Chem. B* **2005**, *109*, 11204.
48. Fanfair, D. D.; Korgel, B. A. *Chem. Mater.* **2007**, *19*, 4943.
49. Hu, J. Q.; Bando, Y.; Golberg, D. *Small* **2005**, *1*, 95.

50. Zhai, T. Y.; Zhong, H. Z.; Gu, Z. J.; Peng, A. D.; Fu, H. B.; Ma, Y.; Li, Y. F.; Yao, J. N. *J. Phys. Chem. C* **2007**, *111*, 2980.
51. Hull, K. L.; Grebinski, J. W.; Kosel, T. H.; Kuno, M. *Chem. Mater.* **2005**, *17*, 4416.
52. Wang, D.; Qian, F.; Yang, C.; Zhong, Z. H.; Lieber, C. M. *Nano Lett.* **2004**, *4*, 871.
53. Hanrath, T.; Korgel, B. A. *J. Am. Chem. Soc.* **2002**, *124*, 1424.
54. QPG was not observed to decompose when heated to 400°C in squalane.

Chapter 10: Optical Properties of Colloidal Germanium Nanorods

10.1 INTRODUCTION

Nanostructures exhibit unique properties due to their sub-wavelength size that are useful for various devices. For instance, semiconductor nanowires can be used in optoelectronic devices such as light concentrators,^{1, 2} waveguides,^{3, 4} solar cells,⁵⁻⁷ photodetectors,^{1, 8-13} and lasers.^{14, 15} Nanowires also boast significantly enhanced optical absorption compared to bulk crystals due to light scattering.¹⁶⁻¹⁹ Ge nanowires have interesting electronic,²⁰ mechanical,^{21, 22} and optical properties¹⁹ due to a high index of refraction, low optical dispersion, and infrared transparency.²³ Ge nanorods are particularly appealing as both length and diameter can be controlled, enabling finely tuned optical properties.²⁴

The discrete dipole approximation (DDA) has been used to calculate scattering and absorption of electromagnetic waves by bodies with arbitrary size and geometry.²⁵⁻³¹ Recently, the discrete dipole approximation was used to interpret experimentally-measured optical spectra of Ge nanowires.¹⁹ An absorbance peak was observed at 600 nm and attributed to a maximum in the index of refraction of Ge. We extend this analysis to Ge nanorods through quantitative investigation of the influence of nanorod length on the optical properties. Colloidal Ge nanorods were grown by arrested solution-liquid-solid (SLS) growth using either Au or Bi nanocrystal seeds. Measured spectra are compared with DDA calculations. The 600 nm absorption feature evolves with increasing nanorod length due to increased light trapping and absorption.

10.2 EXPERIMENTAL DETAILS

10.2.1 Materials

Hexadecylamine (HDA, 90%), tetrahydrofuran (THF, anhydrous, inhibitor free, 99%), lithium triethylborohydrate (LiEt₃BH, 1.0M in THF), bismuth (III) chloride (BiCl₃, ≥ 98.0%), lithium bis(trimethylsilyl)amide (LiHMDS, 99%), toluene (anhydrous, 99.8%),

squalane (99%), tri-*n*-octylphosphine oxide (TOPO, 99%), tri-*n*-dodecylamine (TDDA, $\geq 97.0\%$), oleic acid (OA, $\geq 99\%$), dodecanethiol (DDT, $\geq 98\%$), tetrachloroaurate trihydrate ($\geq 99.9\%$), sodium borohydride (NaBH_4 , $\geq 98\%$), toluene (anhydrous, 99.8%), ethanol (EtOH, 99.9%), tetraoctylammonium bromide (TOAB, 98%), and chloroform (CHCl_3 , 99.8%) were purchased from Sigma Aldrich. Diphenylgermane (DPG, $> 95\%$) was purchased from Gelest. All chemicals were used as received without further purification.

10.2.2 Au-seeded Ge nanorod synthesis

Dodecanethiol-coated Au nanocrystals (2 nm diameter) were synthesized using established methods³² and stored as a dispersion in toluene at a concentration of 50 mg mL⁻¹ in a nitrogen-filled glove box. In a typical Au-seeded Ge nanorod reaction, 2 g TOPO and 4 mL squalane were added to a 4-neck flask and attached to a Schlenk line, degassed under vacuum at 100°C with vigorous stirring (< 500 mTorr) for 30 minutes, and then blanketed with nitrogen. This solvent mixture was then heated to 380°C. Meanwhile, in a nitrogen-filled glove box, 0.2 mL of the Au nanocrystal stock solution was combined with 19 μL of DPG (Ge:Au mole ratio of 2:1) and diluted with 2 mL of TDDA. The solution was drawn into a 3 mL syringe, removed from the glove box and injected into the reaction flask with the squalane/TOPO mixture at 380°C. After 5 min, the flask was removed from the heating mantle and allowed to cool to room temperature. 10 mL of toluene was added. Following brief sonication to remove product from the flask walls, the reaction solution was transferred to a centrifuge tube and centrifuged at 8000 rpm for 5 minutes. The supernatant was discarded and the precipitate was redispersed in 10 mL of chloroform. 2 mL of ethanol was added and the mixture was centrifuged again at 8000 rpm for 5 minutes. This solvent/antisolvent washing procedure was repeated a third time. The nanorods were dispersed in chloroform and stored for further use.

10.2.3 Bi-seeded Ge nanorod synthesis

Ge nanorods were grown from Bi nanocrystals using a modified procedure.²⁴ In a typical reaction, 1 g of HDA was added to a 4-neck flask and attached to a Schlenk line, heated to 100°C with vigorous stirring under vacuum (<500 mTorr) for 30 minutes and then blanketed with nitrogen. In a nitrogen-filled glovebox, 150 mg (0.5 mmol) of BiCl₃ was dissolved in 10 mL of THF. 100 μL of this BiCl₃/THF solution (5 μmol of BiCl₃) was then added to 1 mL of toluene along with 16 mg (0.1 mmol) of LiHMDS (Li:Bi mole ratio of 20:1). A second reactant solution of 10 μL of LiEt₃BH and 90 μL THF was also prepared in the glove box. The two reactant solutions were drawn into syringes, taken out of the glove box and rapidly sequentially into the degassed HDA at 100°C. The BiCl₃ solution was added first, followed by the LiEt₃BH solution, waiting fifteen seconds between each injection. This leads to Bi nanocrystal formation.²⁶ After stirring an additional fifteen seconds, a solution of 2 g TOPO and 200 μL oleic acid in 4 mL squalane was injected into the flask. The flask contents were held at 100°C and placed under vacuum (<500 mTorr) for 15 minutes to degas the squalane/TOPO mixture. After blanketing with nitrogen, the mixture was heated to 350°C. While heating, a DPG reactant solution was prepared in the glove box by adding 180 μL of DPG to 0.5 mL of squalane. This DPG solution was withdrawn from the glove box by syringe (1 mL) and rapidly injected into the Bi nanocrystal-containing reaction mixture at 350°C. The Ge:Bi mole ratio in the reaction was 200:1. Aliquots (0.5 mL) were extracted from the reaction into vials, followed by the addition of 5 mL of toluene to reduce the temperature and quench the reaction.

Nanorods were precipitated from each aliquot by adding 2 mL EtOH followed by centrifugation at 8000 rpm for 5 minutes. The supernatants were discarded and the Ge nanorod precipitate was redispersed in 5 mL toluene. The nanorods were reprecipitated with 2 mL of EtOH and centrifuged again. This purification step was repeated a third time before dispersing the nanorods in chloroform for storage until further use.

10.2.4 Materials characterization

Transmission electron microscopy (TEM) was performed using a FEI Tecnai Spirit BioTwin TEM operated at 80 kV. TEM samples were drop-cast from chloroform onto 200 mesh lacey-carbon copper TEM grids (Electron Microscopy Sciences).

Ultraviolet–visible–near-infrared (UV–Vis–NIR) absorbance spectra were measured at room temperature using a Varian Cary 500 UV-Vis spectrophotometer in transmission mode. Ge nanorod dispersions were diluted enough to have absorbance less than 1 over the entire wavelength range.

10.3 RESULTS AND DISCUSSION

10.3.1 Length Control of Bi-seeded Ge nanorods

Ge nanorods of controlled length can be made using Bi nanocrystal seeds by limiting the reaction time, as shown in Figure 10.1. Immediately following DPG addition, there is an initial lag time before nanorod formation for almost 1 minute, but then nanorod growth proceeds fairly rapidly with little change in nanorod diameter. After two minutes, nanorods are 200–300 nm long, and after 10 minutes they are longer than 5 μm . Table 10.1 summarizes the nanorod dimensions. The average nanorod diameter is close to 50 nm regardless of reaction time with slightly larger Bi seeds (100nm) at the tips of the rods. Many seed particles do not actually participate in the reaction and it appears that once nanorod growth begins, the barrier for continued crystal growth is a significantly lower than the barrier to seed new nanorods.²⁴

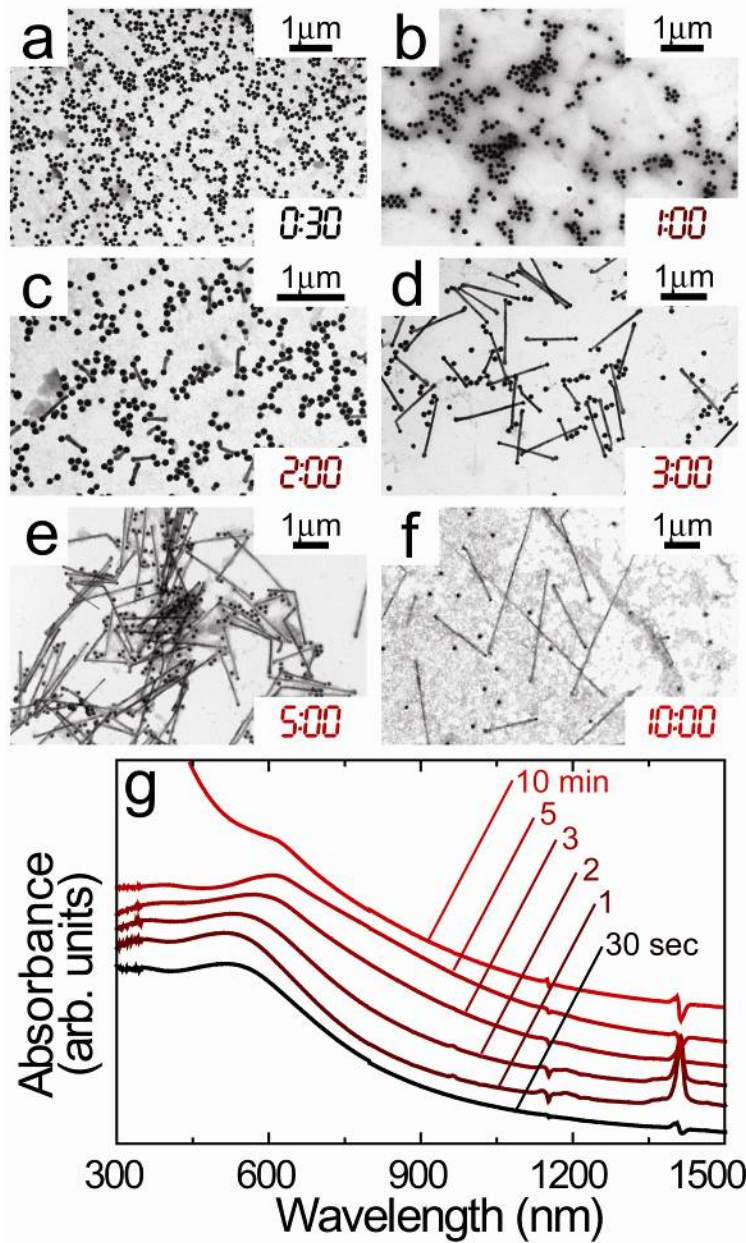


Figure 10.1: TEM images of Ge nanorods isolated at different times during the reaction, (a) 30 sec, (b) 1 min, (c) 2 min, (d) 3 min, (e) 5 min, and (f) 10 min, along with their (g) absorbance spectra. The spectra in (g) are offset for clarity. The sharp peaks at 1400 nm are from chloroform. An absorbance spectrum for Bi nanocrystals in chloroform is provided in Supporting Information.

Table 10.1: Ge nanorod dimensions determined from TEM.

Time	L_{rod} (nm)	D_{rod} (nm)	L_{Rod} / D_{Rod}	D_{Bi} (nm)
30 sec	21 ± 5	42 ± 7	0.5	99 ± 8
1 min	21 ± 8	37 ± 7	0.6	103 ± 10
2 min	265 ± 9	57 ± 11	4.6	101 ± 9
3 min	1180 ± 270	60 ± 11	19.7	105 ± 15
5 min	2430 ± 320	54 ± 14	45.0	105 ± 16
10 min	2670 ± 1150	53 ± 17	50.4	94 ± 21

10.3.2 Bi-seeded Ge nanorod optical properties

Figure 10.1g shows the absorbance spectra of the Bi-seeded Ge nanorods as a function of growth time. The absorbance spectra show a peak that is at 550 nm for nanorods obtained early in the reaction, which evolves to slightly longer wavelength up to about 700 nm as the nanorods increase in length. A similar optical feature has been observed for higher aspect ratio Ge nanowires.^{1,19} As shown in Figure 10.2b, Ge exhibits peaks in both the real and imaginary parts of the complex index of refraction, $\tilde{N} = n + ik$, in this wavelength range. To understand the appearance and length-dependent evolution of the nanorod absorbance spectra, optical properties of Ge nanorods were calculated using the discrete dipole approximation (DDA).

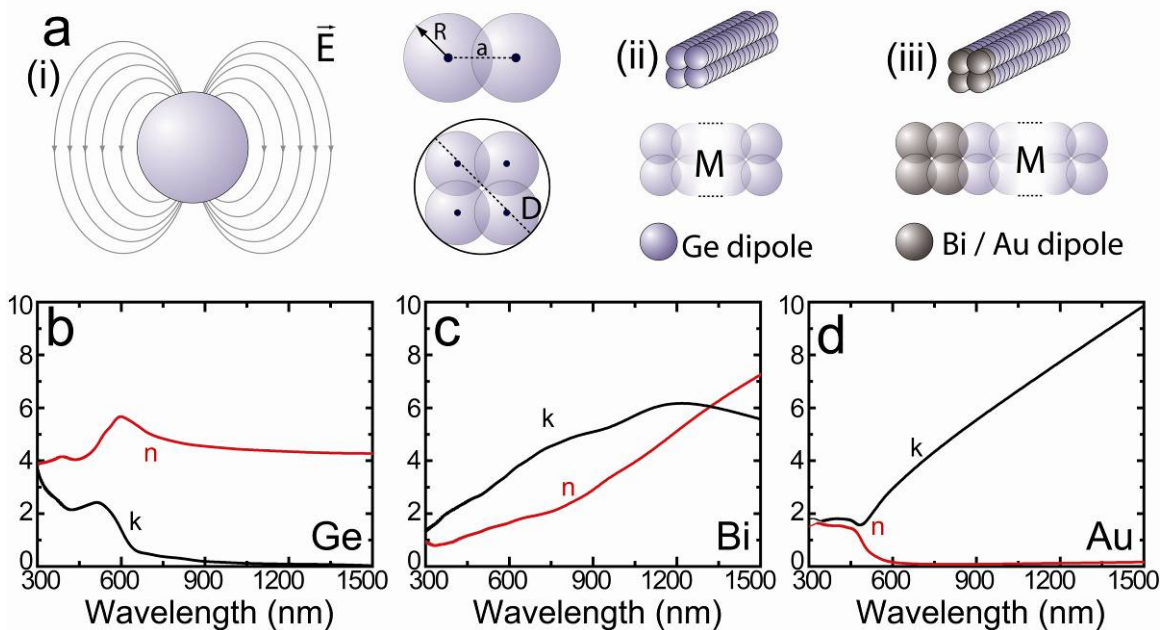


Figure 10.2: (a) Representation of a (i) dipole and interacting dipoles in a (ii) $2 \times 2 \times M$ arrangement (ii) without and (iii) with metal tips. M is the number of dipole layers needed to approximate the nanorod length. The real (n) and imaginary (k) components of the complex index of refraction for (b) Ge,³³ (c) Bi,^{34,35} and (d) Au³³ are shown.

10.3.3 DDA calculations of Ge nanorod absorbance spectra.

10.3.3.1 The DDA Model

Absorbance spectra were calculated by modeling Ge nanorods (either with or without attached Au or Bi seeds) as an array of interacting discrete dipoles.^{19, 24, 36-38} The DDA provides a convenient description of objects of arbitrary shape for calculating optical properties, provided that the inter-dipole spacing is small relative to the wavelength of light.^{19, 25-28} Previously, we used the DDA to interpret absorbance spectra of Ge nanowires, neglecting possible contributions from the Au nanocrystals used to seed growth.¹⁹ For nanorods, the seed particles make up a significant fraction of the structure and should not be ignored.

Ge nanorods were also grown using Au seeds, however, it was not possible to control the nanorod length or adequately prevent aggregation (see Figure H3 in Appendix

H) so absorbance spectra were not measured. Nonetheless, DDA calculations were performed for Au-tipped nanorods to provide a comparison with Bi-tipped nanorods.

Figure 10.2 illustrates the modeling of nanorods as a $2 \times 2 \times M$ array of interacting dipoles with radius R and center-to-center spacing a . The dipole interactions depend on the complex index of refraction of the materials, and bulk values of n and k (also shown in Figure 10.2) were used for the calculations.

The optical extinction, absorption and scattering cross-sections can be calculated if the polarization of each dipole is known. For a three-dimensional collection of interacting dipoles, the polarization of each dipole \vec{P}_j , is determined by solving the set of $3N$ linear equations,

$$\sum_{k=1}^N \tilde{A}_{jk} \vec{P}_j = \vec{E}_{inc,j} \quad (1)$$

where $\vec{E}_{inc,j}$ is the incident electric field and \tilde{A}_{jk} is a 3×3 matrix:

$$\tilde{A}_{jk} = \frac{e^{i\kappa r_{jk}}}{r_{jk}} \left[\kappa^2 (\hat{r}_{jk} \hat{r}_{jk} - \tilde{I}_3) + \frac{i\kappa r_{jk} - 1}{r_{jk}^2} (3\hat{r}_{jk} \hat{r}_{jk} - \tilde{I}_3) \right] \quad (2)$$

$\kappa = 2\pi/\lambda$ (λ is the wavelength of light), r_{jk} is the separation between dipoles j and k , \hat{r}_{jk} is the unit vector along r_{jk} , and \tilde{I}_3 is the 3×3 identity matrix. The self-interaction term, \tilde{A}_{jj} , is:

$$\tilde{A}_{jj} = \tilde{\alpha}_j^{-1} \quad (3)$$

where $\tilde{\alpha}_j$ is the complex polarizability of dipole j , which is related to the complex dielectric function and of the material (e.g., Ge, Au, Bi), ϵ_j , and the surroundings (e.g., chloroform), ϵ_{hst} , through the Clausius–Mossotti relation:

$$\tilde{\alpha}_j = R^3 \frac{\epsilon_j - \epsilon_{hst}}{\epsilon_j + 2\epsilon_{hst}} \quad (4)$$

A radiative corrective term is also used:^{19, 27, 28}

$$\tilde{\alpha}_{cor,j} = \frac{\tilde{\alpha}_j}{1 - i \frac{2\kappa^3}{3} \tilde{\alpha}_j} \quad (5)$$

Dipole periodicity a , and radius R , are related to the nanorod diameter D :

$$D = 2R + \sqrt{2}a \quad (6)$$

with a relationship between a and R of

$$\frac{a}{R} = 1.688 \quad (7)$$

This ratio accounts for multipolar corrections to the depolarization factor, as described by Podolskiy *et al.*³⁹ The extinction, absorption, and scattering cross-sections are calculated using \vec{P}_j :

$$C_{ext} = \frac{4\pi\kappa}{|E_0|^2} \sum_{j=1}^N \text{Im}(\vec{E}_{inc,j}^* \cdot \vec{P}_j) \quad (8)$$

$$C_{abs} = \frac{4\pi\kappa}{|E_0|^2} \sum_{j=1}^N \left\{ \text{Im}[\vec{P}_j \cdot (\tilde{\alpha}_j^{-1})^* P_j^*] - \frac{2}{3} \kappa^3 (\vec{P}_j \cdot \vec{P}_j^*) \right\} \quad (9)$$

$$C_{ext} = C_{abs} + C_{sca} \quad (10)$$

Furthermore, the local electric field for each dipole, $\vec{E}_{loc,j}$, can be calculated:

$$\vec{P}_j = \tilde{\alpha}_j \vec{E}_{loc,j} \quad (11)$$

In Equations 8 and 9, components labeled with ‘*’ are complex conjugates.

10.3.3.2 Calculated extinction cross-sections for Ge nanorods without metal tips

Figure 10.3 shows extinction spectra calculated with incident electric field polarized perpendicular or parallel to the long axis of nanorods with various diameter and aspect ratio. Following this convention, incident fields will be referred to simply as parallel or perpendicular in the remainder of the manuscript. When the incident electric field is perpendicular, the extinction spectra are unaffected by changes in nanorod dimensions. When the incident electric field is parallel, the absorbance peak at around 500 nm for the shortest rods sharpens and red-shifts with increasing aspect ratio. A similar peak sharpening and red-shift of the absorbance peak was observed experimentally with increased nanorod length.

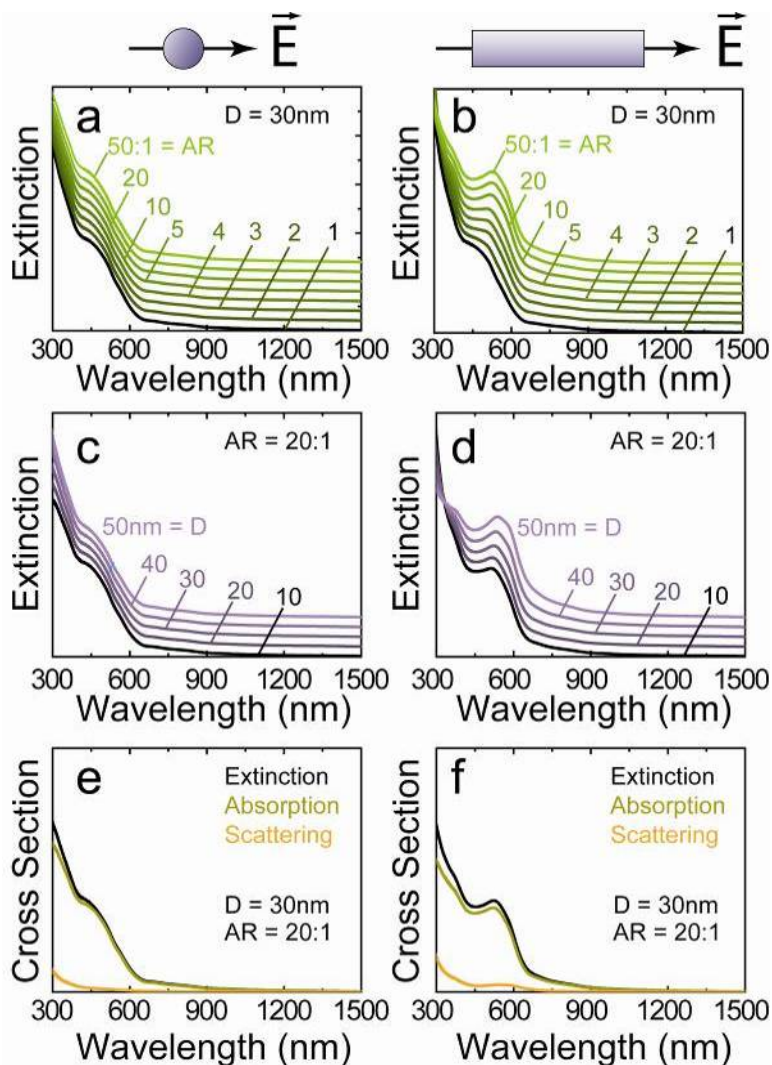


Figure 10.3: Extinction spectra calculated using the DDA approximation for (a, b) 30 nm diameter Ge nanorods with varying aspect ratio (AR) or (c, d) nanorods with AR=20 and varying diameter D . (e, f) Relative contribution of absorption and scattering to the extinction cross-section of a 30 nm diameter nanorod with an aspect ratio of 20. Spectra were calculated with incident electric field polarized either (a, c, e) perpendicular or (b, d, f) parallel to the long axis of the nanorod.

As shown in Figures 10.3c and 10.3d, the calculated spectra are unaffected by differences in diameter, regardless of the polarization orientation of the incident field. Extinction spectra calculated for 200 nm long Ge nanorods (Appendix H) were also unaffected by changes in diameter.

Figures 10.3e and 10.3f show the separate contributions of absorption and scattering to the Ge nanorod extinction cross-section. For these nanorods, with 30 nm diameter and an aspect ratio of 20, absorption is the dominant contributor. Scattering is relatively minor, but becomes more significant for a parallel incident field.

10.3.3.3 Calculated extinction cross-sections for Ge nanorods with Bi or Au tips

Contributions to the optical properties from the Au and Bi seeds at the tips of Ge nanorods were also examined, shown in Figure 10.4. The calculated spectra of Bi-tipped Ge nanorods show qualitative agreement with the experimental data with an absorption peak at around 550 nm and increasing low wavelength absorbance with longer nanorods. Only nanorods with an aspect ratio less than 10, much shorter than those examined experimentally, showed pronounced optical features related to Bi.

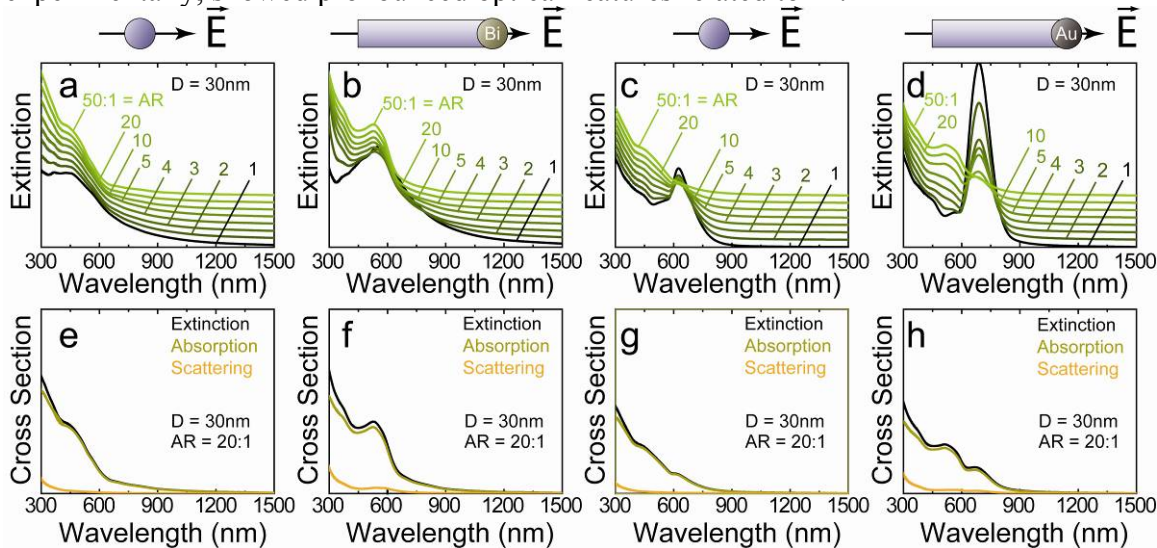


Figure 10.4: Extinction spectra calculated using the DDA for Ge nanorods with (a, b) Bi and (c, d) Au tips. Simulations were performed with the incident electric field polarized either (a, c) perpendicular or (b, d) parallel to the length of the nanorods. (e, f, g, h) Relative contributions of scattering and absorption to the extinction cross-sections. The reported aspect ratios are determined by only considering the Ge portion of the nanorods and do not include the metal tip.

The optical properties of Ge nanorods were affected much more significantly by Au tips, with aspect ratios even as high as 20 showing still a significant Au surface plasmon-related absorption near 700 nm.^{40, 41} Nanorods with an aspect ratio of 20, however, show equally pronounced Ge- and Au-related peaks. When the polarization of the incident field is perpendicular to the nanorod length, the peak associated with the Ge nanorod does not change, but the relative contribution from the Au tip decreases significantly as the nanorods get longer. A similar effect is observed for the nanorods with Bi at their tips. Without metal at the tip of the Ge nanorods, the extinction did not change with differences in length when the polarization of the incident field was perpendicular to the length of the nanorods. However, with Bi at the tips of the nanorods, the low wavelength absorption increases significantly as the length increases (Figure 10.4a). Furthermore, the effect on the optical properties from the metal tips was more significant when the nanorods were oriented parallel to the incident electric field. This suggests coupling between the Ge and Au/Bi dipoles at the junction and is indicative of angle-dependent resonance modes like those observed for Ge nanowires.¹

Figure 10.5 shows the scattering cross-sections calculated for Ge nanorods with and without metal tips. For a perpendicular incident electric fields the scattering cross-section related to the Ge segment is unaffected by changes in aspect ratio. Furthermore, the features related to Au (scattering at 700 nm) and Bi are reduced with increased length. A peak in the scattering cross-section for a parallel incident electric field is observed between 500–600nm for all three cases (Figures 10.5b, 10.5d, and 10.5f). This peak occurs at the same wavelength as observed in the extinction cross-section, discussed above, indicating a minor scattering contribution to this peak. It should be noted, however, that this feature may be due to fundamental limitations of DDA calculations. Since the scattering cross-section is such a small contribution in this case, these peaks could be an artifact resulting from small discrepancies between the calculated absorption and extinction cross sections.²⁶

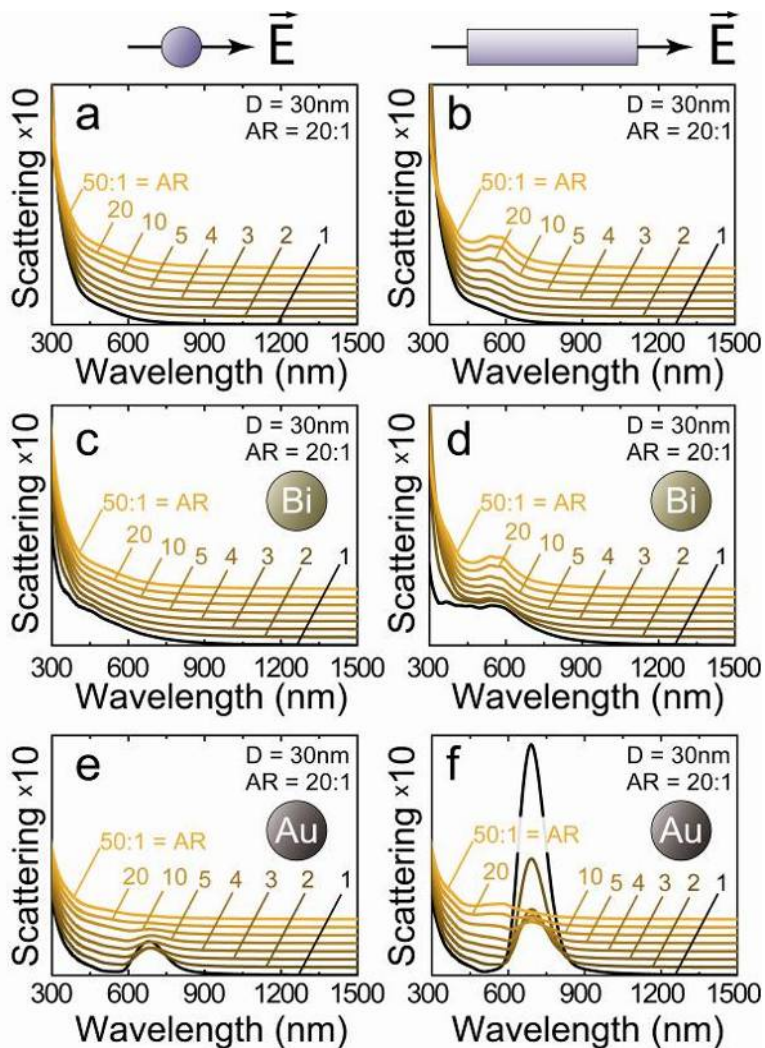


Figure 10.5: Scattering cross-sections (magnified by 10x compared to Figures 10.4e-h) calculated for 30 nm diameter Ge nanorods with (a, b) no metal tips, (c, d) Bi tips or (e, f) Au tips with the incident electric field polarized (a, c, e) perpendicular or (b, d, f) parallel to long axis of the nanorod.

10.3.3.4 Electric field distribution within the Ge nanorods

Figure 10.6 shows electric fields within an illuminated Ge nanorod without a metal tip. The internal electric fields are much more intense for a parallel incident field. The electric field concentrates at the ends of the nanorods. The internal electric field is stronger for a parallel incident field compared to a field with perpendicular incidence and peaks in intensity at 590 nm (2.1 eV). This resonant electric field results from a peak in the imaginary part of the dielectric function (Figure 10.7a), and is responsible for the

observed peak in the extinction cross-section. The complex dielectric function $\varepsilon = \varepsilon' + i\varepsilon''$, is related to the complex index of refraction with $\varepsilon' = n^2 - k^2$ and $\varepsilon'' = 2nk$. ε' is related to energy storage and ε'' to energy dissipation within the medium. Figure 10.7 reveals a peak in the real part of the Ge dielectric constant at 590nm. Ge stores energy best at this wavelength, which manifests in an enhanced electric field at this point. The peak in ε'' occurs at slightly lower wavelength of about 540 nm, and is responsible for the increased absorbance in the experimental data near this wavelength—evident in all calculated extinction cross-sections in a parallel electric field. This is the direct E(1) transition energy in Ge, near the midpoint of Γ and L symmetry points in the Ge Brillouin zone.⁴² As all spectra are nearly equivalent for perpendicular electric fields, the feature at 590 nm in both the calculated extinction spectra and internal electric field is only observed for parallel incident electric fields. An additional observation is that a perpendicular incident field results in low internal electric fields, whereas a parallel incident field causes an enhanced internal field down the length of the rod. Both situations show behavior at the edges that is much different than the rest of the nanorod. Figure 10.7 also shows ε' and ε'' for Bi and Au.

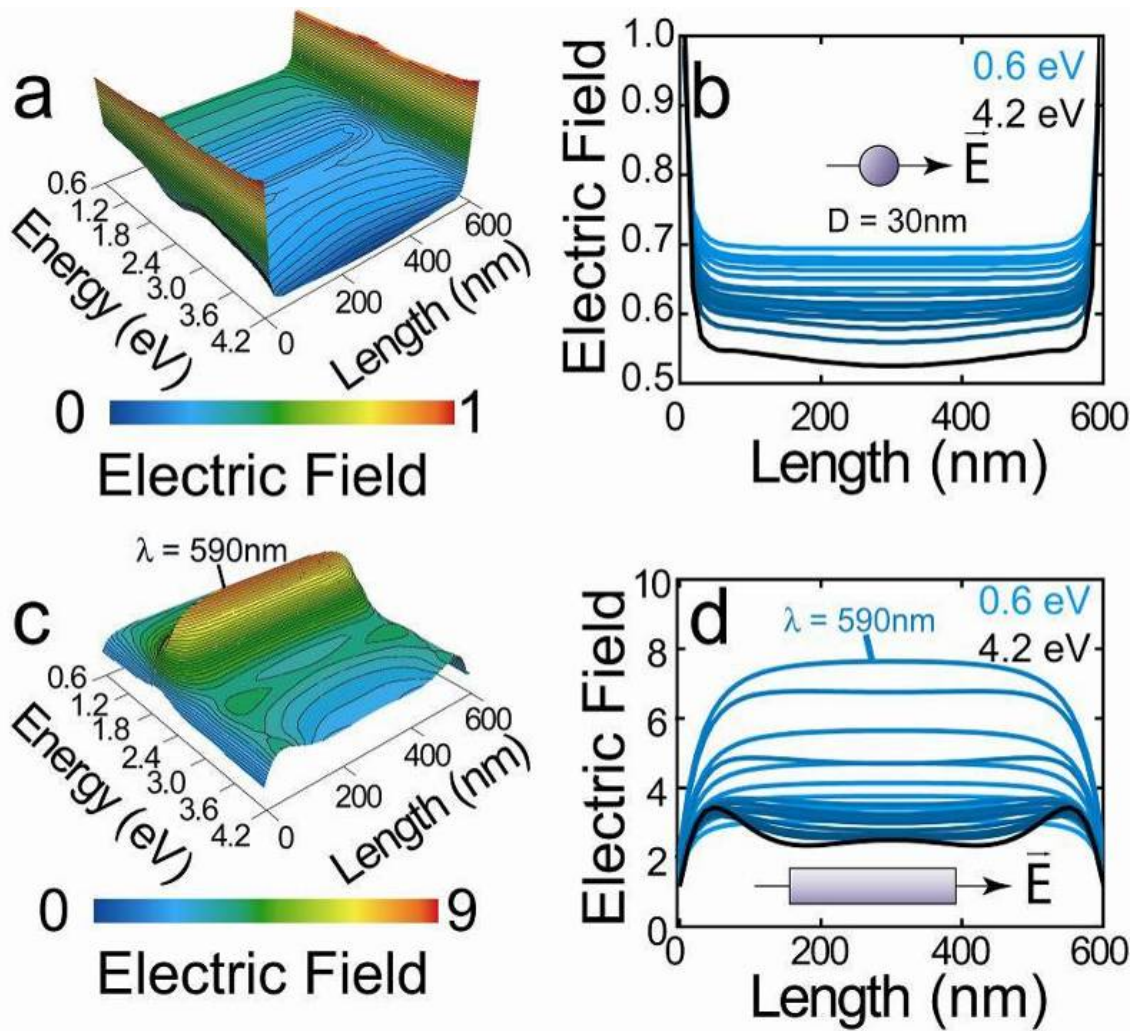


Figure 10.6: Internal electric field calculated using Equation (11) for a 30 nm diameter Ge nanorod with an aspect ratio of 20 with the polarization of the incident field oriented (a, b) perpendicular and (c, d) parallel to the nanorod length.

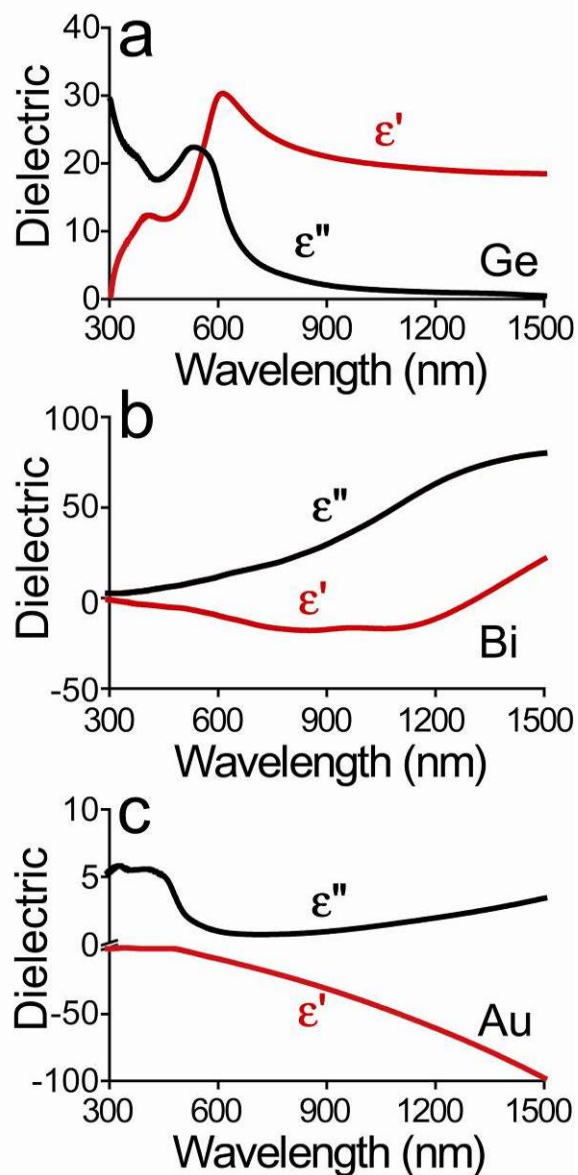


Figure 10.7: Real (ϵ') and imaginary (ϵ'') parts of the complex dielectric function for (A) Ge, (b) Bi, and (c) Au.

10.3.3.5 DDA calculations: varying dipole geometry

Various dipole arrangements were tested to probe the differences in electric field along the edges, faces, and in the interior of the nanorods. The 2x2 dipole cross section is sufficient to simulate extinction and absorption spectra; however, since all of the dipoles in a single 2x2 layer are equivalent, there is no information provided in the calculations regarding local variations in electric field within the nanorod; the calculated electric field

applies only to the nanorod surface. Furthermore, the cross-sectional shape of a true Ge nanorod is more accurately described as rectangular or hexagonal.⁴³ A variety of dipole arrangements were surveyed, including cross, hexagon, and 3x3 arrangements. The extinction spectra are not noticeably affected by the various dipole arrangements (see Figure H5 in Appendix H). Figure 10.8 shows surface and contour plots of the electric field for dipoles located along the edges, faces, and along the central axis of the nanorod for a 3x3 cross-sectional dipole arrangement. Charge builds up at sharp edges, causing the electric field to be most intense along the four corner edges (Figure 10.8a) and weakest in the center of the rod (Figure 10.8c).⁴⁴ Down the length of the structure, the electric field is weakest at the ends of the nanorod. All dipoles show an enhanced electric field at 590 nm, which again is related to ε' . Similar data are shown in Appendix H using a cross (Figure H6) and hexagonal (Figure H7) dipole arrangement. Comparison between these data shows higher electric fields for dipoles with sharper exposed edges. In contrast, the more overlap there is between the center dipole and those that surround it, the more the internal electric field is reduced for that center dipole. For instance, the center dipole in the hexagonal arrangement overlaps with all six surface dipoles and has a lower electric field than the center dipole in either the cross or 3x3 arrangement, which each overlap with only four dipoles (the corner edge dipoles in the 3x3 arrangement do not overlap with the center dipole).

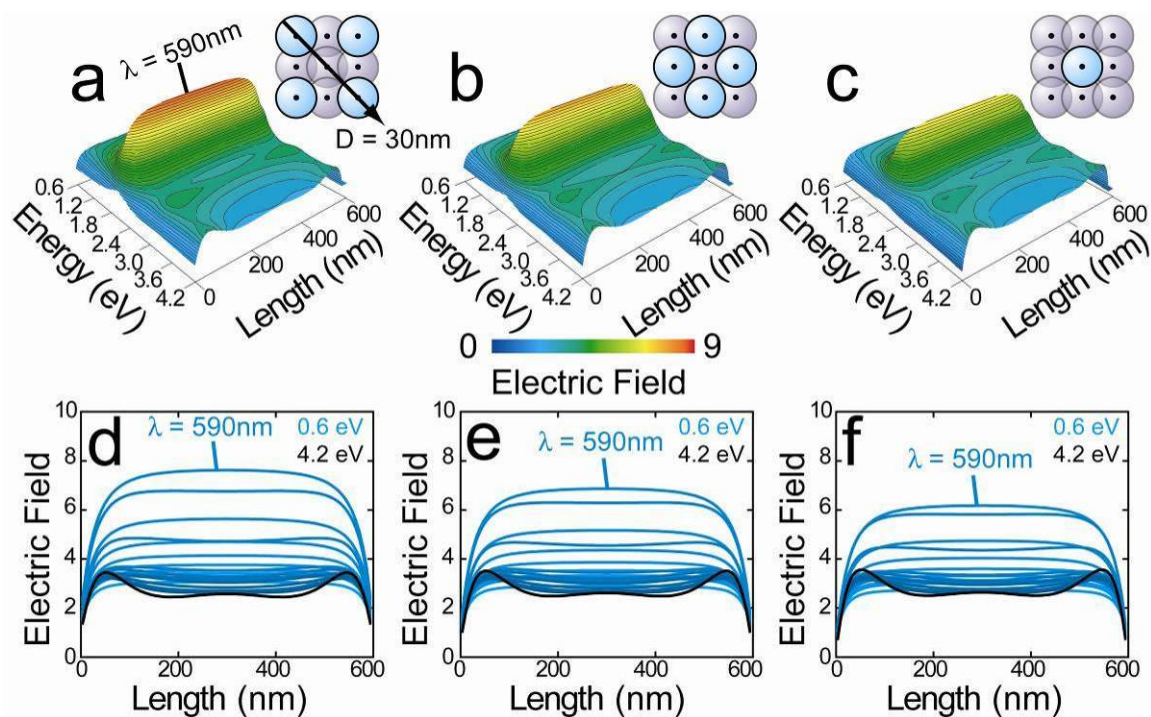


Figure 10.8: Internal electric fields calculated with the polarization of the incident electric field oriented parallel to the nanorod length for (a) corner dipoles (highlighted in blue) along the edges of the nanorod, (b) side dipoles along the faces of the nanorod and (c) central dipoles within the core of the nanorod. (d, e, f) Corresponding cross-sectional plots showing electric field contours for specific wavelengths.

The internal electric field was also calculated for Ge nanorods with Bi tips, shown in Figure 10.9. The internal electric field in the Ge segment is significantly altered near the Bi tip. As energy increases from 0.6 to 4.2 eV, the internal electric field of the Bi tip is depressed, in contrast to a tip-free nanorod, which alters the local electric field in the Ge nanorod in the immediate vicinity of the tip. This manifests itself as a significant peak in electric field intensity in the first 50 nm of Ge immediately adjacent to the Bi tip. A similar effect is observed for a parallel incident electric field. The presence of the Bi tip causes a peak in the internal electric field within the first 20 nm of the Ge nanorod at energies slightly below 1.8 eV. This effect is manifested in the extinction spectrum (Figure 10.4b), where the absorption peak extends beyond 600 nm (compared to 550 nm for the tip-free rods shown in Figure 10.3b, for example). Only the first 200 nm of the

rods are shown. Far away from the metal tip, the internal electric field is unaffected by the metal tip and behaves as shown in Figure 10.6c and Figure 10.8. Au-tipped Ge nanorods were also examined and can be found in Appendix H (Figure H8).

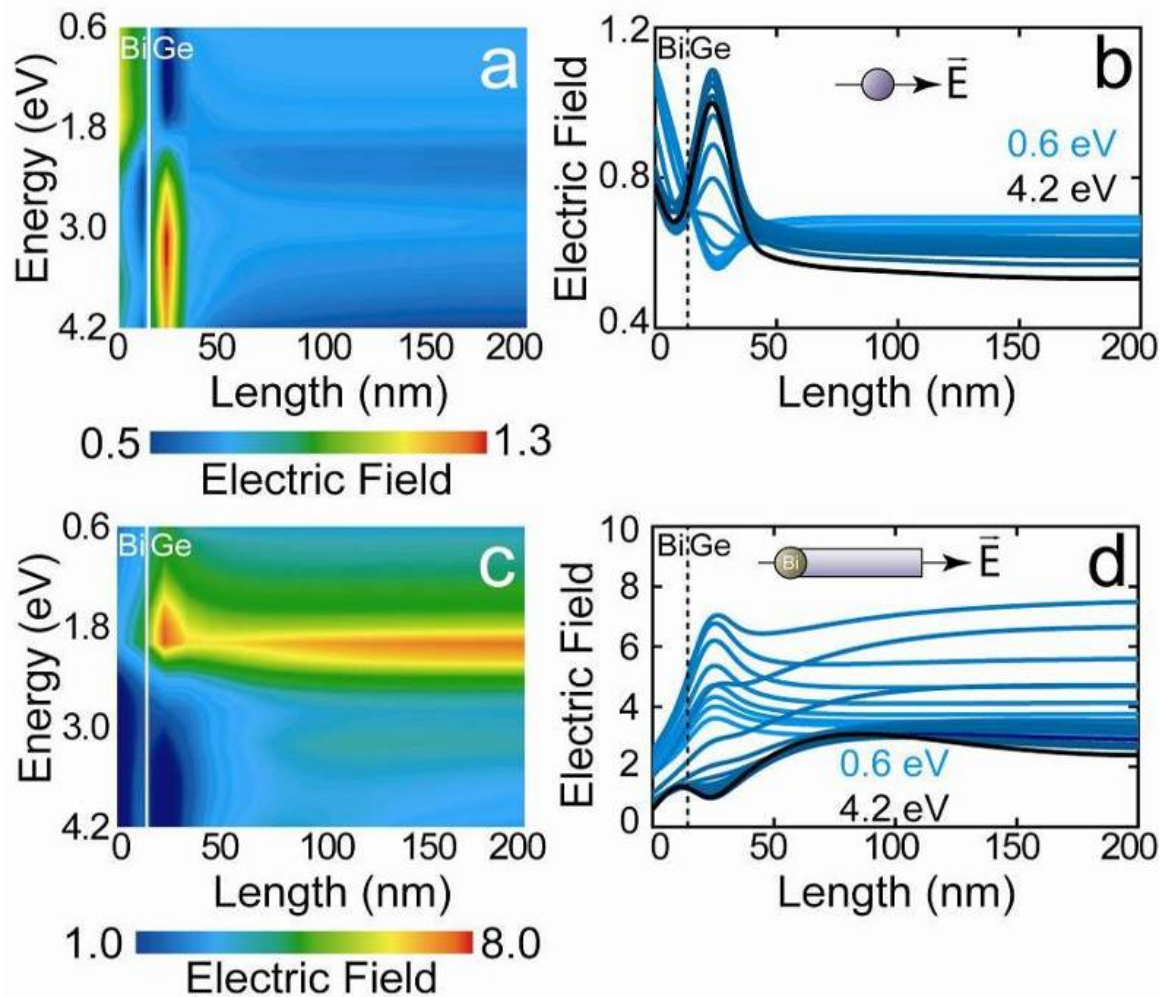


Figure 10.9: Intensity plots showing the local electric field near the tip of Ge nanorod (30 nm diameter; aspect ratio of 20) with Bi seeds for (a) perpendicular and (c) parallel incident electric fields with (b, d) corresponding cross-sectional plots showing constant wavelength contours.

Absorption is enhanced near 600 nm for Ge nanorods of increasing length. We have correlated the evolution of this peak to the optical constants of Ge. As a further explanation of the trend observed in the experimental data, we turn to light refraction. The Ge nanorods are suspended in a solution of chloroform. There is a large difference

between the dielectric constants of chloroform and Ge and incident light can only escape the nanorod if it is traveling normal to the Ge–chloroform interface, plus or minus $\sim 10^\circ$. Figure 10.10 illustrates this point, showing the wavelength-dependent critical angle for total internal reflection of light traveling within a Ge structure suspended in chloroform. For 600 nm light, the critical angle is at its smallest; angles greater than 8° off normal result in total internal reflection. This suggests that significant light trapping occurs in Ge nanorods, effectively increasing the absorption path length. This effect is more pronounced for longer rods, and can be used to engineer nanorod optical devices.¹ The scattering cross-sections are much lower than absorbance due to two main contributing factors. First, light scattering scales with λ^{-4} and is low at most wavelengths. Furthermore, only light with an off-normal incident angle between 0 - 10° to the Ge–chloroform interface is free to escape the nanorod and is absorbed, leaving a small angular window for light scattering.

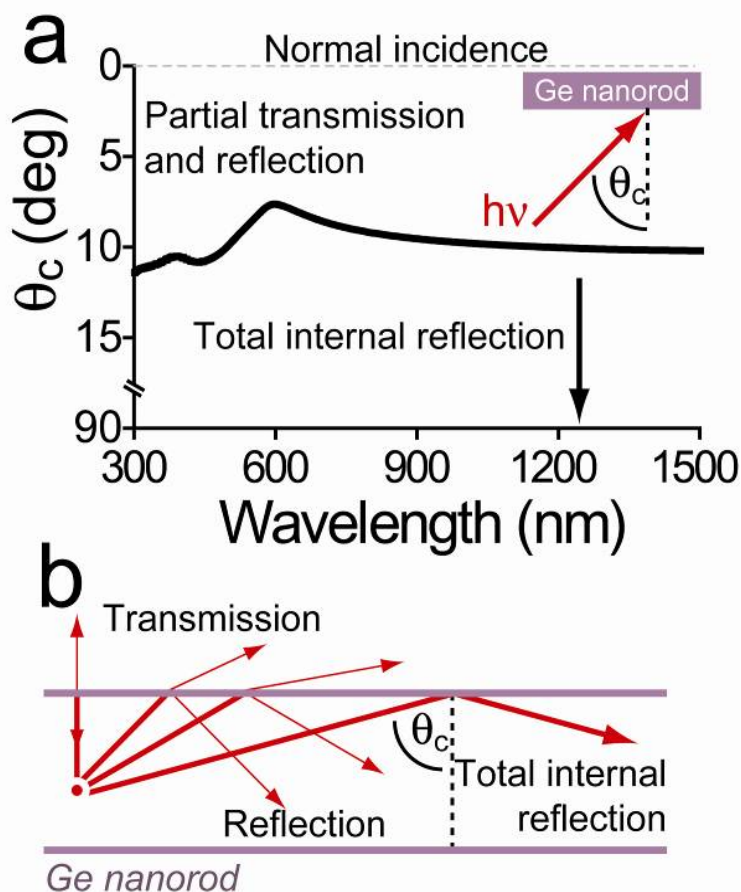


Figure 10.10: (a) Critical angle for total internal reflection within a Ge nanorod suspended in chloroform. (b) Schematic for angle dependence of partial reflection / transmission versus total internal reflection of light impinging on an interface.

Internal electric fields are very different depending on whether the incident field was aligned parallel and perpendicular to the nanorod axis. This is due to the actual orientation (i.e., polarization) of the individual dipoles. When the incident electric field is parallel with the rod axis, the dipoles are aligned and interact more strongly with one another. Figure 10.11 shows the angular dependence of the electric field within the nanorod on the orientation of the incident electric field, displaying the transition from perpendicular to parallel electric field orientation. The general shape of the electric field does not change with increasing angle. As the angle approaches 90° relative to the

surface normal (parallel to the nanorod axis), the dipoles become more aligned and result in an intensified internal electric field.

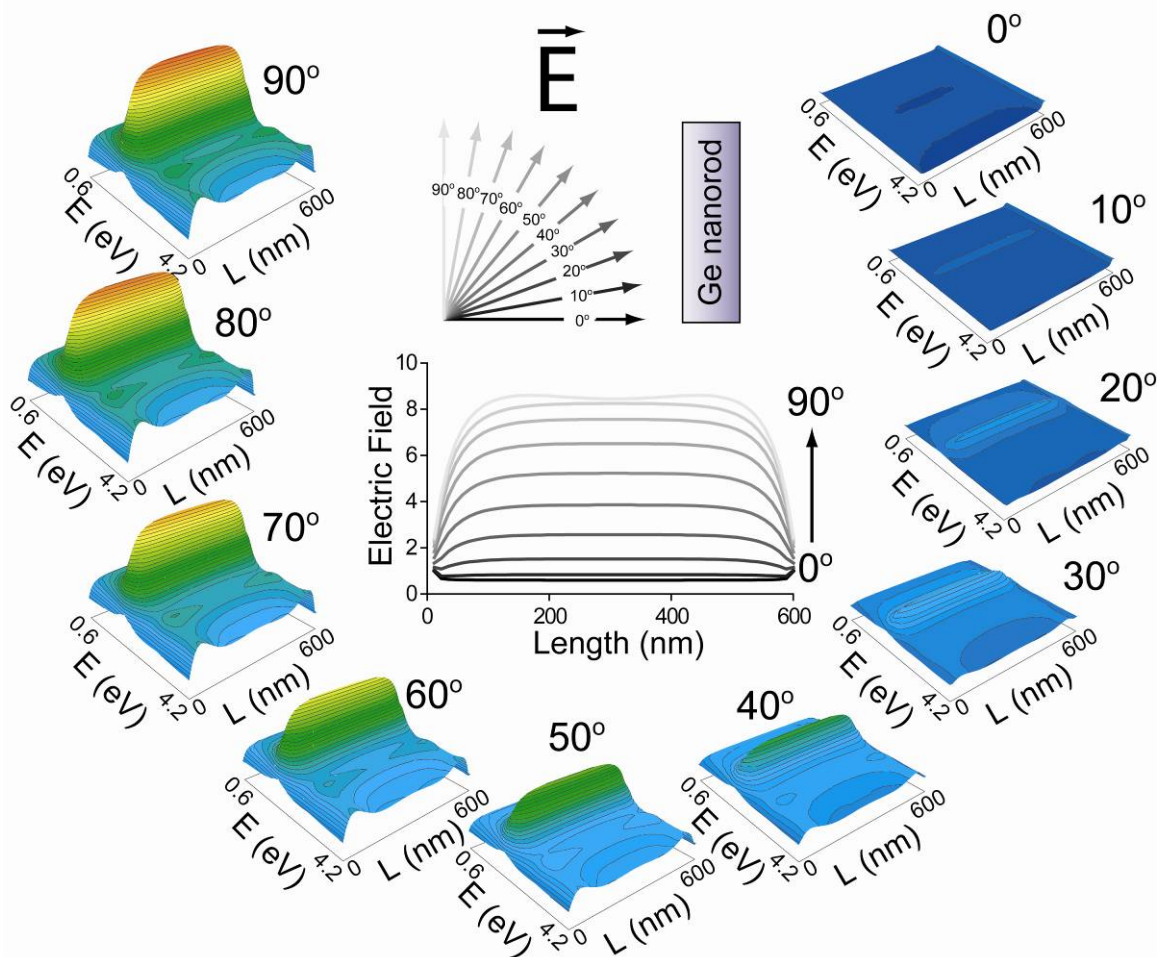


Figure 10.11: Average internal electric field contour plots at 590 nm, calculated for a Ge nanorod (30 nm in diameter with an aspect ratio of 20) with incident electric fields at various angles (center plot) with corresponding surface plots for each angle (surrounding).

10.4 CONCLUSIONS

Ge nanorods were synthesized by arrested Bi- or Au-assisted solution-liquid-solid (SLS) growth. Optical measurements were made and compared to calculations using the discrete dipole approximation (DDA). A peak in the experimental absorbance spectra was observed at 550nm and red-shifted with increasing nanorod length. DDA calculations corroborate this peak, which can be traced back to peaks in the real part of the complex

index of refraction and dielectric function. The peak was also found to be heavily dependent on incident electric field orientation and rod length, but not on rod diameter. We also calculate an enhanced internal electric field at the edges and surfaces of nanorods relative to the central axis of the nanorod. This work shows the potential for fine-tuning of optical properties through controlled growth of Ge nanorods.

10.5 ACKNOWLEDGEMENTS

Authors making contributions to this work include: Vincent C. Holmberg and Brian A. Korgel. Damon A. Smith was helpful with programming DDA calculations. Financial support of this research was provided in part by The Robert A. Welch Foundation (F-1464). V.C.H. acknowledges the Fannie and John Hertz Foundation and the National Science Foundation Graduate Research Fellowship Program for financial support.

10.6 REFERENCES

1. Cao, L. Y.; White, J. S.; Park, J. S.; Schuller, J. A.; Clemens, B. M.; Brongersma, M. L. *Nat. Mater.* **2009**, *8*, 643-647.
2. Chen, G.; Wu, J.; Lu, Q.; Gutierrez, H. R.; Xiong, Q.; Pellen, M. E.; Petko, J. S.; Werner, D. H.; Eklund, P. C. *Nano Lett.* **2008**, *8*, 1341-1346.
3. Law, M.; Sirbuly, D. J.; Johnson, J. C.; Goldberger, J.; Saykally, R. J.; Yang, P. *Science* **2004**, *305*, 1269-1273.
4. Greytak, A. B.; Barrelet, C. J.; Li, Y.; Lieber, C. M. *App. Phys. Lett.* **2005**, *87*, 151103-3.
5. Tian, B. Z.; Zheng, X. L.; Kempa, T. J.; Fang, Y.; Yu, N. F.; Yu, G. H.; Huang, J. L.; Lieber, C. M. *Nature* **2007**, *449*, 885-U8.
6. Kelzenberg, M. D.; Turner-Evans, D. B.; Kayes, B. M.; Filler, M. A.; Putnam, M. C.; Lewis, N. S.; Atwater, H. A. *Nano Lett.* **2008**, *8*, 710-714.
7. Garnett, E. C.; Yang, P. *J. Am. Chem. Soc.* **2008**, *130*, 9224-9225.
8. Wang, J.; Gudixsen, M. S.; Duan, X.; Cui, Y.; Lieber, C. M. *Science* **2001**, *293*, 1455-1457.
9. Hayden, O.; Agarwal, R.; Lieber, C. M. *Nat. Mater.* **2006**, *5*, 352-356.
10. Fan, Z. Y.; Ho, J. C.; Jacobson, Z. A.; Razavi, H.; Javey, A. *P. Natl. Acad. Sci. USA* **2008**, *105*, 11066-11070.

11. Ahn, Y.; Dunning, J.; Park, J. *Nano Lett.* **2005**, *5*, 1367-1370.
12. Soci, C.; Zhang, A.; Xiang, B.; Dayeh, S. A.; Aplin, D. P. R.; Park, J.; Bao, X. Y.; Lo, Y. H.; Wang, D. *Nano Lett.* **2007**, *7*, 1003-1009.
13. Gu, Y.; Kwak, E. S.; Lensch, J. L.; Allen, J. E.; Odom, T. W.; Lauhon, L. J. *App. Phys. Lett.* **2005**, *87*, 043111-3.
14. Huang, M. H.; Mao, S.; Feick, H.; Yan, H.; Wu, Y.; Kind, H.; Weber, E.; Russo, R.; Yang, P. *Science* **2001**, *292*, 1897-1899.
15. Johnson, J. C.; Choi, H. J.; Knutsen, K. P.; Schaller, R. D.; Yang, P. D.; Saykally, R. J. *Nat. Mater.* **2002**, *1*, 106-110.
16. Hu, L.; Chen, G. *Nano Lett.* **2007**, *7*, 3249-3252.
17. Muskens, O. L.; Rivas, J. G. m.; Algra, R. E.; Bakkers, E. P. A. M.; Lagendijk, A. *Nano Lett.* **2008**, *8*, 2638-2642.
18. Muskens, O. L.; Diedenhofen, S. L.; Kaas, B. C.; Algra, R. E.; Bakkers, E. P. A. M.; Gómez Rivas, J.; Lagendijk, A. *Nano Lett.* **2009**, *9*, 930-934.
19. Smith, D. A.; Holmberg, V. C.; Rasch, M. R.; Korgel, B. A. *J. Phys. Chem. C* **2010**, *114*, 20983-20989.
20. Hanrath, T.; Korgel, B. A. *J. Phys. Chem. B* **2005**, *109*, 5518-5524.
21. Smith, D. A.; Holmberg, V. C.; Korgel, B. A. *ACS Nano* **2010**, *4*, 2356-2362.
22. Smith, D. A.; Holmberg, V. C.; Lee, D. C.; Korgel, B. A. *J. Phys. Chem. C* **2008**, *112*, 10725-10729.
23. Claeys, C. *Germanium-Based Technologies: From Materials to Devices* **2007**.
24. Chockla, A. M.; Harris, J. T.; Korgel, B. A. *Chem. Mater.* **2011**, *23*, 1964-1970.
25. Yang, W.-H.; Schatz, G. C.; Van Duyne, R. P. *J. Chem. Phys.* **1995**, *103*, 869-875.
26. Yurkin, M. A.; Hoekstra, A. G. *J. Quant. Spectrosc. Ra.* **2007**, *106*, 558-589.
27. Draine, B. T. *Astrophys. J.* **1988**, *333*, 848-872.
28. Draine, B. T.; Flatau, P. J. *J. Opt. Soc. Am. A* **1994**, *11*, 1491-1499.
29. Draine, B. T.; Flatau, P. J. *J. Opt. Soc. Am. A* **2008**, *25*, 2693-2703.
30. Yurkin, M. A.; Maltsev, V. P.; Hoekstra, A. G. *J. Quant. Spectrosc. Ra.* **2007**, *106*, 546-557.
31. McDonald, J.; Golden, A.; Gerard Jennings, S. *Int. J. High Perform. C.* **2009**, *23*, 42-61.
32. Saunders, A. E.; Sigman, M. B.; Korgel, B. A. *J. Phys. Chem. B* **2003**, *108*, 193-199.
33. Weaver, J. H. W.; Frederikse, H. P. R. *CRC Handbook of Chemistry and Physics, 92nd ed.* **2012**, 12.129-130.

34. Lenham, A. P.; Treherne, D. M.; Metcalfe, R. J. *J. Opt. Soc. Am.* **1965**, *55*, 1072-1074.
35. Wang, P. Y.; Jain, A. L. *Phys. Rev. B-Solid St.* **1970**, *2*, 2978-2983.
36. Lu, X.; Fanfair, D. D.; Johnston, K. P.; Korgel, B. A. *J. Am. Chem. Soc.* **2005**, *127*, 15718-15719.
37. Chockla, A. M.; Korgel, B. A. *J. Mater. Chem.* **2009**, *19*, 996-1001.
38. Hanrath, T.; Korgel, B. A. *Adv. Mater.* **2003**, *15*, 437-440.
39. Podolskiy, V. A.; Sarychev, A. K.; Shalaev, V. M. *J. Nonlinear Opt. Phys.* **2002**, *11*, 65-74.
40. Smith, D. K.; Miller, N. R.; Korgel, B. A. *Langmuir* **2009**, *25*, 9518-9524.
41. Link, S.; El-Sayed, M. A. *Int. Rev. Phys. Chem.* **2000**, *19*, 409-453.
42. Heath, J. R.; Shiang, J. J.; Alivisatos, A. P. *J. Chem. Phys.* **1994**, *101*, 1607-1615.
43. Hanrath, T.; Korgel, B. A. *Small* **2005**, *1*, 717-721.
44. Grillet, N.; Manchon, D.; Bertorelle, F.; Bonnet, C.; Broyer, M.; Cottancin, E.; Lermé, J.; Hillenkamp, M.; Pellarin, M. *ACS Nano* **2011**, *5*, 9450-9462.
45. Heitsch, A. T.; Hessel, C. M.; Akhavan, V. A.; Korgel, B. A. *Nano Lett.* **2009**, *9*, 3042-3047.

Chapter 11: Role of Capping Ligands on Solution-Liquid-Solid (SLS) Growth of Indium Phosphide Nanowires

11.1 INTRODUCTION

Indium phosphide (InP) exhibits strong quantum confinement effects¹⁻⁴ and is an interesting material for optoelectronic applications.⁵ With a broader emission range and lower toxicity, it is also the most promising alternative to CdSe.⁶ As such, there is great interest in developing and understanding the synthesis of InP nanomaterials. The surface chemistry of InP quantum dots has been an area of investigation of late and is relatively well understood.⁶⁻¹⁰ However, surface chemistry of nanowires, grown via the solution-liquid-solid (SLS) growth mechanism, for example, remains ambiguous.^{1, 2, 11-13} There are pronounced differences in the growth of SLS InP nanowires compared to vapor-liquid-solid (VLS) grown InP nanowires. For instance, in SLS InP nanowires exhibit zinc blende structure^{1, 2, 11-13} whereas VLS show a mixture of the zinc blende and wurtzite phases, depending on the reaction conditions.¹⁴⁻¹⁹ This point remains to be addressed directly, but as the phases differ in energy by only 6.8 meV per In-P atom pair,²⁰ the cause is likely due to the presence of the capping ligands in SLS syntheses that form zinc blende structure preferentially.

Introduction of Zn impurities in VLS-grown InP nanowires give rise to formation of twinning super lattices (TSLs) where periodically spaced zinc blende segments are separated by a twin plane caused by a stacking fault.¹⁶ Growth of TSLs in VLS-grown InP nanowires can be controlled and depends critically on the zinc concentration in the seed catalyst.¹⁶ Twinning causes kinks in nanowires which is typically detrimental to the electrical properties.²¹ However, TSLs modify the electronic band structure and alter the optical properties in InP nanowires.²² The formation of TSLs is reported elsewhere²³⁻²⁷ and is attributed to changes in the free energy of formation of wurtzite phase relative to

zinc blende at the solid-liquid (e.g., nanowire-seed droplet) interface. The nature of twinning has been investigated for InP nanowires grown in VLS processes,²³⁻²⁷ but not SLS.¹³ Twinning behavior has been observed in SLS grown InP nanowires, but is less well understood. Here we study the surface chemistry of InP nanowires and show potential solution routes to InP nanowires with TSLs. We also investigate the efficacy of octyl-phosphonic acid, a common surfactant in the growth of InP nanowires, and provide examples of suitable replacements.

11.2 EXPERIMENTAL SECTION

11.2.1 Materials

All chemicals were used as received. Anhydrous tetrahydrofuran (THF, $\geq 99.9\%$), sodium bis(trimethylsilyl)amide (NaTMS₂N), 1.0 M in THF, bismuth (III) chloride (BiCl₃, $\geq 98\%$), diphenyl ether (DPE, $\geq 99\%$), anhydrous toluene (99.8%), anhydrous hexane (95%), poly(1-decene) (1PD, viscosity 50 cSt), *n*-hexadecylamine (HDA, 90%), indium (III) acetate (InAc₃, 99.99%), myristic acid (MyrA, 99%), tri-*n*-octylphosphine oxide (TOPO, 99%), *n*-octylmagnesium bromide (2.0 M in diethyl ether), di-*n*-butyl phosphite (DBP, 96%), diethyl ether (DEE, 99.7%) and phosphoric acid (H₃PO₄, 85% w/w, *aq*) were purchased from Sigma Aldrich, hydrogen peroxide (H₂O₂, 30%), sulfuric acid (H₂SO₄, 96.2% w/w, *aq*) and potassium carbonate (K₂CO₃, anhydrous, 99.8%) were purchased from Fisher, octylphosphonic acid (OPA, 99%) was purchased from Alfa Aesar, and tris(trimethylsilyl)phosphine (TMS₃P, 98%) was purchased from Strem. Polyvinylpyrrolidone-hexadecane (PVP-HDE) copolymer (Ganex V-216, MW = 7300 g mol⁻¹, product ID 72289D) was provided by ISP Technologies, Inc.

11.2.2 Bi nanocrystal preparation

Bi nanocrystals (BiNC) were synthesized according to literature methods.^{28, 29} All synthetic steps were conducted using standard air-free procedures either in an oxygen-free Schlenk flask or a nitrogen-filled glove box. In a typical Bi nanocrystal synthesis, a

growth solution was prepared by combining 5 g PVP-HDE copolymer with 15 g DPE in a 3-neck flask attached to a Schlenk line. The solution was degassed under vacuum with vigorous stirring for 1 hour at 70°C, then blanketed with nitrogen and heated to 200°C. Meanwhile, an injection solution was prepared by dissolving BiCl₃ (158 mg, 0.50 mmol) in THF (1 mL), which yielded a milky suspension. The BiCl₃/THF solution was combined with NaTMS₂N (2 mL, 1.0M in THF) in a 4:1 Na:Bi ratio and plunged into a syringe. The syringe containing the injection mixture was removed from the glovebox and rapidly injected to the hot PVP-HDE copolymer / DPE growth solution, turning the solution black immediately. The mixture was stirred for 30 minutes after which the heating element was removed and the flask contents were allowed to cool. When the temperature dropped to ~100°C, 20 mL of toluene was to the reaction flask and the product was split evenly into 6 centrifuge tubes. 30 mL of methanol was added to each tube followed by centrifugation at 8000 rpm for 5 minutes. The supernatants were discarded being careful to retain the black viscous fluid where the Bi nanocrystals are encased. The viscous phase was redispersed using 2-3 mL of toluene (in each centrifuge tube) and consolidated into 2 centrifuge tubes. 30 mL of methanol was added to each tube followed by centrifugation at 8000 rpm for 5 minutes. The supernatant was discarded, leaving behind a thick black viscous liquid, which was dispersed in chloroform. The chloroform was evaporated using a rotary evaporation (rotovap) system to determine the weight of the black viscous liquid product. In a typical reaction, roughly 4 to 5 g of product is produced, most of which is PVP-HDE copolymer. In order to determine the amount of Bi was collected, a sample of was analyzed using thermogravimetric analysis (TGA). The Bi samples were dispersed in toluene at a concentration of 10 mg mL⁻¹ and stored in a nitrogen filled glove box.

11.2.3 Indium (III) myristate preparation

Indium (III) myristate (InMyr₃) was prepared according to previously described methods.¹³ In a typical procedure InAc₃ (2.5 g, 8.56 mmol) and MyrA (5.87 g, 25.95 mmol) were combined with 1PD (50 g) in a 3-neck flask. The flask was attached to an oxygen-free Schlenk line and stirred vigorously under vacuum (<500 mTorr) for 2 hours at 120 °C. The solution turned optically clear and had a slight yellow hue when heated. Allowing the solution to cool to room temperature and settle results in a thick white precipitate with a clear, colorless supernatant. When shaken, the suspension becomes uniform. InMyr₃ was used from this stock suspension with a concentration of 0.15 mmol g⁻¹ mixture without any further purification.

11.2.4 Di-*n*-octylphosphonic acid preparation

Synthesis of di-*n*-octylphosphonic acid (DOPA) was adapted from literature methods,³⁰ as reported by Wang et al,³¹ through direct oxidation of di-*n*-octylphosphine oxide (DOPO) with excess H₂O₂. To synthesize DOPO, a 3-neck flask containing 50 mL of *n*-octylmagnesium bromide (0.10 mol, 2.0 M in DEE) was connected to a Schlenk line and blanketed with nitrogen. The flask was immersed in an ice bath to maintain the temperature between 10°C and 15°C while DBP (6.88 g, 35.6 mmol) was added dropwise over the course of 30 minutes with vigorous stirring. After injecting DBP, the temperature was raised to reflux the solution for 30 minutes to complete the reaction. After the 30 minute reaction, the flask was again immersed in an ice bath to maintain the temperature between 5°C and 10°C while 37.5 mL of 25% w/w H₂SO₄ (aq) was added dropwise over 30 minutes. After adding H₂SO₄, the flask contents were transferred to a separation funnel where the ether phase was extracted and washed with deionized water (25 mL) three times, K₂CO₃ (25 mL, 15% w/w K₂CO₃, aq) three times, and deionized water (25 mL) three times. The product was returned to a fresh 3-neck flask and the ether removed under vacuum with the solution heated to 65°C. The product was collected

using anhydrous hexane (25 mL) and recrystallized to give the DOPO product. DOPO (5g, 18.2 mmol) was combined with H₂O₂ (30% w/w, 2.3g, 20.3 mmol) in a 3-neck flask and stirred overnight (~15 hours) at 65°C. Water and H₂O₂ were then vacuum distilled at 50°C leaving white chunks of DOPA. Positive ionization mass spectrometry data for the final product can be found in Appendix I, Figure I1.

11.2.5 InP nanowire Synthesis

InP nanowires were synthesized using a variation of previously described methods.¹³ In a typical reaction used to produce high quality InP nanowires, HDA (1.03 g, 4.3 mmol) and OPA (67 mg, 0.34 mmol) were combined with 1PD (3 g) in a 4-neck flask and connected to an oxygen-free Schlenk line. The flask was placed under vacuum (<500 mtorr) and stirred vigorously for 30 minutes at 100 °C. After 30 minutes, the flask was blanketed with nitrogen and heated to the reaction temperature (330 °C).

An injection solution containing 0.1 mL stock BiNC solution (1 mg, 4.8 μmol Bi) dispersed in 0.6 g 1PD was prepared in the glove box and loaded into a syringe. A second injection solution was prepared (also in the glove box) by combining InMyr₃ (3.42 g, 0.51 mmol) with TMS₃P (0.15 mL, 0.51 mmol) dispersed in 0.5 mL 1PD. The InMyr₃/TMS₃P solution was plunged into a syringe. Both injection solutions were removed from the glove box and rapidly injected sequentially into the reaction flask. The BiNC solution was injected first and stirred for 1 minute allowing the temperature to equilibrate at 330 °C. After 1 minute, the InMyr₃/TMS₃P solution was injected drop-wise over 5 minutes. The reaction product turned reddish-brown during this drop-wise addition, and the temperature remained above 320 °C throughout the reaction. The reaction mixture was allowed to stir an additional 5 minutes after the second injection before removing the heating element. The flask contents cooled to 150 °C at which point 10 mL of toluene was added to prevent solidification of HDA and OPA. The reaction mixture was quickly transferred to a glass centrifuge tube and centrifuged at 4000 rpm for

2 minutes while the solution was still hot. The resulting supernatant was discarded and the pellet was redispersed in toluene, followed by centrifugation under the same conditions. This process was repeated several times until the supernatant was clear. The final product was redispersed in chloroform and stored in the glove box until examined with FTIR and XPS.

Additional reactions were done to determine the role of various ligands in the growth of InP nanowires. Beyond to using (1) both HDA and OPA, additional reactions included the use of, (2) OPA only (100 mg, 0.50 mmol), (3) HDA only (1.03 g, 4.3 mmol), (4) neither capping, (5) H₃PO₄ (58 mg 85% H₃PO₄ w/w, 0.50 mmol), (6) DOPA (150 mg, 0.50 mmol), and (7) TOPO (200 mg, 0.50 mmol). Reactions (5)–(7) also contained HDA (1.03g, 4.3 mmol). For reaction (5), the H₃PO₄ was injected immediately before the In/P precursor solution was added in order to prevent the acid from completely evaporating in the hot solvent before hand. These samples were dispersed in chloroform and stored in the glove box until further analyzed.

The interaction between HDA and OPA on the Bi seeds was studied by injecting Bi nanocrystals into the same reaction media used in InP nanowire reactions (1)–(4) without subsequent injection of the InP precursor solution. The Bi seeds were stirred for the same amount of time as a normal reaction, start to finish (i.e., 11 minutes) before following the same cleaning procedure describe for InP nanowire reactions. The product was dispersed in chloroform and stored in a glovebox for characterization.

11.2.6 Materials Characterization

Thermogravimetric analysis (TGA) was performed using a Mettler-Toledo TGA/DSC1. Roughly 1 mg of material was loaded into a 70 μ L alumina crucible by dropcasting from chloroform and dried in ambient atmosphere. TGA was performed under a nitrogen atmosphere (80 mL/min purge rate), increasing the temperature from room temperature to 800°C at a heating rate of 5°C min⁻¹.

Scanning electron microscopy (SEM) images were acquired using a Zeiss Supra 40 SEM with an in-lens arrangement, a working voltage of 5 keV and a working distance of 5 mm. SEM samples were imaged on $1 \times 1 \text{ cm}^2$ silicon wafers (from S.E.H). Transmission electron microscopy (TEM) images were digitally acquired using either a FEI Tecnai Spirit BioTwin TEM operated at 80 kV or a field emission JEOL 2010F TEM operated at 200 kV. Energy-dispersive X-ray spectroscopy (EDS) data were acquired on the JEOL 2010F TEM via an Oxford Inca EDS detector. TEM samples were prepared by drop-casting from chloroform dispersions onto 200 mesh lacey-carbon copper TEM grids (Electron Microscopy Sciences).

X-ray diffraction (XRD) was carried out using either a Rigaku R-Axis Spider Diffractometer with Image plate detector with $\text{Cu } k_{\alpha}$ ($\lambda = 1.5418 \text{ \AA}$) radiation operated at 40 kV and 40 mA, or a Bunker-Nonius D8 Advance diffractometer with $\text{Cu } K_{\alpha}$ source. Measurements using the Spider Diffractometer were taken on particles suspended on a 0.5 mm nylon loop. Samples were scanned for 10 min while rotating at 10° per minute at 298 K in ambient atmosphere. The resulting radial data were integrated from $2\theta = 10$ to 90. Background scattering from the nylon loop was subtracted from the sample measurement. Data were acquired using the Bunker-Nonius from purified product (1~3 mg) dropcast on a quartz substrate using a rotating sample holder with generator voltage and amperage of 40 mV and 40 mA, respectively, at a scan rate of 12 deg min^{-1} in 0.02 deg intervals, with typical collection times of 4 to 6 hours.

X-ray photoelectron spectroscopy (XPS) was performed using a Kratos photoelectron spectrophotometer with monochromatic $\text{Al } K_{\alpha}$ radiation (1487 eV) under a background pressure of 10^{-9} Torr. Samples were prepared by dropcasting nanowires from a 5 mg mL^{-1} solution in chloroform on a UV-ozone cleaned native oxide Si wafer. Spectra were collected at 0.1 eV intervals and 800 ms integration time while charge compensation was taking place through a tungsten coil set at 4.8 V bias with respect to

the substrate. XPS data were corrected by shifting the C1s peak to a binding energy of 285 eV.

XPS data analysis was done using CasaXPS software. The background signal was subtracted using a Shirley background model and peak areas were deconvoluted as Voigt functions (30% Gaussian character). In the In3d region, the InP (5/2), In₂O₃ (5/2), InP (3/2) and In₂O₃ (3/2) peaks at 444.4 eV, 445.2 eV, 452 eV and 452.8 eV binding energies, respectively, were deconvoluted. Total integrated area associated with the 5/2 spins were set to 1.5x of 3/2 spin areas. Full width at half maximum (FWHM) of all the peaks were set equal to each other. For the P2p region, InP (3/2) and InP (1/2) peaks were placed at 128.7 eV and 129.5 eV, respectively. FWHM of these peaks were set equal to each other. The 3/2 spin state total peak area was set 2x the 1/2 spin state. Peaks associated with the suboxides of phosphorous were placed at 129.8 eV, 132.8 eV, and 133.6 eV binding energies. Due to large number of peaks, the two spin states of the suboxides were convoluted into one peak. FWHM of all the suboxide peaks were set equal to each other. For the Bi4f region of the scans, Bi⁰4f (7/2) and Bi⁰4f (5/2) were placed at 157.0 and 162.3 eV, respectively. The FWHM of the different spins set to equal each other, and the total area of the 5/2 spin was set to 75% of the 7/2 spin.

ATR-FTIR spectra were acquired using a Thermo Mattson Infinity Gold FTIR with an attenuated total internal reflectance (ATR) stage made of crystalline ZnSe. The detector is liquid nitrogen cooled and the spectra are acquired from 400–4000 cm⁻¹ with 1 cm⁻¹ resolution by averaging 128 scans. Background scans were collected before sample deposition and are automatically subtracted out of the results. InP nanowires were dropcast onto the ATR stage from a chloroform solution and dried. The sample chamber was purged with dry nitrogen for 5 minutes before collecting data.

11.3 RESULTS AND DISCUSSION

11.3.1 Role of HDA and OPA on InP nanowire growth

Figure 11.1 shows SEM, TEM, HRTEM, and corresponding FFT images of InP nanowires grown from Bi nanocrystals via the SLS growth mechanism in the presence of one of four combinations of OPA and HDA: (1) HDA and OPA; (2) OPA only; (3) HDA only; (4) neither HDA nor OPA. Reaction (1) nanowires are defect-free and single crystalline (Figure 11.1i) while reaction (2) nanowires are ridden with (111) twin plane defects, illustrated in Figure 11.1j. The angle between twin planes is 38° , similar to previous reports.^{32, 33} The periodicity of the plane defects is irregular, but can be controlled through careful introduction of impurities.¹⁶ Samples (1) and (2) both exhibit growth in the $\langle 111 \rangle$ direction. Reaction (3) formed a mixture of crystalline In_2O_3 and InP nanowires (confirmed by XRD shown in Figure 11.2). Figure 11.1k shows TEM of an In_2O_3 nanowire growing in the $\langle 211 \rangle$ direction with d-spacing of 4.14\AA (measured by TEM, expected value: 4.13\AA). Reaction (4) yielded predominantly large particulates. The product is composed of In_2O_3 when no capping ligands are used (see Figure 11.2). The In_2O_3 nanowire shown in Figure 11.1l—typical of reaction (4) conditions—has a $\langle 110 \rangle$ growth direction and a d-spacing of 3.54\AA (measured by TEM, expected value: 3.58\AA). This shows a potential solution route to In_2O_3 nanowires pending improved control over the reaction chemistry and product morphology. This result is significant as In_2O_3 nanowires are typically only grown in high temperature CVD methods.³⁴

In addition to playing a critical role in the formation of single crystalline, defect free InP nanowires, HDA and OPA also affect the nanowire diameters. For example, reaction (1) produced nanowires with an average diameter of 20.8 ± 5.4 nm (the initial Bi seed diameter is 14.0 ± 2.5 nm, shown in Figure I2) while reaction (2) produced InP nanowires with an average diameter of 28.2 ± 9.5 nm. Reactions (3) and (4) yielded wires with an average diameters of 21.0 ± 5.1 nm and 43.1 ± 14.0 nm, respectively (see Figure I3). These results contrast with previous reports that show an empirical relation

between InP nanowire diameters and initial Bi seed diameter.¹³ Here, the nanowire diameter was found to depend on the reaction medium, the reason for which is discussed below.

Twinning in InP nanowires remains a mystery for SLS grown InP nanowires but has been thoroughly investigated for VLS grown wires and—although VLS grown wires exhibit wurtzite structure whereas SLS grown wires are zinc blende—these studies help explain the twinning behavior observed in this study, illustrated in Figure 11.1j. A variety of factors contribute to twin formation in VLS grown InP nanowires: (a) temperature,³⁵ (b) In:P ratio,³⁶ (c) wire diameter,¹³ and (d) zinc impurities.^{16, 37} In this study, the In:P ratio was not changed and the temperature held constant for all reactions, ruling out (a) and (b) as causes for twinning. Reaction (2) wire diameters were larger than reaction (1) (28.2nm compared to 20.8nm), making this a likely factor in twin formation. Furthermore, Zn is present as an impurity in the indium precursor (0.2 ppm)³⁸ and may also play a role.

Twinning superlattices (TSLs) modify the electronic band structure and alter the optical properties in InP nanowires.²² This effect has been observed in quantum well heterostructures and is due to spatial separation of photoexcited electrons that induce band bending.²³⁻²⁷ Controlled growth of TSLs in VLS-grown InP nanowires can be achieved through the introduction of zinc impurities; twins occur with regular periodicity, which depends critically on the zinc concentration in the seed catalyst.¹⁶ The formation of TSLs is attributed to changes in the free energy of formation of wurtzite phase relative to zinc blende at the solid-liquid (e.g., nanowire-seed droplet) interface.^{15, 16} Amines form moderate-strength coordination bonds with Zn^{39, 40} (e.g., amines are used to cap ZnSe nanocrystals),⁴¹ thus the presence of HDA—in reaction (1) for example—prevents twinning by scavenging Zn impurities. Phase purity in InAs nanowires depends on the wire diameter.¹⁵ This same effect could be playing a role in producing twinned wires in reaction (2). The mechanism behind diameter-dependent twinning remains unclear.

While we show a potential solution-phase synthesis to TSLs in SLS-grown InP nanowires, a more systematic study is required to probe the effect of Zn impurities.

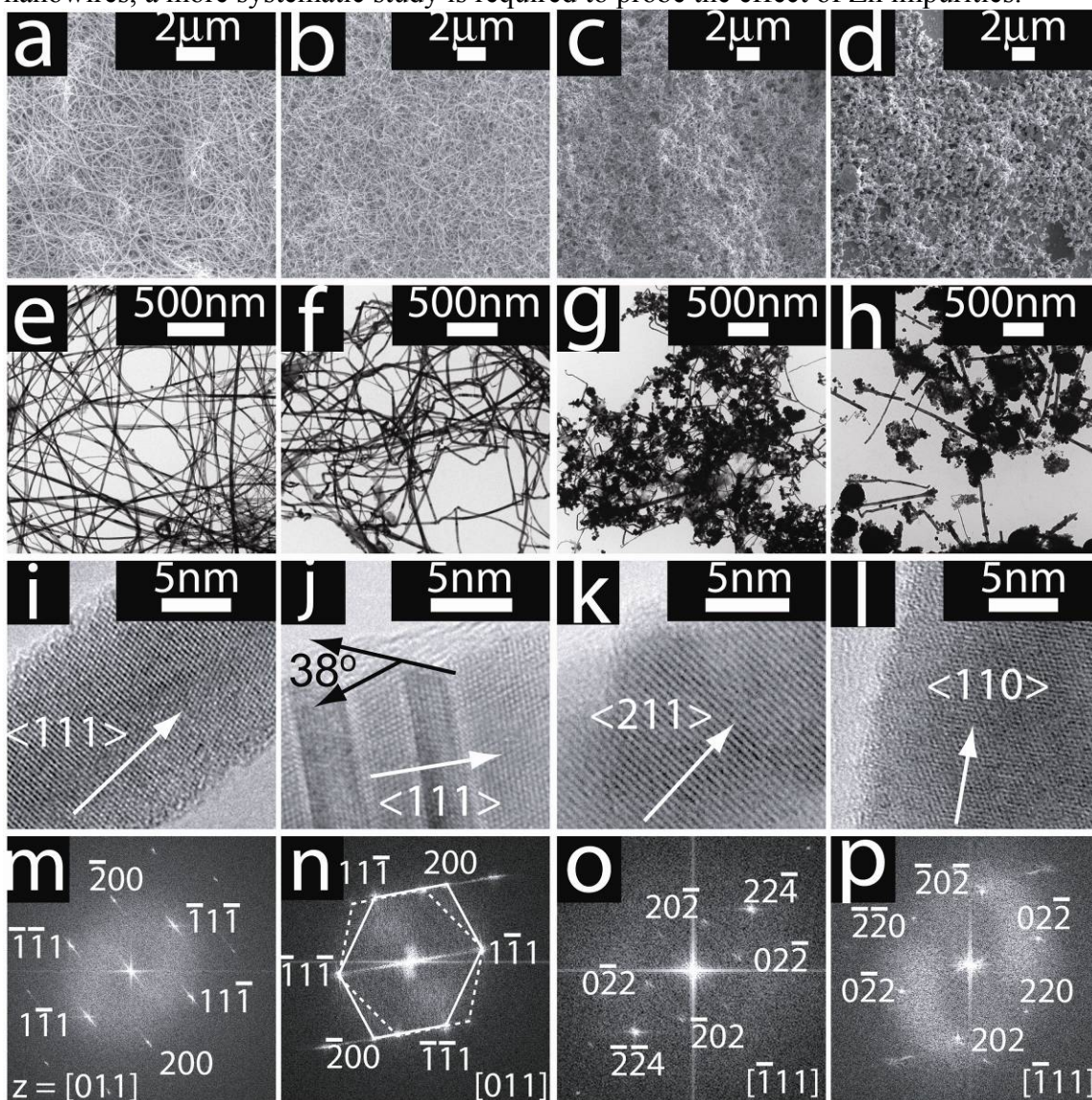


Figure 11.1: (a-d) SEM, (e-h) TEM, (i-l) HRTEM, and (m-p) corresponding FFT images of InP nanowires grown in the presence of (a, e, i, m) OPA and HDA, (b, f, j, n) OPA only, (c, g, k, o) HDA only, and (d, h, l, p) neither ligand.

Figure 11.2 shows XRD data for samples grown from reactions (1) through (4) in curves (i) through (iv), respectively. The data show that InP nanowires form exclusively in reactions (1) and (2) (i.e., reactions where OPA is present). The peak observed in curve (ii) at $2\theta = 27.4$ corresponds to rhombohedral Bi. Reaction (3) shows In_2O_3 in

addition to InP, also illustrated by the In_2O_3 nanowire shown in Figure 11.1j. Reaction (4) yields only a small amount of InP, evident by the limited presence of the InP (111) peak at $2\theta = 26.2$. The majority of the product is In_2O_3 —Figure 11.1l shows an In_2O_3 nanowire, for instance—and metallic indium.

It is clear that OPA is essential to produce crystalline InP nanowires as cubic In_2O_3 forms when OPA is absent. Given that InP nanowires form when HDA is absent, we conclude that the ligand does not play a lead role in promoting InP growth. However, HDA is essential to improve crystallinity (e.g., reaction (2) nanowires are laden with twin planes) and plays a role in controlling nanowire diameter, confirming previous reports.¹³ These observations have been made elsewhere as well. Of further interest is that SLS grown InP nanowires form zinc blende crystal structure exclusively whereas vapor phase methods typically report a mixture of results—some showing zinc blende and some showing the wurtzite crystal structure.^{1, 2, 11-13, 15, 16, 18} While the reason behind this remains unclear, preferential wurtzite formation in VLS grown InP nanowires is attributed to the lower surface energy of the parallel side facets of wurtzite compared to zinc blende nanowires.²⁰ The higher energy facets in zinc blende nanowires are stabilized by the presence of surfactants in SLS syntheses.

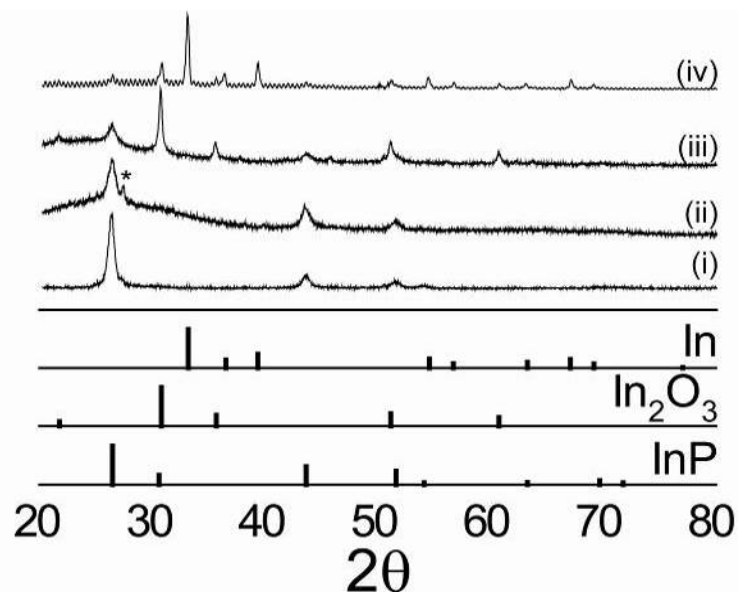


Figure 11.2: Diffraction patterns for InP nanowire reactions done in the presence of (i) HDA and OPA, (ii) OPA only, (iii) HDA only, and (iv) neither ligand. Reference patterns are included for InP (JCPDS: 00-032-0452), In_2O_3 (JCPDS: 01-071-2194) and In (JCPDS: 00-005-0642).

Attenuated total reflectance–Fourier transform infrared (ATR–FTIR) spectroscopy measurements were made on each sample, shown in Figure 11.3 with curves (i)–(iv) corresponding to reactions (1)–(4), respectively. The signal is magnified $10\times$ between 3000 cm^{-1} and 3750 cm^{-1} in curves (i)–(iii) to highlight the peaks in this region. Curves (i)–(iii) show characteristic hydrocarbon signals with symmetric and asymmetric CH_2 methylene stretches at 2852 cm^{-1} and 2922 cm^{-1} , respectively, and asymmetric CH_3 methyl stretching at 2947 cm^{-1} . $\text{C}-\text{CH}_3$ deformation signals are present at 1464 cm^{-1} and 1380 cm^{-1} . The peaks between 1400 cm^{-1} and 1550 cm^{-1} are characteristic of myristic acid. Specifically, the peak at 1530 cm^{-1} is attributed to chelating bidentate coordination between the myristate carboxyl group and a surface indium atom,⁶ and is particularly strong in curve (ii) indicating an increase in surface-bound myristate when HDA is not present. The broad peak centered around 1010 cm^{-1} is attributed to P–O–P due to the formation of a surface InPO_x oxide layer.⁶ Various P=O,

R(OH)₂P=O, and P-O-R stretches also occur in this region corresponding to surface bound OPA in curves (i) and (ii). The P-O-P stretch at 700 cm⁻¹ is also observed.

Phosphonic acid signatures are observed in curves (i) and (ii) at 1692 cm⁻¹ and 1413 cm⁻¹ corresponding to P=O and P-C stretching vibrations, respectively. A broad peak starting at 3640 cm⁻¹ and centered at 3260 cm⁻¹ is due to O-H bonding in OPA. The primary amine N-H stretch (3330 cm⁻¹) and deformation (1640 cm⁻¹) vibrations are present in curve (iii), but are muted in curve (i) due to the presence of the aforementioned signals in the same regions. In the reaction (4) spectra shown in curve (iv), no signals characteristic of OPA, HDA, or myristate were observed, though the P-C stretch at 790 cm⁻¹ was present in all four reactions. XPS measurements were made to further characterize the nanowire surfaces. We present these results below before proposing surface chemistry scheme.

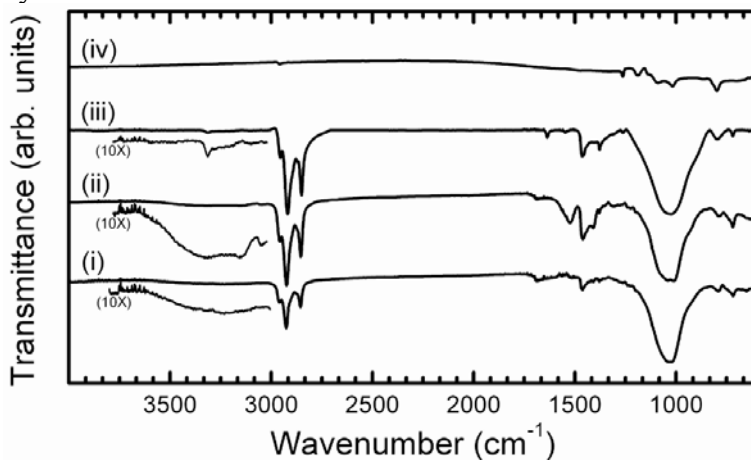


Figure 11.3: ATR-FTIR spectra collected for InP nanowires produced in the presence of (i) HDA and OPA, (ii) OPA only, (iii) HDA only or (iv) neither ligand. The signal between the 3750 cm⁻¹ and 3000 cm⁻¹ was magnified 10× to enhance features in this region.

Figure 11.4 shows XPS spectra of In, P, and Bi for each reaction with curves (i)–(iv) corresponding to reactions (1)–(4). Reaction (1) data show limited oxidation. The In3d region shows peaks at 444.5 eV and 452 eV corresponding to InP.⁴² There is a small shoulder on each of these peaks at higher binding energies that indicates slight

oxidation corresponding to InP_xO_y .⁴² The P2p region shows a doublet with peaks centered at 128.7 eV and 129.5 eV corresponding to InP.⁴² There is also a weak peak centered at 133.2 eV, which can be deconvoluted into various InP_xO_y suboxides.⁴² Phosphorous in OPA has a binding energy of 135 eV⁴³ and is not observed here. The compound is difficult to wash out of the reaction product, so residual OPA is likely the cause for some characteristic FTIR signals, such as OH bonding. XPS, which surveys only a very localized area on the sample, indicates that the OPA is not surface bound. The Bi4f region shows zero-valent Bi oxidation state at 156.7 eV and 162 eV.

Reaction (2) samples show behavior similar to reaction (1), though the Bi seeds in this sample are slightly oxidized, illustrated by the broad, low intensity shoulders in the Bi4f region. These peaks are shifted to slightly higher binding energies (i.e., centered at 159.1 eV and 164.5 eV). HDA therefore prevents oxidation of the Bi nanocrystals. XPS of reaction (3) product reveals increased oxidation of all three elements. The In3d region shows two peaks (444.5 eV and 452 eV) but the peaks are much broader than the In3d signal from reactions (1) and (2) and with a large shoulder at higher binding energies indicating In oxidation. The In3d peak in In_2O_3 occurs at the same binding energy as InP making it impossible to distinguish the two. The P2p peaks for reaction (3) show significant oxidation with a peak at 133.6 eV, but the InP doublet (128.7 eV and 129.5 eV) corroborates the XRD data, confirming the presence of InP.⁴² Zero-valent Bi is detected in reaction (3) along with oxidized Bi shown by the peaks at 159.1 eV and 164.5 eV that correspond to Bi_2O_3 . XPS of reaction (4) product showed trends very similar to reaction (3). The In3d and P2p peaks show significant oxidation. The Bi4f region shows both zero-valent and Bi_2O_3 peaks, the latter of which are more broad and greater in intensity than observed for reaction (3), indicating a greater extent of Bi oxidation.

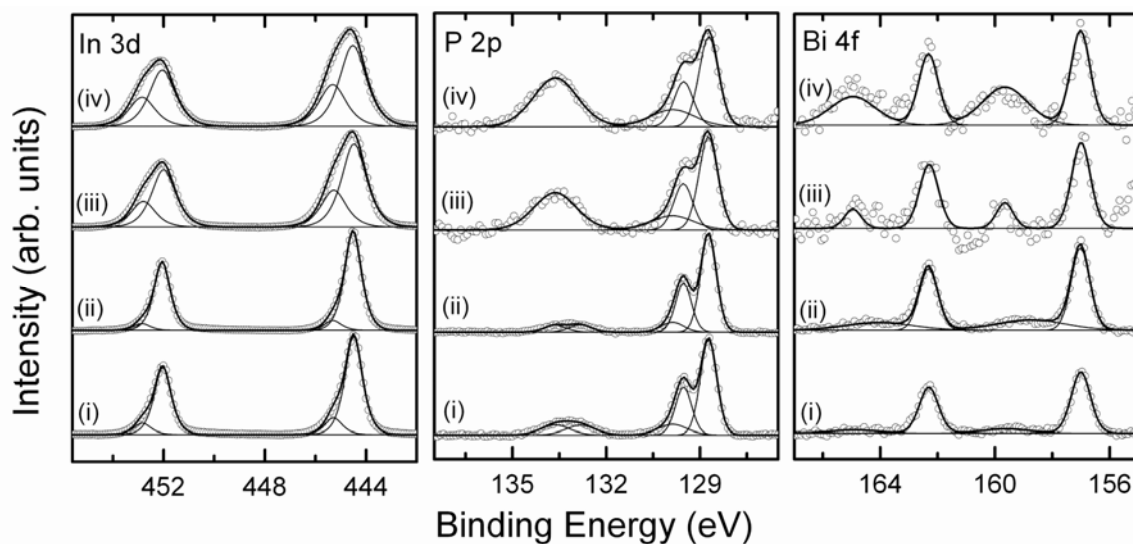


Figure 11.4: XPS spectra of the In3d, P2p, and Bi4f regions for reactions done in the presence of (i) OPA and HDA, (ii) OPA only, (iii) HDA only and (iv) neither ligand.

11.3.2 Role of HDA and OPA on Bi nanocrystal seeds

Bi nanocrystals were injected into the same reaction media used in reactions (1)–(4) without subsequent InP precursor injection to probe ligand-seed interactions. Figure 11.5 shows TEM of the seeds after these injections. Figure 11.5a shows that Bi nanocrystal seeds injected into a solution containing HDA and OPA increased in diameter from the initial seed size (14.0 ± 2.5 nm) to 30.6 ± 6.1 nm. Bi seeds injected into OPA only ($d = 42.5 \pm 3.4$ nm, Figure 11.5b) are to be etched by the OPA; the outer regions of these nanocrystals appear damaged compared to the as-prepared sample. Figure 11.5c shows injection into HDA only ($d = 53.7 \pm 10.6$ nm), and Figure 11.5d shows injection into neither ligand ($d = 85.7 \pm 19.5$ nm).

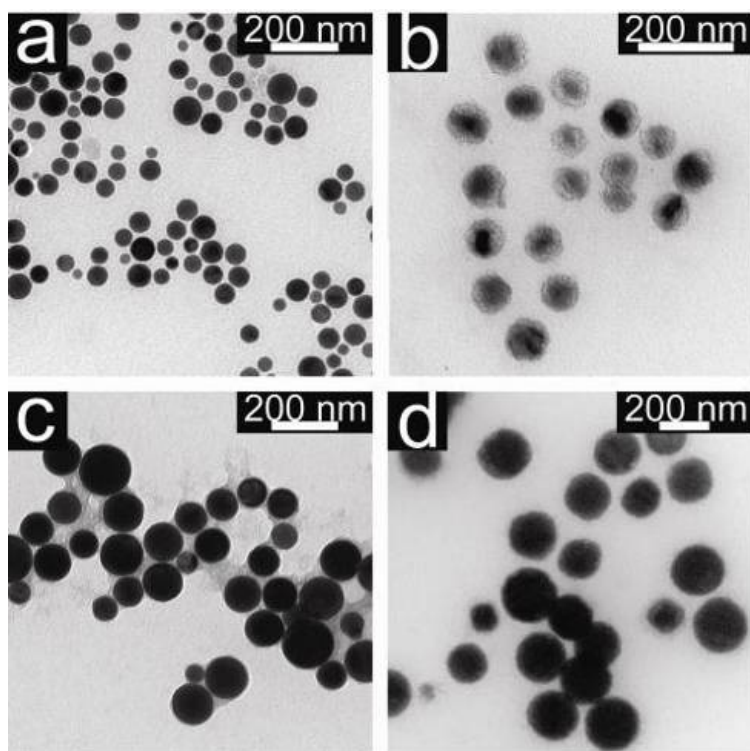


Figure 11.5: TEM of Bi nanoparticles injected into hot solvent containing (a) HDA and OPA, (b) OPA only, (c) HDA only, and (d) neither ligand.

XPS measurements were made on Bi nanocrystals injected into reaction mixtures containing (i) OPA and (ii) HDA and OPA and are shown in Figure 11.6. When only OPA is present, the nanocrystals are completely oxidized, with no Bi^0 observed and Bi_2O_3 peaks present at 159.1 eV and 164.5 eV. When HDA is also present, the extent of Bi oxidation is reduced as Bi^0 are observed (156.7 eV and 162 eV). This is strong evidence that the presence of HDA in the reaction mixture minimizes the oxidation of the Bi nanocrystals by OPA.

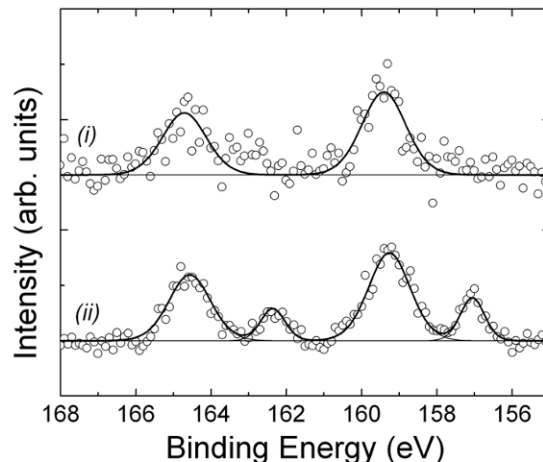


Figure 11.6: XPS spectrum of Bi seeds injected into reaction media containing (i) OPA and (ii) HDA and OPA.

11.3.3 Role of surfactants on InP nanowire growth

A summary of surfactant roles in the growth of InP nanowires follows. When both HDA and OPA are present single crystalline InP nanowires are produced. Removal of HDA from the reaction mixture results in irregularly periodically twinned InP nanowires with larger diameters (compared to when HDA is present). Furthermore, removing HDA results in oxidized Bi seeds indicating that HDA passivates the surface of the Bi nanocrystals. The Bi seeds still agglomerate in the presence of HDA, thus we conclude that the HDA–Bi interaction is weak (i.e., through a dative N–Bi bond). The Bi–N bond is highly polar and very weak. Many $\text{Bi}(\text{NR}_2)_3$ compounds are thermally unstable and decomposed at room-temperature; the Bi–N bond is also light-sensitive.⁴⁴ While HDA protects the Bi seed from oxidation, OPA attacks the seed and etches away the oxide layer. This etching effect helps keep the nanowire diameter narrow in reaction (2). Furthermore, OPA promotes the growth of InP nanowires; In_2O_3 forms when the ligand is absent. It remains unclear how OPA promotes the growth of InP, but XPS shows that the molecule does not bind to the surface of the nanowires. Figure I4 illustrates further the promotion of InP growth by introducing OPA in varying amounts. Myristate is present in all reactions and bonds to the surface of the nanowires. Figure

11.7 illustrates the role played by each ligand. Our data corroborate surface chemistry studies of InP nanostructures, which indicate that the InP surface is coated with a thin layer of InPO_x and passivated with a carboxylic acid and HDA in the case of InP quantum rods and HDA, TOPO, and MyrA in the case of quantum wires.^{6, 7, 12, 13}

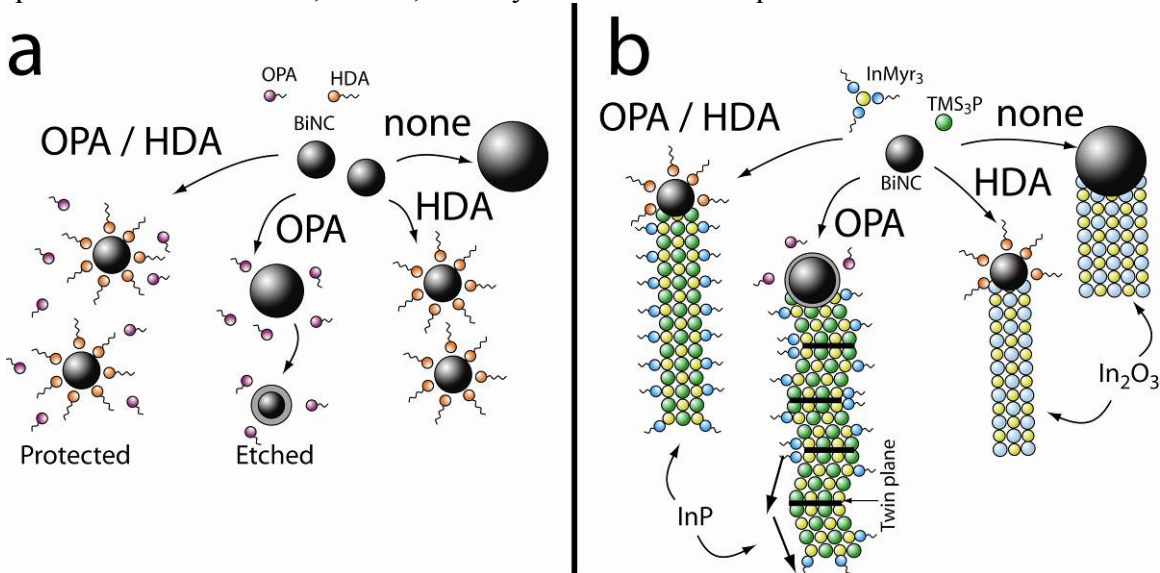


Figure 11.7: Schematic diagram displaying the effect of (a) HDA and OPA on Bi nanocrystals and (b) the role of each in the reaction of InMyr_3 with TMS_3P in the presence of Bi nanocrystals to form InP nanowires.

11.3.4 Effect phosphonic acids

Recent reports show secondary phosphines—such as diphenylphosphine (DPP) or di-*n*-octylphosphine (DOP)—are highly reactive. For instance, diphenylphosphine forms a Pb-phosphine complex promoting formation of PbSe nanocrystals,⁴⁵⁻⁴⁸ improving reaction yield. Furthermore, PbSe growth kinetics improve when DOP is present in small amounts.⁴⁹ These results motivate exploration of alternative phosphonic acids in InP nanowire reactions. Additional InP nanowire reactions were done using HDA and (5) phosphoric acid (H_3PO_4), (6) di-*n*-octylphosphonic acid (DOPA) and (7) tri-*n*-octylphosphine oxide (TOPO). TGA of product from reactions (2) and (5)–(7) was used to determine the reaction yield (see Figures I5 and I6). Table 11.1 summarizes these data, showing OPA has the lowest reaction yield.

Table 11.1: Reaction yield for reactions carried out in the presence of HDA and either H₃PO₄, OPA, DOPA or TOPO.

Reaction	Additive	Conversion (%) [‡]
5	H ₃ PO ₄	28
2	OPA	6
6	DOPA	25
7	TOPO	22

[‡]Based on In an P mass content in precursors (15.9 mg P in TMS₃P, 58.9 mg In in InMyI₃)

Figure 11.8 shows SEM, TEM, HRTEM, and corresponding FFT images for InP nanowires grown from Bi seeds and in the presence of HDA and either (**5**) H₃PO₄, (**2**) OPA, (**6**) DOPA, or (**7**) TOPO. For reaction (**5**), the H₃PO₄ was injected immediately before the In/P precursor solution in order to prevent the acid from evaporating beforehand. XRD for these reactions are shown in Figure 11.10. All phosphoric acid derivatives produce single-crystalline InP nanowires in high yield. Reactions carried out in DOPA produced a significant amount of particles (shown in Figure I7). This may be due to promoted In-P cluster formation due to the presence of DOPA, similar to how DPP induces formation of Pb-Se pairs in PbSe nanocrystal reactions.⁴⁵⁻⁴⁸ Nanowires grown in the presence of H₃PO₄ or TOPO were generally shorter, and had kinks. HRTEM images show wire growth in either the <111> (H₃PO₄–Figure 11.9iv, OPA–Figure 11.9j) or <110> (DOPA–Figure 11.9k, TOPO–Figure 11.9l) directions. Average (**reaction**) nanowire diameters were: (**2**) 16.8 ± 3.5 nm, (**5**) 17.6 ± 6.8 nm, (**6**) 10.2 ± 2.1 nm, (**7**) 12.3 ± 3.0 nm. XRD data shown in Figure 11.10 indicate exclusive growth of InP. Reaction (**2**) had a sufficiently low yield of InP nanowires that Bi diffraction peaks are visible. The use of H₃PO₄ in place of OPA reduces the cost of InP nanowire synthesis and DOPA can be used to produce nanowires with a more narrow distribution.

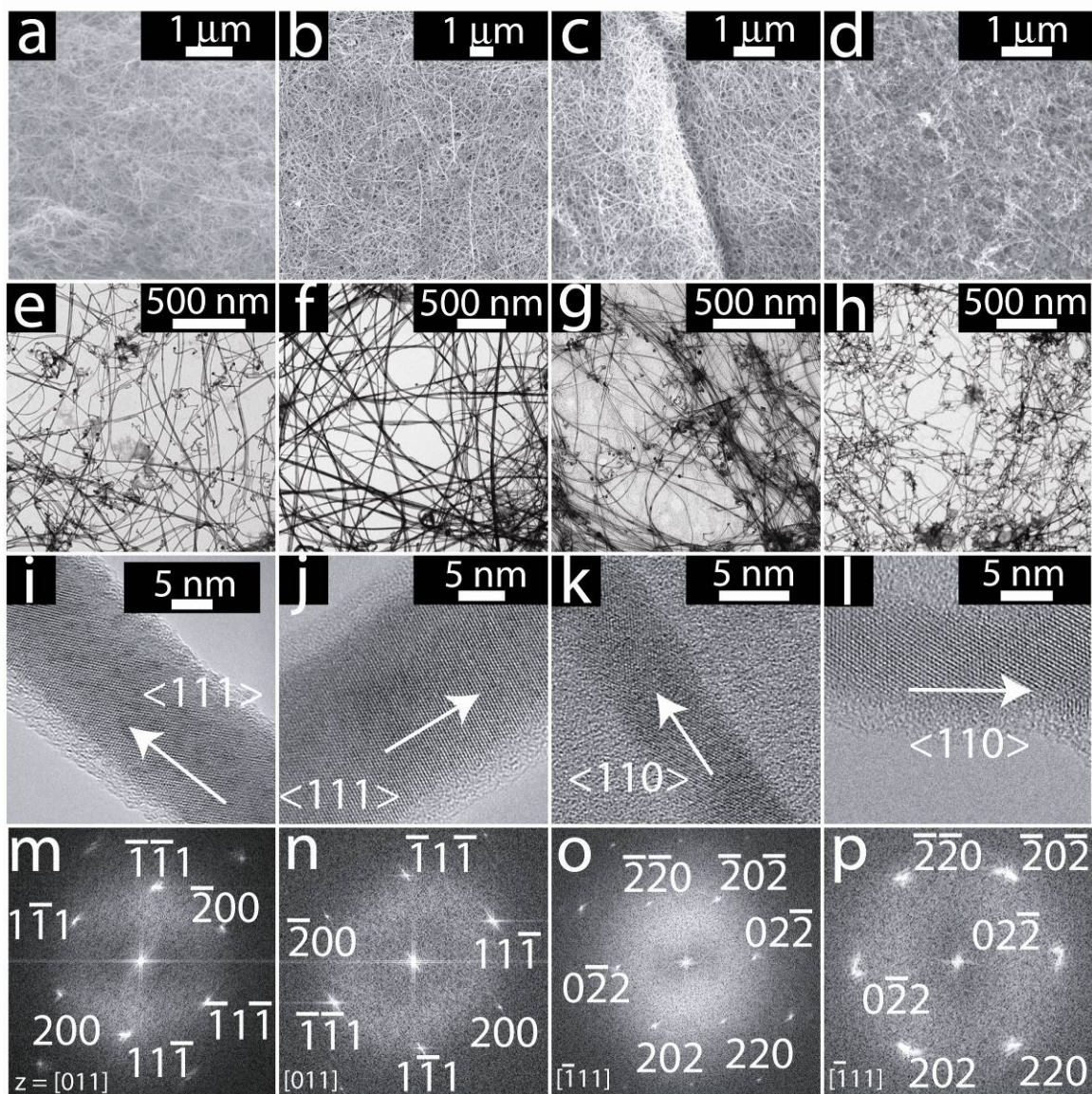


Figure 11.8: (a-d) SEM, (e-h) TEM, (i-l) HRTEM, and (m-p) corresponding FFT images of InP nanowires grown in the presence of HDA and (a, e, i, m) H_3PO_4 , (b, f, j, n) OPA (c, g, k, o) DOPA, and (d, h, l, p) TOPO.

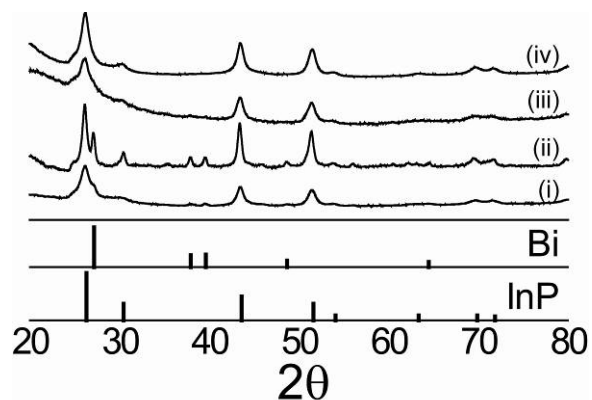


Figure 11.9: XRD InP nanowires grown in the presence of HDA and (i) H_3PO_4 , (ii) OPA (iii) DOPA, and (iv) TOPO.

Figure 11.10 shows XPS of nanowire samples grown in the presence of HDA and (i) H_3PO_4 , (ii) OPA, (iii) DOPA or (iv) TOPO. The XPS measurements reveal that replacement of OPA with these other surfactants does not significantly alter the surface characteristics of the produced wires. The H_3PO_4 reaction shows little presence of the P2p peaks corresponding to the presence of InP. H_3PO_4 oxidizes the surface of the wires, creating an InP_xO_y oxide layer. The InP signal in the P2p region is completely muted in the DOPA sample. This is due to the highly organic nature of the final product. DOPA reactions produce nanowires trapped in a gel-like matrix. As no other reaction forms this matrix, it is likely composed of the DOPA surfactant. Further study is necessary to determine the differences in reaction pathways based on these various ligands.

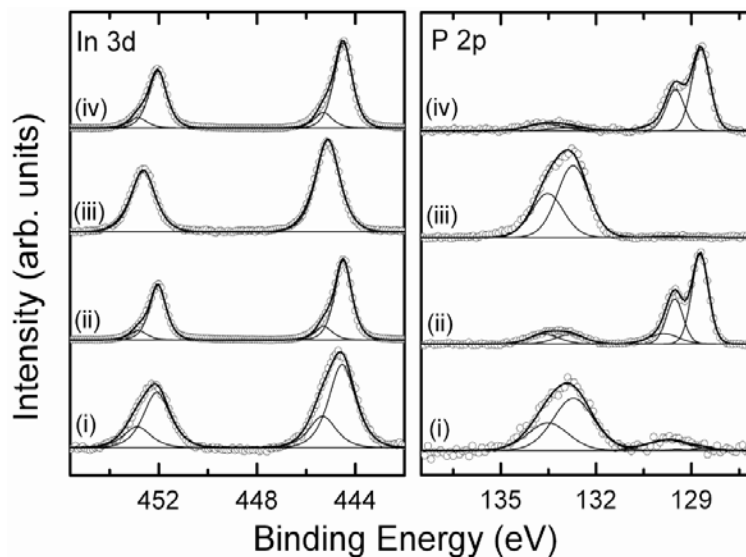


Figure 11.10: XPS spectra of InP nanowires prepared in the presence of HDA and (i) H_3PO_4 , (ii) OPA, (iii) DOPA or (iv) TOPO.

11.4 CONCLUSIONS

We report SLS growth of InP nanowires and study the role of various surfactants on the growth of the nanowires and probe the surface chemistry of InP nanowires grown in the presence of various combinations of ligands. We find that both OPA and HDA are essential for the growth of single crystalline InP nanowires; HDA reduces twinning and prevents Bi agglomeration while OPA promotes the growth of InP over In_2O_3 . The absence of OPA in the reaction yields a mixture of InP and In_2O_3 nanowires indicating a potential solution route to the latter pending improved control of the product morphology. Removing HDA from the reaction mixture yields InP nanowires, indicating that the surfactant does not play a direct role in promoting InP growth. Nanowires grown without HDA are irregularly periodically twinned in a twinning superlattice structure showing a potential solution route to this class of materials, which is of great interest in band gap engineering for optical applications. Furthermore, we report the synthesis of InP nanowires in the presence of DOPA (which produces a more narrow nanowire distribution), TOPO and—remarkably— H_3PO_4 with high yield. This opens up the prospect of using more conventional acid surfactants in place of their more expensive alkylated

derivatives. Further study is required to determine (1) the effect of impurities on SLS grown InP nanowires with TSLs and (2) the interactions between the surfactants—particularly phosphonic acid derivatives—and precursor compounds to elucidate the reaction pathways.

11.5 ACKNOWLEDGEMENTS

Authors making contributions to this work include: Vahid A. Akhavan and Brian A. Korgel. Chet Steinhagen provided helpful discussions pertaining to DOPA synthesis and Justin Harris was helpful in gathering TGA data. We also acknowledge Aaron Rogers and Karin Keller, responsible for mass spec. We thank ISP Technologies for providing the sample of Ganex. Funding for the Rigaku Spider X-ray diffractometer from the National Science Foundation Grant No. 0741973 is also acknowledged.

11.6 REFERENCES

1. Yu, H.; Li, J. B.; Loomis, R. A.; Wang, L. W.; Buhro, W. E. *Nat. Mater.* **2003**, *2*, 517-520.
2. Shweky, I.; Aharoni, A.; Mokari, T.; Rothenberg, E.; Nadler, M.; Popov, I.; Banin, U. *Mater. Sci. Eng. C* **2006**, *26*, 788-794.
3. Micic, O. I.; Sprague, J.; Lu, Z.; Nozik, A. J. *App. Phys. Lett.* **1996**, *68*, 3150-3152.
4. Mičić, O. I.; Jones, K. M.; Cahill, A.; Nozik, A. J. *J. Phys. Chem. B* **1998**, *102*, 9791-9796.
5. Duan, X.; Huang, Y.; Cui, Y.; Wang, J.; Lieber, C. M. *Nature* **2001**, *409*, 66-69.
6. Cros-Gagneux, A.; Delpech, F.; Nayral, C. I.; Cornejo, A.; Coppel, Y.; Chaudret, B. *J. Am. Chem. Soc.* **2010**, *132*, 18147-18157.
7. Moreels, I.; Martins, J. C.; Hens, Z. *Sensor. Actuat. B-Chem.* **2007**, *126*, 283-288.
8. Hens, Z.; Moreels, I.; Martins, J. C. *ChemPhysChem* **2005**, *6*, 2578-2584.
9. Guzelian, A. A.; Katari, J. E. B.; Kadavanich, A. V.; Banin, U.; Hamad, K.; Juban, E.; Alivisatos, A. P.; Wolters, R. H.; Arnold, C. C.; Heath, J. R. *J. Phys. Chem.* **1996**, *100*, 7212-7219.
10. Mičić, O. I.; Ahrenkiel, S. P.; Nozik, A. J. *App. Phys. Lett.* **2001**, *78*, 4022-4024.

11. Fanfair, D. D.; Korgel, B. A. *Cryst. Growth. Des.* **2005**, *5*, 1971-1976.
12. Wang, F.; Buhro, W. E. *J. Am. Chem. Soc.* **2007**, *129*, 14381-14387.
13. Wang, F.; Yu, H.; Li, J.; Hang, Q.; Zemlyanov, D.; Gibbons, P. C.; Wang; Janes, D. B.; Buhro, W. E. *J. Am. Chem. Soc.* **2007**, *129*, 14327-14335.
14. Dick, K. A.; Caroff, P.; Bolinsson, J.; Messing, M. E.; Johansson, J.; Deppert, K.; Wallenberg, L. R.; Samuelson, L. *Semicond. Sci. Tech.* **2010**, *25*, 024009.
15. Caroff, P.; Dick, K. A.; Johansson, J.; Messing, M. E.; Deppert, K.; Samuelson, L. *Nat. Nanotechnol.* **2009**, *4*, 50-55.
16. Algra, R. E.; Verheijen, M. A.; Borgstrom, M. T.; Feiner, L. F.; Immink, G.; van Enckevort, W. J. P.; Vlieg, E.; Bakkers, E. *Nature* **2008**, *456*, 369-372.
17. Kriegner, D.; Wintersberger, E.; Kawaguchi, K.; Wallentin, J.; Borgstrom, M. T.; Stangl, J. *Nanotechnology* **2011**, *22*, 425704.
18. Algra, R. E.; Vonk, V.; Wermeille, D.; Szweryn, W. J.; Verheijen, M. A.; van Enckevort, W. J. P.; Bode, A. A. C.; Noorduyn, W. L.; Tancini, E.; de Jong, A. E. F.; Bakkers, E. P. A. M.; Vlieg, E. *Nano Lett.* **2011**, *11*, 44-48.
19. Xiong, Q.; Wang, J.; Eklund, P. C. *Nano Lett.* **2006**, *6*, 2736-2742.
20. Akiyama, T.; Sano, K.; Nakamura, K.; Ito, T. *Jpn. J. App. Phys* **2006**, *45*, L275-L278.
21. Korgel, B. A. *Nat. Mater.* **2006**, *5*, 521-522.
22. Ikonc, Z.; Srivastava, G. P.; Inkson, J. C. *Phys. Rev. B* **1995**, *52*, 14078-14085.
23. Luo, X. D.; Hu, C. Y.; Xu, Z. Y.; Luo, H. L.; Wang, Y. Q.; Wang, J. N.; Ge, W. K. *App. Phys. Lett.* **2002**, *81*, 3795-3797.
24. Benyattou, T.; Garcia, M. A.; Monéger, S.; Tabata, A.; Sacilotti, M.; Abraham, P.; Monteil, Y.; Landers, R. *Appl. Surf. Sci.* **1993**, *63*, 197-201.
25. Fouquet, J. E.; Minsky, M. S.; Rosner, S. J. *App. Phys. Lett.* **1993**, *63*, 3212-3214.
26. Lu, X. H.; Yu, P. Y.; Zheng, L. X.; Xu, S. J.; Xie, M. H.; Tong, S. Y. *App. Phys. Lett.* **2003**, *82*, 1033-1035.
27. Liu, Q.; Derksen, S.; Lindner, A.; Scheffer, F.; Prost, W.; Tegude, F. J. *J. App. Phys.* **1995**, *77*, 1154-1158.
28. Wang, F.; Buhro, W. E. *Small* **2010**, *6*, 573-581.
29. Chockla, A. M.; Harris, J. T.; Korgel, B. A. *Chem. Mater.* **2011**, *23*, 1964-1970.
30. Williams, R. H.; Hamilton, L. A. *J. Am. Chem. Soc.* **1952**, *74*, 5418-5420.
31. Wang, F.; Tang, R.; Kao, J. L. F.; Dingman, S. D.; Buhro, W. E. *J. Am. Chem. Soc.* **2009**, *131*, 4983-4994.

32. Davidson, F. M.; Lee, D. C.; Fanfair, D. D.; Korgel, B. A. *J. Phys. Chem. C* **2007**, *111*, 2929-2935.
33. Davidson, F. M.; Wiacek, R.; Korgel, B. A. *Chem. Mater.* **2004**, *17*, 230-233.
34. Chen, G.; Wang, L.; Sheng, X.; Liu, H.; Pi, X.; Zhang, Y.; Li, D.; Yang, D. *Nanoscale Res. Lett.* **2010**, *5*, 898-903.
35. Pozuelo, M.; Prikhodko, S. V.; Grantab, R.; Zhou, H.; Gao, L.; Sitzman, S. D.; Gambin, V.; Shenoy, V. B.; Hicks, R. F.; Kodambaka, S. *J. Cryst. Growth* **2010**, *312*, 2305-2309.
36. Joyce, H. J.; Wong-Leung, J.; Gao, Q.; Tan, H. H.; Jagadish, C. *Nano Lett.* **2010**, *10*, 908-915.
37. Shen, G.; Bando, Y.; Liu, B.; Tang, C.; Golberg, D. *J. Phys. Chem. B* **2006**, *110*, 20129-20132.
38. Impurity value obtained from Sigma Aldrich chemical analysis certificate.
39. Airoidi, C.; Silva, M. L. C. P.; Chagas, A. P. *J. Chem. Soc.* **1986**, *9*, 1913-1916.
40. Patiño, R.; Campos, M.; Torres, L. A. *Inorg. Chem.* **2007**, *46*, 9332-9336.
41. Hines, M. A.; Guyot-Sionnest, P. *J. Phys. Chem. B* **1998**, *102*, 3655-3657.
42. Hollinger, G.; Bergignat, E.; Joseph, J.; Robach, Y. *J. Vac. Sci. Technol. A* **1985**, *3*, 2082-2088.
43. Hauffman, T.; Blajiev, O.; Snauwaert, J.; van Haesendonck, C.; Hubin, A.; Tarryn, H. *Langmuir* **2008**, *24*, 13450-13456.
44. Suzuki, H., Komatsu, N., Ogawa, T., Murafuji, T., Ikegami, T., Matano, Y. *Organobismuth Chemistry*. **2001**, 149-150.
45. Yu, K.; Hrdina, A.; Zhang, X. G.; Ouyang, J. Y.; Leek, D. M.; Wu, X. H.; Gong, M. L.; Wilkinson, D.; Li, C. S. *Chem. Commun.* **2010**, *47*, 8811-8813.
46. Yu, K.; Ouyang, J.; Leek, D. M. *Small* **2011**, *7*, 2250-2262.
47. Steckel, J. S.; Yen, B. K. H.; Oertel, D. C.; Bawendi, M. G. *J. Am. Chem. Soc.* **2006**, *128*, 13032-13033.
48. Joo, J.; Pietryga, J. M.; McGuire, J. A.; Jeon, S.-H.; Williams, D. J.; Wang, H.-L.; Klimov, V. I. *J. Am. Chem. Soc.* **2009**, *131*, 10620-10628.
49. Evans, C. M.; Evans, M. E.; Krauss, T. D. *J. Am. Chem. Soc.* **2010**, *132*, 10973-10975.

Chapter 12: Conclusions and Future Directions

12.1 CONCLUSIONS

12.1.1 Nanowire growth

Solution methods to growing single crystalline nanowires (e.g., SLS, SFLS) offer high-throughput, low-cost routes to producing gram-scale quantities in a matter of minutes using lab equipment. SLS-grown Ge nanowires nucleate from Au seeded within seconds and can be easily scaled.¹ Trisilane—a particularly reactive Si source in SFLS synthesis—is capable of producing nanowires at the astonishing rate of 6–8g hr⁻¹.² Due to the extreme reactivity, however, trisilane requires a large concentration of seed particles. As such, Au is typically present in concentrations as high as 25% w/w in the final nanowire reaction product. The presence of Au is detrimental to Li-ion battery performance as lithiation is only partially reversible.^{3, 4} Furthermore, Au hinders optical and electronic properties due to deep trap states within the Si band gap.⁵ Historically, Si and Ge nanowires have been grown predominately using Bi and Au. The demonstrated in-situ growth of Si nanowires from Sn seeds not only addresses this point, but it also paves the way for faster processing by eliminating the need to pre-synthesize seed particles. These nanowires perform better than Au seeded Si nanowires as negative electrodes in Li-ion batteries and may also perform well in nanowire transistors.

12.1.2 Nanowires as negative electrodes in Li-ion batteries

A variety of active material and electrolyte combinations were explored as negative electrodes in Li-ion batteries. Ge nanowires were shown to perform well when mixed with the PVdF binder, even without heat treatment, as is the typical practice.⁶ Furthermore, thanks to fast Li diffusion, Ge nanowires were shown to perform well in batteries cycled under typical end-user conditions, showing capacities between 600 and

700 mA h g⁻¹ for over 1000 cycles at a rate of 1C (where 1C is the current density required to fully lithiate or delithiate the electrode in 1 hour). Though various electrolytes were tested for Ge, only the PVdF binder was employed. A self-healing process occurs for binders that exhibit hydrogen bonding which has shown to improve cyclability in Si systems⁷⁻⁹ and should to be extended to Ge to further improve cyclability. A caveat: these binders are typically dissolved in water, which complicates slurry formation Ge-based electrode systems as Ge forms a water-soluble oxide. In order to test Ge nanowires with these binders the nanowires must be surface passivated to prevent oxidation and etching from water.

A variety of Si nanowire systems were studied. Si nanowires were grown using the extremely reactive trisilane precursor and either pre-synthesized Au nanocrystals or in-situ formed Sn nanoparticles. Au seeded wires were tested as-prepared and with the Au removed through a simple etching procedure. All nanowires were tested with PVdF and NaAlg binders. While only the Sn-seeded nanowires performed well when mixed with PVdF even after heat treatment, NaAlg was found to improve cycling behavior for all systems. The presence of Au is detrimental to the cycling behavior of Si nanowires, which can be improved dramatically through Au-removal. For all electrode systems surveyed, the best performers were those cycled using electrolytes that contained FEC. In the case of Ge nanowires, for example, FEC forms a thin passivating SEI layer on the nanowire surface that allows efficient charge and ion transport. In contrast, non-FEC containing electrolytes form thick SEI layers that grow with repeated cycling. Further surface chemistry analysis, similar to what was done for Ge nanowire films in Chapter 6, is needed to better understand the cycling behavior of these various Si electrodes.

The efficacy of fully flexible electrode materials was also explored using fabric made from Si nanowires grown with the MPS precursor and annealed to convert the

intrinsic poly (phenylsilane) shell to a conductive carbonaceous coating.¹⁰ SFLS Si nanowires grown using trisilane and SLS Ge nanowires grown using DPG were also tested as flexible films supported with RGO, albeit with limited success. Flexible electrodes suffer from poor contact with the current collector.

12.1.3 Nanorods

Ge nanorods were produced using SLS techniques seeded from in-situ formed Bi nanocrystals. Nanorod growth was found to be sensitive to the concentration of PVP/HDE copolymer, a compound necessary for the formation of monodisperse Bi nanocrystals.¹¹ At high copolymer concentrations, for instance, branched Ge nanorods were formed,¹² a phenomenon previously observed for compound semiconductors only. Due to complications caused by this polymer, work pertaining to Ge nanorods was abandoned until a polymer-free Bi nanocrystal synthesis was reported.¹³ This simplified Ge nanorod synthesis allowing for optical studies. Optical measurements were made on these Bi-seeded Ge nanorods and compared to calculations using the DDA. The DDA calculations were used to explain the formation and evolution of an internal reflectance peak that forms between 550 nm and 700 nm in the absorption spectrum, which was correlated to the complex index of refraction and dielectric function. The peak was also found to be heavily dependent on incident electric field orientation and rod length, but not on rod diameter. This work shows the potential for fine-tuning of optical properties through controlled growth of Ge nanorods. The DDA is a powerful tool that can be used to calculate scattering and absorption of electromagnetic waves by bodies with arbitrary size and geometry and can be further extended to other material systems (e.g., Si nanorods).

12.1.4 Ligand chemistry

Indium phosphide nanowires were grown using SLS techniques in the presence of various surfactant molecules. The surface chemistry was examined for nanowires grown using various combinations of ligands. High quality InP nanowires require the presence of an amine (i.e., HDA), which protects the Bi seeds, as well as a phosphoric acid derivative (e.g., OPA, DOPA, TOPO), which promotes InP nanowire growth. A solution route to In₂O₃ nanowires was also reported by simply removing the phosphonic acid ligand from the reaction mixture. By not using an amine, TSL InP nanowires can be grown. Remarkably, H₃PO₄ was found to produce InP nanowires with high yield. This opens up the prospect of using more conventional acid surfactants in place of their more expensive alkylated derivatives for other compound semiconductors with proven solution synthesis routes.

12.2 FUTURE DIRECTIONS

In-situ seeded techniques can be employed to realize large-scale production of nanowires at reduce processing cost. These methods can also be extended to nanorod growth to produce nanorods that exhibit quantum confinement effects that currently remain elusive to Si in this class of materials due to the presence of Au.^{14, 15} In addition, a variety of different seed materials may be employed using such methods. The DDA has proven a powerful tool in interpreting absorption spectra for Ge nanorods and nanowires¹⁶ and can be used to do the same for Si nanorods. Surface fictionalization also remains to be tested for nanowires grown using in-situ seeding methods. Silicon forms a native oxide, which, though not detrimental to Li-ion battery performance, negatively affects electronic characteristics. Controlling the surface properties of solution grown Si and Ge nanowires is essential for the realization of many microelectronic applications.

With a strong understanding of electrochemical and cycling performance of solution grown Si and Ge nanowires as negative electrodes in Li-ion batteries, there are multitude of paths that can be taken moving forward in this area of research. While a large body of literature chronicles the success of Si- and Ge-based electrode systems, a leap in Li-ion battery technology also requires advancement in Li-storage properties of the positive electrodes. Conventional cathode materials act as the source of Li, though alternatives such as sulfur¹⁷ and MF₃ (M = Fe, Ti, V)^{18, 19} have higher Li-storage capacity and are capable of making such advancements. With Li-free anode and cathode materials, it becomes necessary to introduce Li into the system. This can be done one of two ways: (1) pre-lithiation²⁰ of either Si or Ge nanowires, or (2) synthesis of Li_xSi_{1-x} or Li_xGe_{1-x} nanowires. Cycling lithiated Si or Ge nanowires against high capacity cathodes such as sulfur or FeF₃ will produce true working batteries with high overall capacity.

Ge nanowires cycled with FEC-containing electrolytes exhibited interesting temperature-dependent effects warranting further study as well. This material system may prove to be a strong candidate for high-temperature high-power applications like automobile batteries. As mentioned above, a survey of new binder systems is a further area of investigation for Ge nanowires in Li-ion batteries that remains to be explored. In addition to the NaAlg binder, which showed marked improvement for Si nanowire electrodes, CMC, poly(methylmethacrylate) (PMMA), polyacrylic acid (PAA), and polyaniline (PANI) may serve as good binders. PANI may be particularly interesting as it is a conductive polymer that may eliminate the need to add conductive carbon to the electrode slurry.

In the area of materials, SiGe alloys should be explored. SiGe combines the advantages of its two constituent elements into a single material. For instance, the conductivity of SiGe is higher than Si while the maximum theoretical capacity for Li-

insertion is higher than Ge. Negatively doped Si and Ge nanowires show enhanced Li^+ diffusion which improves battery performance under high current densities and should also be t

Fully-flexible power sources may be possible through the use of electrochemically active paper electrodes. This was shown to be the case for Si nanowires grown using MPS and annealed under a reducing atmosphere. Given the high Li-storage capacity of Ge and the superior cycle behavior at high rates, Ge nanowire membranes should be explored as mechanically flexible substrates. This can be done in a similar process as was demonstrated for Si nanowires, for example, by growing a carbonaceous shell on the wires, and making and annealing fabric from these wires in a reducing atmosphere. In general, the gamut of materials available for testing as both positive and negative electrodes for flexible Li-ion batteries needs to grow. Developmental advancements of the methods reported in this manuscript would also show improvement in this area. For instance, in order to improve the RGO supported flexible electrodes, Si and Ge nanowires should be either (1) surface functionalized such that a covalent bond can be formed with the RGO surface or (2) Si / Ge nanowires should be grown straight from Au nanoparticles deposited on the RGO surface. Furthermore, as these materials are conventionally tested in coin-cell type battery cells, methods of fabricating fully functioning flexible Li-ion batteries with high capacity need further development.²¹ Concepts necessary to realize these flexible batteries can also be extended to other flexible devices like solar cells and transistors. Finally, in the area of compound semiconductor nanowires, simplified ligand chemistry may provide greener routes to solution phase synthesis and should be explored for other compound semiconductor systems.

12.3 REFERENCES

1. Chockla, A. M.; Korgel, B. A. *J. Mater. Chem.* **2009**, *19*, 996-1001.
2. Heitsch, A. T.; Akhavan, V. A.; Korgel, B. A. *Chem. Mater.* **2011**, *23*, 2697-2699.
3. Yuan, L.; Liu, H. K.; Maarroof, A.; Konstantinov, K.; Liu, J.; Cortie, M. *J. New Mater. Electr. Sys.* **2007**, *10*, 95-99.
4. Taillades, G.; Benjelloun, N.; Sarradin, J.; Ribes, M. *Solid State Ionics* **2002**, *152-153*, 119-124.
5. Sze, S. M.; Irvin, J. C. *Solid State Electron.* **1968**, *11*, 599-602.
6. Li, J.; Christensen, L.; Obrovac, M. N.; Hewitt, K. C.; Dahn, J. R. *J. Electrochem. Soc.* **2008**, *155*, A234-A238.
7. Kovalenko, I.; Zdyrko, B.; Magasinski, A.; Hertzberg, B.; Milicev, Z.; Burtovyy, R.; Luzinov, I.; Yushin, G. *Science* **2011**, *334*, 75-79.
8. Bridel, J. S.; Azail's, T.; Morcrette, M.; Tarascon, J. M.; Larcher, D. *Chem. Mater.* **2009**, *22*, 1229-1241.
9. Ding, N.; Xu, J.; Yao, Y. X.; Wegner, G.; Lieberwirth, I.; Chen, C. H. *J. Power Sources* **2009**, *192*, 644-651.
10. Chockla, A. M.; Harris, J. T.; Akhavan, V. A.; Bogart, T. D.; Holmberg, V. C.; Steinhagen, C.; Mullins, C. B.; Stevenson, K. J.; Korgel, B. A. *J. Am. Chem. Soc.* **2011**, *133*, 20914-20921.
11. Wang, F.; Buhro, W. E. *Small* **2010**, *6*, 573-581.
12. Chockla, A. M.; Harris, J. T.; Korgel, B. A. *Chem. Mater.* **2011**, *23*, 1964-1970.
13. Yarema, M.; Kovalenko, M. V.; Hesser, G. n.; Talapin, D. V.; Heiss, W. *J. Am. Chem. Soc.* **2010**, *132*, 15158-15159.
14. Heitsch, A. T.; Hessel, C. M.; Akhavan, V. A.; Korgel, B. A. *Nano Lett.* **2009**, *9*, 3042-3047.
15. Hessel, C. M.; Heitsch, A. T.; Korgel, B. A. *Nano Lett.* **2009**, *10*, 176-180.
16. Smith, D. A.; Holmberg, V. C.; Rasch, M. R.; Korgel, B. A. *J. Phys. Chem. C* **2010**, *114*, 20983-20989.
17. Zheng, G.; Yang, Y.; Cha, J. J.; Hong, S. S.; Cui, Y. *Nano Lett.* **2011**, *11*, 4462-4467.
18. Li, T.; Li, L.; Cao, Y. L.; Ai, X. P.; Yang, H. X. *J. Phys. Chem. C* **2010**, *114*, 3190-3195.
19. Li, H.; Richter, G.; Maier, J. *Adv. Mater.* **2003**, *15*, 736-739.

20. Liu, N.; Hu, L.; McDowell, M. T.; Jackson, A.; Cui, Y. *ACS Nano* **2011**, *5*, 6487-6493.
21. Hu, L.; Wu, H.; La, M. F.; Yang, Y.; Cui, Y. *ACS Nano* **2010**, *4*, 5843-5848.

Appendix A[§]

A.1 Solvents and reaction byproducts

Figure A1 shows the chemical structures of the high boiling solvents examined in this study.

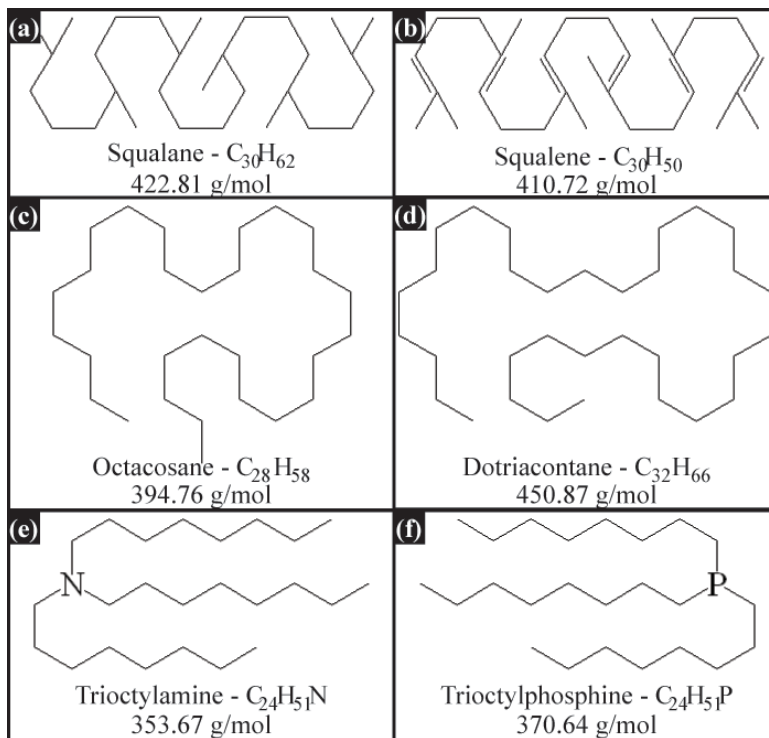


Figure A1: Chemical structure, name, formula and molecular weight for (a) squalane, (b) squalene, (c) octacosane, (d) dotriacontane, (e) trioctylamine and (f) trioctylphosphine. Tri-*n*-octylamine and tri-*n*-phosphine both have coordinating groups, whereas the others are long chain hydrocarbons.

Figure A2 shows SEM images of some of the unwanted reaction byproducts observed with Ge nanowires in some reactions. Figure A3 shows the amorphous Ge

[§] This chapter appears in *Journal of Materials Chemistry* **2009**, *19*, 996-1001, Supplementary Information.

particles that are formed in when DPG was heated to 400°C without the addition of Au nanocrystals.

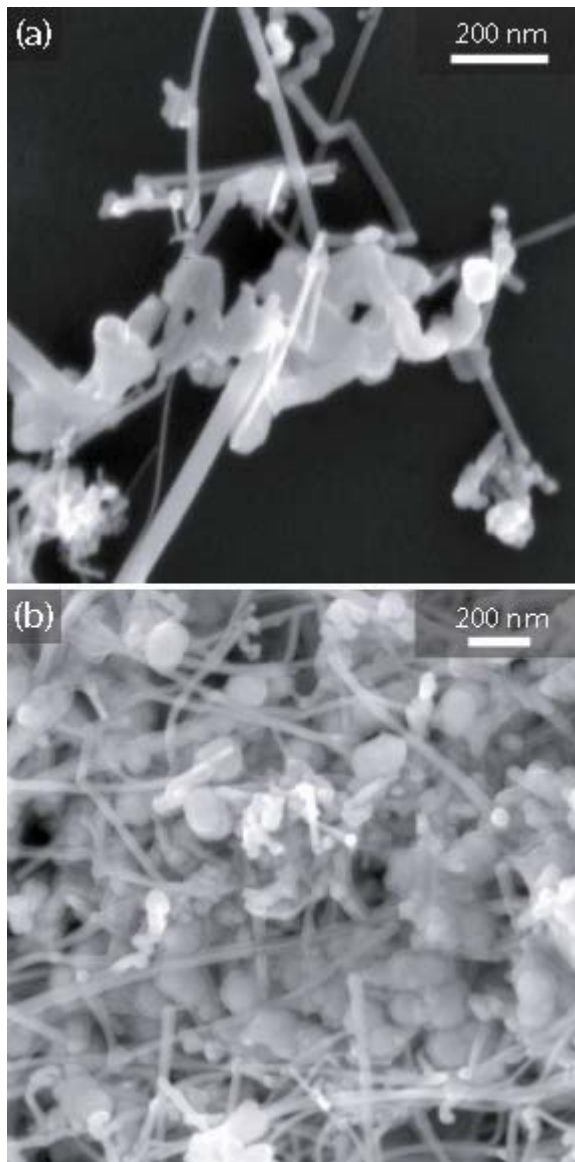


Figure A2: SEM images of reaction byproducts formed during SLS Ge nanowire growth: (a) kinked nanowires and (b) homogeneously nucleated amorphous Ge particles.

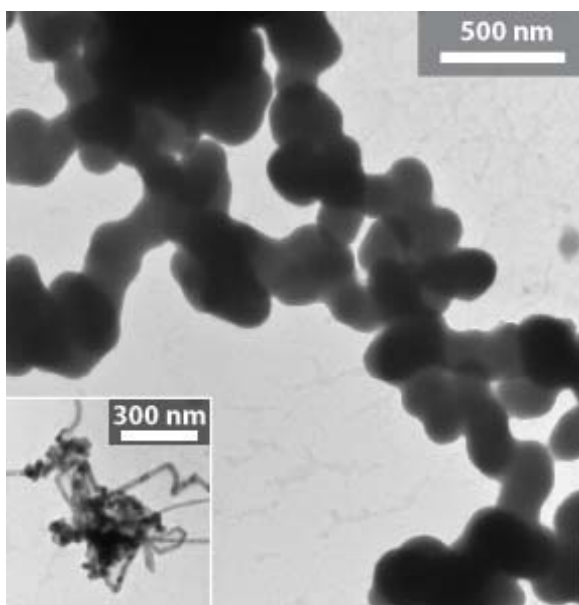


Figure A3: TEM images of the solid reaction product obtained when DPG was heated in squalane at 400°C for 2 hrs in the absence of Au nanocrystals. The product is primarily necked amorphous Ge particles, but there are also a very small number of Ge nanowires that form, such as those in the TEM image in the inset.

A.2 Phenylgermane identification by mass spectrometry

Positive and negative chemical ionization mass spectroscopy (PCI-MS and NCI-MS) was performed on a Thermo Finnigan TSQ700 mass spectrometer. PCI-MS and NCI-MS of as-received DPG was acquired with 300 mM DPG in toluene solutions. PCI-MS and NCI-MS data of the squalane reaction mixture were obtained by diluting a 500 μ L aliquot drawn from the reaction flask with 5 mL of additional toluene.

Several phenylgermane species have similar molecular weights, (*e.g.*, a (phenyl)_(x)germane and a (phenyl)_(x-1)digermane). For example, DPG and MPG₂, differ by less than 2 mass units due to the difference of a phenyl ring (C₆H₅, MW = 77.11 g mol⁻¹) and a germane radical (GeH₃, MW = 75.67). Their nearly equivalent molecular weights make it difficult to distinguish them in the MS data. The same similarities in

molecular weights exist for phenylated trigermane compounds as well. These similarities do not exist for all species, however, and the data indicates conclusively the presence of phenyldigermanes, for example through the peaks observed at mass to charge ratios of 455 (QPG₂) and 530 (PPG₂ not shown). The existence of trigermanes, however, could not conclusively be determined and due to the stability of the Ge-Ge bond were excluded from the analysis. Various phenylgermane species are shown in Figure A4.

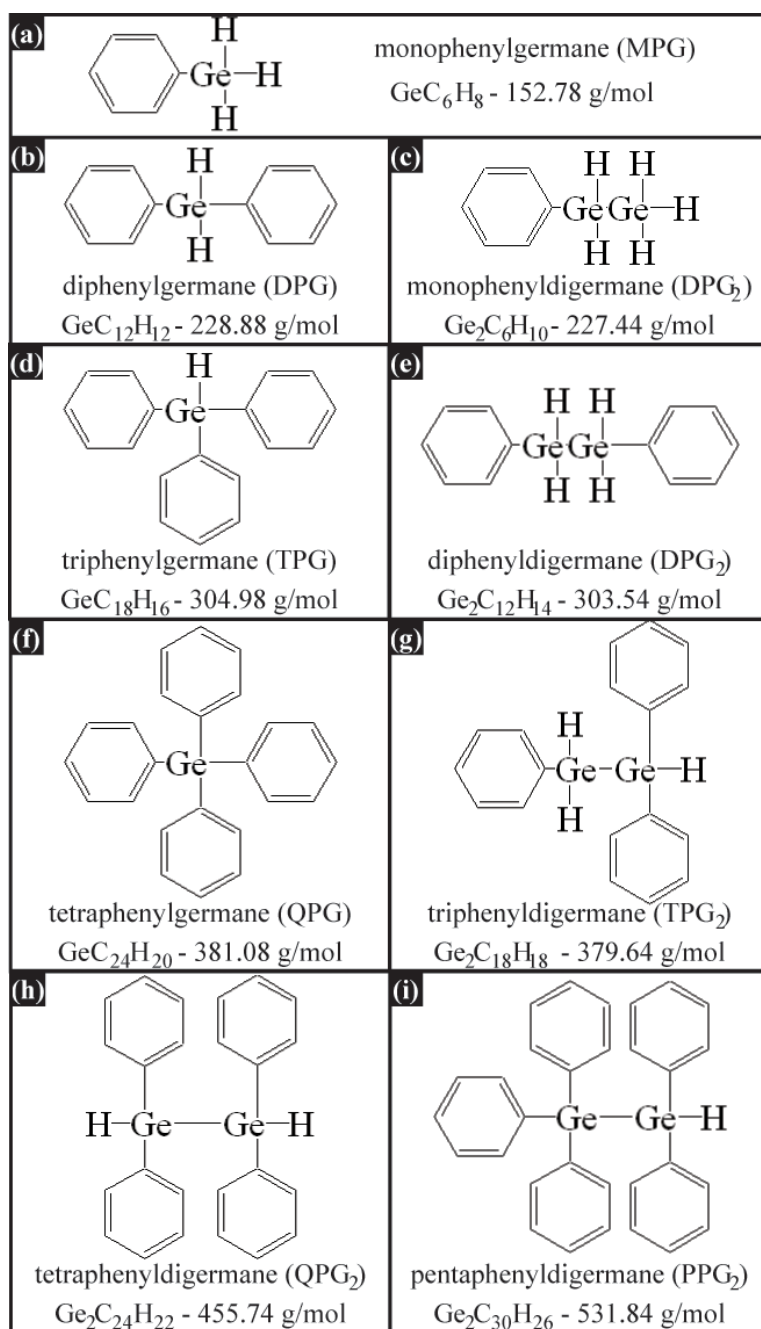


Figure A4: Phenylgermanes observed by mass spectrometry: (a) monophenylgermane, (b) diphenylgermane, (c) monophenyldigermene, (d) triphenylgermane, (e) diphenyldigermene, (f) tetraphenylgermane, (g) triphenyldigermene, (h) tetraphenyldigermene and (g) pentaphenyldigermene. Molecules with similar molecular weights are displayed side-by-side for ease of comparison.

Figure A5 shows PCI-MS and NCI-MS scans of DPG as-received from the supplier and aliquots taken from a DPG decomposition reaction in squalane at 380°C (without Au nanocrystals). MS showed that in addition to DPG, other phenylgermane compounds were present in the as-received compound, including monophenylgermane (MPG), triphenylgermane (TPG), tetraphenylgermane (QPG), tetraphenyldigermene (QPG₂) and pentaphenyldigermene (PPG₂) (peaked at a mass/charge ratio of 530, not shown). When DPG was heated in squalane at 380°C, heavier phenylgermanes increased in relative concentration and DPG disappeared after 10 minutes of heating. TPG also disappeared from the reaction mixture after 10 minutes. These MS data shows that DPG decomposes under these conditions by phenyl redistribution.

Redistribution leads to tetraphenylgermane as a thermally stable, reaction byproduct (which is insoluble in the solvent and therefore does not appear in the MS data). The MS data also revealed that dimeric species like tetraphenyldigermene end up as relatively stable reaction byproducts. (It is possible that some Ge oligomers form in the ionizer during analysis as well). These dimeric species are not desirable because they lead to lower DPG conversions to Ge nanowires.

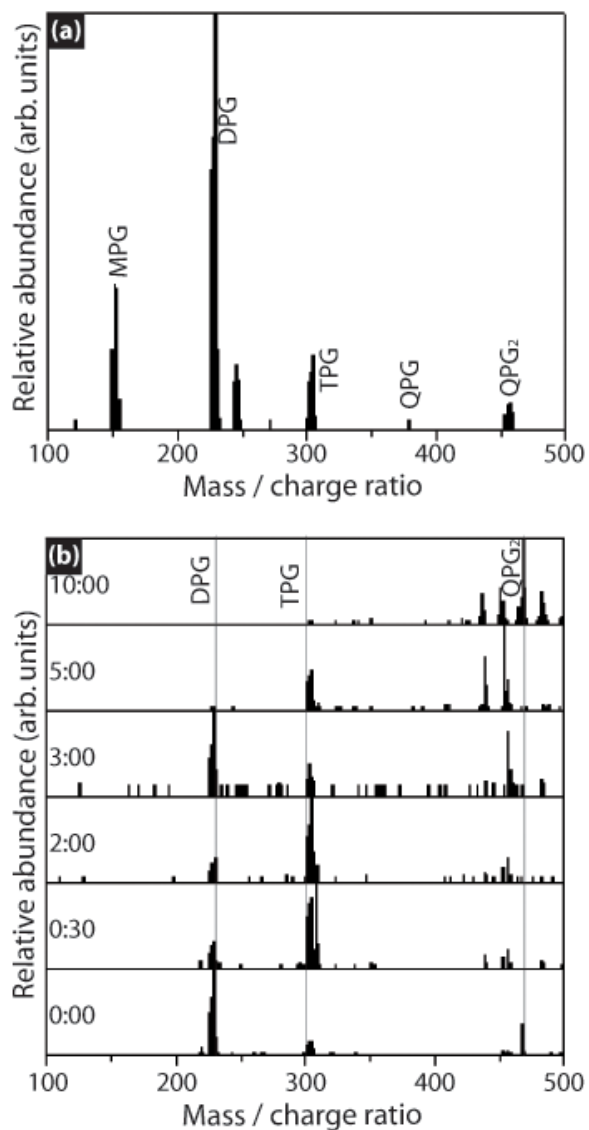


Figure A5: (a) PCI-MS scans of (a) DPG as received from Gelest. (b) NCI-MS scans of aliquots taken from a DPG decomposition reaction in squalane at 380°C without Au nanocrystals. The reaction times are noted in minutes:seconds format next to each spectrum. Peaks are labeled that correspond to diphenylgermane (DPG), triphenylgermane (TPG) and tetraphenyldigermene (QPG₂).

Appendix B[§]

B.1 Cycle rates and additional characterization

Table B1 lists the theoretical charging capacities of Si, Ge and RGO combinations used to determine the C rates reported in the body of the manuscript. X-ray diffraction (XRD) data for the Si and Ge nanowires used in the study are shown in Figure B1.

Table B1: C-rates determined from the theoretical charging capacities of Si, Ge and RGO. Cycling at a rate of 1C is equivalent to charging or discharging 1 g of battery material in 1 hour.

	RGO (% w/w)	Si (% w/w)	Ge (% w/w)	C (mA h g ⁻¹)
Battery 1	0	100	0	3579
Battery 2	25	75	0	2777
Battery 3	50	50	0	1976
Battery 4	75	25	0	998
Battery 5	100	0	0	372
Battery 6	75	0	25	684
Battery 7	50	0	50	996
Battery 8	25	0	75	1308
Battery 9	0	0	100	1620

[§] This chapter was accepted for publication in *The Journal of Physical Chemistry C* **April, 2012**

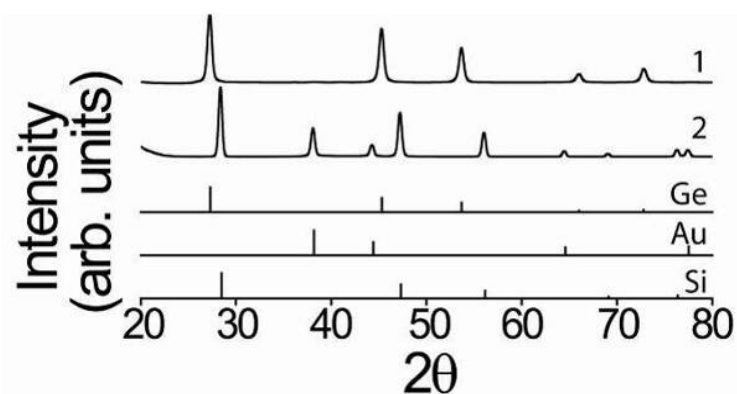


Figure B1: XRD of (1) Ge nanowires and (2) Si nanowires. Data were acquired using a Rigaku R-Axis Spider Diffractometer with Image plate detector, Cu K_{α} radiation ($\lambda = 1.5418 \text{ \AA}$) at 40 kV and 40 mA, with samples on a 0.5 mm nylon loop, scanning for 10 min with sample rotation at 1° per second. Background scattering from the nylon loop has been subtracted. Reference patterns are provided for Ge (JCPDS: 00-004-0545), Au (JCPDS: 00-004-0784), and Si (JCPDS: 00-027-1402).

B.2 Additional electrochemical characterization

Figure B2 shows voltage profiles and differential capacity data for Si nanowires without RGO corresponding to the capacity data in Figure 4.4a. Figure B3 shows an expanded view of the differential capacity curves in the inset of Figure 4.4b for Si nanowire / RGO anodes (75% w/w Si). Figure B4 shows the voltage profiles and differential capacity plots corresponding to the capacity data in Figure 4.6 for Ge nanowire anodes (without RGO). Figure B5 shows an expanded view of the differential capacity curves plotted in the inset of Figure B6b for Ge nanowire / RGO (75% w/w Ge). Figure B6 shows the voltage profiles and differential capacity data corresponding to the capacity data in Figure 4.9 for Ge nanowire/RGO (75% w/w Ge) and Si nanowire / RGO (75% w/w Si) anodes.

The first cycle shown in Figure B2b shows a sharp lithiation peak at 100 mV corresponding to lithiation of crystalline Si to amorphous Si ($a\text{-Li}_x\text{Si}$) along with a peak

at about 50 mV that corresponds to the formation of $\text{Li}_{15}\text{Si}_4$.¹ Delithiation exhibits two peaks: a broad peak at about 300 mV from delithiation of amorphous Si and a much sharper peak at just over 400 mV corresponding to delithiation of $\text{Li}_{15}\text{Si}_4$.¹ Significant irreversible capacity loss occurs with little electrochemical activity in later cycles.

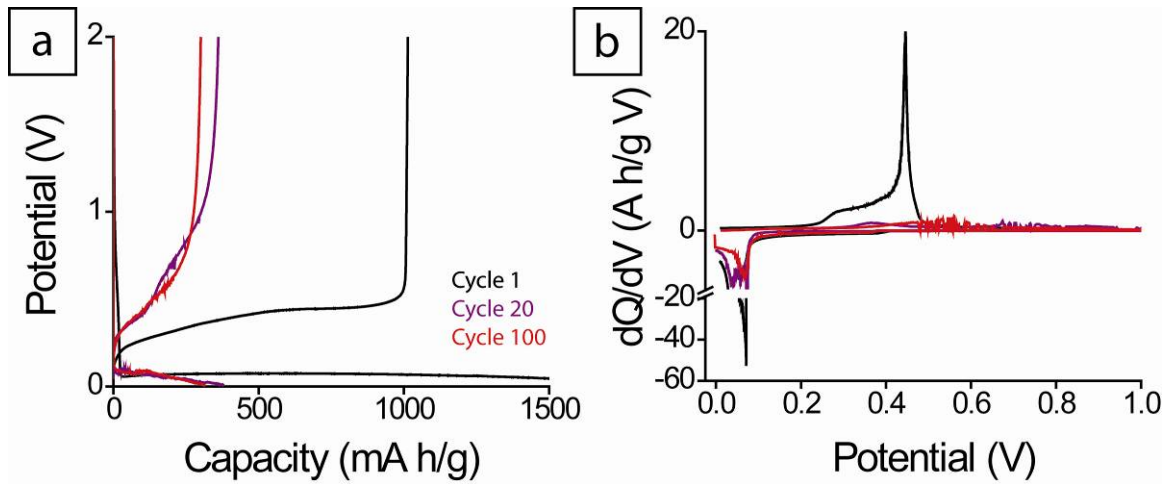


Figure B2: (a) Voltage profiles and (b) differential capacity curves of Si nanowires (without RGO) corresponding to the capacity data in Figure 4.4a.

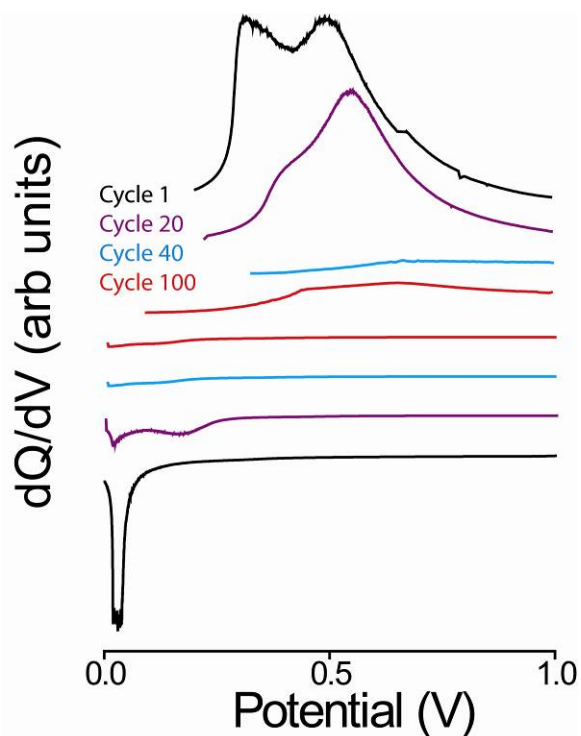


Figure B3: Expanded view of the differential capacity curves for Si nanowire/RGO (75% w/w Si) in the inset in Figure 4.4b. The curves are offset for clarity.

The first cycle differential capacity plot shown in Figure B4b shows a sharp lithiation peak at 300 mV and a delithiation peak at 500 mV, corresponding to the lithiation and delithiation potentials of Ge. The battery failed when the rate was increased above $C/5$, but electrochemical activity was restored when the rate was decreased back to $C/20$.

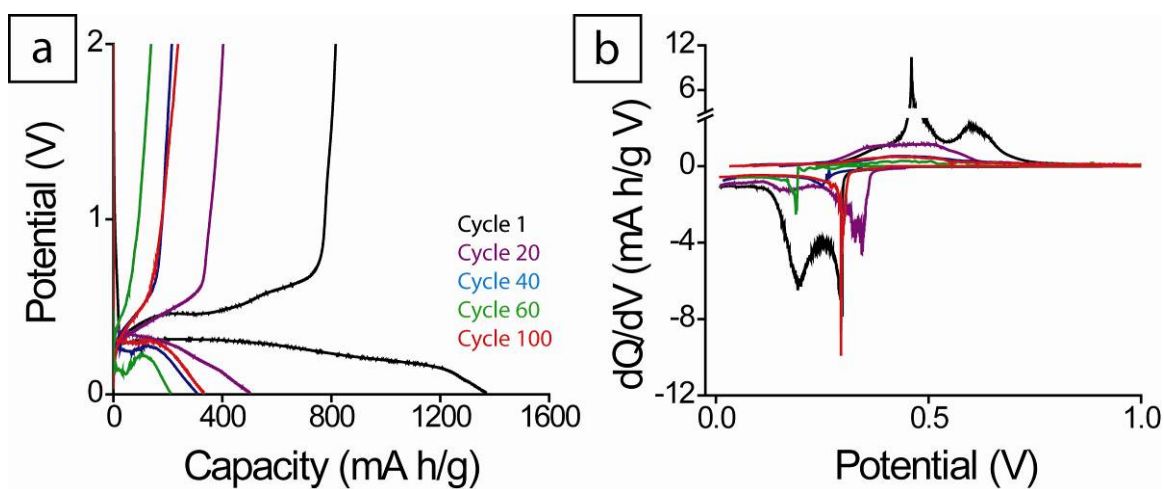


Figure B4: (a) Voltage profiles and (b) differential capacity curves for Ge nanowires (without RGO) corresponding to the capacity data in Figure 4.6.

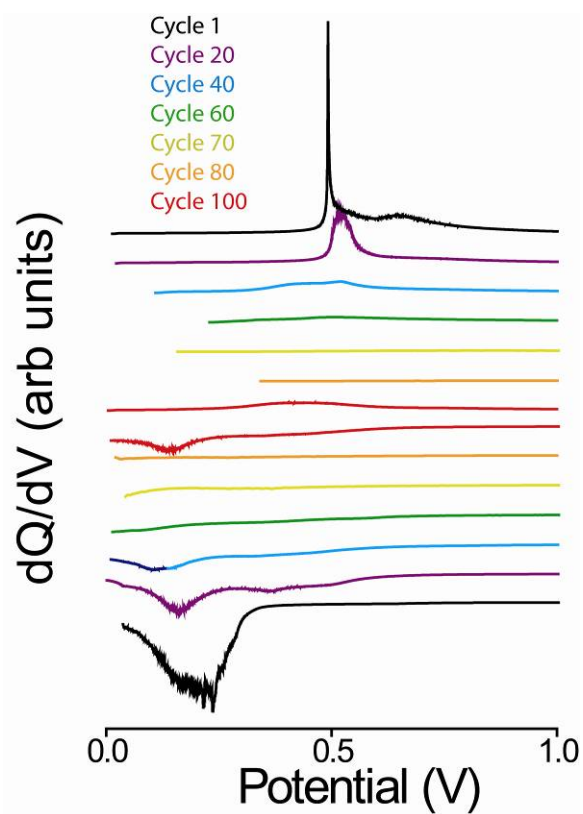


Figure B5: Expanded view of the differential capacity curves in the inset of Figure 4.6b for Ge nanowire / RGO (75% w/w Ge). The curves are offset for clarity.

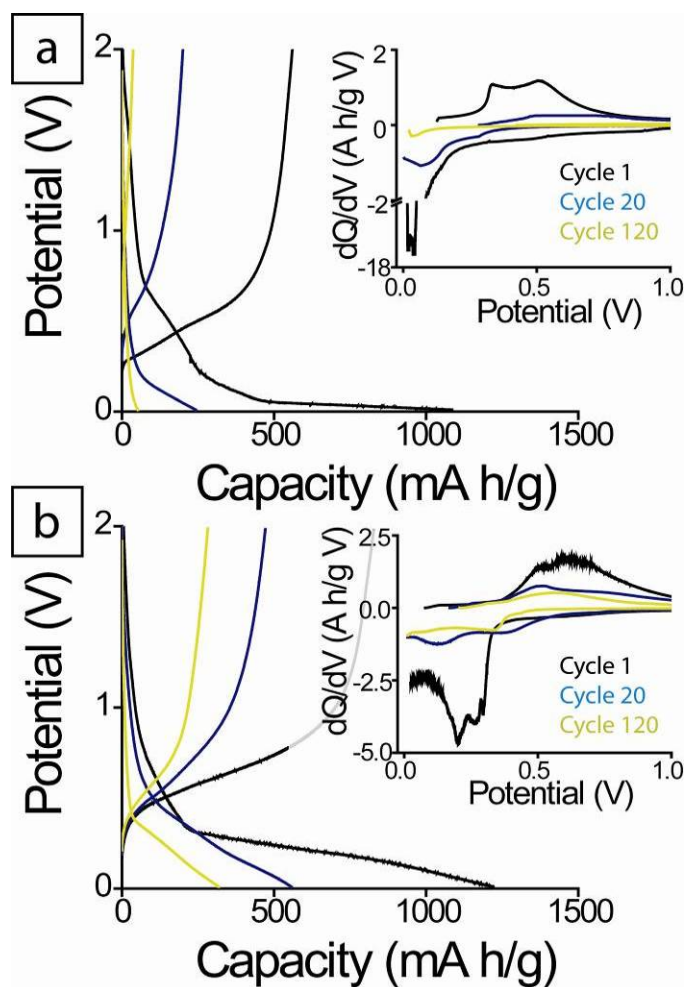


Figure B6: Voltage profiles of (a) Si nanowire / RGO (75% w/w Si) and (b) Ge nanowire / RGO (75% w/w Ge) anodes corresponding to the capacity data plotted in Figure 9. The batteries were cycled at C/20 for 20 cycles and then C/10 for 100 cycles. The corresponding differential capacity curves are plotted in the insets.

B.3 References

1. Obrovac, M. N.; Krause, L. J., *J. Electrochem. Soc.* **2007**, *154*, A103-A108.

Appendix C

C.1 Capacity retention using PC:DMC electrolyte

Figures C1 through C4 show cycling and electrochemical data in greater detail for the PC:DMC electrolyte system. Figure C1 shows the cycling behavior with coulombic efficiencies for this electrolyte with voltage profiles and differential capacity plots. The over potential and lithiation / delithiation peaks are similar to the values reported in the main text. PC:DMC is not a good electrolyte system to use for Ge nanowires. It forms a poor SEI layer that limits Li^+ transfer, evident by the poor coulombic efficiencies.

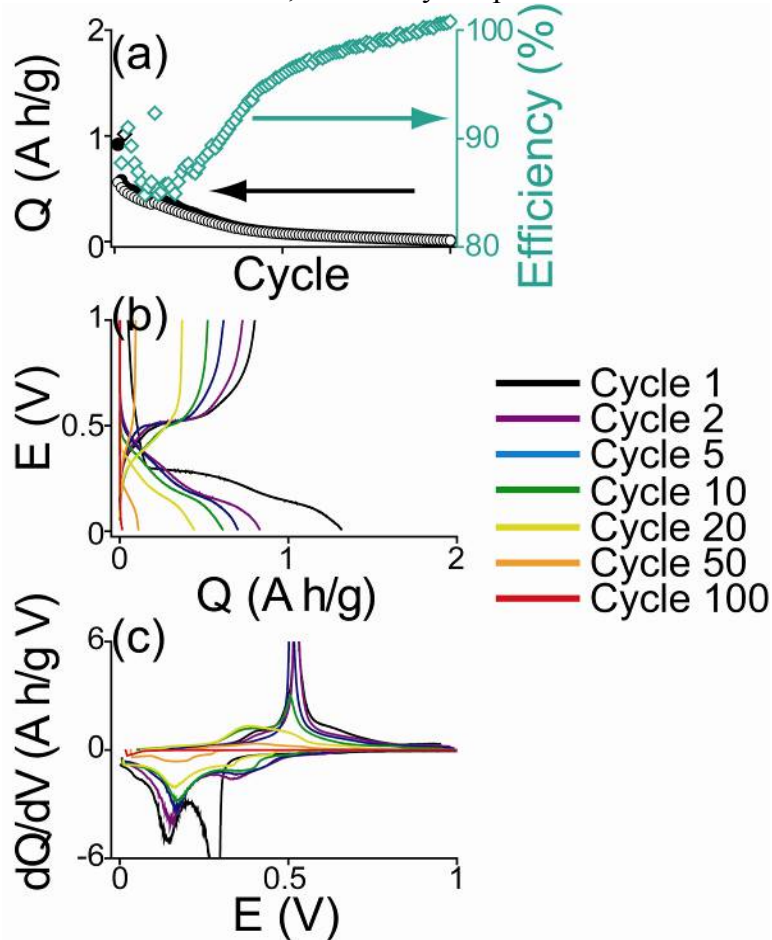


Figure C1: (a) Life cycle data, (b) voltage profiles, and (c) corresponding differential capacity plots for a battery cycled with PC:DMC.

Detailed electrochemical data are shown in Figure C2 that correspond to the data presented in Figure C1. Similar lithiation / delithiation trends are observed as detailed in the main text for the EC:DEC and EC:DMC electrolytes. Namely, lithiation occurs at 200 mV and 500 mV and fades into a single broad peak at lower potentials. Delithiation occurs at 500 mV and fades to lower potentials as well, forming a broad peak.

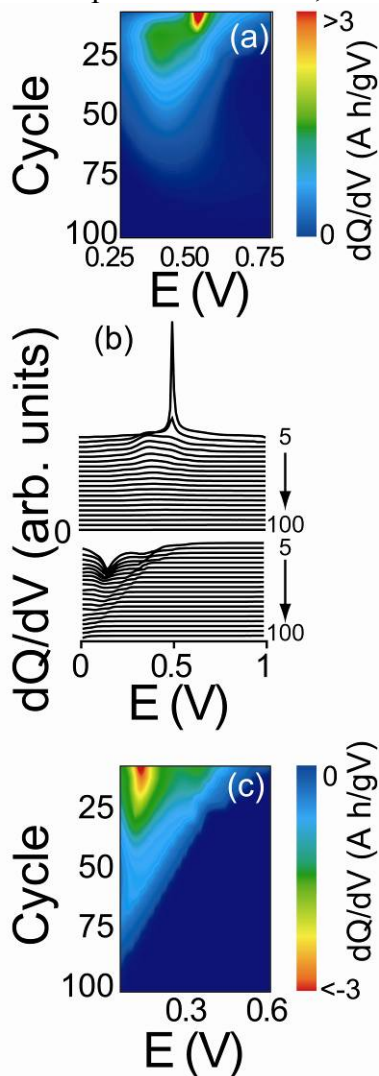


Figure C2: Differential capacity (a) discharge and (c) charge color maps with (b) waterfall plots for a battery cycled using an electrolyte solution of 1M LiPF_6 dissolved in a 1:1 w/w mixture of PC:DMC.

C.2 Rate test using PC:DMC electrolyte

Figure C3 shows the rate-test cycling behavior with coulombic efficiencies for the PC:DMC electrolyte with voltage profiles and differential capacity plots. The over potential and lithiation / delithiation peaks are similar to the values reported in the main text. Shifting peaks are not observed for this electrolyte, indicating that the shift observed in the main text may be due to more than just the non-equilibrium nature of the experiment. Here, charge transport is still the limiting factor. As proposed in the main text, there may be a rate-dependent variance in the lithiation pathway for Ge nanowires.

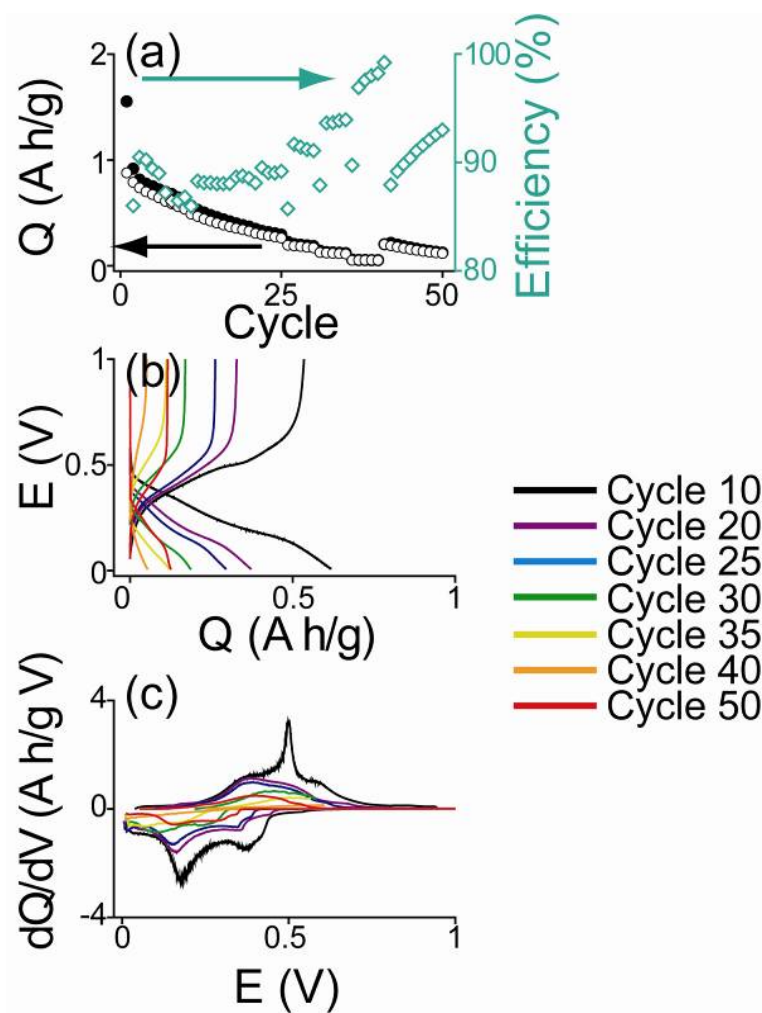


Figure C3: (a) Capacities, (b) voltage profiles and (c) differential capacity plots for a battery cycled using a 1:1 w/w electrolyte solvent mixture of PC:DMC. The battery was cycled at the following rates (number of cycles): C/20 (10), C/10 (10), C/5 (5), C/2 (5), 1C (5), 2C (5), C/10 (10).

Detailed electrochemical data are shown in Figure C4 that correspond to the data presented in Figure C3. Similar lithiation / delithiation trends are observed as discussed above in Figure C2.

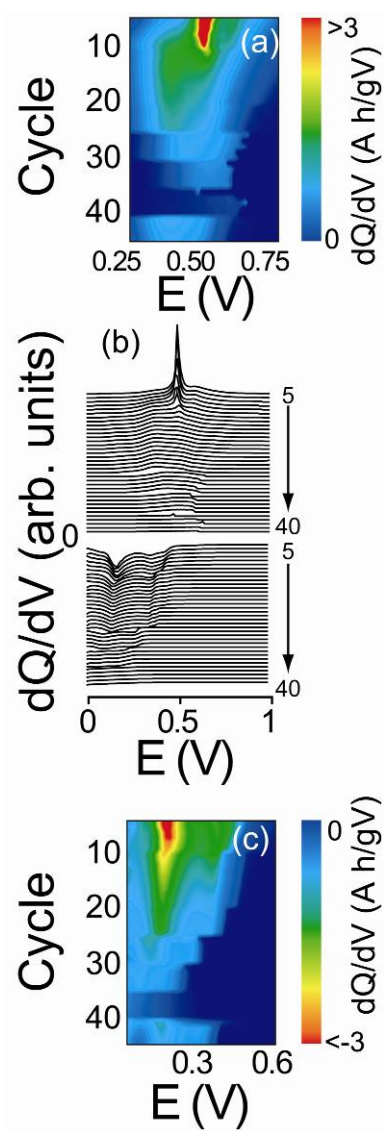


Figure C4: Differential capacity (a) discharge and (c) charge color maps with (b) waterfall plots for a battery cycled at various rates using the PC:DMC electrolyte.

Appendix D

D.1 XPS peak deconvolution of high resolution elemental scans

High resolution elemental XPS scans of the Ge3d orbital are presented in Figure D1 with peak deconvolution envelopes shown for Ge nanowire films cycled with EC:DEC (Figure D1a), EC:DMC (Figure D1b), and FEC:DMC (Figure D1c) electrolyte solutions. Scans were taken before sputtering with Ar⁺ ions (4 keV) and again after sputtering for 20 seconds, 2 minutes, 5 minutes, 15 minutes, and 30 minutes. Similar data are shown for the C1s, O1s, Li1s, F1s, and P2p orbitals in Figures D2–D6, respectively.

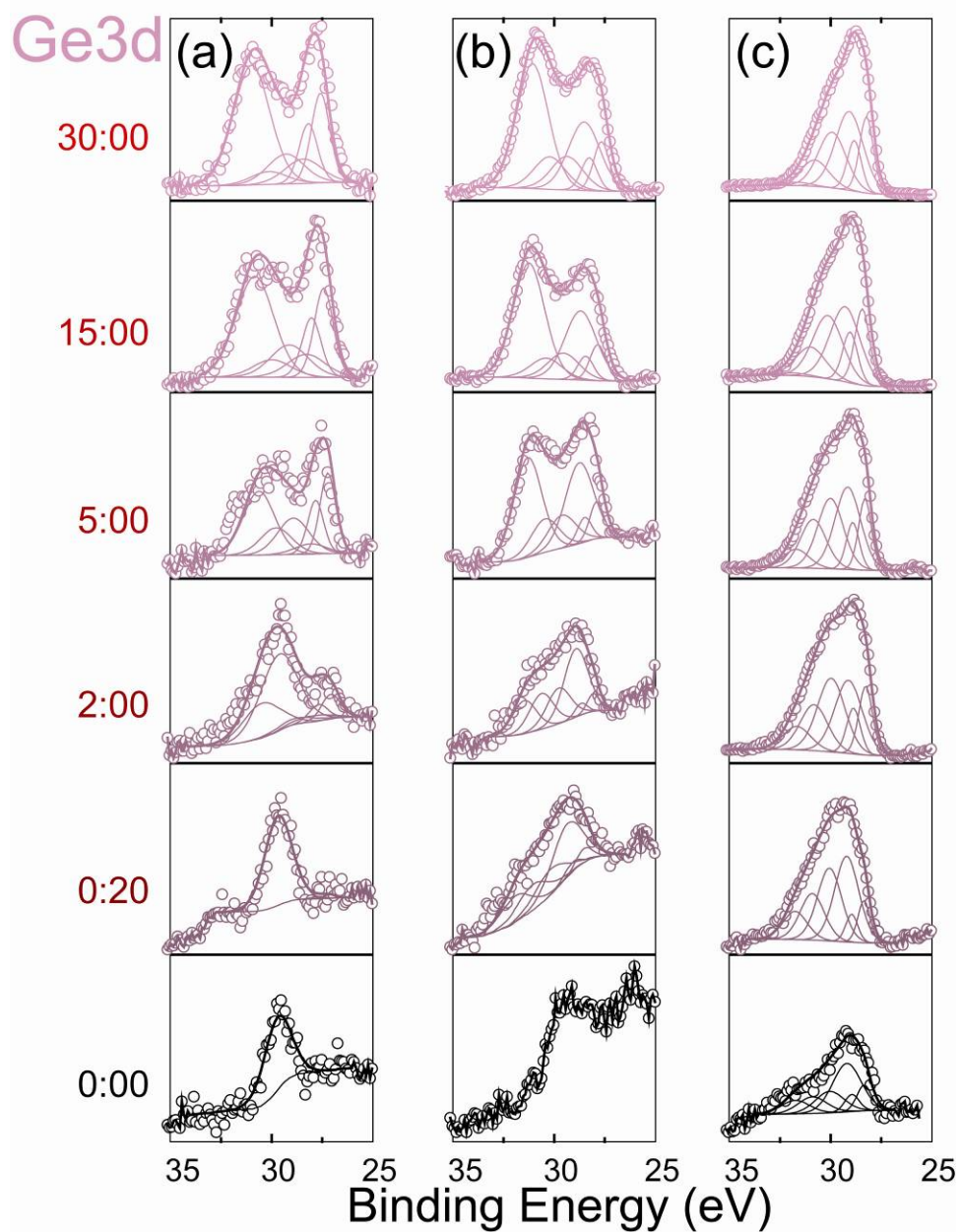


Figure D1: Deconvoluted high-resolution XPS element scans of the Ge3d orbital at the indicated sputtering times for Ge nanowire films cycled using (a) EC:DEC, (b) EC:DMC, and (c) FEC:DMC.

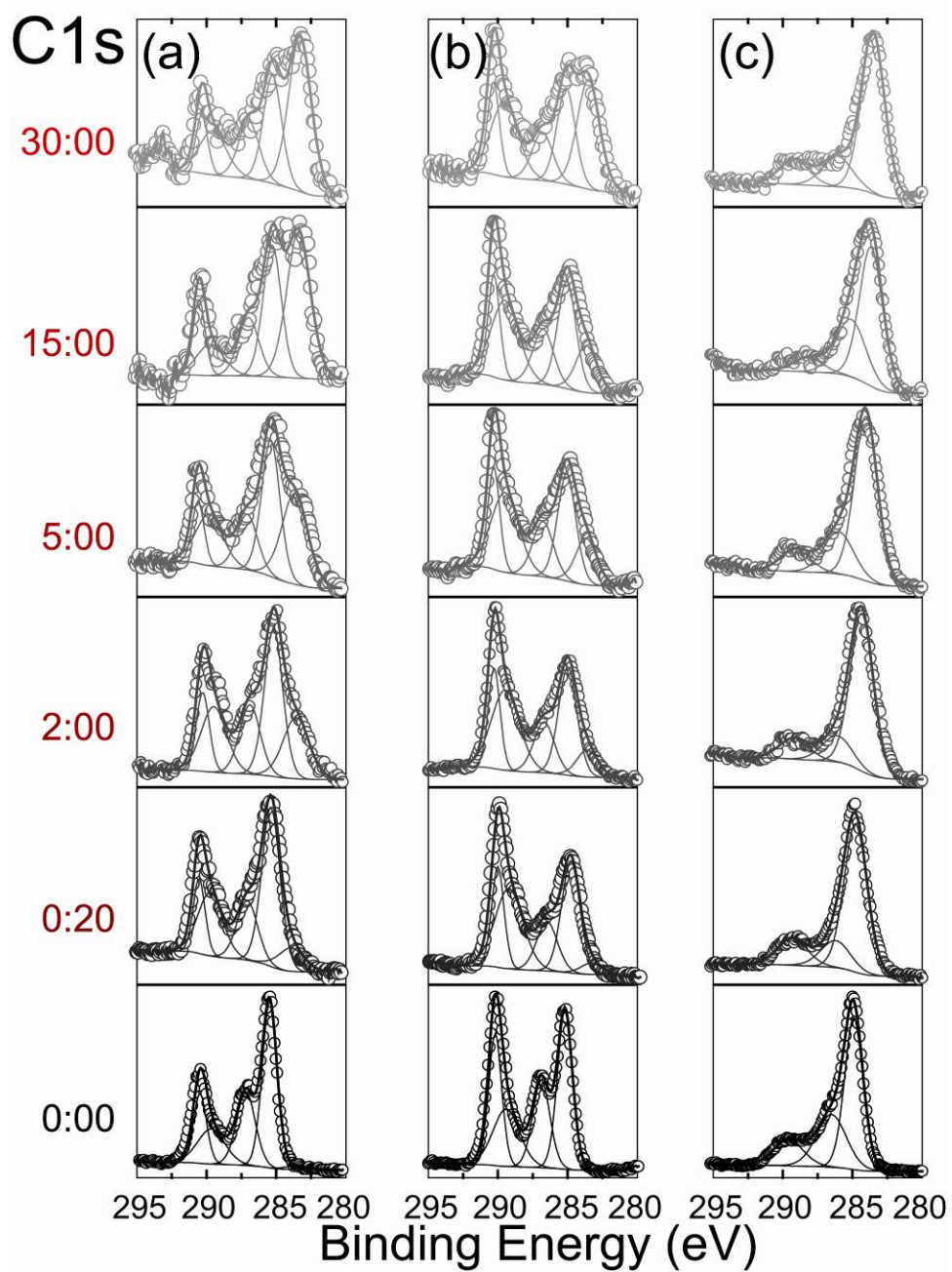


Figure D2: Deconvoluted high-resolution XPS element scans of the C1s orbital at the indicated sputtering times for Ge nanowire films cycled using (a) EC:DEC, (b) EC:DMC, and (c) FEC:DMC.

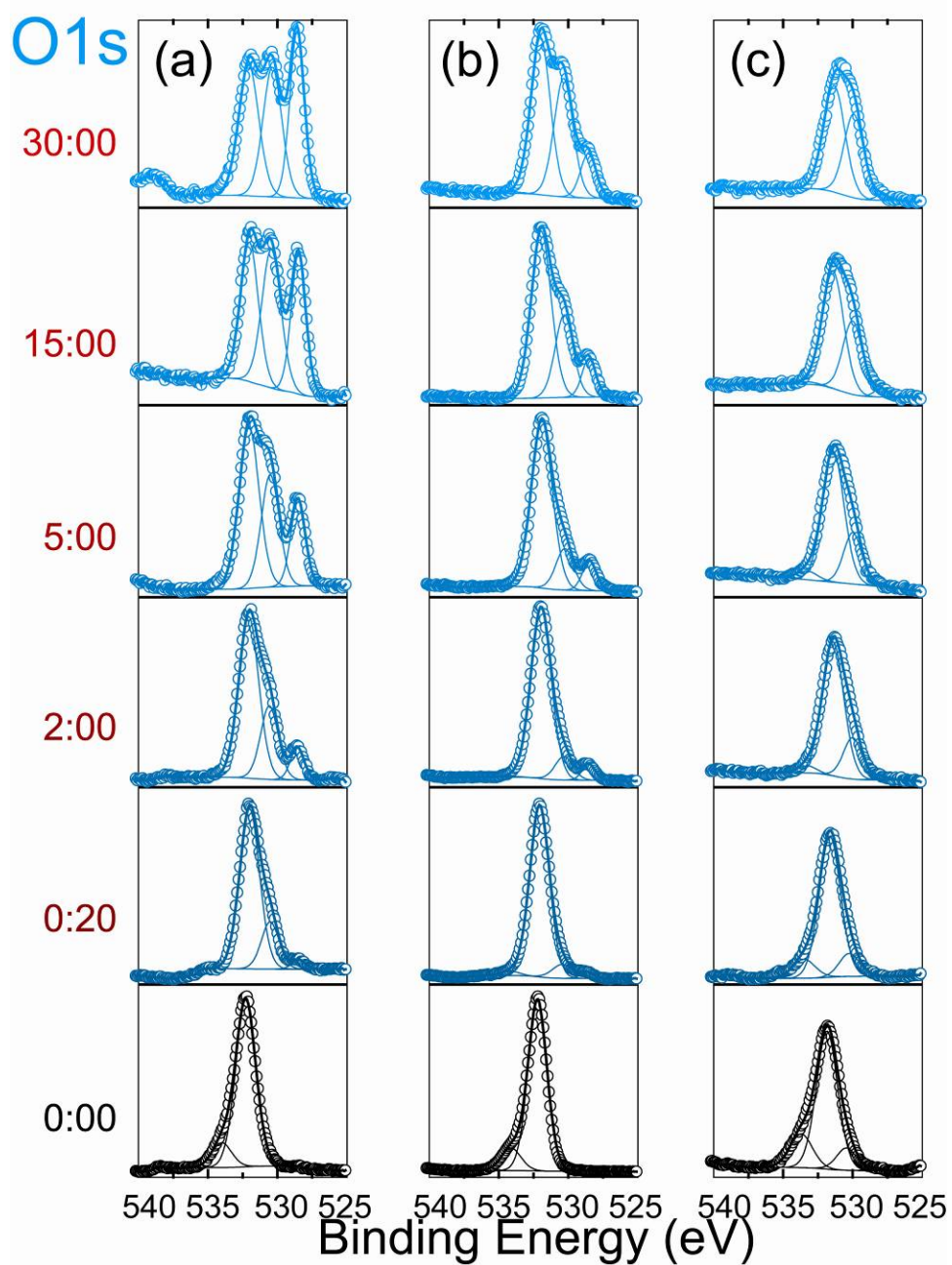


Figure D3: Deconvoluted high-resolution XPS element scans of the O1s orbital at the indicated sputtering times for Ge nanowire films cycled using (a) EC:DEC, (b) EC:DMC, and (c) FEC:DMC.

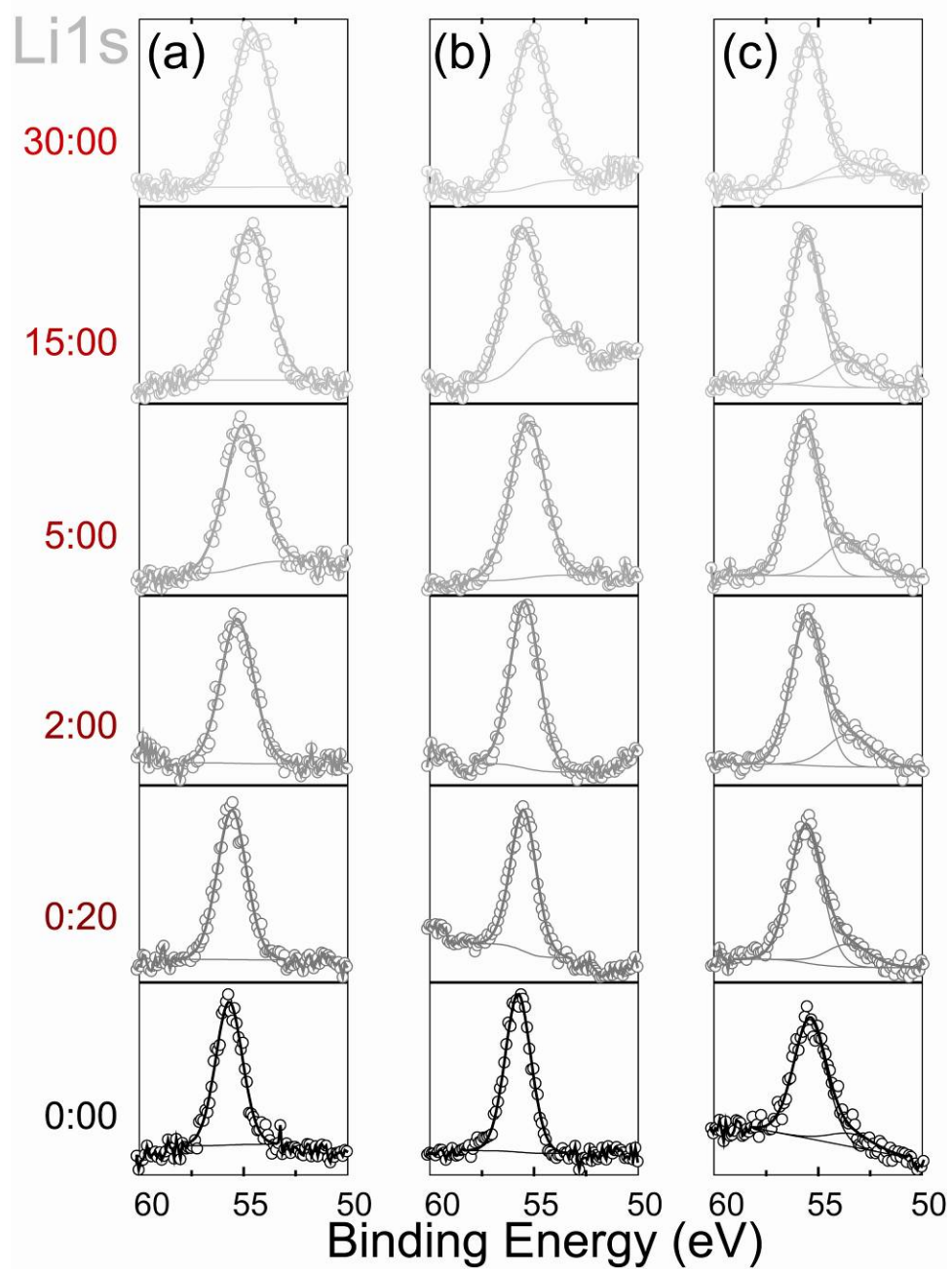


Figure D4: Deconvoluted high-resolution XPS element scans of the Li1s orbital at the indicated sputtering times for Ge nanowire films cycled using (a) EC:DEC, (b) EC:DMC, and (c) FEC:DMC.

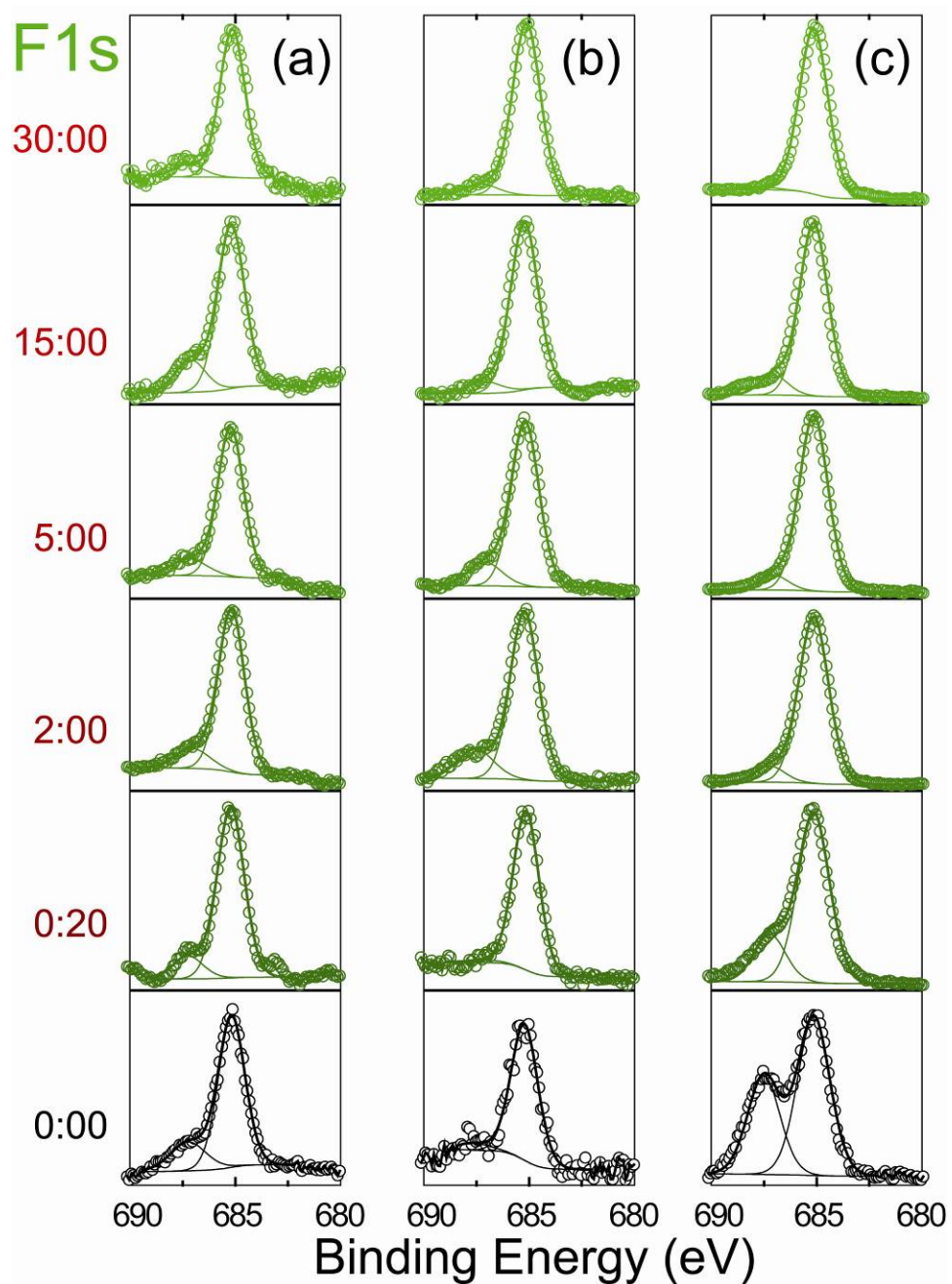


Figure D5: Deconvoluted high-resolution XPS element scans of the F1s orbital at the indicated sputtering times for Ge nanowire films cycled using (a) EC:DEC, (b) EC:DMC, and (c) FEC:DMC.

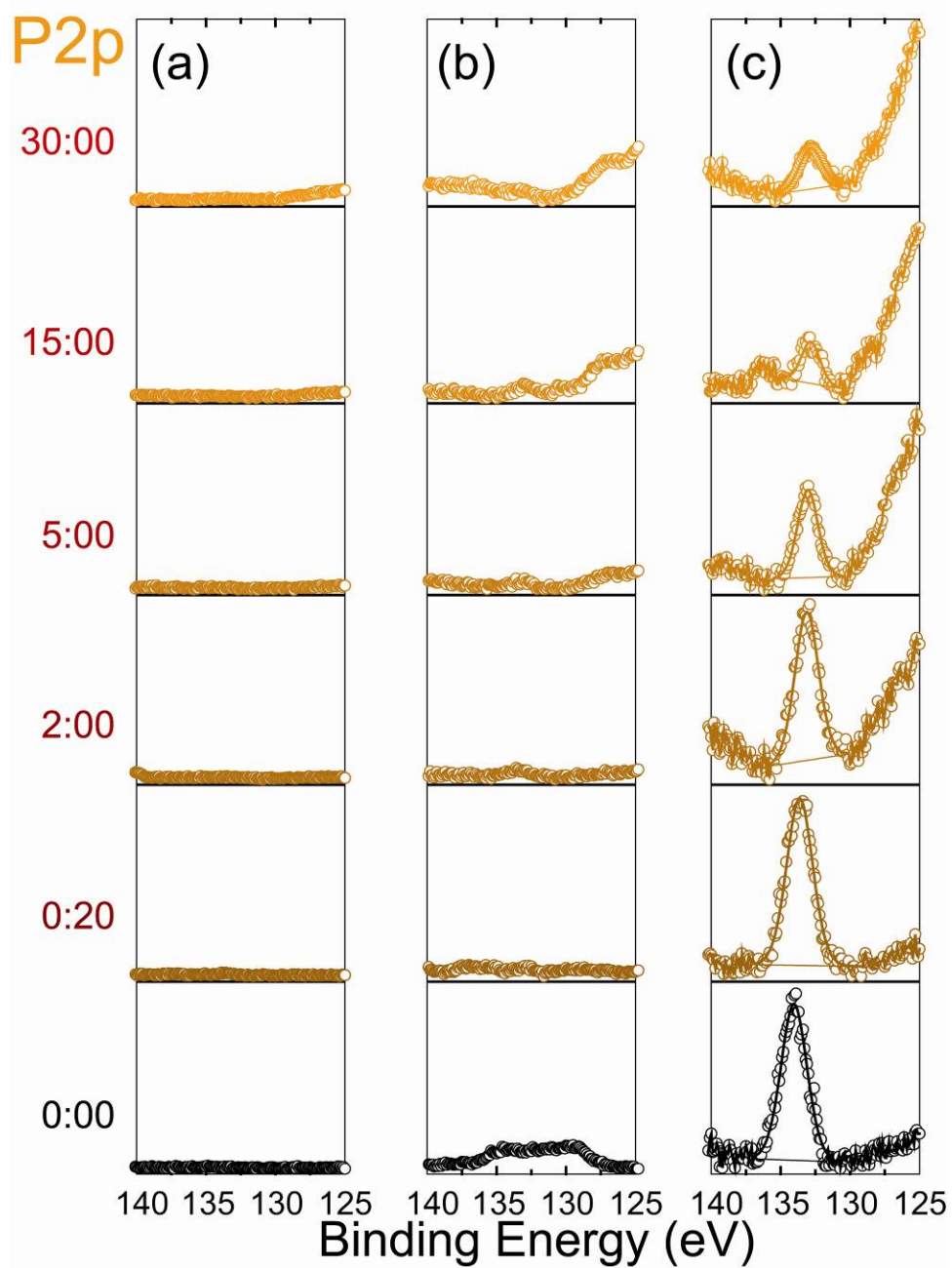


Figure D6: Deconvoluted high-resolution XPS element scans of the P2p orbital at the indicated sputtering times for Ge nanowire films cycled using (a) EC:DEC, (b) EC:DMC, and (c) FEC:DMC.

D.2 XPS characterization of uncycled Ge nanowire films

Figure D7 shows XPS spectra and film composition for an as-made Ge nanowire film. This film was examined by XPS prior to and after 20 seconds and 30 minutes of sputtering. The fluorine signal at 687.5 eV is due to PVdF. The peak at 684 eV after 30 minutes of sputtering is due to elemental fluorine, released by Ar⁺ bombardment. The C1s peak at 285 eV is also due to PVdF. Some oxidation is observed in the un-sputtered and 20-second C1s scans. This is confirmed by the O1s signal. The 30-minute scan shows a very weak (e.g., noisy) O1s signal. The Ge3d signal also shows some oxidation, but only on the surface.

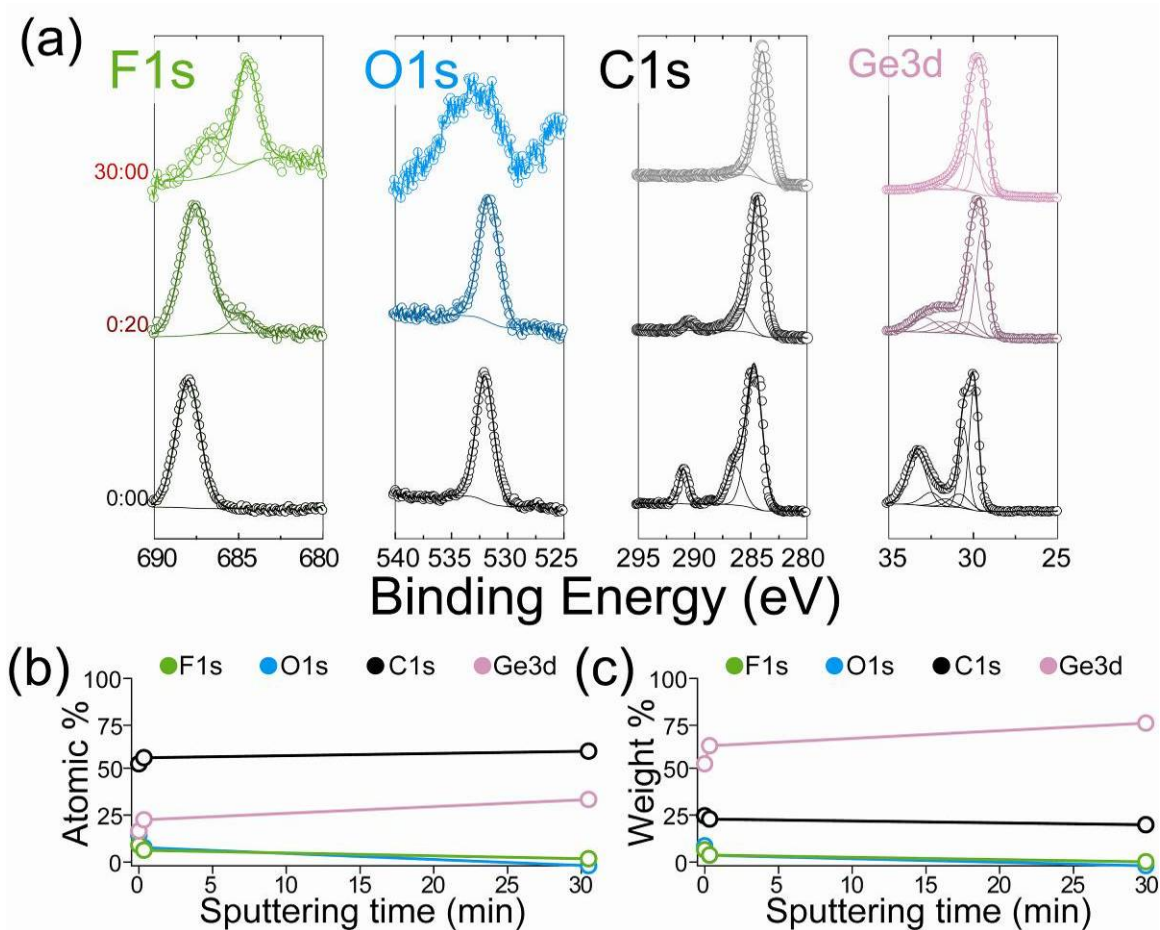


Figure D7: (a) High-resolution XPS elemental scans of F1s, O1s, C1s, P2p, Li1s, and Ge3d at various sputtering times and corresponding (b) atomic and (c) weight compositions of the Ge nanowire film prior to cycling.

D.3 Ge composition: Ge^0 and GeO_x contributions

Figure D8 shows the contributions of Ge suboxides and zero-valent Ge to the Ge3d signal. GeO_x and Ge^0 signals for Ge nanowire films cycled with various electrolyte solutions are shown in Figure D8a. The individual suboxide contributions are shown along with the Ge 5/2 and Ge 3/2 contributions in Figures D8b–D8d for Ge nanowires cycled with EC:DEC, EC:DMC, and FEC:DMC (Figures D8b–d, respectively).

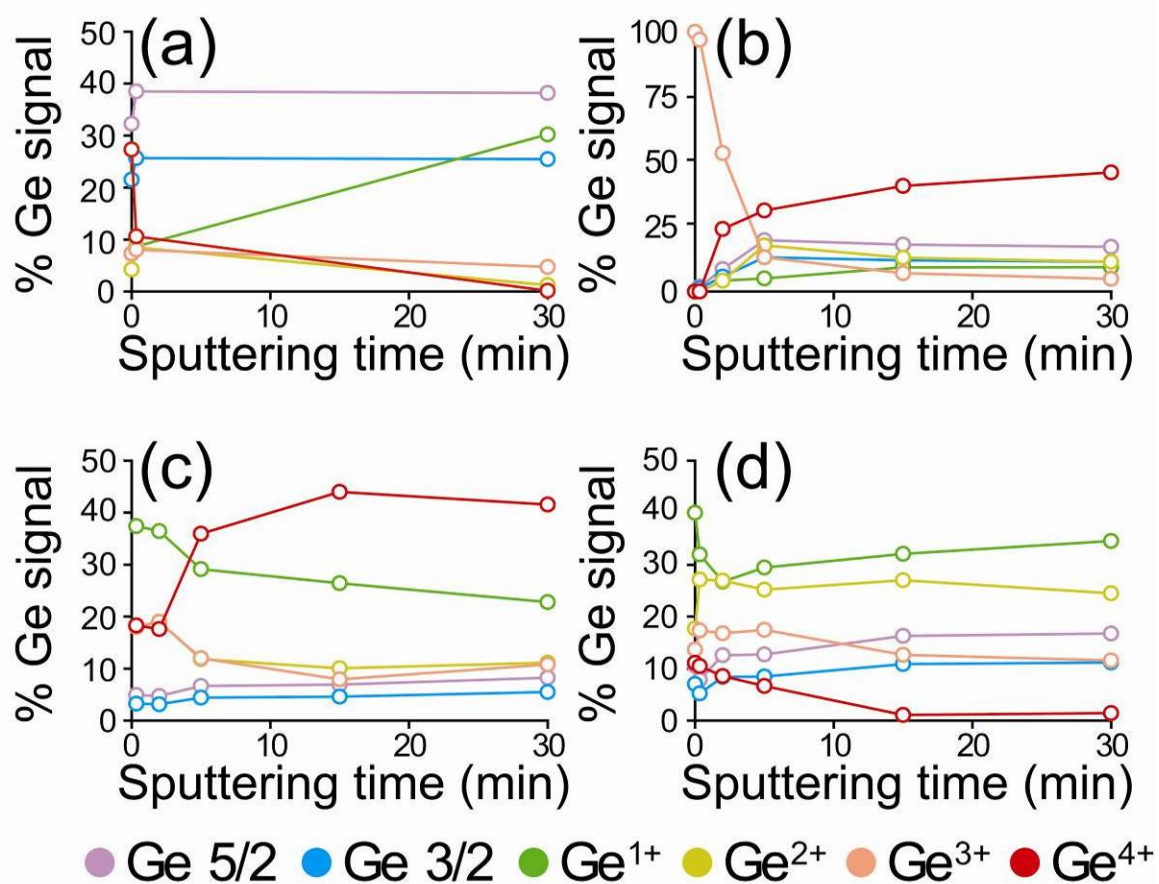


Figure D8: Individual contributions from Ge 5/2, Ge 3/2, Ge¹⁺, Ge²⁺, Ge³⁺, and Ge⁴⁺ for (a) uncycled and (b-d) cycled Ge nanowires using (b) EC:DEC, (c) EC:DMC, and (d) FEC:DMC.

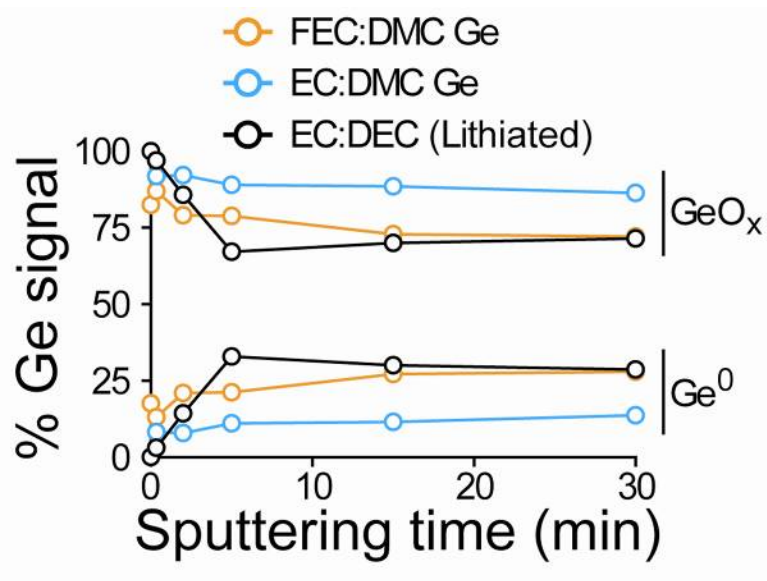


Figure D9: Percent of Ge signal present as either Ge⁰ or GeO_x for films cycled with various electrolytes.

Appendix E

E.1 Electrochemistry of Si nanowires using PVdF binder

Figure E1 shows electrochemical data for film (1) with electrolytes (A)–(E). All batteries show large first cycle irreversible capacity loss and show rapid fade. The FEC:DMC electrolyte shows the most promise for this system.

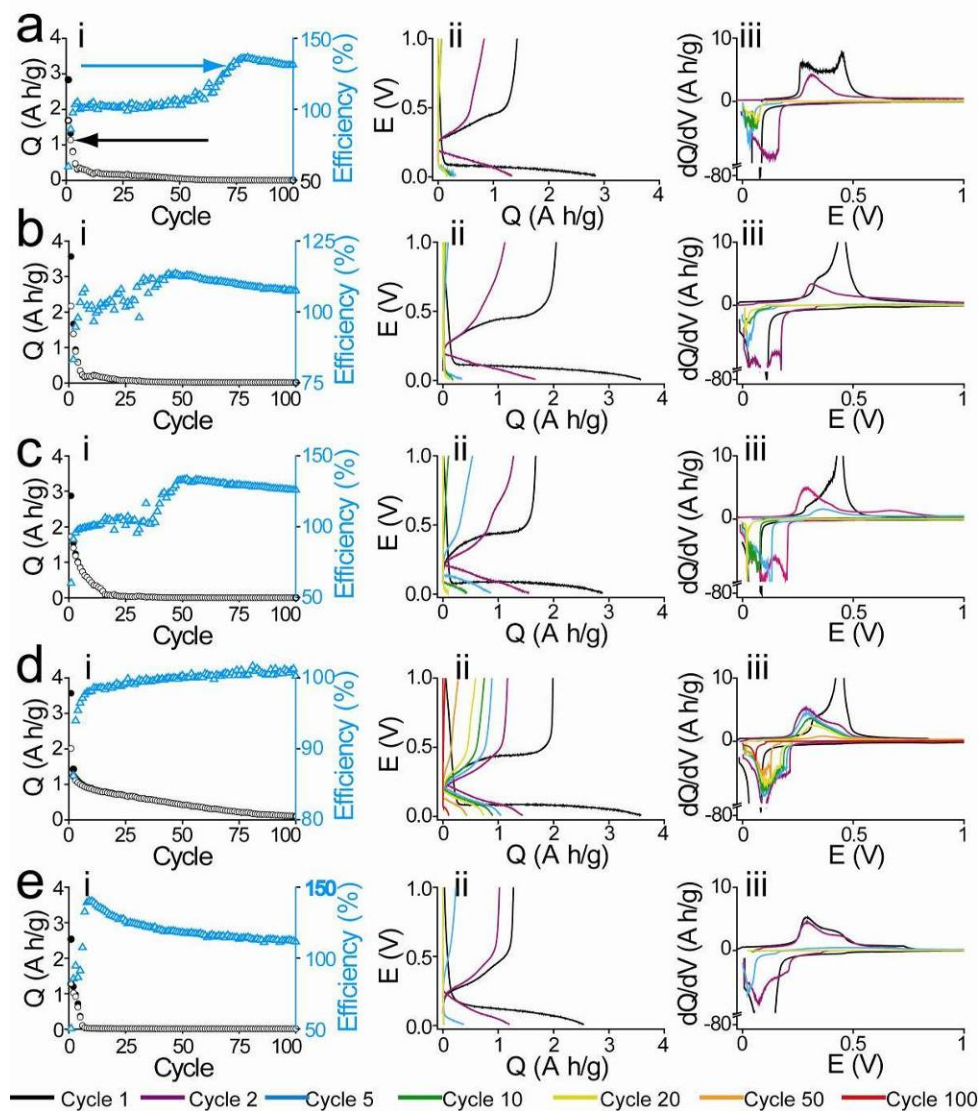


Figure E1: (i) Charge / discharge capacities, coulombic efficiencies, (ii) voltage profiles and (iii) differential capacity for Si nanowires using PVdF and (a) EC:DEC, (b) EC:DMC, (c) EC:DMC+FEC, (d) FEC:DMC, and (e) PC:DMC.

E.2 Electrochemistry of Au-removed Si nanowires

Figure E2 shows electrochemical data for film (1) with electrolytes (A), (B), and (E). All batteries again show large first cycle irreversible capacity loss and show rapid fade. The FEC:DMC electrolyte once more shows the most promise for this system.

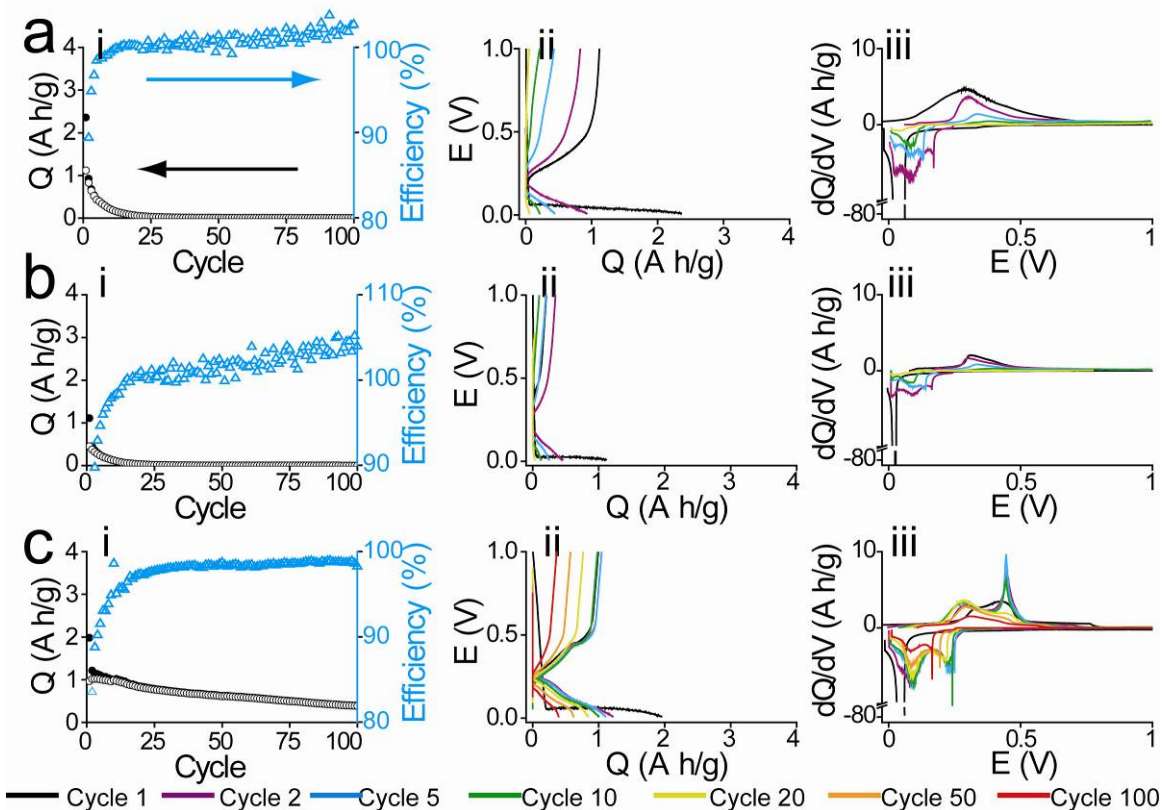


Figure E2: (i) Charge / discharge capacities, coulombic efficiencies, (ii) voltage profiles and (iii) differential capacity for Au-removed Si nanowires using PVdF and (a) EC:DEC, (b) EC:DMC, or (c) FEC:DMC.

Appendix F

F.1 Sn-seeded Si nanowires with varying Si:Sn ratio

Figure F1 shows in-situ Sn seeded Si nanowires grown at various Si:Sn ratios. Wires can be grown at a Si:Sn ratio of 40:1, but when the ratio is increased to 400:1, amorphous Si particles form. This is due to the extremely high reactivity of trisilane that results in homogeneous nucleation when there is not a high enough concentration of seed particles.

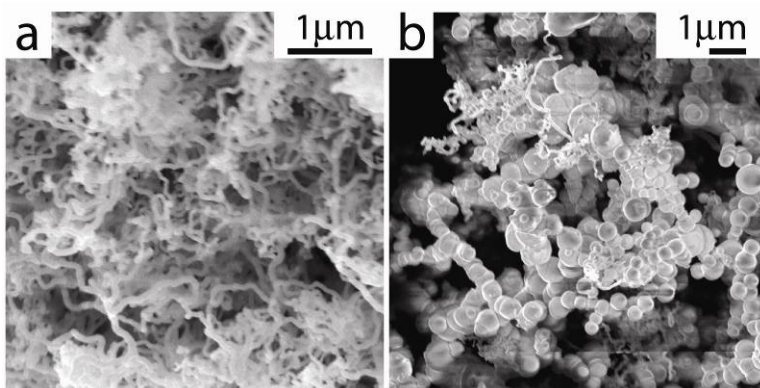


Figure F1: TEM of in-situ Sn-seeded Si nanowires with a Si:Sn ratio of (a) 40:1 and (b) 400:1.

F.2 Electrochemistry Sn-seeded Si nanowires using PVdF

Charge and discharge capacities and corresponding coulombic efficiency curves are shown in Figure F2 for film (1) and a variety of electrolyte solutions. These films were tested as-prepared and performed particularly poorly. PVdF requires thermal treatment to be an effective binder.

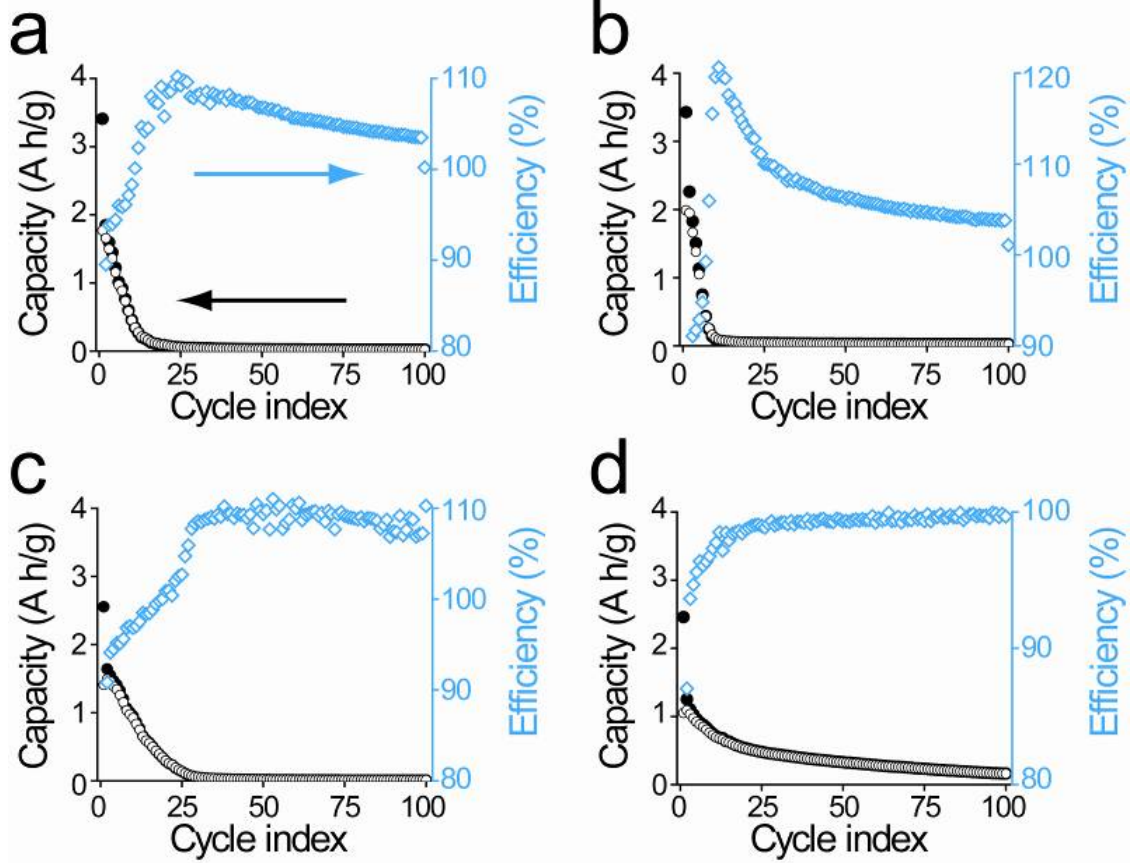


Figure F2: Cycle data with coulombic efficiency for batteries assembled using Sn-seeded Si nanowires with PVdF binder and an electrolyte solvent solutions containing 1.0 M LiPF_6 in a 1:1 w/w mixture of (a) EC:DEC, (b) EC:DMC, (c) EC:DMC + 3% w/w FEC, and (d) FEC:DMC.

Appendix G[§]

G.1 Bi[N(Si(CH₃)₃)₂]₃ characterization

Figure G1 shows mass spectrometry characterization of the reactant, bismuth tris[bis(trimethylsilyl)]amide (Bi[N(Si(CH₃)₃)₂]₃). Figure G2 shows TEM images of reaction product obtained when Bi nanocrystals were not included in the reaction. M/Z ratio of 689 corresponds to the molecular weight of the singly charged total molecule. The recurring M/Z gap of 73 between peaks corresponds to the loss of Si(CH₃)₃ groups upon ionization.

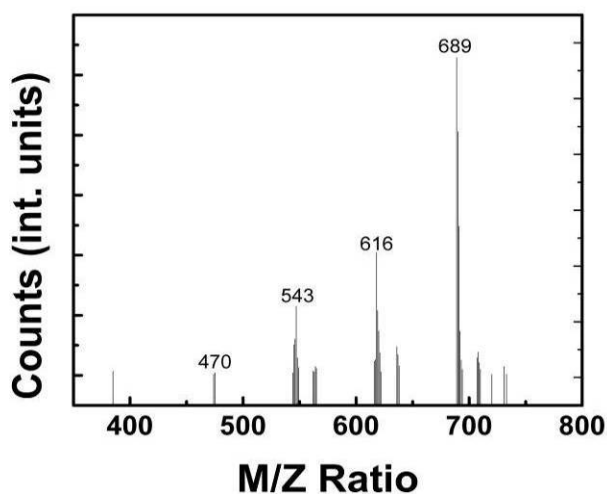


Figure G1: Mass spectrometry of bismuth tris[bis(trimethylsilyl)]amide (Bi[N(Si(CH₃)₃)₂]₃) collected by positive ion chemical ionization.

G.2 Control reactions without the addition of Bi nanocrystals

The reaction products shown in Figure G2 were obtained by carrying out the Ge nanorod synthesis without the addition of Bi nanocrystals. A polymer solution with either 0.5 g PVP/HDE copolymer in 4.5 g of DPE was degassed on a Schlenk line under vacuum with vigorous stirring for 1 hour at 70°C. 2 g of TOPO dissolved in 5 mL of

[§] This chapter appears in *Chemistry of Materials* **2011**, 23, 1964-1970.

toluene and 4 mL of squalane were added by syringe. The temperature was raised to 150°C while under vacuum for 60 minutes to evaporate the DPE. The flask was then blanketed in nitrogen and heated to 350°C (product shown in Figure I2a) or 400°C (product shown in Figure I2b). Under vigorous stirring, a Ge reactant solution of 36 μL of DPG dissolved in 0.5 mL squalane was rapidly injected into the hot solvent mixture. The heating mantle was removed five minutes later to allow the reaction mixture to cool to room temperature. The reaction product was purified using the same procedure used for the Ge nanorod samples as described in the main text.

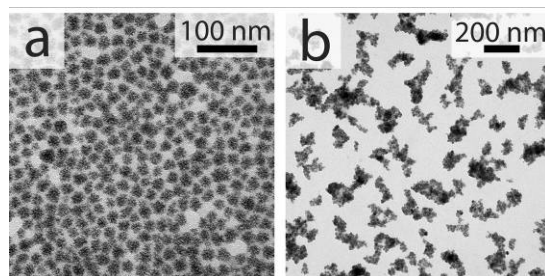


Figure G2: Control reactions at (a) 350°C and (b) 400°C where the typical Ge nanorod procedure was followed except for the injection of Bi precursors. These results show that Ge nanorod growth requires the presence of Bi seeds to proceed through the SLS mechanism.

G.3 Optical properties of Ge nanorods

Aliquots were taken every minute during a Ge nanorod reaction at 350°C. These aliquots are shown in Figures G3 with rod lengths of (1 minute) 31 ± 12 nm, (2 minutes) 52 ± 17 nm, (3 minutes) 72 ± 18 nm, (4 minutes) 79.0 ± 17 nm, (5 minutes) 98.0 ± 19 nm. Absorbance spectra are also presented, showing the evolution of a peak at 550 nm. The nature of this peak is discussed in Chapter 10. Figure G4 shows absorbance spectra for branched and unbranched nanorods. The peak at 550 nm is more pronounced here.

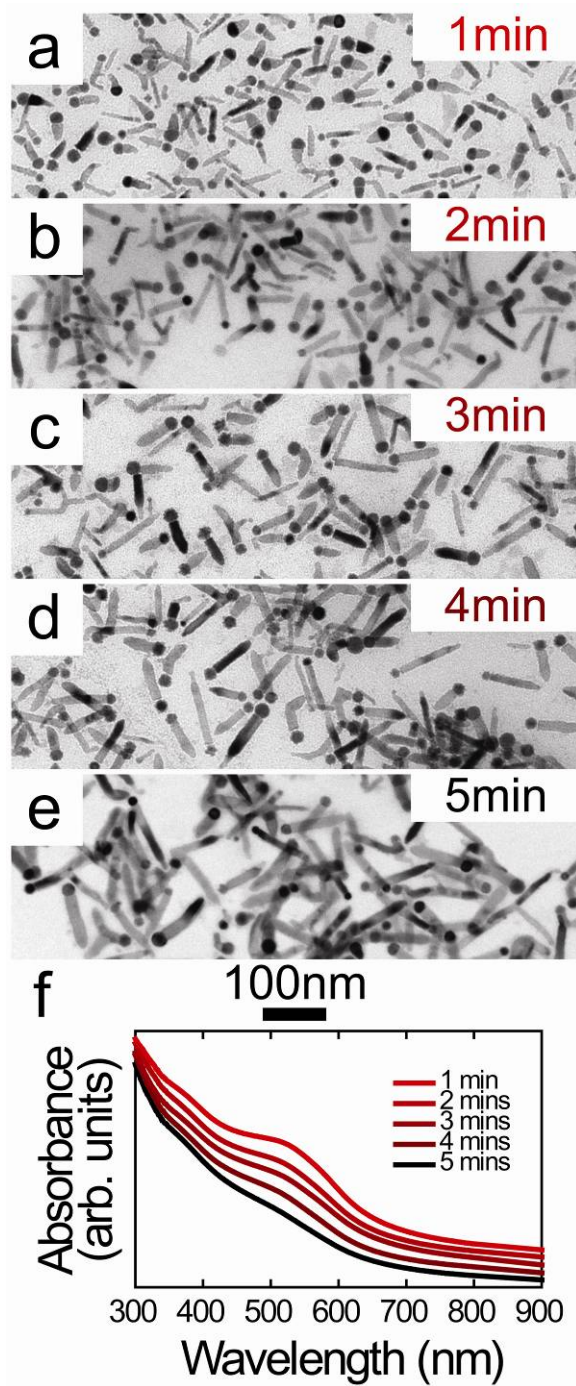


Figure G3: TEM of Ge nanorods grown at 350°C after (a) 1 minute, (b) 2 minutes, (c) 3 minutes, (d) 4 minutes, and (e) 5 minutes with (f) absorbance spectra.

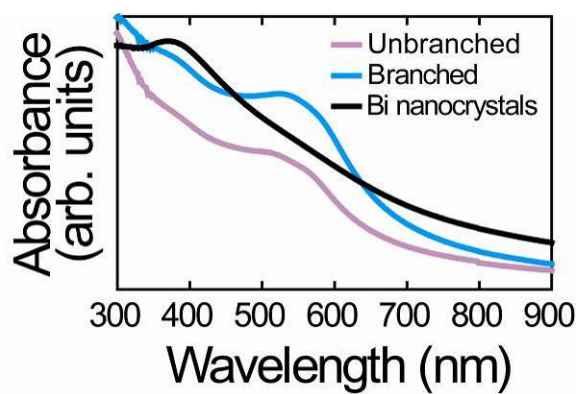


Figure G4: Absorbance spectra of branched and unbranched Ge nanorods and Bi nanocrystals.

Appendix H

H.1 Bi and Au seeded Ge nanorod characterization

Ge clusters form during the Ge nanorod reaction, as shown in Figure H1. It is unclear whether or not these clusters contribute to the growth of the Ge nanorods, though it appears that the presence of these clusters wanes as the reaction progresses.

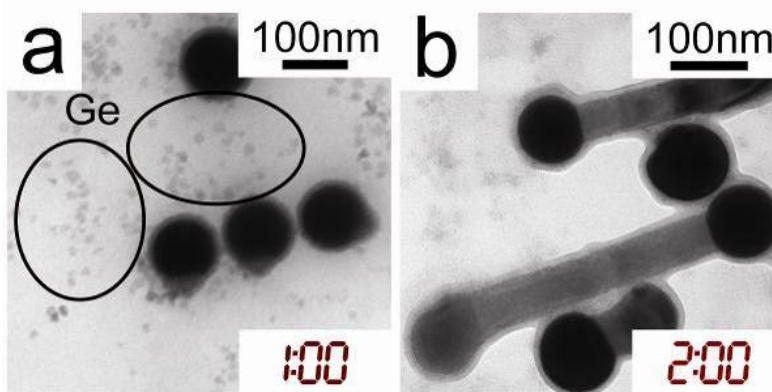


Figure H1: Ge nanorod sample at 30 seconds (or 1 minute) and 2 minutes showing the presence of Ge clusters in the reaction mixtures.

Absorbance measurements were made on as-prepared Bi nanocrystals as a control to be compared against data collected for Ge nanorods of various lengths, shown in Figure H2. The curve is qualitatively similar to the 30 second and 1 minute Ge nanorod aliquots, though the peak for the Bi nanocrystals occurs at 400, whereas the spectra in Figure 10.1 show an initial peak at ~ 550 nm. Though little Ge nanorod growth occurs in the early stages of the reaction, the presence of Ge red-shifts this absorbance feature by 100–200 nm.

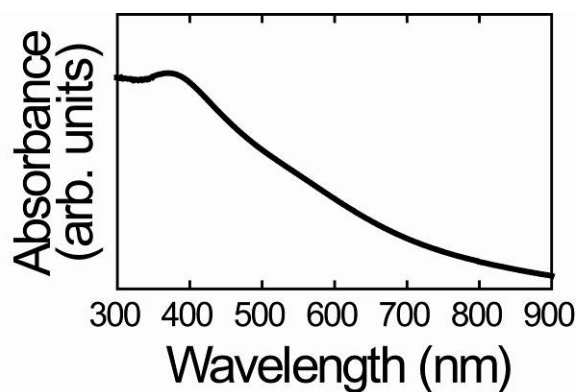


Figure H2: Absorbance spectrum of Bi nanocrystals.

Au seeds agglomerate very quickly, even with the addition of amines, which has been shown to stop Au aggregation. The rods also grow very quickly (within seconds), making aliquot extraction difficult. As such, absorbance data for Au seeded Ge nanorods were not collected. Au seeded Ge nanorods are shown in Figure H3.

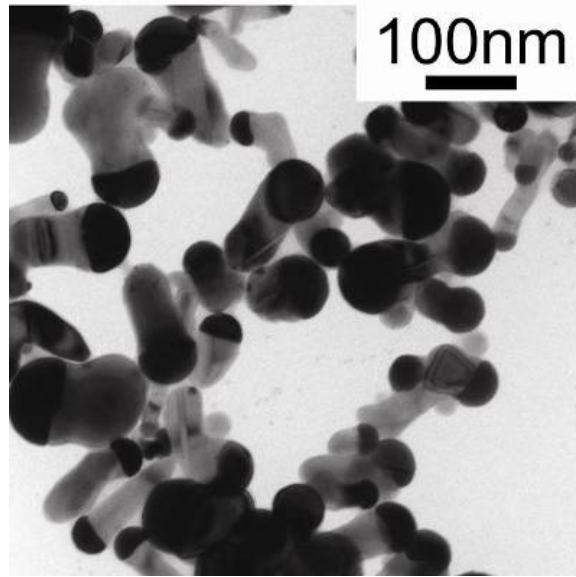


Figure H3: TEM image of solution grown Au seeded Ge nanorods in squalane, TOPO and tri-*n*-dodecylamine.

H.2 Supplemental discrete dipole approximation calculations

Figure H4 shows extinction spectra calculated for 200 nm long Ge nanorods with varying diameter. These calculations show that there is no diameter dependence to the extinction spectra and that the peak that forms at 600nm results from waveguiding down the length of the nanorods.

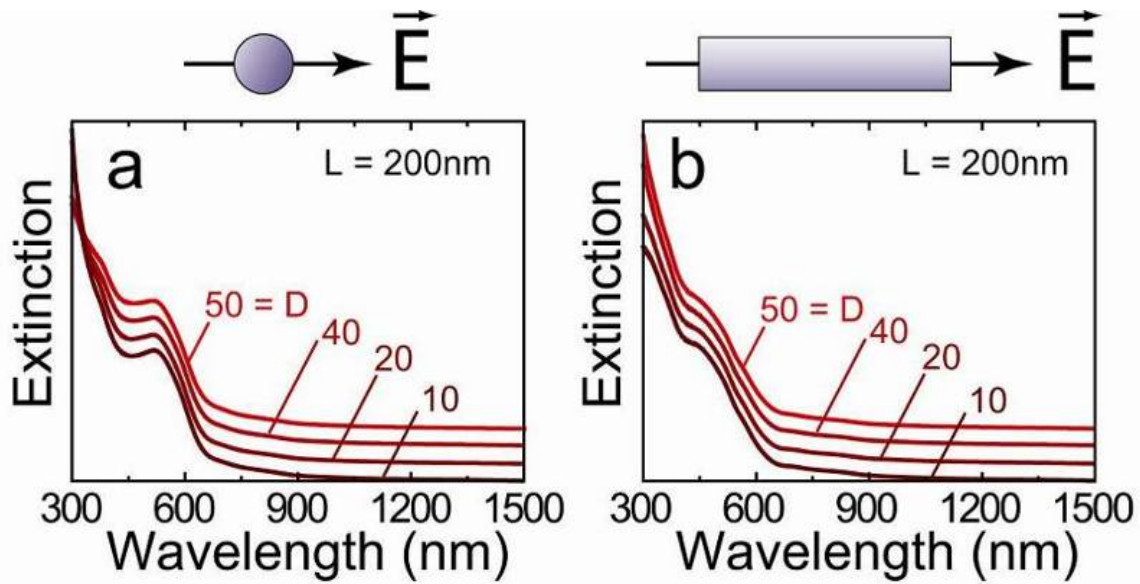


Figure H4: Extinction spectra of 200 nm long Ge nanorods with no metal tip with the incident electric field polarized (a) perpendicular and (b) parallel to the long axis of the nanorods.

Various dipole arrangements were used (in addition to the 2x2 dipole arrangement) to calculate extinction spectra. Figure H5 shows good agreement among these spectra, independent of dipole arrangement. Additional arrangements used included (1) cross, (2) hexagon, and (3) 3x3 cross-sectional dipole arrays. New values for a and R were determined for each dipole configuration with $a/R = 1.688$ and either

$$D = 2R + 2a \quad (12)$$

for the cross (Figure H5b) and hexagonal (Figure H5c) arrangements, or

$$D = 2R + 2\sqrt{2}a \quad (13)$$

for the 3x3 dipole arrangement (Figure H5d). Behavior is examined under a perpendicular (Figure H5e) and parallel (Figure H5f) incident electric field. Figures H5e and H5f show the calculated optical extinction around the 550 nm absorption peak. There is no observed difference among these curves related to the dipole configuration.

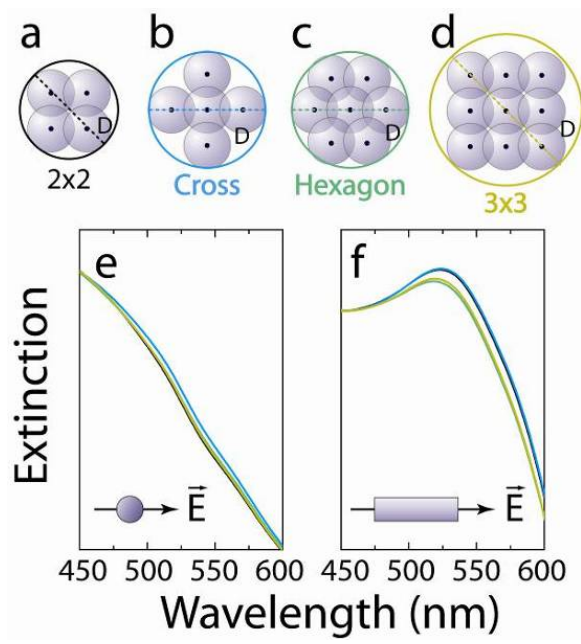


Figure H5: Extinction cross-section calculations using the DDA with various dipole arrangements: (a) 2x2, (b) cross, (c) hexagon, and (d) 3x3, with the polarization of the incident electric field aligned (e) perpendicular and (f) parallel to the long axis of the nanorods.

Figure H6 shows surface and contour plots of the electric field for dipoles located along the edges and along the central axis of the nanorod using the cross dipole arrangement. This arrangement has surface dipoles with the greatest surface exposure, which results in the highest electric fields calculated in this work.

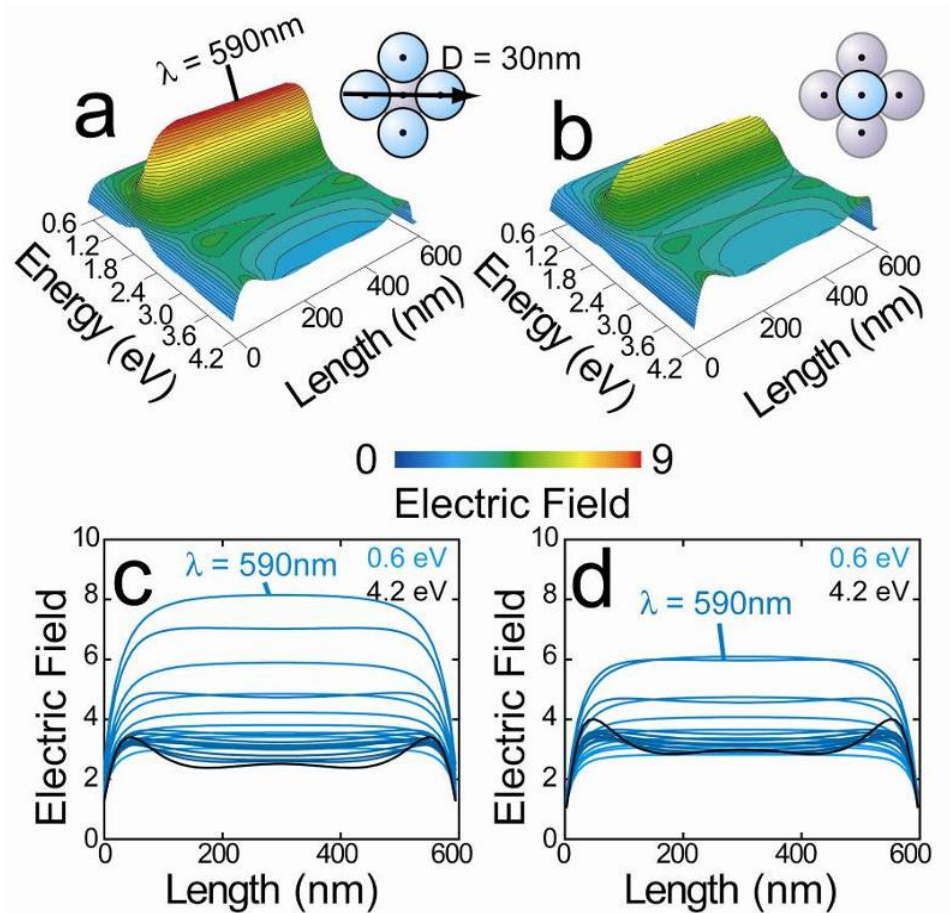


Figure H6: Internal electric field using a parallel incident electric field for (a) edge and (b) central dipoles with (c, d) corresponding cross-sectional plots showing electric field contours for specific wavelengths for a dipole arrangement with a cross cross-section.

Figure H7 shows surface and contour plots of the electric field for dipoles located along the edges and along the central axis of the nanorod using the hexagon dipole arrangement. This arrangement has surface dipoles with the exposed surfaces intermittent to the edge and surface dipoles for the 3x3 arrangement. As such, the edge effects give rise to an electric field with a value intermittent to the 3x3 surface and edge dipoles.

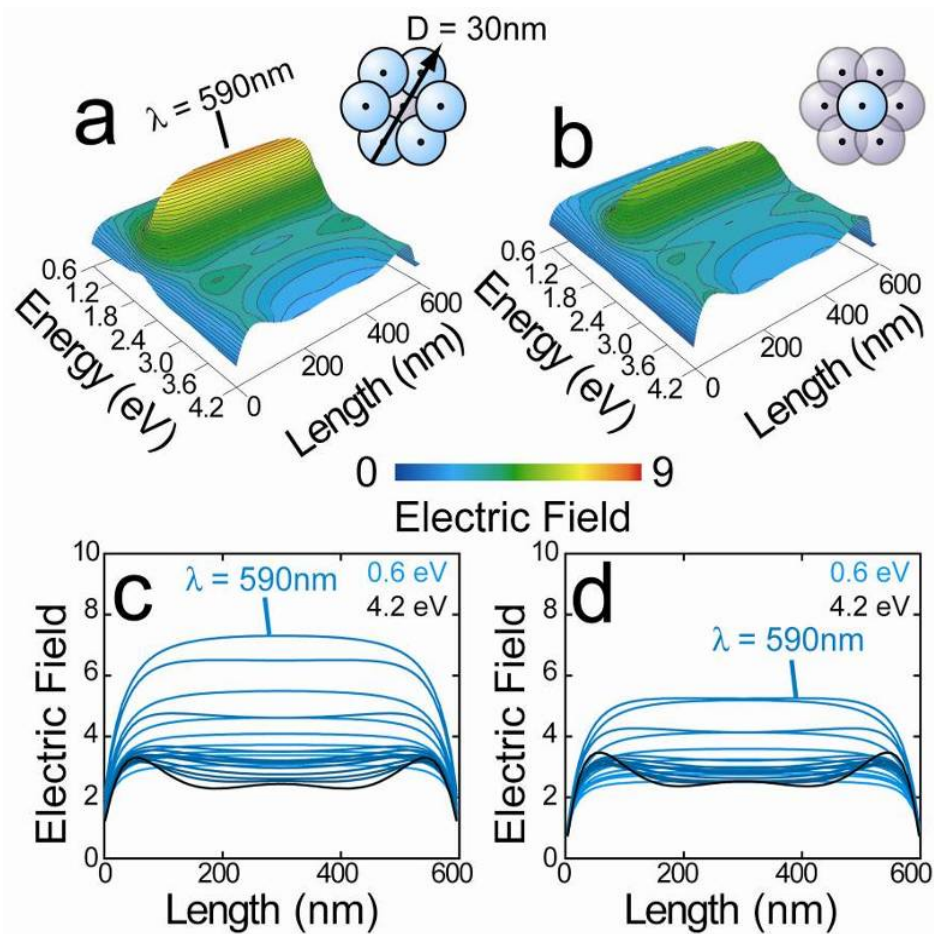


Figure H7: Internal electric field using a parallel incident electric field for (a) face and (b) central dipoles with (c, d) corresponding cross-sectional plots showing electric field contours for specific wavelengths for a dipole arrangement with a hexagonal cross-section.

The internal electric field was examined for Ge nanorods with Au tips using the 2x2 dipole arrangement and is shown in Figure H8. The rods examined were 30 nm in diameter and had an aspect ratio of 20. The presence of the Au tip significantly alters the internal electric field in the Ge near the Au tip. Au has a strong peak just below 1.8 eV, which causes a corresponding peak within the first 20 nm Ge portion of the nanorod.

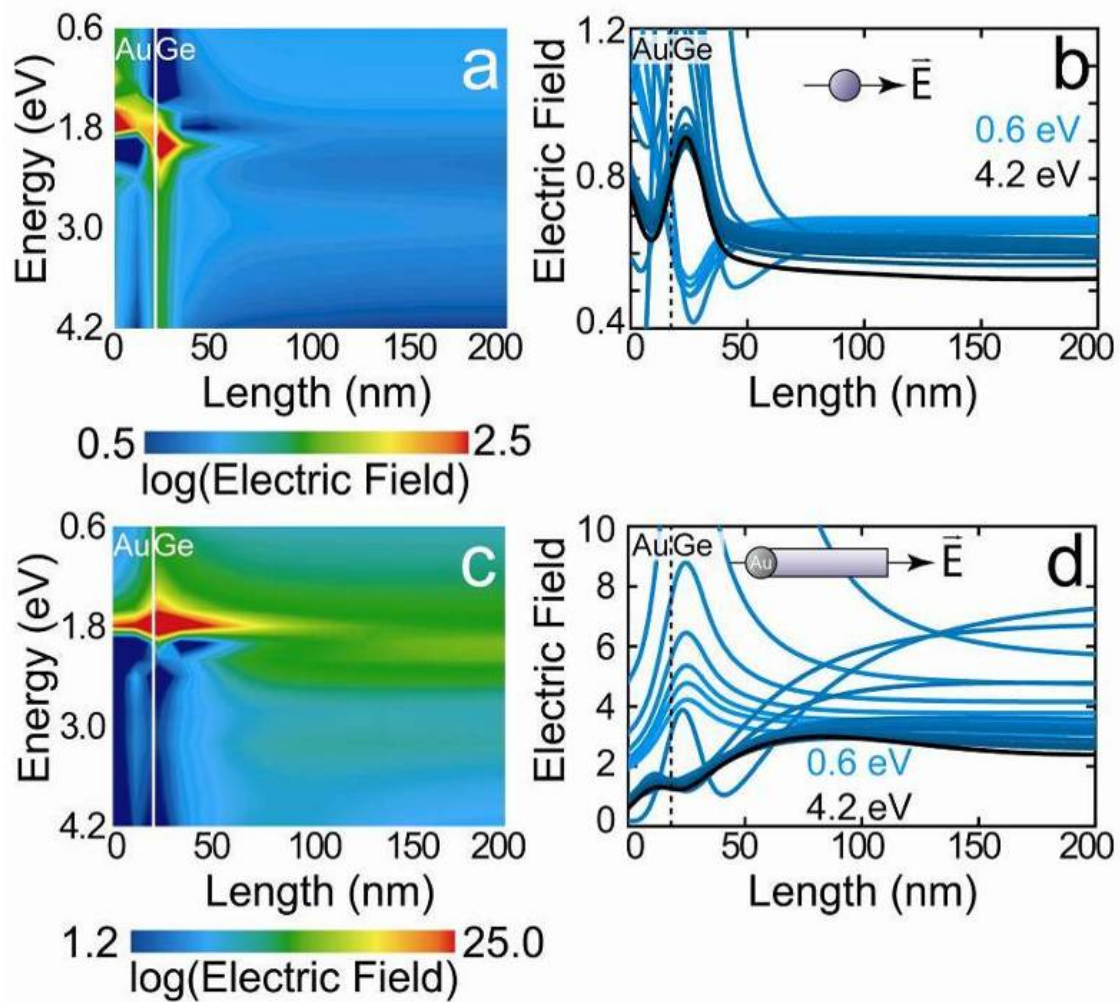


Figure H8: Intensity plots showing the local electric field near the tip of Ge nanorods with Au seeds for (a) perpendicular and (c) parallel incident electric fields with (b, d) corresponding cross-sectional plots showing constant wavelength contours.

Appendix I

I.1 DOPA characterization

Figure I1 shows a positive chemical ionization mass spectrometry spectrum of the final DOPA product. M/Z ratio of 291 corresponds to the molecular weight of the singly charged molecule. M/Z ratios of 581 and 871 correspond to masses of a DOPA dimer and trimer, respectively.

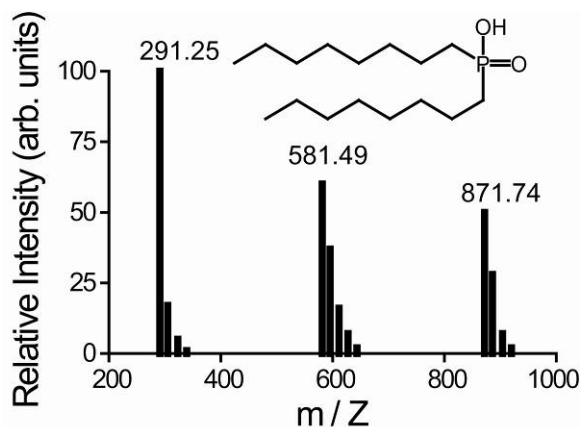


Figure I1: Mass spectrometry of DOPA collected by positive ion chemical ionization.

I.2 Bi nanocrystal and InP nanowire histogram data

Figure I2a shows TEM of the Bi nanocrystal seeds used in this study, which had an average diameter of 14.0 ± 2.5 nm. TGA, shown in Figure I2b, shows that a significant portion of the Bi reaction product is the unctuous PVP-HDE copolymer used to stabilize the nanocrystals. A typical reaction yields product that is 2% w/w Bi nanocrystals.

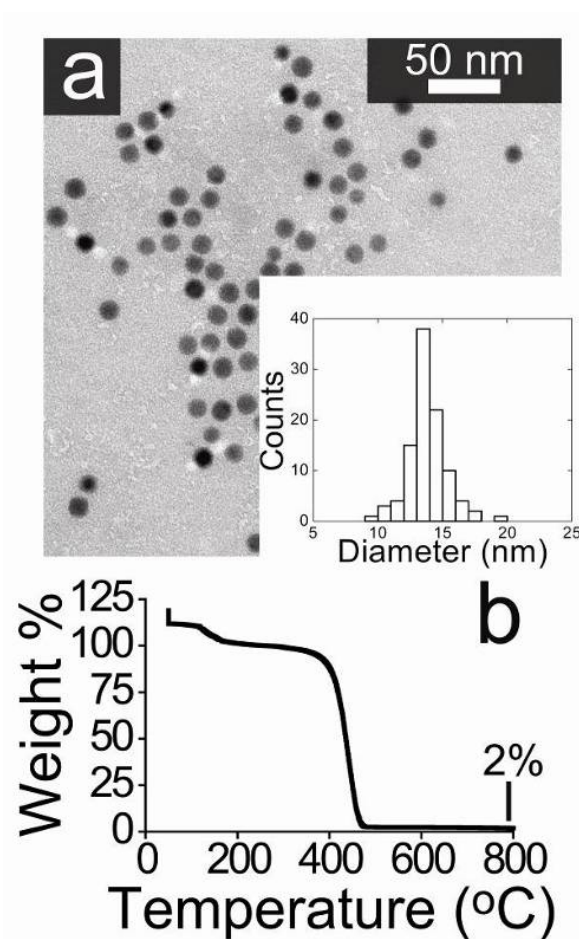


Figure I2: (a) TEM with (inset) diameter histogram of Bi nanocrystals ($d = 14.0 \pm 2.5$ nm) and (b) TGA analysis of the reaction product.

Nanowire diameter histogram data were taken for reactions (1)–(7) and are shown in Figure I3. Figures I3a–I3d correspond to reactions (1)–(4), respectively; 200 nanowires were measured. Figures I3e–I3h corresponding to reactions (5), (2), (6), and (7), respectively; 50 nanowires were measured.

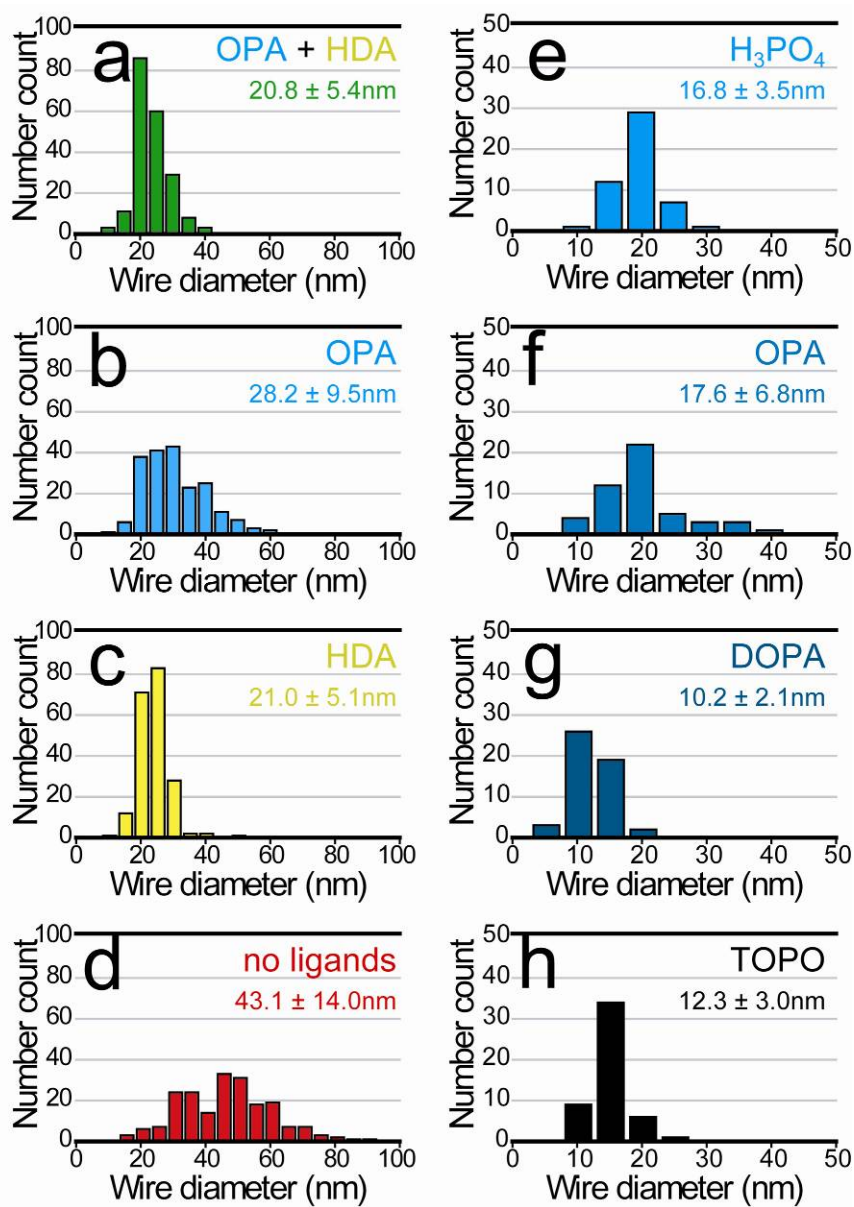


Figure I3: Nanowire histogram plots for InP nanowires grown in the presence of (a) HDA and OPA, (b) OPA only, (c) HDA only, or (d) no ligand. Nanowires were also grown in the presence of HDA and (e) H₃PO₄, (f) OPA, (g) DOPA, or (h) TOPO.

I.3 Effect of *n*-octylphosphonic acid concentration

Promotion of InP nanowire growth through OPA addition is illustrated by varying the amount of OPA in the reaction mixture. Figure I4 shows product formed using reaction (1) reaction media with 0 (Figure I4d.i), 10 mg (Figure I4a, I4d.ii), 100 mg (Figure I4b, I4d.iii), or 1000 mg (Figure I4c, I4d.iv) OPA. Reaction (3), discussed above and shown in curve (i), produces a mixture of InP and In₂O₃ nanowires. Increasing the amount of OPA enhances InP and weakens In₂O₃ signals. Using 1000 mg OPA quenches the reaction entirely and only Bi nanocrystals are recovered; it is interesting to note that at this high OPA concentration, HDA still protects the Bi nanocrystals from etching (Figure I4c). Given that OPA does not bind to the surface of the nanowires, it likely plays a role in catalyzing InP precursor decomposition.

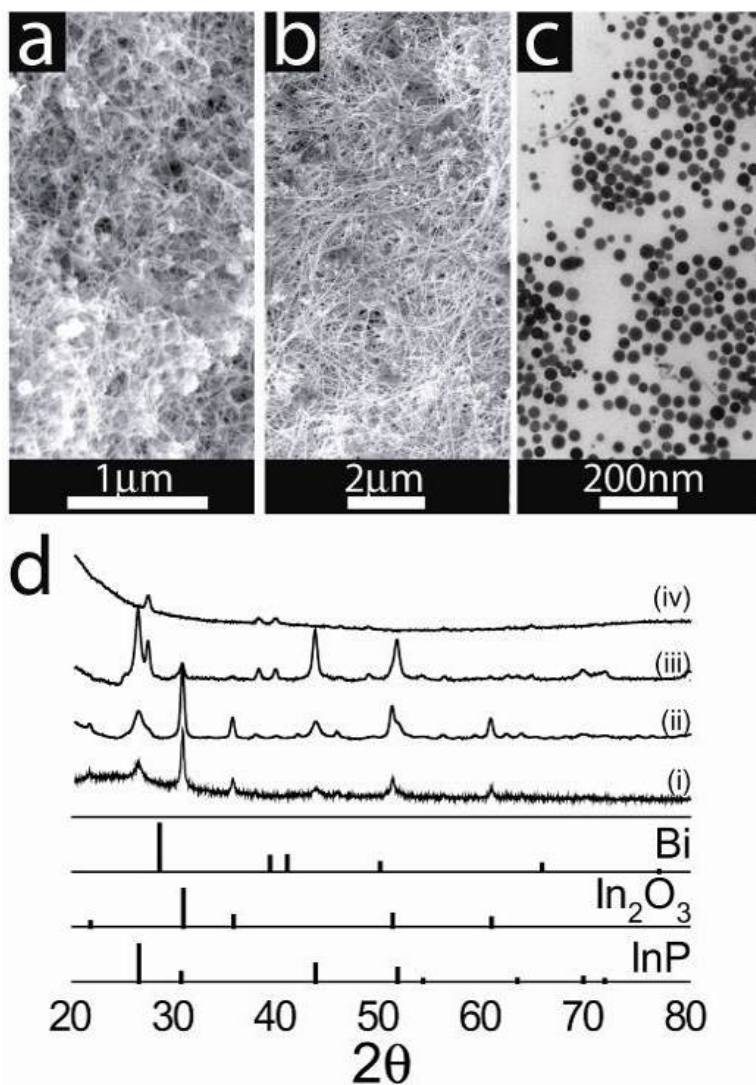


Figure I4: InP nanowires grown in the presence of HDA and (a) 10 mg, (b), 100 mg, and (c) 1000 mg OPA with (d) XRD spectra for each. Reference patterns are included for InP (JCPDS: 00-032-0452), In₂O₃ (JCPDS: 01-071-2194), and Bi (00-044-1246).

I.4 Effect of phosphoric acid derivatives

OPA was replaced with various additives to probe the reactivity of phosphonic acids with various degrees of alkylation (i.e., primary, secondary, etc.). Figure I5 shows ligand molecules used to replace OPA in the reaction of InMyr₃ with TMS₃P in the

presence of Bi nanocrystals. Additives used include: (1) H_3PO_4 , (2) OPA, (3) DOPA, and (4) TOPO.

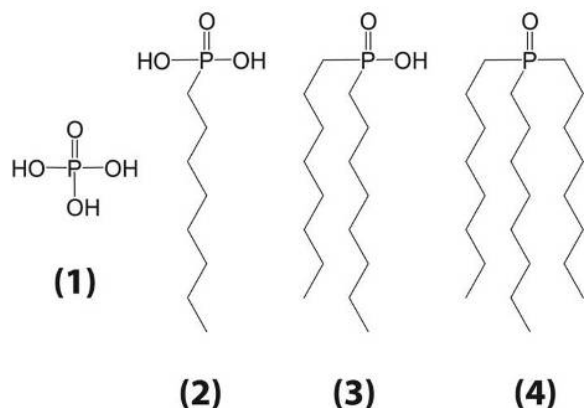


Figure I5: Phosphoric acid derivatives used in reactions included (1) phosphoric acid (H_3PO_4), (2) OPA, (3) DOPA, and (4) (TOPO).

TGA measurements were made on samples for reactions done with various phosphoric acid derivatives, shown in Figure I6. Very little ligand is present in OPA, but all reactions show a mass loss event between 300 and 350°C which due to HDA ($T_b = 330^\circ\text{C}$). The DOPA shows a significant mass loss event starting around 400-450°C. This reaction yields very unctuous, gel-like byproduct in comparison to the other reactions; this mass loss event is likely due to DOPA. The other reactions do not show mass loss events other than HDA further indicating that the phosphonic acids are not surface bound. All samples exhibit oxidation onset at a temperature of 550–600°C.

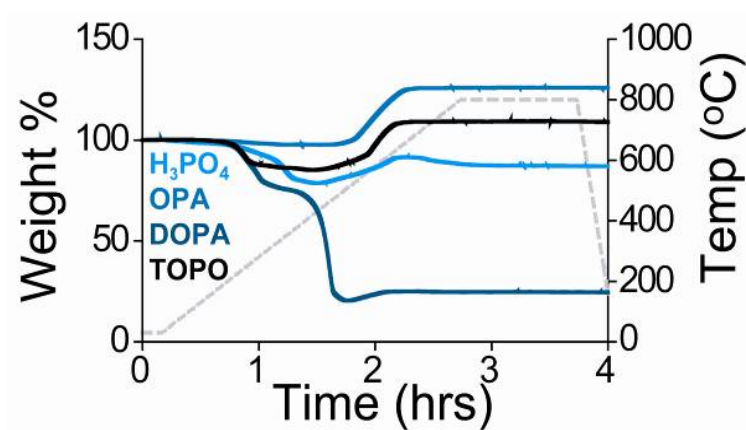


Figure I6: TGA of InP nanowires grown in the presence of HDA and H₃PO₄, OPA, DOPA, and TOPO.

Figure I7 show TEM images of InP nanowires synthesized in the presence of HDA and DOPA. A large portion of this product was nanocrystalline InP. This is evidence that DOPA promotes In-P pair cluster formation, which in turn leads to homogeneous nucleation of InP nanocrystals.

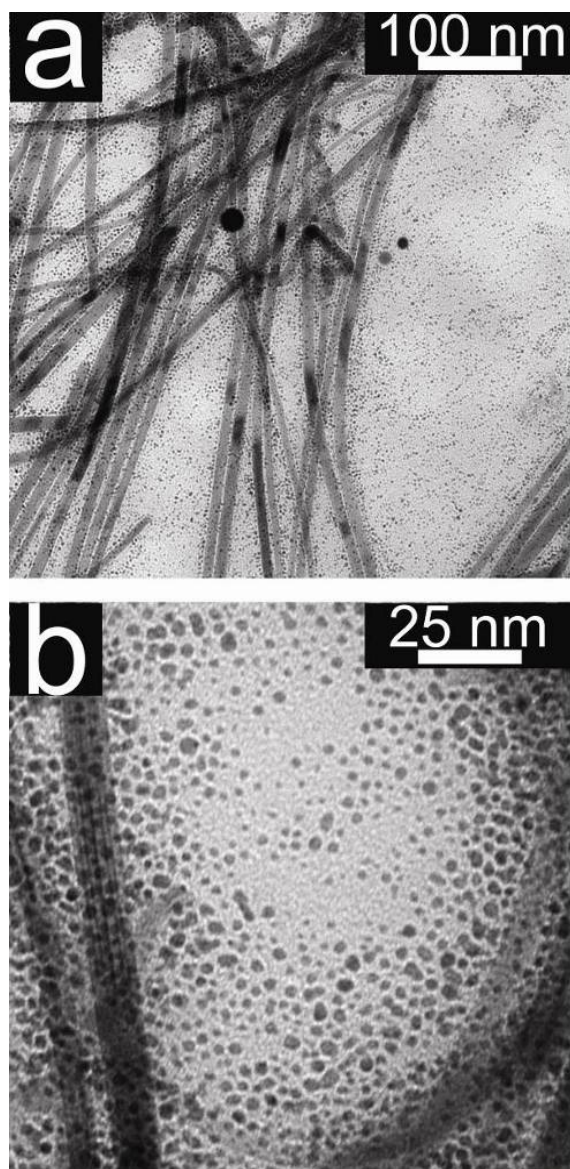


Figure I7: TEM of InP nanowires grown in the presence of HDA and DOPA showing a high yield of nanocrystalline byproduct mixed in with the InP nanowires.

Bibliography

- Ahn, Y.; Dunning, J.; Park, J. "Scanning Photocurrent Imaging and Electronic Band Studies in Silicon Nanowire Field Effect Transistors." *Nano Letters* **2005**, 5(7), 1367-1370.
- Airoldi, C.; Silva, M. L. C. P.; Chagas, A. P. "Heterocyclic Nitrogen-Containing Electron-Pair Donor Ligands: A Thermochemical Study of Adducts with Zinc, Cadmium, and Mercury Chlorides." *Journal of the Chemical Society, Dalton Transactions* **1986**, (9), 1913-1916.
- Akiyama, T.; Sano, K.; Nakamura, K.; Ito, T. "An Empirical Potential Approach to Wurtzite-Zinc-Blende Polytypism in Group III-V Semiconductor Nanowires." *Japanese Journal of Applied Physics* **2006**, 45(8-11), L275-L278.
- Alcantara, R.; Jaraba, M.; Lavela, P.; Tirado, J. L. "Optimizing Preparation Conditions for 5V Electrode Performance, and Structural Changes in $\text{Li}_{1-x}\text{Ni}_{0.5}\text{Mn}_{1.5}\text{O}_4$ spinel." *Electrochimica Acta* **2002**, 47(11), 1829-1835.
- Alcantara, R.; Lavela, P.; Tirado, J. L.; Stoyanova, R.; Zhecheva, E. "Structure and Electrochemical Properties of Boron-Doped LiCoO_2 ." *Journal of Solid State Chemistry* **1997**, 134(2), 265-273.
- Algra, R. E.; Verheijen, M. A.; Borgstrom, M. T.; Feiner, L. F.; Immink, G.; van Enkevort, W. J. P.; Vlieg, E.; Bakkers, E. "Twinning Superlattices in Indium Phosphide Nanowires." *Nature* **2008**, 456(7220), 369-372.
- Algra, R. E.; Vonk, V.; Wermeille, D.; Szweryn, W. J.; Verheijen, M. A.; van Enkevort, W. J. P.; Bode, A. A. C.; Noorduyn, W. L.; Tancini, E.; de Jong, A. E. F.; Bakkers, E. P. A. M.; Vlieg, E. "Formation of Wurtzite InP Nanowires Explained by Liquid-Ordering." *Nano Letters* **2011**, 11(1), 44-48.
- Alivisatos, A. P. "Semiconductor Clusters, Nanocrystals, and Quantum Dots." *Science* **1996**, 271(5251), 933-7.
- Amarilla, J. M.; de Vidales, J. L. M.; Rojas, R. M. "Electrochemical Characteristics of Cobalt-Doped $\text{LiCo}_y\text{Mn}_{2-y}\text{O}_4$ ($0 \leq y \leq 0.66$) Spinel Synthesized at Low Temperature from $\text{Co}_x\text{Mn}_{3-x}\text{O}_4$ Precursors." *Solid State Ionics* **2000**, 127(1-2), 73-81.
- Andersson, A. M. "Surface phenomena in Li-ion batteries." *Ph.D. thesis Acta Universitatis Upsaliensis, Uppsala* **2001**.
- Andersson, A. M.; Abraham, D. P.; Haasch, R.; MacLaren, S.; Liu, J.; Amine, K. "Surface Characterization of Electrodes from High Power Lithium-Ion Batteries." *Journal of The Electrochemical Society* **2002**, 149(10), A1358-A1369.

- Andersson, A. M.; Herstedt, M.; Bishop, A. G.; Edström, K. "The Influence of Lithium Salt on the Interfacial Reactions Controlling the Thermal Stability of Graphite Anodes." *Electrochimica Acta* **2002**, *47*(12), 1885-1898.
- Armand, M.; Tarascon, J. M. "Building Better Batteries." *Nature* **2008**, *451*(7179), 652-657.
- Arora, P.; Popov, B. N.; White, R. E. "Electrochemical Investigations of Cobalt-Doped LiMn_2O_4 as Cathode Material for Lithium-Ion Batteries." *Journal of The Electrochemical Society* **1998**, *145*(3), 807-815.
- ASM International's Binary Alloy Phase Diagrams (2nd edn), U.S.A. 1990.*
- Aurbach, D.; Ein-Eli, Y. "The Study of Li-Graphite Intercalation Processes in Several Electrolyte Systems Using In-Situ X-Ray Diffraction." *Journal of The Electrochemical Society* **1995**, *142*(6), 1746-1752.
- Aurbach, D.; Ein-Eli, Y.; Markovsky, B.; Zaban, A.; Luski, S.; Carmeli, Y.; Yamin, H. "The Study of Electrolyte Solutions Based on Ethylene and Diethyl Carbonates for Rechargeable Li Batteries." *Journal of The Electrochemical Society* **1995**, *142*(9), 2882-2890.
- Aurbach, D.; Ein-Ely, Y.; Zaban, A. "The Surface Chemistry of Lithium Electrodes in Alkyl Carbonate Solutions." *Journal of The Electrochemical Society* **1994**, *141*(1), L1-L3.
- Aurbach, D.; Gamolsky, K.; Markovsky, B.; Gofer, Y.; Schmidt, M.; Heider, U. "On the use of Vinylene Carbonate (VC) as an Additive to Electrolyte Solutions for Li-Ion Batteries." *Electrochimica Acta* **2002**, *47*(9), 1423-1439.
- Aurbach, D.; Gofer, Y.; Langzam, J. "The Correlation Between Surface Chemistry, Surface Morphology, and Cycling Efficiency of Lithium Electrodes in a Few Polar Aprotic Systems." *Journal of The Electrochemical Society* **1989**, *136*(11), 3198-3205.
- Aurbach, D.; Markovsky, B.; Shechter, A.; Ein-Eli, Y.; Cohen, H. "A Comparative Study of Synthetic Graphite and Li Electrodes in Electrolyte Solutions Based on Ethylene Carbonate-Dimethyl Carbonate Mixtures." *Journal of The Electrochemical Society* **1996**, *143*(12), 3809-3820.
- Aurbach, D.; Weissman, I.; Schechter, A.; Cohen, H. "X-ray Photoelectron Spectroscopy Studies of Lithium Surfaces Prepared in Several Important Electrolyte Solutions. A Comparison with Previous Studies by Fourier Transform Infrared Spectroscopy." *Langmuir* **1996**, *12*(16), 3991-4007.
- Aurbach, D.; Zaban, A. "The Application of EQCM to the Study of the Electrochemical-Behavior of Propylene Carbonate Solutions." *Journal of Electroanalytical Chemistry* **1995**, *393*(1-2), 43-53.

- Aurbach, D.; Zaban, A.; Schechter, A.; Ein-Eli, Y.; Zinigrad, E.; Markovsky, B. "The Study of Electrolyte Solutions Based on Ethylene and Diethyl Carbonates for Rechargeable Li Batteries." *Journal of The Electrochemical Society* **1995**, *142*(9), 2873-2882.
- Baggetto, L. c.; Hensen, E. J. M.; Notten, P. H. L. "In-situ X-ray Absorption Spectroscopy of Germanium Evaporated Thin Film Electrodes." *Electrochimica Acta* **2010**, *55*(23), 7074-7079.
- Baggetto, L.; Notten, P. H. L. "Lithium-Ion (De)Insertion Reaction of Germanium Thin-Film Electrodes: An Electrochemical and In-Situ XRD Study." *Journal of The Electrochemical Society* **2009**, *156*(3), A169-A175.
- Barnard, A. S.; Xu, H. "First Principles and Thermodynamic Modeling of CdS Surfaces and Nanorods." *The Journal of Physical Chemistry C* **2007**, *111*(49), 18112-18117.
- Barnard, A. S.; Xu, H.; Li, X.; Pradhan, N.; Peng, X. "Modelling the Formation of High Aspect CdSe Quantum Wires: Axial-Growth Versus Oriented-Attachment Mechanisms." *Nanotechnology* **2006**, *17*(22), 5707-5714.
- Basu, S. *U.S. Patent No. 4,304,825 Dec 8, 1981.*
- Basu, S. *U.S. Patent No. 4,423,124 Dec 27, 1983.*
- Beaulieu, L. Y.; Eberman, K. W.; Turner, R. L.; Krause, L. J.; Dahn, J. R. "Colossal Reversible Volume Changes in Lithium Alloys." *Electrochemical and Solid-State Letters* **2001**, *4*(9), A137-A140.
- Benyattou, T.; Garcia, M. A.; Monéger, S.; Tabata, A.; Sacilotti, M.; Abraham, P.; Monteil, Y.; Landers, R. "Optical characterization of InP / InAlAs / InP interfaces grown by MOVPE." *Applied Surface Science* **1993**, *63*, (1-4), 197-201.
- Bergstrom, O.; Gustafsson, T.; Thomas, J. O. "Electrochemically Lithiated Vanadium Oxide, $\text{Li}_3\text{V}_6\text{O}_{13}$." *Acta Crystallographica Section C-Crystal Structure Communications* **1998**, *54*, 1204-1206.
- Besenhard, J. O.; Eichinger, G. "High Energy Density Lithium Cells: Part I. Electrolytes and Anodes." *Journal of Electroanalytical Chemistry and Interfacial Electrochemistry* **1976**, *68*(1), 1-18.
- Boukamp, B. A.; Lesh, G. C.; Huggins, R. A. "All-Solid Lithium Electrodes with Mixed-Conductor Matrix." *Journal of The Electrochemical Society* **1981**, *128*(4), 725-729.
- Bridel, J. S.; Azaïs, T.; Morcrette, M.; Tarascon, J. M.; Larcher, D. "Key Parameters Governing the Reversibility of Si / Carbon / CMC Electrodes for Li-Ion Batteries." *Chemistry of Materials* **2009**, *22*(3), 1229-1241.
- Briggs, D.; Seah, M.P. *Practical Surface Analysis, 2nd Edition* **1993**.

- Bunge, S. D.; Krueger, K. M.; Boyle, T. J.; Rodriguez, M. A.; Headley, T. J.; Colvin, V. L. "Growth and Morphology of Cadmium Chalcogenides: the Synthesis of Nanorods, Tetrapods, and Spheres from CdO and Cd(O₂CCH₃)₂. *Journal of Materials Chemistry* **2003**, *13*(7), 1705-1709.
- Cao, L. Y.; White, J. S.; Park, J. S.; Schuller, J. A.; Clemens, B. M.; Brongersma, M. L. "Engineering Light Absorption in Semiconductor Nanowire Devices." *Nature Materials* **2009**, *8*(8), 643-647.
- Carmalt, C. J.; Compton, N. A.; Errington, R. J.; Fisher, G. A.; Moenandar, I.; Norman, N. C.; Whitmire, K. H. "Homoleptic Bismuth Amides" *Inorganic Syntheses* **2007**, 98-101.
- Caroff, P.; Dick, K. A.; Johansson, J.; Messing, M. E.; Deppert, K.; Samuelson, L. "Controlled Polytypic and Twin-Plane Superlattices in III-V Nanowires." *Nature Nanotechnology* **2009**, *4*(1), 50-55.
- Chakrapani, V.; Rusli, F.; Filler, M. A.; Kohl, P. A. "Quaternary Ammonium Ionic Liquid Electrolyte for a Silicon Nanowire-Based Lithium Ion Battery." *The Journal of Physical Chemistry C* **2011**, *115*(44), 22048-22053.
- Chan, C. K.; Patel, R. N.; O'Connell, M. J.; Korgel, B. A.; Cui, Y. "Solution-Grown Silicon Nanowires for Lithium-Ion Battery Anodes." *ACS Nano* **2010**, *4*(3), 1443-1450.
- Chan, C. K.; Peng, H.; Liu, G.; McIlwrath, K.; Zhang, X. F.; Huggins, R. A.; Cui, Y. "High-Performance Lithium Battery Anodes Using Silicon Nanowires." *Nature Nanotechnology* **2008**, *3*(1), 31-35.
- Chan, C. K.; Ruffo, R.; Hong, S. S.; Cui, Y. "Surface Chemistry and Morphology of the Solid Electrolyte Interphase on Silicon Nanowire Lithium-Ion Battery Anodes." *Journal of Power Sources* **2009**, *189*(2), 1132-1140.
- Chan, C. K.; Ruffo, R.; Hong, S. S.; Huggins, R. A.; Cui, Y. "Structural and Electrochemical Study of the Reaction of Lithium with Silicon Nanowires." *Journal of Power Sources* **2009**, *189*(1), 34-39.
- Chan, C. K.; Zhang, X. F.; Cui, Y. "High Capacity Li Ion Battery Anodes Using Ge Nanowires." *Nano Letters* **2007**, *8*(1), 307-309.
- Chang, C. C.; Scarr, N.; Kumta, P. N. "Synthesis and Electrochemical Characterization of LiMO₂ (M = Ni, Ni_{0.75}Co_{0.25}) for Rechargeable Lithium Ion Batteries." *Solid State Ionics* **1998**, *112*(3-4), 329-344.
- Chang, S. H.; Ryu, K. S.; Kim, K. M.; Kim, M. S.; Kim, I. K.; Kang, S. G. "Electrochemical Properties of Cobalt-Exchanged Spinel Lithium Manganese Oxide." *Journal of Power Sources* **1999**, *84*(1), 134-137.

- Charlier, J.; Detalle, V.; Valin, F.; Bureau, C.; Lecayon, G. "Study of Ultrathin Polyamide-6, 6 Films on Clean Copper and Platinum." *Journal of Vacuum Science & Technology A: Vacuum, Surfaces, and Films* **1997**, *15*(2), 353-364.
- Chen, C.-C.; Chao, C.-Y.; Lang, Z.-H. "Simple Solution-Phase Synthesis of Soluble CdS and CdSe Nanorods." *Chemistry of Materials* **2000**, *12*(6), 1516-1518.
- Chen, G.; Wang, L.; Sheng, X.; Liu, H.; Pi, X.; Zhang, Y.; Li, D.; Yang, D. "Growth of In₂O₃ Nanowires Catalyzed by Cu via a Solid-Liquid-Solid Mechanism." *Nanoscale Research Letters* **2010**, *5*(5), 898-903.
- Chen, G.; Wu, J.; Lu, Q.; Gutierrez, H. R.; Xiong, Q.; Pellen, M. E.; Petko, J. S.; Werner, D. H.; Eklund, P. C. "Optical Antenna Effect in Semiconducting Nanowires." *Nano Letters* **2008**, *8*(5), 1341-1346.
- Chen, Z.; Christensen, L.; Dahn, J. R. "Large-Volume-Change Electrodes for Li-Ion Batteries of Amorphous Alloy Particles Held by Elastomeric Tethers." *Electrochemistry Communications* **2003**, *5*(11), 919-923.
- Cheng, J.; Du, J. "Facile Synthesis of Germanium-Graphene Nanocomposites and their Application as Anode Materials for Lithium Ion Batteries." *CrystEngComm* **2012**, *14*(2), 397-400.
- Cho, K.-S.; Talapin, D. V.; Gaschler, W.; Murray, C. B. "Designing PbSe Nanowires and Nanorings through Oriented Attachment of Nanoparticles." *Journal of the American Chemical Society* **2005**, *127*(19), 7140-7147.
- Cho, Y. J.; Kim, H. S.; Im, H.; Myung, Y.; Jung, G. B.; Lee, C. W.; Park, J.; Park, M.-H.; Cho, J.; Kang, H. S. "Nitrogen-Doped Graphitic Layers Deposited on Silicon Nanowires for Efficient Lithium-Ion Battery Anodes." *The Journal of Physical Chemistry C* **2011**, *115*(19), 9451-9457.
- Chockla, A. M.; Harris, J. T.; Akhavan, V. A.; Bogart, T. D.; Holmberg, V. C.; Steinhagen, C.; Mullins, C. B.; Stevenson, K. J.; Korgel, B. A. "Silicon Nanowire Fabric as a Lithium Ion Battery Electrode Material." *Journal of the American Chemical Society* **2011**, *133*(51), 20914-20921.
- Chockla, A. M.; Harris, J. T.; Korgel, B. A. "Colloidal Synthesis of Germanium Nanorods." *Chemistry of Materials* **2011**, *23*(7), 1964-1970.
- Chockla, A. M.; Korgel, B. A. "Seeded Germanium Nanowire Synthesis in Solution." *Journal of Materials Chemistry* **2009**, *19*(7), 996-1001.
- Choi, J. W.; Hu, L.; Cui, L.; McDonough, J. R.; Cui, Y. "Metal Current Collector-Free Freestanding Silicon-Carbon 1D Nanocomposites for Ultra-Light Anodes in Lithium Ion Batteries." *Journal of Power Sources* **2010**, *195*(24), 8311-8316.
- Choi, N.-S.; Yew, K. H.; Lee, K. Y.; Sung, M.; Kim, H.; Kim, S.-S. "Effect of Fluoroethylene Carbonate Additive on Interfacial Properties of Silicon Thin-Film Electrode." *Journal of Power Sources* **2006**, *161*(2), 1254-1259.

- Chou, N. H.; Oyler, K. D.; Motl, N. E.; Schaak, R. E. "Colloidal Synthesis of Germanium Nanocrystals Using Room-Temperature Benchtop Chemistry." *Chemistry of Materials* **2009**, *21*(18), 4105-4107.
- Chou, N. H.; Schaak, R. E. "Shape-Controlled Conversion of β -Sn Nanocrystals into Intermetallic M-Sn (M = Fe, Co, Ni, Pd) Nanocrystals." *Journal of the American Chemical Society* **2007**, *129*(23), 7339-7345.
- Claeys, C. *Germanium-Based Technologies: From Materials to Devices* **2007**.
- Codoluto, S. C.; Baumgardner, W. J.; Hanrath, T. "Fundamental Aspects of Nucleation and Growth in the Solution-phase Synthesis of Germanium Nanocrystals." *CrystEngComm* **2010**, *12*(10), 2903-2909.
- Colli, A.; Fasoli, A.; Beecher, P.; Servati, P.; Pisana, S.; Fu, Y.; Flewitt, A. J.; Milne, W. I.; Robertson, J.; Ducati, C.; De Franceschi, S.; Hofmann, S.; Ferrari, A. C. "Thermal and Chemical Vapor Deposition of Si Nanowires: Shape Control, Dispersion, and Electrical Properties." *Journal of Applied Physics* **2007**, *102*(3), 034302.
- Coowar, F.; Abdelsalam, M. E.; Lain, M. *U.K. Patent No. 2481124, Dec 14, 2011*.
- Courtney, I. A.; Tse, J. S.; Mao, O.; Hafner, J.; Dahn, J. R. "Ab Initio Calculation of the Lithium-Tin Voltage Profile." *Physical Review B* **1998**, *58*(23), 15583-15588.
- Cros-Gagneux, A.; Delpech, F.; Nayral, C. L.; Cornejo, A.; Coppel, Y.; Chaudret, B. "Surface Chemistry of InP Quantum Dots: A Comprehensive Study." *Journal of the American Chemical Society* **2010**, *132*(51), 18147-18157.
- Cui, L.-F.; Ruffo, R.; Chan, C. K.; Peng, H.; Cui, Y. "Crystalline-Amorphous Core-Shell Silicon Nanowires for High Capacity and High Current Battery Electrodes." *Nano Letters* **2008**, *9*(1), 491-495.
- Cui, Y.; Lauhon, L. J.; Gudiksen, M. S.; Wang, J.; Lieber, C. M. "Diameter-Controlled Synthesis of Single-Crystal Silicon Nanowires." *Applied Physics Letters* **2001**, *78*(15), 2214-2216.
- Cui, Y.; Lieber, C. M. "Functional Nanoscale Electronic Devices Assembled Using Silicon Nanowire Building Blocks." *Science* **2001**, *291*(5505), 851-853.
- Cui, Y.; Wei, Q.; Park, H.; Lieber, C. M. "Nanowire Nanosensors for Highly Sensitive and Selective Detection of Biological and Chemical Species." *Science* **2001**, *293*(5533), 1289-1292.
- Dahn, J. R.; Zheng, T.; Liu, Y.; Xue, J. S. "Mechanisms for Lithium Insertion in Carbonaceous Materials." *Science* **1995**, *270*(5236), 590-593.
- Datta, M. K.; Maranchi, J.; Chung, S. J.; Epur, R.; Kadakia, K.; Jampani, P.; Kumta, P. N. "Amorphous Silicon-Carbon Based Nano-Scale Thin Film Anode Materials for Lithium Ion Batteries." *Electrochimica Acta* **2011**, *56*(13), 4717-4723.

- Davidson, F. M., III; Lee, D. C.; Fanfair, D. D.; Korgel, B. A. "Lamellar Twinning in Semiconductor Nanowires." *The Journal of Physical Chemistry C* **2007**, *111*(7), 2929-2935.
- Davidson, F. M.; Wiacek, R.; Korgel, B. A. "Supercritical Fluid-Liquid-Solid Synthesis of Gallium Phosphide Nanowires." *Chemistry of Materials* **2004**, *17*(2), 230-233.
- de Heer, W. A.; Bacsá, W. S.; Chatelain, A.; Gerfin, T.; Humphrey-Baker, R.; Forro, L.; Ugarte, D. "Aligned Carbon Nanotube Films: Production and Optical and Electronic Properties." *Science* **1995**, *268*(5212), 845-7.
- Dedryvère, R.; Foix, D.; Franger, S.; Patoux, S.; Daniel, L.; Gonbeau, D. "Electrode / Electrolyte Interface Reactivity in High-Voltage Spinel $\text{LiMn}_{1.6}\text{Ni}_{0.4}\text{O}_4$ / $\text{Li}_4\text{Ti}_5\text{O}_{12}$ Lithium-Ion Battery." *The Journal of Physical Chemistry C* **2010**, *114*(24), 10999-11008.
- Dedryvère, R.; Laruelle, S.; Grugeon, S.; Gireaud, L.; Tarascon, J. M.; Gonbeau, D. "XPS Identification of the Organic and Inorganic Components of the Electrode / Electrolyte Interface Formed on a Metallic Cathode." *Journal of The Electrochemical Society* **2005**, *152*(4), A689-A696.
- Dick, K. A.; Caroff, P.; Bolinsson, J.; Messing, M. E.; Johansson, J.; Deppert, K.; Wallenberg, L. R.; Samuelson, L. "Control of III-V Nanowire Crystal Structure by Growth Parameter Tuning." *Semiconductor Science and Technology* **2010**, *25*(2), 024009.
- Dick, K. A.; Deppert, K.; Larsson, M. W.; Martensson, T.; Seifert, W.; Wallenberg, L. R.; Samuelson, L. "Synthesis of Branched 'Nanotrees' by Controlled Seeding of Multiple Branching Events." *Nature Materials* **2004**, *3*(6), 380-384.
- Dikin, D. A.; Stankovich, S.; Zimney, E. J.; Piner, R. D.; Dommett, G. H. B.; Evmenenko, G.; Nguyen, S. T.; Ruoff, R. S. "Preparation and Characterization of Graphene Oxide Paper." *Nature* **2007**, *448*(7152), 457-460.
- DiLeo, R. A.; Frisco, S.; Ganter, M. J.; Rogers, R. E.; Raffaele, R. P.; Landi, B. J. "Hybrid Germanium Nanoparticle-Single-Wall Carbon Nanotube Free-Standing Anodes for Lithium Ion Batteries." *The Journal of Physical Chemistry C* **2011**, *115*(45), 22609-22614.
- Ding, N.; Xu, J.; Yao, Y. X.; Wegner, G.; Lieberwirth, I.; Chen, C. H. "Improvement of Cyclability of Si as Anode for Li-Ion Batteries." *Journal of Power Sources* **2009**, *192*(2), 644-651.
- Dong, A.; Wang, F.; Daulton, T. L.; Buhro, W. E. "Solution-Liquid-Solid (SLS) Growth of ZnSe-ZnTe Quantum Wires having Axial Heterojunctions." *Nano Letters* **2007**, *7*(5), 1308-1313.
- Draine, B. T. "The Discrete-Dipole Approximation and Its Application to Interstellar Graphite Grains." *Astrophysical Journal* **1988**, *333*(2), 848-872.

- Draine, B. T.; Flatau, P. J. “Discrete-Dipole Approximation for Periodic Targets: Theory and Tests.” *Journal of the Optical Society of America A* **2008**, *25(11)*, 2693-2703.
- Draine, B. T.; Flatau, P. J. “Discrete-Dipole Approximation for Scattering Calculations.” *Journal of the Optical Society of America A* **1994**, *11(4)*, 1491-1499.
- Duan, X.; Huang, Y.; Cui, Y.; Wang, J.; Lieber, C. M. “Indium Phosphide Nanowires as Building Blocks for Nanoscale Electronic and Optoelectronic Devices.” *Nature* **2001**, *409(6816)*, 66-69.
- Duan, X.; Huang, Y.; Lieber, C. M. “Nonvolatile Memory and Programmable Logic from Molecule-Gated Nanowires.” *Nano Letters* **2002**, *2(5)*, 487-490.
- Ehinon, K. K. D.; Naille, S.; Dedryvère, R.; Lippens, P. E.; Jumas, J. C.; Gonbeau, D. “Ni₃Sn₄ Electrodes for Li-Ion Batteries: Li-Sn Alloying Process and Electrode / Electrolyte Interface Phenomena.” *Chemistry of Materials* **2008**, *20(16)*, 5388-5398.
- Eichinger, G.; Besenhard, J. O. “High Energy Density Lithium Cells: Part II. Cathodes and Complete Cells.” *Journal of Electroanalytical Chemistry and Interfacial Electrochemistry* **1976**, *72(1)*, 1-31.
- Endo, M.; Muramatsu, H.; Hayashi, T.; Kim, Y. A.; Terrones, M.; Dresselhaus, M. S. “Nanotechnology: 'Buckypaper' from Coaxial Nanotubes.” *Nature* **2005**, *433(7025)*, 476.
- Etacheri, V.; Haik, O.; Goffer, Y.; Roberts, G. A.; Stefan, I. C.; Fasching, R.; Aurbach, D. “Effect of Fluoroethylene Carbonate (FEC) on the Performance and Surface Chemistry of Si-Nanowire Li-Ion Battery Anodes.” *Langmuir* **2012**, *28(1)*, 965-976.
- Evans, C. M.; Evans, M. E.; Krauss, T. D. “Mysteries of TOPSe Revealed: Insights into Quantum Dot Nucleation.” *Journal of the American Chemical Society* **2010**, *132(32)*, 10973-10975.
- Fan, Z. Y.; Ho, J. C.; Jacobson, Z. A.; Razavi, H.; Javey, A. “Large-Scale, Heterogeneous Integration of Nanowire Arrays for Image Sensor Circuitry.” *Proceedings of the National Academy of Sciences of the United States of America* **2008**, *105(32)*, 11066-11070.
- Fanfair, D. D.; Korgel, B. A. “Bismuth Nanocrystal-Seeded III-V Semiconductor Nanowire Synthesis.” *Crystal Growth & Design* **2005**, *5(5)*, 1971-1976.
- Fanfair, D. D.; Korgel, B. A. “Twin-Related Branching of Solution-Grown ZnSe Nanowires.” *Chemistry of Materials* **2007**, *19(20)*, 4943-4948.
- Fanfair, D. D.; Korgel, B. A. “ZnE (E = S, Se, Te) Nanowires Grown by the Solution-Liquid-Solid Mechanism: Importance of Reactant Decomposition Kinetics and the Solvent.” *Crystal Growth & Design* **2008**, *8(9)*, 3246-3252.

- Ferrari, A. C. "Raman Spectroscopy of Graphene and Graphite: Disorder, Electron-Phonon Coupling, Doping and Nonadiabatic Effects." *Solid State Communications* **2007**, *143*(1-2), 47-57.
- Ferrari, A. C.; Robertson, J. "Interpretation of Raman Spectra of Disordered and Amorphous Carbon." *Physical Review B* **2000**, *61*(20), 14095-14107.
- Föll, H.; Carstensen, J.; Ossei-Wusu, E.; Cojocar, A.; Quiroga-Gonzalez, E.; Neumann, G. "Optimized Cu Contacted Si Nanowire Anodes for Li-Ion Batteries Made in a Production Near Process." *ECS Transactions* **2010**, *33*(27), 131-141.
- Fouquet, J. E.; Minsky, M. S.; Rosner, S. J. "Photoluminescence Excitation Spectroscopy Yields Band Gap of Ga_{0.5}In_{0.5}P Containing Relatively Ordered Domains." *Applied Physics Letters* **1993**, *63*(23), 3212-3214.
- Fu, P. P.; Song, Y. J.; Zhang, H. F.; Yang, H. B.; Zhou, Z. X.; Wu, M. T.; Huang, L. H.; Xu, G. "Amorphous Silicon Film Anode for Lithium-Ion Battery." *Chinese Journal of Inorganic Chemistry* **2006**, *22*(10), 1823-1827.
- Fuller, C. S.; Severiens, J. C. "Mobility of Impurity Ions in Germanium and Silicon." *Physical Review* **1954**, *96*(1), 21-24.
- Gao, B.; Sinha, S.; Fleming, L.; Zhou, O. "Alloy Formation in Nanostructured Silicon." *Advanced Materials* **2001**, *13*(11), 816-819.
- Garnett, E. C.; Yang, P. "Silicon Nanowire Radial p-n Junction Solar Cells." *Journal of the American Chemical Society* **2008**, *130*(29), 9224-9225.
- Ge, M.; Liu, J. F.; Wu, H.; Yao, C.; Zeng, Y.; Fu, Z. D.; Zhang, S. L.; Jiang, J. Z. "Synthesis of Germanium Nanowires." *The Journal of Physical Chemistry C* **2007**, *111*(30), 11157-11160.
- "Germanium—Statistics and Information" *U.S. Geological Survey, Mineral Commodity Summaries*, **2011**.
- Gerung, H.; Boyle, T. J.; Tribby, L. J.; Bunge, S. D.; Brinker, C. J.; Han, S. M. "Solution Synthesis of Germanium Nanowires Using a Ge²⁺ Alkoxide Precursor." *Journal of the American Chemical Society* **2006**, *128*(15), 5244-5250.
- Gilman, H.; Miles, D. H. "Disproportionation Reaction of Diphenylsilane in the Absence of any Added Catalyst." *Journal of Organic Chemistry* **1958**, *23*, 326-328.
- Goebel, J. A.; Black, R. W.; Puthussery, J.; Giblin, J.; Kosel, T. H.; Kuno, M. "Solution-Based II-VI Core / Shell Nanowire Heterostructures." *Journal of the American Chemical Society* **2008**, *130*(44), 14822-14833.
- Goodenough, J. B.; Kim, Y. "Challenges for Rechargeable Li Batteries." *Chemistry of Materials* **2010**, *22*(3), 587-603.

- Graetz, J.; Ahn, C. C.; Yazami, R.; Fultz, B. "Highly Reversible Lithium Storage in Nanostructured Silicon." *Electrochemical and Solid-State Letters* **2003**, *6*(9), A194-A197.
- Graetz, J.; Ahn, C. C.; Yazami, R.; Fultz, B. "Nanocrystalline and Thin Film Germanium Electrodes with High Lithium Capacity and High Rate Capabilities." *Journal of The Electrochemical Society* **2004**, *151*(5), A698-A702.
- Grebinski, J. W.; Hull, K. L.; Zhang, J.; Kosel, T. H.; Kuno, M. "Solution-Based Straight and Branched CdSe Nanowires." *Chemistry of Materials* **2004**, *16*(25), 5260-5272.
- Greytak, A. B.; Barrelet, C. J.; Li, Y.; Lieber, C. M. "Semiconductor Nanowire Laser and Nanowire Waveguide Electro-Optic Modulators." *Applied Physics Letters* **2005**, *87*(15), 151103-3.
- Grillet, N.; Manchon, D.; Bertorelle, F.; Bonnet, C.; Broyer, M.; Cottancin, E.; Lermé, J.; Hillenkamp, M.; Pellarin, M. "Plasmon Coupling in Silver Nanocube Dimers: Resonance Splitting Induced by Edge Rounding." *ACS Nano* **2011**, *5*(12), 9450-9462.
- Gu, Y.; Kwak, E. S.; Lensch, J. L.; Allen, J. E.; Odom, T. W.; Lauhon, L. J. "Near-Field Scanning Photocurrent Microscopy of a Nanowire Photodetector." *Applied Physics Letters* **2005**, *87*(4), 043111-3.
- Gudiksen, M. S.; Lauhon, L. J.; Wang, J.; Smith, D. C.; Lieber, C. M. "Growth of Nanowire Superlattice Structures for Nanoscale Photonics and Electronics." *Nature* **2002**, *415*(6872), 617-620.
- Guzelian, A. A.; Katari, J. E. B.; Kadavanich, A. V.; Banin, U.; Hamad, K.; Juban, E.; Alivisatos, A. P.; Wolters, R. H.; Arnold, C. C.; Heath, J. R. "Synthesis of Size-Selected, Surface-Passivated InP Nanocrystals." *The Journal of Physical Chemistry* **1996**, *100*(17), 7212-7219.
- Höll, R.; Kling, M.; Schroll, E. "Metallogenesis of Germanium-A Review." *Ore Geology Reviews* **2007**, *30*(3-4), 145-180.
- Han, G. B.; Lee, J. N.; Choi, J. W.; Park, J. K. "Tris(pentafluorophenyl) Borane as an Electrolyte Additive for High Performance Silicon Thin Film Electrodes in Lithium Ion Batteries." *Electrochimica Acta* **2011**, *56*(24), 8997-9003.
- Hanrath, T.; Korgel, B. A. "Crystallography and Surface Faceting of Germanium Nanowires." *Small* **2005**, *1*(7), 717-721.
- Hanrath, T.; Korgel, B. A. "Influence of Surface States on Electron Transport through Intrinsic Ge Nanowires." *The Journal of Physical Chemistry B* **2005**, *109*(12), 5518-5524.

- Hanrath, T.; Korgel, B. A. "Nucleation and Growth of Germanium Nanowires Seeded by Organic Monolayer-Coated Gold Nanocrystals." *Journal of the American Chemical Society* **2002**, *124*(7), 1424-1429.
- Hanrath, T.; Korgel, B. A. "Supercritical Fluid-Liquid-Solid (SFLS) Synthesis of Si and Ge Nanowires Seeded by Colloidal Metal Nanocrystals." *Advanced Materials* **2003**, *15*(5), 437-440.
- Hao, Y.; Meng, G.; Ye, C.; Zhang, X.; Zhang, L. "Kinetics-Driven Growth of Orthogonally Branched Single-Crystalline Magnesium Oxide Nanostructures." *The Journal of Physical Chemistry B* **2005**, *109*(22), 11204-11208.
- Hatchard, T. D.; Dahn, J. R. "In-Situ XRD and Electrochemical Study of the Reaction of Lithium with Amorphous Silicon." *Journal of The Electrochemical Society* **2004**, *151*(6), A838-A842.
- Hauffman, T.; Blajiev, O.; Snauwaert, J.; van Haesendonck, C.; Hubin, A.; Terryn, H. "Study of the Self-Assembling of n-Octylphosphonic Acid Layers on Aluminum Oxide." *Langmuir* **2008**, *24*(23), 13450-13456.
- Hayden, O.; Agarwal, R.; Lieber, C. M. "Nanoscale Avalanche Photodiodes for Highly Sensitive and Spatially Resolved Photon Detection." *Nature Materials* **2006**, *5*(5), 352-356.
- Heath, J. R.; LeGoues, F. K. "A Liquid Solution Synthesis of Single Crystal Germanium Quantum Wires." *Chemical Physics Letters* **1993**, *208*(3-4), 263-268.
- Heath, J. R.; Shiang, J. J.; Alivisatos, A. P. "Germanium Quantum Dots: Optical Properties and Synthesis." *The Journal of Chemical Physics* **1994**, *101*(2), 1607-1615.
- Heitsch, A. T.; Akhavan, V. A.; Korgel, B. A. "Rapid SFLS Synthesis of Si Nanowires Using Trisilane with In-Situ Alkyl-Amine Passivation." *Chemistry of Materials* **2011**, *23*(11), 2697-2699.
- Heitsch, A. T.; Fanfair, D. D.; Tuan, H.-Y.; Korgel, B. A. "Solution-Liquid-Solid (SLS) Growth of Silicon Nanowires." *Journal of the American Chemical Society* **2008**, *130*(16), 5436-5437.
- Heitsch, A. T.; Hessel, C. M.; Akhavan, V. A.; Korgel, B. A. "Colloidal Silicon Nanorod Synthesis." *Nano Letters* **2009**, *9*(8), 3042-3047.
- Hens, Z.; Moreels, I.; Martins, J. C. "In-Situ ¹H NMR Study on the Trioctylphosphine Oxide Capping of Colloidal InP Nanocrystals." *ChemPhysChem* **2005**, *6*(12), 2578-2584.
- Hessel, C. M.; Heitsch, A. T.; Korgel, B. A. "Gold Seed Removal from the Tips of Silicon Nanorods." *Nano Letters* **2009**, *10*(1), 176-180.

- Hessel, C. M.; Henderson, E. J.; Veinot, J. G. C. "Hydrogen Silsesquioxane: A Molecular Precursor for Nanocrystalline Si-SiO₂ Composites and Freestanding Hydride-Surface-Terminated Silicon Nanoparticles." *Chemistry of Materials* **2006**, *18*(26), 6139-6146.
- Hessel, C. M.; Rasch, M. R.; Hueso, J. L.; Goodfellow, B. W.; Akhavan, V. A.; Puvanakrishnan, P.; Tunnel, J. W.; Korgel, B. A. "Alkyl Passivation and Amphiphilic Polymer Coating of Silicon Nanocrystals for Diagnostic Imaging." *Small* **2010**, *6*(18), 2026-2034.
- Hessel, C. M.; Reid, D.; Panthani, M. G.; Rasch, M. R.; Goodfellow, B. W.; Wei, J.; Fujii, H.; Akhavan, V.; Korgel, B. A. "Synthesis of Ligand-Stabilized Silicon Nanocrystals with Size-Dependent Photoluminescence Spanning Visible to Near-Infrared Wavelengths." *Chemistry of Materials* **2012**, *24*(2), 393-401.
- Hines, M. A.; Guyot-Sionnest, P. "Bright UV-Blue Luminescent Colloidal ZnSe Nanocrystals." *The Journal of Physical Chemistry B* **1998**, *102*(19), 3655-3657.
- Hollinger, G.; Bergignat, E.; Joseph, J.; Robach, Y. "On the Nature of Oxides on InP Surfaces." *Journal of Vacuum Science & Technology A* **1985**, *3*(6), 2082-2088.
- Holman, Z. C.; Kortshagen, U. R. "Solution-Processed Germanium Nanocrystal Thin Films as Materials for Low-Cost Optical and Electronic Devices." *Langmuir* **2009**, *25*(19), 11883-11889.
- Holmberg, V. C.; Patel, R. N.; Korgel, B. A. "Electrostatic Charging and Manipulation of Semiconductor Nanowires." *Journal Materials Research* **2011**, *26*(17), 2305-2310.
- Holmes, J. D.; Johnston, K. P.; Doty, R. C.; Korgel, B. A. "Control of Thickness and Orientation of Solution-Grown Silicon Nanowires." *Science* **2000**, *287*(5457), 1471-1473.
- Hsieh, G. W.; Beecher, P.; Li, F. M.; Servati, P.; Colli, A.; Fasoli, A.; Chu, D.; Nathan, A.; Ong, B.; Robertson, J.; Ferrari, A. C.; Milne, W. I. "Formation of Composite Organic Thin Film Transistors with Nanotubes and Nanowires." *Physica E* **2008**, *40*(7), 2406-2413.
- Hu, J.; Bando, Y.; Golberg, D. "Sn-Catalyzed Thermal Evaporation Synthesis of Tetrapod-Branched ZnSe Nanorod Architectures." *Small* **2005**, *1*(1), 95-99.
- Hu, J.; Odom, T. W.; Lieber, C. M. "Chemistry and Physics in One Dimension: Synthesis and Properties of Nanowires and Nanotubes." *Accounts of Chemical Research* **1999**, *32*(5), 435-445.
- Hu, L.; Chen, G. "Analysis of Optical Absorption in Silicon Nanowire Arrays for Photovoltaic Applications." *Nano Letters* **2007**, *7*(11), 3249-3252.

- Hu, L.; Wu, H.; Hong, S. S.; Cui, L.; McDonough, J. R.; Bohy, S.; Cui, Y. "Si Nanoparticle-Decorated Si Nanowire Networks for Li-Ion Battery Anodes." *Chemical Communications* **2011**, *47(1)*, 367-369.
- Hu, L.; Wu, H.; La, M. F.; Yang, Y.; Cui, Y. "Thin-Flexible Secondary Lithium-Ion Paper Batteries." *ACS Nano* **2010**, *4(10)*, 5843-5848.
- Hu, Y.-S.; Demir-Cakan, R.; Titirici, M.-M.; Müller, J.-O.; Schlögl, R.; Antonietti, M.; Maier, J. "Superior Storage Performance of a Si@SiO_x / C Nanocomposite as Anode Material for Lithium-Ion Batteries." *Angewandte Chemie International Edition* **2008**, *47(9)*, 1645-1649.
- Huang, M. H.; Mao, S.; Feick, H.; Yan, H.; Wu, Y.; Kind, H.; Weber, E.; Russo, R.; Yang, P. "Room-Temperature Ultraviolet Nanowire Nanolasers." *Science* **2001**, *292(5523)*, 1897-1899.
- Huang, R.; Fan, X.; Shen, W. C.; Zhu, J. "Carbon-Coated Silicon Nanowire Array Films for High-Performance Lithium-Ion Battery Anodes." *Applied Physics Letters* **2009**, *95(13)*, 133119-3.
- Huang, R.; Zhu, J. "Silicon Nanowire Array Films as Advanced Anode Materials for Lithium-ion Batteries." *Materials Chemistry and Physics* **2010**, *121(3)*, 519-522.
- Hull, K. L.; Grebinski, J. W.; Kosel, T. H.; Kuno, M. "Induced Branching in Confined PbSe Nanowires." *Chemistry of Materials* **2005**, *17(17)*, 4416-4425.
- Hwang, C.-M.; Park, J.-W. "Electrochemical Characterization of a Ge-Based Composite Film Fabricated as an Anode Material using Magnetron Sputtering for Lithium Ion Batteries." *Thin Solid Films* **2010**, *518(22)*, 6590-6597.
- Ikonic, Z.; Srivastava, G. P.; Inkson, J. C. "Optical Properties of Twinning Superlattices in Diamond-Type and Zinc-Blende-Type Semiconductors." *Physical Review B* **1995**, *52(19)*, 14078-14085.
- Jo, Y. H.; Jung, I.; Choi, C. S.; Kim, I.; Lee, H. M. "Synthesis and Characterization of Low Temperature Sn Nanoparticles for the Fabrication of Highly Conductive Ink." *Nanotechnology* **2011**, *22(22)*, 225701.
- Johnson, J. C.; Choi, H. J.; Knutsen, K. P.; Schaller, R. D.; Yang, P. D.; Saykally, R. J. "Single Gallium Nitride Nanowire Lasers." *Nature Materials* **2002**, *1(2)*, 106-110.
- Joo, J.; Pietryga, J. M.; McGuire, J. A.; Jeon, S.-H.; Williams, D. J.; Wang, H.-L.; Klimov, V. I. "A Reduction Pathway in the Synthesis of PbSe Nanocrystal Quantum Dots." *Journal of the American Chemical Society* **2009**, *131(30)*, 10620-10628.
- Joo, J.; Son, J. S.; Kwon, S. G.; Yu, J. H.; Hyeon, T. "Low-Temperature Solution-Phase Synthesis of Quantum Well Structured CdSe Nanoribbons." *Journal of the American Chemical Society* **2006**, *128(17)*, 5632-5633.

- Joyce, H. J.; Wong-Leung, J.; Gao, Q.; Tan, H. H.; Jagadish, C. "Phase Perfection in Zinc Blende and Wurtzite III-V Nanowires Using Basic Growth Parameters." *Nano Letters* **2010**, *10*(3), 908-915.
- Jung, H. J.; Park, M.; Han, S. H.; Lim, H.; Joo, S. K. "Amorphous Silicon Thin-Film Negative Electrode Prepared by Low Pressure Chemical Vapor Deposition for Lithium-Ion Batteries." *Solid State Communications* **2003**, *125*(7-8), 387-390.
- Kan, S.; Mokari, T.; Rothenberg, E.; Banin, U. "Synthesis and Size-Dependent Properties of Zinc-Blende Semiconductor Quantum Rods." *Nature Materials* **2003**, *2*(3), 155-158.
- Kanamura, K.; Takezawa, H.; Shiraishi, S.; Takehara, Z. "Chemical Reaction of Lithium Surface During Immersion in LiClO₄ or LiPF₆ / DEC electrolyte." *Journal of The Electrochemical Society* **1997**, *144*(6), 1900-1906.
- Kanamura, K.; Tamura, H.; Shiraishi, S.; Takehara, Z.-I. "XPS Analysis for the Lithium Surface Immersed in γ -Butyrolactone Containing Various Salts." *Electrochimica Acta* **1995**, *40*(7), 913-921.
- Kanamura, K.; Tamura, H.; Shiraishi, S.; Takehara, Z.-I. "XPS Analysis of Lithium Surfaces Following Immersion in Various Solvents Containing LiBF₄." *Journal of The Electrochemical Society* **1995**, *142*(2), 340-347.
- Kanamura, K.; Tamura, H.; Takehara, Z.-I. "XPS Analysis of a Lithium Surface Immersed in Propylene Carbonate Solution Containing Various Salts." *Journal of Electroanalytical Chemistry* **1992**, *333*(1-2), 127-142.
- Kanaras, A. G.; Soennichsen, C.; Liu, H.; Alivisatos, A. P. "Controlled Synthesis of Hyperbranched Inorganic Nanocrystals with Rich Three-Dimensional Structures." *Nano Letters* **2005**, *5*(11), 2164-2167.
- Kang, K.; Lee, H.-S.; Han, D.-W.; Kim, G.-S.; Lee, D.; Lee, G.; Kang, Y.-M.; Jo, M.-H. "Maximum Li Storage in Si Nanowires for the High Capacity Three-Dimensional Li-Ion Battery." *Applied Physics Letters* **2010**, *96*(5), 053110-3.
- Kasavajjula, U.; Wang, C.; Appleby, A. J. "Nano- and Bulk-Silicon-Based Insertion Anodes for Lithium-Ion secondary Cells." *Journal of Power Sources* **2007**, *163*(2), 1003-1039.
- Kayes, B. M.; Atwater, H. A.; Lewis, N. S. "Comparison of the Device Physics Principles of Planar and Radial p-n Junction Nanorod Solar Cells." *Journal of Applied Physics* **2005**, *97*, (11), 114302-11.
- Kelzenberg, M. D.; Turner-Evans, D. B.; Kayes, B. M.; Filler, M. A.; Putnam, M. C.; Lewis, N. S.; Atwater, H. A. "Photovoltaic Measurements in Single-Nanowire Silicon Solar Cells." *Nano Letters* **2008**, *8*(2), 710-714.
- Key, B.; Bhattacharyya, R.; Morcrette, M.; Seznec, V.; Tarascon, J. M.; Grey, C. P. "Real-Time NMR Investigations of Structural Changes in Silicon Electrodes for

- Lithium-Ion Batteries.” *Journal of the American Chemical Society* **2009**, *131*(26), 9239-9249.
- Kim, H.; Cho, J. “Superior Lithium Electroactive Mesoporous Si@Carbon Core-Shell Nanowires for Lithium Battery Anode Material.” *Nano Letters* **2008**, *8*(11), 3688-3691.
- Kim, Y. J.; Kim, M. H.; Yang, J. H.; Park, J. W. “Electrochemical Properties of Aluminum-Doped Silicon Films as Anode Materials for Lithium-Ion Batteries.” *Journal of the Korean Physical Society* **2006**, *49*(3), 1196-1201.
- Kim, Y.; Hwang, H.; Lawler, K.; Martin, S. W.; Cho, J. “Electrochemical Behavior of Ge and GeX₂ (X = O, S) Glasses: Improved Reversibility of the Reaction of Li with Ge in a Sulfide Medium.” *Electrochimica Acta* **2008**, *53*(15), 5058-5064.
- Ko, Y. D.; Kang, J. G.; Lee, G. H.; Park, J. G.; Park, K. S.; Jin, Y. H.; Kim, D. W. “Sn-Induced Low-Temperature Growth of Ge Nanowire Electrodes with a Large Lithium Storage Capacity.” *Nanoscale* **2011**, *3*(8), 3371-3375.
- Korgel, B. A. “Semiconductor Nanowires: Twins Cause Kinks.” *Nature Materials* **2006**, *5*(7), 521-522.
- Kovalenko, I.; Zdyrko, B.; Magasinski, A.; Hertzberg, B.; Milicev, Z.; Burtovyy, R.; Luzinov, I.; Yushin, G. “A Major Constituent of Brown Algae for Use in High-Capacity Li-Ion Batteries.” *Science* **2011**, *334*(6052), 75-79.
- Kriegner, D.; Wintersberger, E.; Kawaguchi, K.; Wallentin, J.; Borgstrom, M. T.; Stangl, J. “Unit Cell Parameters of Wurtzite InP Nanowires Determined by X-Ray Diffraction.” *Nanotechnology* **2011**, *22* (42), 425704.
- Kuno, M.; Ahmad, O.; Protasenko, V.; Bacinello, D.; Kosel, T. H. “Solution-Based Straight and Branched CdTe Nanowires.” *Chemistry of Materials* **2006**, *18*(24), 5722-5732.
- Laforge, B.; Levan-Jodin, L.; Salot, R.; Billard, A. “Study of Germanium as Electrode in Thin-Film Battery.” *Journal of The Electrochemical Society* **2008**, *155*(2), A181-A188.
- Lai, S.-C. “Solid Lithium-Silicon Electrode.” *Journal of The Electrochemical Society* **1976**, *123*(8), 1196-1197.
- Laïk, B.; Eude, L.; Pereira-Ramos, J.-P.; Cojocar, C. S.; Pribat, D.; Rouvière, E. “Silicon Nanowires as Negative Electrode for Lithium-Ion Microbatteries.” *Electrochimica Acta* **2008**, *53*(17), 5528-5532.
- Lambert, T. N.; Andrews, N. L.; Gerung, H.; Boyle, T. J.; Oliver, J. M.; Wilson, B. S.; Han, S. M. “Water-Soluble Germanium(0) Nanocrystals: Cell Recognition and Near-Infrared Photothermal Conversion Properties.” *Small* **2007**, *3*(4), 691-699.

- Lao, J. Y.; Huang, J. Y.; Wang, D. Z.; Ren, Z. F. "Hierarchical Oxide Nanostructures." *Journal of Materials Chemistry* **2004**, *14*(4), 770-773.
- Law, M.; Goldberger, J.; Yang, P. "Semiconductor Nanowires and Nanotubes." *Annual Review of Materials Research* **2004**, *34*, 83-122.
- Law, M.; Sirbuly, D. J.; Johnson, J. C.; Goldberger, J.; Saykally, R. J.; Yang, P. "Nanoribbon Waveguides for Subwavelength Photonics Integration." *Science* **2004**, *305*(5688), 1269-1273.
- Le, H. Q.; Chua, S. J.; Koh, Y. W.; Loh, K. P.; Chen, Z.; Thompson, C. V.; Fitzgerald, E. A. "Growth of Single Crystal ZnO Nanorods on GaN using an Aqueous Solution Method." *Applied Physics Letters* **2005**, *87*, (10), 101908-3.
- Lee, D. C.; Hanrath, T.; Korgel, B. A. "The Role of Precursor-Decomposition Kinetics in Silicon-Nanowire Synthesis in Organic Solvents." *Angewandte Chemie International Edition* **2005**, *44*(23), 3573-3577.
- Lee, D. C.; Pietryga, J. M.; Robel, I.; Werder, D. J.; Schaller, R. D.; Klimov, V. I. "Colloidal Synthesis of Infrared-Emitting Germanium Nanocrystals." *Journal of the American Chemical Society* **2009**, *131*(10), 3436-3437.
- Lee, H.; Kim, H.; Doo, S.-G.; Cho, J. "Synthesis and Optimization of Nanoparticle Ge Confined in a Carbon Matrix for Lithium Battery Anode Material." *Journal of The Electrochemical Society* **2007**, *154*(4), A343-A346.
- Lee, J. K.; Smith, K. B.; Hayner, C. M.; Kung, H. H. "Silicon Nanoparticles-Graphene Paper Composites for Li Ion Battery Anodes." *Chemical Communications* **2010**, *46*(12), 2025-2027.
- Lee, J.-K.; Kung, M. C.; Trahey, L.; Missaghi, M. N.; Kung, H. H. "Nanocomposites Derived from Phenol-Functionalized Si Nanoparticles for High Performance Lithium Ion Battery Anodes." *Chemistry of Materials* **2009**, *21*(1), 6-8.
- Lenham, A. P.; Treherne, D. M.; Metcalfe, R. J. "Optical Properties of Antimony and Bismuth Crystals." *Journal of the Optical Society of America* **1965**, *55*(9), 1072-1074.
- Lespade, P.; Al-Jishi, R.; Dresselhaus, M. S. "Model for Raman Scattering From Incompletely Graphitized Carbons." *Carbon* **1982**, *20*(5), 427-431.
- Li, H. X.; Cheng, F. Y.; Zhu, Z. Q.; Bai, H. M.; Tao, Z. L.; Chen, J. "Preparation and Electrochemical Performance of Copper Foam-Supported Amorphous Silicon Thin Films for Rechargeable Lithium-Ion Batteries." *Journal of Alloys and Compounds* **2011**, *509*(6), 2919-2923.
- Li, H.; Richter, G.; Maier, J. "Reversible Formation and Decomposition of LiF Clusters Using Transition Metal Fluorides as Precursors and Their Application in Rechargeable Li Batteries." *Advanced Materials* **2003**, *15*(9), 736-739.

- Li, J.; Christensen, L.; Obrovac, M. N.; Hewitt, K. C.; Dahn, J. R. "Effect of Heat Treatment on Si Electrodes Using Polyvinylidene Fluoride Binder." *Journal of The Electrochemical Society* **2008**, *155*(3), A234-A238.
- Li, J.; Dahn, J. R. "An In Situ X-Ray Diffraction Study of the Reaction of Li with Crystalline Si." *Journal of The Electrochemical Society* **2007**, *154*(3), A156-A161.
- Li, T.; Li, L.; Cao, Y. L.; Ai, X. P.; Yang, H. X. "Reversible Three-Electron Redox Behaviors of FeF₃ Nanocrystals as High-Capacity Cathode-Active Materials for Li-Ion Batteries." *The Journal of Physical Chemistry C* **2010**, *114*(7), 3190-3195.
- Li, Y.; Li, X.; Yang, C.; Li, Y. "Controlled Synthesis of CdS Nanorods and Hexagonal Nanocrystals." *Journal of Materials Chemistry* **2003**, *13*(10), 2641-2648.
- Liang, M.; Zhi, L. "Graphene-Based Electrode Materials for Rechargeable Lithium Batteries." *Journal of Materials Chemistry* **2009**, *19*(33), 5871-5878.
- Link, S.; El-Sayed, M. A. "Shape and Size Dependence of Radiative, Non-Radiative and Photothermal Properties of Gold Nanocrystals." *International Reviews in Physical Chemistry* **2000**, *19*(3), 409-453.
- Liu, C.; Li, F.; Ma, L. P.; Cheng, H. M. "Advanced Materials for Energy Storage." *Advanced Materials* **2010**, *22*(8), E28-E62.
- Liu, G. Q.; Zeng, C. L.; Yang, K. "Study on the Synthesis and Properties of LiV₃O₈ Rechargeable Lithium Batteries Cathode". *Electrochimica Acta* **2002**, *47*(20), 3239-3243.
- Liu, N.; Hu, L.; McDowell, M. T.; Jackson, A.; Cui, Y. "Prelithiated Silicon Nanowires as an Anode for Lithium Ion Batteries." *ACS Nano* **2011**, *5*(8), 6487-6493.
- Liu, Q.; Derksen, S.; Lindner, A.; Scheffer, F.; Prost, W.; Tegude, F. J. "Evidence of Type-II Band Alignment at the Ordered GaInP to GaAs Heterointerface." *Journal of Applied Physics* **1995**, *77*(3), 1154-1158.
- Liu, S.; Guo, X.; Li, M.; Zhang, W.-H.; Liu, X.; Li, C. "Solution-Phase Synthesis and Characterization of Single-Crystalline SnSe Nanowires." *Angewandte Chemie International Edition* **2011**, *50*(50), 12050-12053.
- Liu, X. H.; Huang, S.; Picraux, S. T.; Li, J.; Zhu, T.; Huang, J. Y. "Reversible Nanopore Formation in Ge Nanowires during Lithiation-Delithiation Cycling: An In-Situ Transmission Electron Microscopy Study." *Nano Letters* **2011**, *11*(9), 3991-3997.
- Liu, X. H.; Zhang, L. Q.; Zhong, L.; Liu, Y.; Zheng, H.; Wang, J. W.; Cho, J.-H.; Dayeh, S. A.; Picraux, S. T.; Sullivan, J. P.; Mao, S. X.; Ye, Z. Z.; Huang, J. Y. "Ultrafast Electrochemical Lithiation of Individual Si Nanowire Anodes." *Nano Letters* **2011**, *11*(6), 2251-2258.

- Liu, Y.; Xue, J. S.; Zheng, T.; Dahn, J. R. "Mechanism of Lithium Insertion in Hard Carbons Prepared by Pyrolysis of Epoxy Resins." *Carbon* **1996**, *34*(2), 193-200.
- Lopez, F. J.; Hemesath, E. R.; Lauhon, L. J. "Ordered Stacking Fault Arrays in Silicon Nanowires." *Nano Letters* **2009**, *9*(7), 2774-2779.
- Lozano, K.; Hernandez, C.; Petty, T. W.; Sigman, M. B.; Korgel, B. "Electrorheological Analysis of Nano Laden Suspensions." *Journal of Colloid and Interface Science* **2006**, *297*(2), 618-624.
- Lu, W.; Lieber, C. M. "Semiconductor Nanowires." *Journal of Physics D: Applied Physics* **2006**, *39*(21), R387-R406.
- Lu, X. H.; Yu, P. Y.; Zheng, L. X.; Xu, S. J.; Xie, M. H.; Tong, S. Y. "Evidence for a Type-II Band Alignment Between Cubic and Hexagonal Phases of GaN." *Applied Physics Letters* **2003**, *82*(7), 1033-1035.
- Lu, X.; Fanfair, D. D.; Johnston, K. P.; Korgel, B. A. "High Yield Solution-Liquid-Solid Synthesis of Germanium Nanowires." *Journal of the American Chemical Society* **2005**, *127*(45), 15718-15719.
- Lu, X.; Hanrath, T.; Johnston, K. P.; Korgel, B. A. "Growth of Single Crystal Silicon Nanowires in Supercritical Solution from Tethered Gold Particles on a Silicon Substrate." *Nano Letters* **2002**, *3*(1), 93-99.
- Luo, X. D.; Hu, C. Y.; Xu, Z. Y.; Luo, H. L.; Wang, Y. Q.; Wang, J. N.; Ge, W. K. "Selectively Excited Photoluminescence of GaAs_{1-x}Sb_x / GaAs Single Quantum Wells." *Applied Physics Letters* **2002**, *81*(20), 3795-3797.
- Lv, R. T.; Cao, C. B.; Zhai, H. Z.; Wang, D. Z.; Liu, S. Y.; Zhu, H. S. "Growth and Characterization of Single-Crystal ZnSe Nanorods via Surfactant Soft-Template Method." *Solid State Communications* **2004**, *130*(3-4), 241-245.
- Möller, K. C.; Hodal, T.; Appel, W. K.; Winter, M.; Besenhard, J. O. "Fluorinated Organic Solvents in Electrolytes for Lithium Ion Cells." *Journal of Power Sources* **2001**, *97-98*(0), 595-597.
- Magasinski, A.; Dixon, P.; Hertzberg, B.; Kvit, A.; Ayala, J.; Yushin, G., "High-Performance Lithium-Ion Anodes using a Hierarchical Bottom-Up Approach." *Nature Materials* **2010**, *9*(4), 353-358.
- Magasinski, A.; Zdyrko, B.; Kovalenko, I.; Hertzberg, B.; Burtovyy, R.; Huebner, C. F.; Fuller, T. F.; Luzinov, I.; Yushin, G. "Toward Efficient Binders for Li-Ion Battery Si-Based Anodes: Polyacrylic Acid." *ACS Applied Materials & Interfaces* **2010**, *2*(11), 3004-3010.
- Manna, L.; Scher, E. C.; Alivisatos, A. P. "Synthesis of Soluble and Processable Rod-, Arrow-, Teardrop-, and Tetrapod-Shaped CdSe Nanocrystals." *Journal of the American Chemical Society* **2000**, *122*(51), 12700-12706.

- Maranchi, J. P.; Hepp, A. F.; Kumta, P. N. "High Capacity, Reversible Silicon Thin-Film Anodes for Lithium-Ion Batteries." *Electrochemical and Solid-State Letters* **2003**, *6*(9), A198-A201.
- Maranchi, J. P.; Kumta, P. N.; Hepp, A. F. "Amorphous Silicon Thin Film Anodes for Lithium-Ion Batteries." *Developments in Solid Oxide Fuel Cells and Lithium Ion Batteries* **2005**, *161*, 121-129.
- Matsuo, Y.; Sugie, Y. "Preparation, Structure and Electrochemical Property of Pyrolytic Carbon from Graphite Oxide." *Carbon* **1998**, *36*(3), 301-303.
- May, S. J.; Zheng, J.-G.; Wessels, B. W.; Lauhon, L. J. "Dendritic Nanowire Growth Mediated by a Self-Assembled Catalyst." *Advanced Materials* **2005**, *17*(5), 598-602.
- Mazouzi, D.; Lestriez, B.; Roue, L.; Guyomard, D. "Silicon Composite Electrode with High Capacity and Long Cycle Life." *Electrochemical and Solid-State Letters* **2009**, *12*(11), A215-A218.
- McAlpine, M. C.; Friedman, R. S.; Jin, S.; Lin, K.-h.; Wang, W. U.; Lieber, C. M. "High-Performance Nanowire Electronics and Photonics on Glass and Plastic Substrates." *Nano Letters* **2003**, *3*(11), 1531-1535.
- McDonald, J.; Golden, A.; Gerard Jennings, S. "OpenDDA: a Novel High-Performance Computational Framework for the Discrete Dipole Approximation." *International Journal of High Performance Computing Applications* **2009**, *23*, 42-61.
- McDowell, M. T.; Lee, S. W.; Ryu, I.; Wu, H.; Nix, W. D.; Choi, J. W.; Cui, Y. "Novel Size and Surface Oxide Effects in Silicon Nanowires as Lithium Battery Anodes." *Nano Letters* **2011**, *11*(9), 4018-4025.
- McMillan, R.; Slegel, H.; Shu, Z. X.; Wang, W. "Fluoroethylene Carbonate Electrolyte and its use in Lithium Ion Batteries with Graphite Anodes." *Journal of Power Sources* **1999**, *81-82*(0), 20-26.
- Mičić, O. I.; Jones, K. M.; Cahill, A.; Nozik, A. J. "Optical, Electronic, and Structural Properties of Uncoupled and Close-Packed Arrays of InP Quantum Dots." *The Journal of Physical Chemistry B* **1998**, *102*(49), 9791-9796.
- Mičić, O. I.; Ahrenkiel, S. P.; Nozik, A. J. "Synthesis of Extremely Small InP Quantum Dots and Electronic Coupling in their Disordered Solid Films." *Applied Physics Letters* **2001**, *78*(25), 4022-4024.
- Mičić, O. I.; Sprague, J.; Lu, Z.; Nozik, A. J. "Highly Efficient Band-Edge Emission from InP Quantum Dots." *Applied Physics Letters* **1996**, *68*(22), 3150-3152.
- Miyachi, M.; Yamamoto, H.; Kawai, H.; Ohta, T.; Shirakata, M. "Analysis of SiO Anodes for Lithium-Ion Batteries." *Journal of The Electrochemical Society* **2005**, *152*(10), A2089-A2091.

- Mogi, R.; Inaba, M.; Jeong, S.-K.; Iriyama, Y.; Abe, T.; Ogumi, Z. "Effects of Some Organic Additives on Lithium Deposition in Propylene Carbonate." *Journal of The Electrochemical Society* **2002**, *149(12)*, A1578-A1583.
- Mohamed, M.; Makino, A.; Dokko, K.; Itoh, T.; Uchida, I. "Electrochemical Investigation of $\text{LiNi}_{0.5}\text{Mn}_{1.5}\text{O}_4$ Thin Film Intercalation Electrodes." *Electrochimica Acta* **2002**, *48(1)*, 79-84.
- Moore, D.; Ding, Y.; Wang, Z. L. "Hierarchical Structured Nanohelices of ZnS." *Angewandte Chemie International Edition* **2006**, *45(31)*, 5150-5154.
- Moreels, I.; Martins, J. C.; Hens, Z. "Solution NMR Techniques for Investigating Colloidal Nanocrystal Ligands: A Case Study on Trioctylphosphine Oxide at InP Quantum Dots." *Sensors and Actuators B: Chemical* **2007**, *126(1)*, 283-288.
- Moulder, J. F.; Stickle, W. F.; Sobol, P. E.; Bomben, K. D. *Handbook of X-Ray Photoelectron Spectroscopy* **1992**.
- Munao, D.; Valvo, M.; van Erven, J.; Kelder, E. M.; Hassoun, J.; Panero, S. "Silicon-Based Nanocomposite for Advanced Thin Film Anodes in Lithium-Ion Batteries." *Journal of Materials Chemistry* **2011**, *22(4)*, 1556-1561.
- Murphy, D. W.; Christian, P. A.; Disalvo, F. J.; Carides, J. N. "Vanadium-Oxide Cathode Materials for Secondary Lithium Cells." *Journal of The Electrochemical Society* **1979**, *126(3)*, 497-499.
- Muskens, O. L.; Diedenhofen, S. L.; Kaas, B. C.; Algra, R. E.; Bakkers, E. P. A. M.; Gómez Rivas, J.; Lagendijk, A. "Large Photonic Strength of Highly Tunable Resonant Nanowire Materials." *Nano Letters* **2009**, *9(3)*, 930-934.
- Muskens, O. L.; Rivas, J. G. m.; Algra, R. E.; Bakkers, E. P. A. M.; Lagendijk, A., "Design of Light Scattering in Nanowire Materials for Photovoltaic Applications." *Nano Letters* **2008**, *8*, (9), 2638-2642.
- Nagao, Y.; Sakaguchi, H.; Honda, H.; Fukunaga, T.; Esaka, T. "Structural Analysis of Pure and Electrochemically Lithiated SiO Using Neutron Elastic Scattering." *Journal of The Electrochemical Society* **2004**, *151(10)*, A1572-A1575.
- Nakai, H.; Kubota, T.; Kita, A.; Kawashima, A. "Investigation of the Solid Electrolyte Interphase Formed by Fluoroethylene Carbonate on Si Electrodes." *Journal of The Electrochemical Society* **2011**, *158(7)*, A798-A801.
- Netz, A.; Huggins, R. A.; Weppner, W. "The Formation and Properties of Amorphous Silicon as Negative Electrode Reactant in Lithium Systems." *Journal of Power Sources* **2003**, *119-121(0)*, 95-100.
- Ng, S. H.; Wang, J.; Guo, Z. P.; Chen, J.; Wang, G. X.; Liu, H. K. "Single Wall Carbon Nanotube Paper as Anode for Lithium-Ion Battery." *Electrochimica Acta* **2005**, *51(1)*, 23-28.

- Obrovac, M. N.; Christensen, L. "Structural Changes in Silicon Anodes during Lithium Insertion / Extraction." *Electrochemical and Solid-State Letters* **2004**, 7(5), A93-A96.
- Obrovac, M. N.; Krause, L. J. "Reversible Cycling of Crystalline Silicon Powder." *Journal of The Electrochemical Society* **2007**, 154(2), A103-A108.
- Ohzuku, T.; Kitagawa, M.; Hirai, T. "Electrochemistry of Manganese-Dioxide in Lithium Nonaqueous Cell II. X-Ray Diffractonal and Electrochemical Characterization on Deep Discharge Products of Electrolytic Manganese-Dioxide." *Journal of The Electrochemical Society* **1990**, 137(1), 40-46.
- Ouyang, L.; Maher, K. N.; Yu, C. L.; McCarty, J.; Park, H. "Catalyst-Assisted Solution-Liquid-Solid Synthesis of CdS/CdSe Nanorod Heterostructures." *Journal of the American Chemical Society* **2006**, 129(1), 133-138.
- Padhi, A. K.; Nanjundaswamy, K. S.; Goodenough, J. B. "Phospho-Olivines as Positive-Electrode Materials for Rechargeable Lithium Batteries." *Journal of The Electrochemical Society* **1997**, 144(4), 1188-1194.
- Pan, D. Y.; Wang, S.; Zhao, B.; Wu, M. H.; Zhang, H. J.; Wang, Y.; Jiao, Z. "Li Storage Properties of Disordered Graphene Nanosheets." *Chemistry of Materials* **2009**, 21(14), 3136-3142.
- Park, M.-H.; Cho, Y.; Kim, K.; Kim, J.; Liu, M.; Cho, J. "Germanium Nanotubes Prepared by Using the Kirkendall Effect as Anodes for High-Rate Lithium Batteries." *Angewandte Chemie International Edition* **2011**, 50(41), 9647-9650.
- Park, S.; An, J. H.; Jung, I. W.; Piner, R. D.; An, S. J.; Li, X. S.; Velamakanni, A.; Ruoff, R. S. "Colloidal Suspensions of Highly Reduced Graphene Oxide in a Wide Variety of Organic Solvents." *Nano Letters* **2009**, 9(4), 1593-1597.
- Park, S.; An, J. H.; Piner, R. D.; Jung, I.; Yang, D. X.; Velamakanni, A.; Nguyen, S. T.; Ruoff, R. S. "Aqueous Suspension and Characterization of Chemically Modified Graphene Sheets." *Chemistry of Materials* **2008**, 20(21), 6592-6594.
- Patiño, R.; Campos, M.; Torres, L. A. "Strength of the Zn-N Coordination Bond in Zinc Porphyrins on the Basis of Experimental Thermochemistry." *Inorganic Chemistry* **2007**, 46(22), 9332-9336.
- Peled, E. "The Electrochemical Behavior of Alkali and Alkaline Earth Metals in Nonaqueous Battery Systems-The Solid Electrolyte Interphase Model." *Journal of The Electrochemical Society* **1979**, 126(12), 2047-2051.
- Peng, K.; Jie, J.; Zhang, W.; Lee, S.-T. "Silicon Nanowires for Rechargeable Lithium-Ion Battery Anodes." *Applied Physics Letters* **2008**, 93(3), 033105-3.
- Peng, X.; Manna, U.; Yang, W.; Wickham, J.; Scher, E.; Kadavanich, A.; Allvisatos, A. P. "Shape Control of CdSe Nanocrystals." *Nature* **2000**, 404(6773), 59-61.

- Peng, Z. A.; Peng, X. "Formation of High-Quality CdTe, CdSe, and CdS Nanocrystals Using CdO as Precursor." *Journal of the American Chemical Society* **2000**, *123(1)*, 183-184.
- Philippe, B.; Dedryvère, R. m.; Allouche, J.; Lindgren, F.; Gorgoi, M.; Rensmo, H. K.; Gonbeau, D.; Edström, K., "Nanosilicon Electrodes for Lithium-Ion Batteries: Interfacial Mechanisms Studied by Hard and Soft X-ray Photoelectron Spectroscopy." *Chemistry of Materials* **2012**, *24(6)*, 107-1115.
- Podolskiy, V. A.; Sarychev, A. K.; Shalaev, V. M. "Plasmon Modes in Metal Nanowires and Left-Handed Materials." *Journal of Nonlinear Optical Physics & Materials* **2002**, *11(1)*, 65-74.
- Pozuelo, M.; Prikhodko, S. V.; Grantab, R.; Zhou, H.; Gao, L.; Sitzman, S. D.; Gambin, V.; Shenoy, V. B.; Hicks, R. F.; Kodambaka, S. "Zincblende to Wurtzite Transition During the Self-Catalyzed Growth of InP Nanostructures." *Journal of Crystal Growth* **2010**, *312(16-17)*, 2305-2309.
- Puthussery, J.; Lan, A.; Kosel, T. H.; Kuno, M. "Band-Filling of Solution-Synthesized CdS Nanowires." *ACS Nano* **2008**, *2(2)*, 357-367.
- Ramesh, T. N.; Lee, K. T.; Ellis, B. L.; Nazar, L. F. "Favorite Lithium Iron Fluorophosphate Cathode Materials: Phase Transition and Electrochemistry of LiFePO_4F - $\text{Li}_2\text{FePO}_4\text{F}$." *Electrochemical and Solid State Letters* **2010**, *13(4)*, A43-A47.
- Rathi, S. J.; Jariwala, B. N.; Beach, J. D.; Stradins, P.; Taylor, P. C.; Weng, X.; Ke, Y.; Redwing, J. M.; Agarwal, S.; Collins, R. T. "Tin-Catalyzed Plasma-Assisted Growth of Silicon Nanowires." *The Journal of Physical Chemistry C* **2011**, *115(10)*, 3833-3839.
- Robert A, H. "Lithium Alloy Negative Electrodes." *Journal of Power Sources* **1999**, *81-82(0)*, 13-19.
- Rong, J. P.; Masarapu, C.; Ni, J.; Zhang, Z. J.; Wei, B. Q. "Tandem Structure of Porous Silicon Film on Single-Walled Carbon Nanotube Macrofilms for Lithium-Ion Battery Applications." *ACS Nano* **2010**, *4(8)*, 4683-4690.
- Ruffo, R.; Hong, S. S.; Chan, C. K.; Huggins, R. A.; Cui, Y. "Impedance Analysis of Silicon Nanowire Lithium Ion Battery Anodes." *The Journal of Physical Chemistry C* **2009**, *113(26)*, 11390-11398.
- Russell, G. A. "Catalysis by Metal Halides I. Mechanism of Disproportionation of Ethyltrimethylsilane." *Journal of the American Chemical Society* **1959**, *81*, 4815-25.
- Ryu, I.; Choi, J. W.; Cui, Y.; Nix, W. D. "Size-Dependent Fracture of Si Nanowire Battery Anodes." *Journal of the Mechanics and Physics of Solids* **2011**, *59(9)*, 1717-1730.

- Saint, J.; Morcrette, M.; Larcher, D.; Laffont, L.; Beattie, S.; Pérès, J. P.; Talaga, D.; Couzi, M.; Tarascon, J. M. "Towards a Fundamental Understanding of the Improved Electrochemical Performance of Silicon–Carbon Composites." *Advanced Functional Materials* **2007**, *17*(11), 1765-1774.
- Sangster, J.; Pelton, A. "The Ge-Li (Germanium-Lithium) System." *Journal of Phase Equilibria* **1997**, *18*(3), 289-294.
- Sato, K.; Zhao, L.; Okada, S.; Yamaki, J.-I. "LiPF₆ / Methyl Difluoroacetate Electrolyte with Vinylene Carbonate Additive for Li-ion Batteries." *Journal of Power Sources* **2011**, *196*(13), 5617-5622.
- Saunders, A. E.; Ghezelbash, A.; Sood, P.; Korgel, B. A. "Synthesis of High Aspect Ratio Quantum-Size CdS Nanorods and Their Surface-Dependent Photoluminescence." *Langmuir* **2008**, *24*(16), 9043-9049.
- Saunders, A. E.; Sigman, M. B.; Korgel, B. A. "Growth Kinetics and Metastability of Monodisperse Tetraoctylammonium Bromide Capped Gold Nanocrystals." *The Journal of Physical Chemistry B* **2003**, *108*(1), 193-199.
- Schechter, A.; Aurbach, D.; Cohen, H. "X-ray Photoelectron Spectroscopy Study of Surface Films Formed on Li Electrodes Freshly Prepared in Alkyl Carbonate Solutions." *Langmuir* **1999**, *15*(9), 3334-3342.
- Seo, M.-H.; Park, M.; Lee, K. T.; Kim, K.; Kim, J.; Cho, J. "High Performance Ge Nanowire Anode Sheathed with Carbon for Lithium Rechargeable Batteries." *Energy & Environmental Science* **2011**, *4*(2), 425-428.
- She, M.; King, T.-J. "Impact of Crystal Size and Tunnel Dielectric on Semiconductor Nanocrystal Memory performance." *Electron Devices, IEEE Transactions on* **2003**, *50*(9), 1934-1940.
- Shen, G.; Bando, Y.; Liu, B.; Tang, C.; Golberg, D. "Unconventional Zigzag Indium Phosphide Single-Crystalline and Twinned Nanowires." *The Journal of Physical Chemistry B* **2006**, *110*(41), 20129-20132.
- Shieh, F.; Saunders, A. E.; Korgel, B. A. "General Shape Control of Colloidal CdS, CdSe, CdTe Quantum Rods and Quantum Rod Heterostructures." *The Journal of Physical Chemistry B* **2005**, *109*(18), 8538-8542.
- Shiraishi, S.; Kanamura, K.; Takehara, Z.-I. "Surface Condition Changes in Lithium Metal Deposited in Nonaqueous Electrolyte Containing HF by Dissolution-Deposition Cycles." *Journal of The Electrochemical Society* **1999**, *146*(5), 1633-1639.
- Shweky, I.; Aharoni, A.; Mokari, T.; Rothenberg, E.; Nadler, M.; Popov, I.; Banin, U. "Seeded Growth of InP and InAs Quantum Rods Using Indium Acetate and Myristic Acid." *Materials Science and Engineering: C* **2006**, *26*(5-7), 788-794.

- Sigman, M. B., Jr.; Korgel, B. A. "Strongly Birefringent Pb₃O₂Cl₂ Nanobelts." *Journal of the American Chemical Society* **2005**, *127*(28), 10089-10095.
- Singh, V.; Joung, D.; Zhai, L.; Das, S.; Khondaker, S. I.; Seal, S. "Graphene Based Materials: Past, Present and Future." *Progress in Materials Science* **2011**, *56*(8), 1178-1271.
- Smart, M. C.; Ratnakumar, B. V.; Ryan-Mowrey, V. S.; Surampudi, S.; Prakash, G. K. S.; Hu, J.; Cheung, I. "Improved Performance of Lithium-Ion Cells with the use of Fluorinated Carbonate-Based Electrolytes." *Journal of Power Sources* **2003**, *119-121*(0), 359-367.
- Smith, D. A.; Holmberg, V. C.; Korgel, B. A. "Flexible Germanium Nanowires: Ideal Strength, Room Temperature Plasticity, and Bendable Semiconductor Fabric." *ACS Nano* **2010**, *4*(4), 2356-2362.
- Smith, D. A.; Holmberg, V. C.; Lee, D. C.; Korgel, B. A. "Young's Modulus and Size-Dependent Mechanical Quality Factor of Nanoelectromechanical Germanium Nanowire Resonators." *The Journal of Physical Chemistry C* **2008**, *112*(29), 10725-10729.
- Smith, D. A.; Holmberg, V. C.; Rasch, M. R.; Korgel, B. A. "Optical Properties of Solvent-Dispersed and Polymer-Embedded Germanium Nanowires." *The Journal of Physical Chemistry C* **2010**, *114*(49), 20983-20989.
- Smith, D. K.; Lee, D. C.; Korgel, B. A. "High Yield Multiwall Carbon Nanotube Synthesis in Supercritical Fluids." *Chemistry of Materials* **2006**, *18*(14), 3356-3364.
- Smith, D. K.; Miller, N. R.; Korgel, B. A. "Iodide in CTAB Prevents Gold Nanorod Formation." *Langmuir* **2009**, *25*(16), 9518-9524.
- Soci, C.; Zhang, A.; Xiang, B.; Dayeh, S. A.; Aplin, D. P. R.; Park, J.; Bao, X. Y.; Lo, Y. H.; Wang, D. "ZnO Nanowire UV Photodetectors with High Internal Gain." *Nano Letters* **2007**, *7*(4), 1003-1009.
- Speier, J. L., Jr.; Zimmerman, R. E. "Disproportionation of Phenylsilanes with Aluminum Chloride as the Catalyst." *Journal of the American Chemical Society* **1955**, *77*, 6395-6.
- Steckel, J. S.; Yen, B. K. H.; Oertel, D. C.; Bawendi, M. G. "On the Mechanism of Lead Chalcogenide Nanocrystal Formation." *Journal of the American Chemical Society* **2006**, *128*(40), 13032-13033.
- Sun, Q.; Zhang, B.; Fu, Z.-W. "Lithium Electrochemistry of SiO₂ Thin Film Electrode for Lithium-Ion Batteries." *Applied Surface Science* **2008**, *254*(13), 3774-3779.
- Sun, Y. K.; Hong, K. J.; Prakash, J.; Amine, K. "Electrochemical Performance of Nano-Sized ZnO-Coated LiNi_{0.5}Mn_{1.5}O₄ Spinel as 5V Materials at Elevated Temperatures." *Electrochemistry Communications* **2002**, *4*(4), 344-348.

- Suzuki, H., Komatsu, N., Ogawa, T., Murafuji, T., Ikegami, T., Matano, Y. *Organobismuth Chemistry* **2001**, 149-150.
- Suzuki, T.; Hasegawa, T.; Mukai, S. R.; Tamon, H. "A Theoretical Study on Storage States of Li Ions in Carbon Anodes of Li Ion Batteries using Molecular Orbital Calculations." *Carbon* **2003**, *41*(10), 1933-1939.
- Szczeczek, J. R.; Jin, S. "Nanostructured Silicon for High Capacity Lithium Battery Anodes." *Energy & Environmental Science* **2011**, *4*(1), 56-72.
- Sze, S. M.; Irvin, J. C. "Resistivity, Mobility and Impurity levels in GaAs, Ge, and Si at 300K." *Solid-State Electronics* **1968**, *11*(6), 599-602.
- Taillades, G.; Benjelloun, N.; Sarradin, J.; Ribes, M. "Metal-Based Very Thin Film Anodes for Lithium Ion Microbatteries." *Solid State Ionics* **2002**, *152-153*(0), 119-124.
- Tang, Z.; Kotov, N. A.; Giersig, M. "Spontaneous Organization of Single CdTe Nanoparticles into Luminescent Nanowires." *Science* **2002**, *297*(5579), 237-240.
- Tarascon, J. M.; Armand, M. "Issues and Challenges Facing Rechargeable Lithium Batteries." *Nature* **2001**, *414*(6861), 359-367.
- Teki, R.; Datta, M. K.; Krishnan, R.; Parker, T. C.; Lu, T. M.; Kumta, P. N.; Koratkar, N. "Nanostructured Silicon Anodes for Lithium Ion Rechargeable Batteries." *Small* **2009**, *5*(20), 2236-2242.
- Tian, B. Z.; Zheng, X. L.; Kempa, T. J.; Fang, Y.; Yu, N. F.; Yu, G. H.; Huang, J. L.; Lieber, C. M. "Coaxial Silicon Nanowires as Solar Cells and Nanoelectronic Power Sources." *Nature* **2007**, *449*(7164), 885-U8.
- Timmons, A.; Todd, A. D. W.; Mead, S. D.; Carey, G. H.; Sanderson, R. J.; Mar, R. E.; Dahn, J. R. "Studies of Si_{1-x}C_x Electrode Materials Prepared by High-Energy Mechanical Milling and Combinatorial Sputter Deposition." *Journal of The Electrochemical Society* **2007**, *154*(9), A865-A874.
- Todd, A. D. W.; Ferguson, P. P.; Fleischauer, M. D.; Dahn, J. R. "Tin-Based Materials as Negative Electrodes for Li-Ion Batteries: Combinatorial Approaches and Mechanical Methods." *International Journal of Energy Research* **2010**, *34*(6), 535-555.
- Totzeck, M.; Ulrich, W.; Gohnermeier, A.; Kaiser, W. "Semiconductor Fabrication: Pushing Deep Ultraviolet Lithography to its Limits." *Nature Photonics* **2007**, *1*(11), 629-631.
- Trentler, T. J.; Hickman, K. M.; Goel, S. C.; Viano, A. M.; Gibbons, P. C.; Buhro, W. E. "Solution-Liquid-Solid Growth of Crystalline III-V Semiconductors: An Analogy to Vapor-Liquid-Solid Growth." *Science* **1995**, *270*(5243), 1791-1794.

- Tsang, C.; Manthiram, A. "Synthesis of Nanocrystalline VO₂ and its Electrochemical Behavior in Lithium Batteries." *Journal of The Electrochemical Society* **1997**, *144*(2), 520-524.
- Tuan, H.-Y.; Korgel, B. A. "Importance of Solvent-Mediated Phenylsilane Decomposition Kinetics for High-Yield Solution-Phase Silicon Nanowire Synthesis." *Chemistry of Materials* **2008**, *20*(4), 1239-1241.
- Tuan, H.-Y.; Lee, D. C.; Korgel, B. A. "Nanocrystal-Mediated Crystallization of Silicon and Germanium Nanowires in Organic Solvents: The Role of Catalysis and Solid-Phase Seeding." *Angewandte Chemie International Edition* **2006**, *45*(31), 5184-5187.
- Tuinstra, F.; Koenig, J. L. "Raman Spectrum of Graphite." *Journal of Chemical Physics* **1970**, *53*(3), 1126-30.
- U.S. Geological Survey, Mineral Commodity Summaries, January 2010.*
- Vivekchand, S. R. C.; Kam, K. C.; Gundiah, G.; Govindaraj, A.; Cheetham, A. K.; Rao, C. N. R. "Electrical Properties of Inorganic Nanowire-Polymer Composites." *Journal of Materials Chemistry* **2005**, *15*(46), 4922-4927.
- Vogdanis, L.; Martens, B.; Uchtmann, H.; Hensel, F.; Heitz, W. "Synthetic and Thermodynamic Investigations in the Polymerization of Ethylene Carbonate." *Makromolekulare Chemie-Macromolecular Chemistry and Physics* **1990**, *191*(3), 465-472.
- Wagner, R. S.; Ellis, W. C. "Vapor-Liquid-Solid Mechanism of Single Crystal Growth." *Applied Physics Letters* **1964**, *4*(5), 89-90.
- Wakihara, M. "Recent Developments in Lithium Ion Batteries." *Materials Science & Engineering R-Reports* **2001**, *33*(4), 109-134.
- Wang, C. Y.; Li, D.; Too, C. O.; Wallace, G. G. "Electrochemical Properties of Graphene Paper Electrodes Used in Lithium Batteries." *Chemistry of Materials* **2009**, *21*(13), 2604-2606.
- Wang, D. H.; Kou, R.; Choi, D.; Yang, Z. G.; Nie, Z. M.; Li, J.; Saraf, L. V.; Hu, D. H.; Zhang, J. G.; Graff, G. L.; Liu, J.; Pope, M. A.; Aksay, I. A. "Ternary Self-Assembly of Ordered Metal Oxide-Graphene Nanocomposites for Electrochemical Energy Storage." *ACS Nano* **2010**, *4*(3), 1587-1595.
- Wang, D.; Qian, F.; Yang, C.; Zhong, Z.; Lieber, C. M. "Rational Growth of Branched and Hyperbranched Nanowire Structures." *Nano Letters* **2004**, *4*(5), 871-874.
- Wang, D.; Yang, Z.; Li, F.; Liu, D.; Wang, X.; Yan, H.; He, D. "Improved Performance for Lithium-Ion Batteries with Nickel Nanocone-Arrays Supported Germanium Anode." *Materials Letters* **2011**, *65*(11), 1542-1544.

- Wang, F.; Buhro, W. E. "An Easy Shortcut Synthesis of Size-Controlled Bismuth Nanoparticles and Their Use in the SLS Growth of High-Quality Colloidal Cadmium Selenide Quantum Wires." *Small* **2010**, *6*(4), 573-581.
- Wang, F.; Buhro, W. E. "Determination of the Rod-Wire Transition Length in Colloidal Indium Phosphide Quantum Rods." *Journal of the American Chemical Society* **2007**, *129*(46), 14381-14387.
- Wang, F.; Dong, A.; Sun, J.; Tang, R.; Yu, H.; Buhro, W. E. "Solution-Liquid-Solid Growth of Semiconductor Nanowires." *Inorganic Chemistry* **2006**, *45*(19), 7511-7521.
- Wang, F.; Tang, R.; Kao, J. L. F.; Dingman, S. D.; Buhro, W. E. "Spectroscopic Identification of Tri-n-Octylphosphine Oxide (TOPO) Impurities and Elucidation of Their Roles in Cadmium Selenide Quantum-Wire Growth." *Journal of the American Chemical Society* **2009**, *131*(13), 4983-4994.
- Wang, F.; Tang, R.; Yu, H.; Gibbons, P. C.; Buhro, W. E. "Size- and Shape-Controlled Synthesis of Bismuth Nanoparticles." *Chemistry of Materials* **2008**, *20*(11), 3656-3662.
- Wang, F.; Yu, H.; Li, J.; Hang, Q.; Zemlyanov, D.; Gibbons, P. C.; Wang; Janes, D. B.; Buhro, W. E. "Spectroscopic Properties of Colloidal Indium Phosphide Quantum Wires." *Journal of the American Chemical Society* **2007**, *129*(46), 14327-14335.
- Wang, H. L.; Cui, L. F.; Yang, Y. A.; Casalongue, H. S.; Robinson, J. T.; Liang, Y. Y.; Cui, Y.; Dai, H. J. "Mn₃O₄-Graphene Hybrid as a High-Capacity Anode Material for Lithium Ion Batteries." *Journal of the American Chemical Society* **2010**, *132*(40), 13978-13980.
- Wang, J.-Z.; Zhong, C.; Chou, S.-L.; Liu, H.-K. "Flexible Free-Standing Graphene-Silicon Composite Film for Lithium-Ion Batteries." *Electrochemistry Communications* **2010**, *12*(11), 1467-1470.
- Wang, J.; Du, N.; Zhang, H.; Yu, J.; Yang, D., "Cu-Ge Core-Shell Nanowire Arrays as Three-Dimensional Electrodes for High-Rate Capability Lithium-Ion Batteries." *Journal of Materials Chemistry* **2012**, *22*(4), 1511-1515.
- Wang, J.; Gudiksen, M. S.; Duan, X.; Cui, Y.; Lieber, C. M. "Highly Polarized Photoluminescence and Photodetection from Single Indium Phosphide Nanowires." *Science* **2001**, *293*(5534), 1455-1457.
- Wang, P. Y.; Jain, A. L. "Modulated Piezoreflectance in Bismuth." *Physical Review B-Solid State* **1970**, *2*(8), 2978-2983.
- Wang, R.-P.; Zhou, G.-W.; Liu, Y.-L.; Pan, S.-H.; Zhang, H.-Z.; Yu, D.-P.; Zhang, Z. "Raman Spectral Study of Silicon Nanowires: High-order scattering and phonon Confinement Effects." *Physical Review B* **2000**, *61*(24), 16827-16832.

- Wang, W.; Kumta, P. N. "Nanostructured Hybrid Silicon / Carbon Nanotube Heterostructures: Reversible High-Capacity Lithium-Ion Anodes." *ACS Nano* **2010**, *4*(4), 2233-2241.
- Wang, Z.; Zhao, B.; Zhang, F.; Mao, W.; Qian, G.; Fan, X. "Novel Single-Crystal PbS Nanowires Directed by [200]." *Materials Letters* **2007**, *61*(17), 3733-3735.
- Wei, Q.; Meng, G.; An, X.; Hao, Y.; Zhang, L. "Temperature-Controlled Growth of ZnO Nanostructures: Branched Nanobelts and Wide Nanosheets." *Nanotechnology* **2005**, *16*(11), 2561-2566.
- Weaver, J. H. W.; Frederikse, H. P. R. "Optical Properties of Selected Elements." *CRC Handbook of Chemistry and Physics*, 92nd ed. **2012**, 12.129-130.
- Wen, C. J.; Huggins, R. A. "Chemical Diffusion in Intermediate Phases in the Lithium-Silicon System." *Journal of Solid State Chemistry* **1981**, *37*(3), 271-278.
- Wen, Z. S.; Cheng, M. K.; Sun, J. C.; Wang, L. A. "Composite Silicon Film with Connected Silicon Nanowires for Lithium Ion Batteries." *Electrochimica Acta* **2010**, *56*(1), 372-375.
- Weydanz, W. J.; Wohlfahrt-Mehrens, M.; Huggins, R. A. "A Room Temperature Study of the Binary Lithium-Silicon and the Ternary Lithium-Chromium-Silicon System for use in Rechargeable Lithium Batteries." *Journal of Power Sources* **1999**, *81*-*82*(0), 237-242.
- Whittingham, M. S. "Electrical Energy Storage and Intercalation Chemistry." *Science* **1976**, *192*(4244), 1126-1127.
- Wieligor, M.; Wang, Y. J.; Zerda, T. W. "Raman Spectra of Silicon Carbide Small Particles and Nanowires." *Journal of Physics-Condensed Matter* **2005**, *17*(15), 2387-2395.
- Wilcoxon, J. P.; Provencio, P. P.; Samara, G. A. "Synthesis and Optical Properties of Colloidal Germanium Nanocrystals." *Physical Review B* **2001**, *64*(3), 035417.
- Williams, R. H.; Hamilton, L. A. "Di-n-Alkylphosphine Oxides I. Synthesis." *Journal of the American Chemical Society* **1952**, *74*(21), 5418-5420.
- Winter, M.; Besenhard, J. O.; Spahr, M. E.; Novák, P. "Insertion Electrode Materials for Rechargeable Lithium Batteries." *Advanced Materials* **1998**, *10*(10), 725-763.
- Winter, M.; Besenhard, J. R. O. "Electrochemical Lithiation of Tin and Tin-Based Intermetallics and Composites." *Electrochimica Acta* **1999**, *45*(1-2), 31-50.
- Wu, P.; Du, N.; Liu, J.; Zhang, H.; Yu, J.; Yang, D. "Solvothetical Synthesis of Carbon-Coated Tin Nanorods for Superior Reversible Lithium Ion Storage." *Materials Research Bulletin* **2011**, *46*(12), 2278-2282.
- Wu, Y.; Yang, P. "Direct Observation of Vapor-Liquid-Solid Nanowire Growth." *Journal of the American Chemical Society* **2001**, *123*(13), 3165-3166.

- Wu, Z. S.; Ren, W. C.; Wen, L.; Gao, L. B.; Zhao, J. P.; Chen, Z. P.; Zhou, G. M.; Li, F.; Cheng, H. M. "Graphene Anchored with Co_3O_4 Nanoparticles as Anode of Lithium Ion Batteries with Enhanced Reversible Capacity and Cyclic Performance." *ACS Nano* **2010**, *4*(6), 3187-3194.
- Xi, L.; Tan, W. X. W.; Boothroyd, C.; Lam, Y. M. "Understanding and Controlling the Growth of Monodisperse CdS Nanowires in Solution." *Chemistry of Materials* **2008**, *20*(16), 5444-5452.
- Xia, Y.; Whitesides, G. M. "Soft Lithography." *Angewandte Chemie International Edition* **1998**, *37*(5), 550-575.
- Xiong, Q.; Wang, J.; Eklund, P. C. "Coherent Twinning Phenomena: Towards Twinning Superlattices in III-V Semiconducting Nanowires." *Nano Letters* **2006**, *6*(12), 2736-2742.
- Xu, Y. H.; Yin, G. P.; Zuo, P. J. "Geometric and Electronic Studies of $\text{Li}_{15}\text{Si}_4$ for Silicon Anode." *Electrochimica Acta* **2008**, *54*(2), 341-345.
- Xue, D.-J.; Xin, S.; Yan, Y.; Jiang, K.-C.; Yin, Y.-X.; Guo, Y.-G.; Wan, L.-J. "Improving the Electrode Performance of Ge through Ge@C Core-Shell Nanoparticles and Graphene Networks." *Journal of the American Chemical Society* **2012**, *134*(5), 2512-2515.
- Yang, J.; Takeda, Y.; Imanishi, N.; Capiglia, C.; Xie, J. Y.; Yamamoto, O. " SiO_x -Based Anodes for Secondary Lithium Batteries." *Solid State Ionics* **2002**, *152*, 125-129.
- Yang, S. B.; Feng, X. L.; Ivanovici, S.; Mullen, K. "Fabrication of Graphene-Encapsulated Oxide Nanoparticles: Towards High-Performance Anode Materials for Lithium Storage." *Angewandte Chemie-International Edition* **2010**, *49*(45), 8408-8411.
- Yang, W.-H.; Schatz, G. C.; Van Duyne, R. P. "Discrete Dipole Approximation for Calculating Extinction and Raman Intensities for Small Particles with Arbitrary Shapes." *The Journal of Chemical Physics* **1995**, *103*(3), 869-875.
- Yao, Y.; McDowell, M. T.; Ryu, I.; Wu, H.; Liu, N.; Hu, L.; Nix, W. D.; Cui, Y. "Interconnected Silicon Hollow Nanospheres for Lithium-Ion Battery Anodes with Long Cycle Life." *Nano Letters* **2011**, *11*(7), 2949-2954.
- Yarema, M.; Kovalenko, M. V.; Hesser, G. N.; Talapin, D. V.; Heiss, W. "Highly Monodisperse Bismuth Nanoparticles and Their Three-Dimensional Superlattices." *Journal of the American Chemical Society* **2010**, *132*(43), 15158-15159.
- Yogeswaran, U.; Chen, S.-M. "A Review on the Electrochemical Sensors and Biosensors Composed of Nanowires as Sensing Material." *Sensors* **2008**, *8*(1), 290-313.

- Yoo, E.; Kim, J.; Hosono, E.; Zhou, H.; Kudo, T.; Honma, I. "Large Reversible Li Storage of Graphene Nanosheet Families for use in Rechargeable Lithium Ion Batteries." *Nano Letters* **2008**, *8*(8), 2277-2282.
- Yoon, S.; Park, C.-M.; Sohn, H.-J. "Electrochemical Characterizations of Germanium and Carbon-Coated Germanium Composite Anode for Lithium-Ion Batteries." *Electrochemical and Solid-State Letters* **2008**, *11*(4), A42-A45.
- Yoshino, A., Nakajima, T., Sanechika, K. *U.S. Patent No. 4,668,595 May 9, 1986*.
- Yoshio, M.; Tsumura, T.; Dimov, N. "Electrochemical Behaviors of Silicon Based Anode Material." *Journal of Power Sources* **2005**, *146*(1-2), 10-14.
- Yu, C. J.; Li, X.; Ma, T.; Rong, J. P.; Zhang, R. J.; Shaffer, J.; An, Y. H.; Liu, Q.; Wei, B. Q.; Jiang, H. Q. "Silicon Thin Films as Anodes for High-Performance Lithium-Ion Batteries with Effective Stress Relaxation." *Advanced Energy Materials* **2012**, *2*(1), 68-73.
- Yu, H.; Li, J. B.; Loomis, R. A.; Wang, L. W.; Buhro, W. E. "Two- Versus Three-Dimensional Quantum Confinement in Indium Phosphide Wires and Dots." *Nature Materials* **2003**, *2*(8), 517-520.
- Yu, H.; Li, J.; Loomis, R. A.; Gibbons, P. C.; Wang; Buhro, W. E. "Cadmium Selenide Quantum Wires and the Transition from 3D to 2D Confinement." *Journal of the American Chemical Society* **2003**, *125*(52), 16168-16169.
- Yu, K.; Hrdina, A.; Zhang, X. G.; Ouyang, J. Y.; Leek, D. M.; Wu, X. H.; Gong, M. L.; Wilkinson, D.; Li, C. S. "Highly-Photoluminescent ZnSe Nanocrystals via a Non-Injection-Based Approach with Precursor Reactivity Elevated by a Secondary Phosphine." *Chemical Communications* **2011**, *47*(31), 8811-8813.
- Yu, K.; Ouyang, J.; Leek, D. M. "In-Situ Observation of Nucleation and Growth of PbSe Magic-Sized Nanoclusters and Regular Nanocrystals." *Small* **2011**, *7*(15), 2250-2262.
- Yuan, J.; Liu, X.; Akbulut, O.; Hu, J.; Suib, S. L.; Kong, J.; Stellacci, F. "Superwetting Nanowire Membranes for Selective Absorption." *Nature Nanotechnology* **2008**, *3*(6), 332-336.
- Yuan, L.; Liu, H. K.; Maarouf, A.; Konstantinov, K.; Liu, J.; Cortie, M. "Mesoporous Gold as Anode Material for Lithium-Ion Cells." *Journal of New Materials for Electrochemical Systems* **2007**, *10*(2), 95-99.
- Yujie, X.; Yi, X.; Zhengquan, L.; Xiaoxu, L.; Shanmin, G. "Aqueous-Solution Growth of GaP and InP Nanowires: A General Route to Phosphide, Oxide, Sulfide, and Tungstate Nanowires." *Chemistry* **2004**, *10*(3), 654-660.
- Yurkin, M. A.; Hoekstra, A. G. "The Discrete Dipole Approximation: An Overview and Recent Developments." *Journal of Quantitative Spectroscopy and Radiative Transfer* **2007**, *106*(1-3), 558-589.

- Yurkin, M. A.; Maltsev, V. P.; Hoekstra, A. G. "The Discrete Dipole Approximation for Simulation of Light Scattering by Particles Much Larger than the Wavelength." *Journal of Quantitative Spectroscopy & Radiative Transfer* **2007**, *106*(1-3), 546-557.
- Zaitseva, N.; Dai, Z. R.; Grant, C. D.; Harper, J.; Saw, C. "Germanium Nanocrystals Synthesized in High-Boiling-Point Organic Solvents." *Chemistry of Materials* **2007**, *19*(21), 5174-5178.
- Zaitseva, N.; Harper, J.; Gerion, D.; Saw, C. "Unseeded Growth of Germanium Nanowires by Vapor-Liquid-Solid Mechanism." *Applied Physics Letters* **2005**, *86*(5), 053105-3.
- Zhai, T.; Zhong, H.; Gu, Z.; Peng, A.; Fu, H.; Ma, Y.; Li, Y.; Yao, J. "Manipulation of the Morphology of ZnSe Sub-Micron Structures Using CdSe Nanocrystals as the Seeds." *The Journal of Physical Chemistry C* **2007**, *111*(7), 2980-2986.
- Zhang, D.; Qi, L.; Cheng, H.; Ma, J. "Preparation of ZnS Nanorods by a Liquid Crystal Template." *Journal of Colloid and Interface Science* **2002**, *246*(2), 413-416.
- Zhang, J.; Yang, Y.; Jiang, F.; Li, J.; Xu, B.; Wang, S.; Wang, X. "Fabrication of Semiconductor CdS Hierarchical Nanostructures." *Journal of Crystal Growth* **2006**, *293*(2), 236-241.
- Zhang, L.; Yu, J. C.; Mo, M.; Wu, L.; Kwong, K. W.; Li, Q. "A General In-Situ Hydrothermal Rolling-Up Formation of One-Dimensional, Single-Crystalline Lead Telluride Nanostructures." *Small* **2005**, *1*(3), 349-354.
- Zhang, S. S. "A Review on Electrolyte Additives for Lithium-Ion Batteries." *Journal of Power Sources* **2006**, *162*(2), 1379-1394.
- Zhang, X.; Shyy, W.; Sastry, A. M. "Numerical Simulation of Intercalation-Induced Stress in Li-Ion Battery Electrode Particles." *Journal of The Electrochemical Society* **2007**, *154*(10), A910-A916.
- Zhao, J.; Wang, L.; He, X.; Wan, C.; Jiang, C. "Kinetic Investigation of LiCoO₂ by Electrochemical Impedance Spectroscopy (EIS)" *International Journal of Electrochemical Science* **2010**, *5*, 478-488.
- Zhaoping, L.; Kai, S.; Wen-Bin, J.; Dan, X.; Yen-Fu, L.; Jiye, F. "Soluble InP and GaP Nanowires: Self-Seeded, Solution-Liquid-Solid Synthesis and Electrical Properties." *Chemistry* **2009**, *15*(18), 4546-4552.
- Zhen, L.; Andreas, K.; Anton, M.; Alf, M. "Formation and Function of Bismuth Nanocatalysts for the Solution-Liquid-Solid Synthesis of CdSe Nanowires." *Small* **2008**, *4*(10), 1698-1702.
- Zheng, G.; Yang, Y.; Cha, J. J.; Hong, S. S.; Cui, Y. "Hollow Carbon Nanofiber-Encapsulated Sulfur Cathodes for High Specific Capacity Rechargeable Lithium Batteries." *Nano Letters* **2011**, *11*(10), 4462-4467.

- Zheng, Y. X.; Xie, J.; Song, W. T.; Liu, S. Y.; Cao, G. S.; Zhao, X. B. "One-Pot Synthesis of Core-Shell Structured Sn/Carbon Nanotube by Chemical Vapor Deposition and its Li-Storage Properties." *Journal of Materials Research* **2011**, *26(21)*, 2719-2724.
- Zhong, Q. M.; Bonakdarpour, A.; Zhang, M. J.; Gao, Y.; Dahn, J. R. "Synthesis and Electrochemistry of $\text{LiNi}_x\text{Mn}_{2-x}\text{O}_4$." *Journal of The Electrochemical Society* **1997**, *144(1)*, 205-213.
- Zhou, G. M.; Wang, D. W.; Li, F.; Zhang, L. L.; Li, N.; Wu, Z. S.; Wen, L.; Lu, G. Q.; Cheng, H. M. "Graphene-Wrapped Fe_3O_4 Anode Material with Improved Reversible Capacity and Cyclic Stability for Lithium Ion Batteries." *Chemistry of Materials* **2010**, *22(18)*, 5306-5313.
- Zou, C.-D.; Gao, Y.-L.; Yang, B.; Zhai, Q.-J. "Size-Dependent Melting Properties of Sn Nanoparticles by Chemical Reduction Synthesis." *Transactions of Nonferrous Metals Society of China* **2010**, *20(2)*, 248-253.

Vita

Aaron Chockla was born in Johnson City, New York. In 1996, he relocated to Cary, North Carolina. Using North Carolina as home base for the next six years, Aaron spent his final two years of high school at Culver Military Academy in Culver, Indiana (2001–2003) and went on to attend the University of Delaware (2003–2007) where he graduated with honors and distinction with a Bachelor of Chemical Engineering and minors in mathematics and biochemical engineering. In the fall of 2007, Aaron enrolled at The University of Texas at Austin where he began his graduate studies in nanomaterial synthesis under supervision of Dr. Brian Korgel. He earned a Master of Science in Engineering in 2009 and completed his Ph.D. in the spring of 2012. Aaron began work as a research investigator at Bristol-Myers Squibb in the summer of 2012.

The author can be reached at aaron.chockla@gmail.com

This dissertation was typed by the author.